Murine murein: The role of *Staphylococcus aureus* cell wall structure during host-pathogen interaction

By:

Joshua A F Sutton BSc (Hons)

(University of Leicester)

A thesis submitted for the degree of Doctor of Philosophy

April 2020

Department of Molecular Biology and Biotechnology, University of Sheffield, Firth Court, Western Bank, Sheffield, S10 2TN

Abstract

The aim of this project was to use the murine sepsis model of *Staphylococcus aureus* infection as a source of *in vivo* derived bacteria for peptidoglycan analysis. A characteristic of this model is the production of kidney abscesses that provide a large quantity of bacteria for analysis. Protocols were developed for optimal peptidoglycan harvesting from infected host organs. Bacteria from kidney infections are smaller and with thicker cell walls than those grown *in vitro.* Muropeptide analysis of purified peptidoglycan from kidney derived cells revealed less crosslinking than *in vitro* exponential phase cells, suggesting an alteration in peptidoglycan metabolism.

To investigate the impact of peptidoglycan metabolism on pathogenesis, the roles of components with known activities were studied using a range of *in vivo* and cellular models. PBP4 is required for the observed high level of peptidoglycan crosslinking found *in vitro*. A *pbp4* mutation led to increased fitness in the murine sepsis model of infection. This was matched by greater survival in human macrophages, suggesting not only that peptidoglycan crosslinking is a key virulence determinant but also that it is manifested during the crucial initial phase of infection during phagocyte interaction. Glucosaminidases hydrolyse the glycan chains in the peptidoglycan and collectively these are important for cell growth and viability. Here, I found differing roles for the enzymes in host-pathogen interaction. The major glucosaminidase SagB is required for virulence in multiple animal models of disease. Analysis of strains bearing mutations in multiple glucosaminidase encoding genes revealed that cell clustering results in reduced pathogenesis in the zebrafish model of infection, but this can be reversed by cluster disruption. This demonstrates that host-pathogen interactions at the outset of disease are crucial for its progression.

My project has given novel insight into host-pathogen interaction and stresses the crucial need for *in vivo* studies to identify key breakpoints in infection for the development of novel control regimes.

Acknowledgements

List of abbreviations

%	Percentage
~	Approximately
°C	Degree Celsius
AFM	Atomic Force Microscopy
BSA	Bovine serum albumin
CDM	Chemically defined media
CFU	Colony forming unit
CWA	Cell wall N-acetyl-L-alanine amidases
CWG	Cell wall glycosylases
CWP	Cell wall peptidase
D-Ala	D-Alanine
D-Glu	D-Glutamic Acid
Da	Daltons
dH$_2$O	Distilled water
DC	Dendritic cell
DNA	Deoxyribonucleic Acid
EDTA	Ethylenediamine tetra-acetic acid
EM	Electron Microscopy
g	Grams
GlcNAc	N-acetyl glucosamine
Glucosaminidase	N-acetyl-β-D-glucosaminidase
Gly	Glycine
h	Hours
HF	Hydrofluoric acid
HMW	High molecular weight
hpf	Hours post fertilisation
hpi	Hours post infection
HPLC	High performance liquid chromatography
IFN	Interferon

IL	Interleukin
Kan	Kanamycin
kb	Kilobase pair
kV	Kilovolt
l	Litre
L-Ala	L-Alanine
LC-MS	Liquid chromatography-mass spectrometry
Lin	Lincomycin
LMW	Low molecular weight
LTA	Lipoteichoic acid
M	Molar
m-DAP	Meso-diaminopimelate
MDM	Monocyte derived macrophages
mg	Milligram
min	Minute
Mino	Minocycline
ml	Millilitre
mM	Millimolar
MRSA	Methicillin resistant *Staphylococcus aureus*
MS	Mass spectrometry
MSCRAMM	Microbial surface components recognizing adhesive matrix molecules
MSSA	Methicillin sensitive *Staphylococcus aureus*
Muramidase	*N*-acetyl-β-D-muramidase
Mur*N*Ac	*N*-acetylmuramic acid
n	Number
Neo	Neomycin
nm	Nanometres
NMR	Nuclear magnetic resonance
OD$_x$	Optical density at wavelength x nm
PAMP	Pathogen associated molecular pattern

vi

PBP	Penicillin binding protein
PBS	Phosphate buffered saline
PCR	Polymerase chain reaction
PG	Peptidoglycan
PRR	Pattern recognition receptor
RP-HPLC	Reverse phase high performance liquid chromatography
rpm	Revolutions per minute
SDS	Sodium dodecyl sulphate
SEM	Scanning electron microscopy
Spec	Spectinomycin
SSTI	Skin and soft tissue infections
TAE	Tris-acetate EDTA
Taq	Thermostable DNA polymerase from *Thermus aquaticus*
TEM	Transmission electron microscopy
TES	Tris-EDTA NaCl
Tet	Tetracycline
TLR	Toll-like receptor
Tris	Tris (hydroxylmethyl) aminomethane
v/v	Volume per volume
VISA	Vancomycin intermediate *Staphylococcus aureus*
VRSA	Vancomycin resistant *Staphylococcus aureus*
w/v	Weight per volume
WTA	Wall teichoic acid
x	Times
xg	Times gravity
x^R	Resistance to antibiotic x
μg	Microgram
μl	Microliter
μM	Micromolar
μm	Micrometre
ϕ	Phage

Table of contents

List of figures

List of tables

Chapter 1
Introduction

1.1 Overview of the bacterial cell wall

The bacterial cell wall is a dynamic structure providing a physical defence from the intracellular and extracellular environment, whilst allowing the assimilation of nutrients from, and release of molecules into, the extracellular milieu (Silhavy *et al.*, 2010). The cell wall also confers mechanical strength, resisting lysis from turgor pressure and defining the morphology of the cell (Egan *et al.*, 2017). The cell wall also plays a role in virulence (Boneca, 2005), and its synthesis is the target of one of the most commonly used group of antibiotics, the β-lactams (Bush and Macielag, 2010).

1.1.1   Structure of the cell envelope

The cell envelopes of bacteria mostly fall into one of two categories based on staining with crystal violet and the counterstain safranin (Coico, 2006). Gram-positive cells retain the primary stain (crystal violet) and Gram-negative the counterstain due to the differences in structure of the cell walls (Silhavy *et al.*, 2010). Despite morphological differences (and the presence or absence of some polysaccharides), the components between these cell envelopes are mostly conserved (Figure 1.1A).
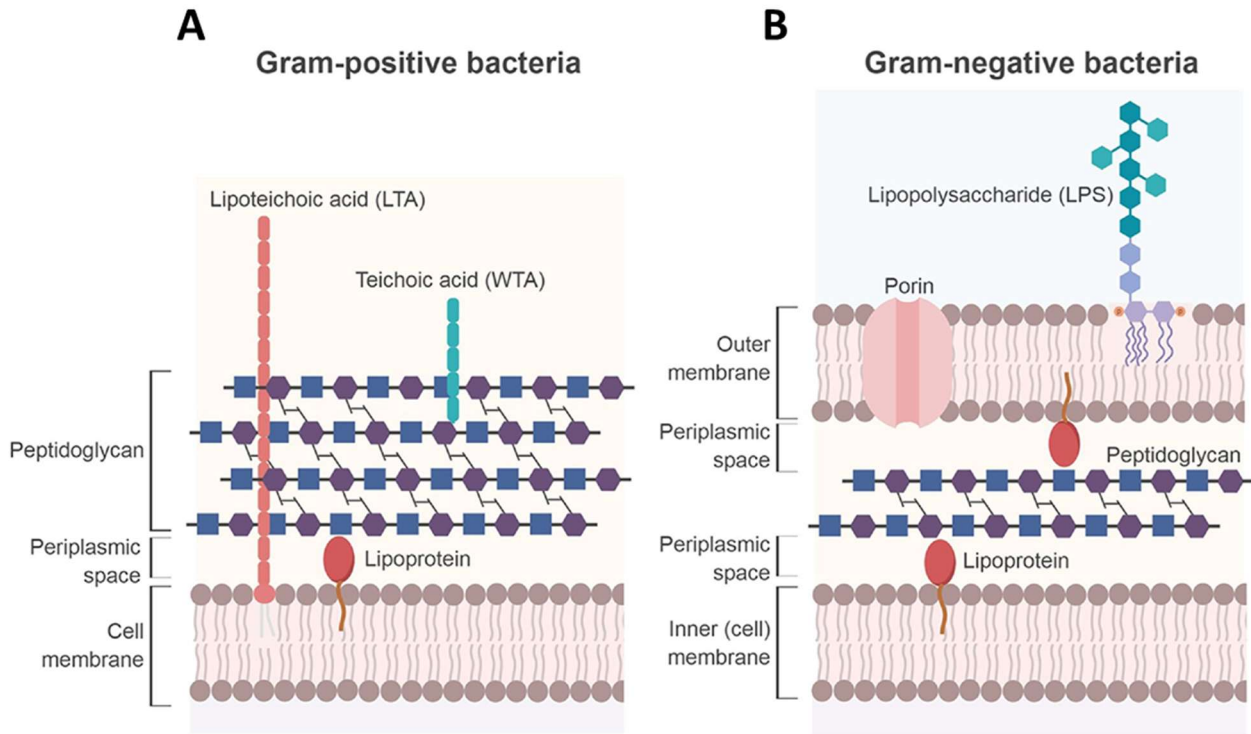
Figure 1.1 The structure of Gram-positive and Gram-negative cell envelopes

Generic cell envelope structures of **(A)** Gram-positive bacteria and **(B)** Gram-negative bacteria. Adapted from Porfírio *et al.* (2019).

1.1.1.1 Gram-positive cell envelope

The Gram-positive envelope consists of a minimum of two layers: the cell membrane and a comparatively thick layer of peptidoglycan (PG) (Malanovic and Lohner, 2016). The cell envelope may also possess an outer capsule (Rajagopal and Walker, 2017) (Figure 1.1B). The PG layer varies in thickness from 30 to 100 nm and is made up of multiple layers of crosslinked PG (Vollmer *et al.*, 2008a), accounting for around 30-70 % dry weight of the Gram-positive envelope (Schleifer and Kandler, 1972). The cross-bridges within the PG provides sites for proteins to be covalently attached to the cell wall. The sortase A enzyme of Gram-positive bacteria covalently bonds surface proteins to the PG crossbridges (Schneewind and Missiakas, 2012). Wall and lipoteichoic acids (WTA, LTA, Chapter 1.3.2) can also be associated with the Gram-positive cell envelope. WTA are covalently attached to the PG while LTA are associated with the cell membrane (Brown *et al.*, 2013). An exoplasmic space has been observed within in *Staphylococcus aureus* between the cell membrane and the PG layer (Matias and Beveridge, 2006), suggesting this may be an overlooked feature of the Gram-positive envelope.

1.1.1.2 Gram-negative cell envelope

The Gram-negative envelope consists of three layers: the inner membrane, the outer membrane and PG. The PG is located within the periplasm; defined as the region between the two membranes (Silhavy *et al.*, 2010). The inner membrane is a phospholipid bilayer, as in Gram-positive organisms. The outer membrane however only has phospholipids within the inner leaflet, with the outer leaflet being composed of lipopolysaccharides (LPS, Chapter 1.3.3, (Egan, 2018)). The outer membrane provides much of the protection from the environment, resulting in a thinner PG layer than that of Gram-positives, being only around 2nm thick in *Pseudomonas aeruginosa* and 6 nm thick in *Escherichia coli* (Vollmer and Seligman, 2010; Turner *et al.*, 2018). The PG polymer is generally only one glycan thick in *E. coli*, although some of the glycan chains have been observed to overlap one another (Turner *et al.*, 2018). PG is essential for the

resistance of turgor pressure, preventing the cell from lysing and maintaining cell shape. The outer membrane in Gram-negative cell envelopes has also been shown to provide much of the stiffness in *E. coli* cells, as well as defining their shape (Rojas *et al.*, 2018). The outer membrane acts as the attachment site for proteins, with nearly half of the outer membrane mass being attributed to proteins (Nikaido and Vaara, 1985). These proteins consist of OMP and lipoproteins (Figure 1.1) that are associated with the inner leaflet of the outer membrane (Ruiz *et al.*, 2006). In *E. coli,* the most abundant protein in the outer membrane is Braun's lipoprotein, which anchors the outer membrane to the PG (Cowles *et al.*, 2011).

1.1.1.3 Other cell envelope structures

Mycobacterium species such as *M. tuberculosis* are said to be acid fast bacteria; meaning that they cannot be decolourised by acids during standard staining techniques (Madison, 2001). This is due to their unique cell envelope. The PG of *M. tuberculosis* is multi-layered, like that of Gram-positive envelopes, but an outer layer of other material is present (Zuber *et al.*, 2008). PG is covalently bound to arabinogalactan, which are covalently bonded to mycolic acids. Mycolic acids are long chain fatty acids, that have been suggested to contribute to virulence and antibiotic resistance (Silhavy *et al.*, 2010).

1.2   Chemical Structures of the Cell Wall

1.2.1   Peptidoglycan

PG is the load bearing molecule in the cell wall of bacteria and exists as a single macromolecule around the cell, forming the sacculus (Turner *et al.*, 2014). PG is comprised of a glycan back bone, peptide side chains and crosslinks. The constituent component of PG is a muropeptide, consisting of an *N*-Acetylmuramic acid (Mur*N*Ac) and an *N*-Acetylglucosamine (Glc*N*Ac) residue, a peptide side chain and species-specific crosslink (Figure 1.2). The biosynthesis of PG is discussed in Chapter 1.4.1.

1.2.2 Glycans

The glycans of PG are long strands of alternating units of GlcNAc and MurNAc residues, linked by β 1-4 glycosidic bonds (de Pedro and Cava, 2015). Glycan strands are produced by the polymerisation of lipid II molecules (Chapter 1.4.1.2) by transglycosylation (Vollmer, 2008). While the chemical structure of these glycans are conserved throughout bacteria, the length of the strands differs amongst species. In the Gram-positive *Bacillus subtilis*, it has been shown that glycan strands are up to 5 μm in length, with an average glycan length of 96 disaccharide (GlcNAc-MurNAc) units (Hayhurst *et al.*, 2008). *S. aureus* has relatively short glycan chains compared to *B. subtilis*, with an average of 6 disaccharides per chain, with only 10-15% of glycans having a length of 26 disaccharides or longer (Boneca *et al.*, 2000). *E. coli,* a Gram-negative bacterium, has an average glycan length of 8.9 disaccharide units with strands of up to around 45 disaccharide units when measured by reverse phase high performance liquid chromatography (Vollmer and Bertsche, 2008). However, when measured using atomic force microscopy, glycan chains up to 200 nm in length were observed, much longer than the proposed maximum of 45 disaccharide units (Vollmer and Bertsche, 2008; Turner *et al.*, 2018). In *E. coli* it has been observed that glycan chains have a spacing of around 3 nm, with chains being an average of 1.4 nm wide (Turner *et al.*, 2018). Glycan chain length can be influenced by PG synthases. *E. coli* penicillin binding protein (PBP) 1A produces glycans of around 30 disaccharide units, whereas PBP1B will produce longer strands, up to 50 disaccharides in length (Wang *et al.*, 2008). PG hydrolases can also determine glycan length. In *S. aureus,* it has been shown that the *N*-acetylglucosaminidase SagB is responsible for cleaving glycans to their mature length (Wheeler *et al.*, 2015; Chan *et al.*, 2016b). Glycan chain length contributes to cell wall mechanics, as without SagB cells show morphological and growth defects, associated with altered glycan length and cell wall stiffness (Wheeler *et al.*, 2015).
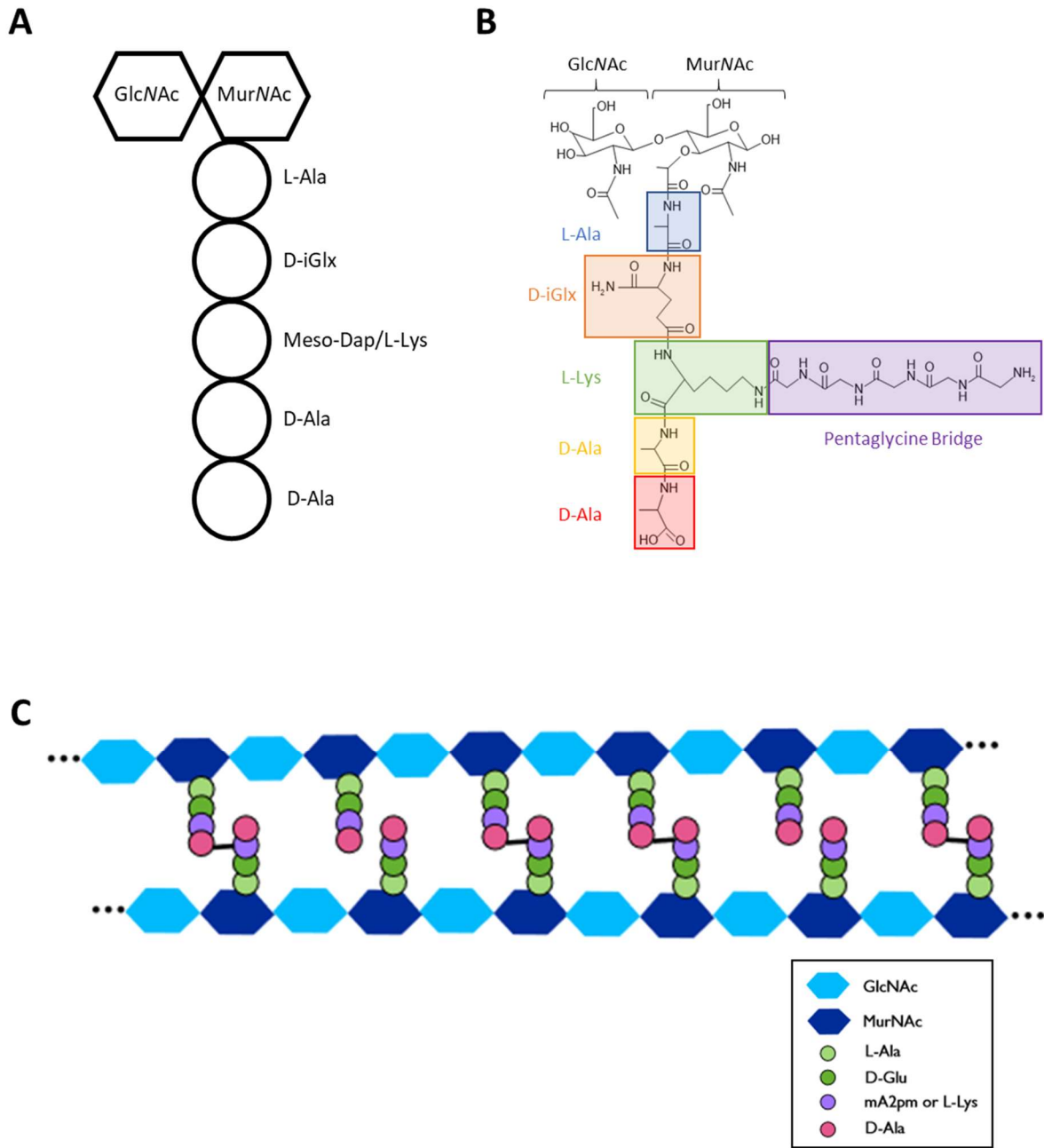
Figure 1.2 The generalised structure of peptidoglycan

(A) Schematic diagram of a generic muropeptide from model Gram-positive and Gram-negative bacteria. Egan *et al.* (2017), Vollmer *et al.* (2008). **(B)** Chemical structure of an *S. aureus* muropeptide. **(C)** The polymerisation of muropeptides forms the polymer of peptidoglycan. Adapted from Kouidmi *et al.* (2014).

1.2.3 Peptide side chains

Peptide side chains are attached to the Mur*N*Ac residue as a substitution for the lactyl group present on Mur*N*Ac (Vollmer *et al.*, 2008a). The peptide side chain contains both D– and L- isoforms of amino acids and is a variable section of the PG (Figure 1.2). The variation between species is often the result of the innate nature of the enzymes involved in PG biosynthesis, but can also be a result of modifications at a later stage of biosynthesis (Bouhss *et al.*, 2008).

The first amino acid typically bound to the Mur*N*Ac residue is L-Ala, which is common to Gram-positives and negatives (Figure 1.2A) (Silhavy *et al.*, 2010). In *Mycobacterium leprae*, the L-Ala residue is replaced by a Gly residue (Mahapatra *et al.*, 2000). The second amino acid is D-*iso*glutamate or D-*iso*glutamine, the latter being produced by amidation of D-*iso*glutamate (Vollmer *et al.*, 2008a). *S. aureus* and other Gram-positive bacteria often have a L-lysine in the third position, whereas Gram-negatives, Bacilli and Mycobacteria have *meso*-diaminopimelic acid (mDAP) (Vollmer *et al.*, 2008a). While these are the most common amino acids, other residues can be present. In *Corynebacterium pointsettiae*, L-homoserine is found in position 3 (Perkins, 1971), and bacteria of the genera *Spirochaeta, Borrelia*, and *Treponema* contain ornithine (Yanagihara *et al.*, 1984). The predominant amino acid in position four is D-Ala, but in rare occasions Gly can also be found in this position in *E. coli* (Glauner *et al.*, 1988). The terminal amino acid is also mostly D-Ala (Vollmer *et al.*, 2008a), but the substitution can confer differing properties to the cell wall, for example, in vancomycin resistant *Staphylococcus aureus* (VRSA) D-alanine can be replaced with D-lactate by the action of VanA acquired from enterococci (Severin *et al.*, 2004).

1.2.4 Crosslinking

Crosslinks in PG produce a three-dimensional mesh with strength and rigidity, compared to non-linked PG (Vollmer and Seligman, 2010). In *E. coli* between 40 and 60% of the muropeptides can be crosslinked (Vollmer and Bertsche, 2008), whereas in the PG of *S. aureus* up to 70 to 80 % of glycine bridges are crosslinked to other stem peptides (Snowden and Perkins, 1990). The levels of crosslinking within a species can change depending on their growth phase. *S. aureus* PG has been shown to have reduced crosslinking in stationary phase compared to exponential phase when grown *in vitro* in synthetic medium (Zhou and Cegelski, 2012), which was hypothesised to be due to glycine depletion. However, in *B. subtilis* it was determined that PG crosslinking was greatest in late stationary phase (Atrih *et al.*, 1999).

These crosslinks fall into two main classifications: a 3-4 or a 2-4 crosslink. The 3-4 crosslink involves the residue in the third position of one stem peptide linked to the residue in the fourth position on the other stem, either directly through their own amino and carboxyl groups, or through an interpeptide bridge (Lovering *et al.*, 2012). The 2-4 link occurs in coryneform bacteria and involves the D-glutamic acid of one chain (in position 2) and the D-alanine of another chain (position 4) being linked (Vollmer *et al.*, 2008a). The interpeptide bridges can vary from one to seven amino acids long, containing a variety of amino acids, or a single type (Figure 1.3).

Crosslinking of peptidoglycan has been shown to be important for virulence. In *Acinetobacter baumannii,* PBP-7/8, an endopeptidase responsible for cleavage of crosslinks (Chapter 1.4.3), has been shown to be required for virulence in both a rat soft-tissue infection model and rat pneumonia model of infection (Russo *et al.*, 2009). As well as this, it was shown that PBP-7/8 was vital for defining the correct shape of the bacterium, as well as survival in human serum *in vitro* (Russo *et al.*, 2009). It has been shown in *S. aureus* that crosslinking is important for both antibiotic resistance and

virulence. Strains of *S. aureus* with reduced PG crosslinking, either induced by antibiotics or due to knockout of PBP4 (Chapter 1.4.2.1), induced increased production of interleukin 1β by the host during infection leading to increased inflammasome activation and a worsened pathology. Strains of *S. aureus* with intermediate resistance to vancomycin (VISA) have been described. As well as having thickened cell walls, these strains have also been found with reduced PG crosslinking, meaning that there are more D-Ala-D-Ala targets to bind vancomycin with no effect on the cell's viability (Gardete and Tomasz, 2014).
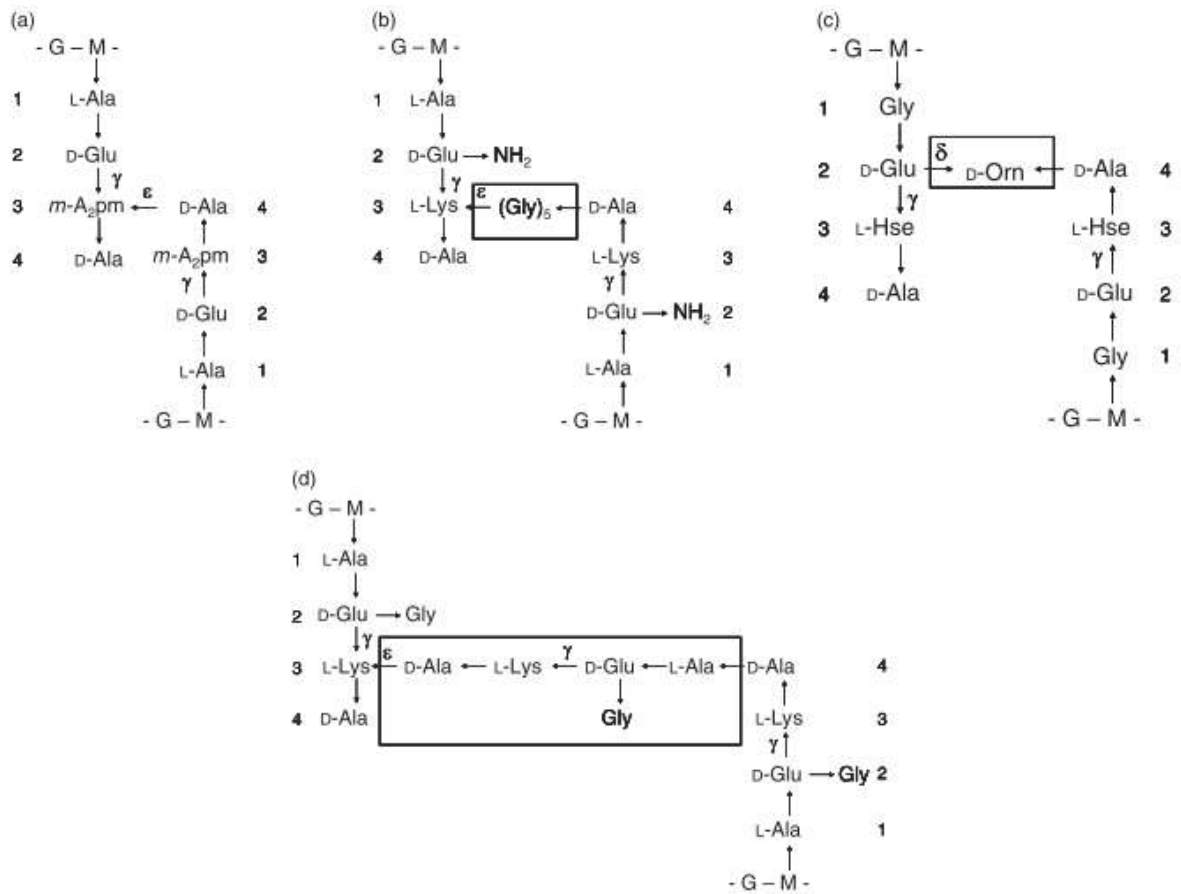
Figure 1.3 Crosslinks in different bacterial PG.

(A) *E. coli* shows a direct linkage from D-alanine in position 4 to meso-A$_2$pm in position 3 on another chain. **(B)** *S. aureus* has a 3-4 crosslink via a pentaglycine bridge. **(C)** *Corynebacterium poinsettiae* has a 2-4 crosslink using a D-ornithine bridge. **(D)** *Micrococcus luteus* has a 3-4 crosslink made from another *M. luteus* peptide stem. Taken from Vollmer *et al.* (2008b).

1.2.5   Peptidoglycan modifications

PG is commonly chemically modified after its synthesis. Deacetylation of the Glc*N*Ac residues in *Streptococcus pneumoniae* (Vollmer and Tomasz, 2002) and *Listeria monocytogenes* (Boneca *et al.*, 2007) are known to provide resistance against host lysozyme, enhancing bacterial evasion of the host innate immune system.

O-acetylation is a common modification of the carbon 6 atom of the Mur*N*Ac residue (Moynihan *et al.*, 2014) that is associated with pathogenicity (Bera *et al.*, 2006; Aubry *et al.*, 2011), and lysozyme resistance (Bera *et al.*, 2005). Depending on the species, strain and growth conditions, between 20–70 % of Mur*N*Ac residues may be O-acetylated by OatA (Moynihan *et al.*, 2014). O-acetylation of Glc*N*Ac is also observed in *Lactobacillus plantarum,* which has been shown to regulate autolysis by the *N*-acetylglucosaminidase Acm2 (Bernard *et al.*, 2011). The O-acetylation of Glc*N*Ac is carried out by OatB and has also been observed in *Lactobacillus sakei* and *Weissella paramesenteroides* (Bernard *et al.*, 2011).

Spore producing bacteria, such as species from the genus *Bacillus,* are known to produce spore specific muramic acid δ-lactam (Atrih *et al.*, 1996; Popham *et al.*, 1996a). For δ-lactam to form, there must be no peptide attached to the lactyl group and the Mur*N*Ac residue must be deacetylated, allowing the conversion by the enzymes CwlD and PdaA in *B. subtilis* (Vollmer, 2008)*.* It has been suggested that the muramic acid δ-lactam modification is required to act as a marker for germination-specific hydrolases required to cleave spore PG and allow out-growth (Popham *et al.*, 1996b).

In Gram-negative bacteria, glycans can be terminated by a 1,6-anhydroMur*N*Ac residue cap (Vollmer, 2008). This modification is also seen in low levels in *B. subtilis* (Atrih *et al.*, 1999)*.* Muropeptides containing such a modification are released from the sacculi during

PG turnover (Vollmer and Höltje, 2001), which can be used as signalling molecules in some bacterial species, resulting in the upregulation of β-lactamase (Höltje *et al.*, 1994; Jacobs *et al.*, 1994). The protein MltG, an endolytic transglycosylase, has been shown to terminate the synthesis of glycan strands of the appropriate length in *E. coli* through the formation of an anhydromuropeptide (Yunck *et al.*, 2016).

1.3   Teichoic Acids

The cell wall of Gram-positive bacteria is associated with other molecules important for virulence and cell adhesion. Teichoic acids are one such molecule and are glycopolymers that are either attached to the PG, called wall teichoic acid (WTA) or to the cell membrane, known as lipoteichoic acid (LTA, Figure 1.4) (Schade and Weidenmaier, 2016).

1.3.1   Wall teichoic acid

WTA consists of a disaccharide linkage (Glc*N*Ac-Man*N*Ac) unit and two glycerol phosphate molecules covalently bound to the C6 hydroxyl of up to every ninth Mur*N*Ac residue within PG (Brown *et al.*, 2013). Bound to the linkage unit are 40-60 molecules of a species (and strain) dependent repeat unit, which in *S. aureus* is commonly ribitol-phosphate (RboP), while in *B. subtilis* glycerol-phosphate (GroP) and RboP units can be found (Schade and Weidenmaier, 2016). Further WTA diversity occurs by chemical modification. The WTA can be decorated with cationic D-alanine (Neuhaus and Baddiley, 2003) which is important in modulating the bacteria's surface charge and promotes virulence and neutrophil survival in *S. aureus* (Collins *et al.*, 2002). WTA can also be modified with mono- or oligosaccharides such as glucose or Glc*N*Ac (Brown *et al.*, 2013).

12

WTA has multiple roles within the cell wall of Gram-positive bacteria. Rod shaped bacteria such as *B. subtilis* and *L. monocytogenes* lacking WTA become spherical, demonstrating a role for WTA in defining cellular morphology (Lazarevic and Karamata, 1995; Soldo *et al.*, 2002; Eugster and Loessner, 2012). It has been suggested that WTA allows the correct cellular localisation/assembly/activation of cell wall elongation and division enzymes, with PG and WTA synthesis enzymes in *B. subtilis* having known interactions (Formstone *et al.*, 2008; Kawai *et al.*, 2011; Brown *et al.*, 2013). WTA also acts as a temporal and spatial regulator of PG metabolism, controlling the level of PG crosslinking in *S. aureus* by regulating PBP4 localization (Atilano *et al.*, 2010). WTA plays a role in horizontal gene transfer, by acting as a receptor allowing bacteriophage infections which can transfer DNA between strains (Schade and Weidenmaier, 2016). For *S. aureus* bacteriophage φ11, GlcNAc modifications on RboP of WTA are essential for infection and potential gene transfer (Xia *et al.*, 2011).

WTA also plays a role in virulence and the formation of biofilms (Brown *et al.*, 2013). The negative charge of RboP and the positively charged ester-linked D-alanine cause the WTA to be zwitterionic, which is a crucial factor for the development of skin abscesses in mice models of *S. aureus* infection (Wanner *et al.*, 2017). The regulation of cell surface charge modulates the binding of molecules, such as host defences including human antibacterial fatty acids, reducing damage caused to the bacterial cell (Kohler *et al.*, 2009). WTA also act as an adhesin, allowing the colonisation of animal models, which has been observed with *S. aureus* and lactobacilli (Weidenmaier *et al.*, 2005; Walter *et al.*, 2007)*.

1.3.2   Lipoteichoic acids

Firmicutes, such as *S. aureus*, have a type 1 LTA consisting of unbranched 1-3 linked polyGroP linked to the cell membrane by a glycolipid anchor (Reichmann and Gründling, 2011; Xia *et al.*, 2011). The hydroxyl groups at C2 of the GroP units can be modified by D-

alanylation or by the addition of glycosyl groups (Percy and Gründling, 2014). In *S. aureus*, it has been shown that a depletion of the *ltaS* gene, required for LTA synthesis, results in aberrant positioning of division septa, with daughter cells producing septa parallel to the previous, rather than the usual perpendicular (Gründling and Schneewind, 2007). LTA have been shown to play a role in osmo-protection, allowing resistance to low osmolarity environments (Oku *et al.*, 2009). The LTAs of *S. aureus* are immunostimulatory, inducing the production of cytokines TNF-α, IL-1β, IL-6 and IL-10 in whole human blood (Hermann *et al.*, 2002) and together with PG can cause shock and multiple organ failure in a rat model of infection (Kimpe *et al.*, 1995). However, it has been suggested that the immunostimulatory effects of LTA is due to contamination by lipoprotein and LTA was not the cause of immune activation in previous experiments (Hashimoto *et al.*, 2006; Zähringer *et al.*, 2008). However, the use of synthetic LTA molecules, that could not be contaminated with lipoprotein, show the same immunostimulatory effect described, providing evidence for the immunostimulatory nature of LTA (Morath *et al.*, 2002; Deininger *et al.*, 2003). The purified LTA of an *lgt* mutant, which does not have lipoproteins, does not show Toll-like receptor 2 stimulation in a murine macrophage line (Hashimoto *et al.*, 2006), but did in whole human blood (Aulock *et al.*, 2007; Bunk *et al.*, 2010). It was suggested that the LTA must be opsonised by antibodies, which results in internalisation and subsequent detection by the immune system (Bunk *et al.*, 2010). Despite conflicting reports, the evidence described suggests that LTA is likely to be immunostimulatory.

1.3.3 Lipopolysaccharides

LPS are endotoxins specific to Gram-negative bacteria. LPS helps the maintenance of cell shape, stabilisation of the cell membrane by providing a net negative charge and protecting the cell from chemical attacks. LPS also elicits strong immunological responses in animal immune systems, playing a key role in pathogenicity (Raetz and Whitfield, 2002).
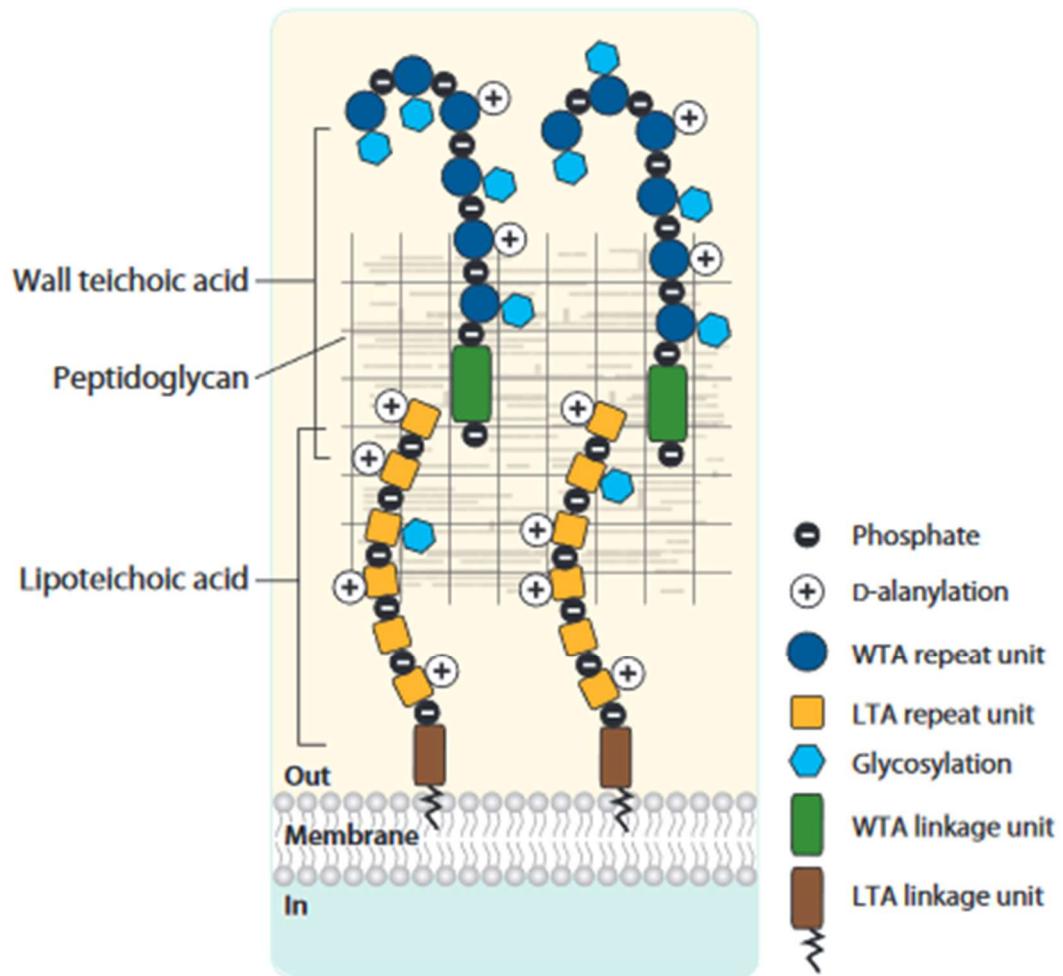
Figure 1.4 The structure of wall- and lipo- teichoic acids

WTA (blue) consist of 40-60 repeating units covalently linked to PG by a linkage unit. LTA (yellow) are also formed of multiple repeating units but are linked to the cell membrane via a linkage unit. Taken from Brown *et al.* (2013).

1.4   Peptidoglycan dynamics

PG is a dynamic molecule, requiring both hydrolysis and synthesis to permit the growth and division of the cell (Nanninga, 1991).

1.4.1   Peptidoglycan biosynthesis

Gram-positive and Gram-negative bacteria share a common PG synthesis pathway. PG synthesis begins in the cytoplasm where PG precursors are made, these membrane bound muropeptides are then flipped to the extracellular environment before finally being incorporated into existing PG (Figure 1.5) (Lovering *et al.*, 2012).

1.4.1.1 Cytoplasmic reactions

The enzymes required to produce PG are found across both Gram-negative and positive bacteria and are essential for viability (Bouhss *et al.*, 2008). Synthesis begins in the cytoplasm where MurA transfers a enolpyruvyl moiety to uridine diphosphate-Glc*N*Ac, which MurB then converts to uridine diphosphate-Mur*N*Ac (Typas *et al.*, 2012). Non-ribosomal peptide synthesis occurs via MurC, MurD, MurE and MurF, which add the species-specific amino acids to the uridine diphosphate-Mur*N*Ac to produce the peptide stem (Chapter 1.2.3). In *Chlamydia trachomatis*, MurC can incorporate L-Ala, L-Ser and Gly with the same efficacy in an *in vitro* context to the first position of the peptide stem (Hesse *et al.*, 2003). MurF incorporates D-Ala-D-Ala into the growing peptide stem (Kouidmi *et al.*, 2014). The D-Ala-D-Ala molecule is produced in two steps. First the racemase Alr converts L-Ala to D-Ala, which is then ligated to another D-Ala molecule to form D-Ala-D-Ala, which is then incorporated into the growing peptide stem (Typas *et al.*, 2012). The uridine diphosphate-Mur*N*Ac-pentapeptide is then linked to a undecaprenyl phosphate (bactoprenol) carrier molecule by the action of MraY, forming lipid I (Bouhss

16

et al., 2008). Lipid I molecules are then converted to lipid II by MurG, which adds a molecule of GlcNAc (Scheffers and Tol, 2015).

In *S. aureus,* the FemABX family of non-ribosomal peptidyltransferases are needed to insert the pentaglycine bridge required to produce PG crosslinks. These proteins utilise glycyl-tRNA as a glycine donor, adding glycine residues to lipid II (Schneider *et al.*, 2004). FemX incorporates the first glycine molecule into the bridge (Rohrer and Berger-Bächi, 2003), followed by FemA incorporating glycines 2 and 3 (Strandén *et al.*, 1997) and FemB adding the final two glycines in position 4 and 5 (Henze *et al.*, 1993). The Fem proteins act immediately after the synthesis of lipid II before it is transported to the outside of the cell (Bouhss *et al.*, 2008). Amidation of D-Glu in the peptide stem to D-Gln by GatD/MurT also occurs to the lipid II molecule (Figueiredo *et al.*, 2012; Münch *et al.*, 2012).

1.4.1.2 Translocation and incorporation of Lipid II

The lipid II molecule is then translocated across the cytoplasmic membrane by the action of flippases, such as MurJ and Amj, to the outer leaflet (Scheffers and Tol, 2015). Lipid II is then incorporated into existing glycan strands by the action of transglycosylases. This occurs by the formation of a glycosidic bond between the MurNAc of lipid II and the GlcNAc of the existing glycan chain (Ward and Perkins, 1973). Undecaprenyl-pyrophosphate is subsequently released from the PG, returned to the cytoplasm (Bouhss *et al.*, 2008) and recycled in the synthesis pathway to form new lipid I after being dephosphorylated (Dam *et al.*, 2009). Transpeptidase reactions then crosslink the newly incorporated strands (Typas *et al.*, 2012).
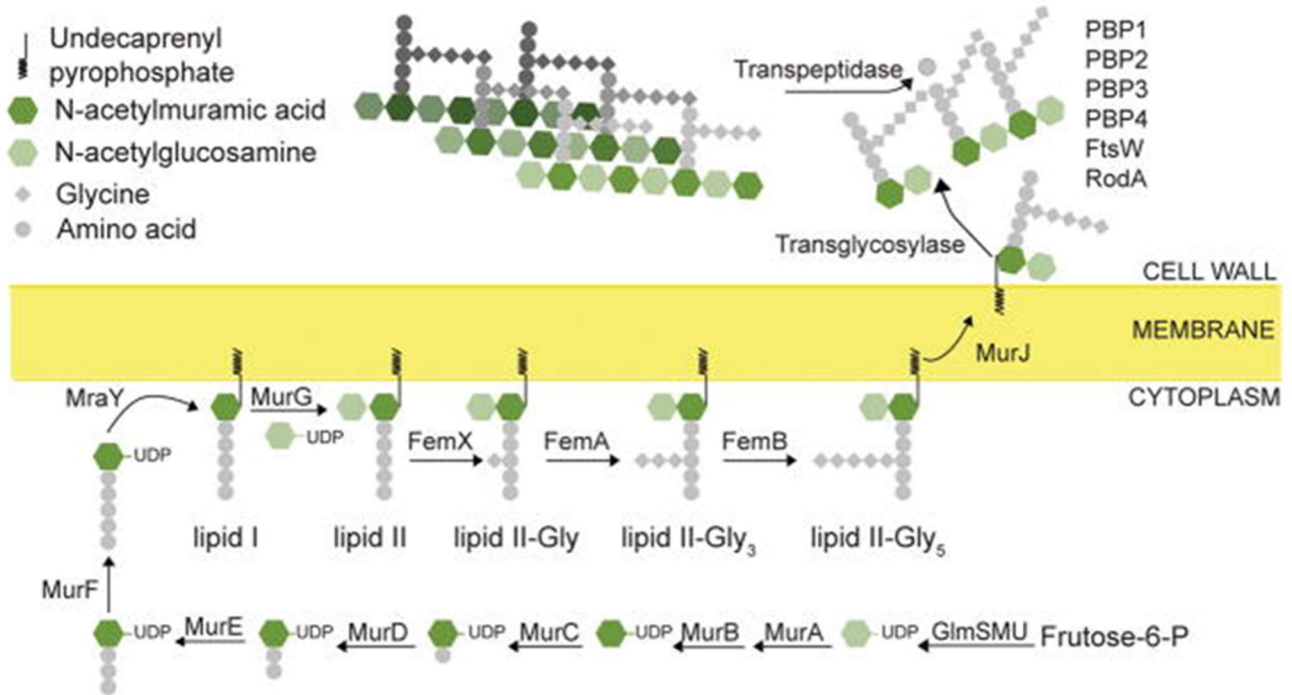
Figure 1.5 PG biosynthesis pathway in *S. aureus*

The PG precursor lipid II is synthesised within the cytoplasm. This is translocated across the membrane, where it is inserted into the existing PG by the action of transglycosylation reactions. Cross-links are added to the PG sacculus by transpeptidation. Taken from Monteiro *et al.* (2018).

1.4.2   Peptidoglycan synthases

1.4.2.1 Penicillin binding proteins

Penicillin binding proteins (PBPs) complete the final stages of PG synthesis, performing the transglycosylation and/or the transpeptidase reactions required to incorporate new muropeptides into the sacculi (Goffin and Ghuysen, 1998). Bacteria contain multiple PBPs which can be categorised into high (HMW) or low molecular mass (LMW) PBPs. High molecular mass PBPs consist of a cytoplasmic tail and a transmembrane anchor, with a catalytic domain on the outer surface allowing PG synthesis (Sauvage *et al.*, 2008). The C-terminal domain of HMW PBPs possesses transpeptidase activity facilitating the formation of crosslinking in the PG (Sauvage *et al.*, 2008). HMW PBPs can be further subdivided into class A or class B depending on the activity of the N-terminus of the PBP. Class A HMW PBPs have an N-terminal domain with transglycosylase activity, elongating glycan chains (Goffin and Ghuysen, 1998; Sauvage *et al.*, 2008). In class B HMW PBP, the N-terminal domain is thought to interact with other proteins involved in growth and division, helping to determine morphology (Zapun *et al.*, 2008b). LMW PBPs usually have either carboxypeptidase or endopeptidase activity, cleaving peptide side chains on PG to regulate crosslinking (Goffin and Ghuysen, 2002; Macheboeuf *et al.*, 2006).

The number of native PBPs varies between bacterial species and even between bacterial strains. *E. coli* has a total of 12 PBP, 5 HMW and 7 LMW (Sauvage *et al.*, 2008). Of the 5 HMW PBP, three are class A (PBP1A, PBP1B and PBP1C) and two are class B (PBP2 and PBP3). The majority of PG synthesis is performed by PBP1A and PBP1B (Egan *et al.*, 2018), and *E. coli* requires at least one of these to be viable (Yousif *et al.*, 1985; Denome *et al.*, 1999). PBP1B, which possesses transglycosylase and transpeptidase activity, is activated by the binding of the lipoprotein LpoB (Egan *et al.*, 2018). PBP2 and PBP3 are monofunctional transpeptidases, with PBP2 playing a role in cell elongation, and PBP3 a key unit of the divisome (Blaauwen *et al.*, 2008). *B. subtilis* contains 16 PBPs, with

specific PBPs involved in sporulation and vegetative PG synthesis (Scheffers, 2005; Sauvage *et al.*, 2008).

S. aureus is a prolate spheroid, which elongates slightly during growth to facilitate cell division (Monteiro *et al.*, 2015; Lund *et al.*, 2018). During *S. aureus* cell division, PG is synthesised at the septum for growth (Pinho *et al.*, 2013). *S. aureus* possesses 4 native PBPs, making it a good minimalist model of PG synthesis (Table 1.1). Two of these PBPs, PBP1 and PBP3, are HMW Class B (Sauvage *et al.*, 2008). PBP1 is essential for growth (Wada and Watanabe, 1998), and depletion studies have shown it is required for the formation of division septa in cells (Pereira *et al.*, 2007). PBP1 has transpeptidase activity, and a loss of this activity results in a reduction in PG crosslinking and failure of cells to divide, but this domain is not essential for cell viability (Pereira *et al.*, 2009). It has been hypothesised that PBP1 may play a role in regulating the activity of autolysis on cells (Dubrac *et al.*, 2007; Pereira *et al.*, 2009). PBP3 is known to be non-essential for viability, with a C-terminal transpeptidase domain assumed to be involved in PG crosslinking and an N-terminal domain of unknown function (Pinho *et al.*, 2000). Recent research has shown that PBP3 interacts with RodA, forming a cognate pair, important for the correct localisation of the proteins at the mid-cell and the insertion of PG at sites other than the septum (Reichmann *et al.*, 2019). *S. aureus* also possesses a HMW class A PBP, PBP2, which localises to the septum of the cell (Pinho and Errington, 2003). PBP2 is essential for transglycosylation and transpeptidation, with deletion mutants not being viable (Pinho *et al.*, 2001a). Methicillin resistant *S. aureus* (MRSA) strains possess the non-native PBP2A, encoded by the *mecA* gene (Zapun *et al.*, 2008a). PBP2A, a HMW class B PBP, is important to perform transpeptidation and crosslink PG in the presence of β-lactam antibiotics (Fishovitz *et al.*, 2014). In the presence of antibiotic, PBP transpeptidase domains are inhibited, preventing PG crosslinking. The transpeptidase domain of PBP2A is β-lactam insensitive and able to continue transpeptidation reactions in the presence of β-lactam antibiotics (Figure 1.6) (Pinho *et al.*, 2001c), but the resulting PG is poorly crosslinked (Müller *et al.*, 2015). PBP4 is the only LMW PBP present in *S. aureus*. PBP4 is known to produce highly crosslinked PG in *S. aureus* (Wyke *et al.*, 1981b). Mutations of the *pbp4* gene, found in the laboratory strain CRB (a *mecA*-

negative *S. aureus* COL variant), have been found to cause increased PG crosslinking and increased tolerance to β-lactam antibiotics (Hamilton *et al.*, 2017; Alexander *et al.*, 2018). A putative interaction has been suggested between PBP4 and PBP2, as a loss of PBP4 resulted in the reduced transcription of PBP2 in both methicillin sensitive *S. aureus* (MSSA) and MRSA strains (Memmi *et al.*, 2008). The expression of PBP2A was found not to be changed with the loss of PBP4 (Memmi *et al.*, 2008). This has resulted in the hypothesis of the cooperative functioning of PBP2, PBP2A and PBP4 within *S. aureus* (Pinho *et al.*, 2001b; Łeski and Tomasz, 2005; Memmi *et al.*, 2008). Other studies have suggested that WTA is required for the co-operative action of PBP2 and PBP4 to produce β-lactam resistance in MRSA strains (Farha *et al.*, 2013).

PBPs are the target of the β-lactam class of antibiotics. β-lactams function by mimicking the terminal D-Ala-D-Ala motif in the stem peptide of PG, and irreversibly bind to and inhibit PBP's function (Rajagopal and Walker, 2017). The serine in the active site of PBPs initiates attack on the carbonyl group of the β-lactam ring, forming a covalent acyl-enzyme complex, which is hydrolysed extremely slowly, preventing the PBPs performing any further reactions (Zapun *et al.*, 2008a).

The PBPs can determine the length of the glycan chains (Chapter 1.2.2). Both PBP2 of *S. aureus* and PBP2A of *Enterococcus faecalis* produce glycan strands of around 15 disaccharide units in length. *E. coli* PBP1A produced glycans of around 30 disaccharide units, and PBP1B 50 units (Wang *et al.*, 2008). These differences show how the intrinsic differences in PBPs both within and between species can cause diversity in and determine PG structure.

PBP	Classification	Description	Reference
PBP1 (*pbp1*)	HMW Class B	Essential for cell growth and division	(Pereira *et al.*, 2009)
PBP2 (*pbp2*)	HMW Class A	Essential for cell division	(Pinho *et al.*, 2001b)
PBP3 (*pbp3*)	HMW Class B	Interacts with RodA for off septal PG synthesis	(Reichmann *et al.*, 2019)
PBP4 (*pbp4*)	LMW	Required for high levels of PG crosslinking	(Wyke *et al.*, 1981)
PBP2A (*mecA*)	HMW Class B	Non-native PBP required for PG synthesis and β-lactam resistance	(Pinho *et al.*, 2001C)

Table 1.1 The PBPs encoded by *S. aureus*

Adapted from Panchal (2018).
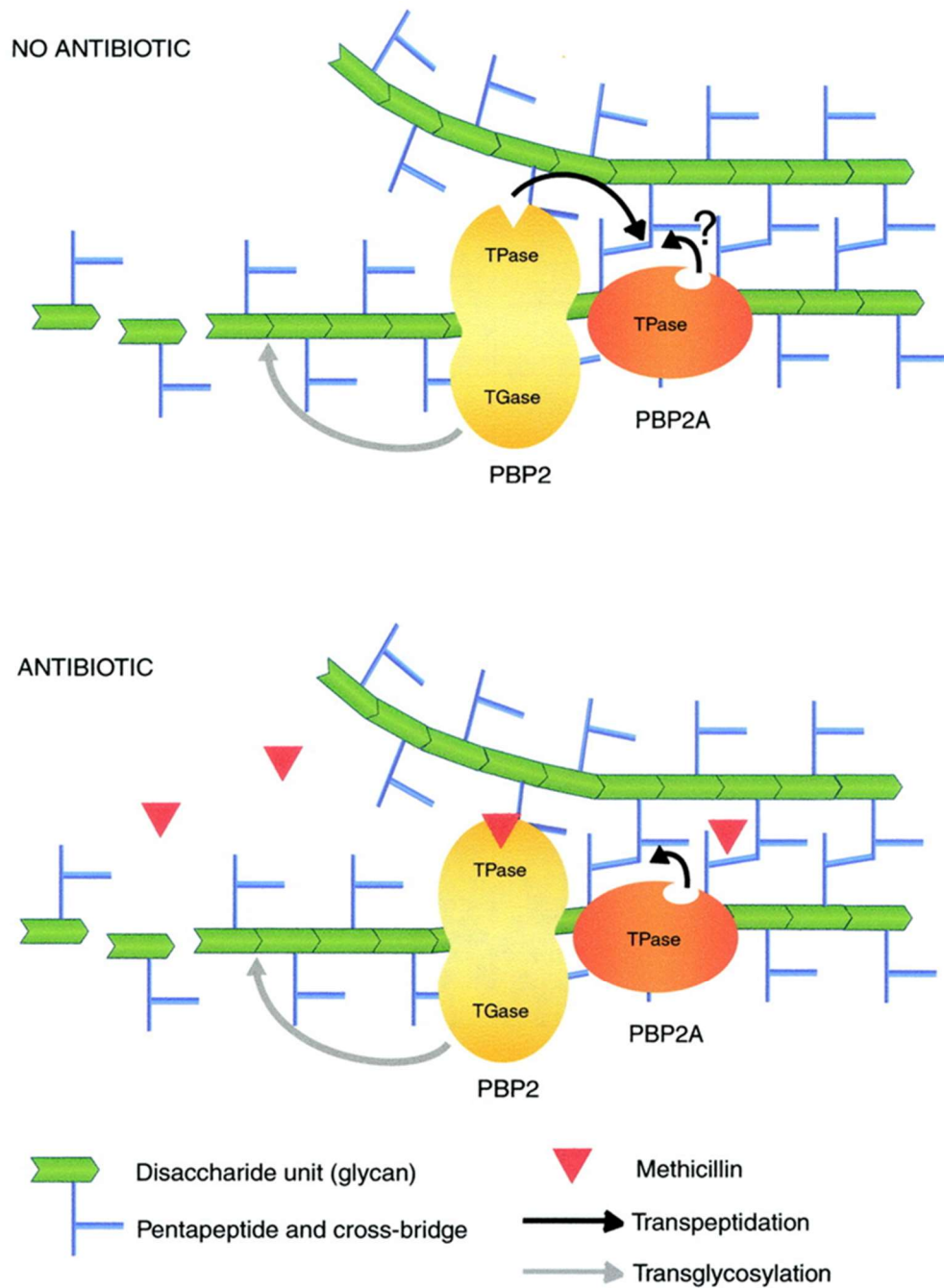
Figure 1.6 The cooperative functioning of PBP2 and PBP2A

With no antibiotic, it is hypothesised that both the transpeptidase and transglycosylase domains of PBP2 contribute to PG synthesis alongside PBP2A. In the presence of antibiotic, the transpeptidase domain of PBP2 is inactivated, while the transglycosylase domain remains functional. The transpeptidase activity of PBP2A compensated for the loss of PBP2 transpeptidase activity. Taken from Pinho *et al*. (2001b).

1.4.2.2 Other *S. aureus* peptidoglycan synthases

As well as four PBP, *S. aureus* possesses two monofunctional transglycosylases: MGT and SgtA (Reed *et al.*, 2015). MGT is a membrane-associated protein shown to have transglycosylase activity (Wang *et al.*, 2001), which has also been found in other species, such as *E. coli,* and all show a high degree of similarity to the glycosyltransferase domain of HMW PBPs (Berardino *et al.*, 1996). Both enzymes are not essential for cell wall synthesis, but *mgt* deletion is synthetically lethal in the absence of PBP2 transglycosylase activity (Reed *et al.*, 2011). Using a bacterial two-hybrid assay, it was found that MGT interacted with itself, SgtA, PBP1, PBP2 and PBP2A (Reed *et al.*, 2011). SgtA was found to interact with itself, MGT, PBP1 and PBP2, suggesting that both SgtA and MGT may function as a multimer within the cell (Reed *et al.*, 2011). It can therefore be hypothesised that *S. aureus* PG synthases may form and function within a complex to facilitate synthesis, as is seen in other bacterial species (Pazos *et al.*, 2017).

FmtA of *S. aureus* has been shown to have weak D-Ala-D-Ala-carboxypeptidase activity *in vitro* and was able to incorporate glycine into cell walls *in vitro,* but with a low activity (Qamar and Golemi-Kotra, 2012), suggesting FmtA may have transpeptidase activity. An inactivation of *fmtA* has shown to result in reduced PG crosslinking in *S. aureus,* providing more evidence for transpeptidase activity (Komatsuzawa *et al.*, 1999). However, more recent research suggests that FmtA acts as a D-amino esterase *in vivo,* acting on teichoic acids removing D-Ala residues, modulating teichoic acid charge and potentially regulating *S. aureus* division, autolysis and host colonisation (Rahman *et al.*, 2016). *S. aureus* FmtB also shares homology with known transpeptidase domains and has been shown to play a role in methicillin resistance. It is thought that FmtB plays a role in cell wall synthesis (Komatsuzawa *et al.*, 2000; Reed *et al.*, 2015).

FtsW, a highly conserved protein amongst bacteria, is required for septum formation and the correct functioning of the divisome as well as the recruitment of FtsI in *E. coli* (Mercer and Weiss, 2002; Mohammadi *et al.*, 2011). *S. aureus* FtsW was recently found

24

to have a role in PG synthesis as it can polymerise lipid II molecules into PG when in complex with PBP1, (Taguchi *et al.*, 2019), highlighting that protein complexes are formed during PG synthesis. FtsW interacts with PBP1 in *S. aureus* which is required for cell viability and the synthesis of PG at the division site (Reichmann *et al.*, 2019). *S. aureus* also possesses RodA, which has been found to interact with PBP3, which is required for the lateral synthesis of PG (i.e. at a site other than the septum) (Reichmann *et al.*, 2019).

1.4.3   Peptidoglycan hydrolases

By utilising *in silico* screens, 21 putative PG hydrolases have been found in *S. aureus* COL (Table 1.2) (Wheeler, 2012). PG hydrolases can be categorised into one of three types depending on the bond in the murein sacculus that they cleave (Figure 1.7). *N*-acetylmuramyl-L-alanine amidases (cell wall amidases, CWA) cleave the amide bond between the L-Ala at the N-terminus of the stem peptide and the *N*-acetylmuramic acid residue of the glycan (Vollmer *et al.*, 2008b; Vermassen *et al.*, 2019). An example is Sle1 of *S. aureus*, a CWA that cleaves the *N*-acetylmuramyl-L-Ala bond in PG, required for cell separation during replication (Kajimura *et al.*, 2005). A mutant lacking Sle1 was shown to be attenuated using a mouse model of infection (Kajimura *et al.*, 2005), highlighting the importance of hydrolases in pathogenesis. Another *S. aureus* CWA is LytH, a membrane bound amidase that was found to remove the stem peptide from uncrosslinked glycan strands (Do *et al.*, 2020b). The authors of this study propose a model whereby LytH regulates the density of PG assembly sites, regulating PG synthesis, promoting PG synthesis to relocate to the mid-cell during division (Do *et al.*, 2020b). The removal of the stem peptides was also found to slow PG synthesis, regulating the expansion of the cell (Do *et al.*, 2020b). LytH is activated when in complex with ActH, which is also a membrane bound protein, but how ActH activates LytH is currently unknown (Do *et al.*, 2020a).

Similarly, cell wall peptidases (CWP) cleave the amide bonds between amino acids and can be further classified into endopeptidases and carboxypeptidases, depending on substrate specificity (Vollmer *et al.*, 2008b). Lysostaphin is an endopeptidase produced by *Staphylococcus simulans* biovar *staphylolyticus* (Schindler and Schuhardt, 1964)*,* which shows activity against staphylococci, including *S. aureus* (Schindler and Schuhardt, 1965)*.* Lysostaphin hydrolyses the pentaglycine cross-bridges present in staphylococcal PG, resulting in cell lysis (Gonzalez-Delgado *et al.*, 2020). The lysostaphin SH3b domain has two binding sites, recognising both the cross-bridge and a peptide side chain, both with weak affinity. This allows lysostaphin to move rapidly around the PG, as one binding site is bound to the PG enabling exploring of the PG and the hydrolysis of glycine bonds (Gonzalez-Delgado *et al.*, 2020). LytM is a *S. aureus* (glycyl-glycine) endopeptidase (Figure 1.7), that cleaves PG crosslinks (Lioliou *et al.*, 2016)*.*

Cell wall glycosidases (CWG) catalyse hydrolysis of the glycosidic linkages in the glycan backbone of PG. CWG can also be further categorised based on substrate specificity. *N*-acetyl-β-D-muramidases (muramidases) cleave specifically after the *N*-acetylmuramic acid residue in the glycan backbone, whereas *N*-acetyl-β-D-acetylglucosaminidases (glucosaminidases) cleave after the *N*-acetylglucosamine moiety (Vermassen *et al.*, 2019).

Protein	Activity	Locus (*Sa*COL)	References
Atl	Amidase and glucosaminidase	1062	(Foster, 1995; Oshida *et al.*, 1995)
SagA	Putative glucosaminidase	2298	(Wheeler *et al.,* 2015; Chan *et al.*, 2016)
SagB	Putative glucosaminidase	1825	(Wheeler *et al.,* 2015; Chan *et al.*, 2016)
Sle1 (ScaA)	Amidase	0507	(Kajimura *et al.*, 2005)
ScaB	Unknown	0723	(Pourmand *et al.*, 2006)
ScaC	Unknown	2581	(Pourmand *et al.*, 2006)
ScaD	Unknown	2291	(Pourmand *et al.*, 2006)
ScaE	Unknown	0820	(Pourmand *et al.*, 2006)
ScaF	Unknown	0270	(Pourmand *et al.*, 2006)
ScaG	Unknown	2557	(Pourmand *et al.*, 2006)
ScaH	Putative glucosaminidase	2666	(Wheeler *et al.,* 2015; Chan *et al.*, 2016)
ScaI	Unknown	1576	(Pourmand *et al.*, 2006)
ScaJ	Unknown	2295	(Pourmand *et al.*, 2006)
IsaA	Putative lytic transglycosylase	2584	(Stapleton *et al.*, 2007)
LytH	Amidase	1739	(Do *et al.*, 2020a)
LytM	Endopeptidase	0263	(Lioliou *et al.,* 2016)
LytN	Amidase and Endopeptidase	1264	(Frankel *et al.*, 2011)
SceD	Putative lytic transglycosylase	2088	(Stapleton *et al.*, 2007)
SA0191	Putative endopeptidase	0191	(Wheeler, 2012)
SA1687	Putative amidase	1687	(Wheeler, 2012)
SA2195	Putative endopeptidase	2195	(Wheeler, 2012)

Table 1.2 Putative peptidoglycan hydrolases of *S. aureus* COL identified by an *in silico* screen

Adapted from Wheeler (2012).
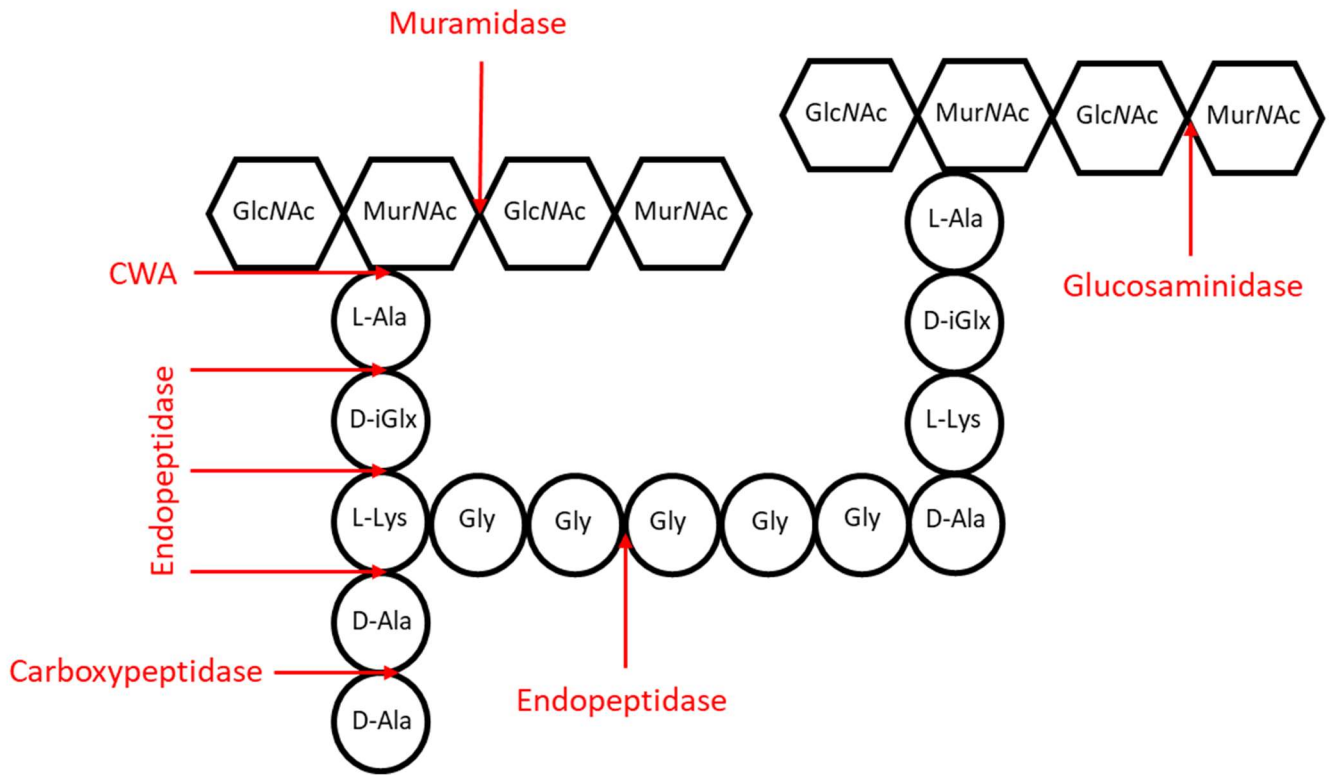
Figure 1.7 The targets of PG hydrolases

The action of hydrolases (red) on the glycan backbone and peptide sidechains of *S. aureus* PG. (Vollmer *et al.*, 2008b). (CWA – Cell wall amidase; D-iGlx – D-iso-glutamine or D-iso-glutamic acid; Glc*N*Ac – *N*-acetylglucosamine; Mur*N*Ac – *N*-acetylmuramic acid).

1.4.3.1 Muramidases

Muramidases cleave the β1,4-glycosidic bond after a Mur*N*Ac residue in the glycan backbone. There are two ways muramidases can achieve this. Firstly, lysozyme like enzymes cleave glycans resulting in a terminal reducing Mur*N*Ac residue. Alternatively, lytic transglycosylases produce a 1,6-anhydroMur*N*Ac residue (Chapter 1.2.5) by an intramolecular transglycosylase reaction (Vollmer *et al.*, 2008b). Two putative lytic transglycosylases have been identified in *S. aureus*: IssA and SceD (Stapleton *et al.*, 2007). Inactivation of *sceD* resulted in a clustering phenotype, with cells failing to divide, but this is not seen in an *issA* mutant (Stapleton *et al.*, 2007). Mutants of *issA* and *sceD* were both shown to be attenuated in a murine septic arthritis model of infection, with *sceD* also being required for nasal colonisation (Stapleton *et al.*, 2007).

Lysozyme is a conserved anti-microbial protein forming part of the innate immune system by hydrolysing PG (Callewaert and Michiels, 2010). Lysozyme is found in the blood, liver, secretions (including at mucosal surfaces) and professional phagocytes of mammals (Callewaert and Michiels, 2010; Lelouard *et al.*, 2010). While lysozyme is a muramidase, cleaving the glycan backbone of PG and causing lysis, human lysozyme is also cationic, allowing it to insert into the negatively charged membrane of bacteria, forming pores and killing bacteria (Ragland and Criss, 2017).

The genome of the *S. aureus* strain Newman has not been found to encode for a muramidase (Chan *et al.*, 2016b).

1.4.3.2 Glucosaminidases

Four putative glucosaminidases have been identified in *S. aureus.* Atl was the first glucosaminidase characterised in *S. aureus* in 1995 and was shown to be bifunctional, containing both an *N*-acetylmuramoyl-L-alanine amidase domain and an endo-β-*N*-acetylglucosaminidase domain (Foster, 1995; Oshida *et al.*, 1995). Atl is the major autolysin of *S. aureus* and is involved in the separation of daughter cells, shown by the

formation of large clusters in *atl* deletion mutants (Oshida *et al.*, 1995). As well as playing a major role in cell division, Atl has been shown to play a role in adherence and biofilm formation (Götz *et al.*, 2014). An *atl* mutant is deficient in the ability to adhere to different surfaces, including polystyrene and glass, resulting in a defect in producing biofilms that may play a role in virulence (Biswas *et al.*, 2006). It has also been suggested that the ability of the glucosaminidase domain of Atl to bind DNA plays a role in the formation of biofilms (Grilo *et al.*, 2014). As well as having a role in adhering to surfaces, Atl can also bind to host matrix proteins such as fibronectin and heparin, suggesting a further role in pathogenesis of the major autolysin (Porayath *et al.*, 2018).

SagB is a glucosaminidase that has been shown to be important for cellular growth. For cells to be able to grow, the newly synthesised PG of the cell wall must be hydrolysed enough to allow physical expansion. *S. aureus* has characteristically short glycan chains of between 3 and 10 disaccharide units (Boneca *et al.*, 2000). SagB cleaves the glycan backbone from long chains to short chains, which has the effect of reducing the surface stiffness (Wheeler *et al.*, 2015). The glycan processing allows the expansion of the cell as loss of such activity results in a growth defect in liquid medium (Wheeler *et al.*, 2015). The correct physiological length of the glycan strands, and by extension the stiffness of the cell wall, is also important for the correct trafficking of proteins through the cell wall and into the extracellular environment (Chan *et al.*, 2016b). A *sagB* mutant has aberrant protein secretion (Chan *et al.*, 2016b).

In contrast, the glucosaminidases SagA and ScaH have been poorly characterised. Mutants with inactive *sagA* or *scaH* genes show similar cell architecture, growth and cell division to wild type *S. aureus* (Wheeler *et al.*, 2015; Chan *et al.*, 2016b). Further analysis of these mutants is needed to understand more about the role of glucosaminidases in *S. aureus.* A degree of redundancy is seen, with mutants missing up to three of the four glucosaminidases being viable (Wheeler *et al.*, 2015). Mutants that all four of the mutants inactive, with *sagB* under the control of an isopropyl β-D-1-thiogalactopyranoside (IPTG) inducible promoter, were only viable in the presence of

IPTG (Wheeler *et al.*, 2015). For *S. aureus* to be viable, at least one of the four glucosaminidases must be active, presumably to produce the correct PG architecture required for growth and division.

1.4.4   WalK/WalR

WalK and WalR (WalKR) form a two-component system in some Gram-positive such as *B. subtilis* (where it was first identified)*, Streptococcus pneumoniae* and *S. aureus* (Dubrac *et al.*, 2008). In *S. aureus* this system is essential, and therefore a potential target for new novel therapeutics (Bem *et al.*, 2015). In this system, WalK is a membrane bound histidine kinase and the response regulator is WalR (Dubrac *et al.*, 2008). Encoded in the *walKR* operon are *yycH* and *yycI,* which negatively regulate WalKR in *B. subtilis* (Szurmant *et al.*, 2007)*,* but research has found that YycHI activates WalKR in *S. aureus*, playing a role in vancomycin resistance (Cameron *et al.*, 2016). In *S. aureus,* once WalK detects the appropriate signal, it phosphorylates the response regulator WalR, which then binds to the regulon DNA promoter sequences and upregulates the expression of autolysins such as *atl* (Chapter 1.4.3.2), *sle1* (Chapter 1.4.3) and *lytM* (Dubrac *et al.*, 2007). WalKR is only active in the exponential phase of growth, becoming inactive during stationary phase (Dubrac *et al.*, 2008). WalKR has also been found to be negatively regulated by Zn^{2+} (Monk *et al.*, 2019). As well as regulating the expression of genes important for cell wall turnover (Dubrac *et al.*, 2007), WalKR is associated with the activation of virulence genes vital for attachment to host, cytolysis and innate immune evasion through the activation of the SaeSR two component system (Delauné *et al.*, 2012), summarised in Figure 1.8.
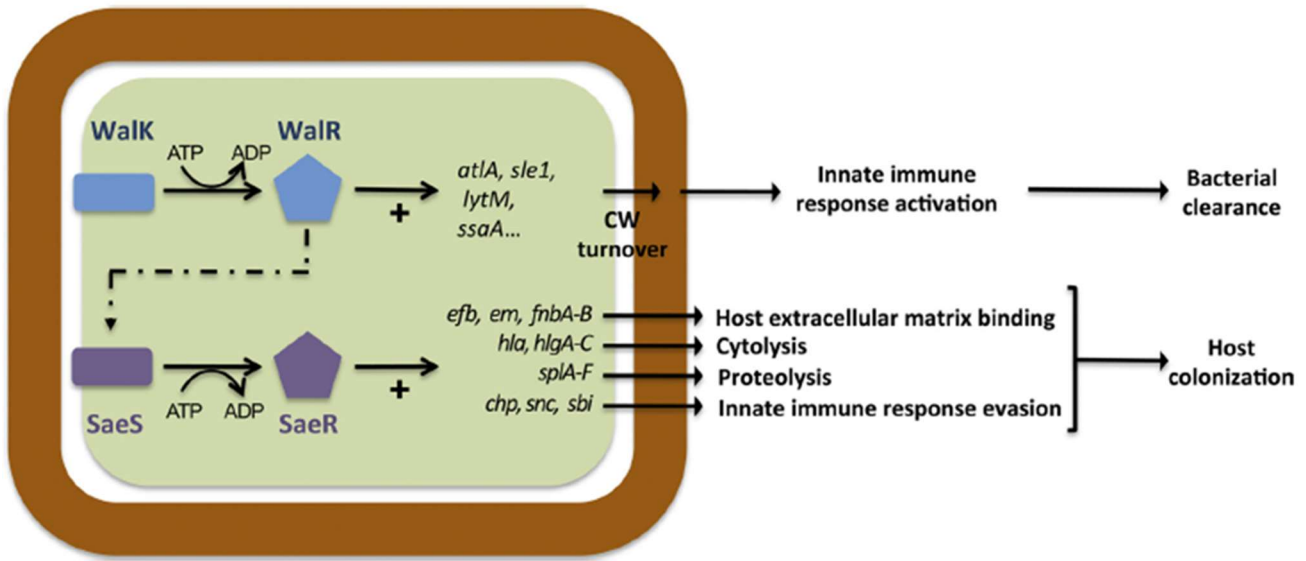
Figure 1.8 The role of WalKR in *S. aureus* cell wall metabolism and virulence

Phosphorylation of WalR by WalK leads to the upregulation of cell wall metabolism genes such as *atl, sle1* and *lytM.* The release of cell wall turnover products may stimulate the innate immune system and lead to clearance from the host. Activated WalR leads to the phosphorylation and activation of SaeR by stimulating the SaeS kinase, resulting in the upregulation of genes required for virulence. WalKR may therefore facilitate the switch to a pathogenic lifestyle. Taken from Delauné *et al.* (2012).

32

1.4.5 Staphylococcal cell division

The *S. aureus* divisome (Figure 1.9), the group of proteins responsible for cell division, contains both PBPs and proteins to coordinate the division process (Lund *et al.*, 2018). FtsZ is an essential protein in most bacteria that, in *E. coli* and *B. subtilis,* has been found to form filaments that act as a scaffold to assemble the divisome components (Bisson-Filho *et al.*, 2017; Yang *et al.*, 2017). The FtsZ assembles into a structure known as the z-ring, which is facilitated by proteins including EzrA (Adams and Errington, 2009), and GpsB (Eswara *et al.*, 2018). GpsB has been shown to interact with FtsZ during initial Z-ring formation, stabilising the structure (Eswara *et al.*, 2018). EzrA is a membrane protein that is crucial for *S. aureus* cell division, acting as a scaffold between FtsZ division proteins and other components of the divisome (Steele *et al.*, 2011). FtsZ, in Z-rings, has been shown to be able to create a constrictive force, and this is hypothesised to play a role in cell separation during division (Erickson *et al.*, 2010). This is finely regulated to prevent the occlusion of the nucleoid by the septum. This is partly regulated by DivIVA , which binds to FtsZ, regulating constriction of the Z-ring, allowing separation of the chromosomes (Bottomley *et al.*, 2017). It has been suggested that the Z-ring is required for the recruitment of at least 12 interacting proteins required to form the divisome (Bottomley *et al.*, 2017).
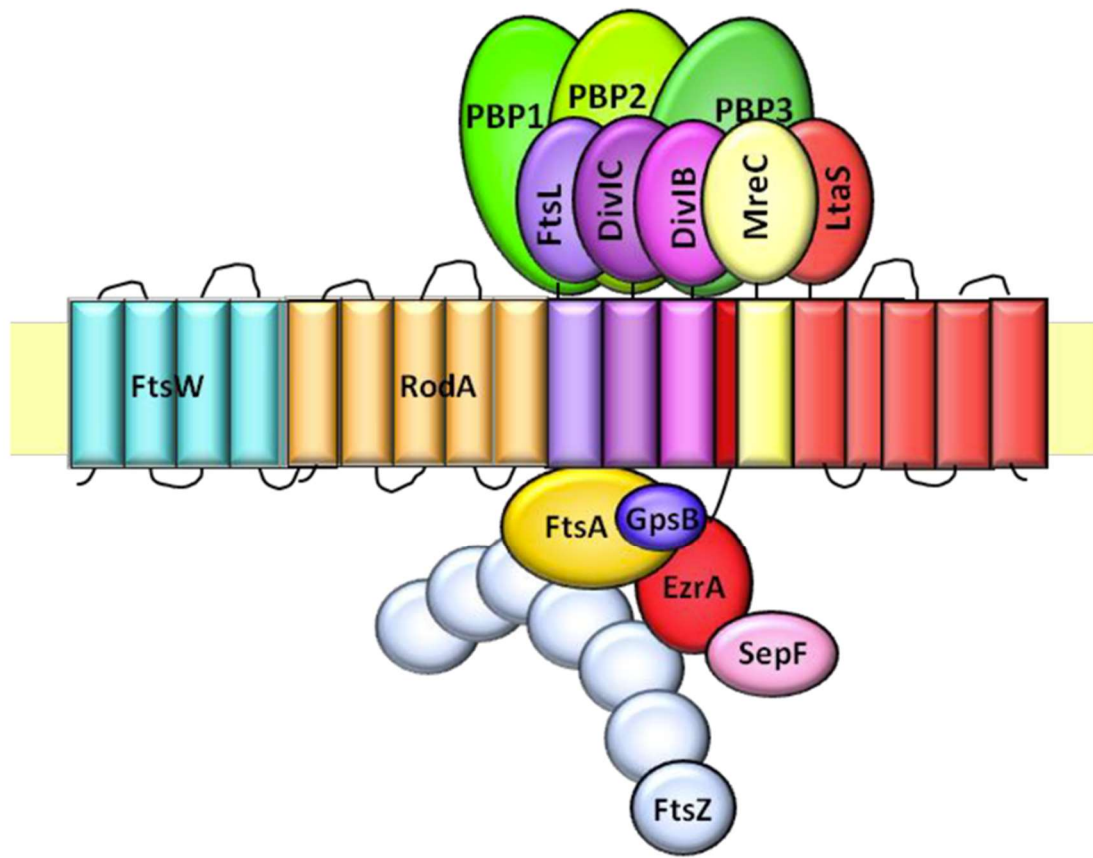
Figure 1.9 The division machinery of *S. aureus*

Schematic representation of the *S. aureus* divisome. Adapted from Wacnik (2016)**.**

PG insertion must be orchestrated during division of the cell (Figure 1.10). PG is synthesised and hydrolysed, allowing the cell to increase in volume at a constant rate (Wheeler *et al.*, 2015; Zhou *et al.*, 2015). The shape of *S. aureus* changes during the cell cycle, which is hypothesised to be due to changing turgor pressure due to PG hydrolysis (Monteiro *et al.*, 2015). As the septa begins to form, a thick band of PG, resembling a 'piecrust', is laid down (Turner *et al.*, 2010a), from which the leading edge of septal PG forms, which is thinner than the rest of the septum (Matias and Beveridge, 2007). While PG is inserted at the leading edge of the septum, it is also incorporated into the rest of the pre-existing cell wall (Lund *et al.*, 2018). Once the septal annulus has closed, the division complex inserts more PG along the length of the septum until it is a uniform thickness (Lund *et al.*, 2018). The major autolysin Atl (1.4.3.2) and other PG hydrolases cleave PG on the outer surface of the cell wall (Komatsuzawa *et al.*, 1997). This results in the rapid separation of daughter cells (Zhou *et al.*, 2015), with the initial 'piecrust' forming scars at the site of division, hypothesised to be a marker of division (Turner *et al.*, 2010a). This can act as an epigenetic marker to allow subsequent divisions to occur on different orthogonal planes.

1.5   Peptidoglycan architecture

A major obstacle in determining the three-dimensional architecture and organisation of PG has been the techniques available to study the cell wall. Techniques such as atomic force microscopy (AFM), nuclear magnetic resonance (NMR) and cryo-electron microscopy have allowed new investigation of this structure (Kim *et al.*, 2015). Two main models have been proposed to explain the architecture: the circumferential (planar) and scaffold models. In the planar model, the glycans run circumferentially around the cell, while in the scaffold model the glycans are arranged perpendicularly the cell (Beeby *et al.*, 2013). It has been suggested that the high-level of crosslinking in *S. aureus* could only be achieved if the stem peptides were packed in the same plane and parallel to one another (Kim *et al.*, 2013). In *B. subtilis* it has been shown that the glycans arrange into

50 nm wide helical cables which then run parallel around the short-axis of the cell (Hayhurst *et al.*, 2008).

1.6   Techniques to analyse PG

1.6.1   Reverse Phase high performance liquid chromatography

Perhaps the most common technique used to study PG has been reverse phase high performance liquid chromatography (RP-HPLC), which was originally proposed in 1988 (Glauner, 1988). RP-HPLC allows differences in the chemical composition in the cell wall to be visualised by separating muropeptides after solubilisation of PG (Desmarais *et al.*, 2013). In RP-HPLC a liquid sample is transported through a hydrophobic column (the stationary phase) by a sodium phosphate/methanol or water/acetonitrile mobile phase. On entering the column, muropeptides interact with the hydrophobic column and are eluted by increasing concentrations of organic solvent present in the mobile phase over time. This produces a UV-absorbance chromatogram with peaks at different retention times, with each peak representing a different muropeptide species (Figure 1.11) (Jonge *et al.*, 1992a). The technique is sensitive enough to detect single amino acid differences between muropeptides (Desmarais *et al.*, 2013).
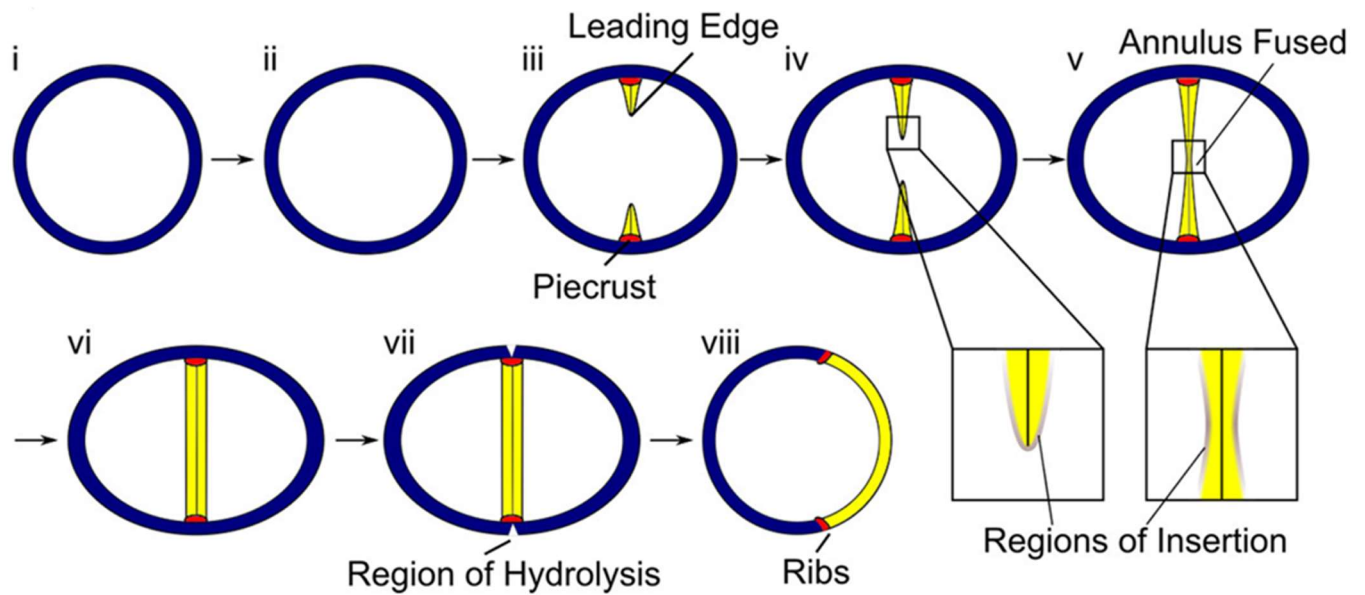
Figure 1.10 Model for *S. aureus* PG insertion and cell division

(i, ii) Cell volume increases with a concomitant shape change, slightly elongating before septum formation. (iii) Septum formation begins with a 'piecrust' (seen in red), (iv) followed by PG being incorporated at the leading edge of the septum, as well as across the cell surface to allow further cell expansion. (v, vi) The septal annulus fuses and new PG is synthesised along the septum to produce a septum of uniform thickness. (vii) PG hydrolases present on the outer surface of the cell cause a split to form which is followed by rapid scission of daughter cells. (viii) Scars (ribs) remain at the site of division. Adapted from Lund *et al.* (2018).
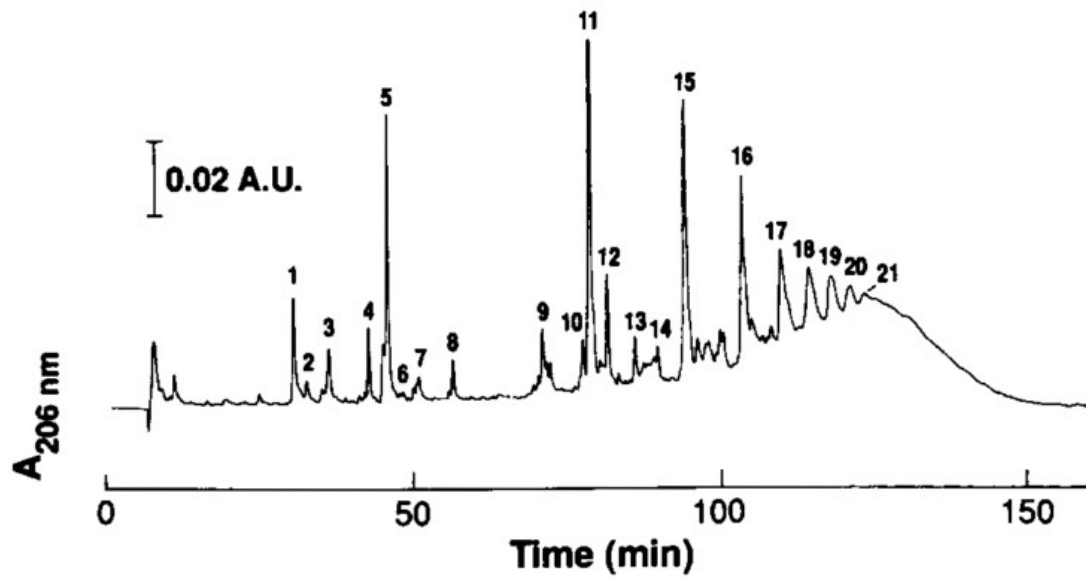
Figure 1.11 Example chromatogram of a *S. aureus* muropeptide RP-HPLC profile

Example chromatogram showing the muropeptide profile of *S. aureus* after separation by RP-HPLC and detection by UV absorbance at 206nm. The numbers above each peak represent the major muropeptide found within each peak as described in de Jonge *et al.* (1992). Adapted from de Jonge *et al.* (1992).

1.6.2   Mass Spectroscopy

While RP-HPLC produces UV absorbance traces of muropeptide composition, it cannot be used to identify muropeptide identity within a UV absorbance peak. Initially, individual muropeptide fractions are collected from the RP-HPLC, desalted by HPLC, and then analysed. One method used was to analyse the amino acids present within a fraction and deducing the muropeptide identity by amino acid relative abundance (Glauner *et al.*, 1988). It is more common for fractions to be analysed by mass spectroscopy (MS) (Bern *et al.*, 2017). This produces a spectrum individually for each fraction, allowing muropeptides to be identified by their mass. If a structure is unknown, MS/MS can be utilised, where ions are fragmented and then subject to further MS to allow muropeptide identification (Boneca *et al.*, 1997). Mass spectroscopy can also be performed in tandem with liquid chromatography (LC-MS), were samples are separated by HPLC, producing a UV absorbance trace and then immediately analysed by MS or MS/MS as they elute from the column, simultaneously producing a ion spectrum (Patti *et al.*, 2008). This methodology is time consuming as manual analysis of the ion spectra is required in order deduce muropeptide structures, but work has been ongoing in order to automate this process (Bern *et al.*, 2017).

1.6.3   Nuclear magnetic resonance

Another method to identify a muropeptide is by utilising nuclear magnetic resonance (NMR). This technique relies on the hydrogen atoms in muropeptides absorbing and emitting electromagnetic radiation in characteristic and detectable ways, allowing identification of a muropeptide species, but requires a relatively large amount of material (Romaniuk and Cegelski, 2015). Solid-state NMR is utilised to analyse to structure of both sacculi and whole cells (Kim *et al.*, 2015), meaning that digestion of the sacculi to muropeptides is not required, and PG can be analysed in a native state. NMR has revealed further details regarding PG architecture of Gram-positive organisms, notably *S. aureus* (Kim *et al.*, 2015). *S. aureus* PG shows 4-fold helical symmetry, with a

periodicity of 40 Å, meaning each peptide stem is rotated 90 ° relative to the previous. The crosslinked peptide stems were shown to be orientated in parallel to one another (Kim *et al.*, 2013, 2015). As previously described (Chapter 1.4.3), NMR has also been used to determine the mechanism of lysostaphin SH3b domains (Gonzalez-Delgado *et al.*, 2020).

1.6.4   Atomic Force Microscopy

To determine the architecture of PG, as in Chapter 1.5, atomic force microscopy (AFM), a form of scanning probe microscopy, is often utilised (Turner *et al.*, 2010b). This technique uses a sharp tip which scans along the sample, and the movement of this tip is converted into an image with a resolution that can be less than a nanometre (Binnig *et al.*, 1986). This method does not require staining of samples, allowing the architecture to be studied without potential interference (Turner *et al.*, 2010b). AFM of *S. aureus* sacculi has allowed the textures of surface PG to be determined (Touhami *et al.*, 2004; Turner *et al.*, 2010a). These textures are seen to consist of concentric rings or a rough 'knobbly' mesh (Turner *et al.*, 2014) (Figure 1.12). The ring structure is associated with newly synthesised PG originating from the most recent division cycle, which over time is processed by PG hydrolases to the mature 'knobbles' (Turner *et al.*, 2014). The ring and mature structures are separated by a thick band of PG resembling a 'piecrust' (Chapter 1.4.5), which are thought to be the initial sites of septation, and play a role in establishing cell polarity (Turner *et al.*, 2010a). Purified sacculi are often used to analyse the PG architecture, but studies have made use of living cells to observe PG structure and cellular processes in a native state in a relevant medium (Viljoen *et al.*, 2020).
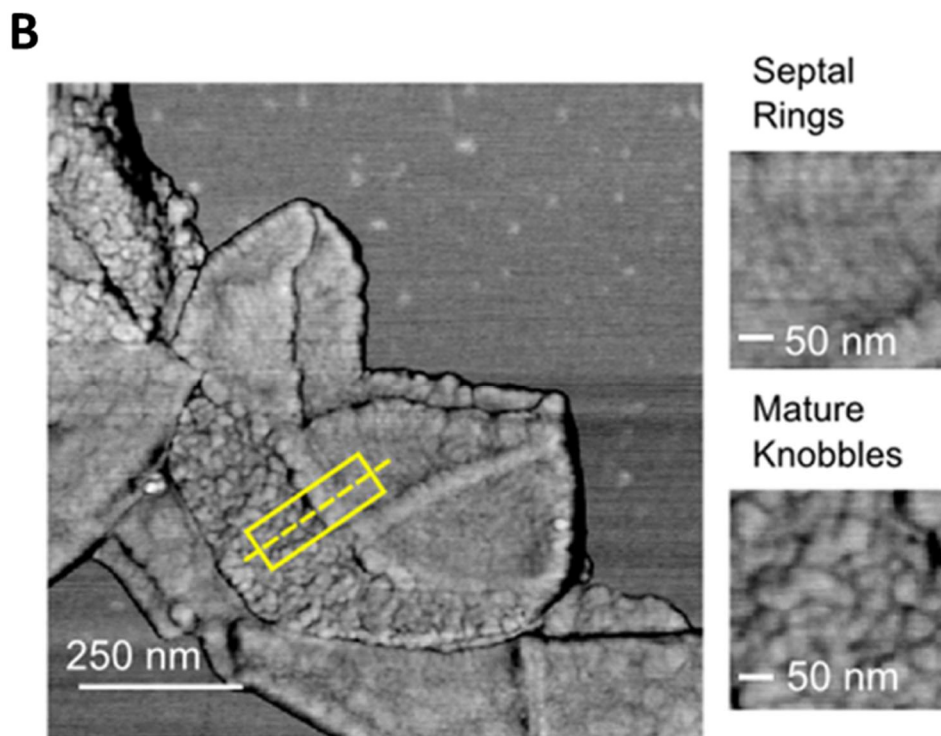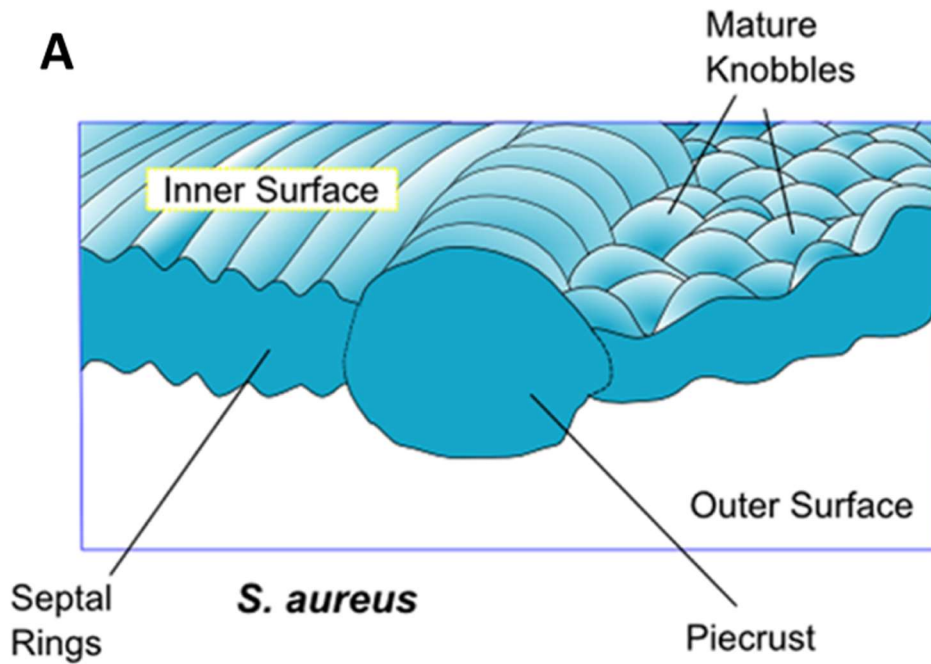
Figure 1.12 Peptidoglycan architecture of *S. aureus* as determined by AFM

(A) Diagram of *S. aureus* surface PG structure based on yellow box region in **(B)** direct AFM observations of PG architecture. Newly synthesised PG is seen as concentric rings, while mature PG adopts a mesh like structure with clear "knobbles". There is a clearly defined transition structure between the rings and the mesh, known as the piecrust, named for its distinctive appearance, and is the first part of the PG synthesised during septation. Adapted from Turner *et al.* (2010; 2014).

1.6.5 Electron Microscopy (EM)

EM has a higher resolving power (around 0.2 nm) than light microscopy due to its use of electrons which have a shorter wavelength than light (Smith, 2008). In thin-section EM samples are chemically fixed, dehydrated and embedded in resin, the samples are thin-sectioned and then stained with heavy metals to increase image contrast, which are then imaged with transmission EM (TEM) (Eltsov and Zuber, 2006). Thin-section EM has shown the basic processes of division in *S. aureus* (Giesbrecht *et al.*, 1997; Sugai *et al.*, 1997), but the accuracy of standard thin-section EM is limited due to the structural artifacts produced due to the harsh chemicals required in sample preparation (Matias and Beveridge, 2007). Cryo-electron microscopy (CryoEM) utilises vitrification of specimens, which rapidly immobilises and preserves morphological structures in a matrix of ice. CryoEM of vitreous sections (CEMOVIS) utilises vitrified samples which are then cut into thin sections and observed by EM, without staining, preserving the structure of the sample (Al-Amoudi *et al.*, 2004). Alternatively, freeze substitution may be utilised where samples are fixed by rapid freezing (cryofixation) preserving the sample's structure. The ice crystals within the sample are then replaced with organic solvent (which may contain chemical fixatives) at low temperatures. The samples can then be thin-sectioned, stained and analysed by EM at room temperature (Matias and Beveridge, 2006). CryoEM has been used to study PG from purified sacculi for both Gram-positive and negative species (Gan *et al.*, 2008; Beeby *et al.*, 2013). CryoEM has shown that a single layer of glycans run parallel to the cell surface of *E. coli* (Gan *et al.*, 2008). Glycan strands run circumferentially around the cell, perpendicular to the long axis of the cell (Gan *et al.*, 2008). This result has also been observed in rod-shaped Gram-positive organisms such as *Bacillus anthracis* and *Listeria monocytogenes* (Beeby *et al.*, 2013). The use of freeze substitution has confirmed the existence of a periplasmic space in *S. aureus* (Matias and Beveridge, 2006), as well as providing further details of the PG architecture within the septa of dividing bacteria (Matias and Beveridge, 2007). Scanning EM (SEM), where electrons are fired at the surface of whole cells, has also been utilised to study the morphology of PG (Henk *et al.*, 1995; Sycuro *et al.*, 2010; Golding *et al.*, 2016).

42

1.6.6 Fluorescence microscopy

While EM can provide high resolution images of the cell and the cell wall, it provides little information about the localisation of cellular components. The fluorescent labelling of proteins has allowed the determination of subcellular localisations, as well as fluorescent D-amino acids to study PG dynamics (Radkov *et al.*, 2018). Standard microscopy techniques are limited by the resolution limit of light to around ~250 nm (Huang *et al.*, 2010). So called super resolution microscopy has been developed to alleviate this limitation, with methods such as structured illumination microscopy (SIM) and stochastic optical reconstruction microscopy (STORM) being utilised to study PG (Huang *et al.*, 2010; Wheeler *et al.*, 2011). Using STORM, the coordination of *S. aureus* cell division has been researched in detail (Chapter 1.4.5) (Lund *et al.*, 2018).

1.7 *Staphylococcus aureus*

S. aureus is a Gram-positive spheroid bacterium found as a commensal organism on around 30 % of the population, commonly colonising the skin and nostrils (Mainous *et al.*, 2006). It is non-motile and a facultative anaerobe as well as being catalase-, coagulase- and phosphatase-positive (Reddy *et al.*, 2017). While *S. aureus* has a commensal relationship with humans, it will adapt to a pathogenic lifestyle on entering host tissues (through injury or medical intervention) (Reddy *et al.*, 2017). Upon entering a host, *S. aureus* can infect a wide repertoire of sites around the body, causing skin and soft tissue infection (SSTIs), sepsis, osteomyelitis, peritonitis, pneumonia and endocarditis (Kim *et al.*, 2014). *S. aureus* can be a causative agent of toxic shock syndrome, predominantly by the production of toxic shock syndrome toxin-1 (TSST-1) (Ferry *et al.*, 2005). *S. aureus* and its associated toxins can also cause gastrointestinal infections and food poisoning. The ingestion of one or more of the preformed *S. aureus* enterotoxins can cause the rapid onset of food poisoning 2 to 8 hours after consumption (Argudín *et al.*, 2010).

It has been suggested that *S. aureus* is the cause of around 40% of all nosocomial infections, demonstrating the importance of research into this organism (Hecker *et al.*, 2010). The biochemistry and microbiology of this organism must be fully understood so that effective treatments can be devised to treat the wide range of diseases that it can cause, with a vaccine not yet being available (Proctor, 2012, 2015).

1.7.1   Antibiotic resistance

Shortly after the introduction of penicillin in the 1940s it was reported that resistant strains of *S. aureus* emerged due to β-lactamase (Rammelkamp and Maxon, 1942; Foster, 2017). The β-lactamase, encoded by *blaZ,* cleaves the β-lactam ring in penicillin (Sabath, 1982). Methicillin-resistant *S. aureus* (MRSA) was first reported in 1961 (Jevons, 1961) shortly after the introduction of methicillin into the clinic to counter the rise of penicillin resistance (Lowy, 2003). Although named for methicillin resistance, MRSA strains are resistant to all β-lactam antibiotics, due to the acquisition of the *mecA* gene (Berger-Bächi and Rohrer, 2002; Stryjewski and Corey, 2014). MRSA infections are associated with significantly high morbidity and mortality rates (Dantes *et al.*, 2013).

The cause of β-lactam resistance was determined to be due to the acquisition of the *mecA* gene on a mobile genetic element called the staphylococcal cassette chromosome (SCC*mec*) (Katayama *et al.*, 2000). The *mecA* gene encodes for a homologue of PBP2 called PBP2A, which is not bound by β-lactam antibiotics (Zapun *et al.*, 2008a). PBP2A only possesses transpeptidase activity, so the transglycosylase activity of the native PBP2 is still required in the presence of β-lactam antibiotics to synthesise PG (Rajagopal and Walker, 2017). The PG produced by PBP2A is less crosslinked than native PG, but still produces viable cells (Müller *et al.*, 2015).

S. aureus strains often acquire resistances to other antibiotics, including glycopeptides such as vancomycin, commonly known as the antibiotic of last resort. Vancomycin binds to the D-Ala-D-Ala dipeptide of lipid II, preventing crosslinking and proper synthesis of the cell wall (Howden *et al.*, 2010). Vancomycin resistant *S. aureus* (VRSA) have obtained the *vanA* gene of Enterococci, causing D-Ala-D-Ala to be replaced with D-Ala-D-lactate (Foster, 2017). It is more common for strains to be vancomycin-intermediate (VISA), which have a higher minimum inhibitory concentration (MIC) for vancomycin than a sensitive strain. This resistance is often associated with an increase in cell wall thickness (Gardete and Tomasz, 2014). The change in cell wall structure in VISA can be associated with single nucleotide substitutions in the *walK* or *walR* genes (Chapter 1.4.4), changing cell wall metabolism (Howden *et al.*, 2011).

1.7.2   *S. aureus* virulence factors

S. aureus possesses a wide range of virulence factors (Figure 1.13), both secreted and cell surface associated, required for disease in a diversity of pathologies (Ukpanah and Upla, 2017). The cell wall of *S. aureus* impacts on virulence, as the PG, WTA and LTA are capable of causing septic shock and multiple organ failure within a host (Kengatharan *et al.*, 1998).

S. aureus produces a range of adhesins that allow binding to the host extracellular matrix and plasma components (Ferry *et al.*, 2005). Microbial surface components recognising adhesive matrix molecules (MSCRAMM) adhesins are commonly anchored to the PG via covalent bonds and allow binding to host tissues (Foster *et al.*, 2014). Sortase is the enzyme responsible for attaching surface proteins to PG via the LPXTG sorting signal motif (Mazmanian *et al.*, 2000). Precursor proteins containing the LPXTG motif are transported to the secretory pathway, whereby they are directed to the cell envelope, and sortase, a transpeptidase, cleaves the motif between the threonine and the glycine residues. This allows a bond to be formed between the threonine of the

protein and the pentaglycine bridge of the PG (Mazmanian *et al.*, 2000). MSCRAMMs in *S. aureus* recognise host fibronectin via fibronectin-binding proteins, such as FnBPA and FnBPB, and fibrinogen with clumping factors A and B (ClfA, ClfB) (Ferry *et al.*, 2005; Foster *et al.*, 2014). It has been shown that ClfB is a major determinant for nasal colonisation (Wertheim *et al.*, 2008).

Protein A (SpA), associated with the cell wall of *S. aureus*, is also an MSCRAMM due to its ability to bind the von Willebrand factor in blood, which is a glycoprotein required for platelet adhesion at the site of tissue damage, as well as binding to blood clotting factors (Cheung *et al.*, 2002). Protein A has a wide variety of other functions in infection, most importantly binding IgG of the host, interfering with opsonisation and phagocytosis (Ukpanah and Upla, 2017). Protein A can activate type I human interferons (IFN), such as IFN-β, which in a mouse pneumonia model has been shown to be important for lung colonisation (Martin *et al.*, 2009).
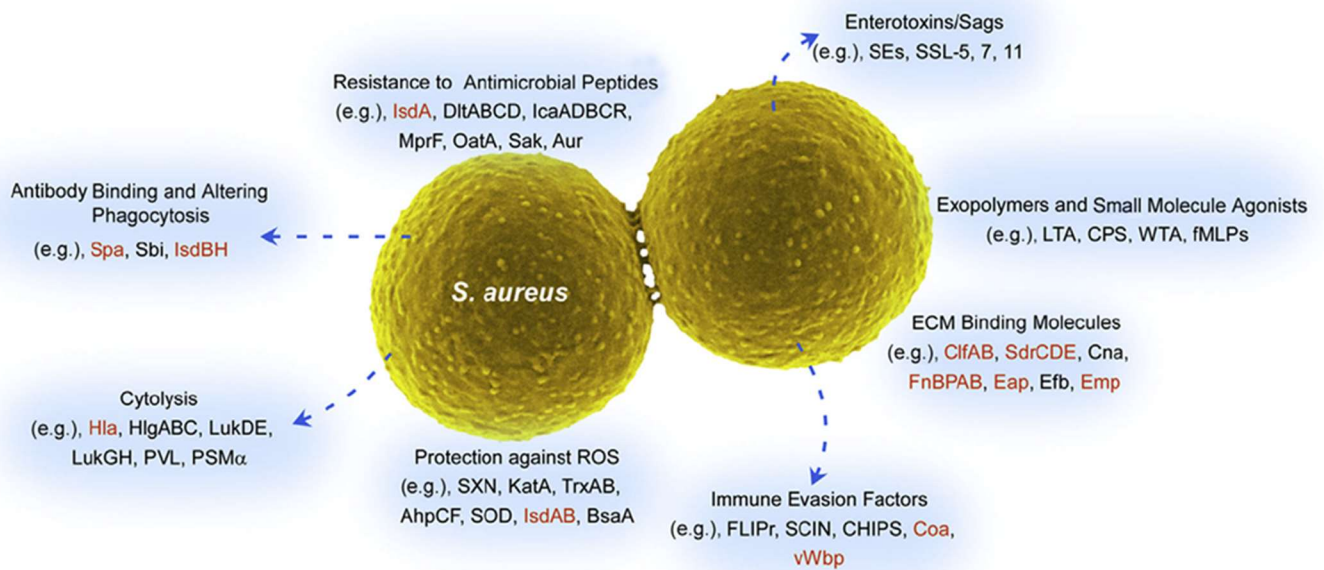
Figure 1.13 Representative *S. aureus* virulence factors

S. aureus produces a wide range of virulence factors to permit pathogenesis once inside a host. Factors in red are those involved in abscess formation. Taken from Kobayashi *et al.*, (2015).

S. aureus are attacked by professional phagocytes during infection and must withstand killing for infection to progress. During infection, *S. aureus* is subjected to the complement system of the innate immune system. The complement system is a cascade of proteins that assists the immune response by opsonising bacteria to enhance phagocytosis, generating inflammatory signals for phagocyte recruitment and killing bacteria through the formation of the membrane attack complex (MAC) (Serruto *et al.*, 2010) (Figure 1.14). There are three complement pathways: classical, alternative and lectin, each consisting of proenzymes that sequentially cleave subsequent proteins, activating them in turn (Buchan *et al.*, 2019). The three complement pathways converge with the cleavage of C3 by the C3 convertase (despite differences in the initial signal) producing C3a, a chemoattractant, and C3b which binds to the pathogen surface and opsonises it (Serruto *et al.*, 2010). C3b binds more C3b molecules and C3 convertases, forming C5 convertases, producing C5a (essential for recruiting and activating phagocytes) and C5b. C5b deposits on the cell surface and binds molecules of C6, C7, C8 and C9, eventually forming a pore known as the membrane attack complex (MAC), killing the bacterium (Merle *et al.*, 2015). As Gram-positives have a thick layer of peptidoglycan covering their cell membrane, they are not affected by the MAC as it cannot reach the cell membrane. Gram-positive bacteria therefore have virulence factors that inhibit C3 and C5 convertases, preventing the production of C3a and C5a (Serruto *et al.*, 2010). *S. aureus* produces the staphylococcal complement inhibitor (SCIN), which acts by binding to the host C3 convertase, halting the complement system from producing the anaphylatoxins C3a and C5a (Rooijakkers and van Strijp, 2007).
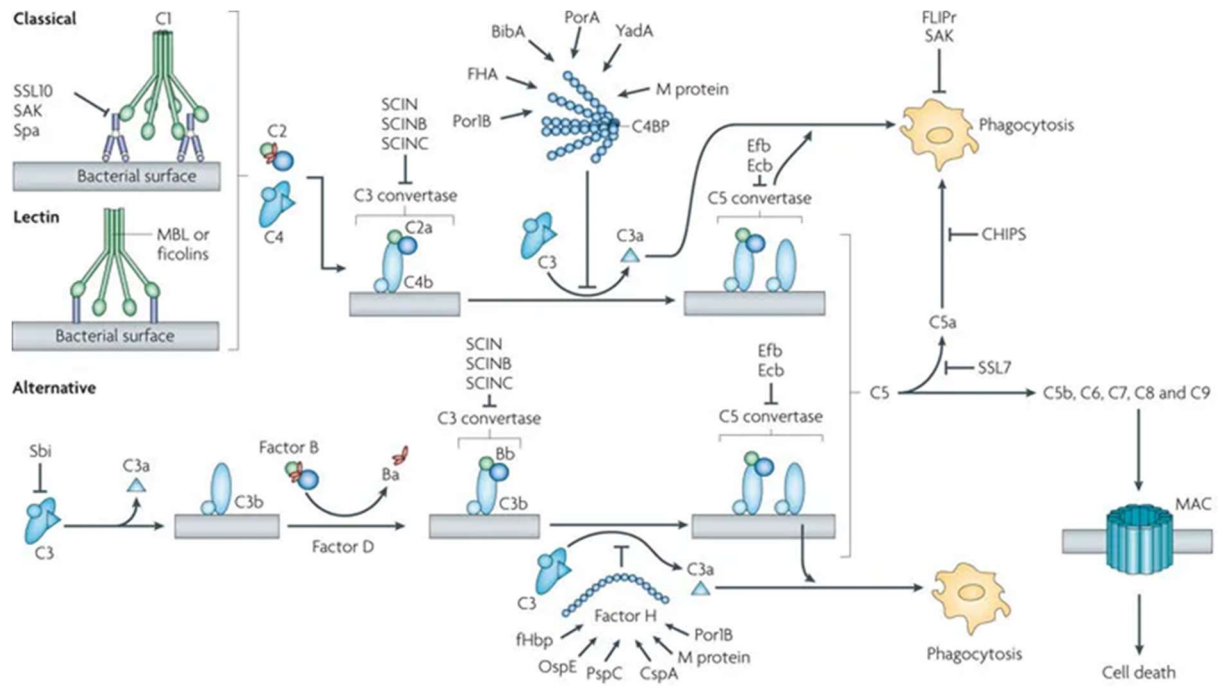
Figure 1.14 The three pathways of the human complement system

The classical, alternative and lectin pathways of the human complement. Representative bacterial factors that target the complement are also shown. Adapted from Serruto *et al.* (2010).

S. aureus has 14 staphylococcal superantigen-like proteins (SSLs), a family of proteins involved in immune evasion (Koymans *et al.*, 2018). Both SSL1 and SSL5 have been found to inhibit matrix metalloproteinases, which are involved in the recruitment of migratory inflammatory cells to the site of bacterial infection (Koymans *et al.*, 2016). Toll-like receptor 2 (TLR2, Chapter 1.8.3) recognises the LTA and PG of *S. aureus* and is important for the activation of pathways leading to *S. aureus* clearance (Fournier and Philpott, 2005)*.* SSL3 has been shown to bind to the extracellular domain of TLR2, inhibiting its binding to *S. aureus* LTA and PG, preventing the production of inflammatory cytokines that would lead to bacterial clearance (Yokoyama *et al.*, 2012). The secreted extracellular adherence protein (Eap) prevents neutrophil recruitment to the site of infection by blocking the interaction between host ICAM-1 and LFA-1, reducing neutrophil transmigration through endothelial cells (Foster, 2009). Phagocyte recruitment is also inhibited by the chemotaxis inhibitory protein of staphylococci (CHIPS) (Ukpanah and Upla, 2017). CHIPS binds to the C5a and formylated peptide receptors on the neutrophil surface, preventing the binding of C5a and formylated peptides, preventing chemotaxis of neutrophils towards C5a and the site of infection (de Haas *et al.*, 2004).

The secretion of enzymes that destroy host structures are important in the spread and dissemination of *S. aureus* throughout the host. The secretion of fibrinolysin, which degrades fibrin, allows the spread of *S. aureus* to surrounding tissues (Ukpanah and Upla, 2017). Hyaluronidases, which degrade the hyaluronic acid in the extracellular matrix, and may also play a role in dissemination and invasive infection tissue (Ukpanah and Upla, 2017).

S. aureus also produces toxins for tissue invasion and nutrient acquisition, as well as to escape immune killing. Alpha toxin (Hla) is a well characterised haemolysin of *S. aureus* that forms β-barrel pores in the membranes of host cells, resulting in host cell lysis (Berube and Bubeck Wardenburg, 2013). Hla binds to host cells via the ADAM10 proteins in the host cell membrane which is expressed on a wide variety of cell types (Berube and Bubeck Wardenburg, 2013). The leukocidins are a group of pore-forming toxins produced by *S. aureus* (Alonzo and Torres, 2014)*.* Leukocidins consist of two subunits, an S-subunit and an F-subunit, which, when secreted, oligomerise into a heptamer which subsequently forms a pore in the host membrane (Alonzo and Torres, 2014)*.* However, LukAB, which targets neutrophils via the CD11b cellular receptor (which binds C3b), is produced as a single heterodimer (DuMont *et al.*, 2013). Panton-Valentine leukocidin (PVL) plays a key role in severe necrotising disease caused by *S. aureus*. PVL induces rapid death of human and rabbit, but not murine or simian, neutrophils (Löffler *et al.*, 2010). Phenol soluble modulins (PSMs) are a group of seven toxins that target erythrocytes and leukocytes (Cheung *et al.*, 2012) and are associated with invasive MRSA infections (Wang *et al.*, 2007). PSMs are receptor independent pore-forming toxins that can target a wide variety of cell types, forming α-helical pores in membranes, resulting in host cell lysis (Buchan *et al.*, 2019). It has been suggested that PSMs can release staphylococcal lipoproteins from the cytoplasmic membrane, resulting in TLR2 signalling, leading to inflammation and sepsis (Chapter 1.7.3) (Buchan *et al.*, 2019).

S. aureus is known to produce abscesses during infection, which is common in the murine sepsis model of infection, where kidney abscesses are a key pathology (Pollitt *et al.*, 2018). An abscess is an aggregation of bacterial cells surrounded by host immune cells, notably macrophages and neutrophils (Figure 1.15) (Kobayashi *et al.*, 2015). Using immune evasion factors as previously discussed, *S. aureus* survives in the bloodstream and disseminates to organ tissues, such as the kidney (Cheng *et al.*, 2011). It has been found that ClfA is important for the formation of an abscess in a rabbit model of skin infection (Malachowa *et al.*, 2016). While in an organ such as the kidney, the iron limiting conditions must be overcome to allow replication to occur. *S. aureus* can scavenge for iron using IsdB, a sortase-anchored cell wall protein that binds

haemoglobin, allowing *S. aureus* to utilise the iron containing haem group (Mazmanian *et al.*, 2003; Torres *et al.*, 2006). The replicating *S. aureus* cause migration of neutrophils and other immune cells to the site of infection (Cheng *et al.*, 2011). Coagulase and von Willebrand factor binding protein (vWbp) are needed to form the fibrous pseudo-capsule surrounding the *S. aureus* within the abscess (Kobayashi *et al.*, 2015). This is surrounded by a layer of necrotic neutrophils and macrophages and also contains tissue debris and fibrin (Cheng *et al.*, 2011; Kobayashi *et al.*, 2015). As the abscess matures, fibroblasts proliferate, resulting in the production of a fibrous capsule encapsulating the abscess, containing the pathogens (Kobayashi *et al.*, 2015).
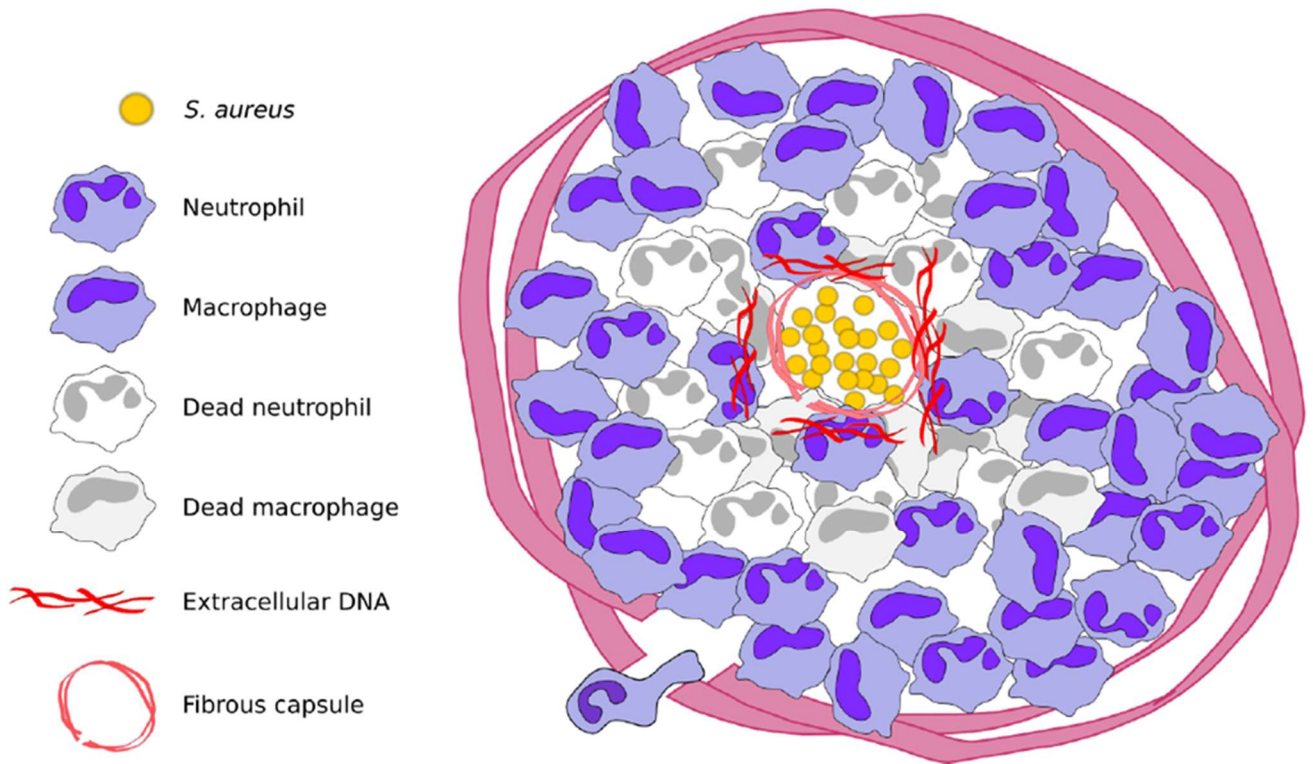
Figure 1.15 Structure of a mature abscess formed by *S. aureus*

S. aureus is found within the centre of the abscess protected by a fibrous pseudo-capsule. The bacteria are surrounded by DNA released from neutrophils. Within the abscess are dead macrophages and neutrophils, as well as some living. The entire abscess is encapsulated with a fibrous capsule of host origin, to isolate the bacteria from the other host tissues. Macrophages and neutrophils can pass through this in order to control the infection. Taken from Wagner (2016).

When phagocytosed by host neutrophils and macrophages, *S. aureus* is subjected to further killing mechanisms. After phagocytosis, *S. aureus* is held within a phagosome that fuses with a lysosome filled with antimicrobial compounds and enzymes which degrade PG, proteins and DNA and produce an oxidative burst to kill pathogens (Buchan *et al.*, 2019). During the oxidative burst (Figure 1.16), superoxide radicals (O_2^-) are produced by NADPH oxidase. Superoxide radicals do not directly contribute much to cell damage or death as *S. aureus* SodA and SodM, superoxide dismutases, convert superoxide radicals to hydrogen peroxide (H_2O_2) and O_2, using manganese as a co-factor (Karavolos *et al.*, 2003). *S. aureus* also produces the membrane-bound carotenoid staphyloxanthin, which gives *S. aureus* its distinctive colour. Staphyloxanthin acts as an anti-oxidant, containing abundant conjugated double bonds, allowing it to quench superoxide without damage to the cell (Clauditz *et al.*, 2006; Buchan *et al.*, 2019). Hydrogen peroxide, a product of both host and *S. aureus* superoxide dismutases, is converted to water and oxygen by *S. aureus* catalase (KatA) (Park *et al.*, 2008). AhpC and AhpF, forming two subunits of *S. aureus* alkyl hydroperoxide reductase, also convert hydrogen peroxide to water and molecular oxygen, or convert alkyl peroxides to water and the corresponding alcohol, neutralising them (Cosgrove *et al.*, 2007; Buchan *et al.*, 2019). Host myeloperoxidase can convert hydrogen peroxide, with a chloride ion, to hypochlorous acid (HOCl), which is the most antimicrobial chemical within the phagolysosome (Buchan *et al.*, 2019). To prevent the function of hypochlorous acid, *S. aureus* inhibits the action of host myeloperoxidase by expressing staphylococcal peroxidase inhibitor (SPIN) (Buchan *et al.*, 2019). SPIN inhibits the active site of myeloperoxidase (Jong *et al.*, 2017).
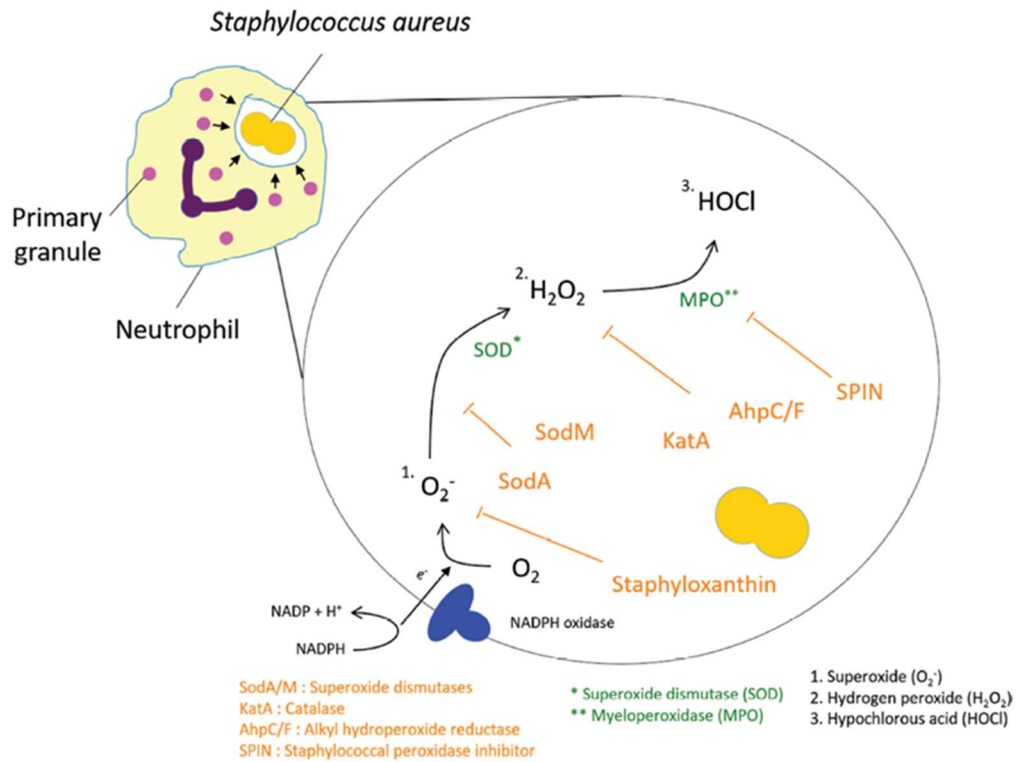
Figure 1.16 Evasion of the oxidative burst by *S. aureus*

The oxidative burst of neutrophils produced superoxide, hydrogen peroxide and hypochlorous acid in order to kill *S. aureus.* In turn *S. aureus* has mechanism to halt the production of and neutralise these chemicals. Taken from Buchan *et al.* (2019).

1.7.3 Host recognition of *S. aureus*

PG is a pathogen associated molecular pattern (PAMP) recognised by the innate immune system via pattern recognition receptors (PRRs) resulting in the transcription of immune modulators, such as pro- or anti-inflammatory chemokines and cytokines (Bourhis and Werts, 2007). Nucleotide-binding oligomerisation domain protein (NOD) 1 and NOD2 are involved in the intracellular recognition of PG within host cells. NOD1 recognises PG, specifically a muropeptide of GlcNAc-MurNAc with a tripeptide stem containing diaminopimelic acid, resulting in the secretion of cytokines such as interleukin (IL) 6 and TNF-α (Chamaillard *et al.*, 2003). NOD2 recognises the PG from both Gram-positive and negative bacteria, specifically detecting MurNAc with a dipeptide of L-Ala-D-iGlx (muramyl dipeptide), common to all PG (Girardin *et al.*, 2003). The detection of PG by NOD2 results in the activation of the NF-κB pro-inflammatory cascade (Girardin *et al.*, 2003), causing the transcription of pro-inflammatory cytokines and leukocyte recruitment to help to clear bacterial infection (Lawrence, 2009). IL-1β and IL-6 are examples of pro-inflammatory cytokines that activate T and B cells respectively, stimulating the adaptive immune system after *S. aureus* is detected via innate immunity (Fournier and Philpott, 2005).The secretion of IL-8 results in the migration of neutrophils to the site of infection, which is important during abscess formation (Fournier and Philpott, 2005; Cheng *et al.*, 2011). *S. aureus* is commonly phagocytosed by professional phagocytes during infection, but *S. aureus* can escape from the phagosome and grow and divide within the host cytoplasm (Kubica *et al.*, 2008; Horn *et al.*, 2018). *S. aureus* has been found to be able to survive within macrophages for days without a change in viability, and it has been suggested that these infected phagocytes may aid in *S. aureus* dissemination during an infection (Kubica *et al.*, 2008; Pollitt *et al.*, 2018).

Toll-like receptor (TLR) 2 has been implicated in resistance to *S. aureus* infection in mouse models (Takeuchi *et al.*, 2000; Hoebe *et al.*, 2005). TLRs are structurally related to *Drosophila* Toll proteins (Medzhitov *et al.*, 1997) and 10 have been found in mammals (Takeda *et al.*, 2003). The activation of TLR2 activates the NF-κB cascade, mediated by

the MyD88 adaptor (Fournier and Philpott, 2005). TLR2 can detect the PG, lipoprotein and LTA (Chapter 1.3.2) of *S. aureus.* Detection of these PAMPs is known to cause the release of the cytokines TNF-α, IL-1β, IL-10, IL-12, IL-8 and the chemoattractant complement factor 5a (Fournier and Philpott, 2005). TLR2 can cooperate with TLR6 and TLR1 to increase the number of bacterial ligands that can be detected, and the formation of a heterodimer with these TLRs, and not a homodimer of TLR2, is required for TNF-α secretion (Ozinsky *et al.*, 2000). The association with TLR1 and TLR6 also allows the discrete recognition of a wide range of PAMPs (Takeda *et al.*, 2003). The α-, β- and γ- haemolysins of *S. aureus* target and cause the lysis of red blood cells in the host, producing an available iron source required for the proliferation of bacteria (Ukpanah and Upla, 2017). The haemolysins, in the presence of *S. aureus* LTA, activate the host NLRP3 inflammasome and the subsequent activation of caspase-1 (Muñoz-Planillo *et al.*, 2009). Caspase-1 cleaves the transcribed pro-IL-1β to the active IL-1β, activating the inflammatory response (Franchi *et al.*, 2009).

1.7.4 Augmentation of *S. aureus* infection by peptidoglycan

S. aureus is present on the skin as part of a mixed microbiome of mostly commensal organisms (Grice *et al.*, 2009). *S. aureus* is subjected to a phagocyte associated immune bottleneck during an infection (McVicker *et al.*, 2014; Pollitt *et al.*, 2018), where only a small proportion of the starting inoculum contributes to the infection (Boldock *et al.*, 2018). As *S. aureus* exists on the skin with other organisms, infection, potentially caused by hospital treatment, can result in a mixed inoculum infecting a patient. It is already known that the CAMP factor secreted by *Propionibacterium acnes,* a near ubiquitous skin bacterium (Brook and Frazier, 1991), enhances the haemolysis of *S. aureus* β- haemolysin, increasing *S. aureus* virulence (Lo *et al.*, 2011). The virulence of *S. aureus* is also augmented in a murine infection model when the inoculum also contains commensal organisms, without proliferation of the commensal bacteria (Boldock *et al.*, 2018). The augmentation could be achieved with purified PG, reducing the infectious dose required for a stable infection by over 1000-fold (Boldock *et al.*, 2018), establishing

a role for the resident skin microbiome, and potentially explaining the need for a large initial inoculum in mammalian models of *S. aureus* disease. The augmentation in mouse sepsis has been shown to be dependent on liver Kupffer cells phagocytosing both the *S. aureus* and augmenting material, resulting in a reduction in the production of reactive oxygen species, and the increased survival of *S. aureus* (Boldock *et al.*, 2018). A murine augmentation model of infection has a unique phenotype whereby multiple liver abscesses form during the infection (Boldock *et al.*, 2018).

1.8 Animal models of *S. aureus* disease

Animal models of disease are required to mimic complex host-pathogen interactions that occur during human interactions. No animal model is perfect to study human disease, with each model presenting advantages and disadvantages (Coulter *et al.*, 1998).

A wide variety of animal models have been developed for studying different *S. aureus* diseases, including: *Galleria mellonella* (Pollitt *et al.*, 2014), *Drosophila melanogaster* (Needham *et al.*, 2004)*,* Zebrafish (*Danio rerio*; Prajsnar *et al.*, 2008) and mammals such as mice and rabbits (Salgado-Pabón and Schlievert, 2014). While mouse models are often considered the 'gold standard' for pre-clinical vaccine studies, many *S. aureus* virulence factors are human specific, and a high starting inoculum is required to initiate infection (von Köckritz-Blickwede *et al.*, 2008; Kim *et al.*, 2014; Salgado-Pabón and Schlievert, 2014).

1.8.1 Invertebrates

Invertebrate models have the advantage of providing high-throughput analysis at a lower cost than using vertebrate models. However, invertebrates do not share as many

immune characteristics with humans and do not have a complex collection of organ systems, meaning disease progression may not be relevant to human infection.

1.8.1.1 *Caenorhabditis elegans*

C. elegans is a soil dwelling nematode roughly 1mm long that has a short life cycle allowing it to be utilised in large quantities (Kenyon, 1988). In this model, *C. elegans* is fed *S. aureus*, and the primary read out of virulence is mortality of the nematodes (Sifri *et al.*, 2003). *S. aureus* with knockouts in *agr* were shown to be less able to cause mortality in *C. elegans,* demonstrating reduced virulence (Sifri *et al.*, 2003). Using transposon insertion mutants of *S. aureus,* high-throughput virulence screens can be performed using the *C. elegans* model, allowing rapid detection of virulence factors important for pathogenesis in this model (Begun *et al.*, 2005). *C. elegans* is cultivated and maintained at 25 °C, which is below the optimum growth temperature for *S. aureus.*

1.8.1.2 *Galleria mellonella*

G. mellonella, the greater wax moth, are a commercially available model organism that are used to study a variety of pathogens, showing correlation in results with mice models (Cotter *et al.*, 2000; Jander *et al.*, 2000). For infection studies, the larvae are used. *G. mellonella* are not as well characterised as *Drosophila* (Chapter 1.8.1.3) but are known to have a circulatory system and immune system reminiscent of mammals, including superoxide producing phagocytes, and the production of antimicrobial peptides (Kemp and Massey, 2007). *G. mellonella* larvae have been used to study the virulence of *S. aureus,* including the involvement of *agr* in virulence and the relative fitness of *S. aureus* mutant strains (Pollitt *et al.*, 2014).

1.8.1.3 *Drosophila melanogaster*

D. melanogaster, a fruit fly, is commonly known as *Drosophila* and is widely used as a host to model disease (Kemp and Massey, 2007). Due to its wide usage, *Drosophila* are well characterised with mutants available for study, as well as being easy to breed and maintain (Kemp and Massey, 2007). *Drosophila* are not a natural host of *S. aureus*, but they have been used as a model organism to study *S. aureus* infection (Needham *et al.*, 2004). The dorsal thorax of *Drosophila* is infected with a needle coated in *S. aureus* culture, with fly death overtime a readout of virulence (Needham *et al.*, 2004). Infection of the fly in this manner results in a systemic *S. aureus* infection and allowed the identification of genes important in virulence (Needham *et al.*, 2004). Bacterial gene expression could be monitored via GFP production. The model also allowed the administration of antibiotics via the fly's food, avoiding the need for further injections (Needham *et al.*, 2004).

1.8.2   Zebrafish

Zebrafish (*Danio rerio*) have historically been utilised to study development due to being transparent, allowing simple imaging. Zebrafish are now commonly used to study infection due to the similarity to the human innate immune system, with both having orthologs of phagocytes and cytokines (van der Vaart *et al.*, 2012). The zebrafish innate immune system is present at one day post fertilisation, with macrophages detectable at 25 hours post fertilisation (hpf) and neutrophils at 18 hpf (Herbomel *et al.*, 1999; Crowhurst *et al.*, 2002). Later in the development, at around 4 – 6 weeks post fertilisation, zebrafish develop a full adaptive immune system (Trede *et al.*, 2004), meaning that the importance of the innate immune system in infection can be investigated separately from that of the adaptive. With adequate infrastructure it is simple to breed and maintain fish allowing the generation of embryos that can be used in studies. Zebrafish are amenable to genetic modification to produce mutants, including transient gene knockdown methods (Trede *et al.*, 2004). Morpholino-modified antisense

oligonucleotides (morpholinos) are commonly used in zebrafish models to study immune components required to control infection (Corey and Abrams, 2001; Bill *et al.*, 2009). The *pu.1* morpholino, injected at the one- to four- cell embryo stage, results in the depletion of myeloid cells (Su *et al.*, 2007), the absence of neutrophils until 36 hpf and macrophages until 48 hpf (Klemsz *et al.*, 1990). The use of the CRISPR/cas9 system has allowed the development of zebrafish mutants to be generated that can be used to study host-pathogen interactions without the need for chemicals and morpholinos (Kimura *et al.*, 2014; Ma and Liu, 2015).

The zebrafish model of infectious disease has been used to study the host-pathogen interactions of a variety of bacterial species, including *Mycobacterium marinum* (Swaim *et al.*, 2006), *S. aureus* (Prajsnar *et al.*, 2008), *S. pneumoniae* (Saralahti *et al.*, 2014; Jim *et al.*, 2016) and *Enterococcus faecalis* (Prajsnar *et al.*, 2013). Injection of 1500 colony forming units of *S. aureus* into the circulation valley of zebrafish embryos (Figure 1.17) results in a systemic infection (Prajsnar *et al.*, 2008), with the innate immune system being the primary defence against infection (Prajsnar *et al.*, 2012). The phagocytes act as an immunological bottleneck for *S. aureus* infection, resulting in a small number of infected phagocytes acting as reservoirs of infection, leading to a clonal dissemination of infection (Prajsnar *et al.*, 2012; McVicker *et al.*, 2014). While the zebrafish model is high throughput, it is maintained at 28.5 °C where important virulence factors may not be expressed, meaning not all aspects of host-pathogen interaction can be investigated (Prajsnar *et al.*, 2008).

1.8.3 Murine

Mice have been used to develop a wide range of infection models where the routes of bacterial administration differ, to mimic the different pathologies bacteria can cause. *S. aureus* can cause a wide range of diseases, including sepsis, arthritis, skin infection, and pneumonia (Kim *et al.*, 2014). By utilising different infectious doses and administration

routes, these pathologies have been modelled by murine infection (Table 1.3). Whilst mouse models are common, there have been many failed human clinical trials based on their use, raising questions as to their suitability to investigate human disease (Proctor, 2012). *S. aureus* naturally colonises mice (Schulz *et al.*, 2017), but most isolates used in research are human specific (Pollitt *et al.*, 2018). A large negative of murine models is a high starting inoculum of bacteria is required to initiate infection, and doses may vary up to 100-fold depending on the *S. aureus* strain and route of administration (Table 1.3) (von Köckritz-Blickwede *et al.*, 2008). This high inoculum requirement may be a consequence of several *S. aureus* virulence factors being human specific. To counter this and improve sensitivity, humanised mice are being developed (Knop *et al.*, 2015; Prince *et al.*, 2017).

1.8.4   Rabbit

Rabbits are commonly used to study bone (osteomyelitis) and joint infections caused by *S. aureus* (Reizner *et al.*, 2014). Staphylococci are the most common cause of orthopaedic infections, with *S. aureus* and *S. epidermidis* able to form a biofilm on the materials used in prosthetics and implants, resulting in a difficult to treat and potentially recurring infection (Montanaro *et al.*, 2011; Arciola *et al.*, 2015). The large size of a rabbit allows implant-based infection models of osteomyelitis to be studied (Zhang *et al.*, 2017). Rabbit models have also been associated with endocarditis (heart) infection models of *S. aureus*, due to the similarity to human endocarditis disease progression (Coulter *et al.*, 1998). Using the rabbit endocarditis model, it was shown that WTA is required for the attachment of *S. aureus* to heart endothelial cells, and a lack of WTA results in attenuation (Weidenmaier *et al.*, 2005).
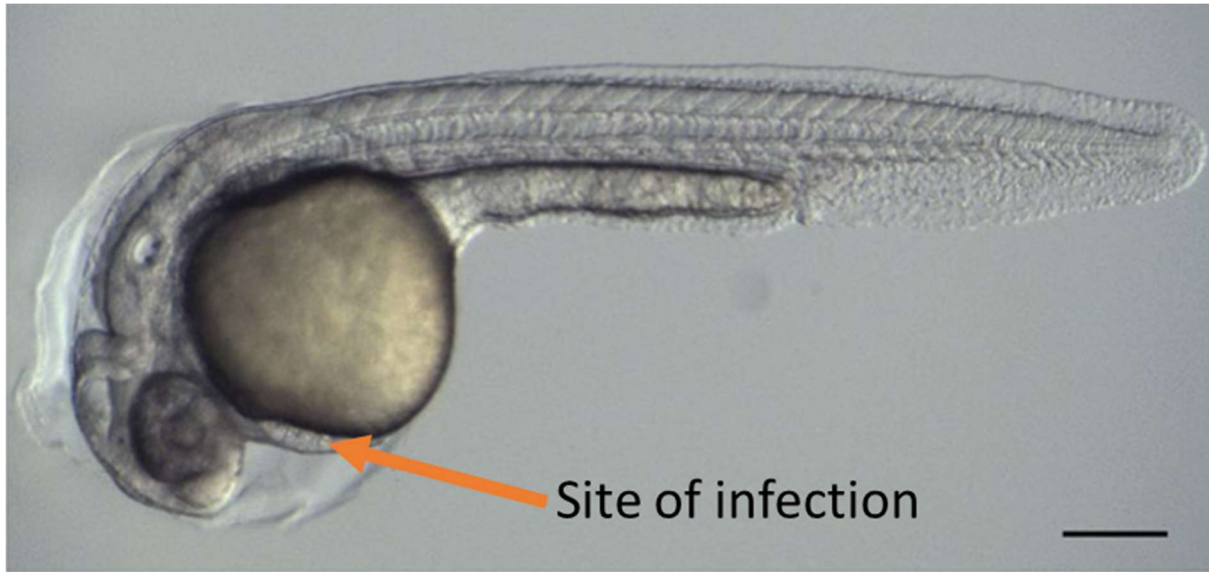
Figure 1.17 Zebrafish embryo 30 hpf

Bright field microscopy image of zebrafish embryo 30 hpf. Scale bar 100 μm. The site of injection is the circulation valley, which is indicated with an orange arrow. Adapted from Huang and Schier (2009).

Disease Model	Infection Route	Infectious dose (CFU)	Phenotype	References
Skin infection	Subcutaneous	1×10^7– 1×10^9	Dermonecrosis caused by secreted toxins	(Kennedy *et al.*, 2010; Malachowa *et al.*, 2013)
Sepsis	Intravenous	1×10^6– 1×10^7	Abscess formation in most internal organs, especially kidneys	(Cheng *et al.*, 2009; McVicker *et al.*, 2014; Boldock *et al.*, 2018; Pollitt *et al.*, 2018)
Survival	Intravenous	5×10^7– 5×10^8	Acute lethal disease within 48 hours of infection; formation of multiple lesions in heart	(Cheng *et al.*, 2010; McAdow *et al.*, 2011; Pollitt *et al.*, 2018)
Peritonitis	Intraperitoneal	5×10^8 (LD_{50}) 6×10^9 (LD_{90})	Acute lethal disease within 12 hours of infection; formation of abscess lesions on peritoneal surfaces	(Rauch *et al.*, 2012)
Arthritis	Local - Intraarticular or Septic - intravenous	Local- 2×10^2 -2×10^6 Septic- 1×10^7	Swelling and erythema of joints with increased levels of TNF-α, IL-1β, IL-6 and NF-κB in knee joint over 28 days.	(Liu *et al.*, 2001; Mohammad *et al.*, 2016; Baranwal *et al.*, 2017)
Pneumonia	Intranasal	2–4×10^8	Acute lethal disease within 72 hours of infection; infiltration of inflammatory cells into alveolar air space	(Kiser *et al.*, 1999; Bubeck Wardenburg *et al.*, 2007)
Gastrointestinal colonization	Gavage	2×10^5 - 8×10^8	Water supplemented with streptomycin to maintain *S. aureus* in the gut for 3 weeks post infection	(Misawa *et al.*, 2015)

Table 1.3 Summary of representative mouse models of *S. aureus* infection

Adapted from Kim *et al.* (2014).

1.9   Project Aims

Previous work has determined the structure of the *S. aureus* cell wall and PG when cultured *in vitro*. The aim of this study was to further the knowledge of *S. aureus* morphology and cell wall architecture during an infection. A further aim was to investigate the importance of PG structure in host-pathogen interaction utilising animal models of infection.

Chapter 2

Materials and Methods

2.1   Media

Media was prepared using distilled water (dH$_2$O) and sterilised by autoclaving solutions at 121 °C and 15 psi for 20 minutes.

2.1.1   Tryptic Soy Broth (TSB)

Tryptic soy broth (Oxoid)   30 g/l

Bacteriological Agar (VWR) was added at 1.5 % (w/v) to produce Tryptic Soy Agar (TSA).

2.1.2   Chemically Defined Media (CDM)

All glassware was rinsed with dH$_2$O before being used for CDM preparation to remove all traces of detergents.

2.1.2.1   Solution 1

Sodium phosphate dibasic ($Na_2HPO_4.2H_2O$)	7 g/l
Potassium phosphate monobasic (KH_2PO_4)	3 g/l
L-Aspartic Acid	0.15 g/l
L-Alanine	0.1 g/l
L-Arginine	0.1 g/l
L-Cysteine	0.05 g/l
Glycine	0.1 g/l
L-Glutamic Acid	0.15 g/l
L-Histidine	0.1 g/l
L-Isoleucine	0.15 g/l
L-Lysine	0.1 g/l
L-Leucine	0.15 g/l
L-Methionine	0.1 g/l
L-Phenylalanine	0.1 g/l
L-Proline	0.15 g/l
L-Serine	0.1 g/l
L-Threonine	0.15 g/l
L-Tryptophan	0.1 g/l
L-Tyrosine	0.1 g/l
L-Valine	0.15 g/l

The pH of solution 1 was measured before mixing and autoclaving and adjusted to 7.2 using NaOH or HCl as appropriate.

2.1.2.2 Solution 2 (1000 x)

Biotin	0.02 g
Nicotinic Acid	0.4 g
D-Pantothenic Acid	0.4 g
Thiamine HCl	0.4 g
Pyridoxal HCl	0.8 g
Pyridoxamine di-HCl	0.8 g
Riboflavin	0.4 g

Chemicals for solution 2 were dissolved in 140 ml of dH_2O and filter sterilised using a Stericup filter unit (milipore) with a 0.1 µm filter. Solution that was diluted to 1x using dH_2O before mixing with other solutions.

2.1.2.3 Solution 3

Adenine Sulphate	0.4 g/l
Guanine HCl	0.4 g/l

Chemicals for solution 3 were dissolved in 0.1 M HCl.

2.1.2.4 Solution 4

Calcium Chloride Hexahydrate ($CaCl_2.6H_2O$)	1 g/l
Ferrous Ammonium Sulphate (($NH_4)_2Fe(SO_4)_2.H_2O$)	0.6 g/l

Chemicals for solution 4 were dissolved in 0.1 M HCl.

2.1.2.5 Solution 5

Glucose	100 g/l
Magnesium sulphate Heptahydrate ($MgSO_4.7H_2O$)	5 g/l

Solution 5 was made using dH_2O and was autoclaved separately to the other solutions used for the preparation of CDM.

2.1.2.6 Preparation of CDM

Solution 1	700 ml
Solution 3	50 ml
Solution 4	10 ml

The three solutions were mixed and autoclaved under standard conditions. Once the mix had reached below 50 °C, 100 ml of solution 2 (at 1x concentration) and 100 ml of solution 5 (also below 50 °C) were added. CDM was stored at 4 °C.

2.1.3 LK Broth

Tryptone	10 g/l
Yeast Extract	5 g/l
KCl	7 g/l

Bacteriological Agar (VWR) was added at 1.5 % (w/v) to produce LK Agar (LK).

2.1.4 Brain Heart Infusion (BHI)

Brain Heart Infusion (Oxoid)   37 g/l

2.1.5 Porcine Serum

Porcine Serum (Gibco – Thermofisher)   500 ml

Serum was left to defrost overnight at 4 °C. After defrosting the serum was used immediately or dispensed into 50 ml aliquots and stored at -20 °C until required.

2.2 Buffers

All buffers were prepared using dH_2O, sterilised by autoclaving (when required), and stored at room temperature or 4 °C as required.

2.2.1 Phosphate Buffered Saline (PBS)

Phosphate Buffered Saline Tablets (Sigma)   2 Tablets /l

2.2.2 50 mM Tris-HCl

Tris base   6.06 g/l

The pH was adjusted to pH 7 or 7.5 with HCl, corrected to the final volume with dH_2O and autoclaved.

2.2.3 50 mM Tris-HCl pH 7.5, SDS, 50 mM DTT, 1.25 mM EDTA

SDS	3 g/l
EDTA	372 mg/l
DTT	7.71 g/l

2.2.4 TAE (50x)

Tris base	242 g/l
Glacial acetic acid	0.57 % (v/v)
EDTA pH 8.0	0.05 mM

A 1x TAE working solution was made by diluting the 50x stock solution with dH_2O.

2.2.5 Tris/EDTA/NaCl buffer (TES)

Tris base	2.42 g/l
EDTA	1.86 g/l
NaCl	5.84 g/l

The pH was adjusted to 8.0 before autoclaving.

2.2.6 Phage buffer

MgSO$_4$	1 mM
CaCl$_2$	4 mM
Tris-HCl pH 7.8	50 mM
NaCl	100 mM
Gelatin	0.1 % (w/v)

2.2.7 Sodium Phosphate Buffer – 200 mM, pH5.5 (10x)

Sodium phosphate monobasic (200 mM) and sodium phosphate dibasic (200 mM) were mixed to produce a solution of pH 5.5.

2.2.8 Sodium Borate Buffer – 250 mM, pH 9

Boric acid (H$_3$BO$_3$) was dissolved in dH$_2$O and adjusted to pH 9 using NaOH before autoclaving.

2.2.8 0.5M Ammonium Buffer, pH9

Ammonium Hydroxide	0.5 M

Ammonium hydroxide was dissolved in dH$_2$O and pH was adjusted to 9 using formic acid.

2.2.10 HPLC buffers

All HPLC buffers were made with Milli-Q filtered water and filtered (0.2 μm pore size, Merck) prior to use. All chemicals used in HPLC analysis were of HPLC grade.

2.2.10.1 Buffer A – Ultra Pure Milli-Q water with formic acid

1 ml of formic acid (98+ % pure) was added to 1 l of ultra-pure Milli-Q water. Buffer was made fresh for each use.

2.2.10.2 Buffer B – Acetonitrile with formic acid

250 μl of formic acid (98+ % pure) was added to 250 ml of acetonitrile. Buffer was made fresh for each use.

2.3   Antibiotics

The antibiotics that were used in this study are listed in Table 2.1. Antibiotics stock solutions were filter sterilised using a 0.2 μm pore filter and then stored at -20 °C. If added to media, antibiotics were added once media had reached a temperature of 50 °C or below.

2.4   Chemicals and Enzymes

All the chemicals and enzymes used in this study were of analytical grade quality and were purchased from Fisher Scientific, MP biomedicals or Merck (Sigma-Aldrich) unless otherwise stated). DNA polymerase and the appropriate buffers were purchased from New England Biolabs. Concentrations, storage conditions and solvents used are shown in Table 2.2.

2.5   Bacterial Strains

2.5.1   *Staphylococcus aureus* strains

The strains of *Staphylococcus aureus* used in this study are listed in Table 2.3. All strains were plated out onto TSA containing the appropriate antibiotic concentrations (Table 2.1) where required for selection, and stored at 4 °C. Each strain was stored as a stock at -80 °C using Microbank Beads which was used to produce the colonies on TSA plates.

2.5.2   Other bacterial strains used

Other bacterial strains used in this study are listed in Table 2.4. Strains were grown and stocked as in Chapter 2.5.1.

Antibiotic	Stock Concentration (mg/ml)	Working concentration (µg/ml)	Solvent
Erythromycin (Ery)	5	5	100% (v/v) Ethanol
Kanamycin (Kan)	50	50	dH_2O
Lincomycin (Lin)	25	25	50% (v/v) ethanol
Minocycline (Mino)	2	2	dH_2O
Neomycin (Neo)	50	50	dH_2O
Spectinomycin (Spec)	50	100	dH_2O
Tetracycline (Tet)	5	5	50% (v/v) ethanol

Table 2.1 Antibiotics used as a part of this study

Stock Solution	Concentration	Solvent	Storage
Mutanolysin	1 mg/ml	200 mM sodium phosphate	-20 °C
Pronase	20 mg/ml	TES pH 8.0	-20 °C
Lysostaphin	5 mg/ml	20 mM sodium acetate (pH 5.2)	-20 °C
Bovine Serum Albumin (BSA)	10% (w/v)	PBS	4 °C
Gentamycin (Sanofi-Aventis)	40 mg/ml	dH_2O	4 °C
Paraformaldehyde	4% (w/v)	100 mM sodium phosphate buffer (pH 7.0)	4 °C
Saponin	10% (w/v)	dH_2O	4 °C
Cellosyl	0.5 mg/ml	5 mM ammonium formate, 10 mM ammonium chloride pH 4.8	-20 °C

Table 2.2 Enzymes and chemicals used as a part of this study

Strain	Genotype	Source
SH1000 (SJF 682)	Functional $rsbU^+$ derivative of 8325-4	(Horsburgh *et al.*, 2002)
SH1000 *atl* (SJF 1367)	SH1000 $atl::ery^R$	(Foster, 1995)
SH1000 *scaH* (SJF 2109)	SH1000 $scaH::kan^R$	(Wheeler *et al.*, 2015)
SH1000 kan^R (SJF 3674)	SH1000 $lysA::kan^R$ lysA+	(McVicker *et al.*, 2014)
SH1000 *pbp3* (SJF 4422)	SH1000 $pbp3::spec^R$	Constructed by Dr K. Wacnik (University of Sheffield)
SH1000 *pbp3 pbp4* (SJF 4423)	SH1000 $pbp3::spec^R$ $pbp4::ery^R$	Constructed by Dr K. Wacnik (University of Sheffield)
SH1000 *pbp4* (SJF 4425)	SH1000 $pbp4::ery^R$	Constructed by Dr K. Wacnik (University of Sheffield)
SH1000 *sagA* (SJF 4606)	SH1000 $sagA::tet^R$	(Wheeler *et al.*, 2015)
SH1000 *scaH* (SJF4607)	SH1000 $scaH::tetM^R$	(Wheeler *et al.*, 2015)
SH1000 *sagB* (SJF 4608)	SH1000 $sagB::kan^R$	(Wheeler *et al.*, 2015)
SH1000 *atl sagA sagB* (SJF 4610)	SH1000 $atl::ery^R$ $sagA::tet^R$ $sagB::kan^R$	(Wheeler *et al.*, 2015)
SH1000 *atl sagA scaH* (SJF 4611)	SH1000 $atl::spec^R$ $sagA::tet^R$ $scaH::tetM^R$	(Wheeler *et al.*, 2015)
SH1000 *sagA sagB scaH* (SJF 4612)	SH1000 $sagA::tet^R$ $sagB::kan^R$ $scaH::tetM^R$	(Wheeler *et al.*, 2015)
SH1000 *atl sagB scaH* (SJF 4613)	SH1000 $atl::ery^R$ $sagB::kan^R$ $scaH::tetM^R$	(Wheeler *et al.*, 2015)
SH1000 *atl sagB* (SJF 4972)	SH1000 $atl::ery^R$ $sagB::kan^R$	(Wheeler *et al.*, 2015)
SH1000 *sagB scaH* (SJF 4973)	SH1000 $sagB::kan^R$	(Wheeler *et al.*, 2015)
SH1000 *sagA sagB* (SJF 4974)	SH1000 $sagA::tet^R$ $sagB::kan^R$	(Wheeler *et al.*, 2015)

SH1000 *sagA scaH* (SJF 5217)	SH1000 *sagA::tet^R scaH::kan^R*	This study
SH1000 *atl* (SJF 5255)	SH1000 *atl::kan^R*	Constructed by Dr B. Salamaga (University of Sheffield)
SH1000 *atl sagA* (SJF 5261)	SH1000 *atl::kan^R sagA::tet^R*	This study
SH1000 *atl scaH* (SJF 5262)	SH1000 *atl::kan^R scaH::tetM^R*	This study
NewHG (SJF 3663)	*S. aureus* Newman with *saeS^L* allele from strain RN1	(Mainiero *et al.*, 2010)
NewHG *kan^R* (SJF 3680)	NewHG *lysA::kan^R lysA+*	(McVicker *et al.*, 2014)
NewHG *tet^R* (SJF 3681)	NewHG *lysA::tet^R lysA+*	(McVicker *et al.*, 2014)
NewHG *sagB* (SJF 4912)	NewHG *sagB::kan^R*	This study
NewHG *pbp4* (SJF 5103)	NewHG *pbp4::ery^R*	This study
NewHG *tet^R pbp4* (SJF 5135)	NewHG *lysA::tet^R lysA+*	This study
NewHG *kan^R pbp4* (SJF 5136)	NewHG *lysA::kan^R lysA+ pbp4::ery^R*	This study
NewHG *sagB pbp4* (SJF 5147)	NewHG *sagB::kan^R pbp4::ery^R*	This study

Table 2.3 The strains of *Staphylococcus aureus* used within this study

ery^R, erythromycin resistance; *kan^R*, kanamycin resistance; *spec^R*, spectinomycin resistance; *tet^R*, tetracycline resistance; *tetM^R*, minocycline resistance.

Species	Strain	Genotype	Source
Enterococcus faecalis	OG1RF	Wildtype background	(Bourgogne *et al.*, 2008)

Table 2.4 Other bacterial strains used in this study

2.6   Growth Conditions

Standard conditions for growth conditions used TSB. Media was inoculated using an overnight culture produced by adding a single colony to 10 ml TSB in a 50 ml Falcon tube, which was left overnight in a water bath (Julabo) at 37 °C with shaking at 200 rpm. The overnight culture was used to inoculate 50 ml fresh media in a 250 ml conical flask to produce an optical density (OD_{600}) of 0.05. Flasks were left in a water bath at 37 °C with shaking at 200 rpm to produce a culture at mid-exponential phase (OD_{600} 0.4-0.8), unless otherwise stated.

2.7   Determination of bacterial density

2.7.1   Optical density measurements

Optical density measurements of liquid culture were taken using a Biochrom WPA Biowave DNA spectrophotometer at a wavelength of 600 nm (OD_{600}), determining the bacterial load of a culture. If required, a 1:10 dilution was made using sterile culture media.

2.7.2   Direct cell counts (CFU/ml)

Direct cell counts were performed to quantify viable bacterial numbers. Bacterial suspensions were serially diluted 1:10 in sterile PBS. 10 µl of each dilution was spotted onto TSA plates, allowed to dry and incubated at 37 °C overnight. The number of colony forming units (CFUs) was directly counted from the plates after incubation.

2.8   Growth Curves

Strains were streaked from Microbank bead frozen stocks (stored at -80 °C) onto TSA containing the appropriate concentration of antibiotic (Chapter 2.3) if required to select for the strain. An overnight culture was made as in Chapter 2.6, which was used to inoculate 50 ml of pre-warmed TSB in 250 ml conical flask to an OD_{600} of 0.01. Cultures were grown in triplicate as in Chapter 2.6, and growth was measured hourly by OD_{600} measurements (Chapter 2.7.1) and/or direct cell counts (Chapter 2.7.2) until stationary phase was reached.

2.9   Centrifugation

The following centrifuges were used to harvest samples:

- Eppendorf microcentrifuge 5418 with a capacity of up to 18 x 1.5- or 2-ml microfuge tubes, maximum speed 16873 x g (14000 rpm).
- Sigma centrifuge 4K15C with a capacity of 16 x 50 ml falcon tubes, maximum speed 5525 x g (5100 rpm).
- Avanti High Speed J25I centrifuge, Beckman Coulter:
  - JA-25.50 rotor with a capacity of up to 6 x 50 ml, maximum speed 75000 x g (25000 rpm).
- Avanti High Speed J-26XP centrifuge, Beckman Coulter:
  - JLA 8.1000 rotor with a capacity of 6 x 1000 ml, maximum speed of 15970 x g (8000 rpm).

2.10   Sonication

Samples were sonicated using a Soniprep 150 Plus bench-top ultrasonic disintegrator (MSE) with an exponential microprobe (tip diameter of 3 mm). Unless otherwise stated, 400 µl of sample was sonicated at an amplitude of 5 microns for 20 seconds on ice.

2.11   DNA techniques

2.11.1 Genomic DNA extraction

1 ml of an overnight culture (Chapter 2.6) was centrifuged at 14000 rpm for 5 min to harvest cells. The pellet was resuspended in 190 μl of dH$_2$O to which 10 μl stock Lysostaphin was added and then incubated at 37 °C for 1 hour. Genomic DNA was then purified using a Qiagen DNeasy Blood and Tissue kit according to manufacturer's instructions.

2.11.2 Primer design

Primers for PCR amplification, 20 - 30 nucleotides in length, were synthesised by Eurofins MWG Operon. Primers were designed based on the genomic DNA sequence of *S. aureus* 8325. Primers were resuspended in nuclease-free water (New England Biolabs) to 100 and 10 μM stock and working solutions respectively and stored at -20 °C. The primers used in this study are listed in Table 2.5.

Primer	Sequence (5'-3')	Application	Source
Atl_TnINS_F	ACATTTACAGGTGATTTAGCTGTGTTG	Amplifies a region of the *atl* gene. Forward primer.	Dr B. Salamaga (University of Sheffield)
Atl_TnINS_R	TCATGATACAGCTAATGATCGTTCGAC	Amplifies a region of the *atl* gene. Reverse primer.	Dr B. Salamaga (University of Sheffield)
psagA_F	TCTCCGATACCAATCCCAGC	Amplifies the *sagA* gene. Forward primer.	This study
psagA_R	GCCAATCAAGCGAGTCCAAA	Amplifies the *sagA* gene. Reverse primer.	This Study
psagB_F	CCGATCAGATATTTTTCAAACA	Amplifies the *sagB* gene. Forward primer.	(Wheeler *et al.*, 2015)
psagB_R	CTTATTCAAATGTTTACTGTCATC	Amplifies the *sagB* gene. Reverse primer.	(Wheeler *et al.*, 2015)
pscaH_F	AGACGACAGCACTTCAGACT	Amplifies a region of the *scaH* gene. Forward primer.	This study
pscaH_R	AACGGGTGTCTCTACAAGTG	Amplifies a region of the *scaH* gene. Reverse primer.	This study
pbp4-1	CTGCAGAAAACTTTATTTTCAAC	Amplifies a region of the *pbp4* gene. Forward primer.	Dr K. Wacnik (University of Sheffield)
pbp4-5	TATATAGAACTATCGATACTAAAC	Amplifies a region of the *pbp4* gene. Reverse primer.	Dr K. Wacnik (University of Sheffield)

Table 2.5 Primers used in this study

2.11.3 Taq polymerase

PCR amplifications were performed using DreamTaq Green Master Mix (Thermo Scientific), as accurate amplification was not needed in this study. Individual reaction volumes were as follows:

DreamTaq Green master Mix (2x)	25 µl
Forward primer (10 µM)	2.5 µl
Reverse primer (10 µM)	2.5 µl
Template DNA	50-100 ng
Nuclease free water	Up to 50 µl

PCR amplification was performed in a Veriti Thermal Cycler (Applied Biosystems). The lid was pre-heated to 105 °C with the following cycling conditions:

1x	Initial denaturation	95 °C	1 min
30x	Denaturation	95 °C	30 s
	Annealing	55-62 °C	30 s
	Extension	72 °C	1 min/kb
1x	Final extension	72 °C	5 min

2.11.4 Agarose gel electrophoresis

A 1% (w/v) agarose gel containing 0.5 µg/ml ethidium bromide was used to separate PCR DNA products in 1 x TAE buffer. Gels had 120 V applied for around 30 min at room temperature. DNA bands were visualised using a UV transilluminator and a photograph was taken using a UVi Tec Digital camera and UVi Doc Gel documentation system. PCR products were compared to fragments of one of two DNA ladders (Table 2.6).

84

Marker	DNA fragment size (kb)
GeneRuler 1 kb DNA ladder (Thermo Scientific)	10.0
	8.0
	6.0
	5.0
	4.0
	3.5
	3.0
	2.5
	2.0
	1.5
	1.0
	0.75
	0.50
	0.25
Quick load purple 2-log DNA ladder (New England Biolabs)	10.0
	8.0
	6.0
	5.0
	4.0
	3.0
	2.0
	1.5
	1.2
	1.0
	0.9
	0.8
	0.7
	0.6
	0.5
	0.4
	0.3
	0.2
	0.1

Table 2.6 DNA fragments used as size markers for agarose gel electrophoresis

2.12   Phage techniques

2.12.1 Bacteriophage

Phage transduction of *S. aureus* was performed using bacteriophage φ11 (Mani *et al.*, 1993).

2.12.2 Preparation of phage lysate

The donor strain of *S. aureus* was grown overnight as in Chapter 2.6. 200 µl of the overnight culture was then mixed with 5 ml of TSB, 5 ml of phage buffer (Chapter 2.2.6) and 100 µl of a φ11 phage lysate stock in a sterile 25 ml Universal tube. This was incubated at 25 °C overnight until the mixture had cleared. The lysate was then filter-sterilised with a 0.2 µm pore filter (Merck) and stored at 4 °C until required.

2.12.3 Phage transduction

A single colony of the recipient *S. aureus* strain was inoculated into a 250 ml conical flask containing 50 ml LK which was incubated overnight in a water bath at 37 °C with shaking at 200 rpm. The resulting overnight culture was harvested by centrifugation at 5000 x g for 10 min at room temperature and resuspended in 3 ml of fresh LK. 500 µl of the recipient strain was then combined with 1 ml fresh LK, 10 µl 1 M $CaCl_2$ and 500 µl donor phage lysate in a 25 ml Universal tube. The tubes were incubated at 37 °C for 25 mins without shaking, and then a further 15 mins with shaking. 1 ml ice cold 0.02 M sodium citrate was added to the mixture, which was then incubated for 5 min on ice. The cells were harvested by centrifugation at 5000 rpm at 4 °C for 10 min and the supernatant was discarded. The pellet was resuspended in 1 ml ice cold 0.02 M sodium citrate and incubated on ice for 45 to 90 min. 100 µl of cells were spread on LK agar plated containing 0.05 % (w/v) sodium citrate and the appropriate antibiotics for selection.

Plates were incubated at 37 °C for 24 to 48 hours until single colonies were visible. These were picked and streaked onto TSA plates containing the selective antibiotics.

2.13   Purification of Sacculi

An overnight culture (made as in Chapter 2.6) was used to inoculate 50 ml of media (normally TSB) in a 250 ml conical flask to an OD_{600} of 0.05. This was incubated at 37 °C, 200 rpm until the desired OD_{600} was reached (generally OD_{600} ~0.6). Cultures were centrifuged to harvest cells and resuspended in Tris HCl pH 7.5 containing 2 % SDS (w/v) and boiled for 10 min to kill cells and inactivate enzymes before being harvested by centrifugation and washed once with dH_2O. Thick suspensions of boiled cells were added to lysing matrix tubes containing 0.1 mm silica beads (Lysing Matrix B, MP Biomedicals). The cells were sheared 10 times at 6.0 m/s for 30 sec using an MP Biomedicals FastPrep 24 Homogeniser, with samples being kept on ice between cycles to prevent overheating. Sacculi were separated from the lysing matrix by centrifuging for 30 sec at 100 x g and collecting the supernatant. The sacculi were harvested from the supernatant and resuspended in 4 % (w/v) SDS and boiled for 30 mins to remove non-covalently bound cell wall components. Cells were harvested again and resuspended in Tris pH 7.5 with SDS/EDTA/DTT (Chapter 2.2.3) and boiled for 30 mins to remove remaining non-covalently bound proteins. Remaining SDS was removed by washing the pellet six times in dH_2O and pellet collected by centrifugation, removing the supernatant each time. Pellets were resuspended in 50 mM Tris HCl pH 7.5 containing 2 mg/ml pronase (Table 2.2) to remove any covalently bound proteins. Wall teichoic acids and any other remaining cell wall polymers were removed by incubating the sacculi in 250 µl 48 % (w/v) hydrofluoric acid (HF) at 4 °C for 48 hours. The purified sacculi were washed in alternating 50 mM Tris HCl pH 7.5 and dH_2O until the pH was raised to at least 5.0, ending on a dH_2O wash to remove Tris HCl residue. Purified sacculi were pelleted and stored at -20 °C until required.

2.14   Digestion of peptidoglycan to produce soluble muropeptides

Purified PG (~2 mg) was resuspended in 10 µl sodium phosphate buffer (Chapter 2.2.7), 90 µl dH$_2$O and 50 µg mutanolysin. This was incubated overnight (~16 hours) at 37 °C and the reaction was stopped by boiling for 5 minutes. Muropeptides were collected by centrifugation at 16873 x g and reservation of the supernatant.

2.15   Reduction of samples by sodium borohydride

Soluble muropeptides were mixed with an equal volume of sodium borate buffer (Chapter 2.2.8) to raise the pH to at least pH 9. Sodium borohydride was added, and the reaction was left for 15 minutes at room temperature. The reaction was stopped by destruction of excess borohydride by the addition of phosphoric acid to a pH of at least 4. The pH was then raised to ~5.6 using NaOH and then filtered (0.2 µm, Merck) to remove any insoluble contaminants from the sample.

2.16   HPLC analysis of muropeptides using the ammonium phosphate buffer system

Samples were analysed using a Thermo Scientific Hypersil GOLD aQ column (200 x 2.1 mm, 1.9 µm particle size), which was pre-equilibrated with Buffer A (Chapter 2.2.4.1) in a Waters HPLC system. *S. aureus* muropeptides were eluted from the 200 x 2.1 mm column using a flow rate of 0.3 ml/min, using a multi-step convex gradient over 63 minutes for *S. aureus* (Table 2.7), and 45 minutes for *E. faecalis* (Table 2.8). Eluted muropeptides were detected by measuring absorbance at 202 nm and analysed using Chromeleon version 6.80.

Time (min)	% Buffer A	% Buffer B
0	100	0
5	95	5
23	90	10
42	85	15
47	70	30
47.1	0	100
55	0	100
55.1	100	0
63	100	0

Table 2.7 RP-HPLC elution gradient for *S. aureus* muropeptides analysis

Time (min)	% Buffer A	% Buffer B
0	100	0
30	70	30
30.1	10	90
35	10	90
35.1	100	0
45	100	0

Table 2.8 RP-HPLC elution gradient for *E. faecalis* muropeptides analysis

2.17   Phosphate free muropeptide digestion and mass spectrometry analysis

When muropeptides were to be analysed by mass spectrometry (MS) a phosphate free buffer was used to remove the need to desalt samples. Purified PG (~2 mg) was resuspended in 90 µl MilliQ water and 10 µl 50 mM ammonium formate buffer pH 4.8 was added, along with 20 µl cellosyl (Table 2.2). This was incubated overnight at 37 °C, 900 rpm in a thermal shaker (Eppendorf). Cellosyl was inactivated at 100 °C for 10 min, and samples were centrifuged at 16873 x g for 10 min, reserving the supernatant. The supernatant was dried using a speed vac vacuum concentrator (Thermofisher) and resuspended in 25 µl of MilliQ water and 25 µl of 0.5 M Ammonium buffer pH 9.0 (Chapter 2.2.8). Samples were reduced at room temperature for 30 min by the addition of tetra methyl ammonium borohydride. Samples were then acidified using 5 % (v/v) formic acid to pH 4.0 – 4.5. Samples were then reduced to around 30 µl using a speed vac, and 15 µl to the HPLC system (Agilent 1100, with an ACE3 C-18AQ column (1 × 150 mm). RP-HPLC conditions were as follows: buffer A (Chapter 2.2.10.1) to a maximum of 50% buffer B (Chapter 2.2.10.2) over 128 min at a flow rate of 0.05 ml/min (Table 2.9). Muropeptides were detected by UV at 205 nm.

MS analysis was performed using a modified protocol of previously published methods (Dembek *et al.*, 2018). Muropeptides were analysed by infusion MS by directing RP-HPLC eluate to the ion source on an LTQ mass spectrometer (Thermo). The spray voltage was set at 3.6 kV and the transfer capillary temperature at 200 °C. Mass spectra were collected over the range m/z = 300–2000 with MS/MS fragmentation spectra triggered for all ion signals >5 × 10^3 intensity. Analysis was performed using Xcalibur QualBrowser v2.0 (Thermo). Relative quantities of muropeptides were calculated by the normalised percentage area under each peak from which the chemical structure had been determined. Peak identity was assigned based on the greatest abundance of an ion within the peak. MS/MS fragmentation spectra confirmed the identity of monomeric and dimeric muropeptide species. Higher crosslinked species were assigned based on observed mass only.

Time (min)	% Buffer A	% Buffer B
0	100	0
5	100	0
10	98	2
30	94	6
58	93	7
100	92	8
110	50	50
112	15	85
117	15	85
118	100	0
128	100	0

Table 2.9 HPLC elution gradient for analysis of *S. aureus* muropeptides by MS

2.18 Animal models of infection

2.18.1 Zebrafish embryo model of infection

2.18.1.1 Zebrafish strains and husbandry

London Wild Type (LWT) strains were used for all zebrafish experiments in this study. Adult zebrafish were maintained by staff at the University of Sheffield Bateson Centre Zebrafish Facility. Adult fish were kept in a continuous re-circulating closed system aquarium with a light/dark cycle of 14/10 hours at 28 °C. LWT zebrafish embryos were kept in E3 medium at 28.5 °C.

2.18.1.2 Zebrafish E3 medium (x 10)

NaCl	50 mM
KCl	1.7 mM
$CaCl_2$	3.3 mM
$MgSO_4$	3.3 mM

A 1 x working stock was made by diluting the 10 x with dH_2O. A final concentration of 0.0005 % methylene blue (Nusslein-Volhard and Dahm, 2002) was added to prevent fungal growth, and the 1 x E3 medium was sterilised by autoclaving.

2.18.1.3 Methylcellulose

A 3.0 % (w/v) solution of methylcellulose was prepared in E3 medium. The solution was stirred, frozen and defrosted multiple times to ensure complete solubilisation (Nusslein-Volhard and Dahm, 2002). The solution was drawn up into 20 ml syringes and stored at -20 °C. Each aliquoted syringe was thawed at 28.5 °C for use, and short-term storage.

2.18.1.4 Zebrafish anaesthesia

Zebrafish embryos were anaesthetised in 0.02 % (w/v) 3-amino benzoic acid ester (tricaine, Sigma) prior to injection. The working stock consisted of 0.4 % (w/v) tricaine in 20 mM Tris-HCl pH 7 (prepared by the staff at the University of Sheffield Bateson Centre Zebrafish Facility). The working stock was kept at 4 °C in the dark.

2.18.1.5 Microinjections of *S. aureus* into zebrafish embryos

S. aureus strains were grown from an overnight culture (Chapter 2.6) used to inoculate 50 ml TSB in a 250 ml conical flask at 37 °C, 200 rpm, until OD_{600} reached approximately 1. 40 ml of the culture was centrifuged in a 50 ml falcon tube at 5100 rpm (Sigma centrifuge 4K15C) for 10 min at 4 °C. The supernatant was discarded, the pellet washed in sterile PBS, centrifuged as before and resuspended in sterile PBS to a known concentration. This known concentration was determined based on the OD_{600} of each culture, with bacterial quantification performed before and after a microinjection experiment. To do this, four injections were performed into 1 ml of sterile PBS, vortexed and, in duplicate, 100 μl was spread onto TSA. After incubation overnight at 37 °C the number of CFU was directly counted from the plate.

Zebrafish embryos were dechorionated manually at roughly 28 hpf, before being injected at roughly 30 hpf with 1 nl of bacterial suspension from a calibrated glass needle. The fine bore glass needles for microinjection were made by heating non-filament glass capillary tubes (World Precision Instruments, WPI) in an electrode puller. Bacterial inoculum was loaded into the microinjection needles using microcapillary pipettes (Fisher Scientific Ltd) and injection volume was calibrated using a graticule slide to 1 nl. Before injection embryos were briefly immersed in 0.02 % (w/v) buffered tricaine anaesthetic solution in E3 before being immobilised onto a glass slide covered with 3.0 % (w/v) methylcellulose. Injections into the zebrafish embryo circulation valley were performed using, a pneumatic micropump (WPI, PV820), a micromanipulator (WPI) and

a dissecting light microscope (Leica). After injection, embryos were removed from the methylcellulose to Petri dishes containing sterile E3 medium and left for 1 – 2 hours at 28.5 °C to allow any remaining methylcellulose to dissolve. Embryos were placed into fresh E3 medium and then placed individually into 96-well plates with 250 µl of E3 per well.

2.18.1.6 Determination of zebrafish embryo mortality

For each experiment, at least 20 fish were injected with *S. aureus* for each strain investigated. Zebrafish embryos were inspected twice a day for the presence of a heartbeat, absence of which was confirmation of death, using a dissecting light microscope (Leica).

2.18.1.7 Determination of *S. aureus* growth within zebrafish embryos

To quantify the bacterial growth within the zebrafish embryos single embryos were collected with 100 µl E3 medium into 2 ml cap containers (Peqlab). Embryos were individually homogenised using a PreCellys 24-dual (Peqlab) and the resulting homogenates were serially diluted in sterile PBS and plated onto TSA as 10 µl spots. The limit of detection for this experiment was 10 CFU/embryo. Clearance was defined as being below the limit of detection.

2.18.2 Murine Sepsis Model

6-7-week-old female BALB/c mice were purchased from Charles River (Margate, UK) and maintained at the University of Sheffield's Biological Services Unit using standard husbandry protocols. Bacteria for inoculum were grown to stationary phase in TSB and washed 3 times in sterile endotoxin free PBS and finally resuspended in PBS containing 10% (w/v) BSA and stored at -80 °C until required. Dilutions were made to the bacterial stocks prior to injection using sterile endotoxin free PBS, with doses ranging from 1×10^5

94

– 1×10^7 CFU per mouse. Purified PG required for injections was centrifuged for 2 minutes at 14000 rpm and then suspended in sterile endotoxin free PBS, before being sonicated (Chapter 2.10) at an amplitude of 10 microns for 30 seconds. PG was injected at a dose of 250 μg per mouse and was injected at the same time as the bacteria.

Mice were kept at 37 °C for 10 mins prior to injections to dilate veins. Mice were intravenously injected in the tail vein, with 100 μl of culture being injected. Viable bacteria in the inoculum were quantified by serial dilution and plating onto TSA, and leaving overnight at 37 °C, before directly counting the CFU to determine injected dose.

Mice were screened for health and wellbeing twice daily throughout the experiment, with weights being recorded daily. At the end of the experiment (normally 72 hpi), or if mice were found to have exceeded severity limits, mice were sacrificed under Schedule 1 using concussion of the brain by striking the cranium with death being confirmed by cervical dislocation. Livers and kidneys (and where possible spleens, lungs and hearts) were then harvested and stored at -20 °C until processing. Sterile PBS (3 ml to livers, 2 ml to other organs) was added and organs were homogenised using a Precellys 24 homogeniser (for 20 seconds). CFU per organ were determined by plating 10 μl spots of serial dilutions of the homogenate onto TSA plates and incubating at 37 °C overnight. The limit of detection within livers was 600 CFU and for all other organs sampled 400 CFU.

2.18.3 Use of clodronate for macrophage depletion

Clodronate liposomes and empty control PBS liposomes (Liposoma research, the Netherlands, clodronateliposomes.com) were ordered and injected as per manufacturer's instructions. For mice, clodronate and control liposomes were injected at a dose of 100 μL of suspension per 10 grams (stock 5 mg clodronate/mL) intravenously 24 hours before infection. Mice were then infected with 1×10^5 CFU of

bacteria as in Chapter 2.18.2. For zebrafish, 1 nl of clodronate or control liposomes were injected into the circulation valley of zebrafish embryos at 24 hpf, before being infected with a dose of around 150 CFU of bacteria at 30 hpf as in Chapter 2.18.1.5.

2.19   Collection of peptidoglycan from murine organs

Organs of one type (n = 10) were pooled from a single mouse experiment that shared the initial starting inoculum. Cells were recovered by centrifugation at 18000 rpm (Avanti centrifuge, JA 25.50 rotor, Chapter 2.9) and resuspended in Tris HCl (50 mM, pH 7.5) containing 2% SDS (w/v) and boiled for 10 min to kill cells. Cells were washed twice in dH_2O, and the pellet resuspended in 10 ml 50 mM Tris HCl pH 7.5. The mixture was transferred to a Braun Homogeniser bottle containing 50 g of sterile, acid-washed glass beads and placed on ice. The contents of the bottle were disrupted using a Braun homogeniser (Braun, Germany). Each bottle was homogenised for 10 x 30 sec, with 5 min on ice in-between each homogenisation. The beads were separated from the broken cells with a vacuum sintered glass filter, and the resulting filtrate centrifuged (18000 rpm, 10 min, 4 °C, Avanti centrifuge, JA 25.50 rotor, Chapter 2.9) to pellet the sacculi. The resulting pellet was then purified in the same way as Chapter 2.13.

2.20   Human cell work

2.20.1 Monocyte derived macrophages (MDMs)

Monocytes were isolated from peripheral blood mononuclear cells (PBMCs) from healthy donors, as previously described (Boldock *et al.*, 2018). Ficoll Plaque (GE Healthcare) density centrifugation was used to isolate PBMCs from donor blood, which were seeded into 24 well plates (Corning) at 2×10^6 cells/ml in RPMI 1640 medium with the addition of 2 mM/l L-glutamine (Lonza) which was further supplemented with 10 % (v/v) new-born foetal calf serum (Gibco). This set up resulted in wells containing approximately 2×10^5 MDM/ml. After incubating for 24 hours at 37 °C with 5 % (v/v) CO_2, the cells were washed with fresh RPMI 1640 with 2 mM/l L-glutamine and with

10 % (v/v) low endotoxin heat inactivated foetal calf serum (Biosera) to remove non-adherent cells. Cells had supernatant removed twice a week which was replaced with fresh supplemented RPMI 1640. Differentiated MDM were used at 14 days.

All media and reagents were warmed to 37 °C before being used with MDMs unless otherwise stated. Differentiated MDMs were challenged with *S. aureus* strains at a MOI of 5 (i.e. 1 x 10^6 CFU per well of 2 x 10^5 MDMs), which were added to the MDMs in fresh RPMI 1640. The MDMs were challenged with *S. aureus* for 4 hours at 37 °C, 5 % (v/v) CO_2, after which infected media was removed and MDMs were washed with ice cold PBS. Any remaining extracellular bacteria were killed by the addition of 100 μg/ml gentamicin in fresh RPMI 1640 media and incubation for 30 min. After this the wells were washed with PBS and the MDM were maintained in fresh RPMI 1640 supplemented with 4 μg/ml gentamycin and 0.8 μg/ml lysostaphin until the desired time point.

At the desired time points MDM were washed with PBS and incubated with 250 μl 2 % (w/v) saponin at 37 °C, 5 % (v/v) CO_2 for 12 min. PBS was added to make well volume 1 ml and cells were further lysed by vigorous pipetting. Cell lysis was confirmed by light microscopy. Viable intracellular CFU was determined by serial dilution, and spotting 10 μl onto TSA plates, which were left at 37 °C overnight. Extracellular bacteria killing by gentamycin and lysostaphin was confirmed by fixing control MDM with 2 % (v/v) paraformaldehyde before bacterial challenge, and then exposing to gentamycin and lysostaphin then lysed as described, showing absence of bacteria in lysates. Other MDM were not infected with *S. aureus* and treated as above, to confirm that all bacteria recovered came from the initial inoculum. All MDM experiments had two biological repeats for each time point and strain.

2.20.2 Neutrophils

Neutrophil work was carried out by Ms Natalia Hajdamowicz (University of Sheffield), following a modified protocol described (Boldock *et al.*, 2018). Neutrophils were purified from anti-coagulated human blood and kept at 37 °C with 5 % CO_2 (v/v) in RPMI 1640 medium. To 96 well Tissue Culture Corning plate containing 90 µl of approximately 2.5 x 10^6 cells/ml (around 225000 neutrophils per well) 10 µl of bacterial stock culture was added to produce a MOI of 5. After 30 minutes, gentamycin was added to 40 mg/ml and a sample was taken without gentamycin treatment to calculate phagocytosed bacteria numbers. After 60 and 120 min of co-culture, 100 µl of sample was transferred to a 1.5 ml Eppendorf tube and centrifuged for 3 min at 400 x g to recover neutrophils. Neutrophils were washed with 1 ml ice cold sterile PBS, and then lysed with 1 ml room temperature alkali water (6 M NaOH added to dH2O until pH 11 and filtered) and vigorous pipetting. Intracellular CFU were determined by serially diluting in sterile PBS and plating 10 µl spots onto TSA, which were left overnight at 37 °C, and CFU calculated the next day by directly counting.

2.21 Transmission electron microscopy (TEM)

After organ CFU had been determined (Chapter 2.18.2) 1 ml of homogenate was centrifuged (16873 x g, 10 min, room temperature) to produce a pellet. The resulting pellet was mixed with 2.5 % (w/v) glutaraldehyde and left overnight at 4 °C to fix samples. Glutaraldehyde was removed from the pellet and washed with PBS. Two further PBS washes were performed, with PBS being left on the sample for 20 min at 4 °C before being removed and discarded. Samples were then mixed with 2 % (w/v) aqueous osmium tetroxide for 2 hours (room temperature) for secondary fixation. Excess osmium tetroxide was removed using two PBS washes, with PBS being left on the sample for 10 min before being discarded. Samples were dehydrated by the addition of incremental concentrations of ethanol (75 % (v/v), 95 % (v/v) and 100 % (v/v) ethanol) for 15 min each before being removed and the higher concentration added. Samples

were then incubated twice with propylene oxide to complete dehydration, each time for 15 min.

Samples were mixed with a 50 % (w/v) propylene oxide to 50 % Epon resin (v/v) mixture and left overnight at room temperature to allow infiltration of the sample. The resin was removed, and any remaining propylene oxide was removed by evaporation over 1 hour. Pure Epon resin was added to the sample, which was left for 4 hours, after which the resin was removed and replaced with fresh pure Epon resin for another 4 hours. Epon resin was removed and the samples were imbedded in fresh resin. Resin polymerisation was performed at 60 °C for 48 – 72 hours. 80 nm thin sections of the samples were produced using an Ultracut E Ultramicrotome (Reichert-Jung) at room temperature. The thin sections were mounted onto 200-square mesh copper TEM grids (Agar Scientific) already treated with a 1.5 % Pyroxylin (w/v, in amyl acetate) film. Mounted sections were stained in 3 % (w/v) aqueous uranyl acetate for 30 min and washed with dH2O. Sections were then stained with Reynold's lead citrate (Reynolds, 1963) for 5 min and washed with dH_2O.

Sections were imaged using a FEI Tecnai T12 Spirit Transmission Electron Microscope operating at 80 kV. Images were recorded using a Gatan Orius™ SC1000B bottom-mounted CCD camera. TEM images were analysed using Fiji software (Schindelin *et al.*, 2012). Cell area was calculated using adapted methodology (Zhou *et al.*, 2015). Two perpendicular measurements were made along the long and short axis the cell, from the edge of the cell wall to the edge of the cell wall. The measured radii were then used to calculate the estimated cell area. For cell wall measurements, four equidistant cell wall measurements were made around the cell where the cell wall was clearly defined (Matias and Beveridge, 2006).

2.22   Flow cytometry

Analysis of *S. aureus* particle size was analysed by measuring the forward scatter (FSC) of particles. Overnight cultures of *S. aureus* strains were grown in Chapter 2.6. These were used to inoculate 1 ml of TSB in a well of a 24 well plate to an OD_{600} of 0.05. The 24 well plate was left at 37 °C and 200 rpm until an OD_{600} of 0.6 (exponential phase) was achieved. Bacteria were diluted 1:100 in PBS filtered through a 0.2 µm syringe filter to remove salt crystals that could interfere with the measurements. FSC was analysed by flow cytometry using a Millipore Guava EasyCyte system. Light scatter data were obtained with logarithmic amplifiers for 2500 events, and each strain was measured in triplicate, from three independent overnight cultures.

2.23   Ethics statement

Murine work was carried out according to UK law in the Animals (Scientific Procedures) Act 1986, under Project License PPL 40/3699 and Project License P3BFD6DB9 (*Staphylococcus aureus* and other pathogens, pathogenesis to therapy). Personal license PIL IF5CD6EC4 (Categories A, B and C).

All zebrafish work was carried out according to the stipulations set out in Project License PPL 40/3574. However, it is important to note that zebrafish embryos fewer than 5 days post fertilization (dpf) are not protected under the Animals (Scientific Procedures) Act 1986 as they are not capable of independent feeding.

Human blood was obtained from healthy volunteers, with informed consent, in compliance with the guidelines of the South Sheffield Research Ethics Committee (07/Q2305/7).

2.24   Statistics

All statistical analysis was performed using Prism version 8.3.0 (GraphPad). Doubling times from growth curves was determined by fitting a curve with non-linear regression (Malthusian growth) using Prism. This was fitted to the most exponential part of the graph.

Zebrafish experiments are representative of at least n = 2 unless otherwise stated. Figures of zebrafish experiments show combined results of replicate experiments. In zebrafish embryo survival experiments, the Kaplan-Meier method was employed. Comparison between survival curves was made using the log-rank (Mantel Cox) test.

For bacterial count and weight change comparison in murine experiments the Mann-Whitney U test was used. For comparison of two or more independent samples simultaneously the Kruskal Wallis test was applied with Dunn's multiple comparison test. For clonality experiments, and. Shannon's diversity index was calculated using the equation $H = -\sum_{i=1}^{R} pi \ln(pi)$, (where H = Shannon diversity index and p_i = the proportion of species i relative to the total number of species present). Species evenness was derived from the Shannon diversity index using the equation $EH = H/\ln S$ (where E_H = species evenness, H = Shannon diversity index and S = the total number of species within the community (species richeness)). Species evenness within an organ over time was then analysed using mean linear regression analysis. For relative fitness experiments, the equation $w = \frac{x_{2(1-x_1)}}{x_{1(1-x_2)}}$ was used and analysed using a one sample Wilcoxon signed rank test (w = relative fitness, X_1 = starting mutant proportion and X_2 = ending mutant proportion).

2.25   Collaborative work

Chapter 3 – TEM samples were given to Ms Lucia Lafage (University of Sheffield), who fixed, stained and sectioned samples. Lucia also assisted me in collecting the images for analysis. Digestion of samples for LC-MS was performed with assistance from Dr Jacob Biboy (University of Newcastle), while samples were analysed by LC-MS with assistance by Dr Joe Gray (University of Newcastle), but all results were analysed by me. *E. faecalis* strain and infected murine kidneys were provided by Dr Josie Gibson (University of Sheffield; Figure 3.10).

Chapter 4 – Ms Simone Tazoll (University of Lübeck, a master's level student) assisted me in producing some repeats of survival curves for some glucosaminidase mutants, including figures 4.1ABC, 4.2BC and 4.3AB. Flow cytometry was performed with the assistance and expertise of Dr Bartłomiej Salamaga (University of Sheffield).

Chapter 5 – Neutrophil experiments were performed by Ms Natalia Hajdamowicz (University of Sheffield), I provided intellectual input into experiment design and analysis of results. Mr William Turnbull was an undergraduate student at the University of Sheffield working on a Harry Smith vacation studentship. William assisted me to produce survival and OD_{600} growth curves for SH1000 *pbp3, pbp4* and *pbp3 pbp4.* Dr Eric Pollitt (University of Sheffield) gave advice on statistical analysis for relative fitness and population dynamics experiments.

All murine experiments were conducted in collaboration with Mr Oliver Carnell, Dr Josie Gibson, Dr Grace Pidwill or Dr Daria Shamarina (University of Sheffield). For all experiments in this study, I wrote the Individual Study Plans (ISPs), prepared the inoculum, infected and culled mice and managed the overall experimental procedures and performed data analysis. Collaborators assisted me in loading needles, writing down weight and wellbeing measurements and the dissection of mice. I also collaborated in the same way for some of their murine experiments.

Chapter 3

Murine murein: The structure of *S. aureus* peptidoglycan during infection

3.1   Introduction

PG structure is discussed in depth in Chapter 1.2. Briefly, almost all bacteria are surrounded by an essential layer of PG (murein) (Vollmer *et al.*, 2008a). PG consists of repeating units of *N*-acetylglucosamine and *N*-acetylmuramic acid linked by β-1-4 glycosidic bonds forming the glycan backbone (de Pedro and Cava, 2015). Peptide side chains are linked to the *N*-acetylmuramic acid residue, which, in *S. aureus,* consist of L-Ala, D-iGlx (Gln or Glu), L-Lys, D-Ala, D-Ala (Vollmer *et al.*, 2008a; Kühner *et al.*, 2014). Stem peptides allow crosslinking of PG. In *S. aureus* these crosslinks consist of an interpeptide bridge consisting of five glycine residues. This interpeptide bridge is known as a 3-4 crosslink, linking the L-Lys of one chain to the D-Ala in position 4 of the other chain (Vollmer *et al.*, 2008a). This single macromolecule maintains cell integrity by withstanding turgor pressure, determines and sustains cell shape as well as providing an anchor for other cell wall components (Vollmer *et al.*, 2008a). These anchored cell wall components include surface proteins which are covalently bonded to the terminal glycine residue of non-crosslinked pentaglycine bridges (Navarre and Schneewind, 1999). Wall teichoic acids (WTA) are anchored to the PG of the cell wall via a linkage unit to carbon-6 of *N*-acetylmuramic acid residues of the glycan backbone (Neuhaus and Baddiley, 2003).

PG is commonly analysed using reverse-phase high performance liquid chromatography (RP-HPLC), methodology originally proposed by Bernd Glauner (Glauner, 1988). PG is purified using proteases, removing covalently bound proteins, and surfactants such as SDS to remove non-covalently bound proteins (Glauner, 1988). The PG is then treated with hydrofluoric acid (HF), removing phosphate linked molecules such as WTA (Jonge *et al.*, 1992b). PG is then digested using a *N*-acetyl-β-D-muramidase, resulting in the

production of soluble disaccharide peptides termed muropeptides (Glauner, 1988, Figure 3.1A). The digestion targets the glycan backbone of PG, leaving pentaglycine crosslinks intact, allowing multimeric muropeptides to be detected and analysed (Figure 3.1B). Muropeptides are then reduced, and analysed by RP-HPLC, and a trace measured by UV-absorbance (Glauner, 1988).

To identify UV-absorbance peaks, individual muropeptide containing fractions are collected, desalted by HPLC and analysed by mass spectrometry (MS) sometimes coupled to MS/MS (Jonge *et al.*, 1992b). This is a time consuming process, and it is now common for muropeptides to be analysed by MS or MS/MS coupled with RP-HPLC (LC-MS), meaning that an ion spectra is produced in tandem to the UV-absorbance trace, reducing the time needed for data collection (Bern *et al.*, 2017), as has been done in my study. This methodology still requires the manual analysis and identification of major ions to identify UV-absorbance peak identity, but work has been published to automate this process (Bern *et al.*, 2017).

Muropeptide traces are often complex, with multiple different species being present on a single trace, due to multimeric muropeptides and modifications (Jonge *et al.*, 1992b; de Jonge and Tomasz, 1993)*.* MRSA strains grown in the presence of methicillin show a greatly changed muropeptide composition, with a large reduction in oligomeric muropeptide species and a shift to monomeric and dimeric species (de Jonge and Tomasz, 1993; Müller *et al.*, 2015). The presence of the *mecA* gene with no antibiotic stimulation results in the same muropeptide composition as a wildtype not containing *mecA* (Jonge *et al.*, 1992b)*. S. aureus* PG structure is also influenced by nutrient availability. As cells reach stationary phase, glycine in the medium becomes depleted, resulting in fewer crosslinked muropeptides (Zhou and Cegelski, 2012).
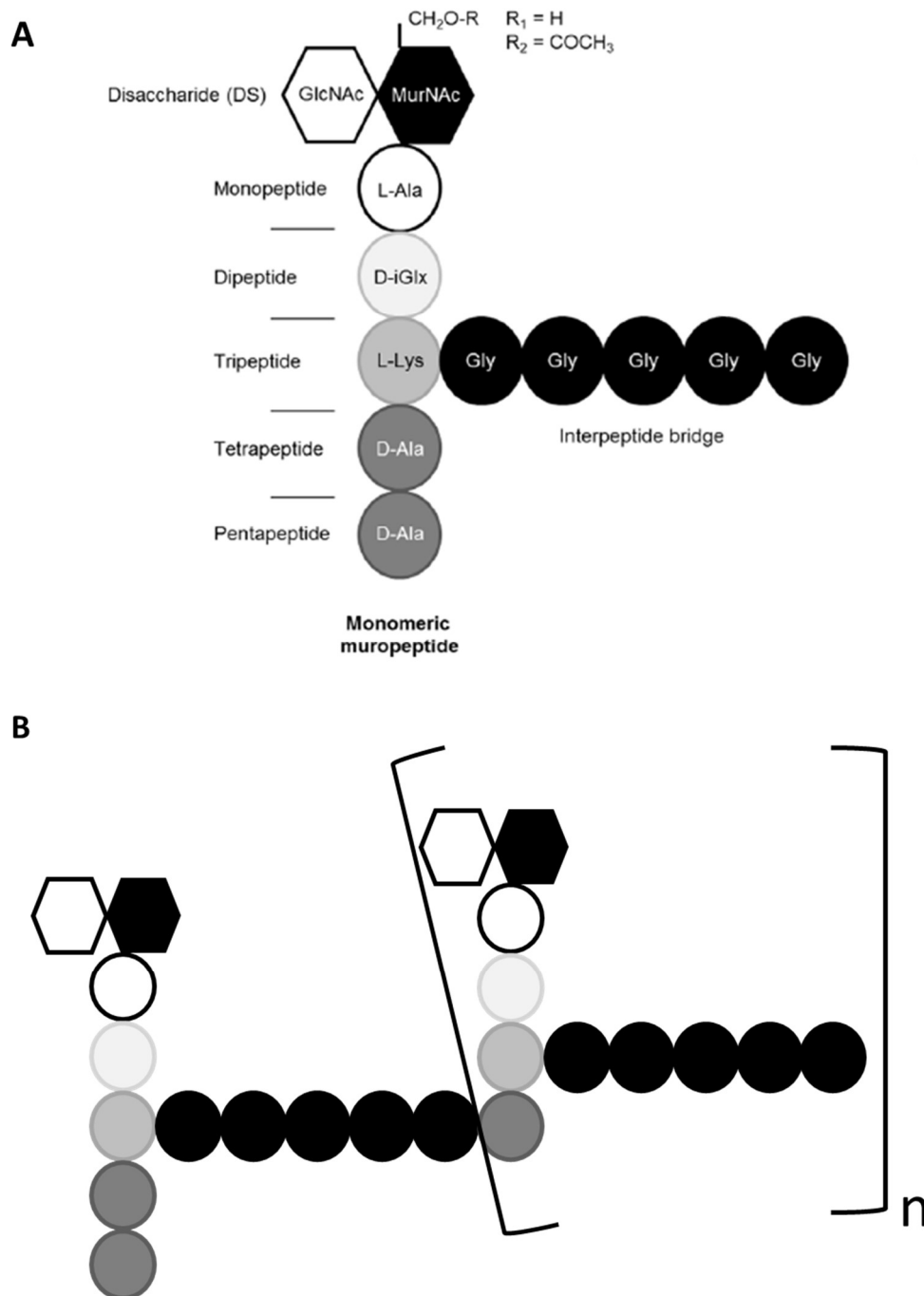
Figure 3.1 Schematic representation of *S. aureus* muropeptides

(A) A *S. aureus* monomeric muropeptide consists of a of an *N*-acetylglucosamine and *N*-acetylmuramic acid residue, with a L-Ala,D-iGlx (Gln or Glu), L-Lys, D-Ala, D-Ala peptide side chain. Bonded to the L-Lys residue is a pentaglycine bridge that can form crosslinks between peptide stems. **(B)** Multimeric monopeptides are formed by crosslinking peptide stems via a pentaglycine bridge, linking adjacent stem peptides. Adapted from Kühner *et al.* (2014).

Several cell wall structural homeostasis mechanisms have also been identified. O-acetylation of *N*-acetylmuramic acid by *oatA* has been shown to render *S. aureus* PG resistant to digestion by lysozyme (Bera *et al.*, 2005), with only pathogenic strains showing this modification (Bera *et al.*, 2006). This modification has been directly shown to contribute to pathogenesis in a murine septic arthritis model of infection (Baranwal *et al.*, 2017). Penicillin binding protein 4 (PBP4) is responsible for the highly crosslinked PG found in *S. aureus* (Wyke *et al.*, 1981a), with around 85% of all muropeptides containing at least one crosslink (Sobral and Tomasz, 2019). Abnormal muropeptide traces have also been produced by inactivating *femA* (de Jonge *et al.*, 1993), a gene required to insert the first and second glycine residues in the pentaglycine bridge (Sobral and Tomasz, 2019). This resulted in an increase of serine containing and mono-glycine crosslinks, as well as being involved in methicillin resistance (de Jonge *et al.*, 1993).

Bacteria live within dynamic and hostile environments, such as a host, which present a variety of different threats to survival. To permit survival within such environments, bacteria may modify their dynamic cell wall to resist environmental conditions. This is described as PG plasticity, with modifications made to PG in response to environmental stimuli, whether that be nutritional status, host interaction or induced by factors such as temperature or oxygen limitation (Cava and de Pedro, 2014; Fang *et al.*, 2016). As *S. aureus* has known cell wall adaptations involved in infection, it can be hypothesised that there may be a plasticity in the muropeptide composition and PG metabolism during an *S. aureus* infection.

3.2 Aims

The aim of this chapter was to determine the structure of *S. aureus* PG during infection, using the murine sepsis model. The specific aims were to:

i. Determine the structure of *S. aureus* PG during infection

ii. Investigate any unique muropeptides of *S. aureus* during infection

iii. Establish *S. aureus* morphology during infection

3.3 Results

3.3.1 Method development

3.3.1.1 Purification optimisation of peptidoglycan from *S. aureus* NewHG

During each purification step for PG isolation (Chapter 2.13) material is lost, reducing the yield of purified material. The number of bacteria recovered from an organ during infection are known (Pollitt *et al.*, 2018) and are likely to be limiting in terms of PG amounts for analysis. For this reason, each purification step was scrutinised to ensure that it was required to produce a high quality muropeptide trace (Figure 3.2). Cells grown in TSB that were only boiled and then treated with mutanolysin showed low levels of muropeptides (Figure 3.2A, all UV absorbance peaks below 400 mAU), whereas treating boiled cells with hydrofluoric acid (HF) increased the yield of muropeptides, with the absorbance reaching 1000 mAU for some UV-absorbance peaks (Figure 3.2B). Boiling cells twice in the presence of SDS (Figure 3.2C,) gave an increased yield compared to boiling the cells in dH_2O (Figure 3.2A), with most UV absorbance peaks having an absorbance of over 500 mAU. However, with a RP-HPLC time of around 30 mins, there is a sharp increase in absorbance (Figure 3.2C) that is not seen in the samples boiled in the presence of SDS and HF treated (Figure 3.2D). This is likely caused by wall teichoic acids (WTA) eluting from the column. As WTA alter the trace, HF treatment will be necessary to purify PG from *in vivo* derived samples. Cells killed by boiling and then treated with pronase (Figure 3.2E, most UV absorbance peaks 500 mAU) show a small increase in yield compared to cells only heat inactivated (Figure 3.2A), but also gives an abnormal increase in absorbance at 30 min, suggesting WTA. This increase abnormality is lost when pronase treated PG is reacted with HF (Figure 3.2F). Treating cells with pronase and boiling cells once in the presence of SDS (Figure 3.2G) also shows increased muropeptide abundance compared to heat inactivating cells (Figure 3.2A), but this also shows the increase in absorbance caused by WTA not seen in the HF treated equivalent (Figure 3.2H). The results suggest that treatment with HF is the most important purification step, improving both the yield and the muropeptide separation of the trace.
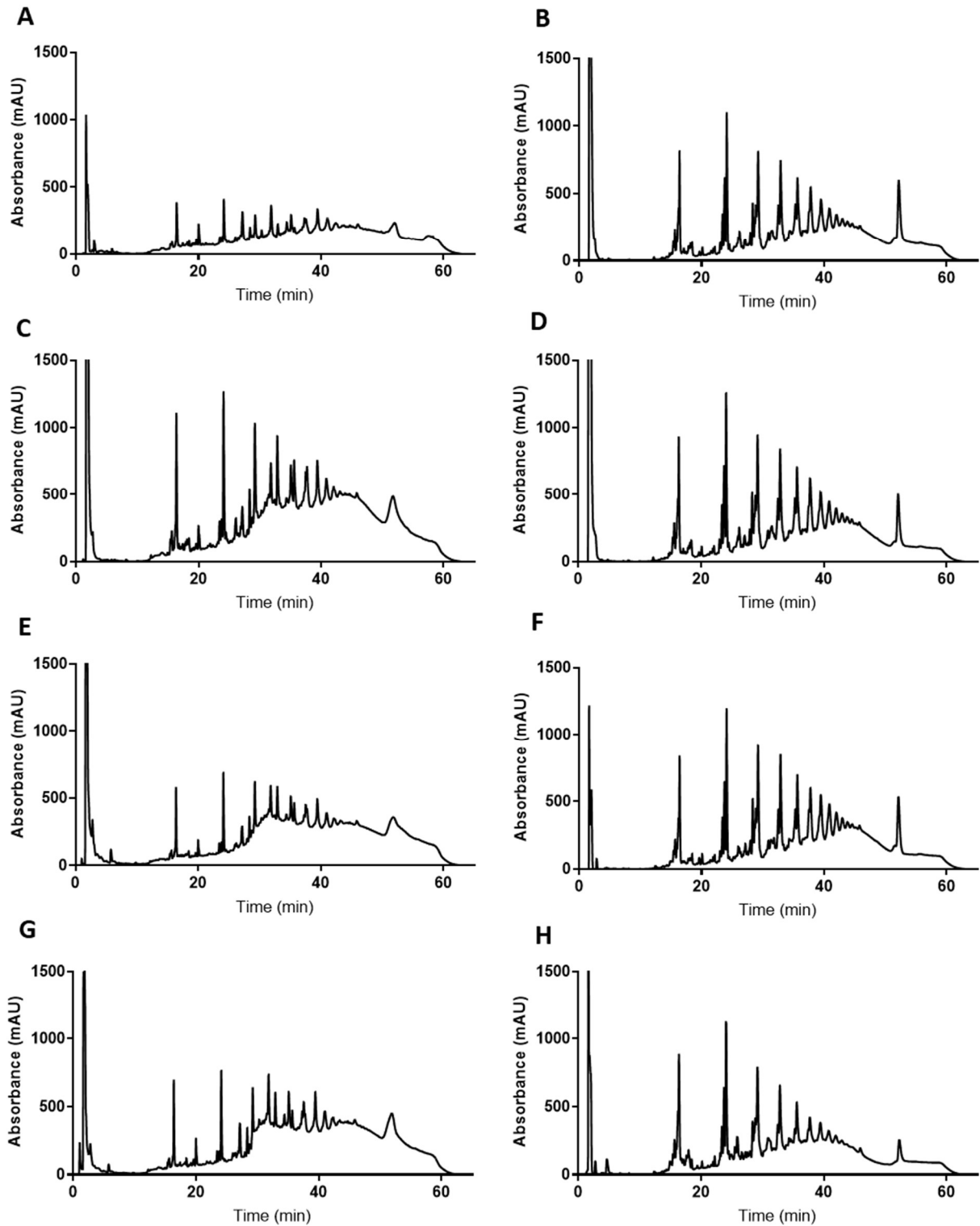
Figure 3.2 Role of purification steps in muropeptide profile determination of *S. aureus* NewHG peptidoglycan by RP-HPLC

Muropeptide profiles of NewHG (SJF 3663) grown in TSB using different purification methods prior to mutanolysin digestion. **(A)** Boiled cells, **(B)** boiled and HF treatment, **(C)** boiled and SDS treated, **(D)** boiled, SDS and HF treated**, (E)** boiled and pronase treated, **(F)** boiled, pronase and HF treated, **(G)** boiled, SDS and pronase treated, **(H)** boiled, SDS, pronase and HF treated.

3.3.1.2 Sensitivity analysis of RP-HPLC muropeptide analysis

A muropeptide trace of PG from *in vivo* grown bacteria has not been reported before. To ensure that this is feasible, the sensitivity of RP-HPLC was scrutinised to determine the fewest number of bacteria possible to produce a muropeptide trace of suitable quality (Figure 3.3). Different volumes of a culture of known CFU/ml were individually purified (Chapter 2.13), digested (Chapter 2.14) and analysed (Chapters 2.15, 2.16). All starting CFU gave recognisable muropeptide profiles. However, the number and UV-absorbance of distinct muropeptides decreased with lower amounts of starting material. A starting CFU of approximately 1.8×10^8 CFU gave a profile suitable for analysis (Figure 3.3F).
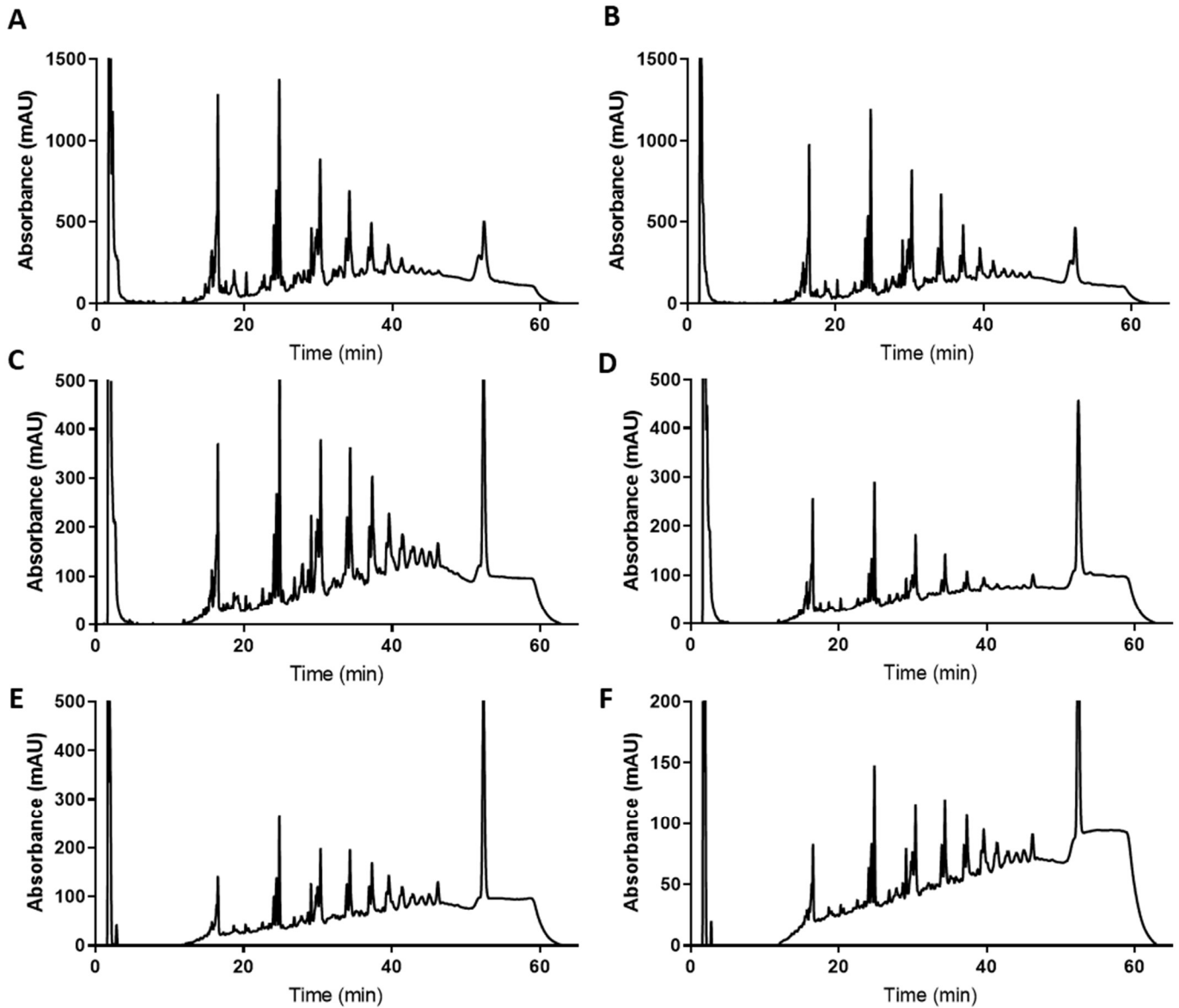
Figure 3.3 Analysis of the effect of initial CFU on muropeptide profile of *S. aureus* NewHG by RP-HPLC

Representative muropeptide profiles of NewHG (SJF 3663) grown in TSB using different starting CFU. Muropeptide profiles from **(A)** 8.8×10^9, **(B)** 3.5×10^9, **(C)** 1.8×10^9, **(D)** 7.0×10^8, **(E)** 3.5×10^8, **(F)** 1.8×10^8 CFU NewHG.

3.3.2 Mass spectrometry analysis of *S. aureus* muropeptides grown to exponential and stationary phase

For all UV-absorbance peak identification of muropeptides by mass spectrometry (MS), the ion of greatest abundance within a peak was used for the peak designation. For monomeric and dimeric muropeptide species, MS/MS was used to confirm the identity of the most abundant observed ion (Appendix 1). For muropeptide species with greater crosslinking (oligomers), the mass of the most abundant ion found by MS was used to identify the UV-absorbance peak.

S. aureus NewHG *kan^R* (SJF 3680) was chosen to produce a reference muropeptide trace, as this strain is used to infect mice (Chapter 2.18.2). NewHG *kan^R* was cultured using standard growth conditions (Chapter 2.6), to exponential phase (OD$_{600}$ of 0.6) or stationary phase (8 hours of growth, OD$_{600}$ of around 9 - 10) in three independent repeats. For MS analysis, samples were digested using a phosphate free methodology to remove the need for desalting, as well as in the absence of sodium to reduce the formation of sodium adducts in the MS ion spectra (Chapter 2.17). Three UV-absorbance muropeptide profiles (with ion spectra) were produced for NewHG *kan^R* cultured in TSB to exponential phase (Figure 3.4A). The representative trace shows the identification of monomeric muropeptide species (3, 4, 5 and 14), dimeric muropeptide species (17 and 24) and higher crosslinked trimeric (28), tetrameric (29) and pentameric (33) muropeptide species. Three independent cultures of NewHG *kan^R* cultured in TSB to stationary phase were used to produce muropeptide profiles (Figure 3.4B). As for exponential phase PG, monomeric species were identified, and crosslinked species (up to pentameric) were also observed in all samples.

The area under each identified UV-absorbance peak was measured and expressed as a percentage of the total area of all identified peaks for each trace (Appendix 2 Tables 1 and 2). These were then grouped based on the level of crosslinking, with monomers having no glycine bridge crosslinking, dimers having one crosslink, and oligomers having

112

a higher level of crosslinking. The extent of crosslinking between exponential and stationary phase cultures was then compared (Figure 3.4C). Stationary phase cells show significantly more monomeric muropeptide species than that of exponential phase cells ($p = 0.0059$). No significant difference could be seen in the abundance of dimeric muropeptides ($p > 0.9999$) between stationary and exponential phase cells. Stationary phase cells show significantly fewer oligomeric (highly crosslinked) muropeptide species compared to exponential phase cells ($p = 0.0055$), suggesting a reduction in PG crosslinking in stationary phase cells.

Figure 3.4 Analysis of muropeptide profiles of *S. aureus* NewHG *kan^R* by RP-HPLC and MS

Representative muropeptide profiles of NewHG *kan^R* (SJF 3680) cultured in TSB in **(A)** exponential phase (OD$_{600}$ ~0.6) or **(B)** stationary phase (OD$_{600}$ ~9). Muropeptides have been labelled after being identified by MS, using muropeptide numbers from Table 3.1. **(C)** Area of eluted identified UV-absorbing peaks, corresponding to different muropeptides, was quantified and is shown as a percentage of the total of all identified peaks grouped based on cross-linking (exponential phase - black bars, stationary phase – blue bars, n = 3, error bars represent the standard deviation of the mean). A two-way ANOVA with Sidak's multiple comparison post-test was used to compare abundance of each muropeptide species (monomers ** p = 0.0059, oligomers ** p = 0.0055).

Muropeptide number	UV retention time (min)	Observed mass (Da)	Charge state (Z)	Calculated neutral mass (Da)	Calculated protonated mass (Da)	Structure
1	24.56	954.37	1	953.40	954.40	GM-Penta(Ala-Gln-Lys-Ala-Gly)
2	29.43-30.59	954.15-954.43	1	953.46	954.46	GM-Tetra(Gln) (G)
3	25.48-31.08	968.07-968.48	1	967.47	968.48	GM-Penta(Gln)
3	26.26	484.57	2	967.47	968.48	GM-Penta(Gln)
4	29.27-32.23	1011.15-1011.47	1	1010.48	1011.48	GM-Tetra(Gln) (GG)
5	30.16-33.77	1025.13-1025.46	1	1024.49	1025.50	GM-Penta(Gln) (G)
5	31.45	513.02513.06	2	1024.49	1025.50	GM-Penta(Gln) (G)
6	27.65-32.76	1068.10-1068.49	1	1067.50	1068.51	GM-Tetra(Gln) (GGG)
7	31.01	541.59	2	1081.51	1082.52	GM-Penta(Gln) (GG)
7	31.31-32.72	1082.03-1082.40	1	1081.51	1082.52	GM-Penta(Gln) (GG)
8	35.66	1083.12	1	1082.50	1083.51	GM-Penta(Glu) (GG)
9	28.2-34.46	1125.17-1125.5	1	1124.52	1125.53	GM-Tetra(Gln) (GGGG)
9	31.07-32.37	563.05-563.44	2	1124.52	1125.53	GM-Tetra(Gln) (GGGG)
10	32.63-33.46	1139.12-1139.90	1	1138.54	1139.54	GM-Penta(Gln) (GGG)
10	31.6-33.04	570.07-570.80	2	1138.54	1139.54	GM-Penta(Gln) (GGG)
11	30.97-32.83	1182.13-1182.53	1	1181.54	1182.55	GM-Tetra(Gln) (GGGGG)
12	35.05	598.61	2	1195.56	1196.56	GM-Penta(Gln) (GGGG)
12	32.52-34.05	1196.21-1196.48	1	1195.56	1196.56	GM-Penta(Gln) (GGGG)
13	31.94	1239.53	1	1238.54	1239.54	GM-Penta(Ala-Gln-Lys-Ala-Gly) (GGGGG)
14	31.92-34.71	1253.13-1253.61	1	1252.58	1253.59	GM-Penta(Gln) (GGGGG)
14	32.83-34.34	626.99-627.11	2	1252.58	1253.59	GM-Penta(Gln) (GGGGG)
15	34.77	1254.42	1	1253.56	1254.57	GM-Penta(Glu) (GGGGG)
16	43.35-44.5	993.14-993.18	2	1984.94	1985.95	GM-pentapeptide (GGGGG) - M-tetrapeptide(G)
17	40.81-43.7	1066.10-1066.60	2	2131.00	2132.01	GM-pentapeptide (GGGGG) - GM-tetrapeptide
18	41.40-45.03	1094.68-1095.21	2	2188.02	2189.03	GM-pentapeptide (GGGGG) - GM-tetrapeptide(g)
19	42.02	1116.54	2	2231.08	2232.09	GM-pentapeptide(Ala-Gln-Lys-Ala-Gly) (GGGGG) - GM-tetrapeptide(GG)
20	42.53-45.60	1123.21-1123.65	2	2245.04	2246.05	GM-pentapeptide (GGGGG) - GM-tetrapeptide(GG)
21	46.38	1152.14	2	2302.07	2303.07	GM-pentapeptide (GGGGG) - GM-tetrapeptide(GGG)
22	44.18	1173.54	2	2345.09	2346.10	GM-pentapeptide (Ala-Gln-Lys,Ala,Gly) (GGGGG) - GM-tetrapeptide(GGGG)
23	46.38	1180.19	2	2359.09	2360.10	GM-pentapeptide (GGGGG) - GM-tetrapeptide(GGGG)
24	43.03-47.36	1209.06-1209.69	2	2417.49	2418.50	GM-pentapeptide (GGGGG) - GM-tetrapeptide (GGGGG)
24	44.51-45.69	806.75-806.83	3	2417.49	2418.50	GM-pentapeptide (GGGGG) - GM-tetrapeptide (GGGGG)

Muropeptide number	UV retention time (min)	Observed mass (Da)	Charge state (Z)	Calculated neutral mass (Da)	Calculated protonated mass (Da)	Structure
25	49.05	1118.03	3	3351.36	3352.37	GM-pentapeptide (GGGGG) - GM-tetrapeptide (GGGGG)- GM-tetrapeptide (G)
26	51.88	1733.9	2	3465.53	3466.54	GM-pentapeptide (GGGGG) - GM-tetrapeptide (GGGGG)- GM-tetrapeptide (GGG)
27	56.61	1175.17	3	3522.64	3523.65	GM-pentapeptide (GGGGG) - GM-tetrapeptide (GGGGG)- GM-tetrapeptide (GGGG)
28	52.52-58.60	1193.88-1194.40	3	3579.64	3580.65	GM-pentapeptide (GGGGG) - GM-tetrapeptide (GGGGG)- GM-tetrapeptide (GGGGG)
28	56.16-58.20	895.80-895.85	4	3579.64	3580.65	GM-pentapeptide (GGGGG) - GM-tetrapeptide (GGGGG)- GM-tetrapeptide (GGGGG)
29	67.35-71.38	1582.19-1582.67	3	4744.13	4745.14	GM-tetrapeptide (GGGGG) - GM-tetrapeptide (GGGGG)- GM-tetrapeptide (GGGGG)- GM-tetrapeptide (GGGGG)
29	69.65-73.82	1186.91-1187.26	4	4744.13	4745.14	GM-tetrapeptide (GGGGG) - GM-tetrapeptide (GGGGG)- GM-tetrapeptide (GGGGG)- GM-tetrapeptide (GGGGG)
30	73.04	1186.83	4	4814.21	4815.22	GM-pentapeptide (GGGGG) - GM-tetrapeptide (GGGGG)- GM-tetrapeptide (GGGGG)- GM-tetrapeptide (GGGGG)
31	85.35-90.42	1477.69-1477.83	4	5907.73	5908.74	GM-pentapeptide (GGGGG) - GM-tetrapeptide (GGGGG)- GM-tetrapeptide (GGGGG)- GM-tetrapeptide (GGGGG)- GM-tetrapeptide (GGGGG) (loss of 2 acetyl groups)
31	85.66	1182.63	5	5907.73	5908.74	GM-pentapeptide (GGGGG) - GM-tetrapeptide (GGGGG)- GM-tetrapeptide (GGGGG)- GM-tetrapeptide (GGGGG)- GM-tetrapeptide (GGGGG) (loss of 2 acetyl groups)
32	90.46	1185.14	5	5920.68	5921.69	GM-tetrapeptide (GGGGG) - GM-tetrapeptide (GGGGG)- GM-tetrapeptide (GGGGG)- GM-tetrapeptide (GGGGG)- GM-tetrapeptide (GGGGG)
33	85.02	1484.69-	4	5934.70	5935.71	GM-pentapeptide (GGGGG) - GM-tetrapeptide (GGGGG)- GM-tetrapeptide (GGGGG)- GM-tetrapeptide (GGGGG)- GM-tetrapeptide (GGGG)
34	86.88-88.01	1498.79-1498.89	4	5991.75	5992.76	GM-pentapeptide (GGGGG) - GM-tetrapeptide (GGGGG)- GM-tetrapeptide (GGGGG)- GM-tetrapeptide (GGGGG)- GM-tetrapeptide (GGGGG)
34	89.4	1199.41	5	5991.75	5992.76	GM-pentapeptide (GGGGG) - GM-tetrapeptide (GGGGG)- GM-tetrapeptide (GGGGG)- GM-tetrapeptide (GGGGG)- GM-tetrapeptide (GGGGG)

Table 3.1 *S. aureus* NewHG muropeptide database

Muropeptide database derived from material from Figures 3.4; 3.6 and 3.9 and from Appendix 2 Tables 1, 2, 3, 4 and 5. Each muropeptide has been given a muropeptide number for this study. Structures of muropeptides are seen in Appendix 1.

3.3.2 Analysis of *S. aureus* muropeptide profile after culture in porcine serum
3.3.2.1 Growth of *S. aureus* in porcine serum

The growth of *S. aureus* NewHG *kan^R* (SJF 3680) in porcine serum was determined under standard conditions (Chapter 2.6, Figure 3.5).

NewHG *kan^R* has a reduced growth rate in porcine serum (doubling time 34.6 min) compared to TSB (doubling time 28.7 min). The yield was 5.9×10^{12} and 4.4×10^9 CFU/ml for TSB and serum respectively after 10 hours (Figure 3.5B). Mid-exponential and stationary phase growth in serum were defined as 3 and 8 hours after inoculation respectively.

3.3.2.2 Analysis of muropeptides of *S. aureus* cultured in porcine serum

Muropeptides from purified PG of NewHG *kan^R* (SJF 3680) cultured, in triplicate, to exponential phase and stationary phase in porcine serum were analysed by MS (Figure 3.6A and B) as in Chapter 3.3.2.1. In both stationary and exponential phase samples, monomeric, dimeric, trimeric, tetrameric and pentameric species were observed. In all serum samples, the most abundant pentameric muropeptide species found was a structure lacking two acetyl groups (muropeptide 31, Table 3.1).

Each identified muropeptide was integrated and expressed as a percentage of the total area of all identified peaks for a single trace (Appendix 2 Tables 3 and 4) and grouped based on crosslinking (Figure 3.6C). No significant differences could be found between the abundance of monomers (p = 0.99), dimers (p = 0.27) or oligomers (p = 0.11) from exponential phase cells grown in TSB or porcine serum. Comparing stationary phase serum to stationary TSB grown muropeptides, there were significantly fewer monomeric (p = 0.0004) and significantly more dimeric (p = 0.0338) muropeptides in the serum sample, but no significant difference between oligomeric muropeptides (p = 0.40) between the two.
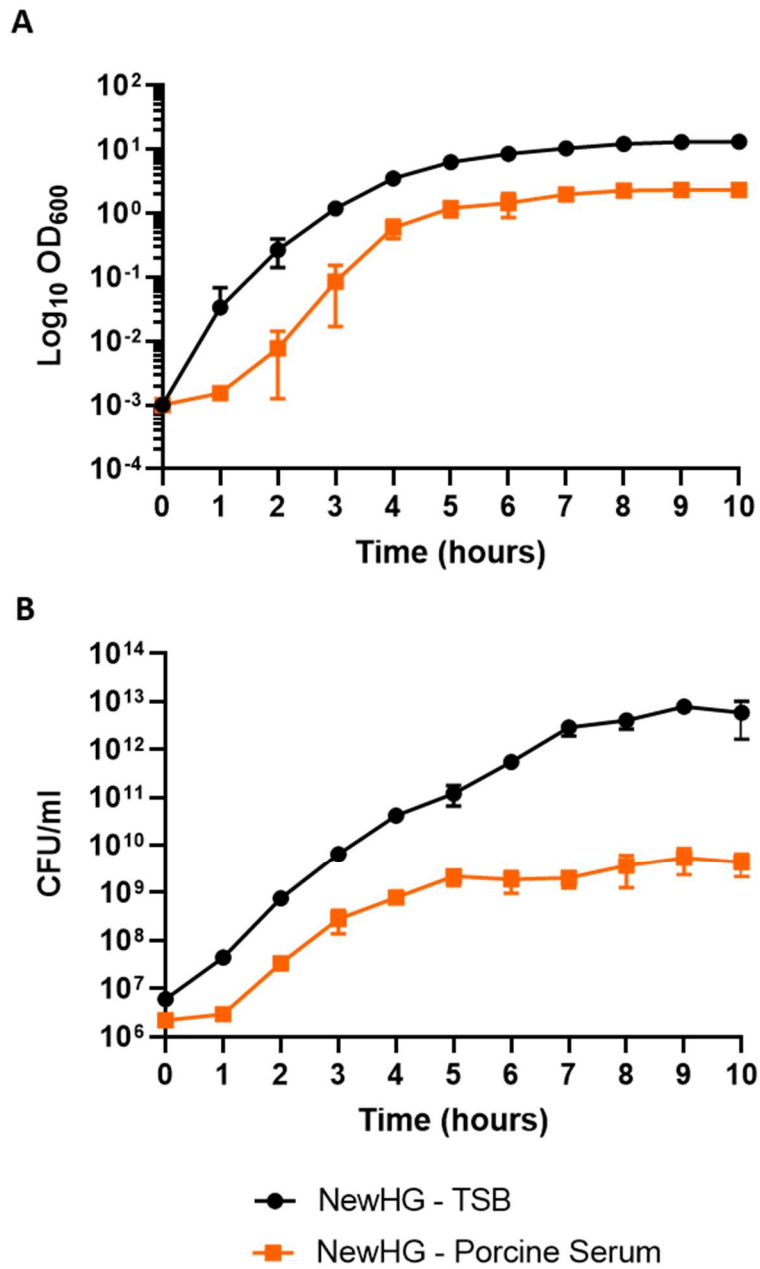
Figure 3.5 Analysis of *S. aureus* NewHG growth in porcine serum

Growth (37 °C) of NewHG *kan^R* (SJF 3680) in TSB (black circles) compared to NewHG *kan^R* in porcine serum (orange squares) measured by (A) absorbance and (B) CFU/ml. Bacterial cultures were prepared in triplicate and error bars represent the standard deviation of the mean. were prepared in triplicate and error bars represent the standard deviation of the mean.
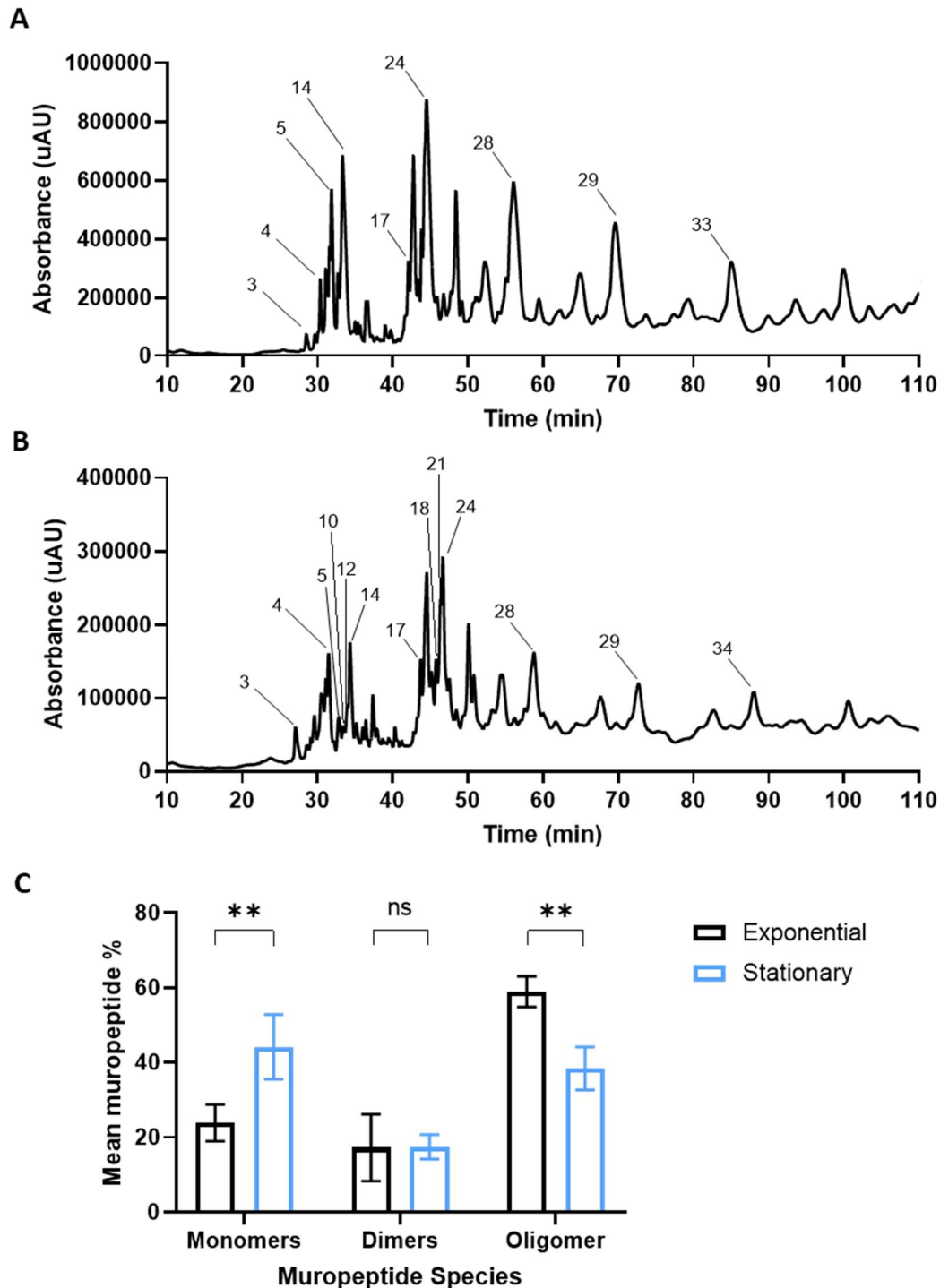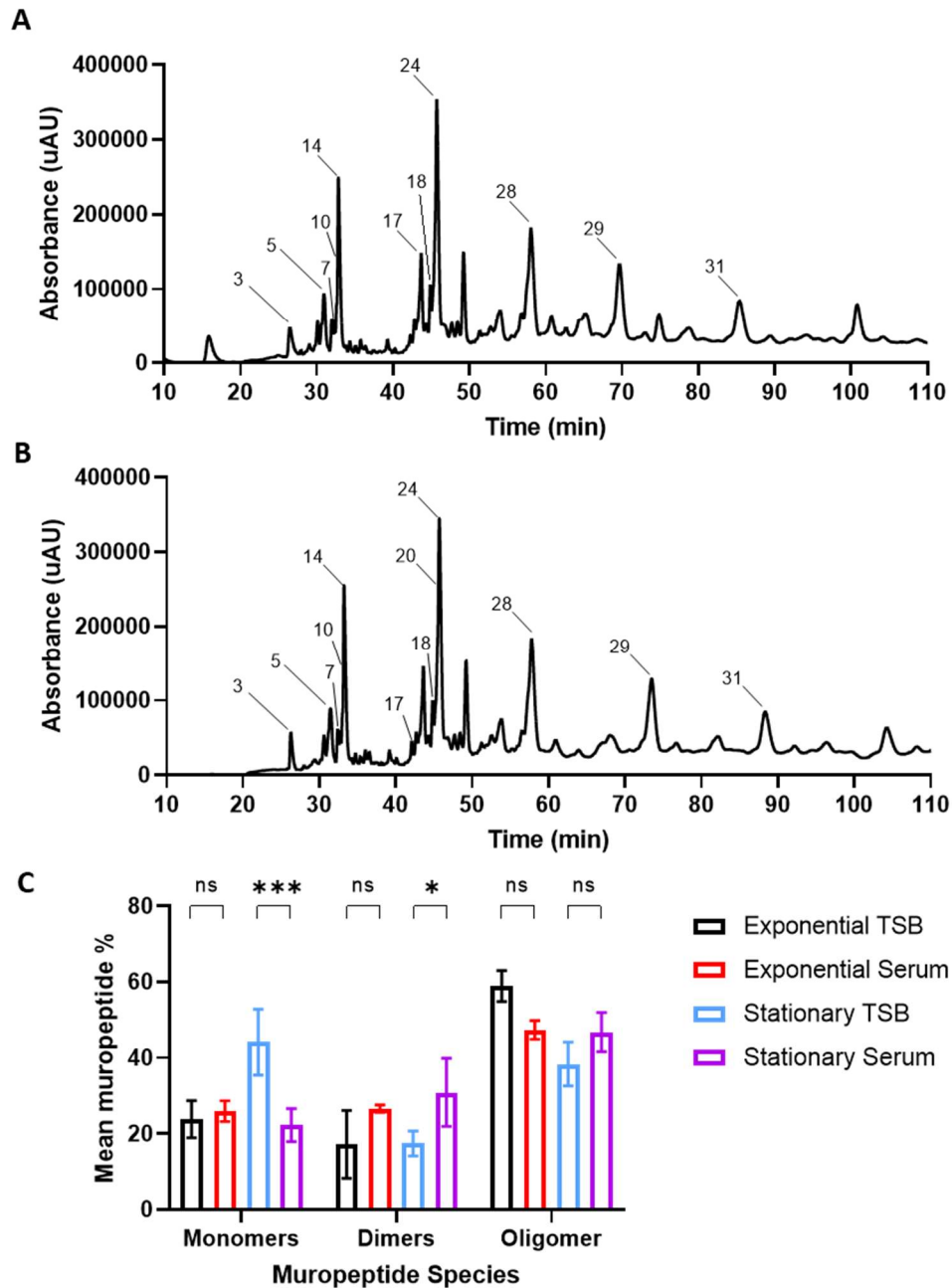
Figure 3.6 Analysis of muropeptide profiles of *S. aureus* NewHG *kan^R* grown in serum by RP-HPLC and MS

Representative muropeptide profiles of NewHG *kan^R* (SJF 3680) cultured in porcine serum in (A) exponential phase or (B) stationary phase. Muropeptides have been labelled after being identified by MS, using muropeptide numbers from Table 3.1. (C) Area of eluted identified UV-absorbing peaks, corresponding to different muropeptides, was quantified and is shown as a percentage of the total of all identified peaks grouped based on cross-linking (exponential phase TSB - black bars, stationary phase TSB – blue bars, exponential phase serum – red bars, stationary phase serum – purple bars, n = 3, error bars represent the standard deviation of the mean). A two-way ANOVA with Sidak's multiple comparison post-test was used to compare abundance of each muropeptide species (monomers *** p = 0.0004, ** p = 0.0030; dimers * p = 0.0308 and 0.0338; oligomers *** p = 0.0009).

3.3.3 Analysis of *S. aureus* cultured in chemically defined media (CDM)
3.3.3.1 Growth of *S. aureus* in CDM

S. aureus NewHG *kan*[R] (SJF 3680) was grown in TSB and CDM under standard conditions (Chapter 2.7.1, Figure 3.7). When cultured in CDM, NewHG *kan*[R] shows a reduced optimal growth rate (doubling time 35.7 mins) and increased lag time compared to TSB (doubling time 30.9 mins). An OD_{600} of around 0.4, was defined as mid-exponential phase in CDM and 8 hours was used for a stationary phase culture.
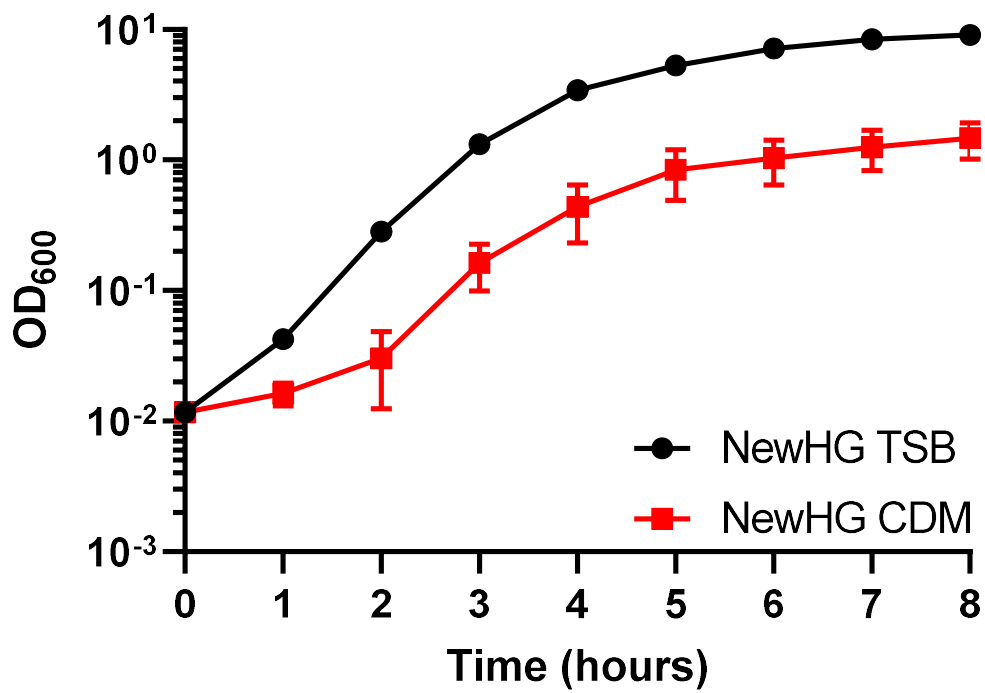
Figure 3.7 Analysis of *S. aureus* NewHG growth in CDM

Growth (37 °C) of NewHG *kan^R* (SJF 3680) in TSB (black circles) and CDM (red squares). Bacterial cultures were prepared in triplicate and error bars represent the standard deviation of the mean.

3.3.3.2 Analysis of muropeptides of *S. aureus* cultured in CDM and modified CDM

A single exponential CDM derived sample of NewHG *kan^R* (SJF 3680) PG was purified and analysed by MS (Chapters 2.13 and 2.17) (Figure 3.8A), as well as a single stationary phase sample cultured in CDM (Figure 3.8B). In both the exponential and stationary phase samples, monomeric, dimeric, trimeric, tetrameric and pentameric species were observed. A trace of NewHG *kan^R* cultured in CDM containing 125 mM of glycine was also produced (Figure 3.8C), but only species up to tetrameric could be identified. This experiment is a repeat of work already published (de Jonge *et al.*, 1996). Three unique muropeptides were also found to be present in this sample, muropeptides: 1, 13 and 22 (Table 3.1), as previously described (de Jonge *et al.*, 1996). These muropeptides show the terminal alanine of the stem peptide substituted with a glycine, unique to this trace. NewHG *kan^R* were also cultured in CDM without glucose, the PG purified and a muropeptide trace produced. In this trace monomeric, dimeric, trimeric and tetrameric muropeptide species were observed.

3.3.3.3 Peptidoglycan crosslinking of *S. aureus* cultured in CDM

All identified peaks were integrated and expressed as a percentage of the total area of all identified peaks (Appendix 2 Table 5) and grouped together based on crosslinking (Figure 3.9). All data sets in this figure consist of one repeat, so serve as preliminary results with no statistical analysis. As seen previously (Figure 3.4C), preliminary results suggest that stationary phase cells grown in CDM have fewer highly crosslinked muropeptides and more monomeric species. Cells grown in CDM containing 125 mM glycine show a drastic reduction in the level of highly crosslinked muropeptides, and a greater amount of monomeric muropeptides. Cells grown in CDM without glucose show an increase in the proportion of dimeric muropeptide species and decrease in oligomeric muropeptides when compared to exponential phase CDM derived PG.

122
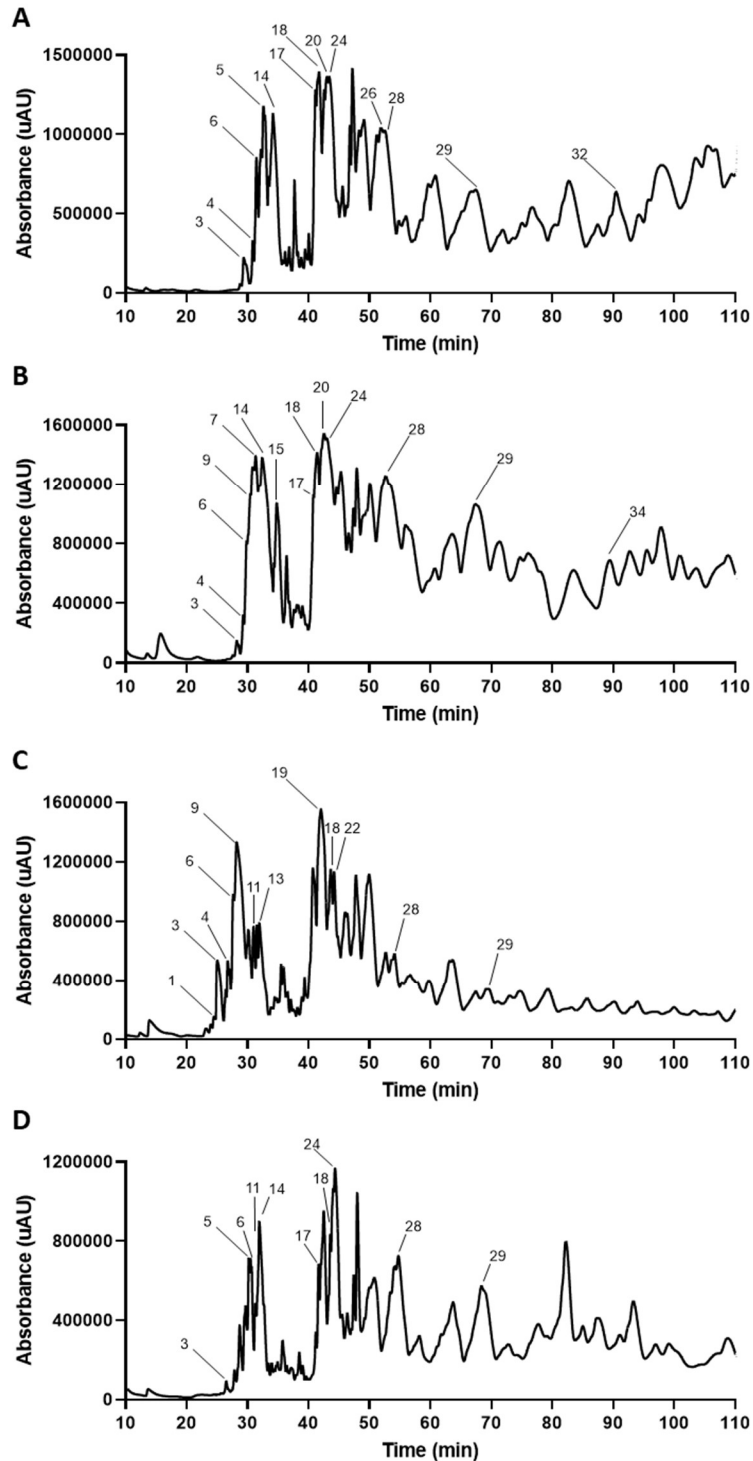
Figure 3.8 Analysis of muropeptide profiles of *S. aureus* NewHG *kan^R* grown in CDM and modified CDM by RP-HPLC and MS

Muropeptide profiles of NewHG *kan^R* (SJF 3680) cultured in CDM to **(A)** exponential phase or **(B)** stationary phase or cultured in **(C)** CDM containing 125 mM glycine to exponential phase or **(D)** CDM lacking glucose to exponential phase. Muropeptides have been labelled after being identified by MS, using muropeptide numbers from Table 3.1.
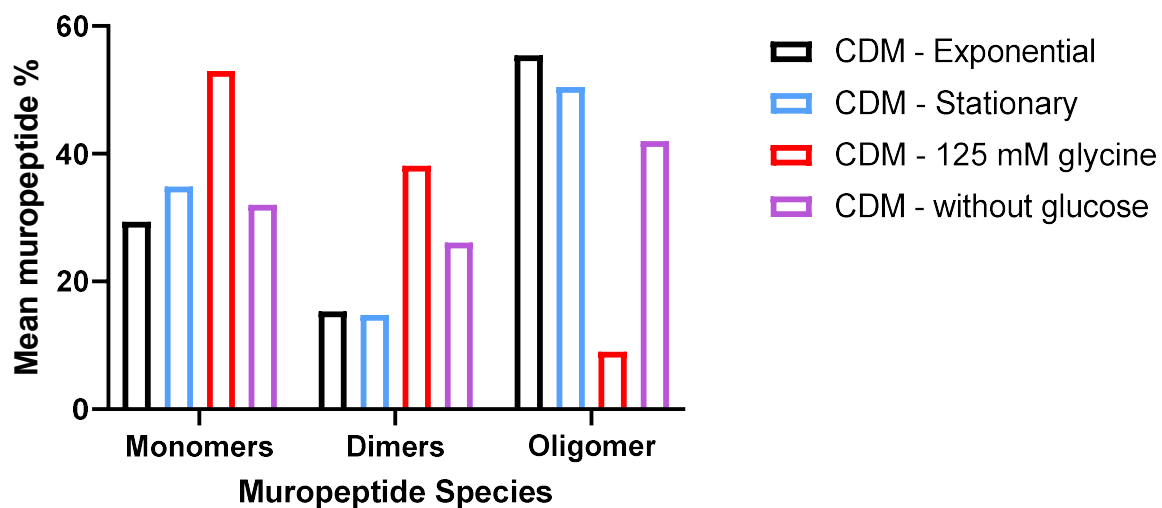
Figure 3.9 Analysis of muropeptide cross-linking of *S. aureus* NewHG *kan^R* grown in CDM or modified CDM

Area of identified UV-absorbing peaks from Figure 3.8, corresponding to different muropeptides, was quantified and shown as a percentage of the total area of all identified peaks grouped based on cross-linking (exponential phase CDM - black bars, stationary phase CDM – blue bars, CDM containing 125 mM glycine – red bars, CDM without glucose – purple bars, n = 1).

3.3.4 *S. aureus* muropeptide database

The identified muropeptides from Figures 3.4, 3.6, 3.8 and Appendix 2 Tables 1, 2, 3, 4 and 5 were combined to produce a database of muropeptides (Table 3.1). Each muropeptide has been allocated a muropeptide number (specific to this study) based on molecular mass. For each muropeptide the structure, the range of retention times and the range of observed masses are recorded. If a muropeptide was observed in different charge states during MS, both ions have been recorded with the same muropeptide number.

3.3.5 Analysis of *S. aureus* peptidoglycan from a murine infection

The murine sepsis model was used as a source of *in vivo* grown bacteria. In this model kidney abscesses are the characteristic pathology (Pollitt *et al.*, 2018). *S. aureus* NewHG *kan*[R] (SJF 3680), at a dose of 1 x 10^7 CFU, was used to inject groups of 10 mice. 72 hpi, mice were culled, and kidneys were harvested, homogenised and CFU determined (Chapter 2.18.2). Kidney homogenates (all from mice from a single experiment, totalling 20 kidneys) were combined and PG was collected (Chapter 2.19) and purified (Chapter 2.13). After purification, the remaining pellet appeared a grey colour rather than the white colour expected of purified PG, which could not be removed with further SDS washes or pronase treatments. To produce a muropeptide trace, 2 mg of this material was digested and analysed by MS (Chapter 2.17).

Two muropeptide traces of NewHG *kan*[R] (SJF 3680) purified from murine kidneys, 72 hpi, were produced and analysed (Figure 3.10A). Monomeric, dimeric, trimeric and tetrameric muropeptide species were detectable in this trace. All muropeptides identified in the trace were also found in the TSB grown samples, with no unique species found (Table 3.1, Appendix 2 Table 6). This may be due to the lower concentration of muropeptides meaning that satellite peaks are not at a concentration where they can be detected by MS.

The extent of crosslinking in PG from NewHG kan^R (SJF 3680) recovered from murine kidneys was determined as previously described (Chapter 2.17). The area of each identified UV-absorbance peak was calculated and expressed as a percentage of the total area of all identified peaks (Appendix 2 Table 6) and expressed based on the level of crosslinking (Figure 3.10B). Significantly more monomeric muropeptides are found in stationary phase TSB samples (p = 0.0180) and kidney samples (p = 0.0081) than exponential phase TSB samples. No significant difference was observed between monomeric muropeptide abundance in stationary TSB PG or kidney PG (p = 0.8734). No significant differences could be found between the abundance of dimeric muropeptides, with no differences found between exponential and stationary phase TSB samples (p = 0.9994), exponential phase TSB and kidney PG (p = 0.1580) or stationary phase TSB and kidney PG (p = 0. 1656). Significantly fewer highly crosslinked muropeptide species were found in stationary phase TSB PG than exponential phase PG (p = 0.0101). It was found that kidney PG contains significantly reduced levels of highly crosslinked muropeptides compared to exponential phase TSB material (p = 0.0002). No significant difference in oligomer abundance in kidney material and stationary phase TSB PG (p = 0.0691) was found. Also, no significant differences could be found between stationary phase TSB PG crosslinking and crosslinking within kidney PG.
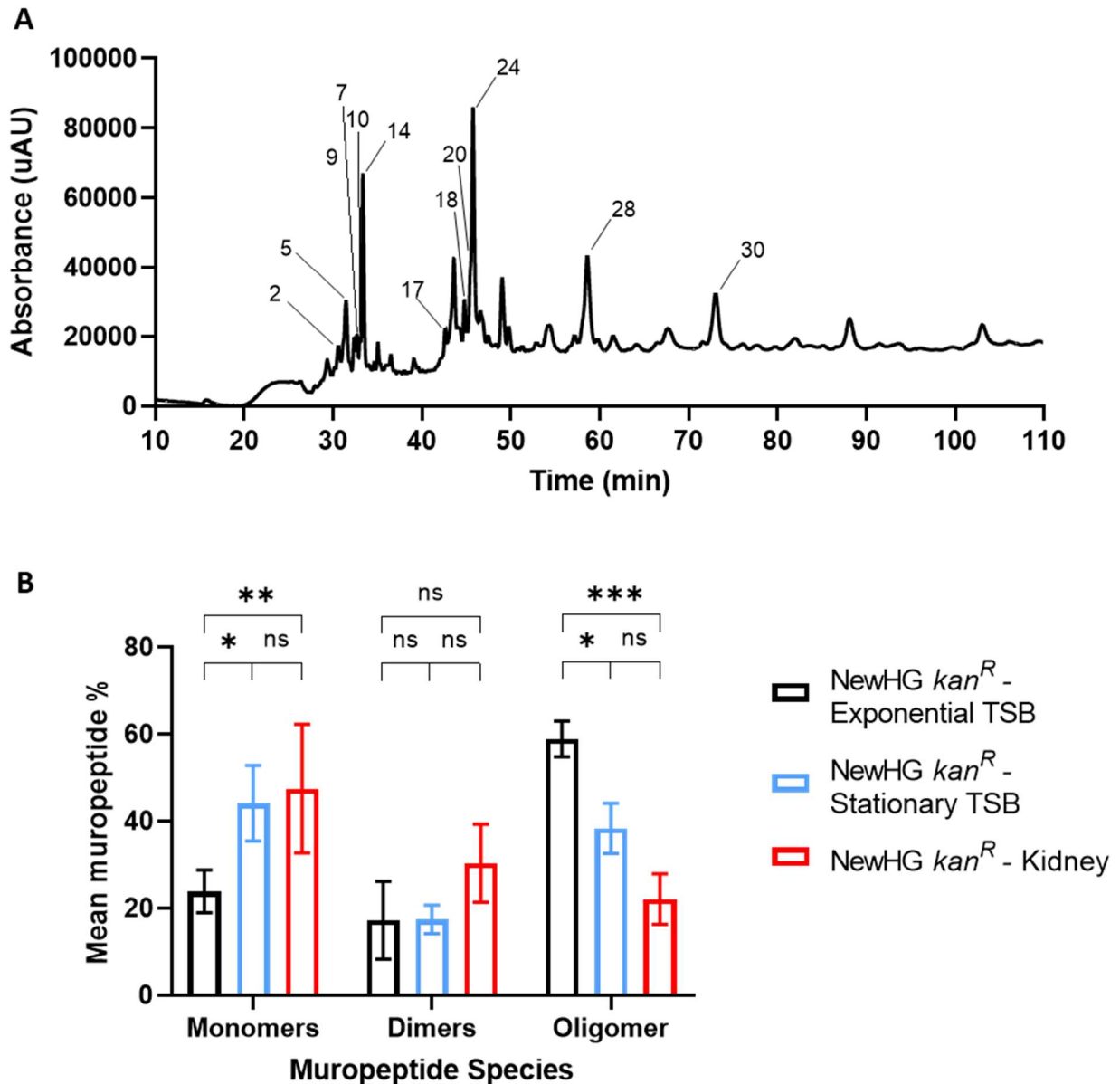
Figure 3.10 Analysis of muropeptide profiles of *S. aureus* NewHG *kan^R* recovered from murine kidneys by RP-HPLC and MS

(A) Representative muropeptide profile of NewHG *kan^R* (SJF 3680) recovered from murine kidneys 72 hpi. Muropeptides have been labelled after being identified by MS, using muropeptide numbers from Table 3.1. **(B)** Area of eluted identified UV-absorbing peaks, corresponding to different muropeptides, was quantified and is shown as a percentage of the total of all identified peaks grouped based on cross-linking (exponential phase TSB - black bars, stationary phase TSB – blue bars, n = 2 NewHG *kan^R* recovered from murine kidney– red bars, n = 3, error bars represent the standard deviation of the mean). A two-way ANOVA with Sidak's multiple comparison post-test was used to compare abundance of each muropeptide species (monomers * p = 0.0108, ** p = 0.0081; oligomers * p = 0.0101, *** p = 0.0002).

3.3.6 Production of *Enterococcus faecalis* peptidoglycan from a murine infection

To determine the wider applicability of the approach, using the established protocols (Chapter 2.18.2), kidneys from 10 mice infected intravenously with *E. faecalis* (72 hpi) were harvested and the PG purified (Chapter 2.19). The sample was then digested (Chapter 2.14), reduced (Chapter 2.15) and analysed by RP-HPLC (Chapter 2.16). The gradient used to analyse *E. faecalis* PG was provided by Dr Stéphane Mesnage (personal communication) using standard HPLC buffers (Chapters 2.2.10.1, Chapter 2.16). To serve as a control, *E. faecalis* PG was purified from bacteria cultured in TSB to exponential phase (Figure 3.11B). Figure 3.11B shows the muropeptide trace produced from murine kidneys infected with *E. faecalis.* Although a low level of muropeptides (absorbance of less than 500 mAu) were recovered using this technique, it suggests that this methodology could be used to investigate the PG structure of other bacterial species during an animal infection.
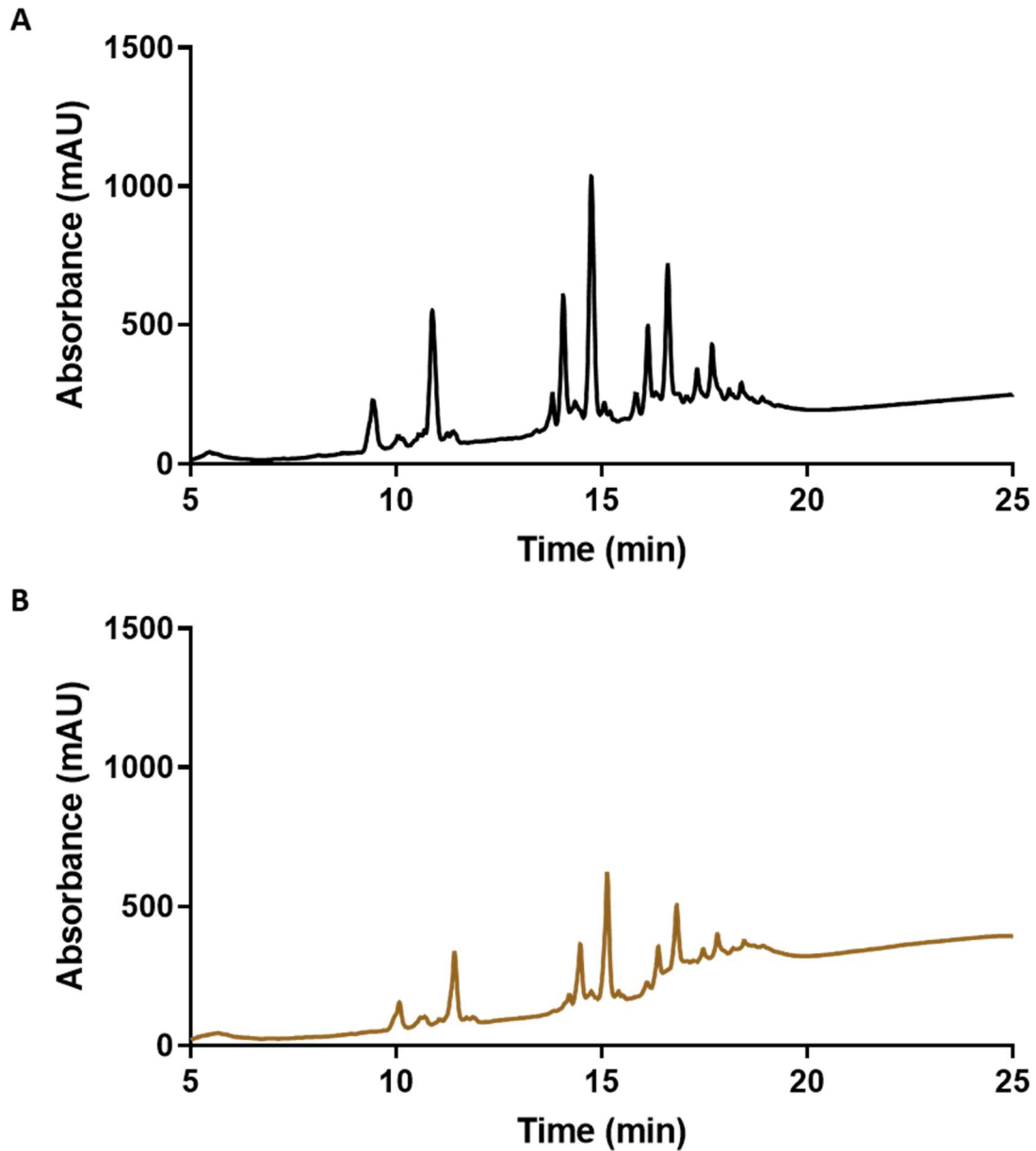
Figure 3.11 Muropeptide profiles of *E. faecalis* recovered from TSB and murine kidneys by RP-HPLC

Muropeptide traces from purified *E. faecalis* peptidoglycan recovered from **(A)** TSB or **(B)** murine kidneys.

3.3.7 Transmission electron microscopy (TEM) analysis of *S. aureus* from an infection

To determine the morphology of *in vivo S. aureus,* TEM was used to visualise cells recovered from a murine kidney infection (Chapter 2.21).

3.3.7.1 TEM images of exponential phase *S. aureus* cultured in TSB

Three independent cultures of *S. aureus* NewHG *kan^R* (SJF 3680) were grown using standard growth conditions (Chapter 2.6) to mid-exponential phase (OD$_{600}$ ~0.6). 1 ml of each culture was centrifuged to harvest cells and fixed and stained as previously described (Chapter 2.21). Sections were then imaged, with representative images shown (Figures 3.12 and 3.13). Background staining seen in some of these images is caused by the precipitation of stain, but this did not impact image analysis.
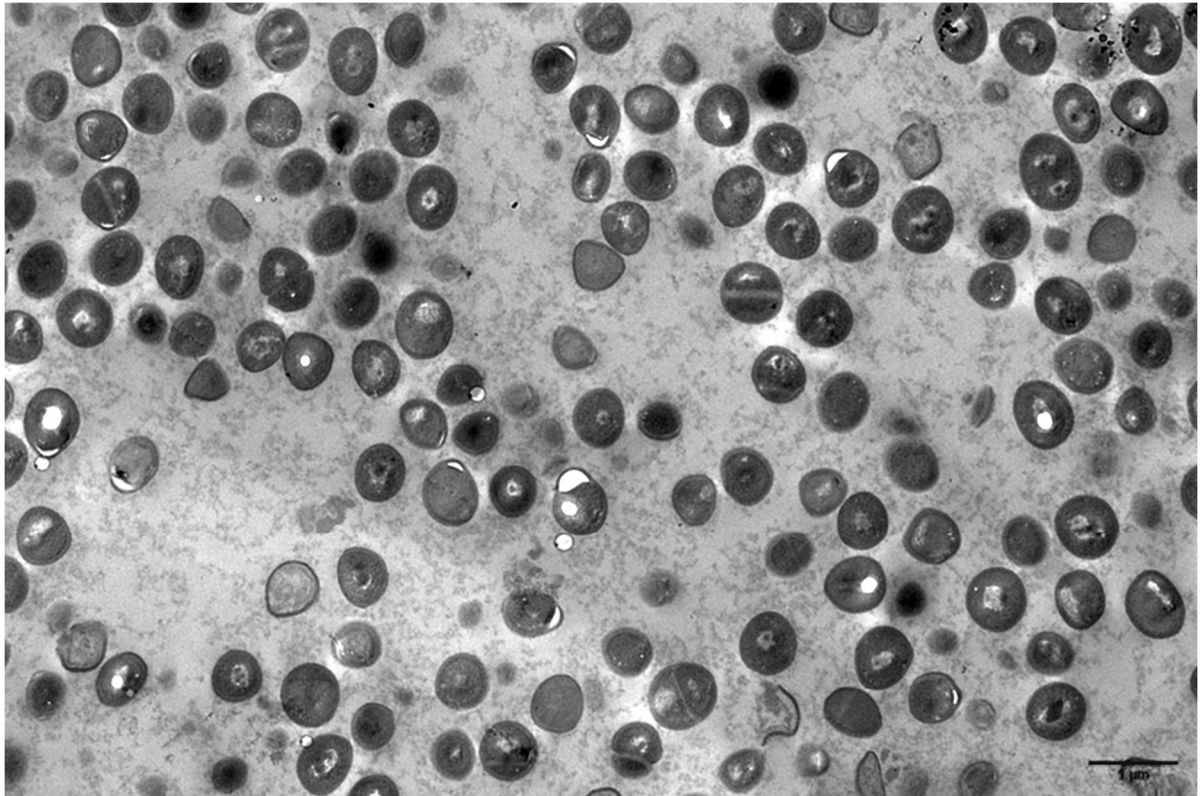
Figure 3.12 Low magnification TEM image of *S. aureus* NewHG in the exponential growth phase

Thin section of chemically fixed *S. aureus* NewHG *kan^R* (SJF 3680) cultured in TSB to exponential phase at low magnification. Scale bar (black line) represents 1 μm.
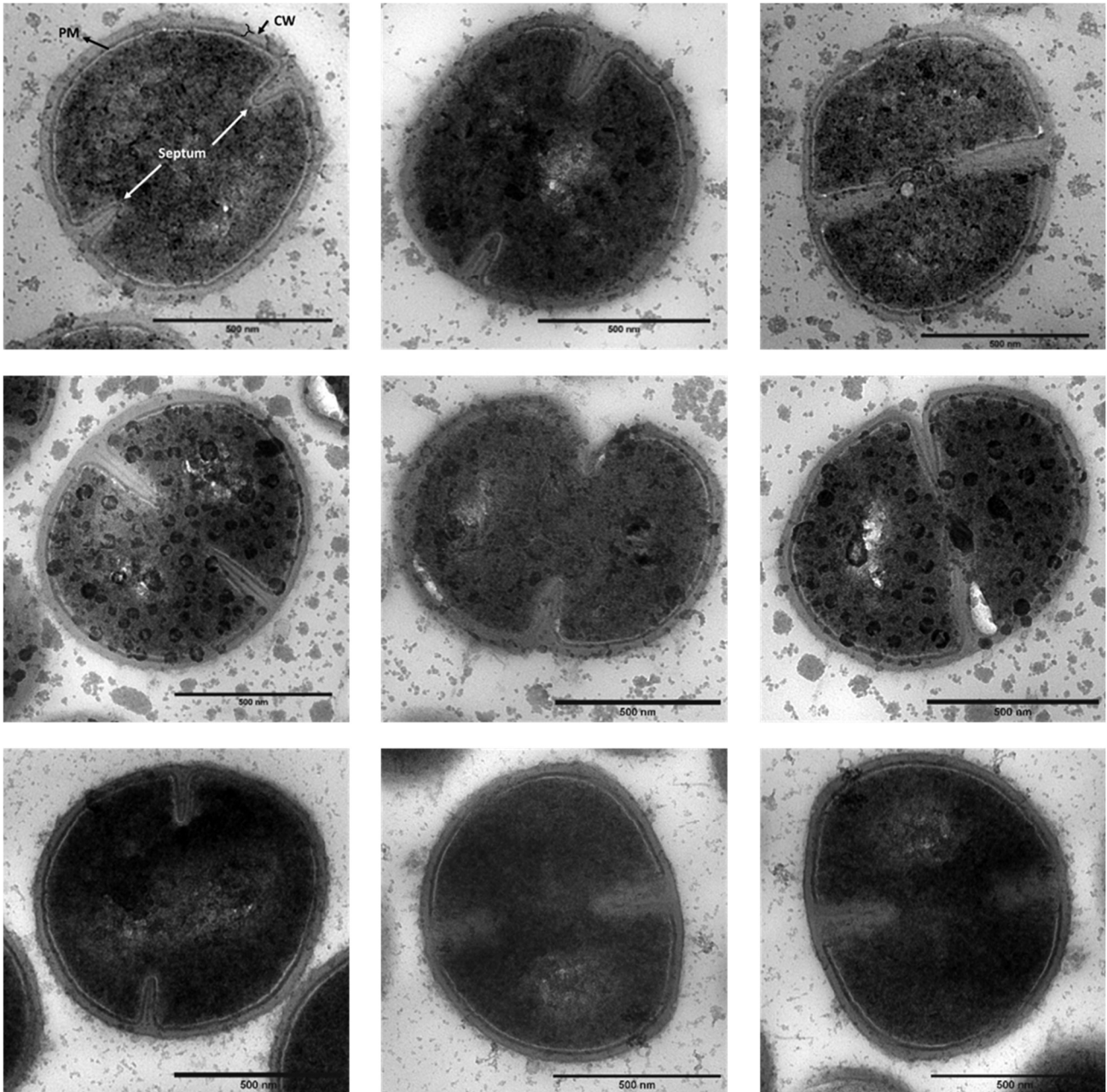
Figure 3.13 TEM images of *S. aureus* NewHG in the exponential growth phase

Thin sections of chemically fixed *S. aureus* NewHG *kan^R* (SJF 3680) cultured in TSB to exponential phase at high magnification. Scale bars (black lines) represent 500 nm. PM: plasma membrane, CW: cell wall.

3.3.7.2 TEM images of stationary phase *S. aureus* cultured in TSB

Using standard growth conditions (Chapter 2.6), three independent cultures *S. aureus* NewHG *kan^R* (SJF 3680) to stationary phase (8 hours after inoculation, OD_{600} 9 – 10). 250 µl of each sample was centrifuged to harvest cells, which were then fixed and stained (Chapter 2.21). Thin sections of each culture were then obtained, with representative images shown (Figures 3.14 and 3.15). White sections within cells are areas of low electron absorption caused by poor infiltration of the stain and did not impact upon image analysis.

3.3.7.3 TEM images of uninfected murine kidney homogenate

Uninfected murine kidney homogenate (1 ml) was centrifuged to harvest insoluble material. This material was fixed, stained and thin sections imaged (Chapter 2.21). These images (Figure 3.16) provide information on what the background stain looks like for bacteria recovered from kidneys using this method.
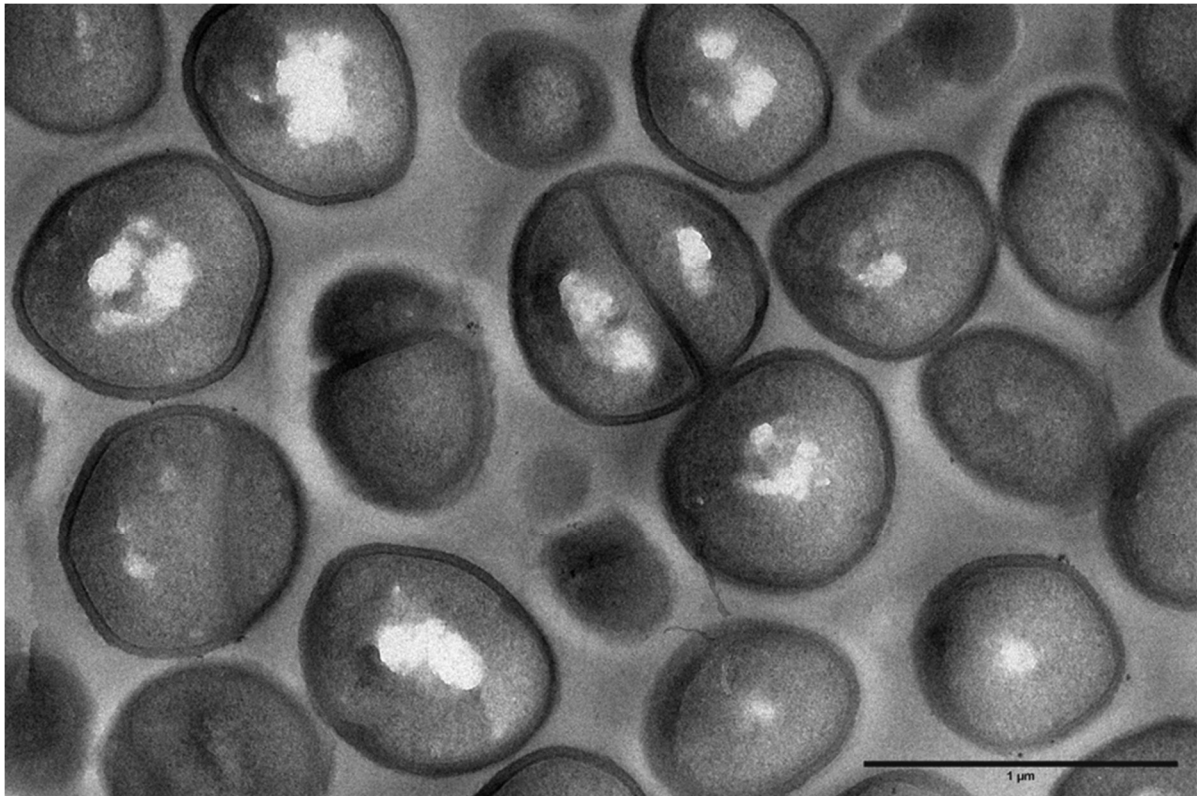
Figure 3.14 Low magnification TEM image of *S. aureus* NewHG in the stationary growth phase

Thin section of chemically fixed *S. aureus* NewHG *kan^R* (SJF 3680) cultured in TSB to stationary phase at low magnification. Scale bar (black line) represents 1 μm.
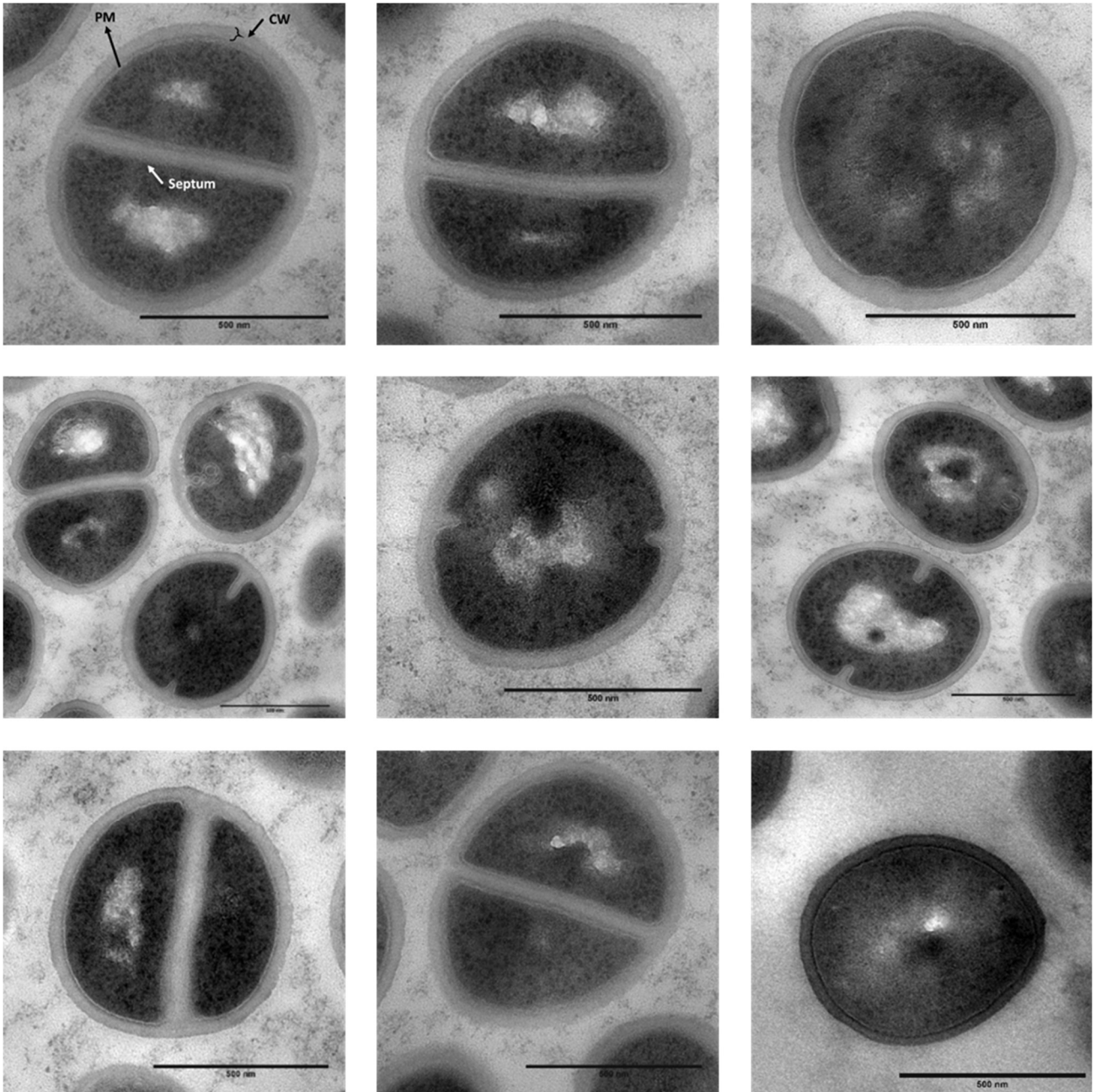
Figure 3.15 TEM images of *S. aureus* NewHG in the stationary growth phase

Thin sections of chemically fixed *S. aureus* NewHG kan[R] (SJF 3680) cultured in TSB to stationary phase at high magnification. Scale bars (black lines) represent 500nm. Scale bar (blue line) shows 500 nm. PM: plasma membrane, CW: cell wall.
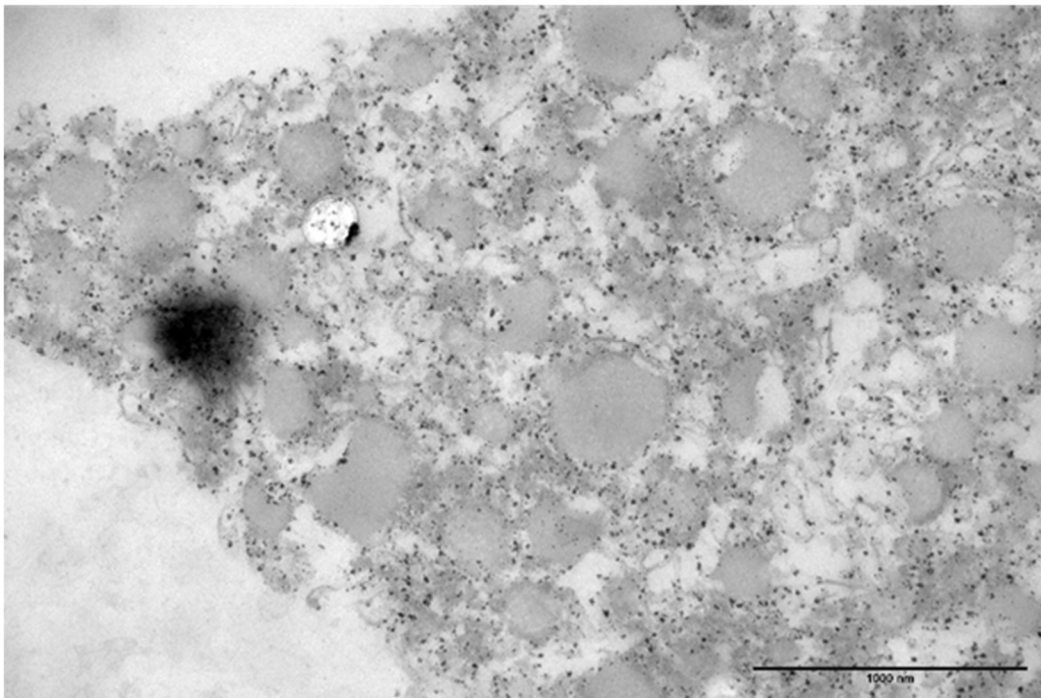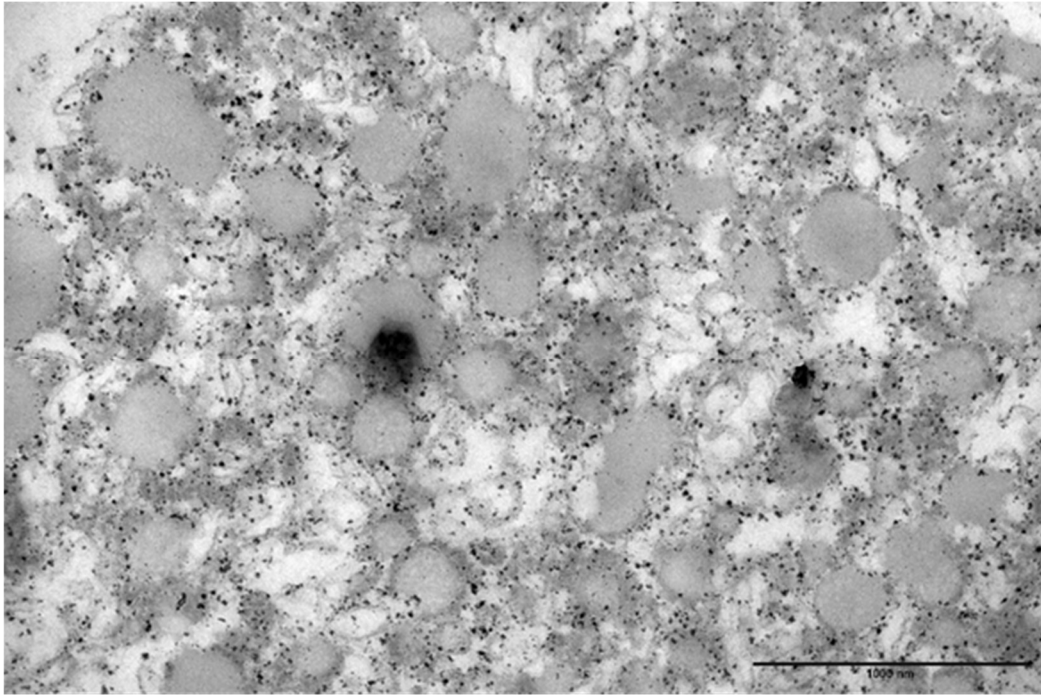
Figure 3.16 TEM images of homogenised uninfected murine kidney

Thin sections of chemically fixed uninfected murine kidney homogenate. Scale bars (black lines) represent 1 μm.

3.3.7.4 TEM images of *S. aureus* recovered from murine kidneys

Mice were infected with 1 x 10^7 CFU NewHG *kan^R* (SJF 3680). 72 hpi, mice were culled, and kidneys were collected, homogenised, and CFU determined (Chapter 2.18.2). After calculating CFU, 1 ml of kidney homogenate was centrifuged to harvest insoluble kidney material and *S. aureus* cells. Pellets were then fixed, stained, thin sectioned and imaged (Chapter 2.21), with representative images shown (Figures 3.17 and 3.18). The high level of background staining is consistent with that seen from uninfected murine kidneys (Figure 3.16). In all images of *S. aureus* isolated from kidneys, a complete or partial zone of low electron density can be seen, which is distinct from the surrounding kidney material (Figures 3.17 and 3.18). *S. aureus* cells were difficult to locate and image when isolated from kidneys, with generally only one being visible in a field of view (Figure 3.17). Images were collected from 2 sets of murine kidneys infected in separate experiments.
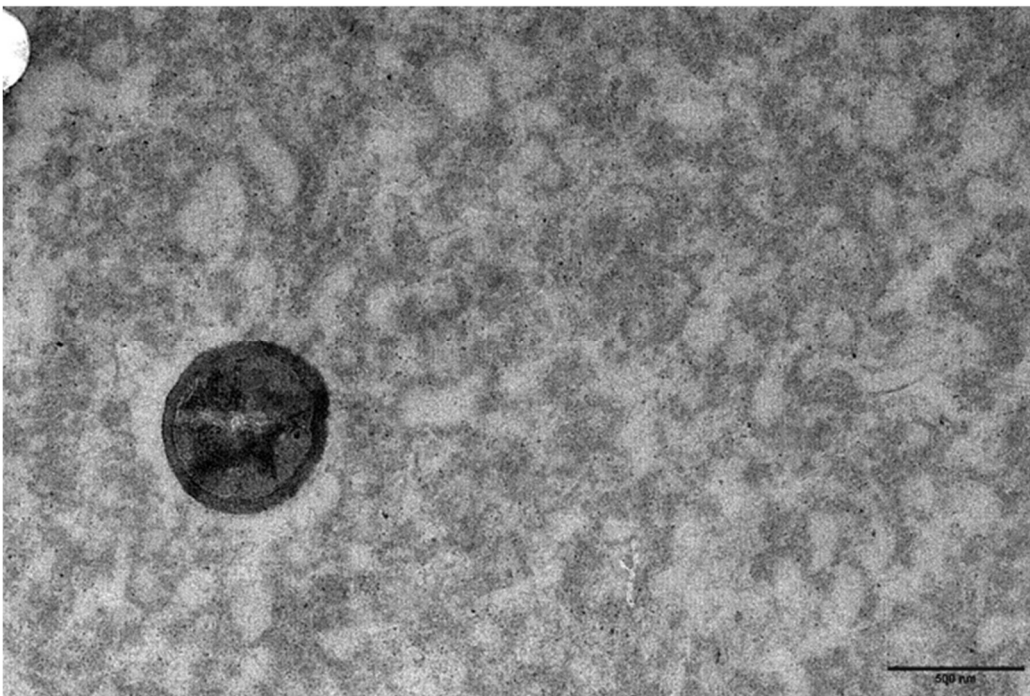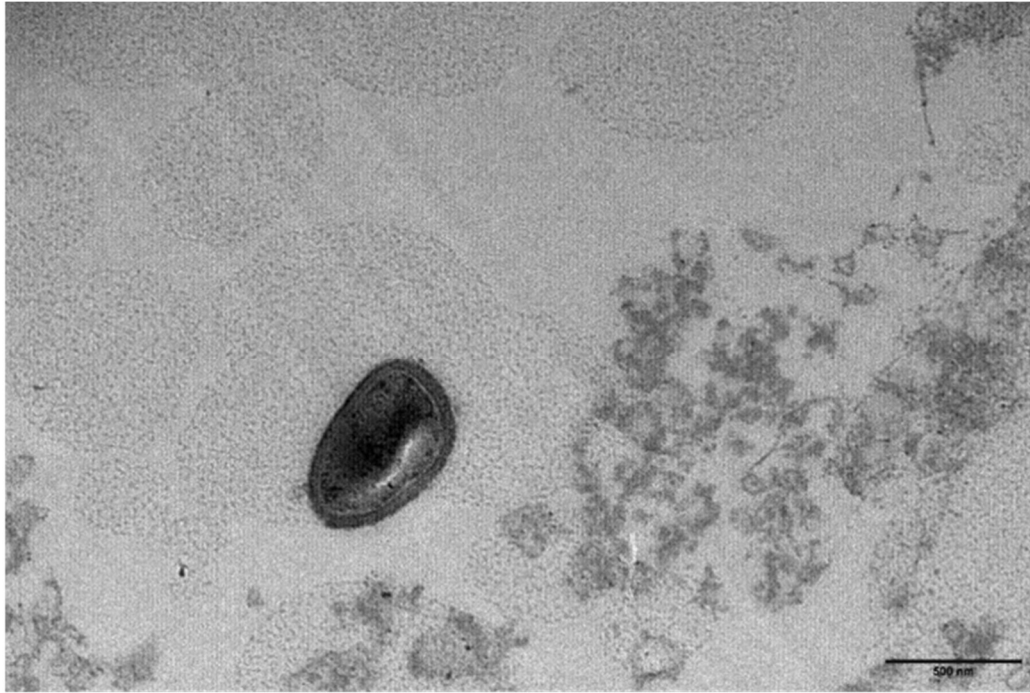
Figure 3.17 TEM images of *S. aureus* NewHG recovered from murine kidneys

Thin sections of chemically fixed *S. aureus* NewHG *kan^R* (SJF 3680) recovered from murine kidney homogenate at low magnification. Scale bars (black lines) represent 500 nm. *S. aureus* cells were found in low densities in all samples.
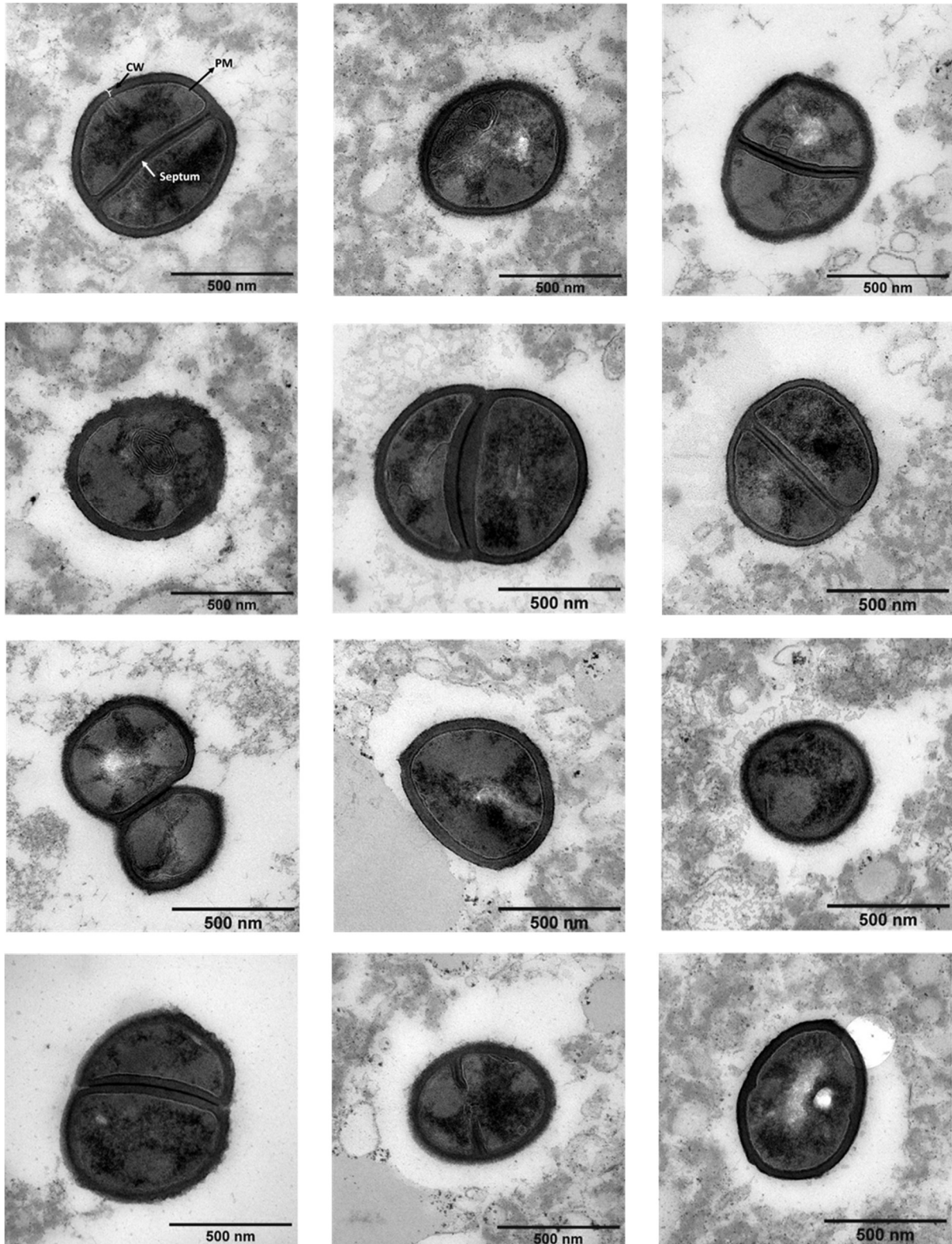
Figure 3.18 TEM images of *S. aureus* NewHG recovered from murine kidneys

Thin sections of chemically fixed *S. aureus* NewHG *kan^R* (SJF 3680) recovered from murine kidney homogenate at high magnification. Scale bars (black lines) 500nm. PM: plasma membrane, CW: cell wall.

3.3.7.5 Analysis of TEM images of *S. aureus*

All images collected for *S. aureus* NewHG *kan^R* (SJF 3680) cultured to exponential phase in TSB, cultured to stationary phase in TSB or isolated from infected murine kidneys were analysed for morphological changes (Figure 3.19). As TEM images thin sections, no Z-axis is available. As such, it cannot be confirmed that cell volume is being measured from the centre of the cell. To counter this, *S. aureus* images were analysed for their cell area (Figure 3.19A). *S. aureus* cells grown to exponential phase have a significantly greater cell area than those cultured to stationary phase in TSB ($p < 0.0001$). *S. aureus* cells recovered from murine kidneys 72 hpi also show a significant reduction in area compared to exponential phase cells ($p < 0.0001$). Cells recovered from infected kidneys were also found to have a significantly smaller area than cells in stationary phase cultured in TSB ($p = 0.0364$). The cell wall of imaged cells was also measured (Figure 3.19B). Exponential phase cells have a significantly thinner cell wall than that of stationary phase cells ($p < 0.0001$) and those recovered from kidneys ($p < 0.0001$). No significant difference between cell wall thickness of stationary phase cells or cells recovered from kidneys could be detected ($p = 0.9611$). Finally, the absence or presence of an incomplete or complete septum in *S. aureus* cells was counted and expressed as the percentage of all cells measured from that growth condition (Figure 3.19C). A significantly greater proportion of stationary phase cells have no septa when compared to exponential phase cells ($p < 0.0001$) and cells recovered from kidneys ($p = 0.0001$). No significant difference could be found between exponential phase cells and cells recovered from kidneys in the proportion of cells with no visible septa ($p = 0.5429$). *S. aureus* cells in exponential phase have a significantly greater proportion of cells possessing an incomplete septum than both stationary phase cells ($p < 0.0001$) and kidney derived cells ($p = 0.0007$). Stationary phase cells and kidney derived cells show no significant difference in the proportion of cells that have an incomplete septum ($p = 0.2617$). Infected kidneys cells have a significantly greater proportion with a complete septum (with daughter cells remaining unseparated) than exponential phase cells ($p = 0.0057$) and stationary phase cells ($p = 0.0034$). No significant difference could be found between the proportion of exponential and stationary phase cells that showed a complete septum ($p = 0.9548$).

140
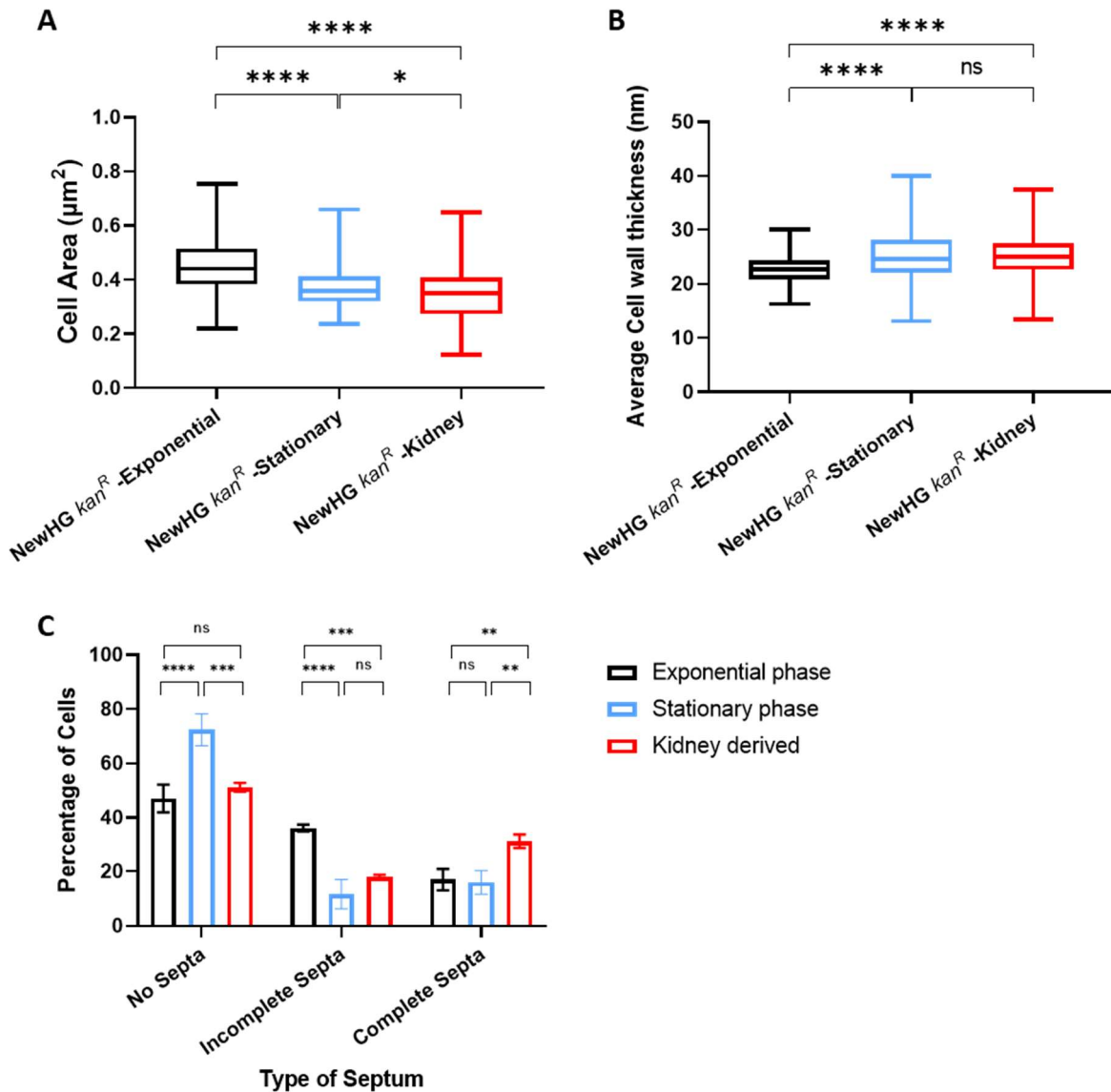
Figure 3.19 Analysis of cell area, cell wall thickness and septa formation in NewHG recovered from murine kidneys

TEM images (Figures 3.10 – 3.17) were analysed to determine the **(A)** cell area, **(B)** cell wall thickness and **(C)** presence of a septum in NewHG *kan^R* (SJF 3680) in different growth conditions. **(A)** The cell area of NewHG *kan^R* (SJF 3680) cultured in TSB to exponential phase (black lines, 3 independent repeats totalling 411 cells), in TSB to stationary phase (blue lines, 3 independent repeats totalling 320 cells) or recovered from murine kidneys 72 hpi (red lines, 2 independent repeats totalling 180 cells). Results analysed using a one-way ANOVA with multiple comparisons (* p = 0.0364, **** p < 0.0001). **(B)** Average cell wall thickness of NewHG *kan^R* (SJF 3680) cultured in TSB to exponential phase (black lines, 3 independent repeats totalling 367 cells), in TSB to stationary phase (blue lines, 3 independent repeats totalling 256 cells) or recovered from murine kidneys 72 hpi (red lines, 2 independent repeats totalling 104 cells). Results analysed using a one-way ANOVA with multiple comparisons (**** p < 0.0001). Box and whiskers for **(A)** and **(B)** represent mean, range and lower and upper quartiles. **(C)** Normalised percentage of NewHG *kan^R* (SJF 3680) that show no septum, an incomplete or completed septa (exponential phase cultured in TSB – black bars, stationary phase cultured in TSB – blue bars, cells recovered from murine kidney homogenate – red bars). Normalised proportions were compared using a two-way ANOVA with multiple comparisons with Tukey's correction (no septa *** p = 0.0001, **** p < 0.0001; incomplete septa *** p = 0.0007, **** p < 0.0001; complete septa ** p = 0.0034 and 0.0057). Error bars represent the standard deviation of the mean.

3.4   Discussion

My work has determined the first peptidoglycan structure from bacteria grown within a host (*in vivo*). During an infection, *S. aureus* NewHG *kan*[R] (SJF 3680) has significantly reduced PG crosslinking than *S. aureus* cultured in TSB to exponential phase. Muropeptide profiles of *S. aureus* purified from infected kidneys 72 hpi resemble that of cells cultured in TSB to stationary phase in terms of crosslinking (Figure 3.10B). TEM analysis also shows that *S. aureus* recovered from murine kidneys 72 hpi have a smaller cell area than stationary and exponential phase cells (Figure 3.19A), as well as a thicker cell wall than exponential phase cells (Figure 3.19B). *S. aureus* also has an increased number of cells with a complete septum visible when analysed by TEM compared to exponential phase cells (Figure 3.19C) but show the same number of cells without a septum. These key findings are summarised overleaf (Table 3.2).

Starvation of *S. aureus* in glucose depleted media for a period of 25 days at 21 °C is associated with a reduction in cell size compared to exponential phase cells (Watson *et al.*, 1998), matching the results of *S. aureus* cells recovered from an infection (Chapter 3.3.7.5). A proportion of glucose starved cells were also found to possess septa when observed by TEM, suggesting that the population is not static, and PG synthesis is occurring, albeit at a reduced rate (Watson *et al.*, 1998). The results shown for *S. aureus* recovered from a murine infection (Figure 3.19C) also show incomplete and complete septa (with the daughter cells remaining attached). This suggests that the cells recovered from an infection are also in a state of starvation, and are not a static population, with PG synthesis and cell division occurring, but at a reduced rate. A reduction in PG crosslinking has also been described in stationary phase *S. aureus* cells when grown in a minimal media, which was hypothesised to be due to the depletion of glycine at the onset of stationary phase (Zhou and Cegelski, 2012).
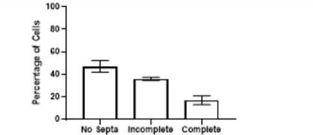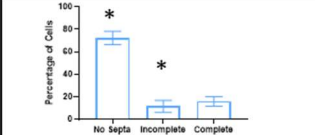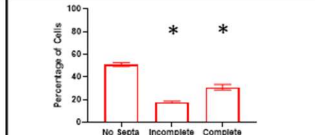
	S. aureus NewHG kan^R growth conditions		
	TSB - Exponential Phase	TSB - Stationary Phase	Murine Kidney – 72 hpi
Peptidoglycan Crosslinking	Crosslinking: 76.2 % (± 4.9)	↓ Crosslinking: 55.82 % (± 8.5) *	↓ Crosslinking: 52.47 % (± 9.5) *
Cell area	0.45 µm² (± 0.09 µm²)	0.37 µm² (± 0.06 µm²) *	0.35 µm² (± 0.1 µm²) *
Cell wall Thickness	22.7 nm (± 2.4 nm)	25.1 nm (± 4.5 nm) *	25.3 nm (± 4.3 nm) *
Septa			

Table 3.2 Summary of key results presented in Chapter 3

The structure and morphology of NewHG kan^R (SJF 3680) in different growth conditions as determined by RP-HPLC, MS and TEM analysis. * indicates a result significantly different from exponential phase cells. ± represents one standard deviation.

No other study has ever determined PG structure from bacteria during an infection. However, several studies have used conditions that mimic this complex environment. *Staphylococcus epidermidis* PG isolated from an *in vitro* biofilm show substitutions in the pentaglycine bridge, with glycine residues being substituted for serine or alanine residues, providing resistance to PG digestion by lysostaphin (Loza-Correa *et al.*, 2019). An increase in O-acetylated *N*-acetylmuramic acid residues was also observed within biofilms, which is vital for resistance to lysozyme based degradation (Bera *et al.*, 2006; Loza-Correa *et al.*, 2019). Using my methodology (Chapter 2.13), the extent of O-acetylation of muropeptides cannot be measured. This is due to the reduction of muropeptides occurring at a basic pH, as well as HF treatment, both of which remove O-acetylation from the cell wall. *S. epidermidis* PG recovered from biofilms cultured in platelet concentrates showed a reduced muropeptide species diversity compared to cells grown in TSB (Loza-Correa *et al.*, 2019). This reduced diversity mirrors my results (Chapter 3.3.5), suggesting that PG from *S. aureus* has reduced complexity and crosslinking during an infection. It has been hypothesised that in *S. epidermidis* PG synthesis is reduced, creating a less complex PG structure. This allows energy to be used in other processes, allowing proliferation of bacteria in a harsh, restrictive environment (Loza-Correa *et al.*, 2019).

Listeria monocytogenes is an intracellular pathogen that encounters a variety of environments during its lifecycle (Quereda *et al.*, 2016). Once within a host cell, the PG structure and proteins associated with the cell wall (including the way they are associated to the PG) are modified, facilitating an intracellular lifecycle (Portillo and Pucciarelli, 2012). In a mouse model of infection, *L. monocytogenes* up regulates two major virulence regulators, PrfA and VirR, which have effects such as remodelling the cell wall surface and release of muropeptides (Camejo *et al.*, 2009). For example, VirR upregulates the expression of *dlt*, which reduces the overall negative charge on WTA and LTA, increasing resistance to cationic antimicrobial peptides. PrfA has been shown to upregulate *inlA* and *inlB*, both essential for entry into host cells to initiate the intracellular phase of infection (Dussurget *et al.*, 2004), as well as *uhpT*, which encodes a

sugar transporter which facilitates rapid proliferation of *L. monocytogenes* when intracellular (Chico-Calero *et al.*, 2002).

Salmonella enterica can colonise the gut and gall bladder due to its bile resistance, which is in part due to changes in the PG structure (Hernández *et al.*, 2015). When the bile salt sodium deoxycholate is introduced to a *S. enterica* culture there is a reduction in the number of muropeptides bound to Braun's lipoprotein and a reduction in the number of L(meso)-diaminopimelyl-D(meso)-diaminopimelic acid peptide bridges, increasing resistance to bile salts (Hernández *et al.*, 2015). *S. enterica* serovar Typhimurium has the capacity for intracellular survival and has been found to remodel PG using the enzyme EcgA, which becomes activated in the nutrient limited environment inside eukaryotic cells (Rico-Pérez *et al.*, 2016). EcgA is a D, L-endopeptidase that cleaves the γ-D-glutamyl-meso-diaminopimelic acid bond in the stem peptide of non-crosslinked muropeptides. It has been hypothesised that this cleavage is also used to avoid recognition of muramyl peptides by the NOD1 receptor, preventing an immune response, allowing persistence and systemic infection in mice (Rico-Pérez *et al.*, 2016). Also when *S. enterica* serovar Typhimurium is cultured within human epithelial cells its PG contains unique muropeptides, a reduction in glycine containing muropeptides and a decrease in crosslinking (Quintela *et al.*, 1997).

The PG of *S. aureus* is known to be influenced by nutrient availability during growth. As cells reach stationary phase glycine depletes as it is used for protein and cell wall production. This results in a thickening of the cell wall and the production of irregular septa with an increased number of non-crosslinked pentaglycine side chains (Zhou and Cegelski, 2012). These changes occur in the newly synthesised PG rather than a modification to existing PG (Zhou and Cegelski, 2012). In a *S. aureus* biofilm, non-crosslinked pentaglycine bridges are used as attachment sites for proteins which is not seen in planktonic culture (Kim *et al.*, 2018). Many surface proteins are required in abscess formation (Cheng *et al.*, 2009, 2011), which are bound to the terminal glycine in the pentapeptide bridge (Navarre and Schneewind, 1999). Therefore, the observed

reduction in crosslinking in PG recovered from infected kidneys (Figure 3.10B) could be due to the glycine bridges being used to anchor proteins required for abscess formation, permitting survival and pathogenesis in the host, rather than crosslinking PG.

A decrease in crosslinking can also be explained by the substitution of D-Ala for glycine in the terminal position of the peptide stem. This was observed in cells cultured with exogenous glycine, which is associated with a decrease in methicillin resistance, demonstrating the effect on nutritional status on PG structure (de Jonge *et al.*, 1996) (Figure 3.8C). However, no muropeptides peak with stem peptides terminating with a glycine residue were detected in *S. aureus* recovered from murine kidneys (Appendix 2 Table 6). Alterations in crosslinking in response to environmental and nutritional factors is carried out by *S. aureus* components. PBP4 is known to result in a high level of crosslinked PG in *S. aureus* (Wyke *et al.*, 1981a)*.* If the expression of *pbp4* (encoding PBP4) is downregulated, it would be expected that the PG would show a reduction in crosslinking, as observed in kidney derived cells (Figure 3.10B). This leads to the hypothesis that PG synthases, such as PBP4, could play a role in *S. aureus* pathogenesis.

S. aureus recovered from murine kidneys shows reduced cell area, increased cell wall thickness and an increase in complete septa while remaining unseparated (Table 3.2). The separation of daughter cells, and therefore the resolution of complete septa, requires PG hydrolases such as Atl (Oshida *et al.*, 1995). An increased number of observed cells with complete septa, but daughter cells remaining joined, could suggest a downregulation of hydrolases, potentially due to a lack of nutrients, resulting in reduced division. PG hydrolases modify PG allowing cellular enlargement (Wheeler *et al.*, 2015). If hydrolases are downregulated in later stages of infection, the reduced cell area could therefore be explained by a more rigid cell wall, a result of reduced hydrolysis, potentially resulting in a reduction in the cell's ability to increase in volume. As previously described (Chapter 1.4.4), the WalKR two-component system upregulates the expression of PG hydrolases such as Atl. WalKR is inactive during stationary phase (Dubrac *et al.*, 2008), suggesting these observations could be due to a change in WalKR

146

activity. A lack of hydrolytic PG processing would also explain an increased cell wall thickness, as less PG is cleaved from the cell wall. It has been shown that the host can influence that transcriptional profile of *S. aureus* during an infection (Thänert *et al.*, 2017). Some strains of mice, such as BALB/c and A/J, have been shown to be highly susceptible to *S. aureus*, whereas C57BL/6 are highly resistant to such infection (von Köckritz-Blickwede *et al.*, 2008), and these differences in resistance influence the bacterial transcription of genes (Thänert *et al.*, 2017). During infection in the resistant C57BL/6, *S. aureus* was shown to upregulate the expression of the hydrolase *lytM* compared to infection in the *S. aureus* susceptible A/J mouse strain (Thänert *et al.*, 2017). In *S. aureus* susceptible A/J mice, no change in PG hydrolase transcription was reported compared to C57BL/6 mice (Thänert *et al.*, 2017). While this suggests that there may be no change in transcription of PG hydrolases during infection of *S. aureus* susceptible BALB/c mice, transcription of genes does not always correlate linearly to translation to a function protein product. These observations lead to the hypothesis that PG hydrolases could also play a role in *S. aureus* pathogenesis.

Chapter 4

The role of four putative glucosaminidases in *S. aureus* pathogenesis

4.1   Introduction

Peptidoglycan hydrolases cleave bonds in the bacterial peptidoglycan sacculus, allowing; the regulation of cell growth, the separation of cells during division and the expansion of the cell wall, amongst other roles (Vollmer *et al.*, 2008b). The turnover of peptidoglycan due to hydrolysis also releases muropeptides into the bacteria's environment. These soluble muropeptides can be detected by the host immune system by proteins such as nucleotide binding and oligomerization domain proteins (NODs) and NOD-like receptors (NLRs) (Martinon and Tschopp, 2005). NOD2 recognises the Mur*N*Ac-D-Ala-D-Glu unit released from the peptidoglycan, present in Gram-positive bacteria such as *S. aureus*, resulting in the activation of signalling cascades activating the nuclear factor-κB (NF-κB) response. NF-κB causes the upregulation of inflammatory responses, and therefore host antimicrobial activity (Irazoki *et al.*, 2019). It has also been shown that insoluble peptidoglycan, in the form of purified sacculi, can augment an *S. aureus* infection in a murine model of infection (Boldock *et al.*, 2018). This insoluble peptidoglycan could potentially be cleaved by the action of peptidoglycan hydrolases and contribute to virulence. The turnover products produced by peptidoglycan hydrolases can therefore interact with the host, and play a role in host-pathogen interactions, specifically within pathogenesis, so warrant investigation.

Peptidoglycan glucosaminidases have been discussed previously (Chapter 1.4.3.2). The genomes of SH1000 and NewHG contain four putative glucosaminidases which were identified using the well characterised Atl glucosaminidase domain as a BLAST template. Four bacterial chromosome encoded glucosaminidases were identified: *atl, sagA, sagB* and *scaH.* The genes *lytP2* and *lytP4* were also identified (Chan *et al.*, 2016b), and both are known to be encoded by the Newman specific prophages φNM2 and φNM4,

respectively (Bae *et al.*, 2006). Bacteriophages are not present, or are differentially present, in the genomes of all strains (Horsburgh *et al.*, 2002), and so to understand the role of the glucosaminidases, the core genome encoded enzymes are key.

S. aureus causes a wide range of pathologies using a diversity of virulence factors (Chapter 1.7.2). Study of the requirements for *S. aureus* pathogenesis may reveal new potential therapeutic targets that will help to combat infections, which is especially relevant in the ever-approaching post-antibiotic era. Due to the medical importance of *S. aureus* as a pathogen, it is common for genetic screens to be used to rapidly detect genes important for pathogenesis. This can be done by using transposon mutagenesis to produce strains with different single gene knockouts that can be studied in a high throughput way (Fey *et al.*, 2013). Transposon mutagenesis studies have not yet reported a role for glucosaminidases in infection (Coulter *et al.*, 1998; Bae *et al.*, 2004; Valentino *et al.*, 2014; Wang *et al.*, 2015)*.* However, other putative peptidoglycan hydrolases have been implicated (Coulter *et al.*, 1998). As well as these studies, targeted studies have been used to directly observe the importance of specific proteins in virulence. The loss of Sle1 activity, a *N*-acetylmuramyl-ʟ-alanine amidase, results in cell clustering and attenuation in a murine model of infection (Kajimura *et al.*, 2005). Conversely, the loss of Atl does not impact virulence in a murine device-related infection model (McCarthy *et al.*, 2016). A major limitation of these studies, however, is the high degree of redundancy seen with PG hydrolases, meaning that the inactivation of one hydrolase may not result in a phenotype, as other hydrolases compensate for its activity. Other *S. aureus* PG metabolism components are known to contribute to virulence (Reed *et al.*, 2015), suggesting that PG homeostasis, by the action of synthases and hydrolases, could be important for virulence. It

As previously discussed (Chapter 1.8), there are a wide range of animal models available to study *S. aureus* infections. Each model has a set of advantages and disadvantages, and by using models in combination more meaningful results can be obtained. For example, the zebrafish embryo model of infection can be utilised as a low-cost, high throughput

screen of strains, which can then be confirmed in a more immunologically relevant murine model. Zebrafish are bred and maintained very easily, with a pair being able to produce 100-200 eggs per mating (Prajsnar *et al.*, 2008). Zebrafish possess TLRs that have a high homology to those of humans (Jault *et al.*, 2004), as well as having circulating macrophages by 25 hpf (Herbomel *et al.*, 1999), and neutrophils by 30 hpf (Prajsnar *et al.*, 2008). In this model, 1500 CFU of *S. aureus* are injected into the zebrafish circulation valley, a dose which does not override the fish's immune system and results in approximately 50 % host mortality (McVicker *et al.*, 2014). The injected inoculum is phagocytosed by macrophages and neutrophils, from which a small subset of *S. aureus* escape, founding a lesion that leads to fish death (McVicker *et al.*, 2014; Pollitt *et al.*, 2018). Likely a single bacterium founds the lesion, meaning that the macrophages and neutrophils act as an immunological bottleneck, resulting in clonal expansion during infection (McVicker *et al.*, 2014; Pollitt *et al.*, 2018).

The well-established murine sepsis model of infection was also chosen in this study to analyse the virulence of *S. aureus* strains. This model has been highly studied, and the dynamics of the infection are well understood (Pollitt *et al.*, 2018) (Figure 4.1). Around 1 x 10^7 CFU of *S. aureus* are injected intravenously into the blood stream of the mice. The majority of the free bacteria are phagocytosed by host macrophages within the liver, with a small minority taken up by neutrophils (Pollitt *et al.*, 2018). There are two possible outcomes once within a phagocyte: the bacteria can be contained, potentially killed and the infection is eventually cleared, or the bacteria can overwhelm the phagocyte and escape into the surrounding environment (Pollitt *et al.*, 2018). Even if bacteria escape the phagocyte, many are then phagocytosed by another immune cell, with only a small proportion escaping this cycle. Free bacteria can potentially form micro-abscesses within the liver, with each micro-abscess being founded by a single bacterium, resulting in clonal expansion (Pollitt *et al.*, 2018). The free bacteria, and those within the micro-abscesses, are in a constant dynamic with phagocytes, and can be further phagocytosed, resulting in their clearance or subsequent escape. The phagocytosis of these bacteria has also been linked to the dissemination of the bacteria into other sites within the host, such as the kidney, where clonally expanded

populations of bacteria can form abscesses (Pollitt *et al.*, 2018). The CFUs recovered from the kidney abscesses, and to a lesser extent the liver, are a major output of the murine sepsis model, and an indicator of virulence (Pollitt *et al.*, 2018).
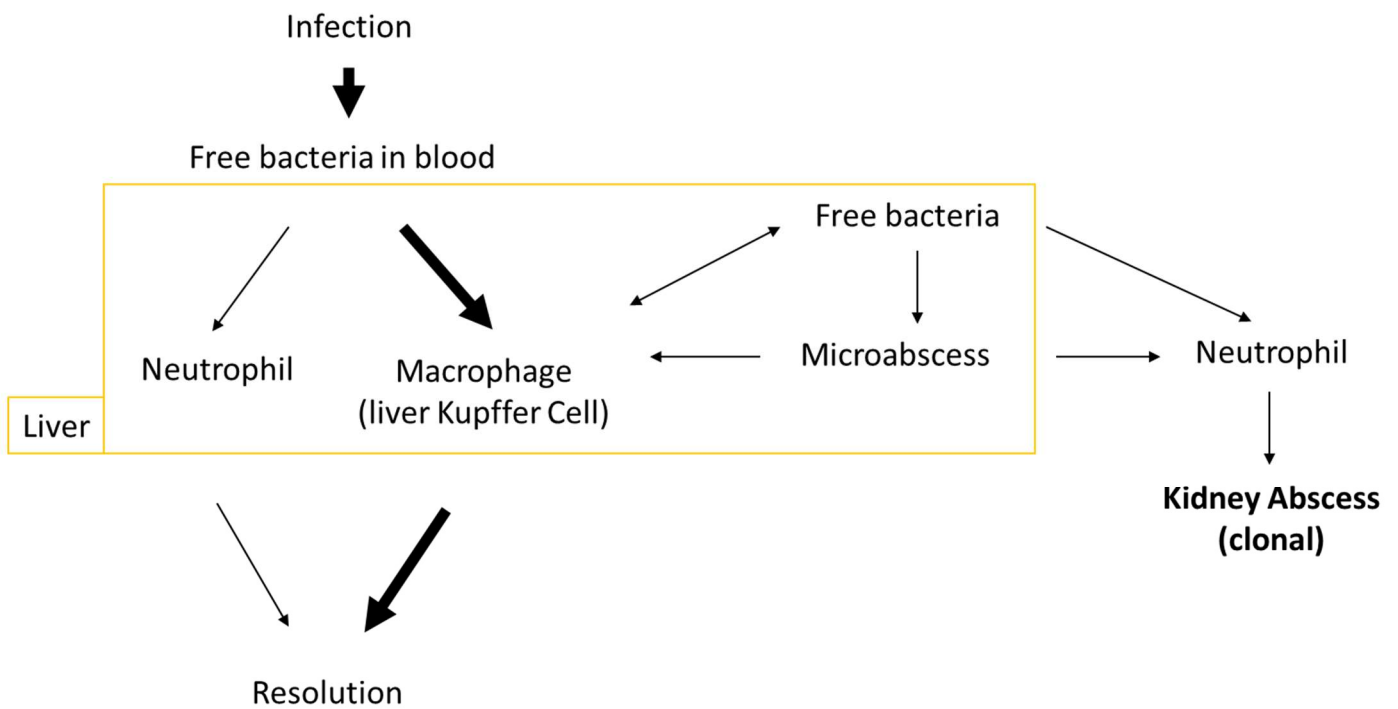
Figure 4.1 Schematic of *S. aureus* infection dynamics in the murine sepsis model of infection

An intravenous infection releases free bacteria into the blood stream, which can be phagocytosed by host neutrophils and macrophages. Most bacteria are taken up by the resident macrophages of the liver; the Kupffer cells. Whatever the phagocyte that captures the *S. aureus*, the bacteria are either killed and cleared from the host, or the bacteria can escape the phagocyte, becoming free bacteria again. After escaping, bacteria can seed the formation of micro-abscesses from which bacteria can be further phagocytosed. It is proposed that neutrophils can facilitate the dissemination of bacteria to other sites in the body, including kidneys, where *S. aureus* can establish abscesses, a major output of the murine sepsis model of infection. The thickness of the arrows represents the proportion of bacteria moving from one state to another. Adapted from Pollitt *et al*. (2018).

4.2   Aims of this chapter

The aim of this chapter was to characterise the role of the glucosaminidases of *S. aureus* in infection. Using *in vivo* models, the role the glucosaminidases play in virulence will be established. The specific aims of this chapter were to:

i.   Investigate the impact of the *S. aureus* glucosaminidases on virulence

ii.   Determine the cause of any observed changes in pathogenesis

4.3 Results

4.3.1 Role of the glucosaminidases (SagB, Atl, SagA and ScaH) in growth

Previous, preliminary studies have shown that a *sagB* mutant in the SH1000 (Wheeler *et al.*, 2015) and Newman (Chan *et al.*, 2016b) genetic backgrounds have a growth defect in liquid medium (BHI and TSB respectively).

Using the *S. aureus* SH1000 genetic background (Wheeler *et al.*, 2015) every single, double and triple mutant lacking an active *sagB* gene in combination with *atl, sagA* and *scaH* was tested for growth in liquid TSB (Figure 4.2). As expected, SH1000 *sagB* (SJF 4608, doubling time 37 min) shows a defect when compared to the wild type SH1000 (SJF 682, doubling time 31 min), taking a longer time to reach a similar OD_{600} over the eight-hour period (Figure 4.2A). The double mutants SH1000 *atl sagB* (SJF 4972, Figure 4.2B, doubling time 41 min) and SH1000 *sagA sagB* (SJF 4974, doubling time 38 min) and SH1000 *sagB scaH* (SJF 4973, Figure 4.2C, doubling time 36 min) all showing a similar growth defect to the single mutant SH1000 *sagB* compared to parental SH1000. Triple mutants containing an inactive *sagB* gene; SH1000 *atl sagA sagB* (SJF 4610, doubling time 47 min), SH1000 *sagA sagB scaH* (SJF 4612, doubling time 51 min) and SH1000 *atl sagB scaH* (SJF 4613, doubling time 48 min) show a slower rate of growth, but still reach a similar end point to the parental SH1000 (Figure 4.2D).
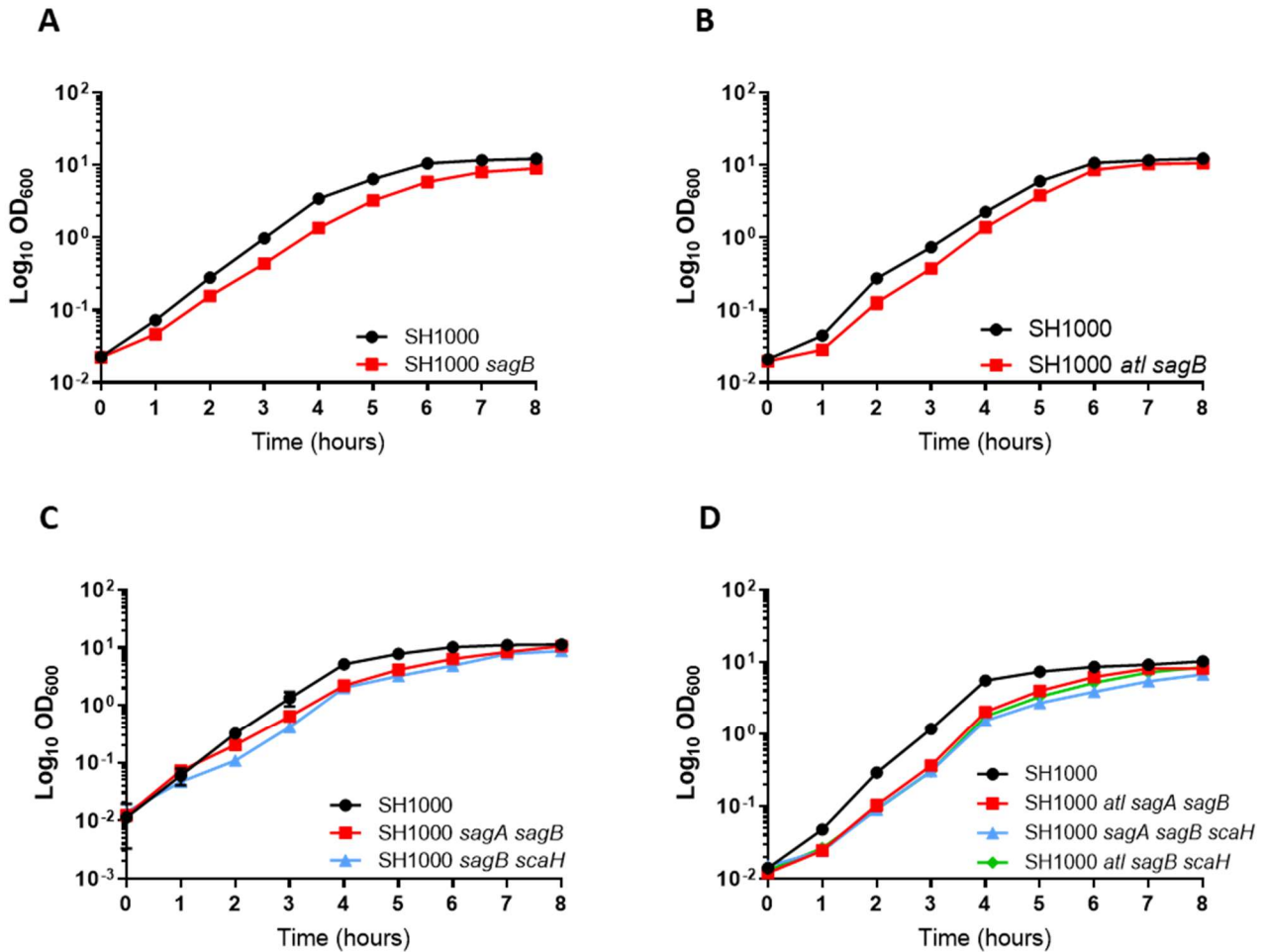
Figure 4.2 Role of glucosaminidases in growth of *S. aureus* SH1000

Strains were grown in TSB at 37 °C with shaking and OD_{600} was measured. Growth of SH1000 (SJF 682, black circles) in TSB compared to **(A)** SH1000 *sagB* (SJF 4608, red squares), **(B)** SH1000 *atl sagB* (SJF 4972, red squares), **(C)** SH1000 *sagA sagB* (SJF 4974, red squares) and SH1000 *sagB scaH* (SJF 4973, blue triangles) or **(D)** SH1000 *atl sagA sagB* (SJF 4610, red squares), SH1000 *sagA sagB scaH* (SJF 4612, blue triangles) and SH1000 *atl sagB scaH* (SJF 4613, green diamonds). Bacterial cultures were prepared in triplicate and error bars represent the standard deviation of the mean.

156

4.3.2 Role of glucosaminidases in *S. aureus* virulence in the zebrafish model

Zebrafish embryos at 30 hpf were injected into the circulation valley with 1500 CFU of bacteria in a volume of 1 nl (Prajsnar *et al.*, 2008). SH1000 *sagB* was found to be significantly attenuated ($p < 0.0001$) compared to the wildtype SH1000 (SJF 682) (Figure 4.3A). SH1000 *atl sagB* (SJF 4972, $p < 0.0001$), SH1000 *sagA sagB* (SJF 4974, $p < 0.0001$) and SH1000 *sagB scaH* (SJF 4973, $p < 0.0001$) were also found to be significantly attenuated when compared to the wildtype (Figure 4.3B). SH1000 *atl sagB* caused no mortality when injected at a dose of 1500 CFU, whereas SH1000 *sagA sagB* had a survival rate of 88% and SH1000 *sagB scaH* a survival rate of 85%. Finally, triple glucosaminidase mutants with an inactive *sagB* gene were analysed using the model. SH1000 *atl sagA sagB* (SJF 4610), SH1000 *sagA sagB scaH* (SJF 4612) and SH1000 *atl sagB scaH* (SJF 4613) were all significantly attenuated when compared to the wild type SH1000 (Figure 4.3C). The data in Figure 4.3 shows that a lack of a functional *sagB* gene is enough to cause attenuation in the SH1000 genetic background.
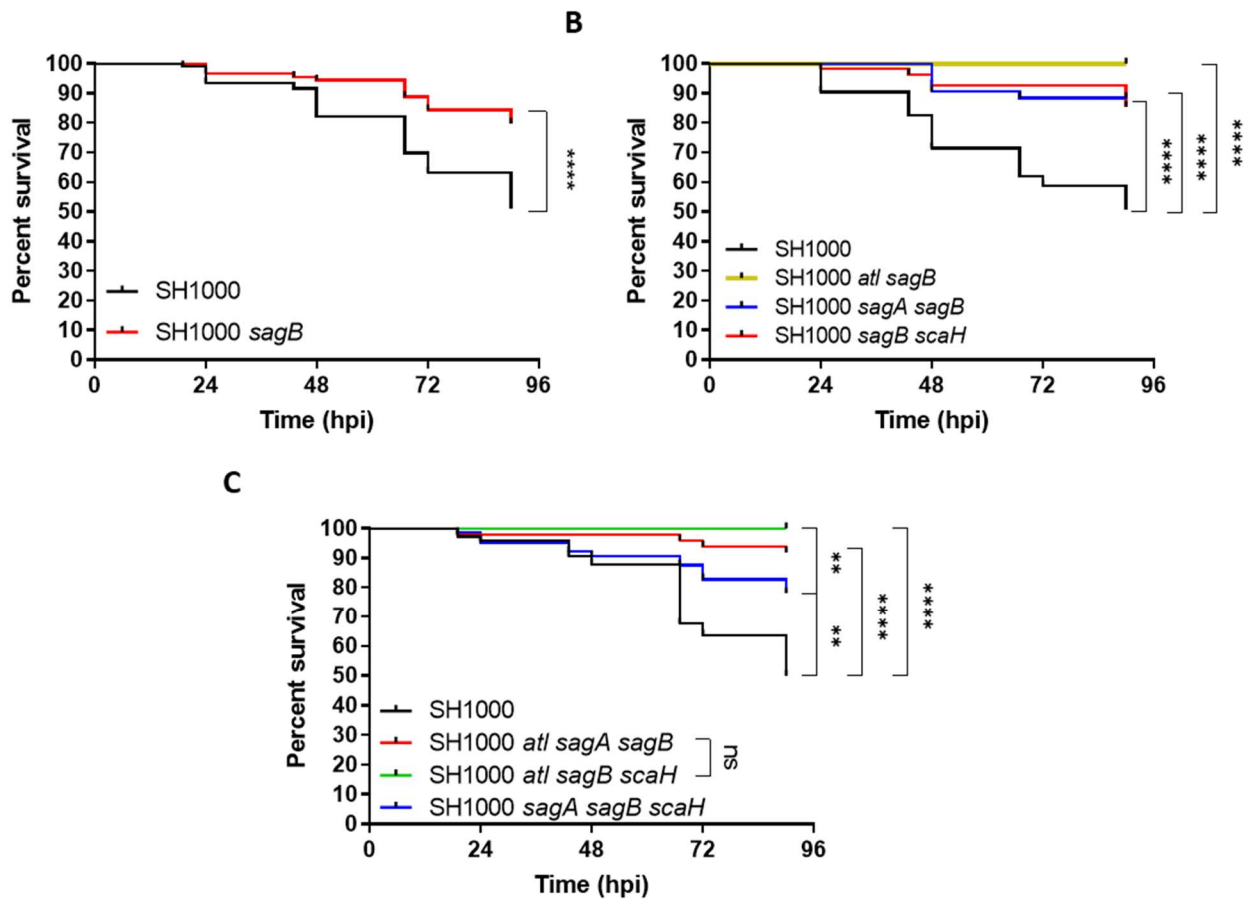
Figure 4.3 Role of the glucosaminidases in *S. aureus* virulence in the zebrafish infection model

(A) Survival curves showing the attenuation of SH1000 *sagB* (SJF 4608, red line) compared to parental SH1000 (SJF 682, black lines) (3 repeats, n>20, **** p < 0.0001). **(B)** Survival curves demonstrating that SH1000 *atl sagB* (SJF 4972, yellow line), SH1000 *sagA sagB* (SJF 4974, blue line) and SH1000 *sagB scaH* (SJF 4973, red line) are all attenuated compared to the parental SH1000 (SJF 682, black lines) (2 repeats, n>20, **** p < 0.0001). **(C)** Survival curves showing the attenuation of SH1000 *atl sagA sagB* (SJF 4610, red line), SH1000 *sagA sagB scaH* (SJF 4612, blue line) and SH1000 *atl sagB scaH* (SJF 4613, green line) are all attenuated compared to the parental SH1000 (SJF 682, black lines) (2 repeats, n>20,**** p < 0.0001). There is no significant difference between SH1000 *atl sagA sagB* and SH1000 *atl sagB scaH*, but both are significantly more attenuated than SH1000 *sagA sagB scaH* (** p = 0.0012).

4.3.3 Growth of SH1000 *sagB in vivo*

The observed virulence attenuation could be attributed to an inability of SH1000 *sagB* (SJF 4608) to grow *in vivo.* To test this the zebrafish embryo model, as described in Chapter 2.18.1.7 (McVicker *et al.*, 2014), was used. At specified time points after inoculation, five infected living zebrafish embryos (and all dead embryos) were collected and homogenised, after which they were plated out to determine bacterial CFU. When wildtype SH1000 (SJF 682) is injected into zebrafish embryos (1500 CFU) bacterial CFU either remain similar to the injected CFU, or increase associated with host death ($10^4 - 10^5$ CFU) (Figure 4.4A). In contrast, embryos injected with the same dose of SH1000 *sagB* (SJF 4608) show a decrease in the number of CFU over time, with some embryos containing bacterial numbers below the limit of detection (10 CFU/embryo), suggesting bacterial clearance (Figure 4.4B). SH1000 was observed to cause mortality in 23 % of observed embryos, while SH1000 *sagB* caused only 2 % mortality.
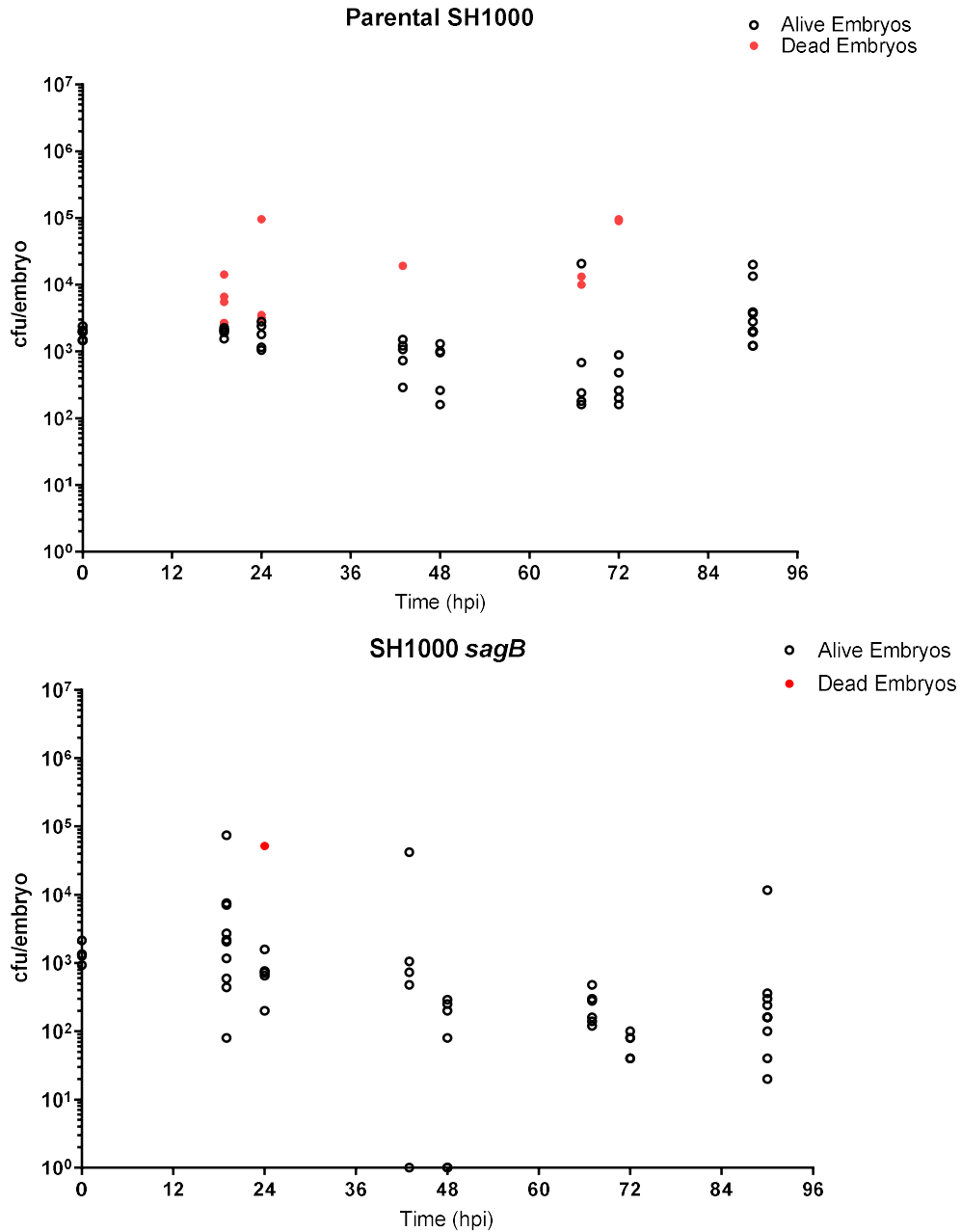
Figure 4.4 Growth of a *S. aureus sagB* strain within the zebrafish infection model

Bacterial CFU were recovered from zebrafish embryos infected with (**A**) SH1000 (SJF 682) or (**B**) SH1000 *sagB* (SJF 4608) (n= 50-60) at times shown. Open black circles are live embryos and red circles are dead embryos.

4.3.4 Construction of a *S. aureus* NewHG *sagB* strain

It is important to verify the attenuation of a *sagB* mutation in another *S. aureus* genomic background, to ensure that the phenotype is not specific to SH1000. The NewHG background is derived from the clinical isolate Newman, isolated in 1952 (Duthie and Lorenz, 1952). For murine studies of *S. aureus* infection, Newman is commonly used as the genomic background for studying virulence. However, a single nucleotide change in the *saeS* gene (a global virulence regulator) results in a higher level of toxin expression than that of other *S. aureus* strains (Mainiero *et al.*, 2010). The *saeS* gene of NewHG has been repaired, resulting in toxin gene expression equivalent to levels in other *S. aureus* strains.

The *sagB* mutation was transduced into the NewHG parental background (SJF 3663) using bacteriophage φ11 to produce NewHG *sagB* (SJF 4912). This was confirmed using PCR, where amplification of the *sagB* gene produced the expected mutant band in the transduced strain (Figure 4.5A; Wheeler *et al.*, 2015).

4.3.5 Virulence of NewHG *sagB* in the zebrafish embryo model of infection
4.3.5.1 NewHG *sagB* virulence phenotype

The NewHG *sagB* strain (SJF 4912) was investigated for its virulence in the zebrafish model of infection compared to the parental strain (SJF 3663). NewHG *sagB* was significantly attenuated (70% survival, p = 0.0043) compared to the same dose (1500 CFU) wildtype (46% survival) (Figure 4.5B). This confirms that the *sagB* mutant virulence phenotype is not specific to SH1000.

4.3.5.2 NewHG *sagB in vivo* growth kinetics

The *in vivo* growth kinetics of NewHG *sagB* were also studied using the zebrafish infection model. The CFU recovered from embryos infected with parental NewHG were found to be equal to those of the starting inoculum (10^3 CFU) or higher (up to 10^6 CFU), showing the growth of NewHG within the embryo. Dead embryos infected with NewHG had ~1 x 10^{3-6} recovered CFU, demonstrating that bacteria multiplied within the embryo (Figure 4.5C). However, as some fish were found dead containing ~10^3 CFU, this would imply that low numbers of bacteria (the same as the starting inoculum) can cause mortality in the zebrafish embryo. NewHG *sagB* infected fish also showed a maintenance or increase in recovered CFU over time, suggesting that NewHG *sagB* can grow in the zebrafish host (Figure 4.5D). Embryos infected with NewHG *sagB* can also clear infection, which was not seen in embryos infected with parental NewHG (Figure 4.5C and D, limit of detection 10 CFU/embryo), indicating that NewHG *sagB* has a growth defect *in vivo* in this model. Dead embryos infected with NewHG *sagB* have CFU around 1 x 10^{4-6} CFU.
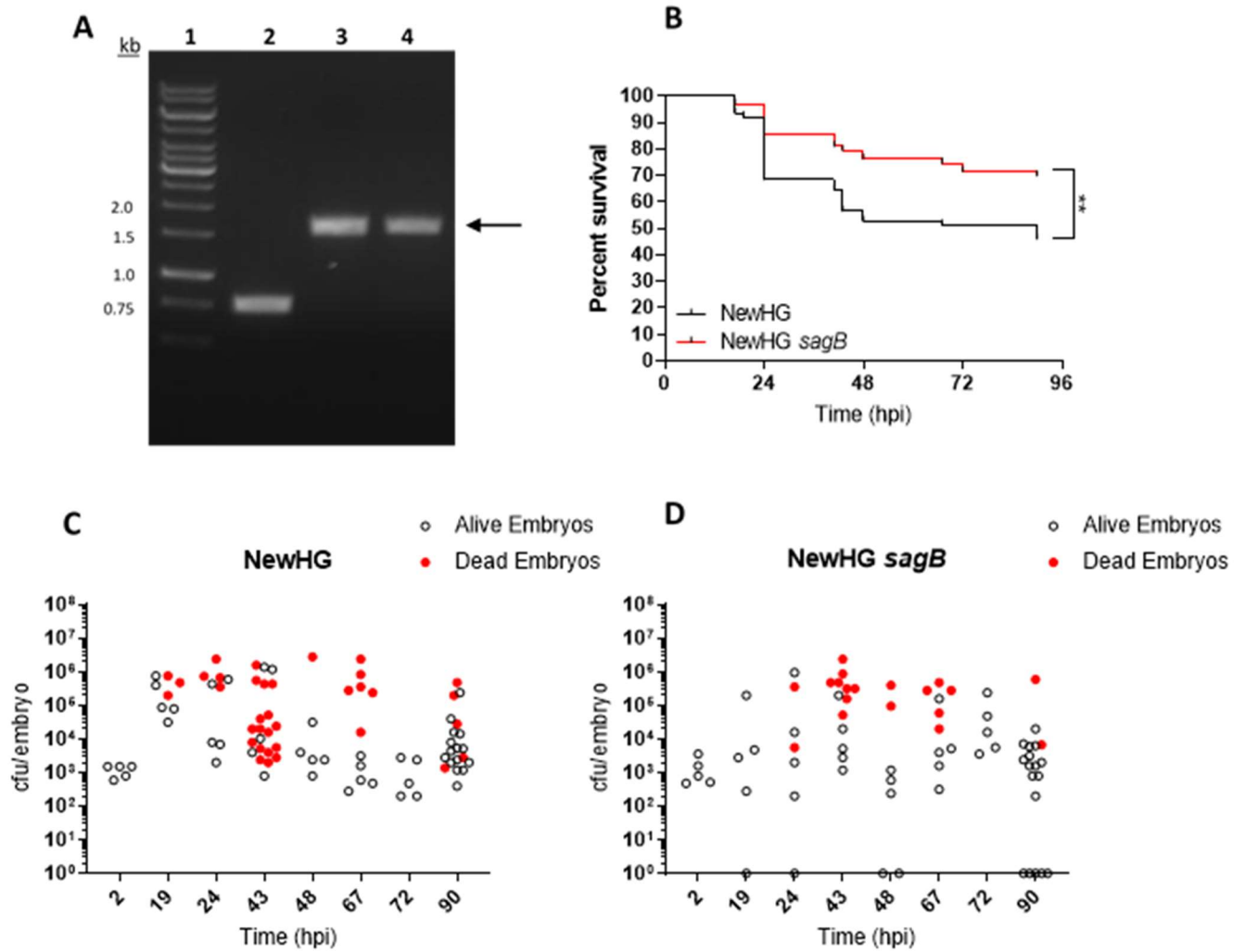
Figure 4.5 The role of SagB in virulence in the *S. aureus* NewHG background in the zebrafish model of infection

(A) 1% (w/v) TAE agarose gel showing PCR amplification of the *sagB* gene from wildtype NewHG (lane 2), positive control SH1000 *sagB* (lane 3) and NewHG *sagB* (SJF4912) (lane 4) using primers *psagB_F* (forwards) and *psagB_R* (reverse). The wildtype band of 761 bp can be seen in lane 2. The expected mutant band of 1700 bp, shown in lane 3 and indicated with a black arrow, is also seen in lane 4. Relevant sizes of DNA ladder (GeneRuler 1 kb DNA ladder, Thermo Scientific) are shown in kb (lane 1). **(B)** Survival curves showing the attenuation of NewHG *sagB* (SJF 4912, red line) compared to parental NewHG (SJF 3663, black lines) (2 repeats, n>20, ** p = 0.0043). **(C, D)** Bacterial CFU were recovered from zebrafish embryos infected with approximately 1500 CFU **(C)** NewHG (SJF 3663) or **(D)** NewHG *sagB* (SJF 4912) (n= 70-85) at times shown. Open black circles are live embryos and red circles are dead embryos.

4.3.6 Analysis of *sagB* virulence in murine models of infection
4.3.6.1 The murine sepsis model of infection

The well-established mouse sepsis model of infection was used (Chapter 2.18.2) to investigate NewHG *sagB* (SJF 4912) (Jonsson *et al.*, 2004; Kim *et al.*, 2014; Pollitt *et al.*, 2018). In murine experiments, NewHG *kan^R* (SJF 3680) was used as the parental type *S. aureus* strain. NewHG (SJF 3663) and NewHG *kan^R* have been shown to have the same virulence in both the zebrafish embryo model and murine sepsis models of infection (McVicker *et al.*, 2014), so can be used interchangeably and NewHG *kan^R* can be selected for using kanamycin from organ homogenates.

To investigate the virulence of *sagB* in the murine sepsis model of infection, groups of 10 mice were injected with 1 x 10^7 CFU of NewHG *kan^R* or NewHG *sagB* (Figure 4.6). Weight loss after infection is a measure of general sickness. Mice infected with NewHG *sagB* (SJF 4912) show significantly reduced weight loss that those infected with NewHG *kan^R*, with most mice infected with NewHG *sagB* maintaining their weight over the 72-hour infection period (Figure 4.6A, p = 0.0005). Significantly fewer *S. aureus* were recovered from the livers (p = 0.0178) and kidneys (p = 0.0178) of mice infected with NewHG *sagB* than compared to those infected with NewHG *kan^R* (Figure 4.6B, C).

164
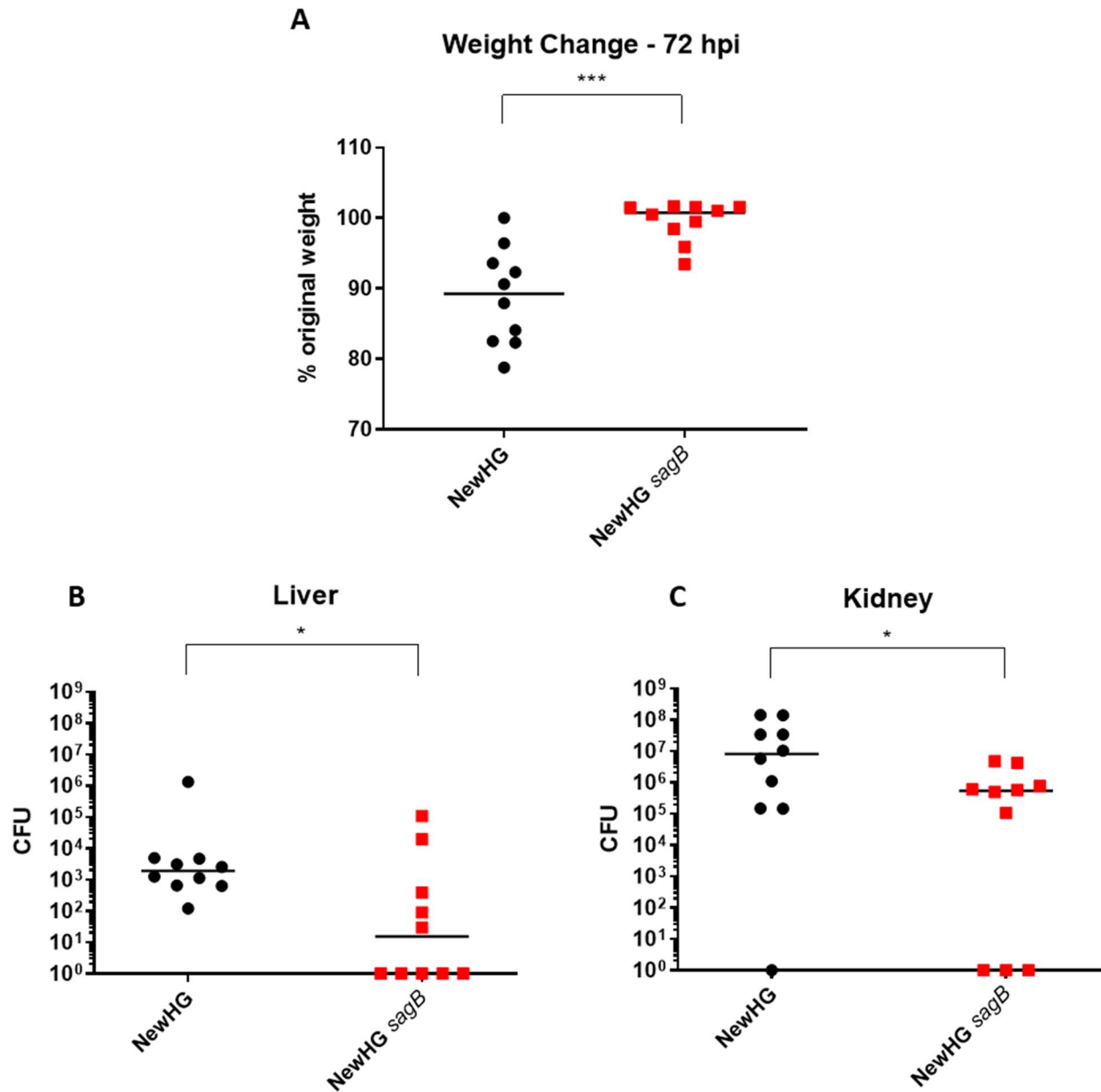
Figure 4.6 The role of SagB in virulence in the murine sepsis model of infection

Approximately 1 x 10^7 CFU of *S. aureus* NewHG *kan*[R] (SJF 3680) or NewHG *sagB* (SJF 4912) were injected intravenously into mice (n=10). Weight loss 72 hpi (**A**, *** p = 0.0005), liver CFU (**B**, * p = 0.0178) and kidney CFU (**C**, * p = 0.0368). Groups were compared using a Mann-Whitney U test (NewHG *kan*[R] – black circles, NewHG *sagB* red squares).

4.3.6.2 Augmentation of *sagB* in the murine sepsis model of infection

Augmentation in *S. aureus* infection has been described in detail in chapter 1.7.4. Briefly, insoluble purified peptidoglycan co-injected with *S. aureus* enhances pathogenicity (Boldock *et al.*, 2018). In the mouse sepsis model of infection, augmentation depends on co-internalisation of both the bacteria and the peptidoglycan by the resident macrophages of the liver, Kupffer cells (Boldock *et al.*, 2018). Augmentation with peptidoglycan was shown to reduce the reactive oxygen species burst and acidification of *S. aureus* containing phagolysosomes in Kupffer cells. The addition of peptidoglycan in infection allows *S. aureus* to survive more within macrophages, and therefore more *S. aureus* can seed abscesses, and worsen infection (Boldock *et al.*, 2018). Augmentation results in a large CFU of *S. aureus* within the livers of mice.

NewHG *kan*^{R} (SJF 3680) or NewHG *sagB* (SJF 4912), at a low dose (around 1×10^6 CFU) were injected intravenously either with or without 250 µg of purified PGN (NewHG *kan*^{R}, SJF 3680). When injected with low dose NewHG *kan*^{R} or NewHG *sagB* alone, mice either maintained or gained weight over the infection period. When NewHG *kan*^{R} was co-injected with peptidoglycan, mice lost significantly more weight than mice receiving NewHG *kan*^{R} alone (p = 0.0079). Mice infected with NewHG *sagB* and peptidoglycan also lose significantly more weight than those mice infected with NewHG *sagB* alone (Figure 4.7A, p = 0.0159). The positive control of NewHG *kan*^{R} shows a significant increase of CFU in the livers of mice when peptidoglycan is co-injected with NewHG *kan*^{R} (p = 0.0079), demonstrating augmentation has occurred (Figure 4.7B). NewHG *sagB,* however, does not appear to be augmented when co-injected with peptidoglycan, as there is no significant increase in CFU recovered from the livers, although the median is higher (Figure 4.7B, p = 0.0952). While there are no significant differences in the kidneys between low dose bacteria and co-injection groups (Figure 4.7C), there is a clear trend for higher CFU recovered from mice infected with NewHG *kan*^{R} with peptidoglycan than NewHG *kan*^{R} alone, whereas for NewHG *sagB* this trend is less apparent. There were no significant differences found between the bacteria only and co-injection groups in the spleen (Figure 4.7D).

The results of this experiment suggest that NewHG *sagB* cannot be augmented using NewHG *kan^R* purified peptidoglycan, as there are no significant differences in CFU between the NewHG *sagB* alone and augmented NewHG *sagB* groups.
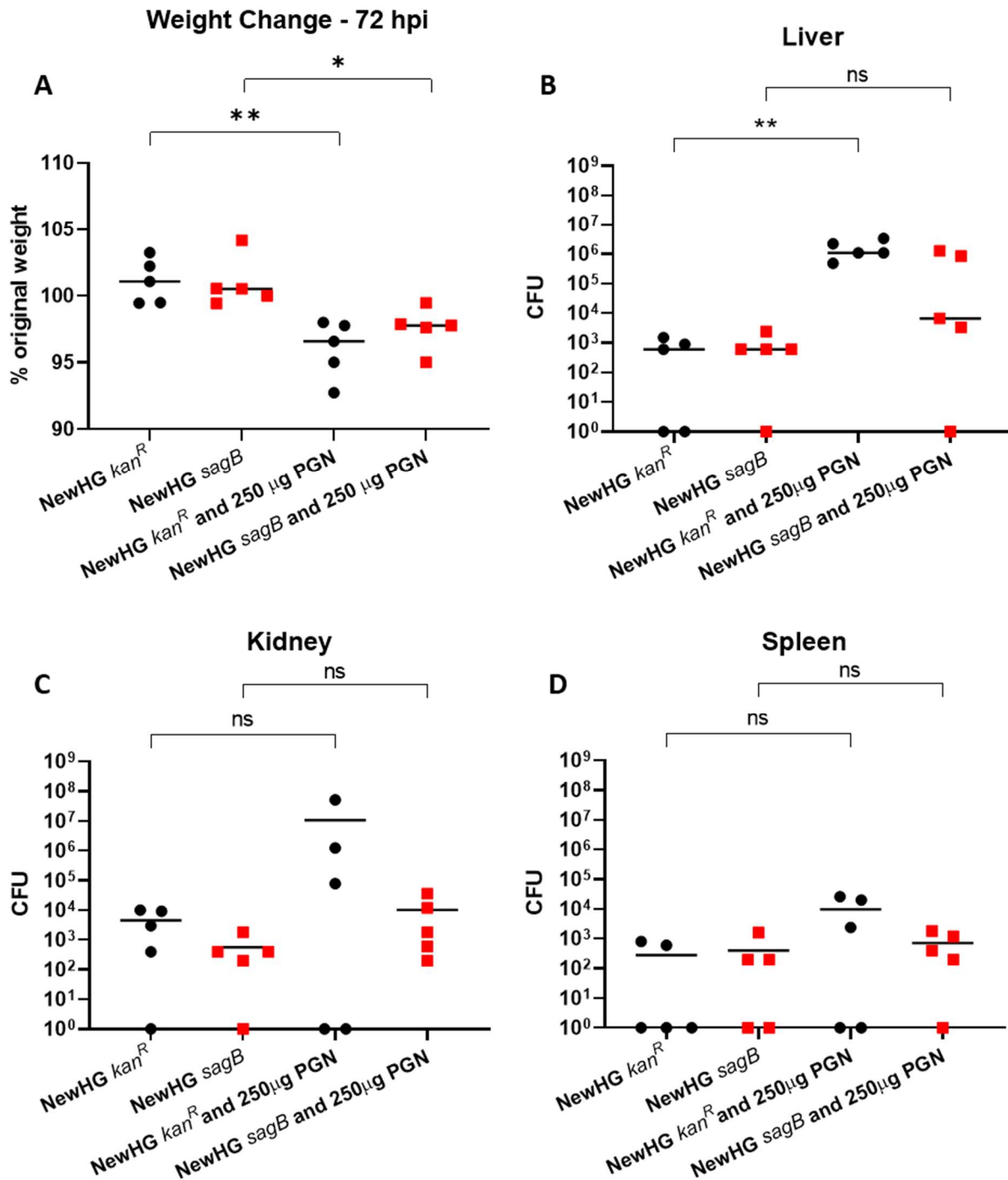
Figure 4.7 Augmentation of the *S. aureus sagB* mutant using staphylococcal peptidoglycan

Approximately 1x10^6 CFU *S. aureus* NewHG *kan*^{R} (WT, SJF 3680) or NewHG *sagB* (SJF 4912) with or without 250 µg WT *S. aureus* PGN was injected intravenously into mice (n=5)*.* Weight loss 72 hpi (**A**) and CFUs recovered from livers (**B**), kidneys (**C**) and spleen (**D**) were recorded to determine if the *sagB* mutant could be augmented. Groups were compared using Mann-Whitney U tests (NewHG *kan*^{R} – black circles, NewHG *sagB*-red squares) (* p = 0.0159, ** p = 0.0079).

4.3.6.3 Augmentation using purified peptidoglycan from NewHG *sagB*

As NewHG *sagB* (SJF 4912) cannot be augmented by wildtype NewHG (SJF 3663) peptidoglycan, it was investigated if purified NewHG *sagB* peptidoglycan can augment a NewHG infection.

To investigate if *sagB* peptidoglycan could augment a wild type infection in the murine model, mice were injected with either: low-dose (1×10^6 CFU) NewHG *kan^R*, low-dose NewHG *kan^R* with 250 µg NewHG peptidoglycan or low-dose NewHG *kan^R* with 250 µg NewHG *sagB* peptidoglycan. Mice co-injected with low-dose NewHG *kan^R* and NewHG *sagB* peptidoglycan show a significant weight loss than mice injected with NewHG *kan^R* alone (Figure 4.8A, p = 0.0029). The bacterial CFU recovered from the livers of mice co-infected with low-dose NewHG *kan^R* with 250 µg NewHG peptidoglycan or infected with low-dose NewHG *kan^R* and 250 µg NewHG *sagB* peptidoglycan where both significantly higher than those infected with low-dose NewHG *kan^R* alone (Figure 4.8B, p = 0.0079). From the numbers of bacteria recovered from the kidneys, it is clear there is a trend for more bacteria being recovered from mice receiving NewHG *kan^R* with NewHG peptidoglycan than NewHG *kan^R* alone, despite the lack of significance (p = 0.1667). Co-injecting with NewHG *sagB* peptidoglycan significantly increases the number of bacteria recovered from the kidney, further confirming that augmentation has occurred using *sagB* mutant peptidoglycan (Figure 4.8C, p = 0.0317). No significant differences in CFU could be found in the spleens, lungs or hearts of any group (Figure 4.8D, E and F respectively). The conclusion from this experiment is that *sagB* peptidoglycan can be used to augment an *S. aureus* infection.
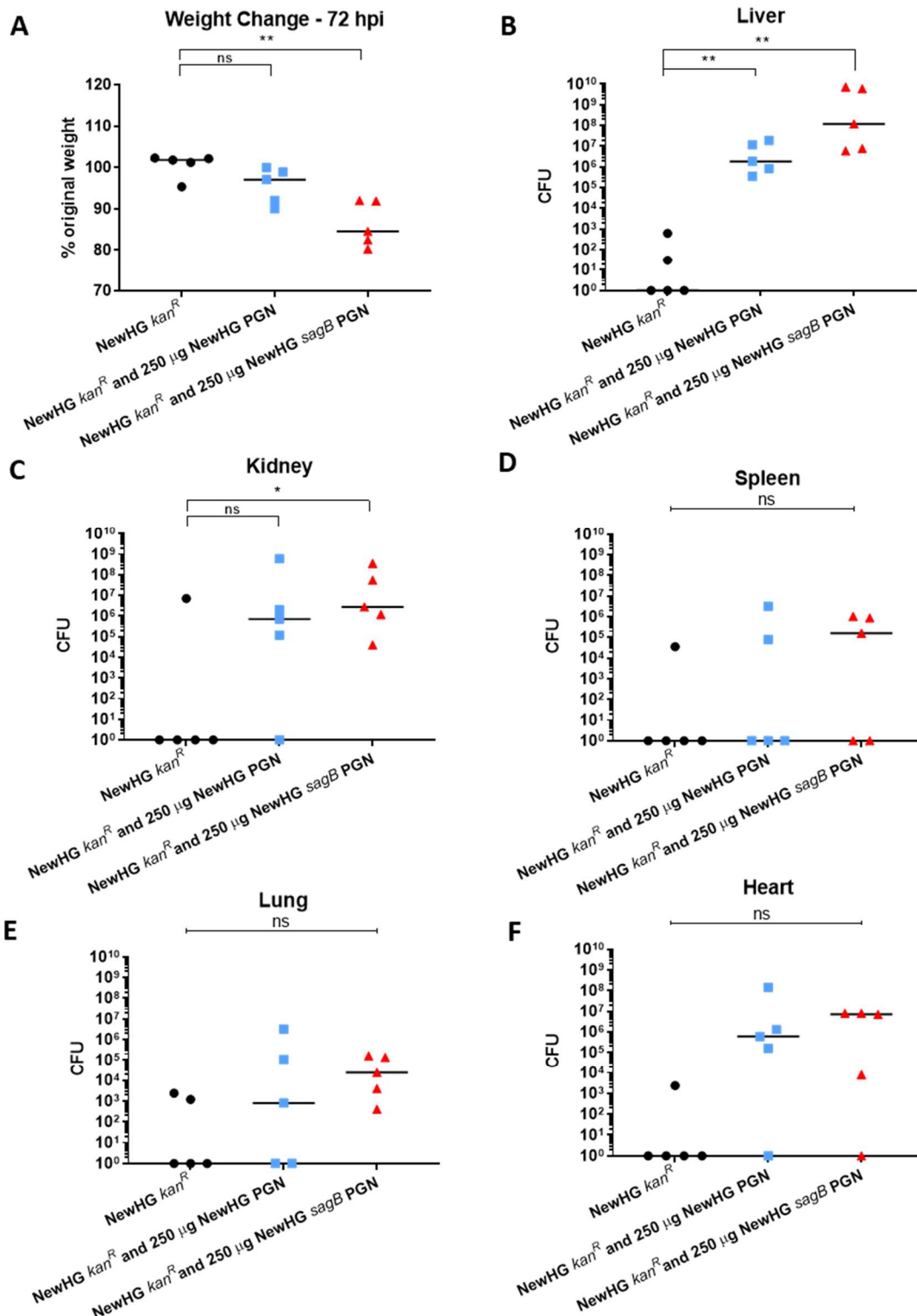
Figure 4.8 Augmentation of *S. aureus* NewHG using peptidoglycan from wildtype and *sagB S. aureus* strains

Mice (n=5) were injected with approximately 1x10^{6} CFU *S. aureus* NewHG *kan*[R] (WT, SJF 3680) alone, or with 250 μg NewHG *kan*[R] PGN or 250 μg NewHG *sagB P*GN. Weight loss 72 hpi (**A**, p= 0.0029) and CFUs recovered from livers (**B,** p = 0.0079), kidneys (**C**), spleen (**D**), lungs (**E**) and heart (**F**) were determined. Groups were compared using a Mann-Whitney U test (NewHG *kan*[R] *only* – black circles, NewHG *kan*[R] with wild type PGN - blue squares and NewHG *kan*[R] with NewHG *sagB* PGN – red triangles).

4.3.7 *S. aureus sagB* survival in human macrophages

While murine models share similarities to human infection the differences between the systems means that results may not translate through to be relevant in a clinical setting (Jonsson *et al.*, 2004). Research has shown that during the mouse sepsis model of infection, bacteria move through the blood to the liver, where they are phagocytosed by the resident macrophages Kupffer cells (Pollitt *et al.*, 2018). As macrophages may play a role in the attenuation of *sagB*, and to ensure that the attenuation results translate to a clinically relevant model, the ability of NewHG *sagB* (SJF 4912) to survive in human macrophages compared to NewHG *kan*[R] (SJF 3680) was investigated using monocyte derived macrophages (MDMs) (chapter 2.20.1).

Approximately 2×10^5 MDMs were infected with either NewHG *kan*[R] (SJF 3680) or NewHG *sagB* (SJF 4912) at a multiplicity of infection (MOI) of 5 for a period of 4 hours. Extracellular bacteria were removed by gentamycin, and MDMs were lysed at specified time points to determine intracellular CFU (Boldock *et al.*, 2018). When NewHG *kan*[R] is used to infect MDMs, a significant (~10 fold) drop in intracellular CFU was seen in the first 30 min after gentamycin treatment (Figure 4.9). After this, the number of intracellular CFU remains roughly stable (5 – 6.5 hpi). This could be due to MDMs being unable to kill anymore bacterial cells, or because the remaining *S. aureus* are able to withstand killing by MDMs. Intracellular numbers of NewHG *sagB* recovered also show roughly a 10-fold drop in the first 30 min after gentamycin treatment. However, at time points past 5 hpi, the intracellular recovered CFU continue to drop, suggesting killing of NewHG *sagB* by the MDMs (Figure 4.9). The intracellular NewHG *sagB* CFU recovered 5 (p = 0.0250), 5.5 (p = 0.0075) and 6 hpi (p = 0.0003) are all significantly lower than those recovered for NewHG *kan*[R], demonstrating NewHG *sagB* is less able to survive within host macrophages.
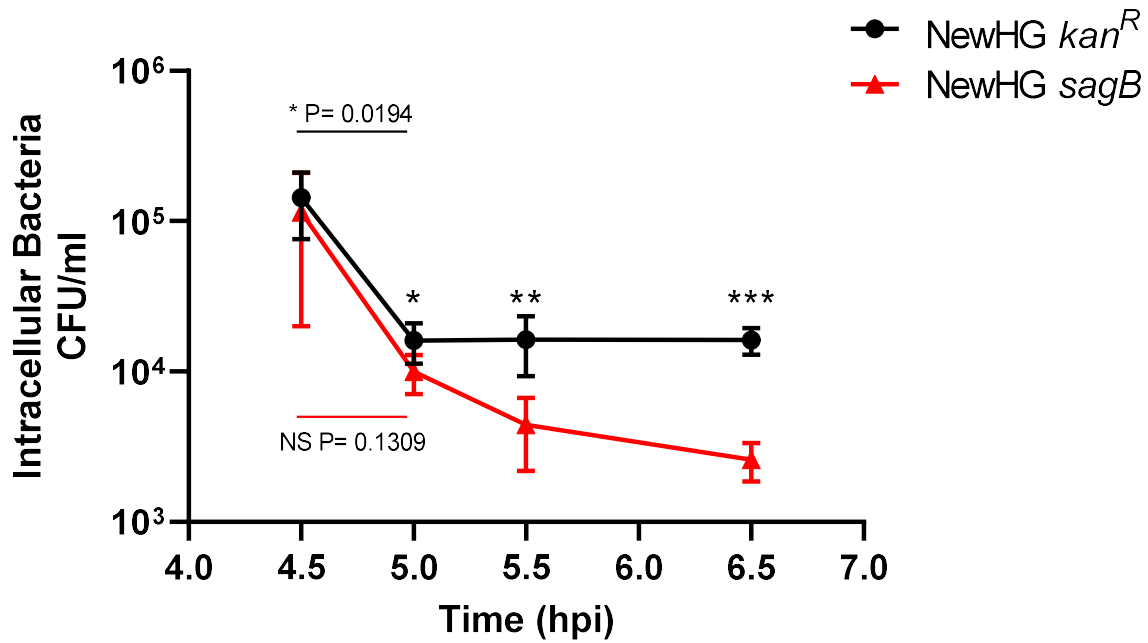
Figure 4.9 The role of SagB in intracellular killing of *S. aureus* by human MDMs

MDMs were incubated with *S. aureus* NewHG *kan*[R] (SJF 3680, black circles) or NewHG *sagB* (SJF 4912) at a MOI of 5 (1 x 10^{6} CFU) for 4 hours before being treated with gentamycin for 0.5 hours to kill extracellular bacteria. MDMs were lysed at specific time points and intracellular bacterial numbers were determined. A two-way ANOVA with Tukey's multiple comparison post-test was used to compare the first two time points for each strain, while paired two-tailed t-tests were used to compare between the strain CFU at subsequent time points. (* p = 0.0250, ** p = 0.0075, *** p = 0.0003). Error bars show ±SD. (n = 3, each consisting of 2 intra-assay repeats).

4.3.8   The interrelationship between SagB and macrophages within infection models

The *sagB* mutant is less able to survive within human MDMs. If SagB has an important role in macrophage interaction, then depletion of these phagocytes may restore virulence of the *sagB* mutant. This can be achieved by injecting animal hosts with liposomes containing clodronate before infection with *S. aureus*. Clodronate itself is non-toxic, as are liposomes (Rooijen and Sanders, 1994). However when delivered in liposomes, which are selectively taken up by macrophages, clodronate accumulates within the macrophages, resulting in their death and depletion (Rooijen and Sanders, 1994).

4.3.8.1 Role of macrophages in the zebrafish embryo model of infection

Macrophages can be depleted from the zebrafish model using the methods in chapters 2.18.3 and 2.18.1.5. The injection of clodronate liposomes into the circulation valley of zebrafish embryos 24 hpf depletes the macrophages without killing the zebrafish embryo (Shwartz *et al.*, 2019).

At 24 hpf, zebrafish embryos were injected with either clodronate containing liposomes or liposomes only containing PBS (control liposomes). At 30 hpf, both groups were injected with either 150 CFU SH1000 (SJF 682) or SH1000 *sagB* (SJF 4608) (Figure 4.10). A low dose of bacteria (150 CFU) was used as it has been previously shown that removal of macrophages renders the host more pathogen susceptible (Prajsnar *et al.*, 2020). Embryos injected with control liposomes show a significant difference in survival between those injected with 150 CFU of SH1000 or SH1000 *sagB*, showing that at this dose a *sagB* mutant is also attenuated (p = 0.0254). Embryos that had been treated with clodronate liposomes, to deplete macrophages, saw no significant difference in survival in embryos injected with either SH1000 or SH1000 *sagB* (Figure 4.10, p = 0.2733)*.* Embryos injected with clodronate liposomes show significantly higher mortality than those treated with control liposomes when infected with either SH1000 or SH1000 *sagB*

(p < 0.0001). Without macrophages in the infection model, SH1000 *sagB,* which is otherwise attenuated, has a virulence equivalent to the wildtype SH1000. This suggests that in the zebrafish model of infection, macrophage interaction is the cause for the attenuation of the *sagB* mutant.
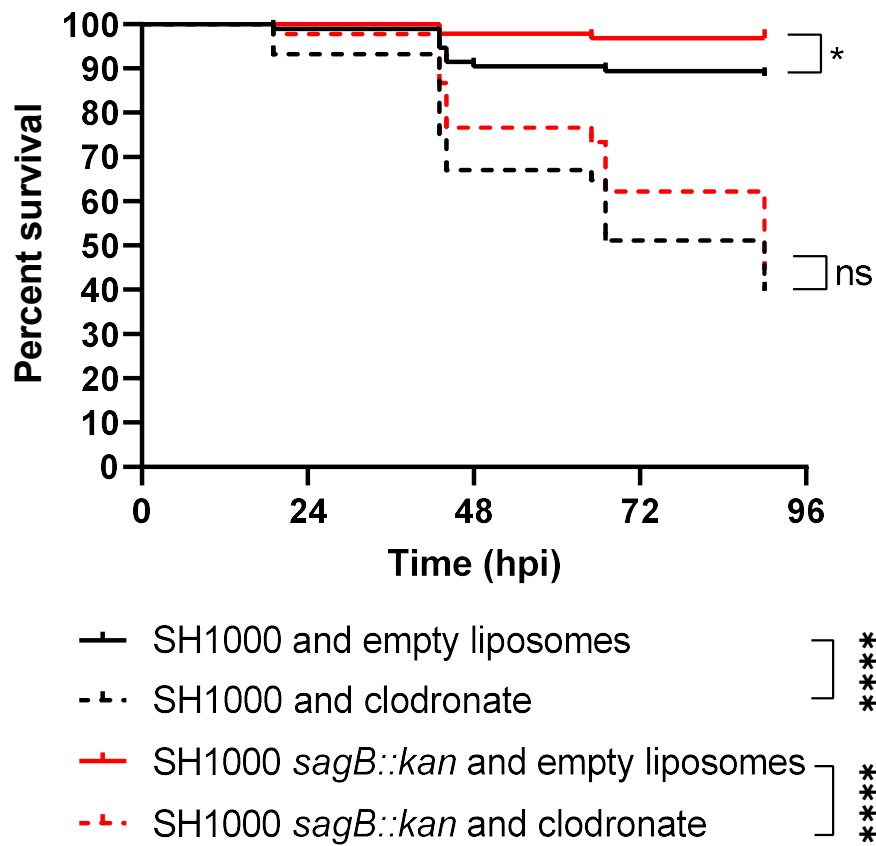
Figure 4.10 The role of macrophages in the attenuation of *S. aureus sagB* in the zebrafish infection model

At around 24 hpf, zebrafish embryos were injected with either empty liposomes or clodronate containing liposomes. At 30 hpf, around 150 CFU of SH1000 (SJF 682) or SH1000 *sagB* (SJF 4608) were injected. (Black lines – SH1000, red lines – SH1000 *sagB*, solid lines – empty liposome, broken lines – clodronate treated) (3 repeats, n>20, * p = 0.0254, **** p < 0.0001).

4.3.8.2 Role of macrophages in the murine sepsis model

The methods used to deplete macrophages are described in Chapters 2.18.2 and 2.18.3. Clodronate containing liposomes are injected into the tail vein of mice 24 hours before *S. aureus* infection (Verdrengh and Tarkowski, 2000; Boldock *et al.*, 2018; Pollitt *et al.*, 2018).

Mice were injected with either clodronate or control liposomes 24 hours before being injected intravenously with 1×10^5 CFU NewHG *kan^R* (SJF 3680) or NewHG *sagB* (SJF 4912) (Figure 4.11). For mice injected with control liposomes and NewHG *kan^R* or NewHG *sagB*, no significant difference could be found between the weight loss, liver CFU, kidney CFU or spleen CFU recovered from infected mice (Figure 4.11A, B, C and D respectively). Despite the lack of significance, there is a trend for fewer recovered CFU and greater clearance in mice infected with NewHG *sagB.* The lack of significance may be due to the low inoculum. Concomitantly, low numbers of bacteria were recovered from the organs of infected mice (Figure 4.11). Clodronate treatment led to a dramatic increase in recovered CFU for both strains (Figure 4.11). This allowed the two bacterial strains to be compared.

Clodronate treated mice injected with NewHG *sagB* lost significantly less weight over a period of 72 hpi compared to mice injected with NewHG *kan^R* (Figure 4.11A). Interestingly the CFU recovered from the liver, kidneys and spleen of clodronate treated mice infected with NewHG *sagB* were consistently and significantly lower than those recovered from mice infected with NewHG *kan^R* (Figure 4.11 B, C and D)*.* Thus, although macrophages are important in the control of both the wildtype and *sagB* strains, they are not solely responsible for the observed *sagB* attenuation.

176
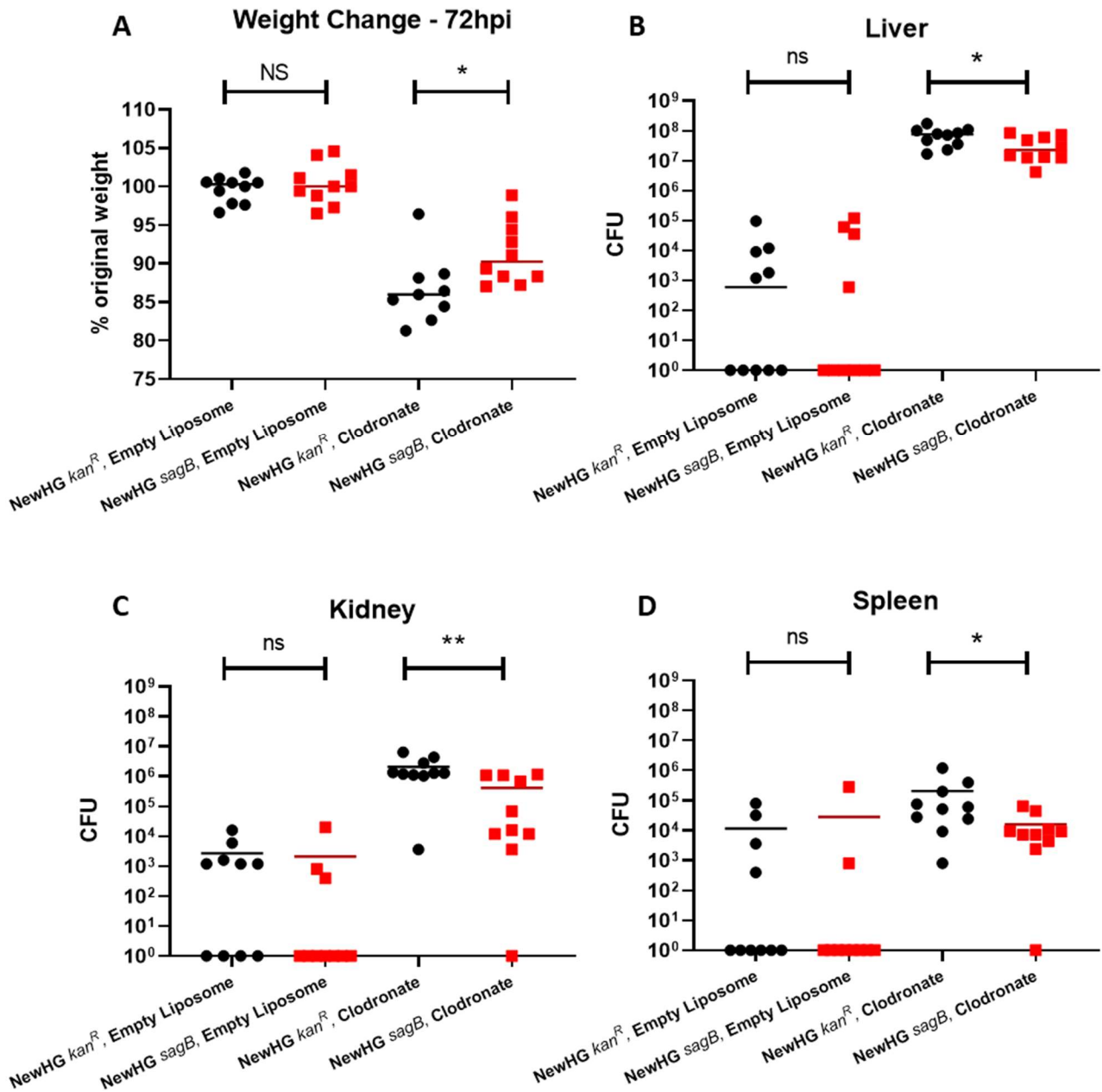
Figure 4.11 The role of macrophages in the murine sepsis model in the attenuation of *S. aureus sagB* mutants

Mice (n=10) were injected with approximately 1×10^5 CFU of NewHG *kan*[R] (SJF 3680) or NewHG *sagB* (SJF 4912) 24 hours post treatment with empty liposomes or clodronate containing liposomes. 72 hpi, mice were sacrificed and the weight change (**A,** * p = 0.0254) and liver (**B,** * p = 0.0243), kidney (**C,** ** p = 0.0030) and spleen (**D,** * p = 0.0196) CFU were determined. Groups were compared using Mann-Whitney U tests (NewHG *kan*[R] – black circles, NewHG *sagB*- red squares). One mouse in the NewHG *kan*[R] clodronate treated group was culled at 48 hpi due to reaching severity limits and has been excluded from the graph and statistical analysis.

4.3.9 The role of multiple glucosaminidases in staphylococcal pathogenesis

The results from Figure 4.3B and 4.3C suggest that all the glucosaminidases may play a role in virulence of *S. aureus*. The remaining glucosaminidases: Atl, SagA and ScaH were interrogated for their role and importance in the growth and virulence of *S. aureus.*

4.3.9.1 Role of glucosaminidases in growth

Existing glucosaminidase mutants in the SH1000 background were analysed for their growth as described in Chapter 2.8. At each hourly timepoint, the OD_{600} and the CFU per ml culture was determined for both the mutant and the control parental strain. It is already known that *atl* mutants form clusters of cells, due to an inability to properly divide daughter cells (Takahashi *et al.*, 2002; Wheeler *et al.*, 2015).

SH1000 *atl* (SJF 1367) was grown at 37 °C, 200 rpm in 50 ml TSB in a 250 ml conical flask, with absorbance at 600 nm and CFU per ml being determined (Chapter 2.7.1, 2.7.2), compared to the parental SH1000 (SJF 682). As SH1000 *atl* forms particles consisting of many bacteria the CFU at each timepoint was determined for an unsonicated sample, the CFU of which represents the number of particles per ml, and a sonicated sample, the CFU of which represents the number of bacteria per ml (Chapter 2.10). The growth of SH1000 *atl* as determined by optical density shows the same growth kinetics as the parental SH1000 (Figure 4.12A). However, the CFU growth shows that, when unsonicated, the SH1000 *atl* mutant has fewer particles than SH1000 (Figure 4.12A). This can be explained as the *atl* mutant results in the formation of clusters. When sonicated, SH1000 *atl* follows the same growth kinetics as the sonicated SH1000 strain. This shows that SH1000 *atl* grows at the same rate as parental SH1000 but cannot complete division. Both SH1000 *sagA* (SJF 4606) and SH1000 *scaH* (SJF 4607) were also analysed (Figure 4.12B and C respectively). Both mutants showed the same growth kinetics as parental SH1000 (SJF 682) when analysed by optical density, and by CFU, with both unsonicated and sonicated CFU being comparable at all time points. The results in Figure

4.12 show that SH1000 *atl* (SJF 1367), SH1000 *sagA* (SJF 4606) and SH1000 *scaH* (SJF 4607) all have the same growth kinetics as the parental SH1000. The only exception is that SH1000 *atl* forms clusters.

Figure 4.12 The role of *S. aureus* SH1000 glucosaminidases in growth in TSB

Growth of parental SH1000 (SJF 682, black circles solid line) or parental SH1000 sonicated (open black circles and broken line) in TSB compared to: **(A)** SH1000 *atl* (SJF 1367, yellow squares) and sonicated SH1000 *atl* (yellow open squares, broken lines), **(B)** SH1000 *sagA* (SJF 4606, blue squares) and sonicated SH1000 *sagA* (blue open squares, broken lines) or **(C)** SH1000 *scaH* (SJF 4607, red squares) and sonicated SH1000 *scaH* (red open squares, broken lines). Bacterial cultures were prepared in triplicate and error bars represent the standard deviation of the mean. Sonicated strains were sonicated for 20 seconds at an amplitude of 5 microns.

4.3.9.2 Virulence of glucosaminidase mutants in the zebrafish embryo model of infection

To determine if the glucosaminidases play a role in virulence, 1500 CFU of each strain was injected into the circulation valley of zebrafish embryos. As SH1000 *atl* (SJF 1367) forms clusters during growth, defining the injected CFU was vital. Around 500 particles of SH1000 *atl* were injected into zebrafish embryos, which was the equivalent of roughly 1500 bacteria. To ensure that the correct number of bacteria for each glucosaminidase strain was correct, the parental and mutant strains were plated on TSA unsonicated, to determine the number of particles injected, and sonicated, to determine the number of bacteria injected.

Zebrafish infected with 500 CFU (particles) of unsonicated SH1000 *atl* were compared to a group injected with 1500 CFU of unsonicated parental SH1000 (Figure 4.13A). SH1000 *atl* was shown to cause the same amount of mortality in zebrafish embryos as the wild type SH1000, suggesting that the clusters formed by SH1000 *atl* do not impact upon pathogenesis in the zebrafish model. This matches with data of a murine implant model, where a JE2 *atl* mutant was found to have no significant difference in virulence compared to the wild type JE2 (McCarthy *et al.*, 2016). Zebrafish injected with 1500 CFU of unsonicated SH1000 *sagA* also showed no difference in virulence when compared to mortality of zebrafish injected with the same CFU of parental SH1000 (Figure 4.13B). SH1000 *scaH* (1500 CFU) also shows the same virulence as the parental SH1000 (Figure 4.13C).

Figure 4.13 Role of the glucosaminidases Atl, SagA and ScaH in *S. aureus* virulence in the zebrafish infection model

Survival curves of zebrafish embryos injected with approximately 1500 CFU of *S. aureus* SH1000 (SJF 682, black lines) or **(A)** approximately 500 CFU SH1000 *atl* (1500 CFU after sonication) (SJF 1367, yellow line) **(B)** approximately 1500 CFU SH1000 *sagA* (SJF 4606, blue line) or **(C)** approximately 1500 CFU SH1000 *scaH* (SJF 4607, red line). (3 repeats, n>20), all groups are not significantly different from the parental SH1000 strain.

4.3.9.3 Construction of double glucosaminidase mutant strains

Double glucosaminidase mutants were constructed in the SH1000 genomic background using phage transduction (chapter 2.12.3). To produce SH1000 *atl sagA* (SJF 5261), a phage lysate was produced from SH1000 *atl* (SJF 5255), which was used to transfer the *atl* mutation into SH1000 *sagA* (SJF 4606). The PCR confirmation for this strain can be seen in Figure 4.14A, where mutant bands can be seen in lanes 4 and 8. SH1000 *atl scaH* (SJF 5262) was made in the same fashion, with the *atl* gene transduced into SH1000 *scaH* (SJF 4607), confirmed by PCR amplification of the target genes (Figure 4.14B). Finally, SH1000 *sagA scaH* (SJF 5217) was constructed by transducing a *scaH* mutation (SJF 2109) into SH1000 *sagA* (SJF 4606). The success of this transduction was confirmed by PCR of the *sagA* and *scaH* genes to ensure both contained the marked insertion, inactivating the genes (Figure 4.14C).

184
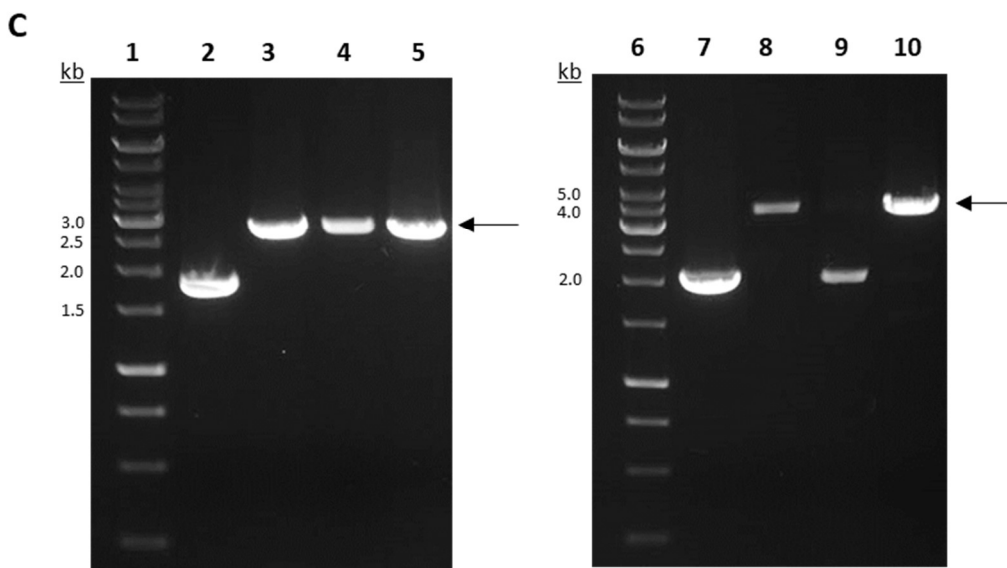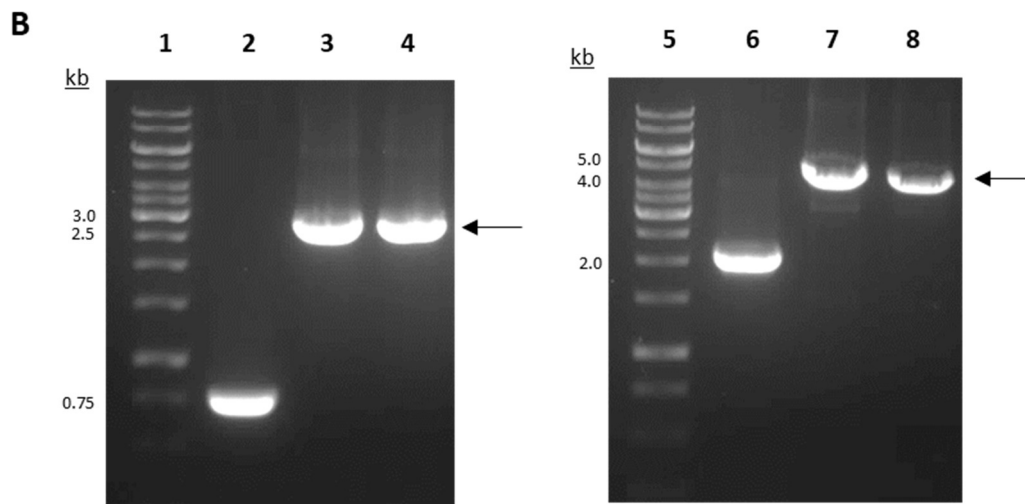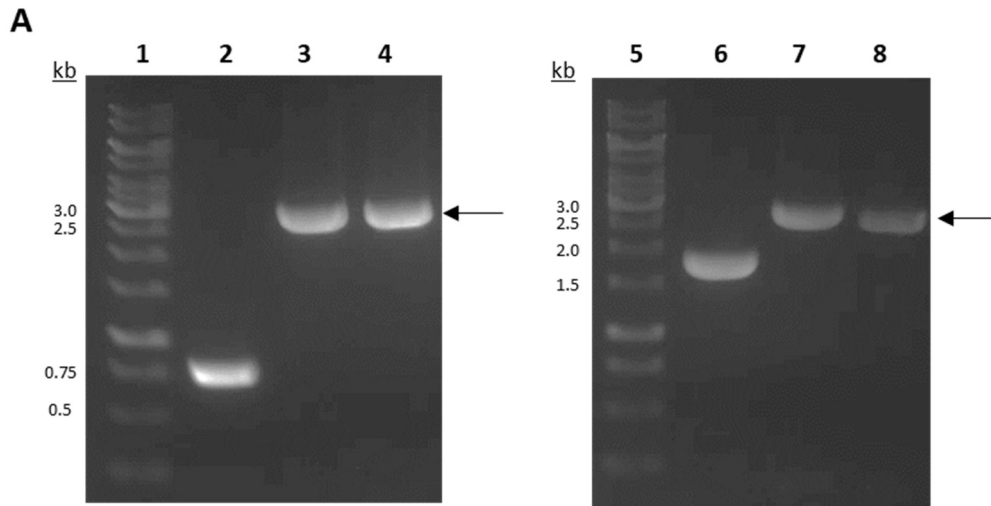
Figure 4.14 Verification of double glucosaminidase mutants

(A) 1% (w/v) TAE agarose gels showing PCR amplification of the *atl* and *sagA* genes from *S. aureus*. Lane 2 shows wild type *atl* band (777 bp) expected from the primer set (*Atl_TnINS_F* and *Atl_TnINS_R*). The expected mutant band (donor strain SH1000 *atl* mutant, SJF 5255, 2500 bp), shown in lane 3 and indicated with a black arrow, is also seen in lane 4 of the SH1000 *atl sagA* (SJF 5261). Lane 6 shows the wild type *sagA* band (1835bp) expected from the primer set (*psagA_F* and *psagA_R*). The expected mutant band (3000 bp), indicated with an arrow, from SH1000 *sagA* (SJF 4606) can be seen in lane 7, and in lane 8 for SH1000 *atl sagA* (SJF 5261). **(B)** 1% (w/v) TAE agarose gel showing PCR amplification of the *atl* and *scaH* genes from *S. aureus*. Lane 2 shows wild type *atl* band (777 bp) expected from the primer set (*Atl_TnINS_F* and *Atl_TnINS_R*). The expected mutant band (donor strain SH1000 *atl* mutant, SJF 5255, 2500 bp), shown in lane 3 and indicated with a black arrow, is also seen in lane 4 of SH1000 *atl scaH* (SJF 5262). Lane 6 shows the wild type *scaH* band (2074 bp) expected from the primer set (*pscaH_F* and *pscaH_R*). The expected mutant band (4000 bp), indicated with an arrow, from SH1000 *scaH* (SJF 4607) can be seen in lane 7. Lane 8, SH1000 *atl scaH* (SJF 5262), also shows the mutant band. **(C)** 1% (w/v) TAE agarose gel showing PCR amplification of the *sagA* and *scaH* genes from *S. aureus*. Lane 2 shows wild type *sagA* band (1835bp) expected from the primer set (*psagA_F* and *psagA_R*). The expected mutant band (donor strain SH1000 *sagA* mutant, SJF 4606, 3000 bp), shown in lane 3 and indicated with a black arrow, is also seen in lane 5 of SH1000 *sagA scaH* (SJF 5217). Lane 7 shows the wild type *scaH* band (2074 bp) expected from the primer set (*pscaH_F* and *pscaH_R*). The expected mutant band (4000 bp), indicated with an arrow, from SH1000 *scaH* (SJF 4607) can be seen in lane 8. Lane 10, SH1000 *sagA scaH* (SJF 5217), also shows the mutant band. Relevant sizes of DNA ladder (GeneRuler 1 kb DNA ladder, Thermo Scientific) are shown in kb (lane 1 and 5 of **A, B** and 1 and 6 of **C**).

4.3.9.4 Growth kinetics of double glucosaminidase mutants

The double glucosaminidase mutants constructed (Chapter 4.3.9.3) were analysed for growth kinetics compared to the parental SH1000 (SJF 682). As an *atl* mutant is known to form clusters (Chapter 4.3.9.1, Takahashi *et al*., 2002), all mutants were plated unsonicated, to measure number of particles, and sonicated, to measure the number of bacteria in the culture (chapter 2.10).

SH1000 *atl sagA* (SJF 5261) showed the same growth kinetics as parental SH1000 (SHF 682) when compared by measuring optical density (Figure 4.15A). Similarly, to SH1000 *atl* (SJF 1367), SH1000 *atl sagA* shows clustering by CFU. The unsonicated CFU of SH1000 *atl sagA* was consistently around 10-fold lower than the unsonicated wildtype SH1000. When sonicated, SH1000 *atl sagA* shows similar CFU to sonicated SH1000. SH1000 *atl sagA* had the same growth rate as SH1000, whilst forming clusters.

SH1000 *atl scaH* (SJF 5262) shows the same phenotype as SH1000 *atl sagA*. SH1000 *atl scaH* shows the same growth pattern as parental SH1000 when optical density was measured. SH1000 *atl scaH* also showed clustering, with unsonicated CFU lower than unsonicated wildtype SH100, but sonicated CFU matching sonicated SH1000 CFU (Figure 4.15B).

The SH1000 *sagA scaH* (SJF 5217) mutant showed the same optical density growth as parental SH1000 (Figure 4.15C). Unsonicated and sonicated SH1000 *sagA scaH* CFU match the corresponding SH1000 CFU. This demonstrates that SH1000 *sagA scaH* has the same growth rate as parental SH1000 and does not form clusters during growth under these conditions.
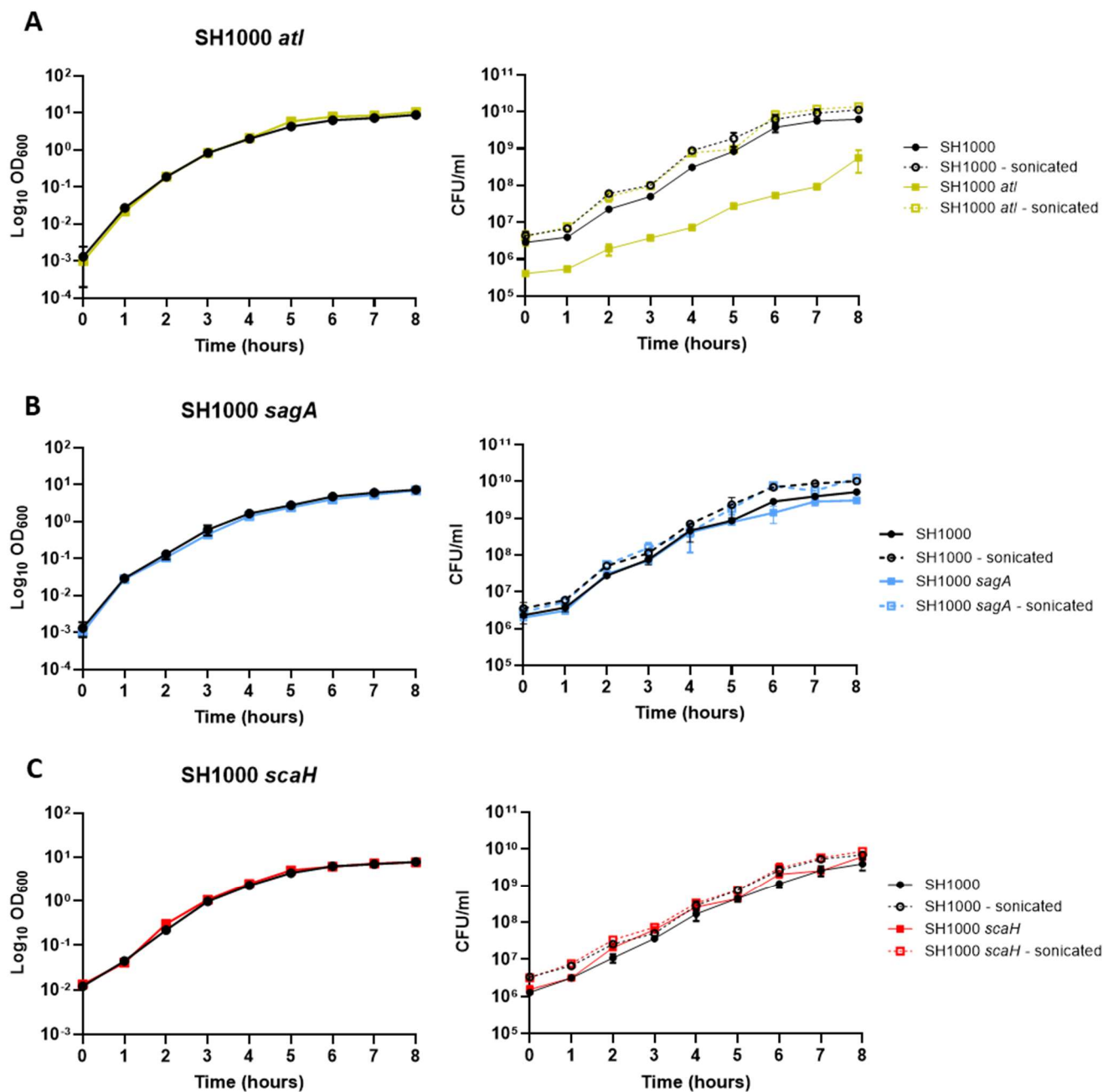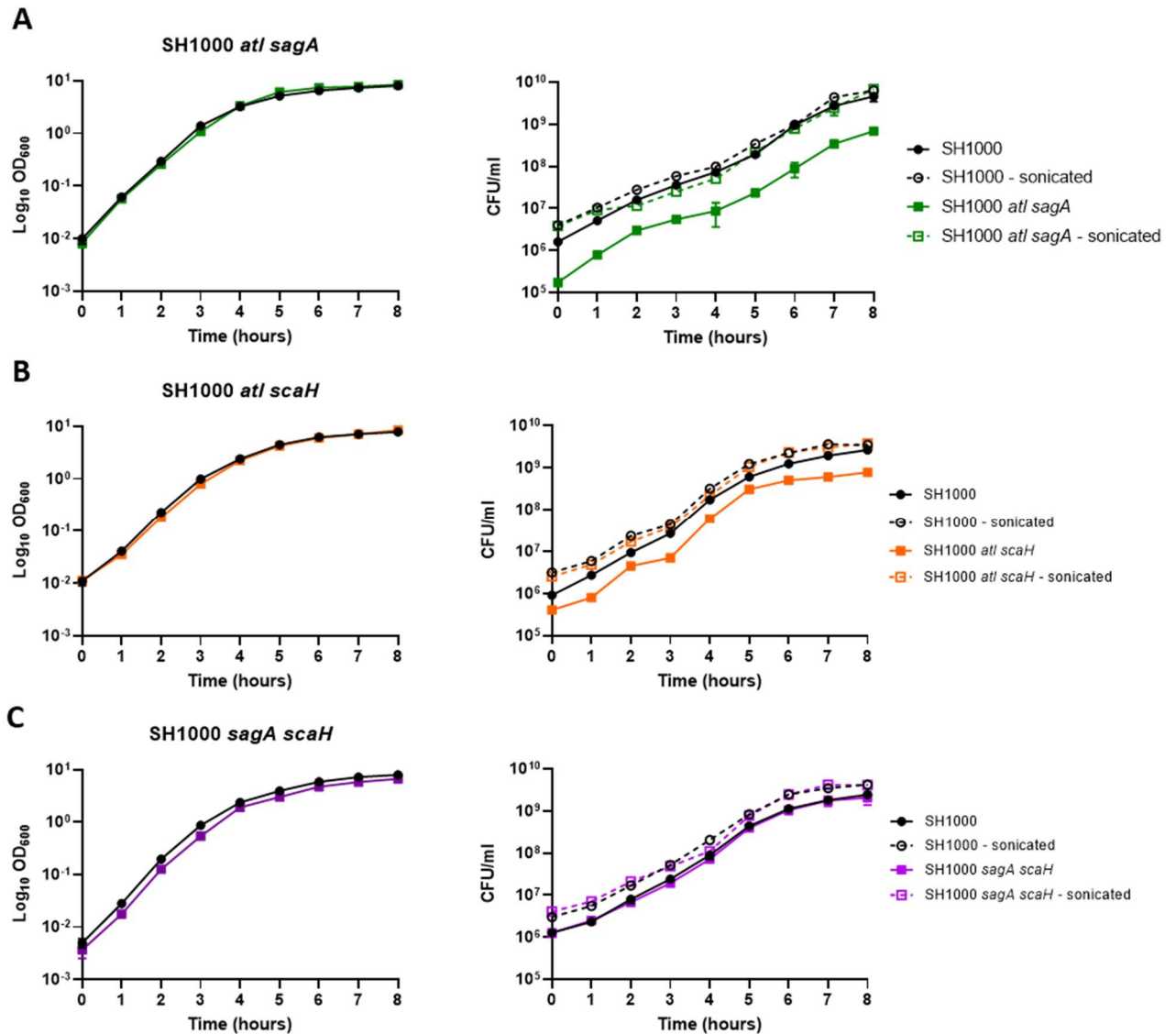
Figure 4.15 Role of glucosaminidases in growth of _S. aureus_

Growth of parental SH1000 (SJF 682, black circles solid line) or parental SH1000 sonicated (open black circles and broken line) in TSB compared to: **(A)** SH1000 _atl sagA_ (SJF 5261, green squares) and sonicated SH1000 _atl sagA_ (green open squares, broken lines). **(B)** SH1000 _atl scaH_ (SJF 5262, orange squares) and sonicated SH1000 _atl scaH_ (orange open squares, broken lines). **(C)** SH1000 _sagA scaH_ (SJF 5217, purple squares) and sonicated SH1000 _sagA scaH_ (purple open squares, broken lines). Bacterial cultures were prepared in triplicate and error bars represent the standard deviation of the mean. Sonicated strains were sonicated for 20 seconds at an amplitude of 5 microns.

4.3.9.5 Virulence phenotype of double glucosaminidase mutants

To determine if the double glucosaminidase mutants had a different virulence phenotype than that of the parental SH1000 (SJF 682), strains were analysed in the zebrafish embryo model of infection (Chapter 2.18.1). To ensure the same number of bacteria were injected for each strain, CFU were determined from both sonicated and unsonicated samples of the inoculum used. Unsonicated mutant strains, and parental SH1000 (SJF 682) were injected into embryos. 400 particles of SH1000 *atl sagA* (SJF 5261), 300 particles of SH1000 *atl scaH* (SJF 5262) and 1300 particles of SH1000 *sagA scaH* (SJF 5217), all consisting of around 1300 bacteria, were injected into embryos and compared to an injection of 1300 bacteria of parental SH1000 (SJF 682) (Figure 4.16A). SH1000 *sagA scaH* is as virulent as the parental SH1000 (p = 0.9189). Both SH1000 *atl sagA* and SH1000 *atl scaH* cause significantly lower mortality than the parental SH1000 (both p < 0.0001). SH1000 *atl scaH* causes significantly reduced mortality than SH1000 *atl sagA* (p = 0.0203)*.* As SH1000 *sagA scaH* is not attenuated, and SH1000 *atl scaH* is significantly more attenuated than SH1000 *atl sagA* it can be inferred that Atl is the most important hydrolase with glucosaminidase activity for virulence (excluding SagB), followed by ScaH and then SagA.

As *atl* mutants have been shown to form clusters that separate upon sonication (Figures 4.12 and 4.15) the effect of sonicating the glucosaminidase mutants (Chapter 2.10) on virulence was investigated. For all strains, the equivalent of 1300 bacteria were injected into the embryos. 400 particles of unsonicated SH1000 *atl sagA* (1300 bacteria), 1300 CFU of sonicated SH1000 *atl sagA* or 1300 CFU SH1000 (Figure 4.16B). Unsonicated SH1000 *atl sagA* is significantly attenuated compared to parental SH1000 (p < 0.0001). Sonicated SH1000 *atl sagA* has equivalent virulence to parental SH1000 (p = 0.9413). An injection of 300 particles of unsonicated SH1000 *atl scaH* (1300 bacteria) is significantly attenuated compared to the equivalent bacterial numbers of wildtype SH1000 (p < 0.0001). Injecting 1300 CFU of sonicated SH1000 *atl scaH* causes the same mortality as an inoculum consisting of 1300 CFU of SH1000 (Figure 4.16C) (p = 0.1252). Sonication of

SH1000 *sagA scaH* caused no change in virulence compared to an equivalent dose of wildtype SH1000 (Figure 4.16D) (p = 0.7724).

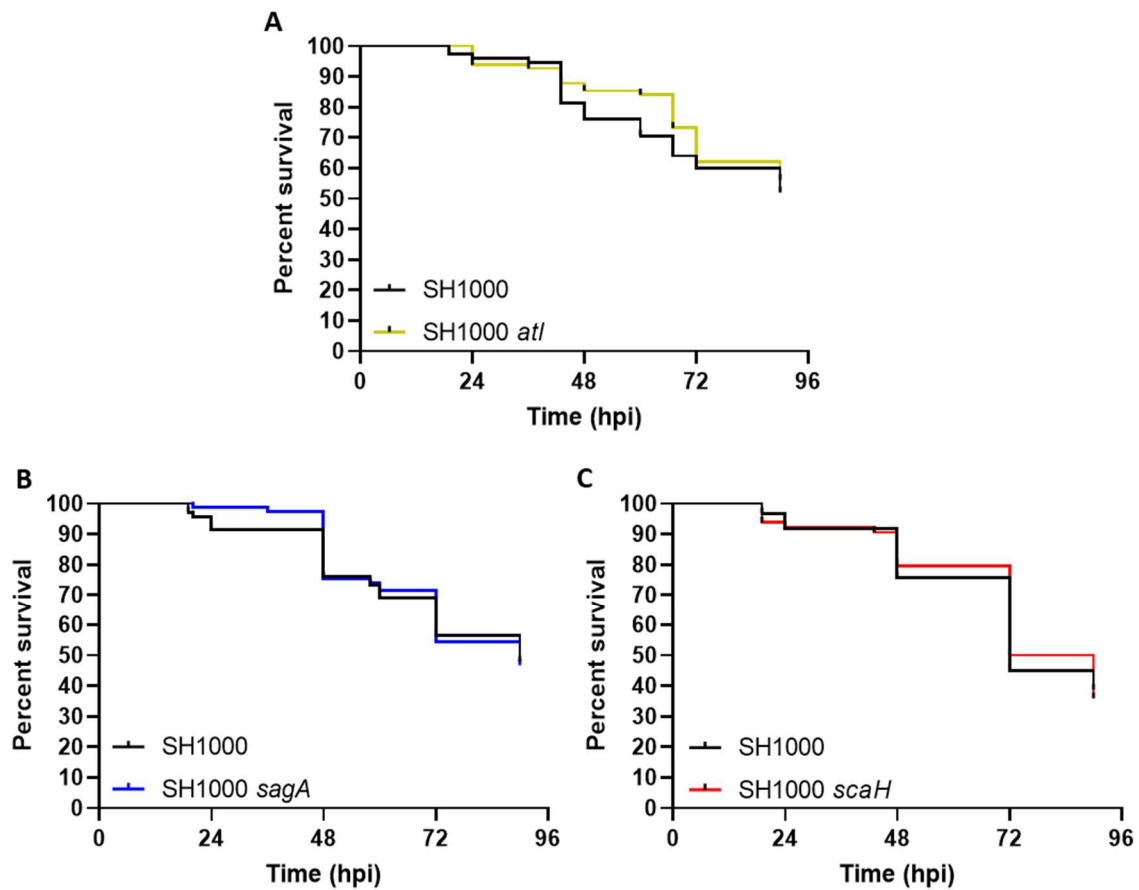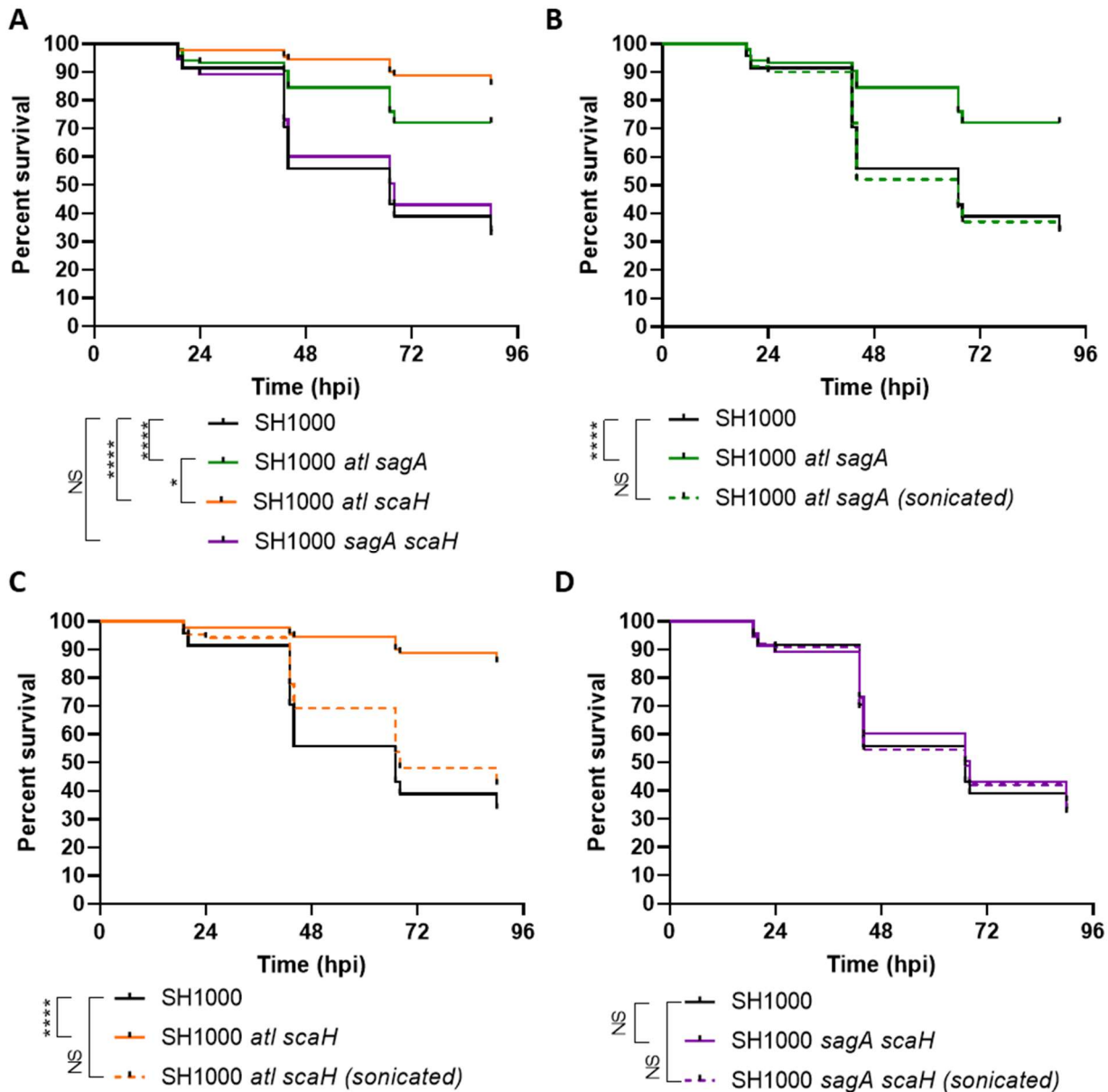**Figure 4.16 Role of the glucosaminidases Atl, SagA and ScaH in *S. aureus* virulence in the zebrafish infection model in double mutant bacteria**

Survival curve of zebrafish embryos injected with approximately 1300 CFU of *S. aureus* SH1000 (SJF 682, black lines) or: **(A)** 400 particles of unsonicated SH1000 *atl sagA* (SJF 5261, solid green line) consisting of 1300 bacteria (when sonicated), 300 particles of unsonicated SH1000 *atl scaH* (SJF 5262, solid orange line) consisting of 1300 bacteria (after sonication) or 1300 CFU unsonicated SH1000 *sagA scaH* (SJF 5217, solid purple line, sonication did not change CFU). (3 repeats, n>20, **** $p < 0.0001$). **(B)** 400 particles unsonicated SH1000 *atl sagA* (SJF 5261, solid green line) consisting of 1300 bacteria (when sonicated) or approximately 1300 CFU of sonicated SH1000 *atl sagA* (broken green line) (3 repeats, n>20, all stated CFU are approximate, **** $p < 0.0001$, * $p = 0.0203$). **(C)** 300 particles of unsonicated SH1000 *atl scaH* (SJF 5262, solid orange line) *consisting* of 1300 bacteria (after sonication) or 1300 CFU sonicated SH1000 *atl scaH* (broken orange line). (3 repeats, n>20, all stated CFU are approximate, **** $p < 0.0001$). **(D)** 1300 CFU unsonicated SH1000 *sagA scaH* (SJF 5217, solid purple line, sonication did not change CFU) or 1300 CFU sonicated SH1000 *sagA scaH (*3 repeats, n>20, all stated CFU are approximate).

4.3.9.6 Particle size of double glucosaminidase mutants

The cause of attenuation of SH1000 *atl sagA* (SJF 5261) and SH1000 *atl scaH* (SJF 5262) is likely due to the bacteria being unable to separate and clustering, much like an *atl* mutant (Takahashi *et al.*, 2002; Wheeler *et al.*, 2015). To measure the change in particle size, flow cytometry was utilised to measure changes in the forward scatter (FSC) of light caused by different glucosaminidase mutants (Chapter 2.22). FSC values are comparable to the size of the particle being measured, allowing strains to be compared for particle size by their differing FSC values; the larger the FSC value, the larger the particle (Salamaga *et al.*, 2017). It has previously been shown by light microscopy that *S. aureus* without functional Atl form clusters (Wheeler *et al.*, 2015). An assumption of this experiment is when strains are sonicated, they are becoming single cells, i.e. individual bacteria not connected to other daughter cells.

First, glucosaminidase mutants, both single and double, where analysed by flow cytometry to determine their relative particle size (Figure 4.17A). As previously described, SH1000 *atl* (SJF 1367) shows an increase in particle size compared to parental SH1000 (SJF 682) (p = 0.0013). Both SH1000 *sagA* (SJF 4606) and SH1000 *scaH* (SJF 4607) show no significant difference in particle size to the parental SH1000, indicating no clustering (p = 0.9996 and 0.9998 respectively). SH1000 *atl sagA* (SJF 5261) and SH1000 *atl scaH* (SJF 5262) both show a significant increase in FSC value compared to parental SH1000, suggesting they have an increased particle size, and therefore are clustering (p < 0.0001 for both strains). This matches with previously described data, where sonication increased CFU on plating (Figures 4.15 and 4.16). SH1000 *sagA scaH* (SJF 5217) shows no difference in FSC value to parental SH1000, so also does not show clustering (p = 0.9996). When sonicated, the FSC of both SH1000 *atl sagA* and SH1000 *atl scaH* are seen to drop (Figure 4.17B), suggesting that the cells have gone from clusters to individual cells. When these values were compared to sonicated wildtype SH1000, the glucosaminidase mutants, including SH1000 *sagA scaH*, were found to have significantly lower FSC values.
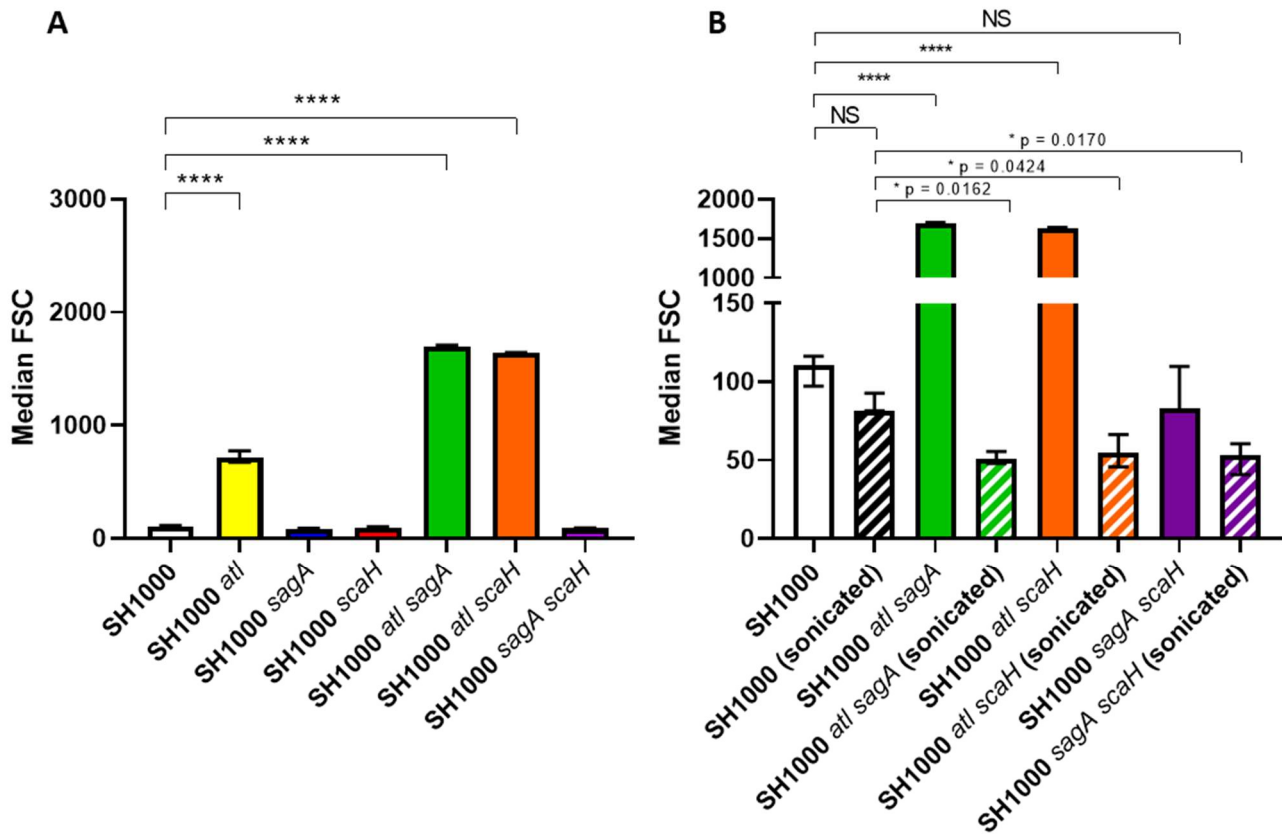
Figure 4.17 Analysis of glucosaminidase mutant particle size by flow cytometry

(A) Comparison of the median forward scattered (FSC) light values of parental SH1000 (SJF 682, white bar), SH1000 *atl* (SJF 1367, yellow bar), SH1000 *sagA* (SJF 4606, blue bar), SH1000 *scaH* (SJF 4607, red bar), SH1000 *atl sagA* (SJF 5261, green bar), SH1000 *atl scaH* (SJF 5262, orange bar) and SH1000 *sagA scaH* (SJF 5217, purple bar). (n = 3, **** p < 0.0001). **(B)** Comparison of the median FSC light values of parental SH1000 (unsonicated white bar, sonicated black and white bar), SH1000 *atl sagA* (unsonicated green bar, sonicated green and white bar), SH1000 *atl scaH* (unsonicated orange bar, sonicated orange and white bar) and SH1000 *sagA scaH* (unsonicated purple bar, sonicated purple and white bar). (n = 3, **** p < 0.0001). Error bars show ±SD, Median FSC values were compared using a one-way ANOVA with Dunnet's multiple comparison test, strains were sonicated for 20 seconds at an amplitude of 5 microns.

4.3.9.7 Does sonication restore *sagB* virulence?

It has been reported in the literature that *sagB* mutants also have a clustering phenotype (Wheeler *et al.*, 2015; Chan *et al.*, 2016b). As an *atl* mutant has a more pronounced clustering phenotype, and *atl sagA/scaH* double mutants regain virulence on being sonicated, it was examined if sonication could restore virulence to SH1000 *sagB* (SJF 4608), using the zebrafish embryo model of infection.

Figure 4.18 shows that the sonication of SH1000 (SJF 682) does not change the virulence when compared to the same CFU of unsonicated SH1000 (p = 0.8672). Unsonicated SH1000 *sagB* (SJF 4608) (1500 CFU) has no difference in mortality in zebrafish embryos than the same dose of sonicated SH1000 *sagB* (p = 0.4381)*.* Unsonicated SH1000 *sagB* is significantly attenuated compared to unsonicated SH1000 (p = 0.0053) and sonicated SH1000 *sagB* is significantly attenuated compared to sonicated SH1000 (p = 0.0099).
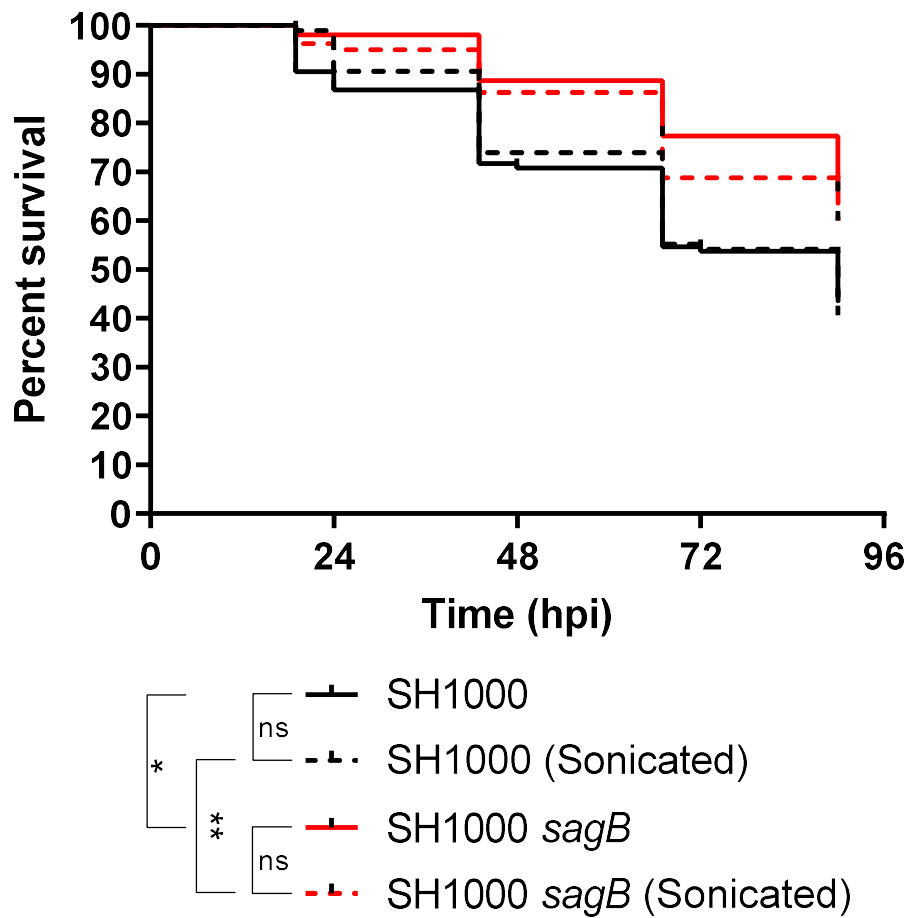
Figure 4.18 The effect of sonication on the virulence of SH1000 *sagB* in the zebrafish model of infection

At around 30 hpf, zebrafish embryos were injected with approximately 1500 CFU of SH1000 (SJF 682) or SH1000 *sagB* (SJF 4608). These strains were either injected unsonicated or having been sonicated for 20 seconds at an amplitude of 5 microns (sonication of these strains did not change CFU, data not shown). (Black lines – SH1000, red lines – SH1000 *sagB*, solid lines – unsonicated bacteria, broken lines – sonicated bacteria) (3 repeats, n>20, * p = 0.0053, ** p = 0.0099).

4.3.9.8 Phenotypic analysis of a triple glucosaminidase mutant

As the double glucosaminidase mutant analysis shows virulence phenotypes, strain SH1000 *atl sagA scaH* (SJF 4611) was used to determine the combined role of all three glucosaminidases in infection (Wheeler *et al.*, 2015).

The growth of SH1000 *atl sagA scaH* (SJF 4611) was compared to the parental SH1000 (SJF 682) using both direct CFU counts and optical density measurements (Figure 4.19A). The optical density measurements show a slower growth rate for SH1000 *atl sagA scaH* (doubling time 34.8 min) than the wildtype strain (25.9 min). However, at 7 hours, SH1000 *atl sagA scaH* reaches the same optical density as SH1000. The CFU counts are for sonicated and unsonicated mutant and wildtype. Unsonicated SH1000 *atl sagA scaH* shows around 10-fold lower CFU than unsonicated parental SH1000 and sonicated SH1000 *atl sagA scaH,* suggesting clustering and the inability for daughter cells to separate correctly. When comparing the sonicated SH1000 *atl sagA scaH* CFU (doubling time 44.8 min) to sonicated wildtype SH1000 CFU (doubling time 25.9 min), SH1000 *atl sagA scaH* CFU are consistently lower than SH1000, and do not reach the same numbers until 8 hours. This confirms that SH1000 *atl sagA scaH* has a reduced growth rate compared to wildtype SH1000, and forms clusters of cells during growth.

To confirm the clustering, flow cytometry was used to measure the particle size of SH1000 *atl sagA scaH* by the FCS value compared to wildtype SH1000 (Chapter 2.22). SH1000 *atl sagA scaH* has a significantly higher FSC value than that of parental SH1000 (Figure 4.19B, $p < 0.0001$), confirming clustering. Upon sonication of SH1000 *atl sagA scaH*, the FSC value drops to that of wildtype SH1000, suggesting that sonication of SH1000 *atl sagA scaH* also reverts the clusters to single cells ($p < 0.0001$).

The virulence of SH1000 *atl sagA scaH* (SJF 4611) in the zebrafish embryo model of infection was analysed (Chapter 2.18.1). When zebrafish were injected with around 100 particles of SH1000 *atl sagA scaH* (consisting of around 1500 bacteria), there was

significantly reduced mortality than when embryos were injected with 1500 CFU of unsonicated SH1000 (Figure 4.19C). However, when sonicated, SH1000 *atl sagA scaH* (1500 CFU) has an equivalent virulence to SH1000, matching the results of the double mutants SH1000 *atl sagA* (SJF 5261) and SH1000 *atl scaH* (SJF 5262).
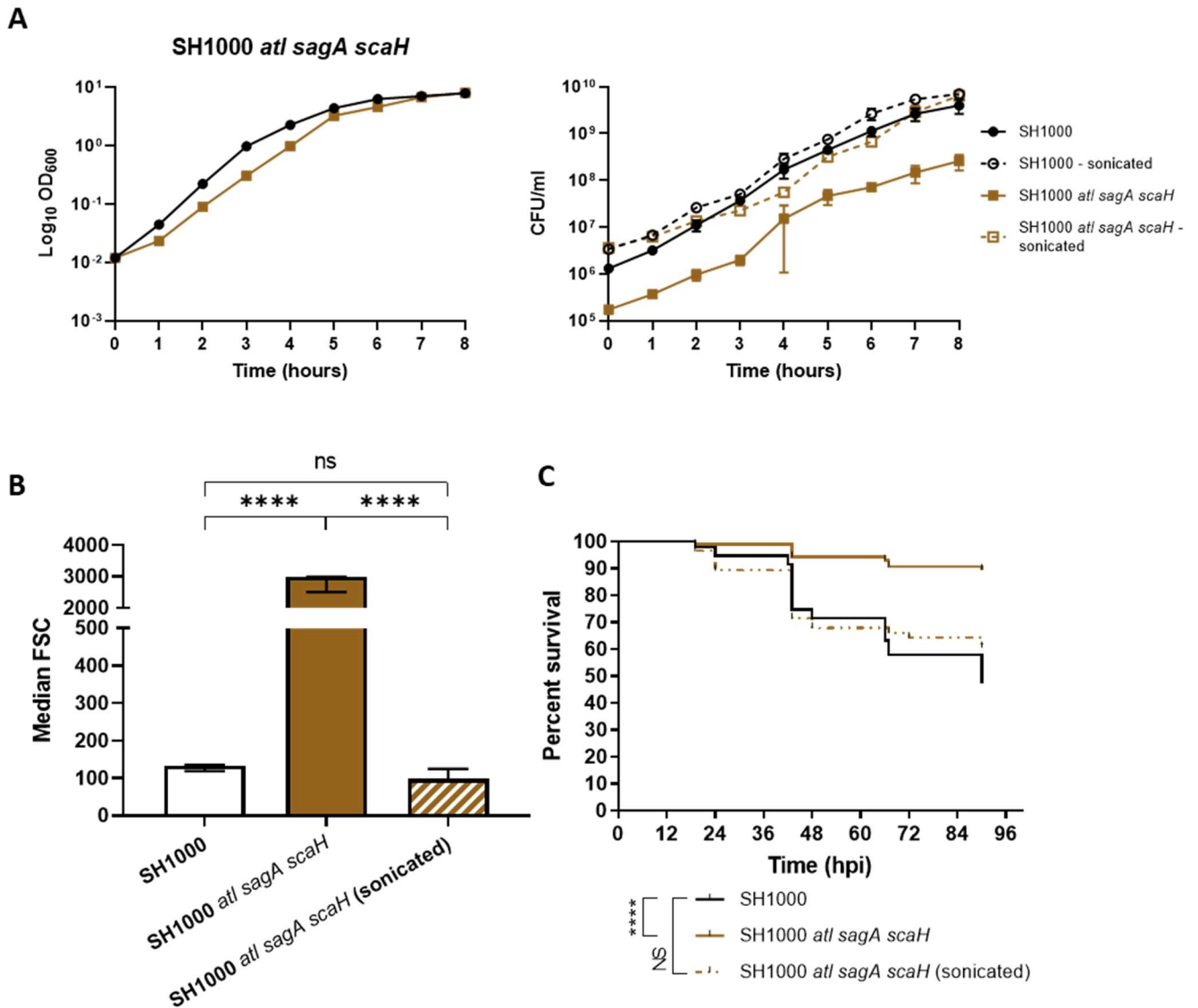
Figure 4.19 Analysis of growth and virulence of SH1000 *atl sagA scaH*

(A) Growth of parental SH1000 (SJF 682, black circles solid line) or parental SH1000 sonicated (open black circles and broken line) in TSB compared to SH1000 *atl sagA scaH* (SJF 4611, brown squares) and sonicated SH1000 *atl sagA scaH* (brown open squares, broken lines). **(B)** Comparison of the median forward scattered (FSC) light values of parental SH1000 (white bar) and SH1000 *atl sagA scaH* (unsonicated brown bar, sonicated white and brown bar) (n = 3, **** p < 0.0001). Error bars show ±SD, Median FSC values were compared using a one-way ANOVA with Tukey multiple comparison test, strains were sonicated for 20 seconds at an amplitude of 5 microns. **(C)** 100 particles of unsonicated SH1000 *atl sagA scaH* (consisting of 1500 bacteria, solid brown line), 1500 CFU of sonicated SH1000 *atl sagA scaH* (broken brown line) or 1500 CFU of parental SH1000 (solid black line). 3 (repeats, n>20, all stated CFU are approximate, **** p < 0.0001).

4.3.9.9 Virulence phenotype of SH1000 *atl sagA scaH*

In this experiment, the genetic background SH1000 was used to analyse the virulence of SH1000 *atl sagA scaH* (SJF 4611) to allow comparisons to be made with other glucosaminidase mutants. The wildtype strain used contained a kanamycin resistance cassette to allow selection of *S. aureus* from organ homogenate to determine CFU. SH1000 *kan^R* (SJF 3674) has been shown to have equivalent virulence to the wildtype SH1000 (SJF 682) (McVicker *et al.*, 2014).

Mice were injected with unsonicated or sonicated SH1000 *kan^R* (SJF 3674) or SH1000 *atl sagA scaH* (SJF 4611). Number of bacteria in a sample was determined by sonication of the inoculum and plating to determine CFU, and number of particles was determined by plating unsonicated inoculum. Mice were injected with 1.65×10^7 bacteria in 1.47×10^7 particles of unsonicated SH1000 *kan^R* (SJF 3674), and 1.62×10^7 CFU of sonicated SH1000 *kan^R* (SJF 3674). Mice received 1.43×10^7 bacteria in 5.5×10^6 particles of unsonicated SH1000 *atl sagA scaH* (SJF 4611) and 1.51×10^7 CFU of sonicated SH1000 *atl sagA scaH* (SJF 4611).

Mice injected with unsonicated SH1000 *kan^R* (SJF 3674) show a significantly greater weight loss than mice injected with SH1000 *atl sagA scaH* (SJF 4611, p = 0.0314), indicating a reduced virulence in the SH1000 *atl sagA scaH* (SJF 4611) mutant. Mice infected with sonicated SH1000 *atl sagA scaH* (SJF 4611) show a trend for causing reduced weight loss than the sonicated wild type SH1000 *kan^R* (SJF 3674) (Figure 4.20A). Both sonicated and unsonicated SH1000 *atl sagA scaH* (SJF 4611) show significantly fewer CFU recovered from the livers of mice infected with the corresponding SH1000 *kan^R* (SJF 3674) strains (Figure 4.20B, unsonicated p = 0.0003, sonicated p = 0.0014). In fact, mice infected with SH1000 *atl sagA scaH* (SJF 4611) had no recoverable CFU from the liver, indicating that CFU present were below 600 particles, the limit of detection for the assay. Given that SH1000 *atl sagA scaH* (SJF 4611) is known to form clusters, the livers were sonicated (chapter 2.10). When infected livers were sonicated, bacteria could

be detected in both SH1000 *atl sagA scaH* (SJF 4611) infected groups. However, significantly fewer unsonicated and sonicated SH1000 *atl sagA scaH* (SJF 4611) CFU were recovered than the corresponding SH1000 *kan^R* (SJF 3674) group (Figure 4.20C, unsonicated p = 0.0364, sonicated p = 0.0009).

There is a trend for fewer CFU recovered from kidneys of mice infected with SH1000 *atl sagA scaH* (SJF 4611) than unsonicated SH1000 *kan^R* (SJF 3674) (Figure 4.20D). Significantly fewer CFU are recovered from the kidneys of mice infected with sonicated SH1000 *atl sagA scaH* (SJF 4611) than sonicated SH1000 *kan^R* (SJF 3674, p = 0.0096). This is also seen when infected kidneys are sonicated, where kidneys infected with unsonicated or sonicated with SH1000 *atl sagA scaH* (SJF 4611) have significantly fewer recovered CFU than SH1000 *kan^R* (SJF 3674) (Figure 4.20E, unsonicated p = 0.0364, sonicated p = 0.0009). In all cases (Figure 4.20 A, B, C, D and E) no significance could be found between recovered CFU values (and weight changes) from mice infected with sonicated and unsonicated inoculum bacteria of the same strain. This would suggest that unlike in the zebrafish embryo model, sonication of bacteria has no impact on virulence in a murine sepsis model of infection.

A Weight Change - 72 hpi
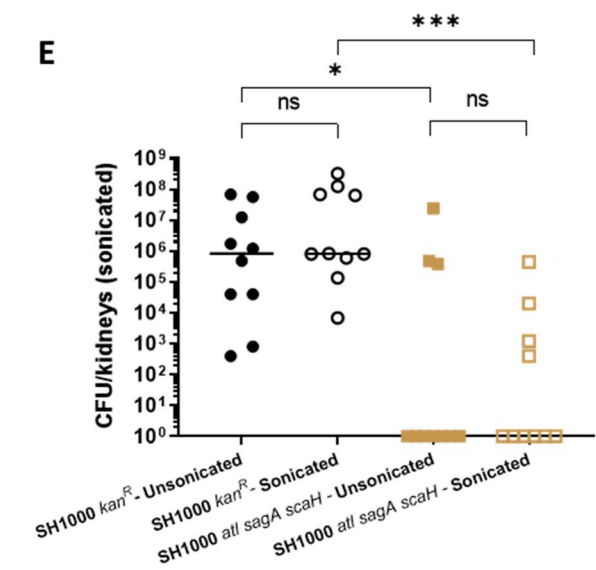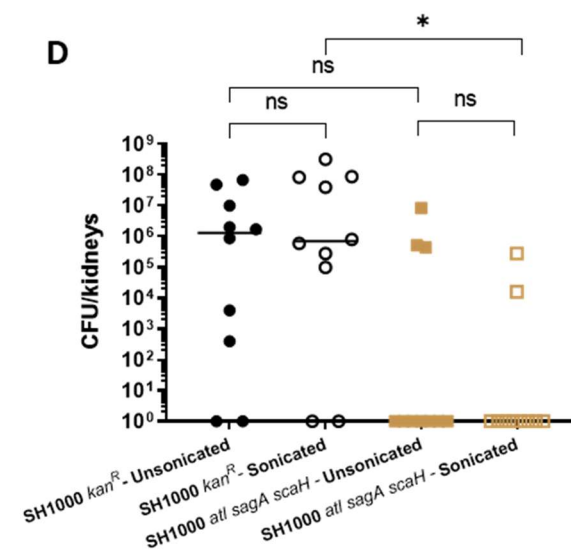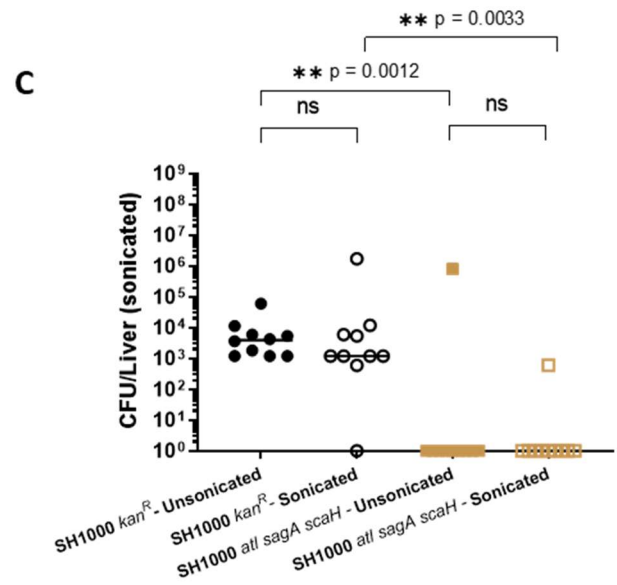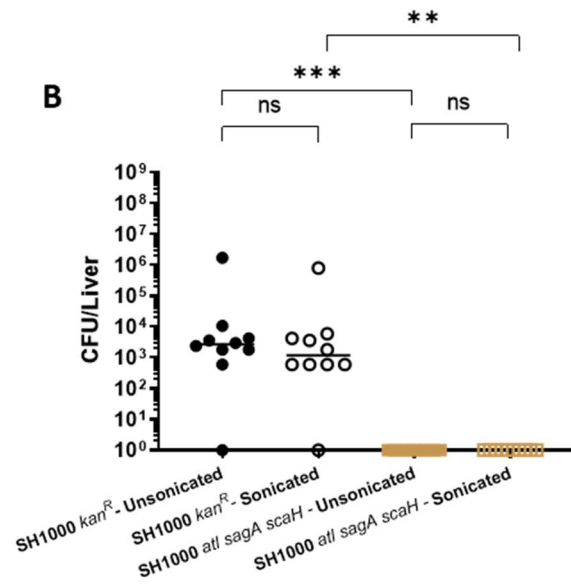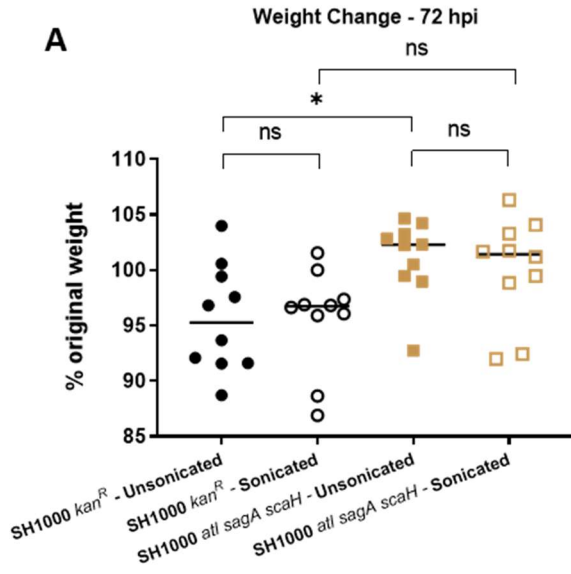
Figure 4.20 The role of Atl, SagA and ScaH in virulence in a murine sepsis model of infection

S. aureus SH1000 *kanR* (SJF 3674) or SH1000 *atl sagA scaH* (SJF 4611) were injected intravenously into mice (n=10). Approximately 1 x 10^7 bacteria were injected in unsonicated and sonicated groups. Sonication had no effect on SH1000 *kan*^{R}, but 1 x 10^7 bacteria in 5 x 10^6 particles of unsonicated SH1000 *atl sagA scaH* was injected. Weight loss 72 hpi (**A**, * p = 0.0314), liver CFU (**B**, ** p = 0.0014, *** p = 0.0003) and kidney CFU (**D**, ** p = 0.0096) were determined. Organ homogenates were also sonicated to get a better representation of bacterial load in livers (**C**, p values on graph) and kidneys (**E**, * p = 0.0364, *** p = 0.0009). Groups were compared using a Kruskal-Wallis test with multiple comparisons (Unsonicated SH1000 *kan*^{R} – black circles, sonicated SH1000 *kan*^{R} – open black circles, unsonicated SH1000 *atl sagA scaH* - brown squares and sonicated SH1000 *atl sagA scaH* – open brown squares). Strains and organ homogenates were sonicated for 20 seconds at an amplitude of 5 microns.

4.3.9.10 Augmentation of SH1000 *atl sagA scaH*

Mice were injected with 1 x 10^7 CFU of sonicated SH1000 *atl sagA scaH* (SJF 4611). This dose is 10-fold higher than the low dose for SH1000 for augmentation (Boldock *et al.*, 2018) but was used as this strain is highly attenuated (Figure 4.20). Augmented doses also contained 250 µg of wild type SH1000 (SJF 682) purified peptidoglycan (wild type peptidoglycan) or 250 µg of SH1000 *atl sagA scaH* (SJF 4611) purified peptidoglycan (mutant peptidoglycan). The weight of mice injected with SH1000 *atl sagA scaH* (SJF 4611) were roughly constant during the 72 hours of the experiment, while those mice co-injected with SH1000 *atl sagA scaH* (SJF 4611) with wild type (p = 0.0159) or mutant peptidoglycan (p = 0.0079) showed significant greater weight loss 72 hpi (Figure 4.21A). The CFU recovered from the livers of mice co-injected with SH1000 *atl sagA scaH* (SJF 4611) with wild type or mutant peptidoglycan were significantly higher than those of mice only infected with SH1000 *atl sagA scaH* (SJF 4611) (Figure 4.21B, p for both = 0.0159). Significantly higher CFU were also recovered from the kidneys of augmented mice groups compared to mice injected with SH1000 *atl sagA scaH* (SJF 4611) alone (Figure 4.21 C, p = 0.0159, p = 0.0317). For spleens, lungs and hearts, no significant difference between recovered CFU could be seen between groups (Figure 4.21 D, E and F respectively).

The results of this experiment demonstrate that SH1000 *atl sagA scaH* (SJF 4611) can be augmented by purified *S. aureus* peptidoglycan. Peptidoglycan of SH1000 *atl sagA scaH* (SJF 4611) can augment an infection, indicating that any change in peptidoglycan due to loss of glucosaminidases does not impact upon the augmentation capacity of peptidoglycan.
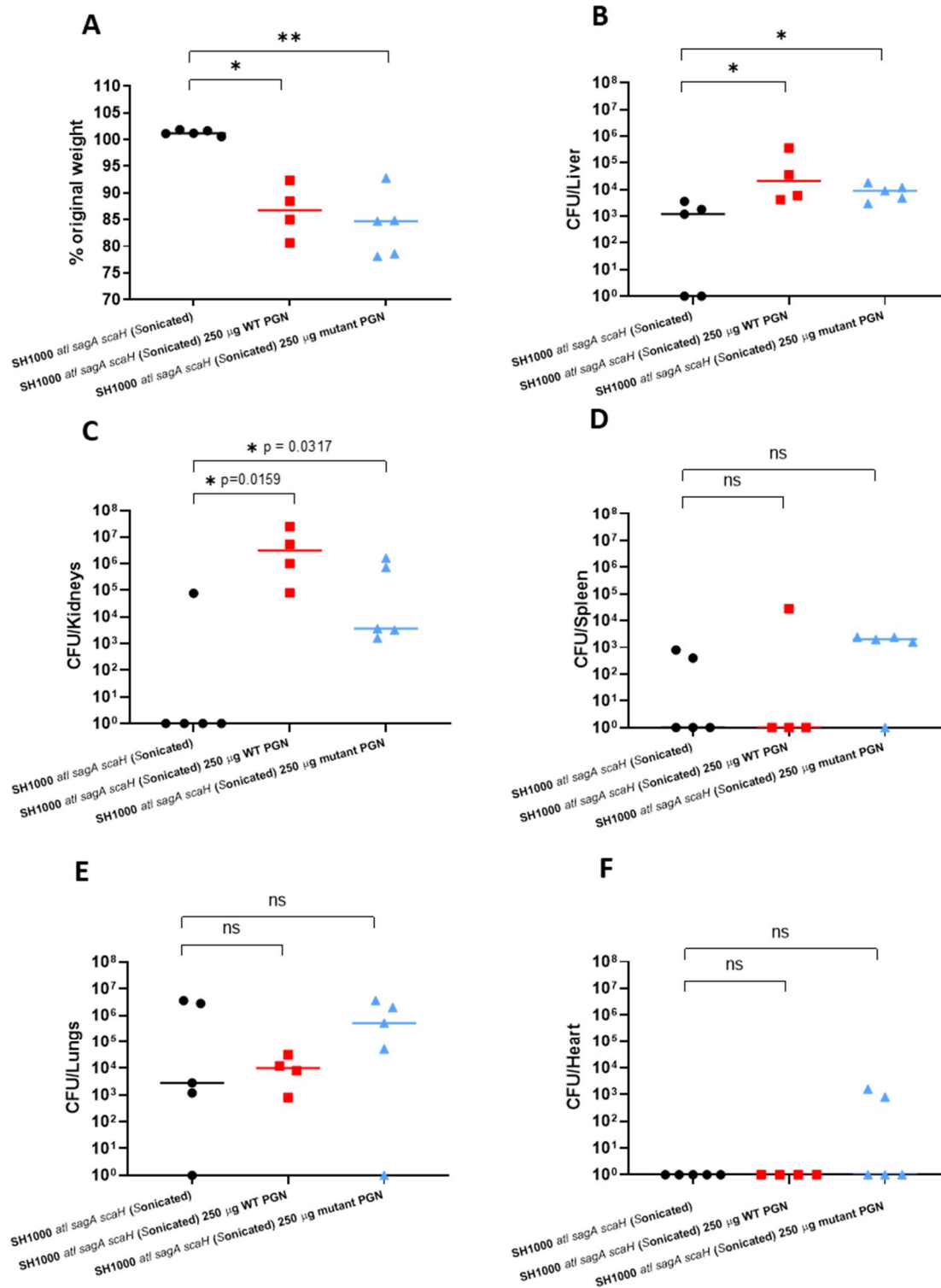
Figure 4.21 Augmentation of *S. aureus* SH1000 *atl sagA scaH* using wildtype and mutant peptidoglycan

Mice (n=5) were injected with approximately 1x10^7 CFU sonicated *S. aureus* SH1000 *atl sagA scaH* (SJF 4611) alone, or with 250 µg SH1000 PGN (SJF 682, WT PGN) or 250 µg SH1000 *atl sagA scaH* PGN (mutant PGN). Weight loss 72 hpi (**A**, ** p= 0.0079, * p = 0.0159) and CFUs recovered from livers (**B,*** p = 0.0159) , kidneys (**C,** p values on graph) , spleen (**D**) , lungs (**E**) and heart (**F**) were determined. Groups were compared using a Mann-Whitney U test. (SH1000 *atl sagA scaH* only – black circles, SH1000 *atl sagA scaH* with wild type PGN - red squares SH1000 *atl sagA scaH* with mutant PGN – blue triangles). One mouse in the SH1000 *atl sagA scaH* and WT PGN group reached severity limits at 48 hpi and was culled and has been excluded from analysis.

4.3.9.11 The role of macrophages in SH1000 *atl sagA scaH* host interaction

During augmentation it is thought that peptidoglycan interacts within macrophages to potentially neutralise the effect of ROS on staphylococcal cells (Boldock *et al.*, 2018). As SH1000 *atl sagA scaH* (SJF 4611) infection has been shown to be augmented by peptidoglycan, macrophages may also play a role in the attenuation of this strain. To test this hypothesis, the zebrafish embryo infection model was utilised, with clodronate depletion of macrophages (Chapters 2.18.1 and 2.18.3).

Figure 4.22A shows the effect of sonicating bacteria on the virulence of parental SH1000 (SJF 682) in zebrafish embryos pre-treated with clodronate containing, or control, liposomes. There is no significant difference in the mortality of zebrafish embryos treated with empty control liposomes infected with sonicated or unsonicated SH1000 (SJF 682, p = 0.5141). This is also true of clodronate treated zebrafish embryos, suggesting that there is no impact of sonication on the virulence of SH1000 (SJF 682, p = 0.8262). There was a significantly higher mortality in embryos treated with clodronate liposomes than the control liposomes, for groups infected with either unsonicated (p = 0.0057) or sonicated (p = 0.0455) SH1000 (SJF 682). Figure 4.22A serves as a control to show that sonication has no impact on wildtype SH1000 (SJF 682) virulence, but clodronate does increase the mortality observed in zebrafish embryos.

In embryos treated with control liposomes, sonicated SH1000 *atl sagA scaH* (SJF 4611) causes significantly more mortality than unsonicated SH1000 *atl sagA scaH* (SJF 4611, p = 0.0013), corroborating with previous results (Figure 4.19C; Figure 4.22B). There is significantly less mortality in embryos treated with control liposomes and infected with unsonicated SH1000 *atl sagA scaH* (SJF 4611), than embryos that are clodronate treated and infected with unsonicated SH1000 *atl sagA scaH* (SJF 4611, p = 0.0005). No difference can be seen in clodronate treated embryo mortality infected with sonicated or unsonicated SH1000 *atl sagA scaH* (SJF 4611). Also, no difference in mortality is

observed between clodronate treated fish injected with unsonicated SH1000 *atl sagA scaH* (SJF 4611) and fish receiving control liposomes infected with sonicated SH1000 *atl sagA scaH* (SJF 4611). Finally, no difference in mortality can be seen in embryos infected with sonicated SH1000 *atl sagA scaH* (SJF 4611), whether they have received clodronate or control liposomes. These results show that sonication or clodronate treatment can restore the virulence of SH1000 *atl sagA scaH* (SJF 4611). However, the action of sonication and clodronate together do not further increase the mortality observed in zebrafish embryos, suggesting the effect of sonication is lost (or redundant) upon the loss of macrophages. This implies that a change in interaction with macrophages play a role in the attenuation of SH1000 *atl sagA scaH* (SJF 4611).

The experiment was repeated by infecting two-day old fish, which have a more developed innate immune system, to test if the same results would be seen in a more immune competent embryo (Figure 4.22C). Embryos were treated with control liposomes or clodronate at 24 hpf but were not infected with bacteria until around 54 hpf. The results in Figure 4.22C match those of 4.22B with the exception that clodronate treated embryos have a significantly higher mortality than those treated with control liposomes when infected with sonicated SH1000 *atl sagA scaH* (SJF 4611).
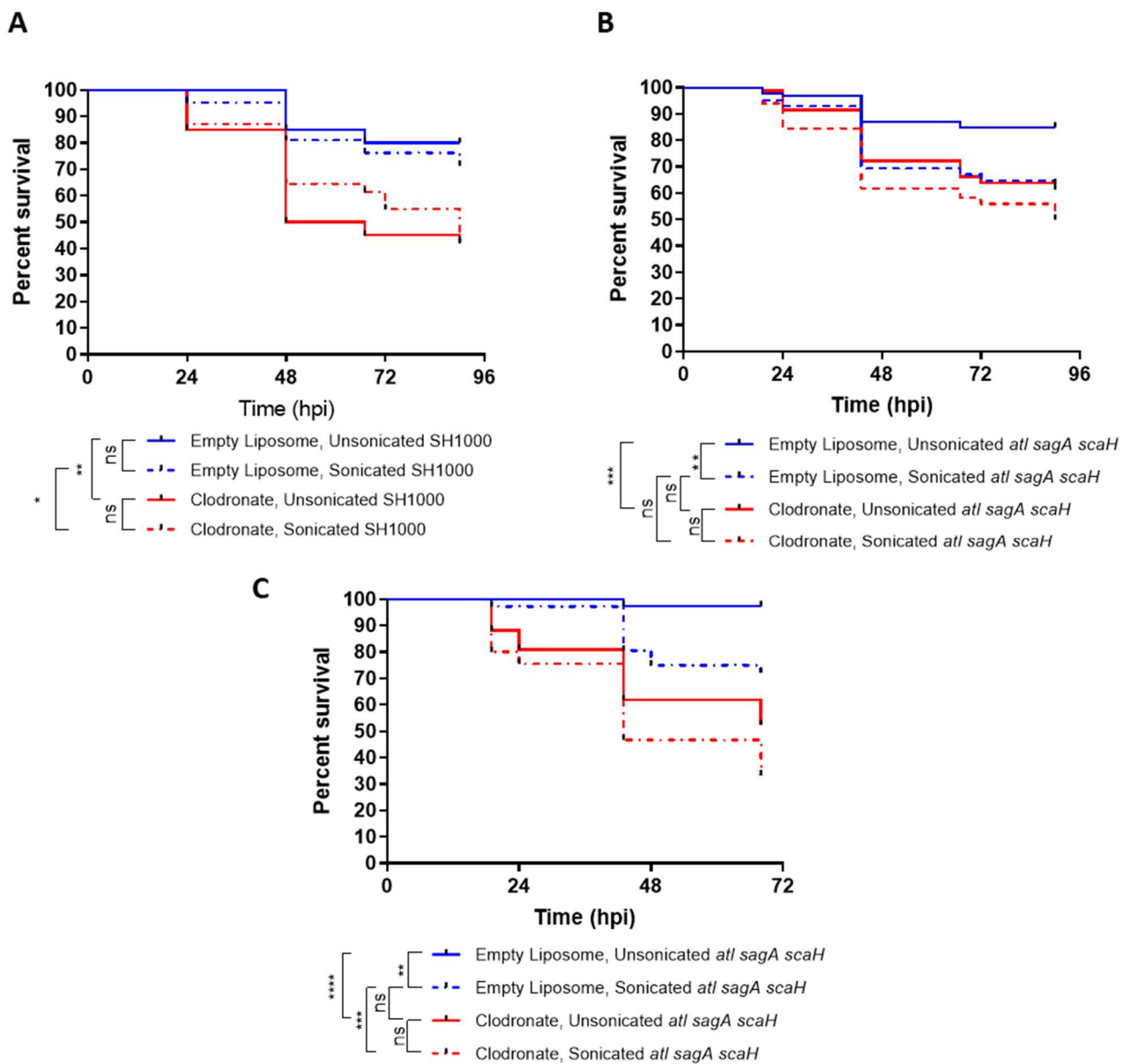
Figure 4.22 The role of macrophages in the zebrafish model in the attenuation of _S. aureus atl sagA scaH_

At around 24 hpf, all zebrafish embryos were injected with either empty liposomes or clodronate containing liposomes. **(A)** At approximately 30 hpf embryos were injected with approximately 150 CFU of sonicated or unsonicated SH1000 (SJF 682) (3 repeats, n>20, * p =0.0455, ** p = 0.0057). **(B)** At approximately 30 hpf embryos were injected with approximately 150 CFU of sonicated or 150 bacteria in 10 particles of unsonicated SH1000 _atl sagA scaH_ (SJF 4611) (3 repeats, n>20, ** p = 0.0013, *** p = 0.0005). **(C)** At approximately 54 hpf embryos were injected with approximately 150 CFU of sonicated or 150 bacteria in 10 particles of unsonicated SH1000 _atl sagA scaH_ (SJF 4611) (3 repeats, n>20, ** p = 0.0021, *** p = 0.0004, **** p < 0.0001). (Blue lines – empty liposomes, red lines – clodronate treated, solid lines – unsonicated bacteria, broken lines – sonicated bacteria).

206

4.4 Discussion

The virulence of a wide range of *S. aureus* glucosaminidase strains have been investigated as a part of my study, using different animal models of infection. These results have been summarised in Table 4.1.

4.4.1 The role of SagB in virulence

The data presented in this chapter shows that a *sagB* mutant has a reduced growth rate compared to the wildtype (Figure 4.2) and is attenuated in the zebrafish model of infection (Figure 4.3). This attenuation can be seen in the murine sepsis infection model (Figure 4.6). The *sagB* mutant was less able to survive within human MDMs than a wild type strain (Figure 4.9), suggesting the attenuation was due to a change in the interaction with macrophages. However, while clodronate depletion of macrophages in mice increased the virulence of the *sagB* mutant, it was still significantly less than a wildtype (Figure 4.11) suggesting that factors other than macrophages also play a role in the attenuation.

The *sagB* mutant showed a reduced growth rate *in vitro* (Figure 4.2), which is also seen *in vivo* (Figure 4.4). While SH1000 *sagB* (SJF 4608) has a reduced CFU increase *in vivo* compared to wildtype (Figure 4.4B), this trend is not so clear for NewHG *sagB* (SJF 4912) (Figure 4.5D). However, zebrafish embryos do clear the NewHG *sagB* inoculum*,* while embryos do not clear wildtype NewHG. *S. aureus* without active SagB shows longer glycan chains, and a stiffer cell wall than wild type when measured by AFM (Wheeler *et al.*, 2015). The inability of the *sagB* mutant to process glycan strands may lead to a reduction in the ability of cells to increase in volume, in turn reducing the growth rate. During an infection, this reduced growth rate is exacerbated by the stringent *in vivo* conditions, potentially resulting in the attenuation of the strain in zebrafish and murine models of infection.

As well as growth defects, work by Chan *et al.* (2016) shows changes in the secretome of *sagB* mutants. Secreted proteins, including those important to virulence, such as: staphylococcal complement inhibitor, staphylococcal superantigen-like protein 1 (SSL1), SSL7, SSL11 and Coa were found in reduced concentrations in the culture medium when compared to wild type (Chan *et al.*, 2016b). As these proteins are important virulence factors, this could explain the reduction in virulence seen in a *sagB* mutant in both zebrafish embryo and murine sepsis models of infection (Figures 4.3A, 4.5B and 4.6). The secretion defect was also found to include the increased secretion of 251 proteins, 90.5% (227 proteins) of which were predicted to be cytoplasmic proteins (Chan *et al.*, 2016b). The increased secretion of cytoplasmic proteins would help to explain both the reduced growth rate *in vitro* and reduced virulence, as intracellular proteins erroneously excreted to the extracellular environment cannot perform their function. *S. aureus sagB* mutants have been reported to not show an autolysis phenotype (Chan *et al.*, 2016b), so lysis is unlikely to be an explanation for the presence of cytoplasmic proteins outside of the cell. *S. aureus atl* mutants have also been found to have an aberrant secretion of extracellular proteins (Pasztor *et al.*, 2010). A wildtype *S. aureus* was found to excrete 22 typically cytoplasmic proteins, but an *atl* mutant showed a reduction in the excretion of these proteins as well as a reduction in extracellular proteases, but the increased release of PG hydrolases (Pasztor *et al.*, 2010).

Invasion of, and survival within, host phagocytes may be a fundamental part of *S. aureus* disease (Kubica *et al.*, 2008; Prajsnar *et al.*, 2012; Pollitt *et al.*, 2018), providing a reservoir for infection. While my study has shown that *sagB* mutants are less able to survive within MDMs than wild type *S. aureus* (Chapter 4.3.7) it has not determined if there is a change in bacterial uptake. With an altered glycan structure from the loss of SagB (Wheeler *et al.*, 2015), it is possible that the mutant is less readily phagocytosed by host phagocytes due to a change in the recognition of bacterial peptidoglycan (Peterson *et al.*, 1978; Dziarski and Gupta, 2005).

The results of my study have raised further questions on the impact of SagB on virulence. It has been shown through Figures 4.9, 4.10 and 4.11 that *sagB* mutants (SJF 4608 and SJF 4912) have a different interaction with the host macrophages than the parental *S. aureus* strains (SJF 682 and SJF 3680), resulting in the mutant being less able to survive within host macrophages. This could be caused by a change in the acidification of the macrophages that *S. aureus* are contained within during an infection. The structure of PG made by cells without *sagB* may be more susceptible to the oxidative burst of phagocytes (Chapter 1.7.2). This could also be a result of the aberrant protein secretion described for *sagB* mutants (Chan *et al.*, 2016b) resulting in the incorrect localisation of proteins required for defence against the oxidative burst. This may also have an impact on the secretion of proteins required for the protection against the action of antimicrobial peptides, resulting in the reduced survival of *sagB* strains *in vivo* (DeLeo *et al.*, 2009; Buchan *et al.*, 2019)*.* The change in glycan structure may alter host recognition of peptidoglycan by receptors such as NOD2, possibly resulting in increased cytokine signalling by an increased expression of NF-κB and the subsequent production of inflammatory cytokines such as IL-1β (Irazoki *et al.*, 2019).

S. aureus strain	Zebrafish embryo model	Murine sepsis model
SH1000 *atl* (SJF 1367)	Virulent (p = 0.4709)	
SH1000 *sagA* (SJF 4606)	Virulent (p = 0.9672)	
SH1000 *scaH* (SJF 4607)	Virulent (p = 0.9666)	
SH1000 *sagB* (SJF 4608)	Attenuated (p < 0.0001)	
NewHG *sagB* (SJF 4912)	Attenuated (p = 0.0043)	Attenuated (Figure 4.6)
SH1000 *atl sagA* (SJF 5261)	Attenuated (p < 0.0001) Sonication restores virulence (P = 0.9413)	
SH1000 *atl scaH* (SJF 5262)	Attenuated (p < 0.0001) Sonication restores virulence (p = 0.1252)	
SH1000 *sagA scaH* (SJF 5217)	Virulent (p = 0.7724)	
SH1000 *atl sagA scaH* (SJF 4611)	Attenuated (p < 0.0001) Sonication restores virulence (p = 0.2191)	Attenuated, Sonication doesn't restore virulence (Figure 4.20)
SH1000 *atl sagB* (SJF 4972)	Attenuated (p < 0.0001)	
SH1000 *sagA sagB* (SJF 4974)	Attenuated (p < 0.0001)	
SH1000 *sagB scaH* (SJF 4973)	Attenuated (p < 0.0001)	
SH1000 *atl sagA sagB* (SJF 4610)	Attenuated (p < 0.0001)	
SH1000 *sagA sagB scaH* (SJF 4612)	Attenuated (p = 0.0012)	
SH1000 *atl sagB scaH* (SJF 4612)	Attenuated (p < 0.0001)	

Table 4.1 Summary of virulence phenotypes of different *S. aureus* glucosaminidase mutant strains

Summary of observed virulence phenotypes for *S. aureus* in the zebrafish embryo and murine sepsis models of infection. Stated p values compare the strain to the parental strain.

4.4.2 The impact of clustering on *S. aureus* virulence

Single mutations of *atl, sagA* or *scaH* have no impact upon virulence (Figure 4.13), although Figure 4.12A does show the clustering of *atl* mutants that has previously been described (Takahashi *et al.*, 2002; Wheeler *et al.*, 2015). Despite the clustering, it is interesting to note that a single *atl* mutant is not attenuated in the zebrafish model of infection. This result matches the finding that a JE2 *atl* mutant had no difference in virulence to wildtype JE2 in a murine device-related infection model (McCarthy *et al.*, 2016). SH1000 *atl sagA* (SJF 5261) and SH1000 *atl scaH* (SJF 5262) mutants were found to be attenuated in a zebrafish embryo model of infection, but virulence was restored upon sonication of the strains (Figure 4.16A, B and C). No difference in virulence was found for SH1000 *sagA scaH* (Figure 4.16D). SH1000 *atl sagA scaH* (SJF 4611) was also found to cluster and had a reduced growth rate. For clustering mutants, it was found that sonication restored bacteria to single cells and restored virulence in the zebrafish embryo model of infection, but not in the murine sepsis model of infection. The impact of clustering in the zebrafish model of infection have been summarised in Figure 4.23. Finally, it was found that depletion of macrophages by clodronate treatment in zebrafish embryos resulted in the same level of embryo mortality when injected with unsonicated SH1000 *atl sagA scaH* (SJF 4611) as control liposome treated embryos injected with sonicated SH1000 *atl sagA scaH* (SJF 4611) (Figure 4.22B).

It is curious that an *atl* mutant is not attenuated, but if both *atl* and *sagA* or *scaH* are inactivated, attenuated is observed. This is also compounded by the fact that a *sagA scaH* double mutant is not attenuated. This demonstrates the functional redundancy of the glucosaminidases as reported by Wheeler *et al.* (2015). The glucosaminidases SagA, ScaH and SagB can compensate for the loss of Atl activity in virulence (despite the clustering). However, once SagA or ScaH activity is also lost, the remaining enzymes cannot perform the function. A SH1000 *sagA scaH* mutant is also not attenuated, presumably because the activities of Atl and SagB provide enough glucosaminidase activity to maintain the cell.
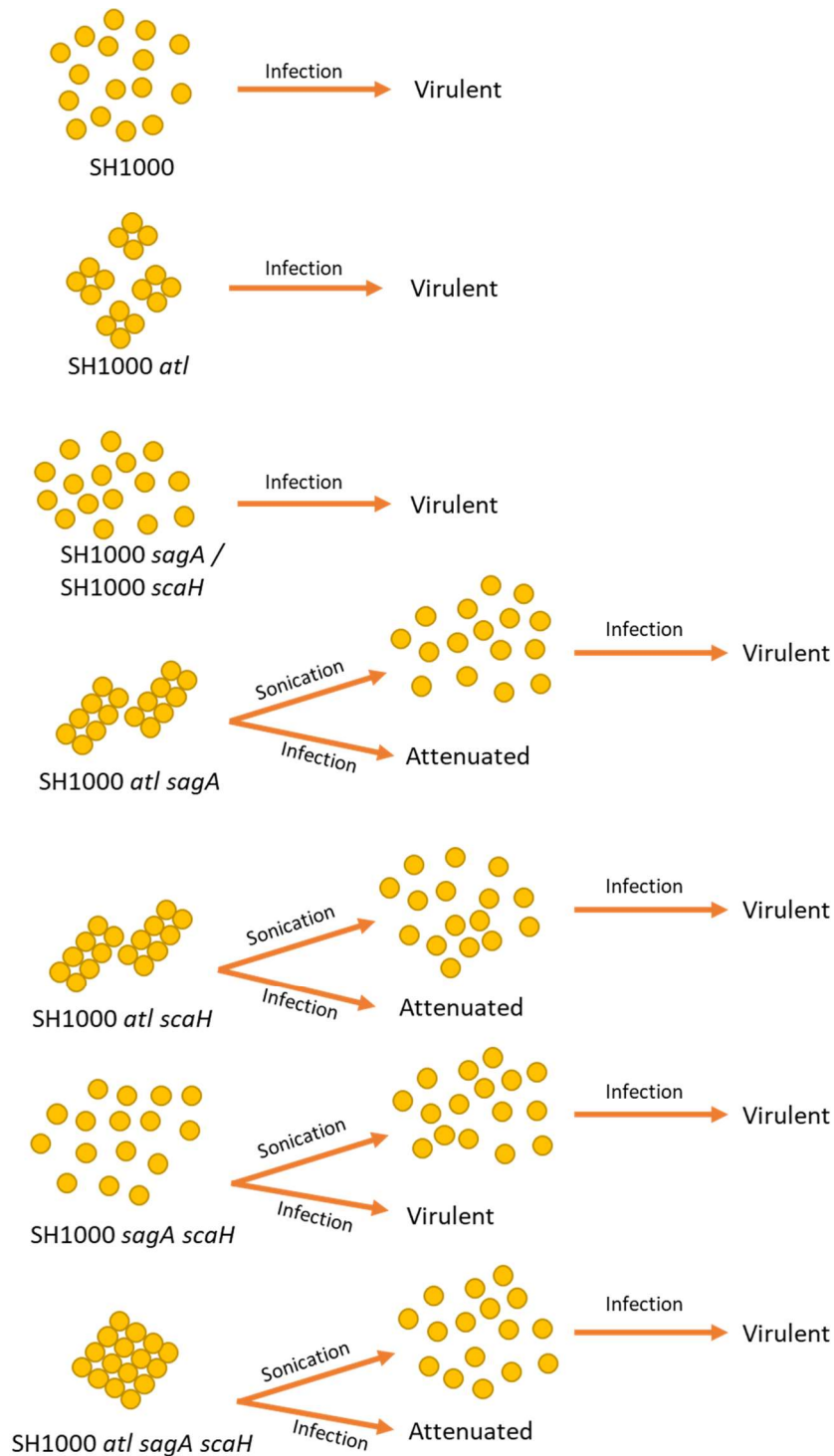
Figure 4.23 Summary of the impact of clustering on *S. aureus* virulence in the zebrafish model of infection

Parental SH1000 (SJF 682) does not show cell clustering and is virulent in the zebrafish model of infection. Single mutations in *atl, sagA* or *scaH* are not attenuated, but SH1000 *atl* (SJF 1367) does show a clustering phenotype. Both SH1000 *atl sagA* (SJF 5261) and SH1000 *atl scaH* (SJF 5262) show a clustering phenotype. While in clusters, the strains are attenuated, but sonication to disrupt the clustering restores virulence. SH1000 *sagA scaH* (SJF 5217) does not show clustering and is virulent regardless of sonication. SH1000 *atl sagA scaH* (SJF 4611) also displays clustering and is attenuated when injected into zebrafish embryos, but virulence is restored upon sonication.

The attenuation of SH1000 *atl sagA scaH* can partly be explained due to the loss of several glucosaminidases, but Atl has also been shown to have other activities, including amidase activity. It has been found that Atl is able to bind to fibronectin, heparin (Porayath *et al.*, 2018) and DNA (Grilo *et al.*, 2014). The ability of Atl to bind to fibronectin is likely due to the repeat sequences of Atl (R_1, R_2 and R_3) (Houston *et al.*, 2011). The binding of Atl to these molecules has been found to be involved in the establishment of biofilms (Bose *et al.*, 2012). Loss of Atl may therefore cause a reduction in the ability of *S. aureus* to produce a biofilm *in vivo*. SagA and ScaH are both poorly studied enzymes, which may also have other, yet undiscovered, roles in the cell.

The increase in particle size (measured by FSC) of SH1000 *atl sagA scaH* (Figure 4.19C) matches that found with *atlA* mutants of *Enterococcus faecalis* (Salamaga *et al.*, 2017). The lack of AtlA in *E. faecalis* produces chains of bacteria rather than the clusters seen in SH1000 *atl sagA scaH,* which are also found to be attenuated in the zebrafish embryo model of infection. When chains of *E. faecalis* Δ*atlA* were sonicated or incubated with purified AtlA, virulence was restored in the zebrafish embryo model of infection. The reason for attenuation of *E. faecalis* Δ*atlA* was determined to be an increase in uptake by phagocytes (Salamaga *et al.*, 2017).

Sonication of SH1000 *atl sagA scaH* (SJF 4611) did not restore virulence in the murine model of infection, while it did in the zebrafish. This discrepancy could be explained by the nature of *S. aureus* infection dynamics. *S. aureus* is thought to go through bottlenecks during infection, with only a small number of the starting inoculum going on to seed the characteristic abscesses or lesions, depending on the infection model (McVicker *et al.*, 2014; Pollitt *et al.*, 2018). This may explain the need for such high CFU for infection in mammalian models of *S. aureus* disease (Pollitt *et al.*, 2018). The immune bottleneck is associated with phagocytes in both zebrafish and murine models of infection. The bacteria that survive this phagocyte mediated bottleneck, go on to form abscesses. As previously described (Chapter 1.8.2, 4.1) zebrafish below 5 dpf have only an innate immune system (Prajsnar *et al.*, 2008), while mice have a more complex

immune system, including adaptive immunity, and infection progression is more complex (Figure 4.1). There are more bottlenecks that SH1000 *atl sagA scaH* (SJF 4611) must go through in mice than the zebrafish embryos. SH1000 *atl sagA scaH* (SJF 4611) will continue to form clusters when it grows and divides even after mechanical separation by sonication. Sonicated SH1000 *atl sagA scaH* (SJF 4611) can cause mortality in zebrafish embryos, as it passes through fewer bottlenecks causing mortality before the mutant becomes clustered and therefore attenuated. In the mice however, the sonicated SH1000 *atl sagA scaH* (SJF 4611) must contend with a more complex infection process. Host lysozyme, a muramidase (Chapter 1.4.3.1) may act on the PG of *S. aureus* during an infection, and this may modify its structure. While the loss of glucosaminidases results in a clustering phenotype, it is possible that host lysozyme would provide muramidase activity that could result in the reversal of the bacterial clustering, restoring virulence. It would therefore be pertinent to investigate the sensitivity of the glucosaminidase strains to lysozyme, and the strains' clustering status *in vivo* during an infection.

The Atl autolysin has also been associated with cell division and virulence in other staphylococcal species. *Staphylococcus lugdunensis* is a commensal skin organism, but like *S. aureus* can adapt to a pathogenic lifestyle, causing abscess and wound infections, endocarditis, urinary tract infections, and infections of catheters and other medical devices (Frank *et al.*, 2008). AtlL of *S. lugdunensis* is also bifunctional like Atl of *S. aureus* (Bourgeois *et al.*, 2009). Loss of AtlL activity results in clustering in *S. lugdunensis,* reduction in the ability to form biofilms, as well as reduced virulence in a *C. elegans* model of infection (Gibert *et al.*, 2014). Loss of AtlE of *Staphylococcus epidermidis* has also been associated with clustering and a reduction in biofilm formation (Heilmann *et al.*, 1997; Biswas *et al.*, 2006).

Glucosaminidases have been shown to play a role in cell separation in rod shaped bacteria as well as spheroid bacteria like staphylococcal species. *Clostridium perfringens* is a Gram-positive, spore-forming rod shaped bacterium implicated in foodborne disease, as well as a causative agent of gas gangrene (Brynestad and Granum, 2002).

Amidases and muramidases are important for the sporulation and germination of *C. perfringens* (Chen *et al.*, 1997; Miyata *et al.*, 1997). The *C. perfringens* PG hydrolase Acp has been shown to have glucosaminidase activity and is predominantly expressed during vegetative growth (Camiade *et al.*, 2010). A loss of Acp activity resulted in the observation of long chains of undivided *C. perfringens* (Camiade *et al.*, 2010), matching the clustering of *S. aureus,* suggesting a role in other species for glucosaminidases in cell division and separation.

4.4.3 The combined role of glucosaminidases

The loss of glucosaminidase activity suggests that there will be a reduction in the concentration of peptidoglycan turnover products, such as soluble muropeptides. It is known that *Pseudomonas aeruginosa* senses and responds to peptidoglycan from Gram-positive bacteria to upregulate virulence factors and increase pathogenesis (Korgaonkar *et al.*, 2013). *S. aureus* has regulatory systems, such as PknB, that can respond to components of the cell wall (Hardt *et al.*, 2017). PknB is a eukaryotic-like serine/threonine kinase that is believed to be involved in the regulation of cell wall metabolism, virulence and antibiotic susceptibility (Beltramini *et al.*, 2009; Débarbouillé *et al.*, 2009). PknB consists of a C-terminal extracellular receptor region that has three PASTA (PBP and serine/threonine kinase–associated) domains (thought to bind PG), a transmembrane domain and an intracellular kinase domain at the N-terminus (Ohlsen and Donat, 2010). The kinase domain of PknB has been shown to be activated by binding lipid II, specifically the L-Lys-D-Ala-D-Ala motif (Hardt *et al.*, 2017). PknB has been found to be able to phosphorylate WalR, activating it, and upregulating the expression of PG hydrolases important for PG turnover (Chapter 1.4.3) (Hardt *et al.*, 2017). PknB was also found to phosphorylate FtsZ, regulating its polymerisation, and subsequent recruitment of the divisome (Hardt *et al.*, 2017).

This chapter has given important insight into the individual and collective role of glucosaminidases in *S. aureus* pathogenesis. The loss of *sagB* results in a growth defect

and the attenuation of *S. aureus* in zebrafish and murine models of infection, which has been linked to a change in macrophage interaction. The individual loss of *atl, sagA* or *scaH* is not enough to cause attenuation, despite the clustering phenotype of an *atl* mutant, which is likely because of the high degree of redundancy seen in bacterial PG hydrolases. The simultaneous loss of *atl* and another glucosaminidase results in clustering and the attenuation of strains in a zebrafish model of infection, with virulence restored when the clusters are mechanically disrupted. A mutant lacking *atl, sagA* and *scaH* also displayed a clustering phenotype associated with attenuation in the zebrafish model, with virulence being restored with sonication. The attenuation of this mutant could not be restored by mechanical disruption of the clusters in a murine sepsis model of infection.

Chapter 5

The role of *S. aureus* penicillin binding proteins in pathogenesis

5.1   Introduction

Cell wall PG must be cleaved to allow growth associated with the insertion of new material by the action of PG synthases (Vollmer *et al.*, 2008b). Penicillin binding proteins (PBPs) with transglycosylase activity add new muropeptides by polymerising new glycans into existing cell wall material. New crosslinks between the glycans can be added by some PBPs by transpeptidation. *S. aureus* possesses four native PBPs: PBP1, PBP2, PBP3 and PBP4. Of these PBP3 and PBP4 are non-essential (Sauvage *et al.*, 2008).

MRSA strains also encode the non-native *mecA* gene, producing the non-essential PBP2A responsible for high level β-lactam antibiotic resistance (Blázquez *et al.*, 2014). *S. aureus* COL, an MRSA strain, is viable with only PBP1 and PBP2 (Reed *et al.*, 2015). This PBP minimal strain does not show a growth defect in rich or minimal media, and cells show normal cell morphology when observed by TEM and Structured Illumination Microscopy (SIM). While growth rate and morphology were unaffected, the minimal strain is highly sensitive to cell wall targeting antibiotics such as β-lactams, compared to the wildtype (Reed *et al.*, 2015). The loss of non-essential PG synthesis enzymes also results in the attenuation of the strain compared to the wildtype in a *Drosophila* model of infection, which was suggested to be caused by reduced PG crosslinking resulting in more susceptibility to host killing (Reed *et al.*, 2015). Collectively PG synthesis enzymes therefore play a role in virulence, but their individual functions are unknown.

PBP4 is the only low molecular mass PBP of *Staphylococcus aureus,* a type-5 PBP with transpeptidase activity (Sauvage *et al.*, 2008). The transpeptidase activity of PBP4 is required to produce the high level of crosslinking found in *S. aureus* PG (Wyke *et al.*, 1981a). Increased production of PBP4 has also been associated with low-level resistance to β-lactam

antibiotics (Henze and Berger-Bächi, 1995), an important virulence phenotype in clinical settings. Upregulation of PBP4 has been associated with a reduction in *S. aureus* sensitivity to β-lactam antibiotics (Hamilton *et al.*, 2017). The increased resistance to β-lactam antibiotics from PBP4 has also been established in community-acquired MRSA strains that do not encode for PBP2a (Memmi *et al*., 2008; Chan *et al*., 2016), but the mechanism remains unclear (Hamilton *et al.*, 2017). PBP4 is therefore important in a clinical setting and may also play a role in virulence. A PBP4 deletion mutant was associated with larger skin lesions in a mouse skin model of infection (Müller *et al.*, 2015), suggesting an increased virulence from exacerbated disease presentation. A fitness cost is associated with the acquisition of antibiotic resistance (Geisinger and Isberg, 2017) as well as PG metabolism, but the trade-off between PBP4 and *in vivo* fitness has not been studied.

Less information is known about the role of PBP3 in the cell (Reed *et al.*, 2015). Recent work has shown an interaction between PBP3 and RodA, which is thought to be important for the localisation of both proteins to the mid-cell for PG insertion (Reichmann *et al.*, 2019). The loss of PBP3 does not alter the muropeptide composition of the cell wall, and causes no change in the resistance of the cell to methicillin (Pinho *et al.*, 2000). Observations of cell morphology by TEM suggest that PBP3 may play a role in septum formation and separation (Pinho *et al.*, 2000), as when cells are treated with selective inhibitors of PBP3 cells failed to separate after division (Georgopapadakou *et al.*, 1986; Okonog *et al.*, 1995). Due to the high level of redundancy of the PG synthases (Reed *et al.*, 2015) it is possible that when studied *in vitro* other synthases may be able to substitute for loss of PBP3 function, hence the lack of a distinct phenotype.

5.2   Aims of this chapter

The aim of this chapter was to characterise the role of PBP3 and PBP4 of *S. aureus* in animal models of infection. The specific aims of this chapter were to:

i.   Investigate the role of *S. aureus* PBP3 and PBP4 in virulence

ii.   Determine the cause of any observed changes in pathogenesis

5.3 Results

5.3.1 Role of non-essential PBPs in growth

The growth rates of *pbp3* and *pbp4* mutants have previously been analysed, with no difference in growth being reported (Curtis *et al.*, 1980; Pinho *et al.*, 2000).

Using the *S. aureus* SH1000 genetic background, SH1000 *pbp3* (SJF 4422), SH1000 *pbp4* (SH1000 4425) and SH1000 *pbp3 pbp4* (SJF 4423) were tested for growth in liquid TSB (Figure 5.1). SH1000 *pbp3* (doubling time 33.6) shows no difference in growth rate to parental SH1000 (SJF 682, doubling time 33.7 min, Figure 5.1A). SH1000 *pbp4* (doubling time 34.9 min) also shows the same growth kinetics *in vitro* as the wildtype SH1000 (doubling time 35.3, Figure 5.1B). A SH1000 *pbp3 pbp4* (doubling time 36.8) double mutant also shows no difference in growth rate compared to SH1000 (doubling time 36.8, Figure 5.1C). The inactivation of *pbp3* and/or *pbp4* causes no change in the growth of *S. aureus* SH1000.
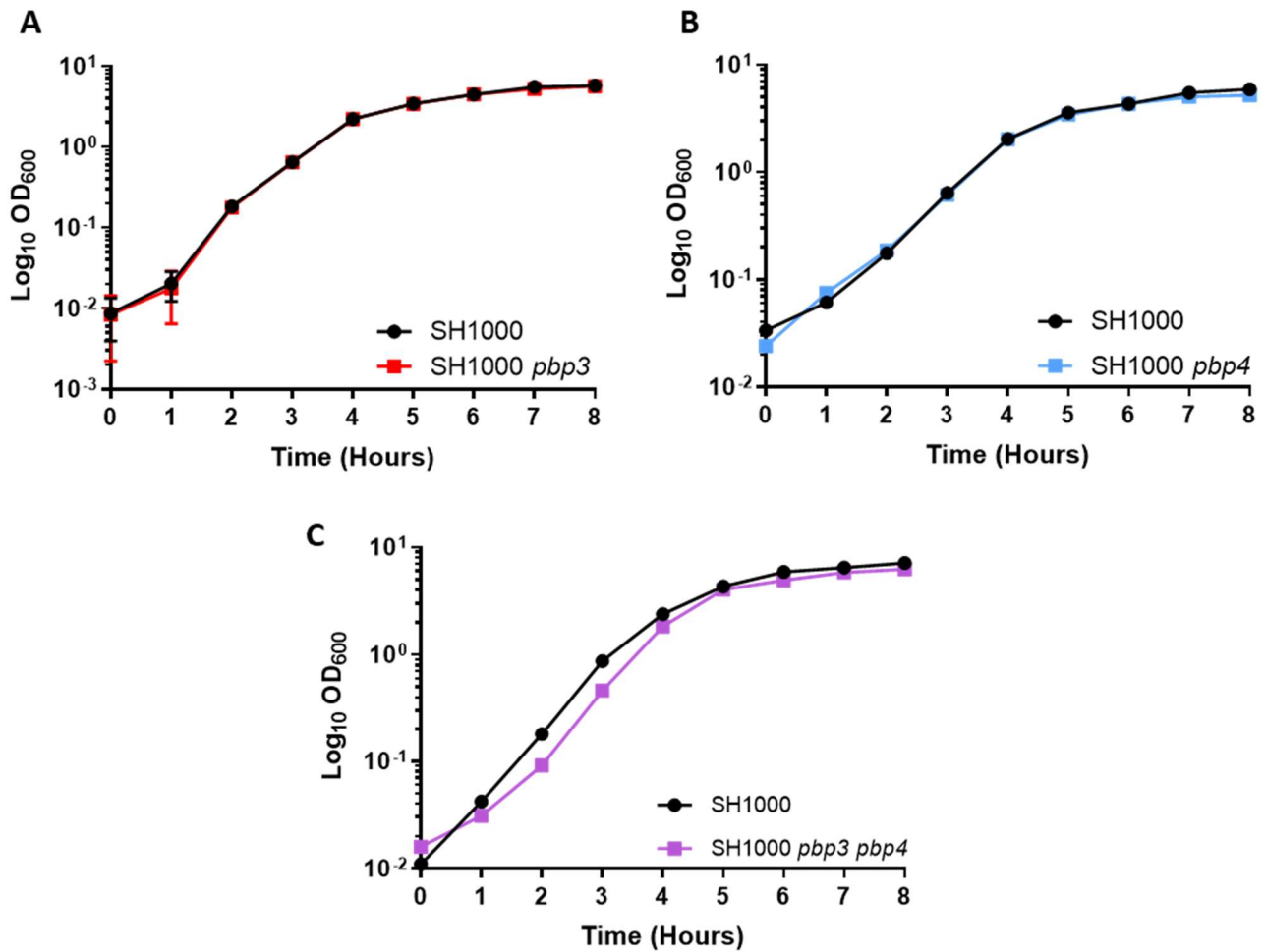
Figure 5.1 Role of *S. aureus* SH1000 PBPs in growth

Growth of parental SH1000 (SJF 682, black circles) in TSB compared to **(A)** SH1000 *pbp3* (SJF 4422, red squares), **(B)** SH1000 *pbp4* (SJF 4425, blue squares) and **(C)** SH1000 *pbp3 pbp4* (SJF 4423, purple squares). Bacterial cultures were prepared in triplicate and error bars represent the standard deviation of the mean.

5.3.2 Role of *S. aureus* PBP3 and PBP4 in the zebrafish model of infection

SH1000 *pbp3* (SJF 4422), SH1000 *pbp4* (SJF 4425) and SH1000 *pbp3 pbp4* (SJF 4423) strains were analysed for virulence in the zebrafish embryo infection model (Chapter 2.18.1). 1500 CFU of each strain were injected into the circulation valley of 30 hpf embryos and compared to the mortality caused by SH1000 (SJF 682) (Figure 5.2). SH1000 *pbp3* caused 63 % mortality 90 hpi compared to 55 % caused by the wildtype SH1000, which was found to not be significantly different (Figure 5.2A, p = 0.9505). There was no significant difference in mortality seen between SH1000 *pbp4* and SH1000 (Figure 5.2B, p = 0.3154), despite SH1000 *pbp4* causing a higher mortality (64 %) than SH1000 (54 %). The mortality caused by SH1000 *pbp3 pbp4* (47 %) was found to not be significantly different from that of SH1000 (53 %) (Figure 5.2C, p = 0.7958). The loss of non-essential PBPs has no overall impact on virulence in this model.
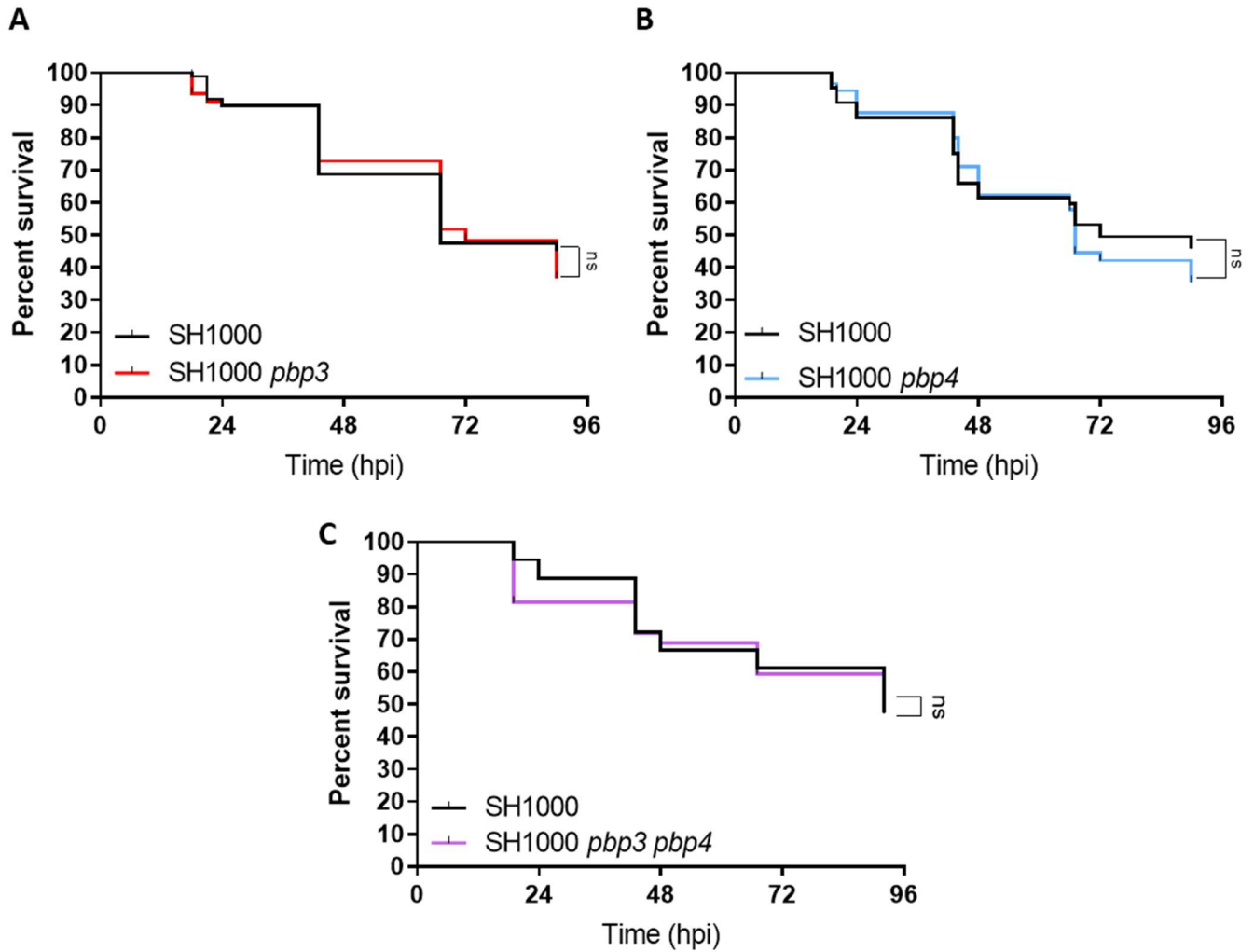
Figure 5.2 Role of PBPs in _S. aureus_ virulence in the zebrafish infection model

Approximately 1500 CFU of bacteria (mutant or wild type) was injected into the circulation valley of LWT zebrafish embryos around 30 hpf. **(A)** Survival curves comparing the virulence of parental SH1000 (SJF 682, WT, black lines) to SH1000 _pbp3_ (SJF 4422, red lines) (3 repeats, n>20). **(B)** Survival curves comparing the virulence of parental SH1000 (SJF 682, WT, black lines) to SH1000 _pbp4_ (SJF 4425, blue lines) (3 repeats, n>20). **(C)** Survival curves comparing the virulence of parental SH1000 (SJF 682, WT, black lines) to SH1000 _pbp3 pbp4_ (SJF 4423, purple lines) (3 repeats, n>20).

5.3.3 Construction of a *S. aureus* NewHG *pbp4* strain

SH1000 *pbp4* (SJF 4425) shows a trend for increased virulence in the zebrafish infection model (Figure 5.2B). PBP4 is known to be responsible for the high level of *S. aureus* PG crosslinking (Wyke *et al.*, 1981a). For these reasons, it was decided to further investigate the role of PBP4 in virulence in the NewHG genetic background, as described in Chapter 4.3.4, as it is a well-established strain in the murine sepsis model of infection (Pollitt *et al.*, 2018).

The SH1000 *pbp4* (SJF 4425) strain is derived from the Nebraska Transposon library, which uses a *bursa aurealis* transposon to inactivate non-essential genes of *S. aureus* (Fey *et al.*, 2013). This insertion in the *pbp4* gene (Figure 5.3B) was transduced into the NewHG genetic background (SJF 3663) using bacteriophage φ11 to produce NewHG *pbp4* (SJF 5103). The transduction was confirmed using PCR, where amplification of the *pbp4* gene produced the expected band of 4773 bp in the NewHG *pbp4* strain (Figure 5.3A; Fey *et al.*, 2013).

A
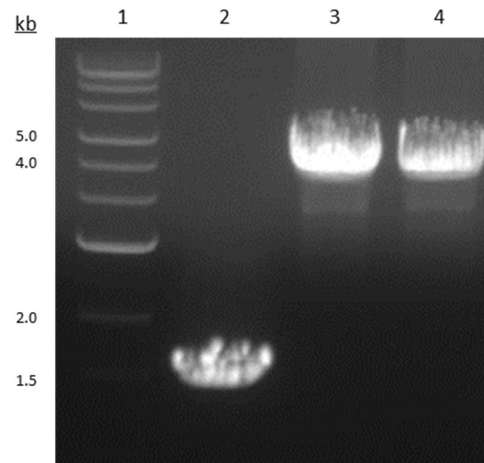
B

Figure 5.3 Verification of NewHG *pbp4* by PCR

(A) 1% (w/v) TAE agarose gel showing PCR amplification of the *pbp4* gene from wildtype NewHG (lane 2), positive control SH1000 *pbp4* (lane 3) and NewHG *pbp4* (SJF 5103) (lane 4) using primers *pbp4-1* (forwards) and *pbp4-5* (reverse). The wildtype band of 1535 bp can be seen in lane 2. The expected mutant band of 4773 bp, shown in lane 3 and indicated with a black arrow, is also seen in lane 4. Relevant sizes of DNA ladder (Quick load purple 2-log DNA ladder, NEB) are shown in kb (lane 1). **(B)** Map showing the *pbp4 gene* (blue, 1296 bp) and the location of the transposon within the gene (bp 606). Primers *pbp4-1* and *pbp4-5* (purple) and are also shown.

5.3.4   Virulence of NewHG *pbp4* in the zebrafish embryo model of infection
5.3.4.1 NewHG *pbp4* virulence phenotype

The virulence of NewHG *pbp4* (SJF 5103) compared to the wildtype NewHG (SJF 3663) was analysed using the zebrafish model of infection. When 1500 CFU of bacteria were injected, NewHG *pbp4* caused 64 % mortality in embryos, which was not significantly different to the 50% mortality caused by NewHG (Figure 5.4A, p = 0.1364). While not significant, the trend for increased killing for a *pbp4* mutant, as for the SH1000 background (Figure 5.2B), is present in the NewHG background.

5.3.4.2 NewHG *pbp4 in vivo* growth kinetics

The zebrafish model of infection was used to determine the *in vivo* growth kinetics of NewHG *pbp4* (SJF 5103) compared to parental NewHG (SJF 3663). 1500 CFU were injected into embryos and the CFU of infected embryos were recovered over time. When embryos are infected with NewHG, the CFU recovered at later timepoints from living embryos are higher than (up to 10^7 CFU), or equal to that of the initial inoculum. One living embryo at 24 hpi had CFU below the limit of detection. Dead embryos infected with NewHG had between ~1 x 10^{3-7} recovered CFU (Figure 5.4B). Embryos injected with NewHG *pbp4* showed similar results to the wildtype strain. Living embryos had recovered CFU similar or greater than (up to 10^7) the initial inoculum CFU. Two living embryos were found to have cleared the infection, one at 48 hpi and one at 67 hpi. Dead embryos infected with NewHG *pbp4* were found to have ~1 x 10^{3-7} recovered CFU (Figure 5.4C). The *in vivo* growth of NewHG *pbp4* is comparable with the wildtype NewHG in the zebrafish model of infection.
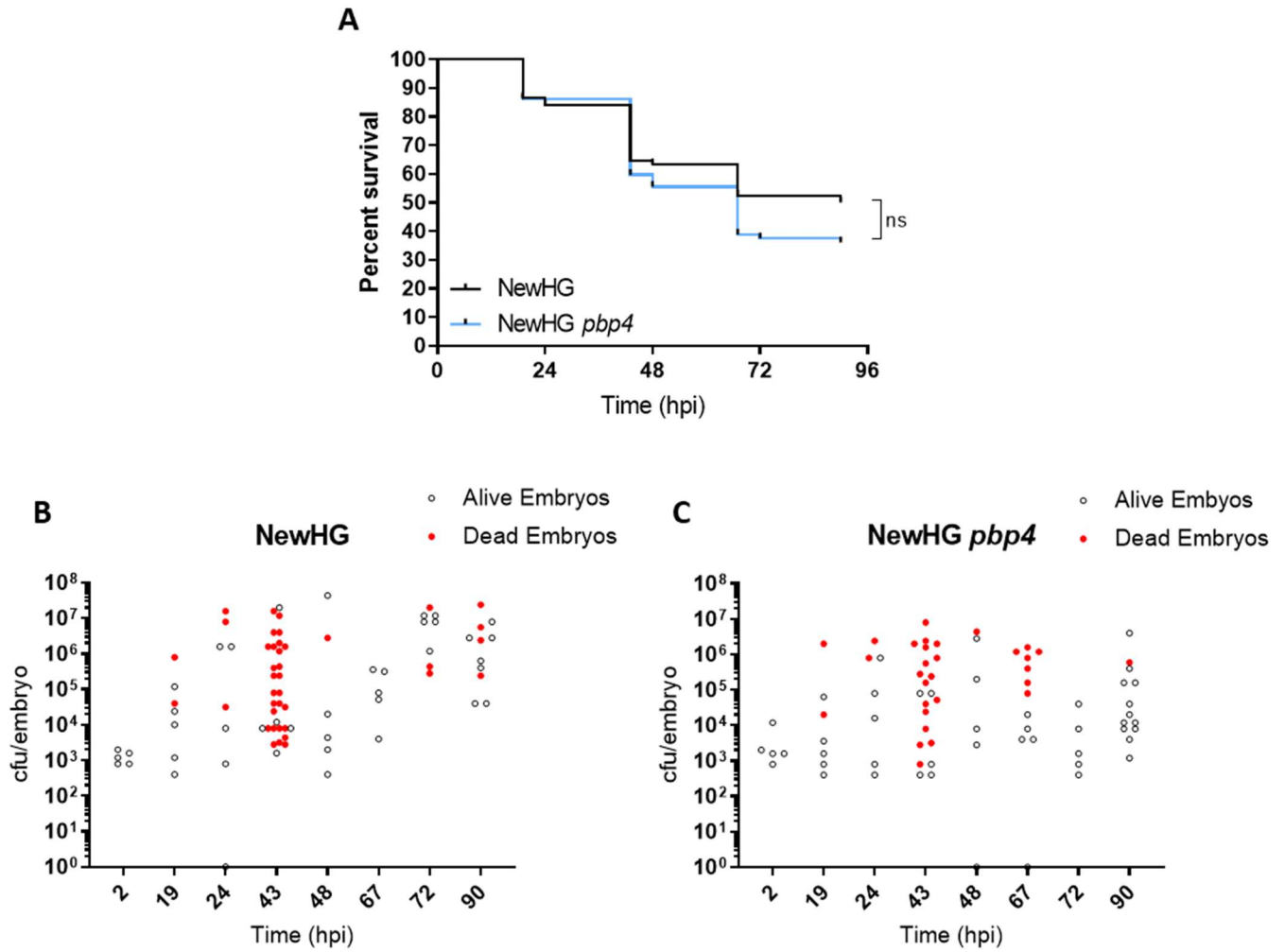
Figure 5.4 The role of PBP4 in *S. aureus* virulence and growth in the zebrafish model of infection

(A) Approximately 1500 CFU of bacteria (mutant or wild type) were injected into the circulation valley of LWT zebrafish embryos around 30 hpf. Survival curve produced to compare the virulence of parental NewHG (SJF 3663, WT, black line) to NewHG *pbp4* (SJF 5103) (3 repeats, n>20). Bacterial CFU were recovered and determined at specified timepoints after LWT zebrafish embryos were infected with (**B**) NewHG (SJF 3663) or (**C**) NewHG *pbp4* (SJF 5103) (n= 75-85) Open black circles are live embryos and red circles are dead embryos.

5.3.5   Analysis of NewHG *pbp4* virulence in the murine model of infection
5.3.5.1 The murine sepsis model

The virulence of NewHG *pbp4* (SJF 5103) was further interrogated using the murine sepsis model of infection (Chapter 2.18.2). NewHG *kan^R* (SJF 3680) was used as the wildtype strain as previously described (Chapter 4.3.6.1).

The virulence of NewHG *pbp4* was examined by injecting groups of 10 mice with 1 x 10^7 CFU of NewHG *pbp4* or NewHG *kan^R* (Figure 5.5). No significant difference in the weight change between the two groups of mice could be seen after 72 hours (Figure 5.5A, p = 0.8421). NewHG *pbp4* has significantly higher CFU recovered from the livers of infected mice than those infected with NewHG *kan^R* (Figure 5.5B, p = 0.0294). No significant difference could be seen in the CFU recovered from the kidneys of mice infected with NewHG *kan^R* or NewHG *pbp4* (Figure 5.5C, p = 0.4829). The CFU recovered from spleens, lungs and hearts all show no significant difference whether mice were injected with NewHG *kan^R* or NewHG *pbp4* (Figures 5.5D, E and F, p = 0.7612, 0.4336 and 0.1223 respectively). These results show an increased colonisation for NewHG *pbp4* specifically within the liver of the murine infection model, compared to NewHG *kan^R*.
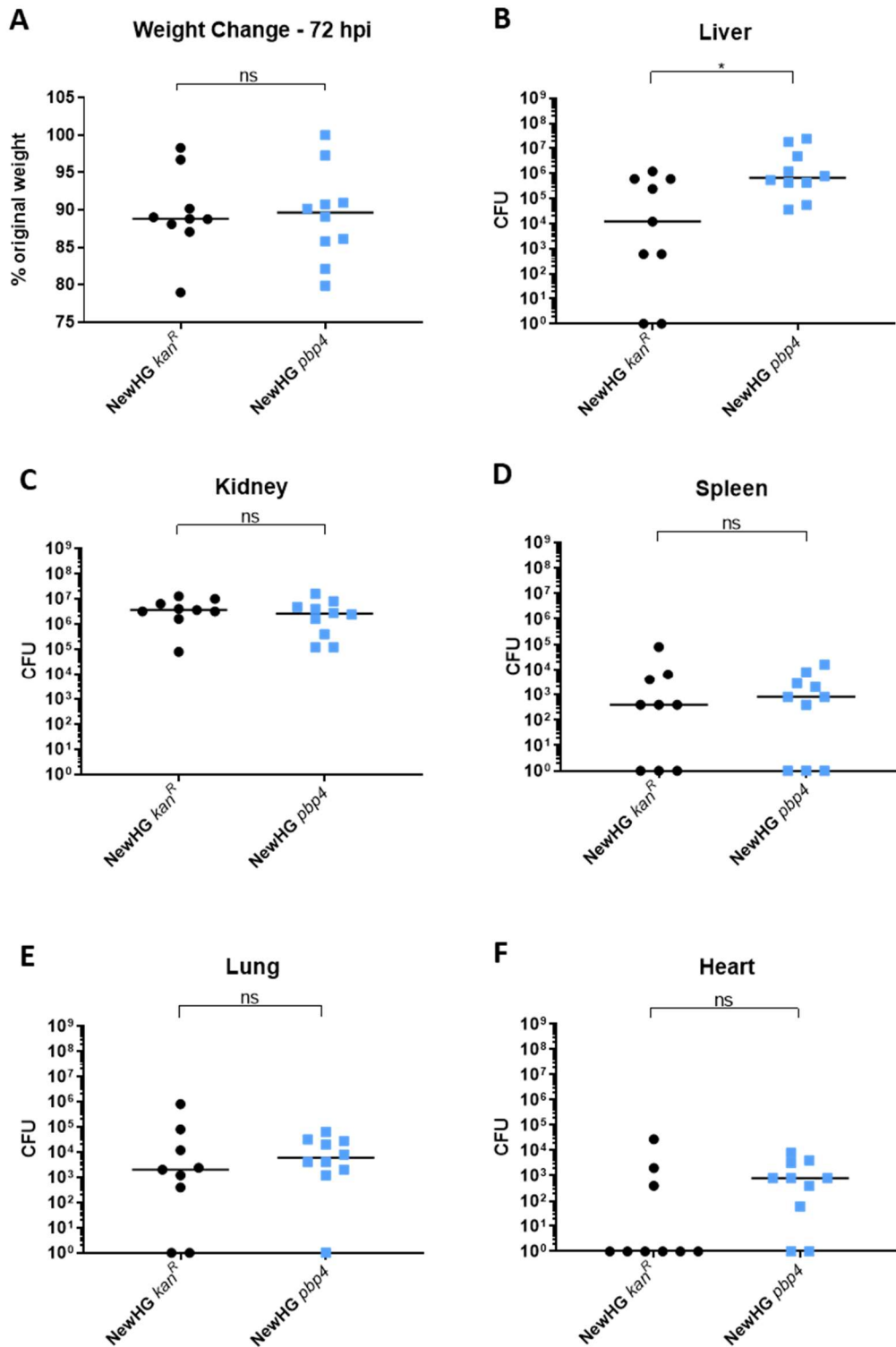
Figure 5.5 Role of PBP4 in *S. aureus* pathogenesis in the murine sepsis model of infection.

Mice (n=10) were injected with approximately 1×10^{7} CFU *S. aureus* NewHG *kan*[R] (WT, SJF 3680) or NewHG *pbp4* (SJF 5103)*.* Weight loss 72 hpi (**A**) and CFUs recovered from livers (**B**), kidneys (**C**), spleen (**D**), lungs (**E**) and heart (**F**) were determined. Groups were compared using a Mann-Whitney U test (NewHG *kan*[R] – black circles, NewHG *pbp4* blue squares) (* p = 0.0294) One mouse was found dead 72 hpi in the NewHG *kan*[R] group and was excluded from the analysis.

5.3.5.2 A low dose infection in the murine sepsis model

If NewHG *pbp4* (SJF 5103) is able to colonise the livers of mice more effectively, then a lower infectious dose may make an increase in mutant virulence more apparent.

Groups of 10 mice were injected with 5 x 10^6 CFU of NewHG *kan^R* (SJF 3680) or NewHG *pbp4* (SJF 5103) (Figure 5.6). No significant difference was found between the weight change in mice infected with either NewHG *kan^R* or NewHG *pbp4* after 72 hours (Figure 5.6A, p = 0.3930). Mice infected with NewHG *pbp4* show a higher number of recovered CFU from the liver than mice infected with NewHG *kan^R* (Figure 5.6B, p = 0.0051), confirming the increased colonisation of the liver. No significant difference could be seen between recovered CFU in the kidneys of mice infected with NewHG *kan^R* or NewHG *pbp4* (Figure 5.6C, p = 0.2878). While there is no significant difference between CFU recovered from spleens infected with NewHG *kan^R* or NewHG *pbp4* (Figure 5.6D, p = 0.5314) less clearance can be seen in spleens infected with NewHG *pbp4.* Significantly more NewHG *pbp4* is recovered from the lungs of infected mice than from lungs of mice infected with NewHG *kan^R* (Figure 5.6E, p = 0.0410). No significant difference can be seen between the recovered CFU from infected mouse hearts (Figure 5.6F, p > 0.9999).
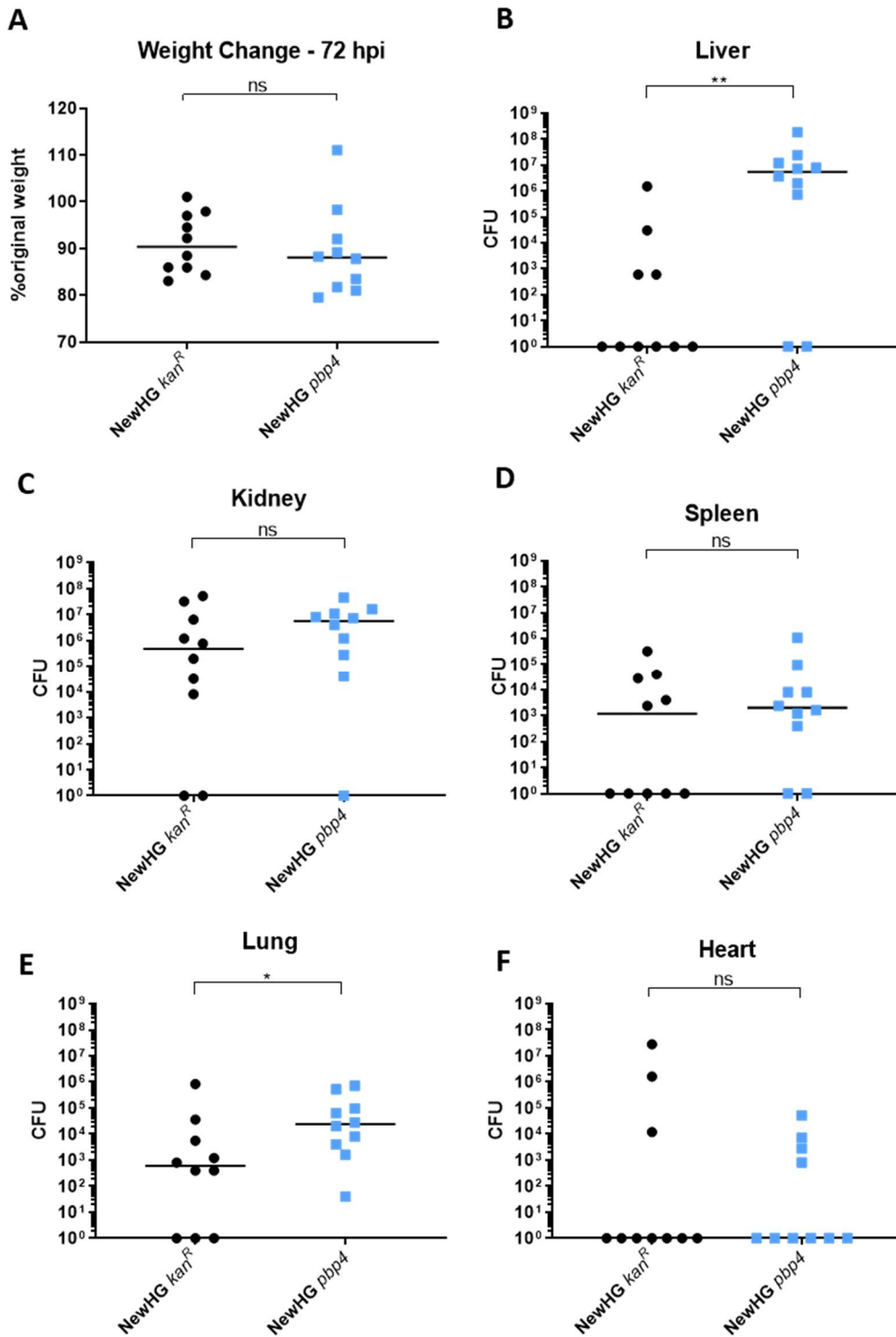
Figure 5.6 Role of PBP4 in *S. aureus* infection at low dose in the murine sepsis model

Mice (n=10) were injected with approximately 5x10^6 CFU *S. aureus* NewHG *kan*^{R} (WT, SJF 3680) or NewHG *pbp4* (SJF 5103). Weight loss 72 hpi (A) and CFUs recovered from livers (B), kidneys (C), spleen (D), lungs (E) and heart (F) were determined. Groups were compared using a Mann-Whitney U test (NewHG *kan*^{R} – black circles, NewHG *pbp4* blue squares) (** p = 0.0051, * p = 0.0410).

5.3.6 Construction of *pbp4* strains for clonality experiments

To investigate the dynamics of a NewHG *pbp4* (SJF 5103) infection, two marked strains were constructed, by transducing the *pbp4* mutation into NewHG *kan^R* (SJF 3680) and NewHG *tet^R* (SJF 3681). Both NewHG *kan^R* and NewHG *tet^R* have been shown to have the same virulence as NewHG (SJF 3663) in the murine sepsis model, so can be used as the marked strains with no effects on virulence (Prajsnar *et al.*, 2012; McVicker *et al.*, 2014).

5.3.6.1 Construction of NewHG *kan^R pbp4*

The *pbp4* mutation from SH1000 *pbp4* (SJF 4425) was transduced into NewHG *kan^R* (SJF 3680) using bacteriophage φ11 to produce NewHG *kan^R pbp4* (SJF 5136). This was confirmed by PCR, where amplification of *pbp4* gene of NewHG *kan^R pbp4* produced the expected wild type band (Figure 5.7A). The mutant was also able to grow in the presence of standard levels of kanamycin (Chapter 2.3).

5.3.6.2 Construction of NewHG *tet^R pbp4*

Using bacteriophage φ11, the *pbp4* mutation was transduced into NewHG *tet^R* (SJF 3681), producing strain NewHG *tet^R pbp4* (SJF 5135). The amplification of the *pbp4* gene in NewHG *tet^R pbp4* gave the mutant band (Figure 5.7B), confirming transduction. The strain was also able to grow in the presence of the standard concentration of tetracycline (Chapter 2.3).
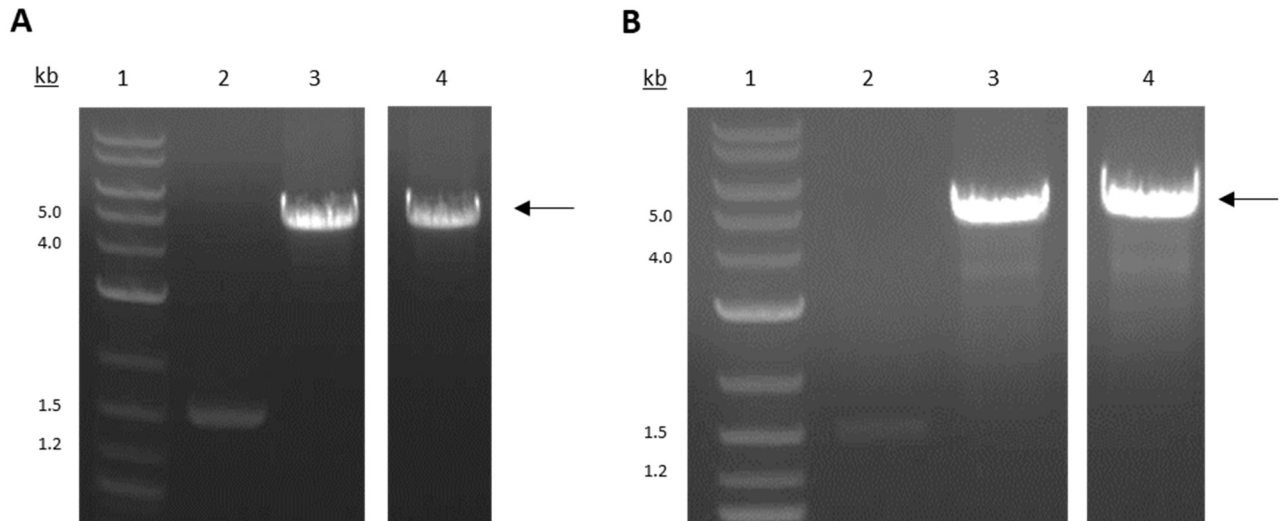
Figure 5.7 Verification of kanamycin and tetracycline resistant NewHG *pbp4* strains

(A) 1% (w/v) TAE agarose gel showing PCR amplification of the *pbp4* gene from NewHG *kan*[R] (lane 2, SJF 3680), positive control SH1000 *pbp4* (lane 3) and NewHG *kan*[R] *pbp4* (SJF 5136) (lane 5) using primers *pbp4-1* (forwards) and *pbp4-5* (reverse). The wildtype band of 1535 bp can be seen in lane 2. The expected mutant band of 4773 bp, shown in lane 3 and indicated with a black arrow, is also seen in lane 5. **(B)** 1% (w/v) TAE agarose gel showing PCR amplification of the *pbp4* gene from NewHG *tet*[R] (lane 2, SJF 3681), positive control SH1000 *pbp4* (lane 3) and NewHG *tet*[R] *pbp4* (SJF 5135) (lane 4) using primers *pbp4-1* (forwards) and *pbp4-5* (reverse). The wildtype band of 1535 bp can be seen in lane 2. The expected mutant band of 4773 bp, shown in lane 3 and indicated with a black arrow, is also seen in lane 4. Relevant sizes of DNA ladder (Quick load purple 2-log DNA ladder, NEB) are shown in kb (lane 1).

5.3.7 Analysis of NewHG *pbp4* infection dynamics in the murine sepsis model
5.3.7.1 Ratios of NewHG and NewHG *pbp4* variants in mice organs over time

The dynamics of a NewHG *pbp4* (SJF 5103) infection was interrogated using established protocols (Pollitt *et al.*, 2018). The liver is the first infectious site in the murine sepsis model of infection, with *S. aureus* being taken up from the blood by liver Kupffer cells. Within Kupffer cells *S. aureus* can be killed, but a small number survive the killing and pass through this immunological bottleneck and are able to form a micro abscess (Pollitt *et al.*, 2018). Bacteria can escape from the micro abscess, from whence they can disseminate to other organs such as the kidneys, a process that involves neutrophils (Pollitt *et al.*, 2018).

20 mice were injected with a 1:1 ratio of NewHG *kan^R* (SJF 3680) and NewHG *tet^R* (SJF 3681) totalling 1 x 10^7 CFU, and 20 mice were injected with a 1:1 ratio of NewHG *kan^R pbp4* (SJF 5136) and NewHG *tet^R pbp4* (SJF 5135) totalling 1 x 10^7 CFU. Mice were culled at 2, 24, 48 and 72 hpi and the CFU of the differently marked strains (*kan^R* or *tet^R*) were determined in the liver, right kidney, left kidney, spleen, lung and heart of each mouse for wildtype and *pbp4* strains (Figure 5.8).

The ratios of each variant that was recovered from each organ at different time points post infection are shown in pie charts where green represents the proportion of recovered *kan^R* strain, and blue the *tet^R* strain (Figure 5.9). Mice injected with a 1:1 ratio of NewHG *kan^R* (SJF 3680) and NewHG *tet^R* (SJF 3681) show a drop in recovered CFU in the liver between 2 and 24 hpi, but an increase at 48 and 72 hpi (Figure 5.8A). At 48 and 72 hpi, the murine organs, excluding the liver, are shown to be predominantly infected with one variant of NewHG, indicating clonality in the infection (Figure 5.9). Mice infected with a 1:1 ratio of NewHG *kan^R pbp4* (SJF 5136) and NewHG *tet^R pbp4* (SJF 5135) maintain CFU in the liver between 2 and 24 hpi (Figure 5.8A). At 72 hpi, all murine organs infected with NewHG *kan^R pbp4* and NewHG *tet^R pbp4* are predominantly infected with one of the injected variants.
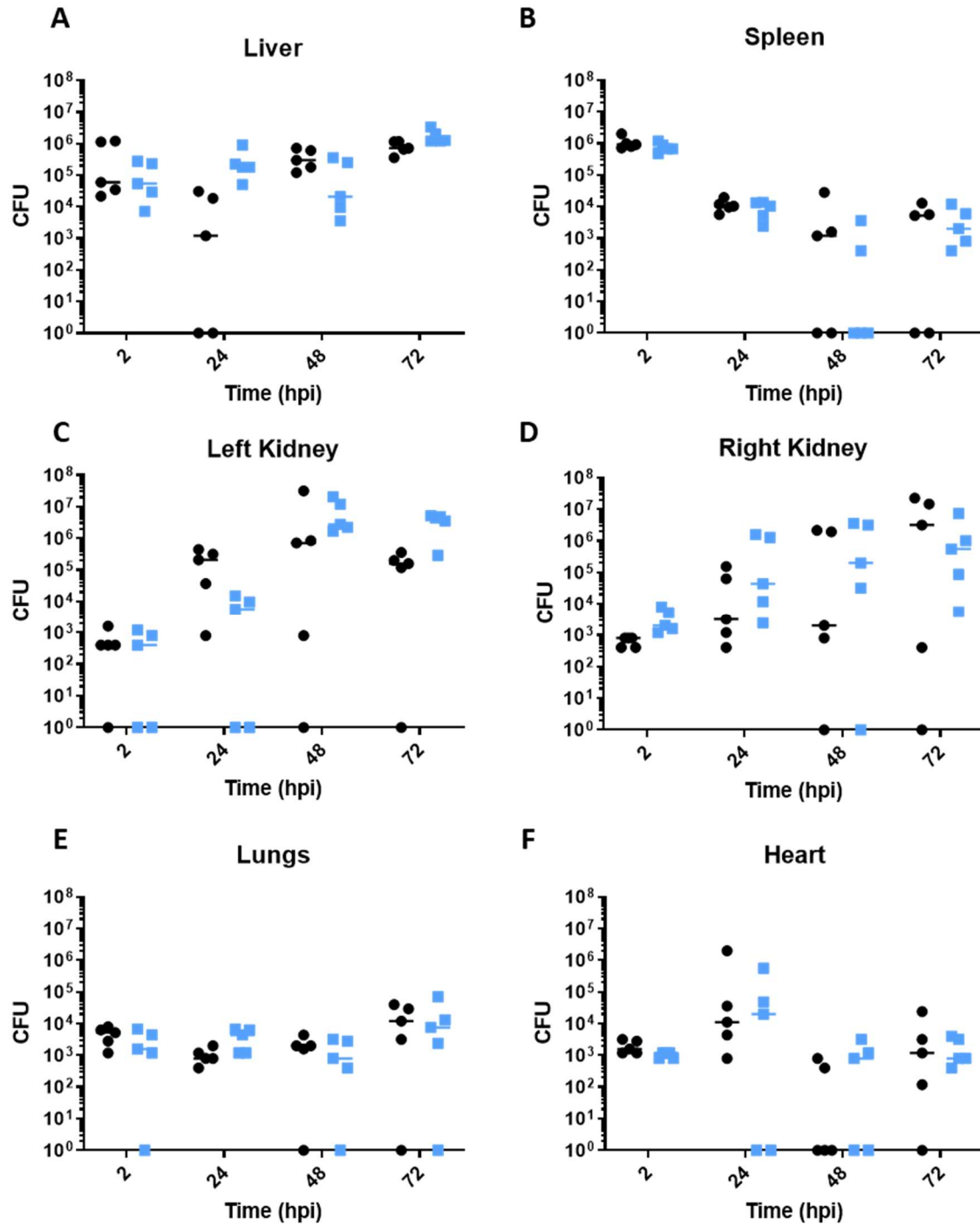
Figure 5.8 Total recovered CFU of *S. aureus* NewHG strains in the murine sepsis model over time

Mice (n=20) were injected with a 1:1 ratio (totalling approximately 1 x 10^7 CFU) of 2 resistance marker tagged NewHG variants (black circles), or 2 resistance marker tagged NewHG *pbp4* variants (blue squares). 5 mice were culled at each time point and the CFU ratios in the **(A)** liver, **(B)** spleen, **(C)** left kidney, **(D)** right kidney, **(E)** lungs and **(F)** heart were determined. Total CFU of recovered NewHG *kan^R* (SJF 3680) and NewHG *tet^R* (SJF 3681) are seen in black circles for each organ. Total CFU of recovered NewHG *kan^R pbp4* (SJF 5136) and NewHG *tet^R pbp4* (SJF 5135) are seen in blue squares for each organ.

A

B

Figure 5.9 The distribution of *S. aureus* NewHG strains in the murine sepsis model over time

Mice (n=20) were injected with a 1:1 ratio (totalling approximately 1 x 10^7 CFU) of two resistance marker tagged NewHG variants. 5 mice were culled at each time point and the CFU ratios in the liver, left kidney, right kidney, spleen, lungs and heart were determined. **(A)** The proportions of NewHG *kan*^{R} (SJF 3680, green) and NewHG *tet*^{R} (SJF 3681, blue) recovered at each time point from each organ in each mouse. **(B)** The proportions of NewHG *kan*^{R} *pbp4* (SJF 5136, green) and NewHG *tet*^{R} *pbp4* (SJF 5135, blue) recovered at each time point from each organ in each mouse. The number in each pie chart represents the log number of bacteria recovered (i.e. 10^6 CFU = 6). H.P.I: hours post infection, M.N.: Mouse number.

236

5.3.7.2 Ratio of NewHG and NewHG *pbp4* variants in liver abscesses at 72 hpi

While dissecting livers of mice at 72 hpi, some livers were found to have superficial abscesses that could be cleanly isolated from the liver tissue. Mice 17, 20 and 37 were found to have such abscesses. These abscesses were individually homogenised and plated, to determine the ratio of each antibiotic variant within an individual abscess, compared to the whole liver (Figure 5.10). Mice 17 and 20 were infected with NewHG *kan*^R (SJF 3680) and NewHG *tet*^R (SJF 3681), while mouse 37 was infected with NewHG *kan*^R *pbp4* (SJF 5136) and NewHG *tet*^R *pbp4* (SJF 5135). All three of the tested abcesses were found to contain a single variant from the infected inoculum, showing that for both NewHG and NewHG *pbp4,* a single bacterial cell likely founds an abcess.
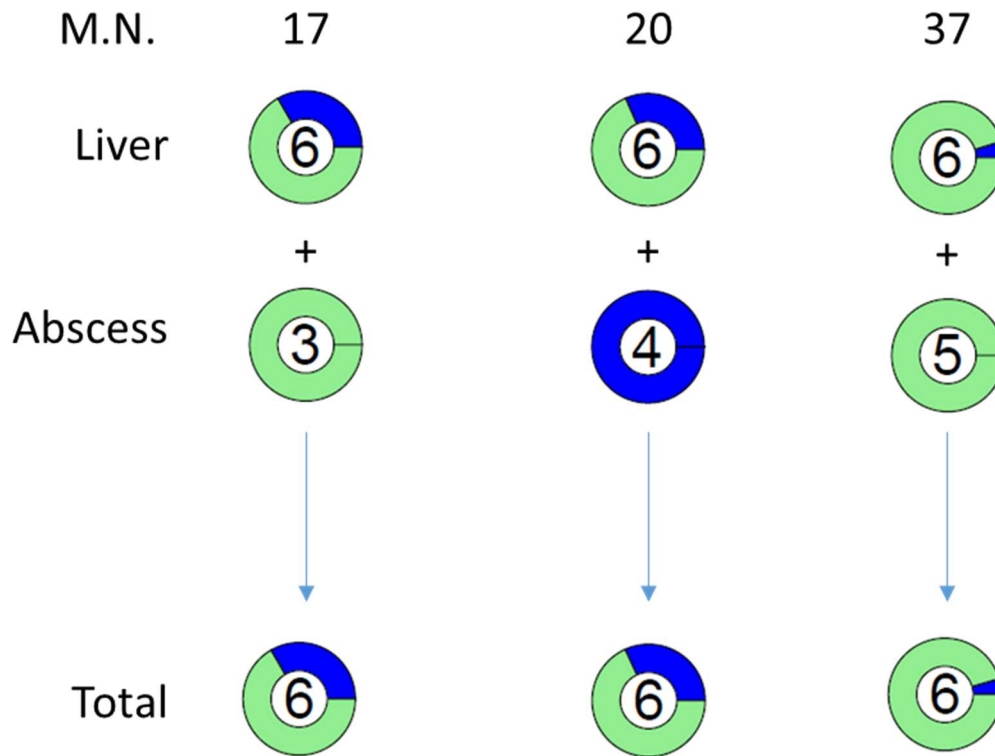
Figure 5.10 The ratio of *S. aureus* NewHG in liver abscesses in the murine sepsis model

CFU and strain ratios were determined from liver abscesses found in mice 17, 20 and 37 from Figures 5.8 and 5.9. "Liver" shows the CFU/proportions found in the remaining liver, "abscess" the CFU/proportions from the abscess and "total" the liver and abscess CFU/proportions combined (the total is reported in Figure 5.8). Mice 17 and 20 proportions of NewHG *kan*[R] (SJF 3680, green) and NewHG *tet*[R] (SJF 3681, blue), and mouse 37 show proportions of NewHG *kan*[R] *pbp4* (SJF 5136, green) and NewHG *tet*[R] *pbp4* (SJF 5135, blue). M.N.: Mouse number.

5.3.7.3 Species evenness of NewHG *pbp4* in the murine model compared to the wildtype

The proportion of each strain recovered (Figure 5.9) was used to calculate the species evenness index for each organ (Chapter 2.24) (Mulder *et al.*, 2004). This metric is used to determine how even populations of different organisms are within an environment, with an evenness of 1 equating to an equal ratio of strains in the environment, and 0 equating to one organism being present within an environment (Pollitt *et al.*, 2018). Population evenness is based on Shannon's diversity index, commonly used in studies (Morris *et al.*, 2014; Pollitt *et al.*, 2018), and can be used to analyse species that are uncommon and abundant within a sample. This is important as in this study organs could contain evenly mixed populations or only a single variant. After calculating population evenness for each organ, a mean linear regression was calculated for each data set (using Prism version 8.3.0) and compared for each strain (Figure 5.10). To remove skew caused by low numbers of recovered CFU, only organs that had at a total of least 10 colonies counted (consisting of either marked strain) were included in this analysis.

In the livers, both NewHG *kan^R* (SJF 3680), NewHG *tet^R* (SJF 3681) (wildtype strains), and NewHG *kan^R pbp4* (SJF 5136), NewHG *tet^R pbp4* (SJF 5135) (*pbp4 strains*) infections become more clonal over time. The linear regressions for both wildtype (p = 0.0448) and *pbp4* strains (p = 0.0036) are significantly decreasing in population evenness (Figure 5.11A). The wildtype and *pbp4* strains do not have a significantly different decrease in population evenness from one another (p = 0.6077). The spleens show a significant decrease in population evenness for both wildtype strains (p = 0.0001) and *pbp4* strains (p = 0.0049), but these decreases are not significantly different from one another (Figure 5.11B, p = 0.2339). The left kidney does not show a significant decrease in evenness for wildtype strain (p = 0.0878) or *pbp4* strains (p = 0.2248), and these lines are not significantly different from one another (Figure 5.11C, p = 0.7691). In the right kidney, wildtype strains show no significant change in population evenness (p = 0.5730) whereas *pbp4* strains show a significant decrease (p = 0.0441), which are not significantly different from one another (Figure 5.11D, p = 0.6604). While a trend for a decrease in population evenness is seen in the lungs for both wildtype strains (p = 0.2503) and *pbp4* strains (p = 0.0770), these decreases are not significant, and not significant from

one another (Figure 5.11E, p = 0.6758). The same pattern can be seen in the heart (Figure 5.11F), with neither wildtype strains (p = 0.5809) or *pbp4* strains (p = 0.6494) showing a significant decrease in population evenness. No significant difference could be seen in the heart between the population evenness change between the two groups (p = 0.9300). Wild type and *pbp4* strains show no difference in infection dynamics from one another within each organ. NewHG *pbp4* therefore goes through the same immunological bottleneck as wildtype strains (Pollitt *et al.*, 2018).
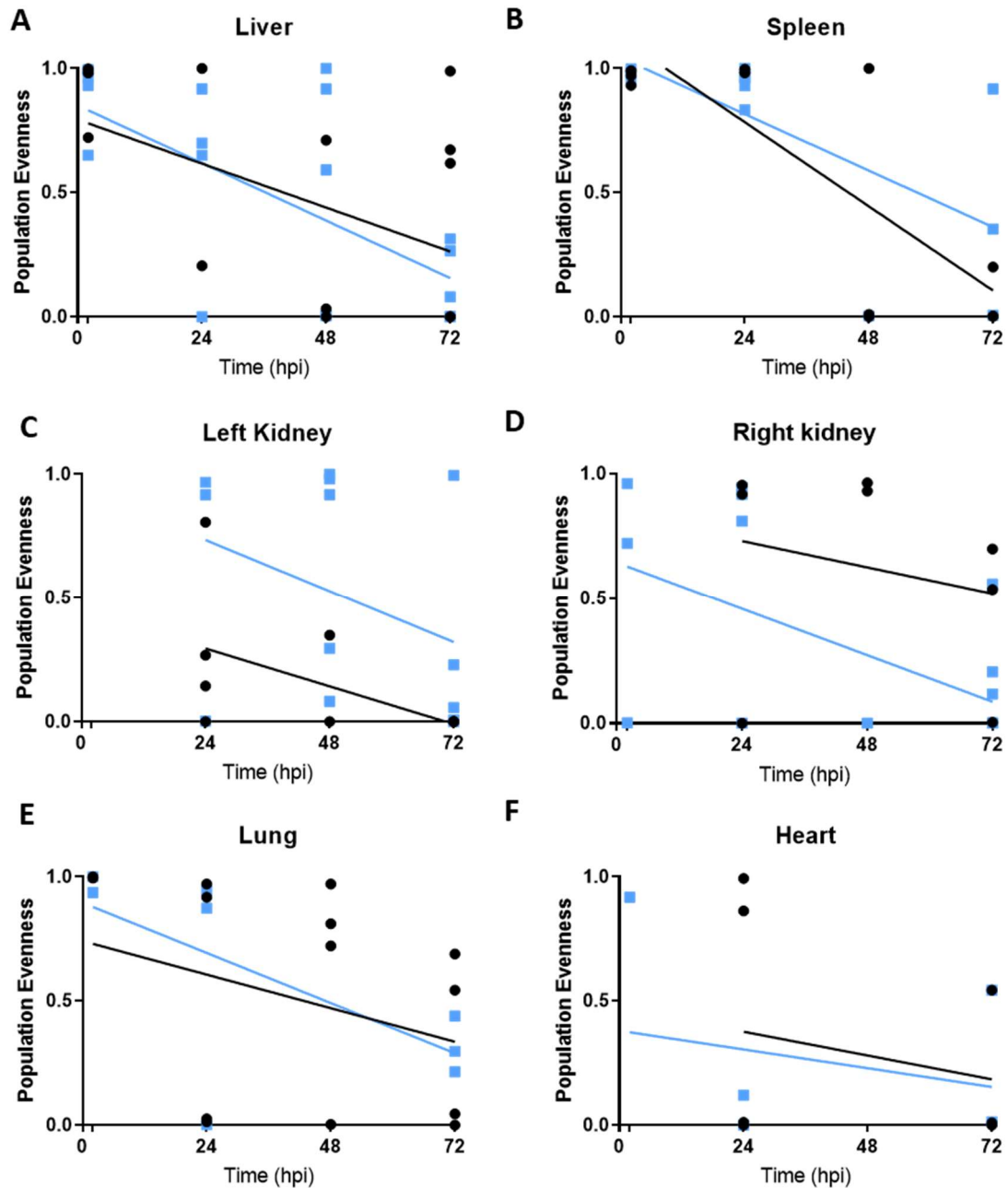
Figure 5.11 *S. aureus* NewHG *kan^R* and NewHG *pbp4* population evenness in the mouse sepsis model over time

The population evenness from each mouse at different time points for NewHG *kan^R* (SJF 3680) and NewHG *tet^R* (SJF 3681) (black circles and line) and NewHG *kan^R pbp4* (SJF 5136) and NewHG *tet^R pbp4* (SJF 5135) (blue squares and lines) for **(A)** livers, **(B)** spleen, **(C)** left kidney, **(D)** right kidney, **(E)** lungs and **(F)** heart. Lines are mean linear regression, which were calculated and compared using Prism software. All linear regressions were found to be non-significant, so the slopes of the lines are not significantly different from one another. Livers p = 0.6077, Spleen p = 0.2339, Left kidney: p = 0.7691, Right kidney p = 0.6604, Lungs p = 0.6758 and Heart p = 0.9300.

5.3.8   Fitness of NewHG *pbp4* compared to NewHG *kan^R* in the murine sepsis model

5.3.8.1 Population ratios of NewHG *pbp4* to NewHG *kan^R* in the murine sepsis model

It was hypothesised that the NewHG *pbp4* (SJF 5103) had a greater relative fitness in the livers of mice compared to the wildtype strain. To test this hypothesis, 20 mice were injected with a 1:1 ratio (totalling 7 x 10^6 CFU) of NewHG *kan^R* (SJF 3680) and NewHG *pbp4* (SJF 5103). Mice were infected for a period of 72 hours, before being culled and organs dissected. The total number, and ratio of each strain, recovered from each organ was calculated (Figure 5.12). The pie charts show that at 72 hpi, most of the organs are dominated by a single strain, showing clonality of infection, as found in Chapter 5.3.7.3.

Figure 5.12 Fitness of *S. aureus* NewHG versus NewHG *pbp4* in the murine sepsis model

Mice (n=20) were injected with a 1:1 ratio (totalling 7×10^6 CFU) of NewHG *kan*[R] (SJF 3680, red) and NewHG *pbp4* (SJF 5103, blue). At 72 hpi mice were culled and the CFU ratios between the strains in the liver, left kidney, right kidney, spleen, lungs and heart were determined. The number in each pie chart represents the log total number of bacteria recovered (i.e. 10^6 CFU = 6). Mice 9 and 12 reached severity limits at 54 hpi, so were culled, but have been included here. Mouse 18 was found dead at 72 hpi, so has been excluded from the analysis.

5.3.8.2 Relative fitness of NewHG *pbp4 compared* to NewHG *kan^R*

To determine if the ratios of the two strains recovered (Figure 5.12) are significantly different from the infectious dose, the relative fitness of NewHG *pbp4* (SJF 5103) was calculated using the formula $w = \frac{x_{2(1-x_1)}}{x_{1(1-x_2)}}$ (where *w* = relative fitness, X_1 = starting mutant proportion and X_2 = ending mutant proportion) (Pollitt *et al.*, 2014). This gives a numerical value for the relative fitness of NewHG *pbp4,* where a value of 1 indicates an equal fitness between NewHG *pbp4* and NewHG *kan^R* (SJF 3680), a value greater than 1 shows a greater relative fitness for NewHG *pbp4*, and a value less than 1 a greater relative fitness for NewHG *kan^R* (Pollitt *et al.*, 2014). These values were plotted for each organ of each mouse (Figure 5.13). Relative fitness within each organ was analysed using a one sample Wilcoxon signed rank test, comparing the results to a theoretical median of 1, testing if strains deviate from equal fitness.

In the livers of mice infected with NewHG *pbp4* (SJF 5103) and NewHG *kan^R* (SJF 3680), the median relative fitness of NewHG *pbp4* is significantly greater than 1 (p = 0.0105), demonstrating that NewHG *pbp4* has a greater fitness relative to NewHG *kan^R* in livers (Figure 5.13A). NewHG *pbp4* also shows significantly higher relative fitness in the spleens of mice infected with both strains (Figure 5.13B, p = 0.0476). No difference in fitness was found between NewHG *pbp4* and NewHG *kan^R* in the left kidneys of infected mice (Figure 5.13C, p = 0.3258). However, a significantly higher relative fitness can be observed for NewHG *pbp4* in the right kidney (Figure 5.13D, p = 0.0327). No significant difference in fitness was observed between NewHG *pbp4* and NewHG *kan^R* in the lungs or hearts of infected mice (Figures 5.13 E, F, p = 0.3396 and 0.4375 respectively). The results show there is a fitness cost associated with having a functional *pbp4* gene in the livers and spleen of the murine sepsis model.
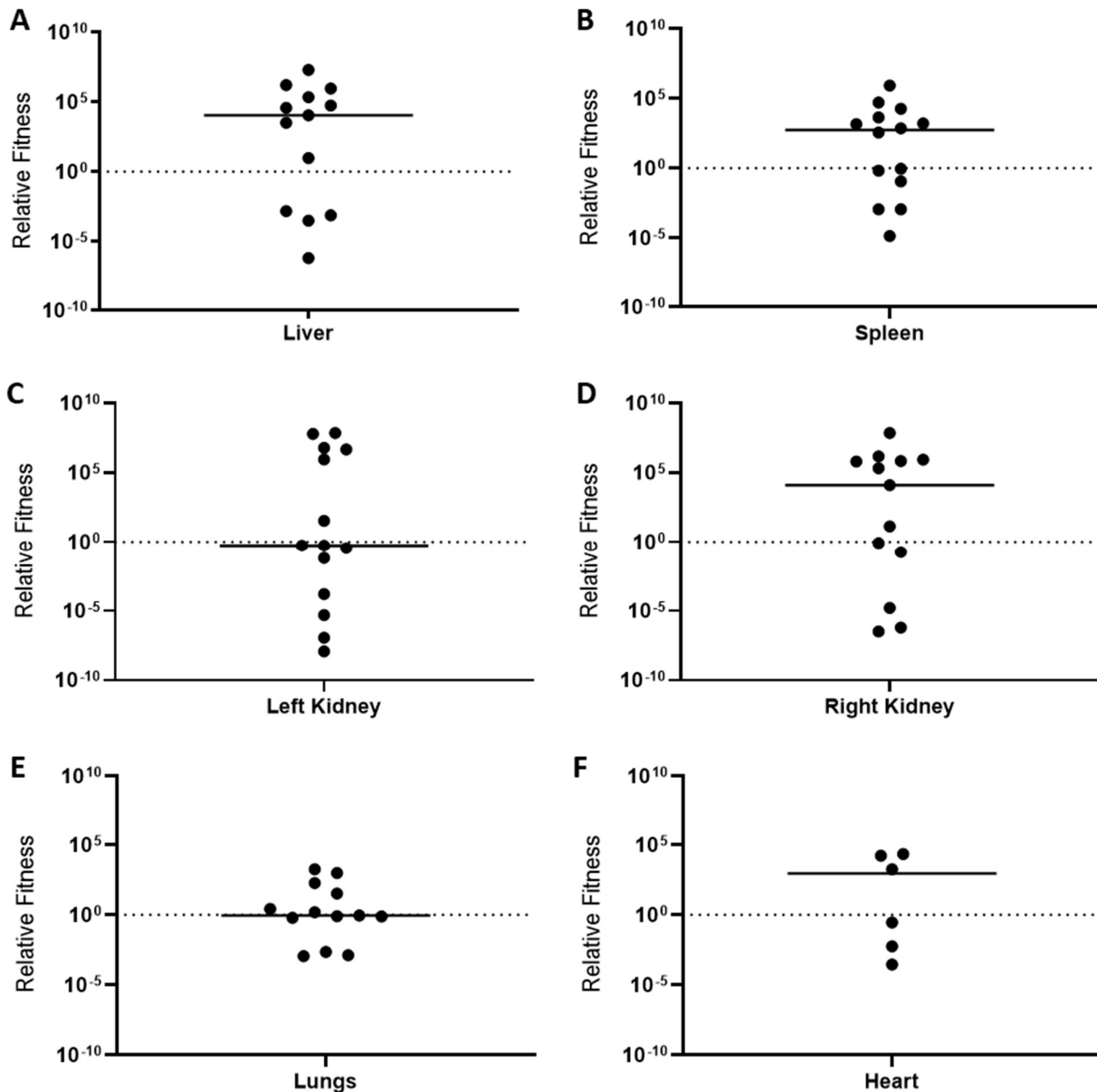
Figure 5.13 The relative fitness of NewHG *pbp4* compared to NewHG *kan^R* in different organs in the murine sepsis model

The relative fitness of NewHG *pbp4* (SJF 5103) against NewHG *kan^R* (SJF 3680) was calculated from the data in figure 5.12 using the formula $w = \frac{x_{2(1-x_1)}}{x_{1(1-x_2)}}$ (where *w* = relative fitness, X_1 = starting mutant proportion and X_2 = ending mutant proportion). This was calculated for the liver (**A**, * p = 0.0105), spleen (**B**, * p = 0.0476)**,** left kidney (**C**, p = 0.3258), right kidney (**D**, * p = 0.0327), lungs (**E,** p = 0.3396) and heart (**F**, p = 0.43275). Line on graph depicts the median. Statistical significance was determined using a one sample Wilcoxon signed rank test, comparing the results to a theoretical median of 1, which would indicate an equal fitness between the strains.

5.3.9 The role of phagocytes in NewHG *pbp4* infection
5.3.9.1 The ability of NewHG *pbp4* to survive in human macrophages

As previously described (Chapter 4.3.7), bacteria are first phagocytosed by Kupffer cells in the liver during the murine sepsis model (Boldock *et al.*, 2018; Pollitt *et al.*, 2018). As NewHG *pbp4* (SJF 5103) has been shown to have a greater relative fitness in the liver of mice this could be due to a change in the strain's interaction with macrophages. The interaction of NewHG *pbp4* with MDMs was investigated to test this hypothesis.

MDMs (2×10^5) were infected with 1×10^6 CFU NewHG *pbp4* (SJF 5103) or NewHG *kan^R* (SJF 3680) (MOI of 5) for 4 hours. Extracellular bacteria were killed by the addition of gentamycin for 30 min, which was then removed. MDMs were lysed at specified time points to determine the intracellular CFU of *S. aureus* strains (Chapter 2.20.1). In the first 30 min after gentamycin treatment, there is a significant drop in recovered intracellular NewHG *kan^R* CFU (Figure 5.14, p = 0.0194). At 5 – 6.5 hpi, the intracellular NewHG *kan^R* CFU remains constant, likely due to MDMs being unable to further kill, and the remaining *S. aureus* able to withstand MDM killing. Intracellular numbers of NewHG *pbp4* show a non-significant (p = 0.0802) decrease in the first 30 min after gentamycin treatment. At 5 hpi, there was significantly more intracellular NewHG *pbp4* within MDMs than NewHG *kan^R* (p = 0.0008). At 5.5 and 6.5 hpi, there are no significant differences between intracellular CFU of NewHG *pbp4* and NewHG *kan^R* (p = 0.5638 and 0.3565 respectively).
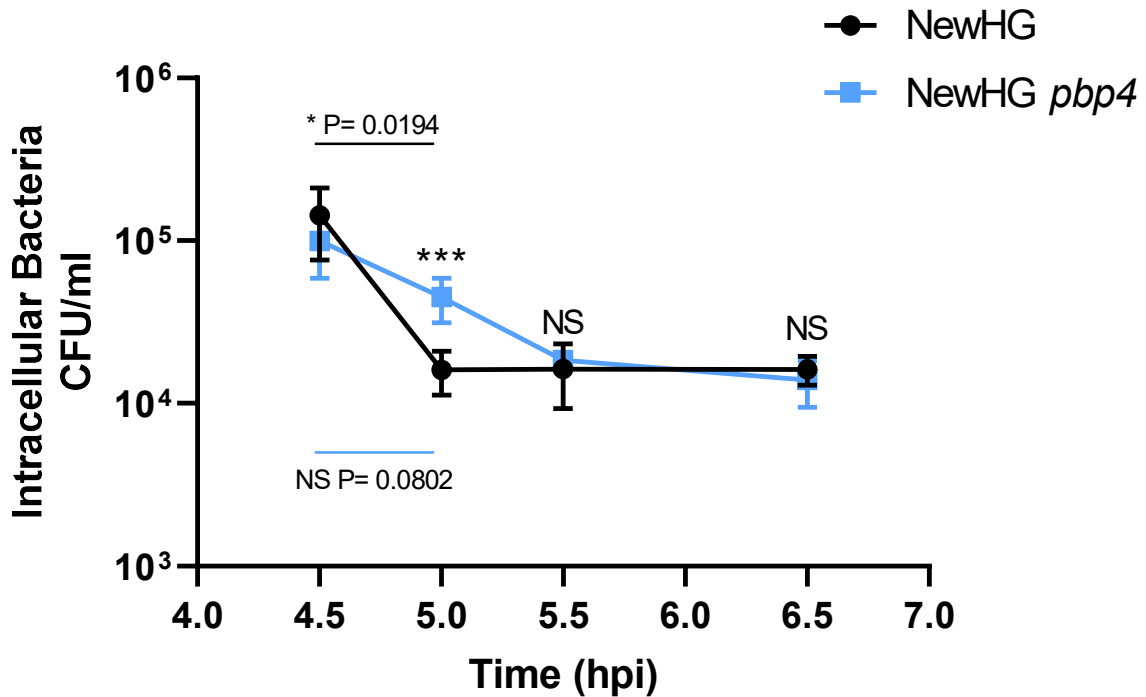
Figure 5.14 Survival of *S. aureus* strains in human MDMs

MDMs were infected with *S. aureus* NewHG *kan*[R] (SJF 3680, black circles) or NewHG *pbp4* (SJF 5103, blue squares) at a MOI of 5 (1 x 10^6 CFU) for 4 hours before being treated with gentamycin for 0.5 hours to kill extracellular bacteria. MDMs were lysed at specific time points and intracellular bacterial numbers were determined. A two-way ANOVA with Tukey's multiple comparison post-test was used to compare the first two time points for each strain, while paired two-tailed t-tests were used to compare between the strain CFU at subsequent time points. (*** p = 0.0008). Error bars show ±SD. (n = 3, each consisting of 2 intra-assay repeats).

5.3.9.2 The ability of NewHG *pbp4* to survive in human neutrophils

Circulating neutrophils have been shown to play a role in disseminating *S. aureus* to other organs from the liver in a murine sepsis model of infection (Pollitt *et al.*, 2018). As a significantly increased fitness was only observed in the right kidney of mice (Figure 5.13D) but not in the left kidney, lungs or heart (Figures 5.13 C, E and F), neutrophils are unlikely to play a role in the NewHG *pbp4* (SJF 5103) increase in liver colonisation. This hypothesis was tested by co-incubating human neutrophils with *S. aureus* strains (Chapter 2.20.2).

Approximately 2.25×10^5 neutrophils were incubated with NewHG *kan*[R] (SJF 3680) or NewHG *pbp4* (SJF 5103) at a MOI of 5 (1.125×10^6 CFU). No significant difference could be seen in the CFU recovered in the pellet (internalised in neutrophils) 30 min after co-incubation with NewHG *kan*[R] or NewHG *pbp4* (Figure 5.15A, p = 0.2107), showing no difference in internalisation.

After 60 min of co-incubation, no significant difference could be found between intracellular NewHG *kan*[R] and NewHG *pbp4* CFU (Figure 5.15B, p = 0.9869). No significant difference was also found between intracellular NewHG *kan*[R] and NewHG *pbp4* CFU after 120 min of co-incubation (Figure 5.15B, p = 0.9942).
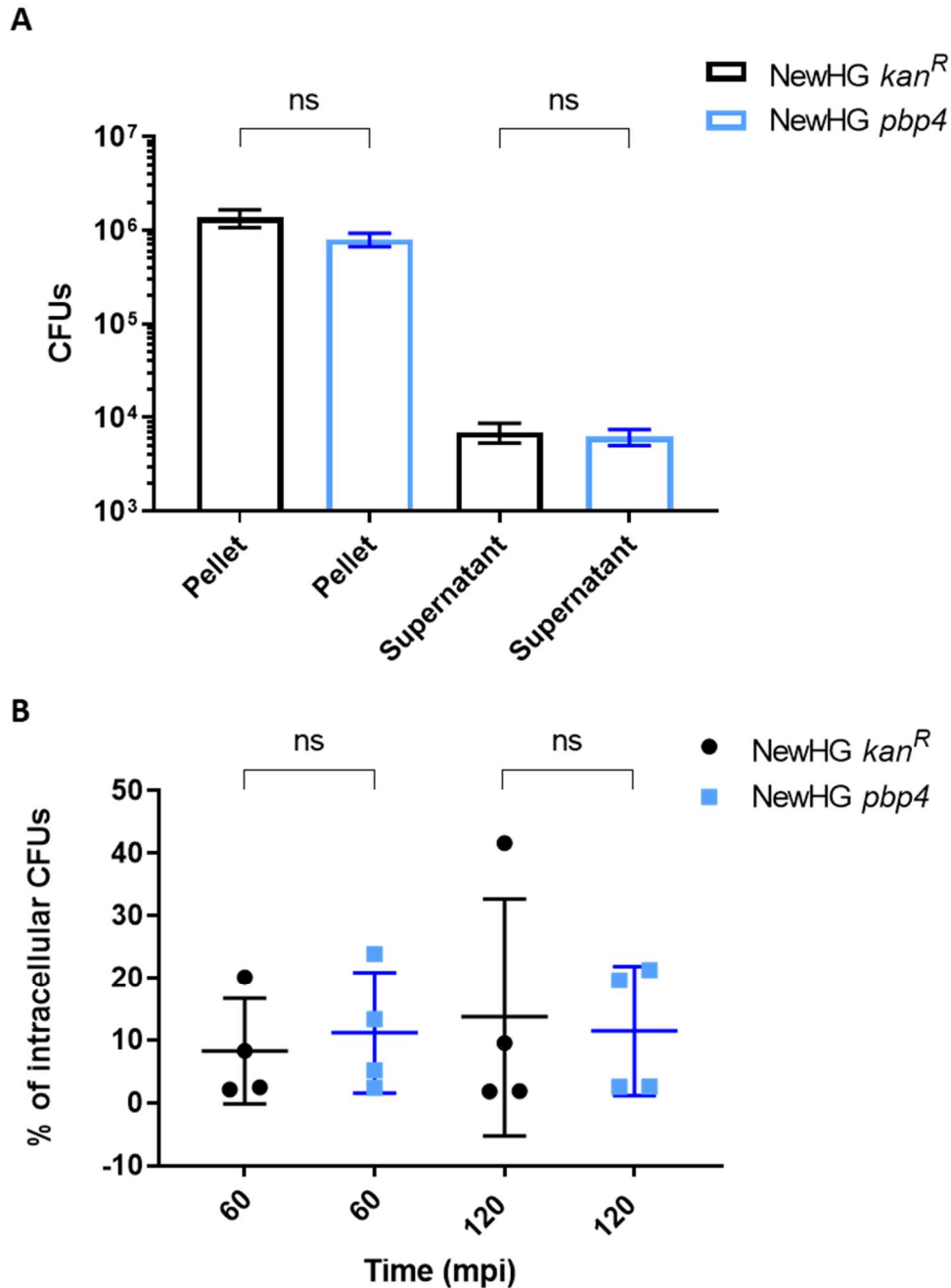
Figure 5.15 Survival of *S. aureus* strains in human neutrophils

(A) The number of internalised NewHG *kan^R* (SJF 3680, black bars) and NewHG *pbp4* (SJF 5103, blue bars) and the number remaining in the extracellular supernatant after 30 min of co-incubation with human neutrophils. Error bars represent the standard deviation of the mean. (n = 4, each consisting of 3 intra-assay repeats). Results analysed with a one-way ANOVA with Tukey's multiple comparison post-test. **(B)** Intracellular NewHG *kan^R* (SJF 3680, black circles) and NewHG *pbp4* (SJF 5103, blue squares) CFU after co-incubation with neutrophils for 60 or 120 minutes. (n = 4, each consisting of 3 intra-assay repeats). Error bars represent the mean and standard deviation of the mean. Results analysed with a two-way ANOVA with Tukey's correction.

5.3.10 Role of macrophages in the murine sepsis model

As previously described (Chapter 4.3.8, 4.3.8.2) clodronate was used to deplete the macrophages within the murine sepsis model of infection (Chapter 2.18.2, 2.18.3). Groups of 10 mice were injected with either clodronate, or control, liposomes 24 hours before being intravenously injected with 1 x 10^5 CFU NewHG *kan*^{R} (SJF 3680) or NewHG *pbp4* (SJF 5103) (Figure 5.16). No significant difference could be found in the weight change 72 hpi for mice injected with control liposomes and NewHG *kan*^{R} or NewHG *pbp4* (p = 0.7812) or for mice injected with clodronate liposomes and NewHG *kan*^{R} or NewHG *pbp4* (Figure 5.16A, p = 0.3865). No significant differences could be found in the CFU recovered from the liver (p = 0.1196), kidneys (p = 0.8592) or spleen (p = 0.9150) of mice treated with control liposomes and infected with and NewHG *kan*^{R} or NewHG *pbp4* (Figures 5.16B, C and D respectively). Despite the lack of significance, a trend for increased CFU recovered from the livers and spleens of mice infected with and NewHG *pbp4* can be seen. The lack of significance may be due to low inoculum CFU.

Clodronate treatment led to a dramatic increase in recovered CFU for both strains, allowing the bacterial strains, and effect of clodronate to be compared (Figure 5.16). When mice are treated with clodronate no significant difference can be seen in CFU recovered from the livers of mice infected with NewHG *kan*^{R} or NewHG *pbp4* (Figures 5.16B, p = 0.5659). No significant difference can be seen in the CFU of kidneys (Figures 5.16C, p = 0.0626) or spleens (Figures 5.16D, p = 0.2245) of clodronate treated mice infected with NewHG *kan*^{R} or NewHG *pbp4.*
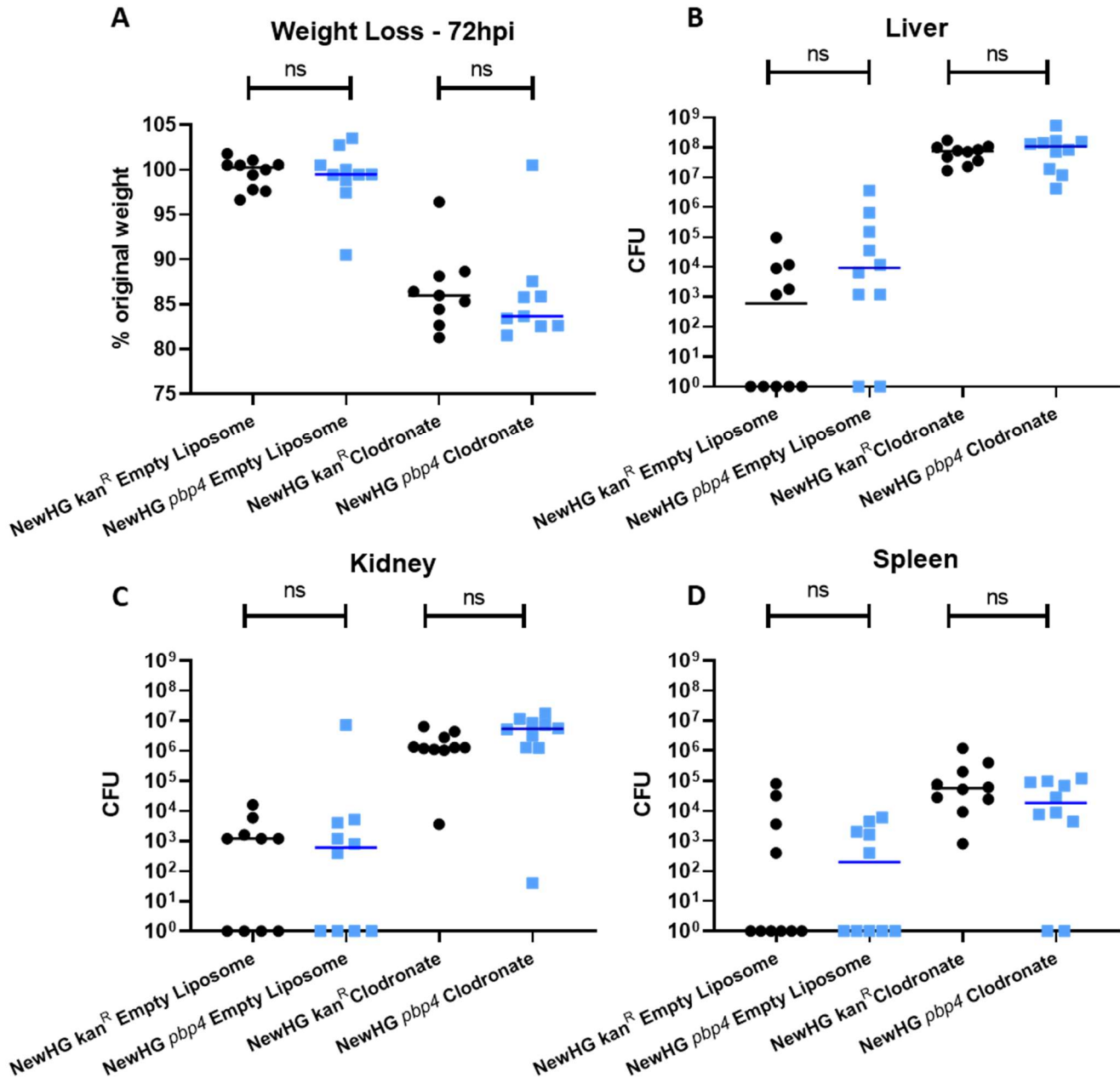
Figure 5.16 The role of macrophages in *S. aureus* host-pathogen interaction in the murine sepsis model

Mice (n=10) were injected with approximately 1 x 10^5 CFU of NewHG *kan*^{R} (SJF 3680) or NewHG *pbp4* (SJF 5103) 24 hours post treatment with empty liposomes or clodronate containing liposomes. 72 hpi, mice were sacrificed and the weight change (**A**) and liver (**B**), kidney (**C**) and spleen (**D**) CFU were determined. Groups were compared using Mann-Whitney U tests (NewHG *kan*^{R} – black circles, NewHG *pbp4* - blue squares). One mouse in the NewHG *kan*^{R} clodronate treated group and one in the NewHG *pbp4* clodronate treated group were culled at 48 hpi due to reaching severity limits and have been excluded from the graph and statistical analysis.

5.3.11 Augmentation of NewHG *pbp4* in the murine sepsis model

Augmentation has previously been described in Chapter 1.7.4 and Chapter 4.3.6.2, where the addition of purified peptidoglycan to an *S. aureus* inoculum greatly increases virulence. The addition of PG allows greater survival of *S. aureus* within macrophages (Boldock *et al.*, 2018).

Groups of 5 mice were injected with 1 x 10^6 NewHG *kan^R* or NewHG *pbp4* with or without the addition of 250 µg purified NewHG *kan^R* PG (Figure 5.17). If mice were injected with NewHG *kan^R* or NewHG *pbp4,* mice maintained their weight over 72 hours, with one NewHG *pbp4* infected mouse at 82.7 % of its original weight (Figure 5.17A). This difference was not statistically significant (p = 0.3095). When only injected with bacteria, the CFU of NewHG *pbp4* recovered from livers are significantly higher than the recovered CFU from mice infected with NewHG *kan^R* (Figure 5.17B, p = 0.0397). No significant difference could be found between recovered CFU in kidneys and spleens of mice infected with NewHG *kan^R* or NewHG *pbp4* only (Figures 5.17C, D, p = 0.5397 and 0.2857 respectively). When NewHG *kan^R* or NewHG *pbp4* were co-injected with 250 µg PG, no significant difference can be seen in the recovered CFU for either strain (Figure 5.17B, p = 0.2857). No significant differences could be found in kidneys (p = 0.4127) and spleens (p = 0.6508) injected with NewHG *kan^R* or NewHG *pbp4* with 250 µg of PG (Figure 5.17C and D).
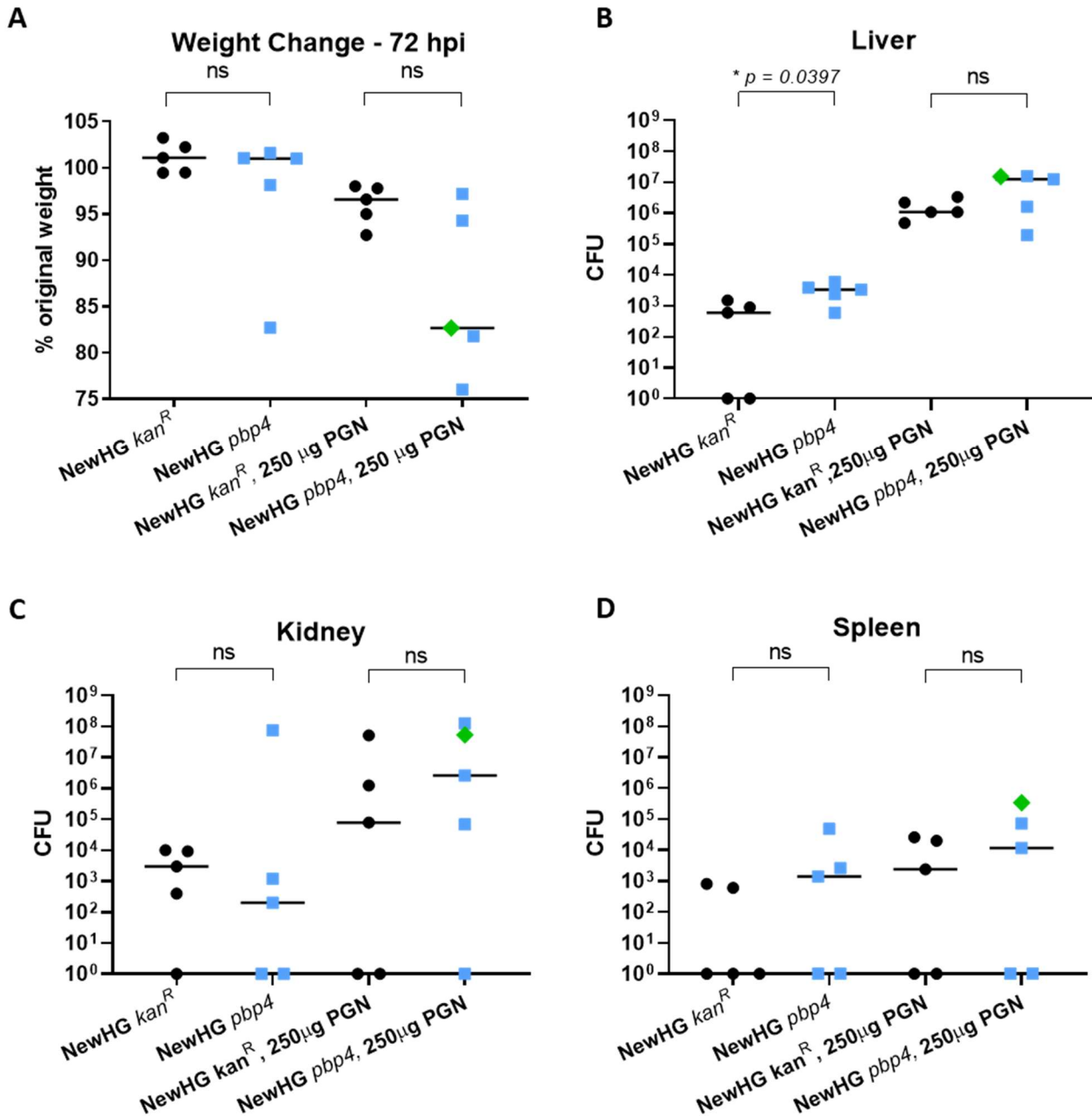
Figure 5.17 Augmentation of *S. aureus* strains using staphylococcal peptidoglycan in the murine sepsis model

Approximately 1x10^6 CFU *S. aureus* NewHG *kan*^{R} (WT, SJF 3680) or NewHG *pbp4* (SJF 5103) with or without 250 µg WT *S. aureus* PG injected intravenously into mice (n=5). Weight loss 72 hpi (**A**) and CFUs recovered from livers (**B**), kidneys (**C**) and spleen (**D**) were determined. Groups were compared using Mann-Whitney U tests (NewHG *kan*^{R} – black circles, NewHG *pbp4* blue squares) (* p = 0.0397). One mouse (infected with NewHG *pbp4* and 250 µg PG) was culled at 56 hpi due to reaching severity limits, so was culled. This data is represented as a green diamond but has been excluded from statistical analysis.

5.3.12 The combined role of peptidoglycan synthases and hydrolases in *S. aureus*

The cell wall is a dynamic structure that requires both the hydrolysis and synthesis of PG to produce the correct cell wall structure (Vollmer *et al.*, 2008a). It was hypothesised that mutations in both a hydrolase and synthase could have an impact on growth and virulence. This was tested by using NewHG *sagB pbp4* (SJF 5147).

5.3.12.1 Construction of NewHG *sagB pbp4*

Bacteriophage φ11 was used to transduce the *sagB* mutation into NewHG *pbp4* (SJF 5103), producing strain NewHG *sagB pbp4* (SJF 5147). Amplification of the *sagB* gene in NewHG *sagB pbp4* produced the mutant band (Figure 5.18A), confirming transduction. The strain also had a mutated *pbp4* gene after being amplified by PCR, confirming inactivation of *sagB* and *pbp4* genes (Figure 5.18A).

5.3.12.2 Role of SagB and PBP4 in growth

NewHG *sagB pbp4* (SJF 5147), NewHG (SJF 3663), NewHG *pbp4* (SJF 5103) and NewHG *sagB* (SJF 4912) were grown in liquid TSB (Figure 5.18B). NewHG had a doubling time of 30.9 min, which is similar to the growth of NewHG *pbp4* (doubling time 33.0 min). As previously described (Chapter 4.3.1) *sagB* mutants have a decreased growth rate, which is seen in NewHG *sagB* (doubling time 37.5 min). NewHG *sagB pbp4* shows a slight decreased growth rate (doubling time 34.2 min) compared to parental NewHG, which is a higher rate than NewHG *sagB*.

5.3.12.3   Role of SagB and PBP4 in the zebrafish embryo model of infection

NewHG (SJF 3663), NewHG *pbp4* (SJF 5103), NewHG *sagB* (SJF 4912) and NewHG *sagB pbp4* (SJF 5147) were injected into embryos 30 hpf at a dose of 1500 CFU (Figure 5.18C). When injected with NewHG, 46 % of embryos survive infection. Embryos injected with NewHG *pbp4* showed a survival rate of 34 %, which shows no significant difference to the wildtype (p = 0.2002). As seen previously (Chapter 4.3.5.1), embryos injected with NewHG *sagB* have a significantly higher survival rate than injection with NewHG (66 %, p = 0.0157). When injected with NewHG *sagB pbp4*, embryos have a survival rate of 54 %, which is not significantly different to survival when injected with NewHG (p = 0.1602). This shows that NewHG *sagB pbp4* has equivalent virulence to wildtype NewHG.

5.3.12.4   Particle size of NewHG *sagB pbp4*

The particle size of NewHG *sagB pbp4* (SJF 5147) was analysed using flow cytometry, as previously described (Chapters 2.22 and 4.3.9.6). The FSC value for each mutant was determined and compared to wildtype NewHG (SJF 3663) as a measure of relative particle size (Figure 5.18D).

NewHG *pbp4* (SJF 5103) shows no significant difference in FSC compared to the wildtype NewHG (SJF 3663, p = 0.3545). NewHG *sagB* (SJF 4912) was found to have a significantly lower FSC than parental NewHG (p = 0.0002). NewHG *sagB pbp4* (SJF 5147) shows no significant difference in FSC, and therefore particle size, to wildtype NewHG (p = 0.7463), suggesting a loss of PBP4 can compensate for the loss of SagB.
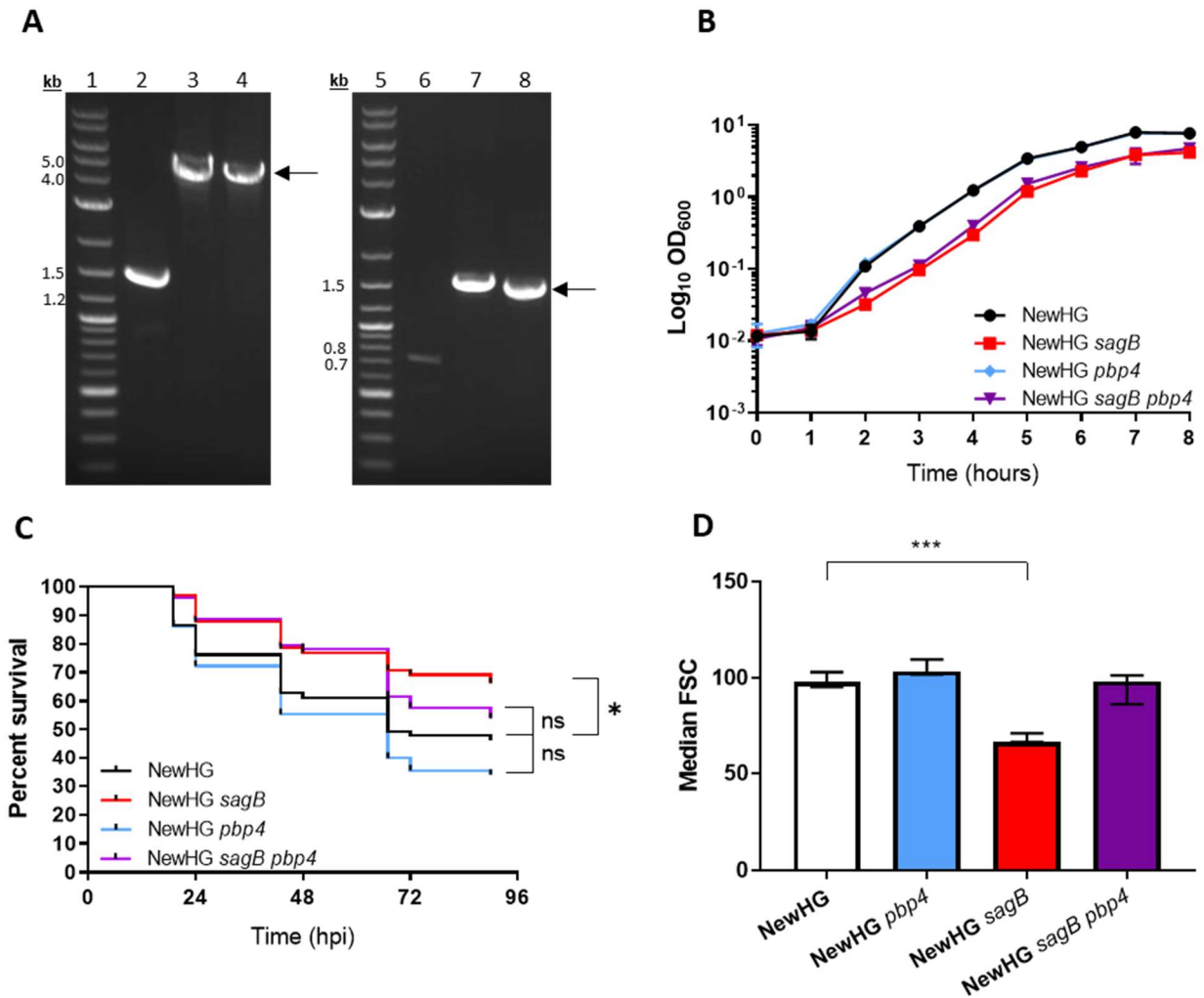
Figure 5.18 Analysis of growth and virulence of NewHG *sagB pbp4*

(A) 1% (w/v) TAE agarose gels showing PCR amplification of the *pbp4* and *sagB* genes from *S. aureus*. Lane 2 shows wild type *pbp4* band (1296 bp) expected from the primer set (*pbp4-1* and *pbp4-5*). The expected mutant band (donor strain SH1000 *pbp4*, 4773 bp), shown in lane 3 and indicated with a black arrow, is also seen in lane 4 of the NewHG *sagB pbp4* mutant (SJF 5147). Lane 6 shows the wild type *sagB* band (777 bp) expected from the primer set (*psagB_F* and *psagB_R*). The expected mutant band (1700 bp), indicated with an arrow, from SH1000 *sagB* (SJF 4608) can be seen in lane 7, and in lane 8 for NewHG *sagB pbp4* (SJF 5147). **(B)** Growth of parental NewHG (SJF 3663, black circles) in TSB compared to: NewHG *sagB* (SJF 4912, red squares), NewHG *pbp4* (SJF 5103, blue diamonds) and NewHG *sagB pbp4* (SJF 5147, purple triangles). Bacterial cultures were prepared in triplicate and error bars represent the standard deviation of the mean. **(C)** Approximately 1500 CFU of bacteria (mutant or wild type) was injected into the circulation valley of LWT zebrafish embryos around 30 hpf. A survival curve was produced comparing the virulence of parental NewHG (SJF 3663, black line) to: NewHG *sagB* (SJF 4912, red line), NewHG *pbp4* (SJF 5103, blue line) and NewHG *sagB pbp4* (SJF 5147, purple line). (3 repeats, n>20, * p = 0.0157). **(D)** Comparison of the median forward scattered (FSC) light values of parental NewHG (SJF 3663, white bar), NewHG *pbp4* (SJF 5103, blue bar), NewHG *sagB* (SJF 4912, red bar) and NewHG *sagB pbp4* (SJF 5147, purple bar) (n = 3, *** p = 0.0002). Error bars show ±SD, Median FSC values were compared using a one-way ANOVA with Dunnet's multiple comparison test.

5.3.12.5   Pathogenesis of NewHG *sagB pbp4* in the murine sepsis model of infection

The virulence of NewHG *sagB pbp4* (SJF 5147) was compared to NewHG *kan^R* (SJF 3680), as previously described (Chapter 5.3.5) (Figure 5.19).

No difference in weight change 72 hpi could be seen between NewHG *kan^R* (SJF 3680) and NewHG *sagB* (SJF 4912, p = 0.0524), NewHG *pbp4* (SJF 5103, p = 0.8534) or NewHG *sagB pbp4* (SJF 5147, p = 0.5787) (Figure 5.19A). While there is greater clearance observed in the livers of mice infected with NewHG *sagB,* no significant difference between the recovered CFU compared to the CFU livers infected with NewHG *kan^R* could be detected (Figure 5.19B, p = 0.3171). As previously seen (Figures 5.5 and 5.6) significantly more CFU were recovered from the livers of mice infected with NewHG *pbp4* than NewHG *kan^R* (p = 0.0119). No significant difference could be seen in recovered liver CFU between mice infected with NewHG *sagB pbp4* or NewHG *kan^R* (p = 0.8654).

Significantly fewer CFU were recovered from the kidneys of mice infected with NewHG *sagB* than NewHG *kan^R* (Figure 5.19C, p = 0.0053). No significant difference could be seen between the recovered kidney CFU of mice infected with NewHG *pbp4* or NewHG *kan^R* (p = 0.2544). Despite a higher level of clearance in the kidneys of mice infected with NewHG *sagB pbp4*, no significant difference could be detected between the recovered CFU of NewHG *sagB pbp4* and NewHG *kan^R* (p = 0.3752). No significant differences between NewHG *kan^R* and the mutant strains could be seen in the recovered CFU from the spleen, lungs and heart (Figures 5.19 D, E and F).
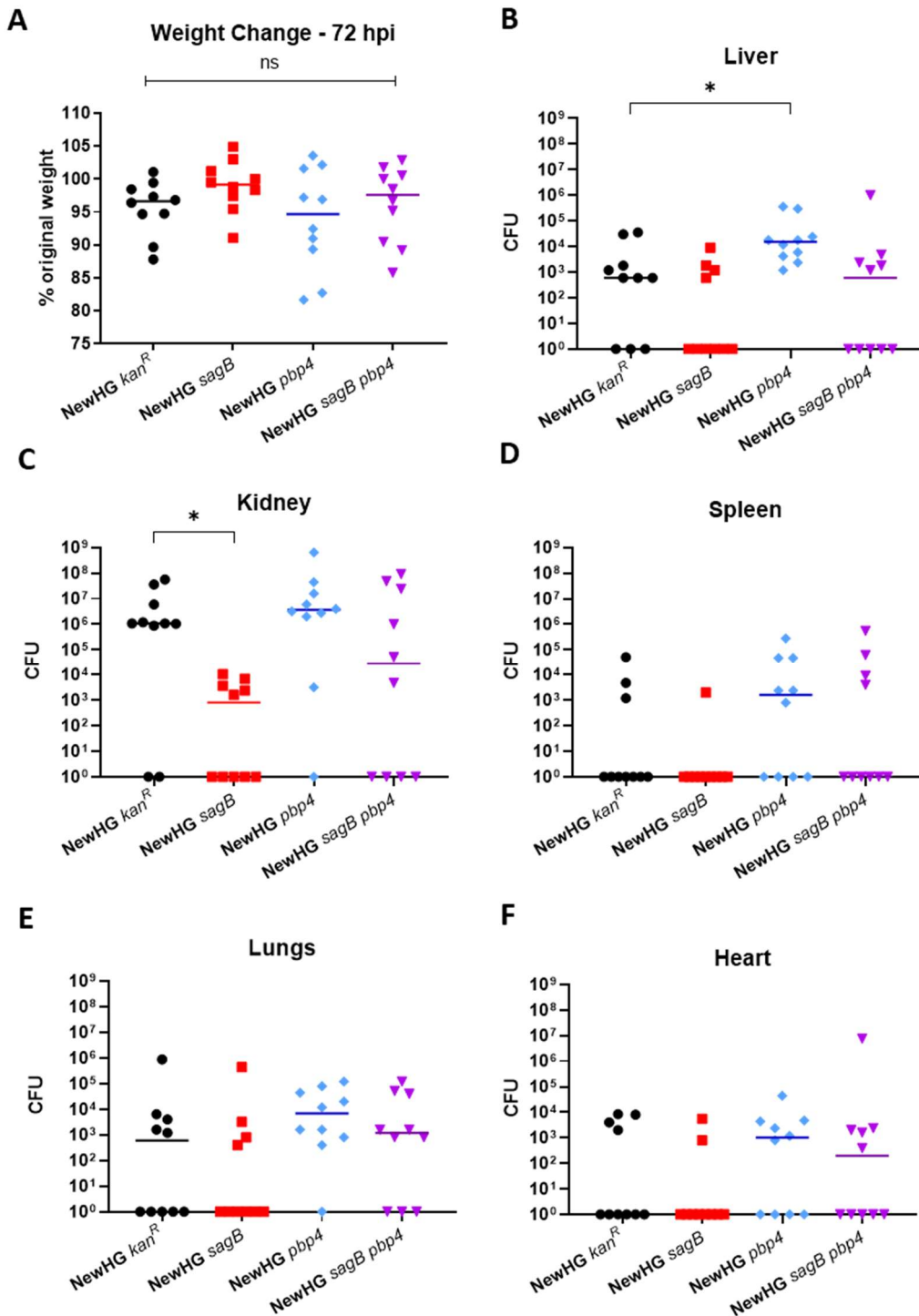
Figure 5.19 The role of PG synthases and hydrolases in *S. aureus* virulence in the murine sepsis model of infection.

Mice (n=10) were injected intravenously with approximately 1x10^7 CFU *S. aureus* NewHG *kan*[R] (WT, SJF 3680), NewHG *sagB* (SJF 4912), NewHG *pbp4* (SJF 5103) or NewHG *sagB pbp4* (SJF 5147). Weight loss 72 hpi (**A**) and CFUs recovered from livers (**B,** * p = 0.0119), kidneys (**C**, * p = 0.0055), spleen (**D**), lungs (**E**) and heart (**F**) were determined. Groups were compared using a Mann-Whitney U test (NewHG *kan*[R] – black circles, NewHG *sagB* – red squares, NewHG *pbp4* blue diamonds, NewHG *sagB pbp4* – purple triangles).

5.4 Discussion

5.4.1 The role of PBP4 in *S. aureus* pathogenesis

NewHG *pbp4* (SJF 5103) shows greater colonisation of mouse livers in the murine sepsis model of infection (Figures 5.5, 5.6). While NewHG *pbp4* goes through the same immunological bottle neck as its parent (Figure 5.11), it has a greater relative fitness (Figure 5.13). A proposed model for NewHG *pbp4* infection dynamics is summarised in Figure 5.20. Bacteria injected intravenously results in free bacteria entering the circulation (Pollitt *et al.*, 2018). Both wildtype and *pbp4* are then taken up by Kupffer cells (resident macrophages) in the liver (Pollitt *et al.*, 2018). A greater number of NewHG *pbp4* are recovered from the livers of mice than those infected with NewHG (Figures 5.5, 5.6). This is likely due to a change in interaction within macrophages, as seen by an increased resistance to early macrophage killing (Figure 5.14), leading to increased NewHG *pbp4* survival and release from macrophages (Figure 5.20). The free bacteria can form liver abscesses, increasing the observed recovered liver CFU.

A *pbp4* mutant causes increased size of skin lesions in mice infected using the skin infection model, which was suggested to be caused by an increase in production of IL-1β (Müller *et al.*, 2015). In this model, strains with a reduction in crosslinked muropeptides were more susceptible to macrophage killing and degradation (Müller *et al.*, 2015). This was not found in my study, with NewHG *pbp4* being more resistant initially to macrophage killing (Figure 5.14). Müller *et al*. (2015) show no evidence for increased killing of *pbp4* deletion strains within macrophages. The increased liver colonisation of NewHG *pbp4* matches the observed phenotype when *S. aureus* is augmented by the addition of purified peptidoglycan to the inoculum; an increase in CFU recovered from the livers of mice (Boldock *et al.*, 2018). Without PBP4, PG is less crosslinked than the wildtype (Wyke *et al.*, 1981a). As the PG is less crosslinked, it can be hypothesised that cleavage of PG by hydrolases is more likely to release muropeptides into the environment, as there are fewer bonds to keep the muropeptides linked to the sacculus. The increase in release of muropeptides, if released within macrophages, may neutralise ROS (Boldock *et al.*, 2018) and augment NewHG *pbp4* during infection. However, a change in PG recognition and cytokine signalling could be the

cause for the observed increase in liver colonisation seen with the *pbp4* mutant. In a *Drosophila* model of infection, a *S. aureus* strain with no PG synthases except the essential PBP1 and PBP2 is attenuated (Reed *et al.*, 2015). The *Drosophila* PG recognition protein SA (PGRP-SA) recognises PG and activates the Toll pathway, clearing bacteria (Chang *et al.*, 2004). Without PGRP-SA, the synthase depleted strain has restored virulence, suggesting the reduced crosslinking of the strain changes its recognition by the host (Reed *et al.*, 2015). The reduction in crosslinking associated with *pbp4* mutants (Wyke *et al.*, 1981a) could cause a change in the interaction with mammalian extracellular receptors such as Toll-like receptor 2 (Dziarski and Gupta, 2005) and cytosolic, muropeptide detecting NOD2 (Carneiro *et al.*, 2008). A change in interaction with these PG receptors, possibly caused by the increased proportion of monomeric muropeptides, would change downstream signalling, altering the host response with differing inflammasome activation, potentially through cytokines, such as IL-1β (Shimada *et al.*, 2010; Müller *et al.*, 2015).

PBP4 has been shown to contribute to β-lactam resistance in *S. aureus* (Memmi *et al.*, 2008; Chan *et al.*, 2016; Hamilton *et al.*, 2017)*,* which is usually associated with a reduction in fitness (Andersson and Hughes, 2010; Geisinger and Isberg, 2017). NewHG *pbp4* has a greater relative fitness in the liver and spleens of mice compared to the wildtype (Chapter 5.3.8.2), which could indicate that there is a fitness cost for producing highly crosslinked PG (Wyke *et al.*, 1981a), and this structure is not required in the mouse sepsis model of infection. However, as *pbp4* is in the core genome of *S. aureus,* it can be assumed that PBP4 is required to produce highly crosslinked PG for environments outside of a murein sepsis infection.

The increased fitness of NewHG *pbp4* in the livers of mice is unusual, as many species lose fitness when PBPs are inactivated. *Vibrio cholerae* lacking PBP1a shows a reduced growth and survival in an infant mouse intestine (Dörr *et al.*, 2014). The same is true for *Listeria monocytogenes,* with bacteria missing Lmo0540, Lmo1438, Lmo2229 (all encoding PBPs) or PBP5 showing attenuation within macrophages and the spleens of infected mice (Guinane *et al.*, 2006). *Acinetobacter baumannii* with a transposon inactivation of *pbpG* (encoding PBP7/8) also shows attenuation compared to a wildtype strain (Russo *et al.*, 2009). This

strain demonstrated attenuation in both rat soft-tissue and pneumonia models of infection, as well as being killed when cultured in 90 % human serum *in vitro*. The attenuation phenotype was described to have been caused by an increased susceptibility to complement (Russo *et al.*, 2009). In the three examples however, the loss of virulence was associated with growth defects *in vitro*, not observed for NewHG *pbp4* (Figure 5.1B). In *Streptococcus pneumoniae*, strains have been isolated that possess β-lactam resistance (Rieux *et al.*, 2001). These strains showed mutations within the *pbp2b* and *pbpX* genes responsible for the acquisition of resistance, but these mutations were also associated with avirulence (Rieux *et al.*, 2001).

Neutrophils are thought to be involved in the dissemination of *S. aureus* to other organs during sepsis (Thwaites and Gant, 2011). Mice infected with NewHG *pbp4* do not show increased CFU recovered from the kidneys, suggesting no change in dissemination, which is confirmed by the same level of neutrophil killing of NewHG *pbp4* and wildtype (Figure 5.14).
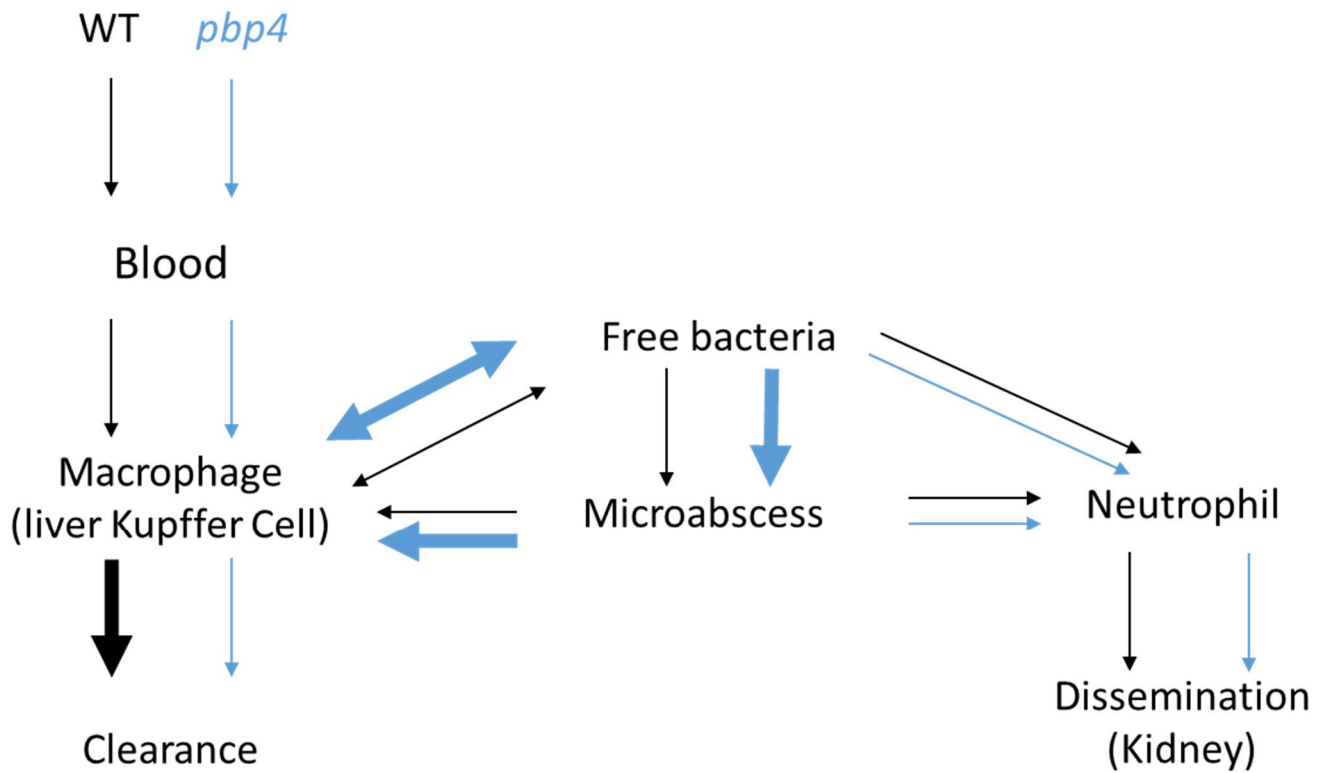
Figure 5.20 Proposed infection dynamics of NewHG *pbp4* compared to wildtype NewHG in the murine sepsis model

When mice are intravenously infected with *S. aureus,* free bacteria are released into the blood stream that are phagocytosed by Kupffer cells (resident macrophages) in the liver. Macrophages contain and kill the *S. aureus*, but some bacteria survive, escaping the macrophage and form extracellular micro-abscesses. It is proposed that more NewHG *pbp4* survive within the macrophages than NewHG. The same amounts of both strains are phagocytosed and killed by neutrophils, resulting in the same level of dissemination to different organs. Arrow sizes indicated the number of bacteria moving between states relative to the other strain. Adapted from Pollitt *et al.* (2018).

5.4.2 NewHG *sagB pbp4* phenotype

It was previously shown that NewHG *sagB* (SJF 4912) was attenuated in zebrafish embryo infection (Figure 4.4B) and murine sepsis (Figure 4.5). NewHG *pbp4* was shown to be more effective at liver colonisation in the murine sepsis model (Figures 5.5, 5.6). As hydrolases and synthases are both needed to maintain the PG sacculus (Vollmer *et al.*, 2008b), it was hypothesised that NewHG *sagB pbp4* (SJF 5147) could have its own distinct phenotype.

When analysed *in vitro*, NewHG *sagB pbp4* (SJF 5147) has a slightly reduced growth rate compared to parental NewHG (Figure 5.17B). While NewHG *sagB* (SJF 4912) has a decreased particle size compared to wild type NewHG, NewHG *sagB pbp4* has no difference in particle size to the wildtype (Figure 5.17D). *In vivo,* NewHG *sagB* is attenuated in the zebrafish model of infection, whilst NewHG *sagB pbp4* is not (Figure 5.17D). In the murine sepsis model of infection, despite significantly higher CFU recovered from the livers of mice infected with NewHG *pbp4* (SJF 5103) and significantly lower from kidneys infected with NewHG *sagB*, no differences could be seen between NewHG *sagB pbp4* and the wildtype (Figure 5.18). Overall, NewHG *sagB pbp4* shows no differences, except a slightly slower growth rate, to parental NewHG.

A *sagB* mutant has an increased cell wall stiffness (Wheeler *et al.*, 2015), aberrant protein trafficking and secretion and morphological defects (Chan *et al.*, 2016b), and it has been hypothesised that this may be a cause for the attenuation of this strain in animal models of infection (Chapter 4.4.1). The inability to process the glycans results in longer and stiffer chains (Wheeler *et al.*, 2015), with an associated reduction in the ability to increase in cell volume. This is supported by the particle size of NewHG *sagB* (Figure 5.17D) being significantly lower than wildtype NewHG. Previous studies have shown that *pbp4* mutants have reduced cell wall stiffness compared to a wild type strain (Loskill *et al.*, 2014), likely due to the reduction in crosslinking (Wyke *et al.*, 1981a). NewHG *sagB pbp4* has the same particle size as NewHG, suggesting the increased cell wall stiffness is reversed by the *pbp4* mutation (Figure 5.17D), resulting in an increase in cell volume, and the same virulence as the wildtype. The *sagB* mutant has abnormal secretion of proteins, proposed to be due to

the change in PG (Chan *et al*., 2016), which could also be a cause of the attenuation. As *pbp4* mutations cause reduced crosslinking (Wyke *et al.*, 1981a) and a reduced cell wall stiffness (Loskill *et al.*, 2014), it is possible that the loss of PBP4 can cause changes in the cell wall structure that may revert its biophysical properties to a wildtype state. If this is true, the protein secretion defect associated with *sagB* which could be a cause of attenuation, may be reverted with a *pbp4* mutation.

Chapter 6

General Discussion

S. aureus is a current healthcare issue due to the emergence of multiple antibiotic resistant strains such as MRSA (Jensen and Lyon, 2009). The rise of antimicrobial resistant nosocomial *S. aureus* infections is a challenge, both in terms of available treatments and the cost of care. Therefore, new treatments must be developed to combat potentially fatal *S. aureus* disease. A large proportion of antibiotics target the cell wall of bacteria, specifically PG biosynthesis (Zaman *et al.*, 2017). The structure of *S. aureus* PG is relatively well studied (Jonge *et al.*, 1992a; de Jonge and Tomasz, 1993; Kim *et al.*, 2013; Lund *et al.*, 2018), but the focus has been on *in vitro* growth, which does not truly reflect the conditions of an infection. My research aimed to fill this gap in our knowledge by providing data for the structure of *S. aureus* PG during pathogenesis. PG has also been shown to play a role in disease (Boneca, 2005; Boldock *et al.*, 2018), so the study of its metabolism and structure is important to fully understand the infection process. This may provide insight into potential new treatments and drug targets that could help in the fight against antimicrobial resistance and prevent the onset of the so-called post antibiotic era.

Using a combination of RP-HPLC, MS and TEM, my study has shown that during an infection *S. aureus* cells are smaller with a thicker (but less crosslinked) PG cell wall than exponential phase cells (Table 3.2). It has previously been found that *S. aureus* cells in stationary phase have a thicker cell wall with reduced PG crosslinking (Watson *et al.*, 1998; Zhou and Cegelski, 2012), hypothesised to be due to a change in available nutrients, which my study also demonstrates. This observation suggests that during an infection *S. aureus* cells have a similar cell wall structure to that of stationary phase cells, which could also be caused by a change in nutrient availability during an infection.

The impact of PG metabolism on virulence was also investigated using glucosaminidase and *pbp4* mutants, to further assess how thickened cell walls and reduced PG crosslinking

impact upon pathogenesis. A *sagB* mutant was shown to be attenuated in both zebrafish and murine models of infection (Figures 4.3A, 4.5B, 4.6), and this was associated with a reduced ability of the *sagB* mutant to survive in human MDMs (Figure 4.9). Other glucosaminidase mutants, *atl, sagA* and *scaH*, are not attenuated in a zebrafish model of infection (Figure 4.13). When in combination, attenuation is associated with a clustering phenotype (Figure 4.23), with virulence being restored in the zebrafish model (but not the murine) when bacterial clusters are disrupted by sonication. These results suggest that autolysin activity is required during infection to produce the correct cell wall architecture and to separate daughter cells, which in turn permits pathogenesis to occur.

A *pbp4* mutant shows increased colonisation, and relative fitness, in the livers of mice during sepsis (Figures 5.7, 5.8, 5.13). The *pbp4* mutant was shown to have greater survival in human MDMs than a wildtype (Figure 5.14). However, as the increased fitness was only seen within the livers and spleens of mice (Figure 5.13), the change in crosslinking is only beneficial within these tissues. This difference across host tissues could be due to a result of differing host nutritional status, such as heterogenous levels of iron, within each organ of the body (Cassat *et al.*, 2018). It has also been described that abscesses within the same organ can have different nutritional statuses and within a single abscess microdomains of differing concentrations of calcium, phosphorus and manganese exist (Cassat *et al.*, 2018). The differences in fitness in each organ could also be due to varying immune responses between organs. Using the methodology developed in my study, it will be important to investigate the PG structure of *S. aureus* infecting organs other than the kidney, to see if the potential differences in immune response and nutritional status result in the same PG structure as described in my study.

As the loss of hydrolases was shown to reduce fitness, but the loss of a synthase was shown to increase fitness, the impact of the simultaneous loss of hydrolases and synthases on virulence was investigated. A *S. aureus* strain lacking both *sagB* and *pbp4* had the same virulence as the wild type in the murine sepsis model (Figure 5.19). The results suggest that

the reduction in fitness caused by a *sagB* mutation can be reversed by a reduction in crosslinking caused by *pbp4* inactivation.

Overall, my results show that during infection, *S. aureus* has reduced PG crosslinking and a thicker cell wall, much like that of stationary phase. My work demonstrates the importance of cell wall structure in virulence, as a reduction in crosslinking results in the increased fitness of *S. aureus* in the livers and spleens of mice. While it has been speculated that these changes may be due to changes in the nutrient availability for *S. aureus* within a host, these changes could be due to changes in the cell wall architecture and the host response.

6.1   Cell morphology and peptidoglycan architecture

Throughout this study, the importance of PG structure in *S. aureus* infection has been highlighted. During infection, the morphology of the cell, cell wall and PG all show a distinct difference compared to exponentially growing cells (Table 3.2). In addition to this, mutations in genes required for PG metabolism change the outcome of infection, with loss of putative glucosaminidases resulting in attenuation, and the loss of the synthase *pbp4* resulting in increased fitness (Chapter 5.3.5). While the causes of these changes are only just being understood, it can be speculated that a change in the PG architecture is a factor. The architecture of PG has been briefly discussed in Chapter 1.5. Using molecular resolution AFM, more insight has been acquired (Figure 6.1) (Pasquina-Lemonche *et al.*, 2020). The Gram-positive cell wall contains a single macromolecule of PG that is tens of nanometres thick (Matias and Beveridge, 2007; Turner *et al.*, 2014). While being essential for viability by resisting internal turgor (Vollmer and Seligman, 2010), the cell wall has a porosity that allows the acquisition of nutrients from the environment, as well as the secretion of molecules, such as toxins, into the environment (Green and Mecsas, 2016). The external PG forms the interface with the environment and adopts a "mature" architecture, consisting of pores up to 60 nm in diameter and up to 23 nm deep (Pasquina-Lemonche *et al.*, 2020). These pores narrow as they reach the cell membrane, and the inner face of the PG can be seen to adopt a disordered mesh architecture. The internal mesh is likely to be formed from

single glycan chains, whereas the mature external surface is described as a porous gel formed of randomly orientated strands consisting of multiple bunched glycan chains (Pasquina-Lemonche *et al.*, 2020). The cytoplasmic facing PG of division septa has a tight disordered mesh reminiscent of the internal surface previously described. The PG within the septum forming the external division plane is seen to be organised into dense concentric rings. This immature ring architecture is seen on the surface of PG of recently divided cells, consisting of circumferentially oriented densely packed strands (Turner *et al.*, 2010a; Pasquina-Lemonche *et al.*, 2020). The interface between the mature mesh and nascent ring is sharp, suggesting that the transition from ring to mature mesh takes place within a single division cycle (Turner *et al.*, 2010a; Pasquina-Lemonche *et al.*, 2020). The varied and dynamic PG architecture across a cell raises the question of what the PG architecture is during an infection, and if this infectious architecture plays a role in supporting virulence.

The final architecture of the cell wall is specified by the activities of both PG synthases and hydrolases as seen by mutant studies. When *sagB* is inactivated, PG is initially thinner, and a transition between the ring and the mature mesh can be visualised, suggesting a role for *sagB* in this transition. A *pbp4* mutant was found to have a denser ring structure, which was observed to occasionally persist past a division cycle (Pasquina-Lemonche *et al.*, 2020). It could be suggested that the crosslinking introduced by PBP4 is required for the efficient conversion of ring architecture PG to the mature mesh, as the results obtained from the *sagB* mutant (Pasquina-Lemonche *et al.*, 2020) suggest that hydrolase activity is required for the maturation of PG to the mesh architecture. As a *sagB* mutant was seen to be attenuated in zebrafish (Chapter 4.3.2) and murine models of infection (Chapter 4.3.6), and a *pbp4* mutant showed increased fitness in murine livers (Chapter 5.3.5) it is reasonable to hypothesise that the change in the PG architecture may influence host-pathogen interactions, leading to the observed changes in virulence. It was suggested in Chapter 3.4 that the increase in cell wall thickness and increase in undivided cells with a complete septum observed in *S. aureus* recovered from a kidney could be due to a decrease in the expression of PG hydrolases. If this is true, then the PG architecture during infection may show a similar phenotype to the *sagB* mutant (Pasquina-Lemonche *et al.*, 2020), with a transition structure being observable by AFM.

268
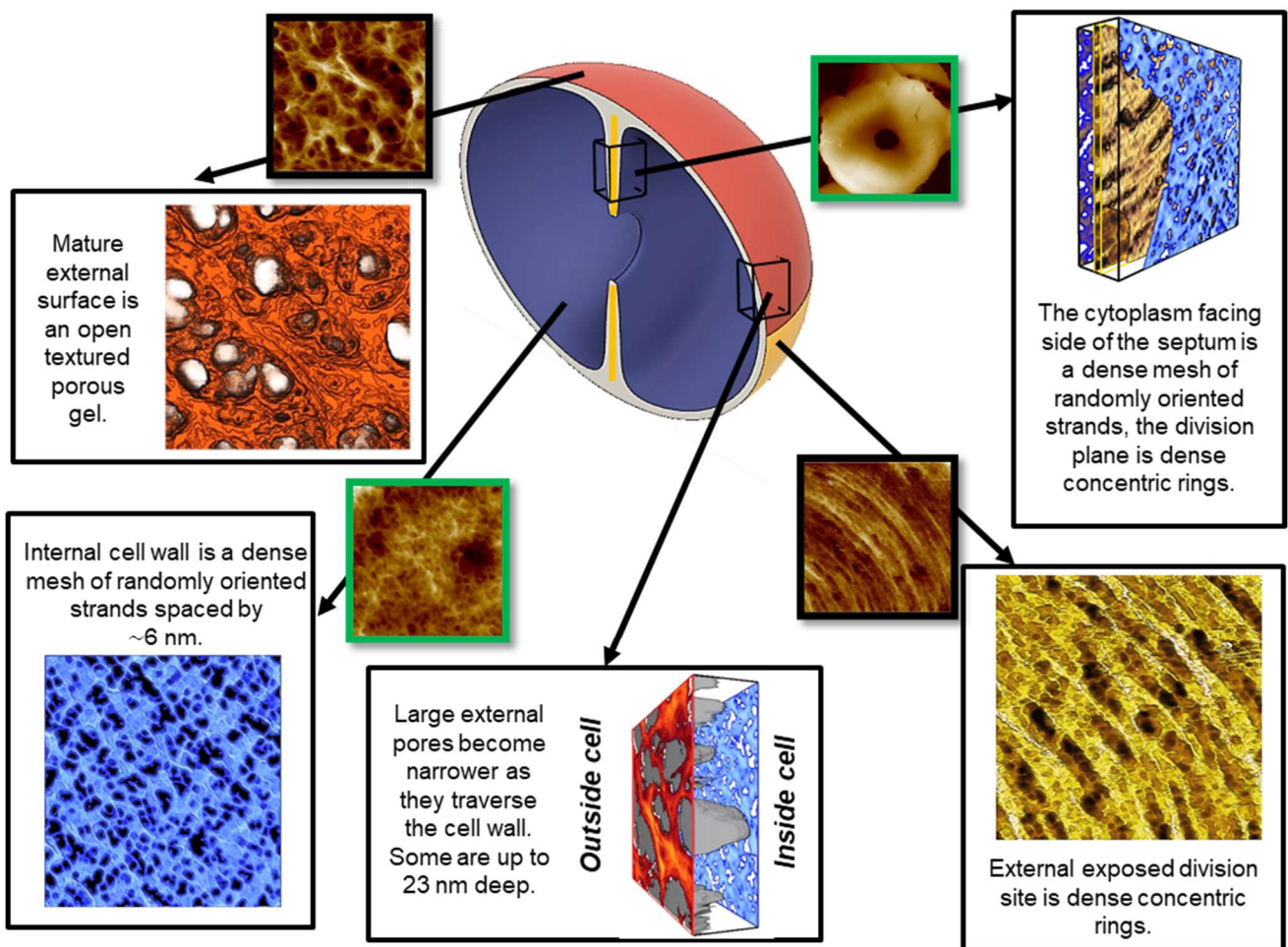
Figure 6.1 The 3D structure of *S. aureus* peptidoglycan using AFM

The architecture of *S. aureus* PG derived from AFM observations. Representative AFM images show the different PG architectures and areas with distinct morphology found in the cell during division. Adapted from Pasquina-Lemonche *et al.* (2020).

6.2   Host response to *S. aureus* infection

An alteration in PG architecture resulting in a change in host-pathogen interaction has been suggested by recent work comparing the effects of exponential and stationary phase *S. aureus* on human dendritic cells (DCs) (Balraadjsing *et al.*, 2019). Exponential phase *S. aureus* cells were found to be highly phagocytosed by DCs, which promoted the secretion of IL-12 and an intracellular clearance response (Figure 6.2) (Balraadjsing *et al.*, 2019). This was also found when murine DCs were used (Lund *et al.*, 2016). Stationary phase *S. aureus* cells were phagocytosed less than exponential phase cells, resulting in the reduced production of IL-12, and a shift to IL-23 production, and an extracellular host response (Figure 6.2) (Balraadjsing *et al.*, 2019). The phagocytosis of *S. aureus* leads to the intracellular activation of NOD2 and TLR2, resulting in cytokine production (Balraadjsing *et al.*, 2019). The cause for the reduced phagocytosis of stationary phase *S. aureus* cells was not confirmed, but speculated to be caused by factors such as ClfA that inhibit phagocytosis (Higgins *et al.*, 2006; Balraadjsing *et al.*, 2019). However, a presumed change in PG architecture between stationary and exponential phase cells may alter phagocytosis of *S. aureus* (van Kessel *et al.*, 2014). PG architectural dynamics during infection may lead to a differential DC and subsequent T cell response, allowing survival within the host (Balraadjsing *et al.*, 2019).

Exponential phase *S. aureus*

IL-12 Th1 INFγ

Increased intracellular bactericidal responses

S. aureus DC Stimulation

IL-23 Th17 IL-17

Neutrophil recruitment leading to extracellular clearance

Stationary phase *S. aureus*
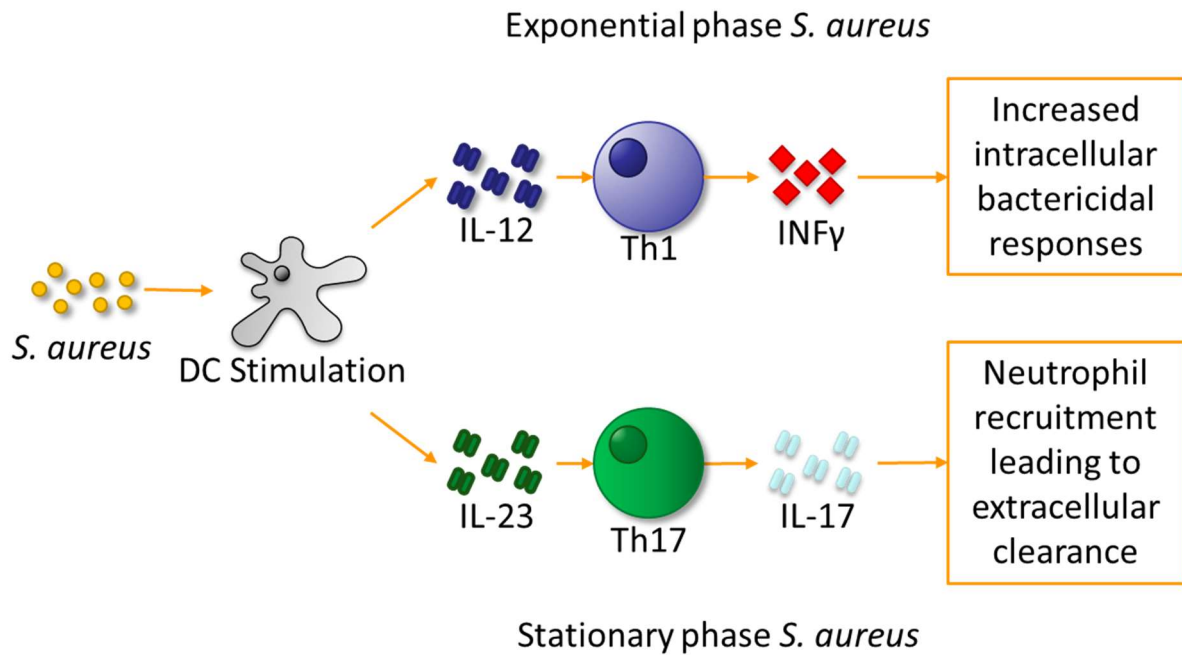
Figure 6.2 Schematic of dendritic cell response to *S. aureus* infection

The stimulation of DCs by *S. aureus* results in the production of T cell polarising cytokines to modify the host response. The production of IL-12 results in the production of Th1 cells, which produce INFγ, resulting in the increased expression of factors required for intracellular clearance of *S. aureus.* The production of IL-23 stimulates the formation of Th17 cells producing IL-17 to recruit neutrophils and result in the clearance of *S. aureus* from the extracellular environment. DCs – Dendritic cells; INF – Interferon; IL – Interleukin; Th – T helper cells. (Balraadjsing *et al.*, 2019).

A *sagB* mutant was found to be less able to survive in human MDMs than wildtype *S. aureus* (Chapter 4.3.7), and is associated with a different PG architecture and biochemistry (Wheeler *et al.*, 2015; Pasquina-Lemonche *et al.*, 2020). A contributing factor to *sagB* mutant attenuation could be the altered host recognition of the mutant PG architecture resulting in the increased expression of intracellular bactericidal factors and explaining the decreased survival of *sagB* in human MDMs. Research has shown that PG is naturally shed during growth in Gram-positive bacteria (Borisova *et al.*, 2016). The PG from a *pbp4* mutant could be more readily shed into the extracellular milieu due to the decreased number of crosslinks in the sacculi. When DCs were preincubated with purified *S. aureus* PG, it was found that IL-12 expression was inhibited, and IL-23 production was stimulated, resulting in an increased Th17 response (Balraadjsing *et al.*, 2019). A reduction in IL-12 results in the shift to an extracellular clearance response by neutrophils (Figure 6.2), rather than activation of phagocytes for intracellular bacterial clearance, which may explain increased survival in MDMs (Chapter 5.3.9.1).

The increased fitness of the *pbp4* mutant in murine livers should be further investigated. Clodronate can be used to deplete macrophages from mice (Chapter 4.3.8.2), and these macrophage depleted mice could be used to compare the relative fitness of NewHG *pbp4* to the wildtype, as in Chapter 5.3.8.2. If increased fitness in the murine liver of *pbp4* is a result of changes in macrophage interactions, the depletion of the macrophages should result in no difference in relative fitness being observed. This could be further investigated by using qPCR to quantify the levels of *pbp4* expressed by *S. aureus* within the isolated infected kidneys (Rivera *et al.*, 2015; Taylor *et al.*, 2019). The qPCR experiment could be performed using samples collected over the whole course of the experiment, to see when (and if) the expression of *pbp4* changes. Poorly crosslinked PG is known to result in the increased production of IL-1β host cells (Müller *et al.*, 2015), and a *pbp4* mutant shows reduced PG crosslinking (Wyke *et al.*, 1981b). It would therefore be important to perform cytokine analysis on the serum of mice infected with *S. aureus* NewHG *pbp4* compared to the wildtype, and to confirm a reduction in IL-12 expression.

Results presented in Chapter 4 show that clustering of bacteria due to the loss of PG hydrolases results in attenuation in zebrafish and murine models of infection. Subsequent research should aim to find why clustering causes attenuation. The attenuation likely results from a differing interaction with host macrophages and neutrophils. Uptake and killing assays using these host cells and SH1000 *atl sagA scaH* (SJF 4611) could be utilised to help refine the cause of attenuation.

My work has produced the first PG structure from *S. aureus*, or any bacterium, during an infection. This, paired with TEM analysis, has helped to elucidate the structure of the *S. aureus* cell wall during an infection. This paves the way for a fuller understanding of how *S. aureus* causes disease and assists the discovery of new ways to control this insidious pathogen.

References

Adams, D.W., Errington, J., (2009). Bacterial cell division: assembly, maintenance and disassembly of the Z ring. Nat Rev Microbiol 7, 642–653.

Al-Amoudi, A., Chang, J.-J., Leforestier, A., McDowall, A., Salamin, L.M., Norlén, L.P.O., Richter, K., Blanc, N.S., Studer, D., Dubochet, J., (2004). Cryo-electron microscopy of vitreous sections. EMBO J 23, 3583–3588.

Alexander, J.A.N., Chatterjee, S.S., Hamilton, S.M., Eltis, L.D., Chambers, H.F., Strynadka, N.C.J., (2018). Structural and kinetic analyses of penicillin-binding protein 4 (PBP4)-mediated antibiotic resistance in Staphylococcus aureus. J. Biol. Chem. 293, 19854–19865.

Alonzo, F., Torres, V.J., (2014). The Bicomponent Pore-Forming Leucocidins of Staphylococcus aureus. Microbiol Mol Biol Rev 78, 199–230.

Andersson, D.I., Hughes, D., (2010). Antibiotic resistance and its cost: is it possible to reverse resistance? Nat Rev Microbiol 8, 260–271.

Arciola, C.R., Campoccia, D., Ehrlich, G.D., Montanaro, L., (2015). Biofilm-Based Implant Infections in Orthopaedics, in: Donelli, G. (Ed.), Biofilm-Based Healthcare-Associated Infections: Volume I, Advances in Experimental Medicine and Biology. Springer International Publishing, Cham, pp. 29–46.

Argudín, M.Á., Mendoza, M.C., Rodicio, M.R., (2010). Food Poisoning and Staphylococcus aureus Enterotoxins. Toxins 2, 1751–1773.

Atilano, M.L., Pereira, P.M., Yates, J., Reed, P., Veiga, H., Pinho, M.G., Filipe, S.R., (2010). Teichoic acids are temporal and spatial regulators of peptidoglycan cross-linking in Staphylococcus aureus. PNAS 107, 18991–18996.

Atrih, A., Bacher, G., Allmaier, G., Williamson, M.P., Foster, S.J., (1999). Analysis of Peptidoglycan Structure from Vegetative Cells of Bacillus subtilis 168 and Role of PBP 5 in Peptidoglycan Maturation. Journal of Bacteriology 181, 3956–3966.

Atrih, A., Zöllner, P., Allmaier, G., Foster, S.J., (1996). Structural analysis of Bacillus subtilis 168 endospore peptidoglycan and its role during differentiation. Journal of Bacteriology 178, 6173–6183.

Aubry, C., Goulard, C., Nahori, M.-A., Cayet, N., Decalf, J., Sachse, M., Boneca, I.G., Cossart, P., Dussurget, O., (2011). OatA, a Peptidoglycan O-Acetyltransferase Involved in Listeria monocytogenes Immune Escape, Is Critical for Virulence. J Infect Dis 204, 731–740.

Aulock, S. von, Hartung, T., Hermann, C., (2007). Comment on "Not Lipoteichoic Acid but Lipoproteins Appear to Be the Dominant Immunobiologically Active Compounds in Staphylococcus aureus." The Journal of Immunology 178, 2610–2610.

Bae, T., Baba, T., Hiramatsu, K., Schneewind, O., (2006). Prophages of Staphylococcus aureus Newman and their contribution to virulence. Molecular Microbiology 62, 1035–1047.

Bae, T., Banger, A.K., Wallace, A., Glass, E.M., Åslund, F., Schneewind, O., Missiakas, D.M., (2004). Staphylococcus aureus virulence genes identified by bursa aurealis mutagenesis and nematode killing. PNAS 101, 12312–12317.

Balraadjsing, P.P., Lund, L.D., Souwer, Y., Zaat, S.A.J., Frøkiær, H., Jong, E.C. de, (2019). The Nature of Antibacterial Adaptive Immune Responses against Staphylococcus aureus Is Dependent on the Growth Phase and Extracellular Peptidoglycan. Infection and Immunity 88.

Baranwal, G., Mohammad, M., Jarneborn, A., Reddy, B.R., Golla, A., Chakravarty, S., Biswas, L., Götz, F., Shankarappa, S., Jin, T., Biswas, R., (2017). Impact of cell wall peptidoglycan O-acetylation on the pathogenesis of Staphylococcus aureus in septic arthritis. International Journal of Medical Microbiology 307, 388–397.

Beeby, M., Gumbart, J.C., Roux, B., Jensen, G.J., (2013). Architecture and assembly of the Gram-positive cell wall. Molecular Microbiology 88, 664–672.

Begun, J., Sifri, C.D., Goldman, S., Calderwood, S.B., Ausubel, F.M., (2005). Staphylococcus aureus Virulence Factors Identified by Using a High-Throughput Caenorhabditis elegans-Killing Model. Infection and Immunity 73, 872–877.

Beltramini, A.M., Mukhopadhyay, C.D., Pancholi, V., (2009). Modulation of Cell Wall Structure and Antimicrobial Susceptibility by a Staphylococcus aureus Eukaryote-Like Serine/Threonine Kinase and Phosphatase. Infection and Immunity 77, 1406–1416.

Bem, A.E., Velikova, N., Pellicer, M.T., Baarlen, P. van, Marina, A., Wells, J.M., (2015). Bacterial histidine kinases as novel antibacterial drug targets. ACS Chem. Biol. 10, 213–224.

Bera, A., Biswas, R., Herbert, S., Götz, F., (2006). The Presence of Peptidoglycan O-Acetyltransferase in Various Staphylococcal Species Correlates with Lysozyme Resistance and Pathogenicity. Infection and Immunity 74, 4598–4604.

Bera, A., Herbert, S., Jakob, A., Vollmer, W., Götz, F., (2005). Why are pathogenic staphylococci so lysozyme resistant? The peptidoglycan O-acetyltransferase OatA is the major determinant for lysozyme resistance of Staphylococcus aureus. Molecular Microbiology 55, 778–787.

Berardino, M.D., Dijkstra, A., Stüber, D., Keck, W., Gubler, M., (1996). The monofunctional glycosyltransferase of Escherichia coli is a member of a new class of peptidoglycan-synthesising enzymes. FEBS Letters 392, 184–188.

Berger-Bächi, B., Rohrer, S., (2002). Factors influencing methicillin resistance in staphylococci. Arch Microbiol 178, 165–171.

Bern, M., Beniston, R., Mesnage, S., (2017). Towards an automated analysis of bacterial peptidoglycan structure. Anal Bioanal Chem 409, 551–560.

Bernard, E., Rolain, T., Courtin, P., Guillot, A., Langella, P., Hols, P., Chapot-Chartier, M.-P., (2011). Characterization of O-acetylation of N-acetylglucosamine: A novel structural variation of bacterial peptidoglycan. Journal of Biological Chemistry 286, 23950–23958.

Berube, B.J., Bubeck Wardenburg, J., (2013). Staphylococcus aureus α-toxin: nearly a century of intrigue. Toxins (Basel) 5, 1140–1166.

Bill, B.R., Petzold, A.M., Clark, K.J., Schimmenti, L.A., Ekker, S.C., (2009). A Primer for Morpholino Use in Zebrafish. Zebrafish 6, 69–77.

Binnig, G., Quate, C.F., Gerber, Ch., (1986). Atomic Force Microscope. Phys. Rev. Lett. 56, 930–933.

Bisson-Filho, A.W., Hsu, Y.-P., Squyres, G.R., Kuru, E., Wu, F., Jukes, C., Sun, Y., Dekker, C., Holden, S., VanNieuwenhze, M.S., Brun, Y.V., Garner, E.C., (2017). Treadmilling by FtsZ filaments drives peptidoglycan synthesis and bacterial cell division. Science 355, 739–743.

Biswas, R., Voggu, L., Simon, U.K., Hentschel, P., Thumm, G., Götz, F., (2006). Activity of the major staphylococcal autolysin Atl. FEMS Microbiol Lett 259, 260–268.

Blaauwen, T.D., Pedro, M.A.D., Nguyen-Distèche, M., Ayala, J.A., (2008). Morphogenesis of rod-shaped sacculi. FEMS Microbiology Reviews 32, 321–344.

Blázquez, B., Llarrull, L.I., Luque-Ortega, J.R., Alfonso, C., Boggess, B., Mobashery, S., (2014). Regulation of the Expression of the β-Lactam Antibiotic-Resistance Determinants in Methicillin-Resistant Staphylococcus aureus (MRSA). Biochemistry 53, 1548–1550.

Boldock, E., Surewaard, B.G.J., Shamarina, D., Na, M., Fei, Y., Ali, A., Williams, A., Pollitt, E.J.G., Szkuta, P., Morris, P., Prajsnar, T.K., McCoy, K.D., Jin, T., Dockrell, D.H., Strijp, J.A.G. van, Kubes, P., Renshaw, S.A., Foster, S.J., (2018). Human skin commensals augment Staphylococcus aureus pathogenesis. Nat Microbiol 3, 881–890.

Boneca, I.G., (2005). The role of peptidoglycan in pathogenesis. Current Opinion in Microbiology, Host--microbe interactions: bacteria 8, 46–53.

Boneca, I.G., Dussurget, O., Cabanes, D., Nahori, M.-A., Sousa, S., Lecuit, M., Psylinakis, E., Bouriotis, V., Hugot, J.-P., Giovannini, M., Coyle, A., Bertin, J., Namane, A., Rousselle, J.-C., Cayet, N., Prévost, M.-C., Balloy, V., Chignard, M., Philpott, D.J., Cossart, P., Girardin, S.E., (2007). A critical role for peptidoglycan N-deacetylation in *Listeria* evasion from the host innate immune system. PNAS 104, 997–1002.

Boneca, I.G., Huang, Z.-H., Gage, D.A., Tomasz, A., (2000). Characterization of Staphylococcus aureus Cell Wall Glycan Strands, Evidence for a New β-N-Acetylglucosaminidase Activity. J. Biol. Chem. 275, 9910–9918.

Boneca, I.G., Xu, N., Gage, D.A., de Jonge, B.L., Tomasz, A., (1997). Structural characterization of an abnormally cross-linked muropeptide dimer that is accumulated in the peptidoglycan of methicillin- and cefotaxime-resistant mutants of Staphylococcus aureus. J. Biol. Chem. 272, 29053–29059.

Borisova, M., Gaupp, R., Duckworth, A., Schneider, A., Dalügge, D., Mühleck, M., Deubel, D., Unsleber, S., Yu, W., Muth, G., Bischoff, M., Götz, F., Mayer, C., (2016). Peptidoglycan Recycling in Gram-Positive Bacteria Is Crucial for Survival in Stationary Phase. mBio 7.

Bose, J.L., Lehman, M.K., Fey, P.D., Bayles, K.W., (2012). Contribution of the Staphylococcus aureus Atl AM and GL Murein Hydrolase Activities in Cell Division, Autolysis, and Biofilm Formation. PLOS ONE 7, e42244.

Bottomley, A.L., Liew, A.T.F., Kusuma, K.D., Peterson, E., Seidel, L., Foster, S.J., Harry, E.J., (2017). Coordination of Chromosome Segregation and Cell Division in Staphylococcus aureus. Front Microbiol 8.

Bouhss, A., Trunkfield, A.E., Bugg, T.D.H., Mengin-Lecreulx, D., (2008). The biosynthesis of peptidoglycan lipid-linked intermediates. FEMS Microbiol Rev 32, 208–233.

Bourgeois, I., Camiade, E., Biswas, R., Courtin, P., Gibert, L., Götz, F., Chapot-Chartier, M.-P., Pons, J.-L., Pestel-Caron, M., (2009). Characterization of AtlL, a bifunctional autolysin of Staphylococcus lugdunensis with N-acetylglucosaminidase and N-acetylmuramoyl-l-alanine amidase activities. FEMS Microbiol Lett 290, 105–113.

Bourgogne, A., Garsin, D.A., Qin, X., Singh, K.V., Sillanpaa, J., Yerrapragada, S., Ding, Y., Dugan-Rocha, S., Buhay, C., Shen, H., Chen, G., Williams, G., Muzny, D., Maadani, A., Fox, K.A., Gioia, J., Chen, L., Shang, Y., Arias, C.A., Nallapareddy, S.R., Zhao, M., Prakash, V.P., Chowdhury, S., Jiang, H., Gibbs, R.A., Murray, B.E., Highlander, S.K., Weinstock, G.M., (2008). Large scale variation in Enterococcus faecalis illustrated by the genome analysis of strain OG1RF. Genome Biology 9, R110.

Bourhis, L.L., Werts, C., (2007). Role of Nods in bacterial infection. Microbes Infect. 9, 629–636.

Brook, I., Frazier, E.H., (1991). Infections caused by Propionibacterium species. Rev. Infect. Dis. 13, 819–822.

Brown, S., Santa Maria, J.P., Walker, S., (2013). Wall Teichoic Acids of Gram-Positive Bacteria. Annu. Rev. Microbiol. 67, 313–336.

Brynestad, S., Granum, P.E., (2002). Clostridium perfringens and foodborne infections. International Journal of Food Microbiology, Memorial Issue for Gordon Stewart 74, 195–202.

Bubeck Wardenburg, J., Patel, R.J., Schneewind, O., (2007). Surface proteins and exotoxins are required for the pathogenesis of Staphylococcus aureus pneumonia. Infect. Immun. 75, 1040–1044.

Buchan, K.D., Foster, S.J., Renshaw, S.A., (2019). Staphylococcus aureus: setting its sights on the human innate immune system. Microbiology, 165, 367–385.

Bunk, S., Sigel, S., Metzdorf, D., Sharif, O., Triantafilou, K., Triantafilou, M., Hartung, T., Knapp, S., Aulock, S. von, (2010). Internalization and Coreceptor Expression Are Critical for TLR2-Mediated Recognition of Lipoteichoic Acid in Human Peripheral Blood. The Journal of Immunology 185, 3708–3717.

Bush, K., Macielag, M.J., (2010). New β-lactam antibiotics and β-lactamase inhibitors. Expert Opinion on Therapeutic Patents 20, 1277–1293.

Callewaert, L., Michiels, C.W., (2010). Lysozymes in the animal kingdom. J. Biosci. 35, 127–160.

Camejo, A., Buchrieser, C., Couvé, E., Carvalho, F., Reis, O., Ferreira, P., Sousa, S., Cossart, P., Cabanes, D., (2009). In Vivo Transcriptional Profiling of Listeria monocytogenes and Mutagenesis Identify New Virulence Factors Involved in Infection. PLoS Pathog 5.

Cameron, D.R., Jiang, J.-H., Kostoulias, X., Foxwell, D.J., Peleg, A.Y., (2016). Vancomycin susceptibility in methicillin-resistant Staphylococcus aureus is mediated by YycHI activation of the WalRK essential two-component regulatory system. Sci Rep 6, 1–11.

Camiade, E., Peltier, J., Bourgeois, I., Couture-Tosi, E., Courtin, P., Antunes, A., Chapot-Chartier, M.-P., Dupuy, B., Pons, J.-L., (2010). Characterization of Acp, a Peptidoglycan Hydrolase of Clostridium perfringens with N-Acetylglucosaminidase Activity That Is Implicated in Cell Separation and Stress-Induced Autolysis. Journal of Bacteriology 192, 2373–2384.

Carneiro, L. a. M., Magalhaes, J.G., Tattoli, I., Philpott, D.J., Travassos, L.H., (2008). Nod-like proteins in inflammation and disease. The Journal of Pathology 214, 136–148.

Cassat, J.E., Moore, J.L., Wilson, K.J., Stark, Z., Prentice, B.M., Van de Plas, R., Perry, W.J., Zhang, Y., Virostko, J., Colvin, D.C., Rose, K.L., Judd, A.M., Reyzer, M.L., Spraggins, J.M., Grunenwald, C.M., Gore, J.C., Caprioli, R.M., Skaar, E.P., (2018). Integrated molecular imaging reveals tissue heterogeneity driving host-pathogen interactions. Sci Transl Med 10.

Cava, F., de Pedro, M.A., (2014). Peptidoglycan plasticity in bacteria: emerging variability of the murein sacculus and their associated biological functions. Current Opinion in Microbiology, Cell regulation 18, 46–53.

Chamaillard, M., Hashimoto, M., Horie, Y., Masumoto, J., Qiu, S., Saab, L., Ogura, Y., Kawasaki, A., Fukase, K., Kusumoto, S., Valvano, M.A., Foster, S.J., Mak, T.W., Nuñez, G., Inohara, N., (2003). An essential role for NOD1 in host recognition of bacterial peptidoglycan containing diaminopimelic acid. Nat Immunol 4, 702–707.

Chan, L.C., Gilbert, A., Basuino, L., Costa, T.M. da, Hamilton, S.M., Santos, K.R. dos, Chambers, H.F., Chatterjee, S.S., (2016a). PBP 4 Mediates High-Level Resistance to New-Generation Cephalosporins in Staphylococcus aureus. Antimicrobial Agents and Chemotherapy 60, 3934–3941.

Chan, Y.G.Y., Frankel, M.B., Missiakas, D., Schneewind, O., (2016b). SagB Glucosaminidase Is a Determinant of Staphylococcus aureus Glycan Chain Length, Antibiotic Susceptibility, and Protein Secretion. Journal of Bacteriology 198, 1123–1136.

Chang, C.-I., Pili-Floury, S., Hervé, M., Parquet, C., Chelliah, Y., Lemaitre, B., Mengin-Lecreulx, D., Deisenhofer, J., (2004). A Drosophila Pattern Recognition Receptor Contains a Peptidoglycan Docking Groove and Unusual L,D-Carboxypeptidase Activity. PLoS Biol 2, e277.

Chen, Y., Miyata, S., Makino, S., Moriyama, R., (1997). Molecular characterization of a germination-specific muramidase from Clostridium perfringens S40 spores and nucleotide sequence of the corresponding gene. J. Bacteriol. 179, 3181–3187.

Cheng, A.G., DeDent, A.C., Schneewind, O., Missiakas, D., (2011). A play in four acts: Staphylococcus aureus abscess formation. Trends in Microbiology 19, 225–232.

Cheng, A.G., Kim, H.K., Burts, M.L., Krausz, T., Schneewind, O., Missiakas, D.M., (2009). Genetic requirements for Staphylococcus aureus abscess formation and persistence in host tissues. The FASEB Journal 23, 3393–3404.

Cheng, A.G., McAdow, M., Kim, H.K., Bae, T., Missiakas, D.M., Schneewind, O., (2010). Contribution of Coagulases towards Staphylococcus aureus Disease and Protective Immunity. PLoS Pathog 6.

Cheung, A.L., Projan, S.J., Gresham, H., (2002). The Genomic Aspect of Virulence, Sepsis, and Resistance to Killing Mechanisms in Staphylococcus aureus. Curr Infect Dis Rep 4, 400–410.

Cheung, G.Y.C., Duong, A.C., Otto, M., (2012). Direct and synergistic hemolysis caused by Staphylococcus phenol-soluble modulins: implications for diagnosis and pathogenesis. Microbes Infect 14, 380–386.

Chico-Calero, I., Suárez, M., González-Zorn, B., Scortti, M., Slaghuis, J., Goebel, W., Consortium§, T.E.L.G., Vázquez-Boland, J.A., (2002). Hpt, a bacterial homolog of the microsomal glucose- 6-phosphate translocase, mediates rapid intracellular proliferation in Listeria. PNAS 99, 431–436.

Clauditz, A., Resch, A., Wieland, K.-P., Peschel, A., Götz, F., (2006). Staphyloxanthin Plays a Role in the Fitness of Staphylococcus aureus and Its Ability To Cope with Oxidative Stress. Infect Immun 74, 4950–4953.

Coico, R., (2006). Gram Staining. Current Protocols in Microbiology 00, A.3C.1-A.3C.2.

Collins, L.V., Kristian, S.A., Weidenmaier, C., Faigle, M., van Kessel, K.P.M., van Strijp, J.A.G., Götz, F., Neumeister, B., Peschel, A., (2002). Staphylococcus aureus Strains Lacking d-Alanine Modifications of Teichoic Acids Are Highly Susceptible to Human Neutrophil Killing and Are Virulence Attenuated in Mice. J Infect Dis 186, 214–219.

Corey, D.R., Abrams, J.M., (2001). Morpholino antisense oligonucleotides: tools for investigating vertebrate development. Genome Biol 2, reviews1015.1-reviews1015.3.

Cosgrove, K., Coutts, G., Jonsson, I.-M., Tarkowski, A., Kokai-Kun, J.F., Mond, J.J., Foster, S.J., (2007). Catalase (KatA) and alkyl hydroperoxide reductase (AhpC) have compensatory roles in peroxide stress resistance and are required for survival, persistence, and nasal colonization in Staphylococcus aureus. J. Bacteriol. 189, 1025–1035.

Cotter, G., Doyle, S., Kavanagh, K., (2000). Development of an insect model for the in vivo pathogenicity testing of yeasts. FEMS Immunol. Med. Microbiol. 27, 163–169.

Coulter, S.N., Schwan, W.R., Ng, E.Y.W., Langhorne, M.H., Ritchie, H.D., Westbrock-Wadman, S., Hufnagle, W.O., Folger, K.R., Bayer, A.S., Stover, C.K., (1998). Staphylococcus aureus genetic loci impacting growth and survival in multiple infection environments. Molecular Microbiology 30, 393–404.

Cowles, C.E., Li, Y., Semmelhack, M.F., Cristea, I.M., Silhavy, T.J., (2011). The free and bound forms of Lpp occupy distinct subcellular locations in Escherichia coli. Molecular Microbiology 79, 1168–1181.

Crowhurst, M.O., Layton, J.E., Lieschke, G.J., (2002). Developmental biology of zebrafish myeloid cells. Int. J. Dev. Biol. 46, 483–492.

Curtis, N.A.C., Hayes, M.V., Wyke, A.W., Ward, J.B., (1980). A mutant of Staphylococcus aureus H lacking penicillin-binding protein 4 and transpeptidase activity in vitro. FEMS Microbiol Lett 9, 263–266.

Dam, V. van, Olrichs, N., Breukink, E., (2009). Specific Labeling of Peptidoglycan Precursors as a Tool for Bacterial Cell Wall Studies. ChemBioChem 10, 617–624.

Dantes, R., Mu, Y., Belflower, R., Aragon, D., Dumyati, G., Harrison, L.H., Lessa, F.C., Lynfield, R., Nadle, J., Petit, S., Ray, S.M., Schaffner, W., Townes, J., Fridkin, S., Emerging Infections Program–Active Bacterial Core Surveillance MRSA Surveillance Investigators, (2013). National burden of invasive methicillin-resistant Staphylococcus aureus infections, United States, 2011. JAMA Intern Med 173, 1970–1978.

de Haas, C.J.C., Veldkamp, K.E., Peschel, A., Weerkamp, F., Van Wamel, W.J.B., Heezius, E.C.J.M., Poppelier, M.J.J.G., Van Kessel, K.P.M., van Strijp, J.A.G., (2004). Chemotaxis inhibitory protein of Staphylococcus aureus, a bacterial antiinflammatory agent. J. Exp. Med. 199, 687–695.

de Jonge, B.L., Chang, Y.S., Xu, N., Gage, D., (1996). Effect of exogenous glycine on peptidoglycan composition and resistance in a methicillin-resistant Staphylococcus aureus strain. Antimicrob Agents Chemother 40, 1498–1503.

de Jonge, B.L., Sidow, T., Chang, Y.S., Labischinski, H., Berger-Bachi, B., Gage, D.A., Tomasz, A., (1993). Altered muropeptide composition in Staphylococcus aureus strains with an inactivated femA locus. J Bacteriol 175, 2779–2782.

de Jonge, B.L., Tomasz, A., (1993). Abnormal peptidoglycan produced in a methicillin-resistant strain of Staphylococcus aureus grown in the presence of methicillin: functional role for penicillin-binding protein 2A in cell wall synthesis. Antimicrob. Agents Chemother. 37, 342–346.

de Pedro, M.A., Cava, F., (2015). Structural constraints and dynamics of bacterial cell wall architecture. Front. Microbiol. 6.

Débarbouillé, M., Dramsi, S., Dussurget, O., Nahori, M.-A., Vaganay, E., Jouvion, G., Cozzone, A., Msadek, T., Duclos, B., (2009). Characterization of a Serine/Threonine Kinase Involved in Virulence of Staphylococcus aureus. Journal of Bacteriology 191, 4070–4081.

Deininger, S., Stadelmaier, A., Aulock, S. von, Morath, S., Schmidt, R.R., Hartung, T., (2003). Definition of Structural Prerequisites for Lipoteichoic Acid-Inducible Cytokine Induction by Synthetic Derivatives. The Journal of Immunology 170, 4134–4138.

Delauné, A., Dubrac, S., Blanchet, C., Poupel, O., Mäder, U., Hiron, A., Leduc, A., Fitting, C., Nicolas, P., Cavaillon, J.-M., Adib-Conquy, M., Msadek, T., (2012). The WalKR System Controls Major Staphylococcal Virulence Genes and Is Involved in Triggering the Host Inflammatory Response. Infection and Immunity 80, 3438–3453.

DeLeo, F.R., Diep, B.A., Otto, M., (2009). Host Defense and Pathogenesis in Staphylococcus aureus Infections. Infect Dis Clin North Am 23, 17–34.

Dembek, M., Kelly, A., Barwinska-Sendra, A., Tarrant, E., Stanley, W.A., Vollmer, D., Biboy, J., Gray, J., Vollmer, W., Salgado, P.S., (2018). Peptidoglycan degradation machinery in Clostridium difficile forespore engulfment. Molecular Microbiology 110, 390–410.

Denome, S.A., Elf, P.K., Henderson, T.A., Nelson, D.E., Young, K.D., (1999). Escherichia coli mutants lacking all possible combinations of eight penicillin binding proteins: viability, characteristics, and implications for peptidoglycan synthesis. J. Bacteriol. 181, 3981–3993.

Desmarais, S.M., De Pedro, M.A., Cava, F., Huang, K.C., (2013). Peptidoglycan at its peaks: how chromatographic analyses can reveal bacterial cell wall structure and assembly. Mol. Microbiol. 89, 1–13.

Do, T., Page, J.E., Walker, S., (2020a). Uncovering the activities, biological roles, and regulation of bacterial cell wall hydrolases and tailoring enzymes. J. Biol. Chem. jbc.REV119.010155.

Do, T., Schaefer, K., Santiago, A.G., Coe, K.A., Fernandes, P.B., Kahne, D., Pinho, M.G., Walker, S., (2020b). Staphylococcus aureus cell growth and division are regulated by an amidase that trims peptides from uncrosslinked peptidoglycan. Nat Microbiol 5, 291–303.

Dörr, T., Möll, A., Chao, M.C., Cava, F., Lam, H., Davis, B.M., Waldor, M.K., (2014). Differential Requirement for PBP1a and PBP1b in In Vivo and In Vitro Fitness of Vibrio cholerae. Infection and Immunity 82, 2115–2124.

Dubrac, S., Bisicchia, P., Devine, K.M., Msadek, T., (2008). A matter of life and death: cell wall homeostasis and the WalKR (YycGF) essential signal transduction pathway. Molecular Microbiology 70, 1307–1322.

Dubrac, S., Boneca, I.G., Poupel, O., Msadek, T., (2007). New insights into the WalK/WalR (YycG/YycF) essential signal transduction pathway reveal a major role in controlling cell wall metabolism and biofilm formation in Staphylococcus aureus. J. Bacteriol. 189, 8257–8269.

DuMont, A.L., Yoong, P., Day, C.J., Alonzo, F., McDonald, W.H., Jennings, M.P., Torres, V.J., (2013). Staphylococcus aureus LukAB cytotoxin kills human neutrophils by targeting the CD11b subunit of the integrin Mac-1. Proc. Natl. Acad. Sci. U.S.A. 110, 10794–10799.

Dussurget, O., Pizarro-Cerda, J., Cossart, P., (2004). Molecular Determinants of Listeria monocytogenes Virulence. Annual Review of Microbiology 58, 587–610.

Duthie, E.S., Lorenz, L.L., (1952). Staphylococcal Coagulase: Mode of Action and Antigenicity. Microbiology, 6, 95–107.

Dziarski, R., Gupta, D., (2005). Staphylococcus aureus Peptidoglycan Is a Toll-Like Receptor 2 Activator: a Reevaluation. Infection and Immunity 73, 5212–5216.

Egan, A.J.F., (2018). Bacterial outer membrane constriction. Molecular Microbiology 107, 676–687.

Egan, A.J.F., Cleverley, R.M., Peters, K., Lewis, R.J., Vollmer, W., (2017). Regulation of bacterial cell wall growth. The FEBS Journal 851–867.

Egan, A.J.F., Maya-Martinez, R., Ayala, I., Bougault, C.M., Banzhaf, M., Breukink, E., Vollmer, W., Simorre, J.-P., (2018). Induced conformational changes activate the peptidoglycan synthase PBP1B. Mol. Microbiol. 110, 335–356.

Eltsov, M., Zuber, B., (2006). Transmission electron microscopy of the bacterial nucleoid. Journal of Structural Biology 156, 246–254.

Erickson, H.P., Anderson, D.E., Osawa, M., (2010). FtsZ in Bacterial Cytokinesis: Cytoskeleton and Force Generator All in One. Microbiol. Mol. Biol. Rev. 74, 504–528.

Eswara, P.J., Brzozowski, R.S., Viola, M.G., Graham, G., Spanoudis, C., Trebino, C., Jha, J., Aubee, J.I., Thompson, K.M., Camberg, J.L., Ramamurthi, K.S., (2018). An essential Staphylococcus aureus cell division protein directly regulates FtsZ dynamics. eLife 7.

Eugster, M.R., Loessner, M.J., (2012). Wall Teichoic Acids Restrict Access of Bacteriophage Endolysin Ply118, Ply511, and PlyP40 Cell Wall Binding Domains to the Listeria monocytogenes Peptidoglycan. Journal of Bacteriology 194, 6498–6506.

Fang, F.C., Frawley, E.R., Tapscott, T., Vázquez-Torres, A., (2016). Bacterial Stress Responses during Host Infection. Cell Host & Microbe 20, 133–143.

Farha, M.A., Leung, A., Sewell, E.W., D'Elia, M.A., Allison, S.E., Ejim, L., Pereira, P.M., Pinho, M.G., Wright, G.D., Brown, E.D., (2013). Inhibition of WTA synthesis blocks the cooperative action of PBPs and sensitizes MRSA to β-lactams. ACS Chem. Biol. 8, 226–233.

Ferry, T., Perpoint, T., Vandenesch, F., Etienne, J., (2005). Virulence determinants in Staphylococcus aureus and their involvement in clinical syndromes. Curr Infect Dis Rep 7, 420–428.

Fey, P.D., Endres, J.L., Yajjala, V.K., Widhelm, T.J., Boissy, R.J., Bose, J.L., Bayles, K.W., (2013). A Genetic Resource for Rapid and Comprehensive Phenotype Screening of Nonessential Staphylococcus aureus Genes. mBio 4.

Figueiredo, T.A., Sobral, R.G., Ludovice, A.M., de Almeida, J.M.F., Bui, N.K., Vollmer, W., de Lencastre, H., Tomasz, A., (2012). Identification of Genetic Determinants and Enzymes Involved with

the Amidation of Glutamic Acid Residues in the Peptidoglycan of Staphylococcus aureus. PLoS Pathog 8, e1002508.

Fishovitz, J., Hermoso, J.A., Chang, M., Mobashery, S., (2014). Penicillin-binding protein 2a of methicillin-resistant Staphylococcus aureus. IUBMB Life 66, 572–577.

Formstone, A., Carballido-López, R., Noirot, P., Errington, J., Scheffers, D.-J., (2008). Localization and Interactions of Teichoic Acid Synthetic Enzymes in Bacillus subtilis. Journal of Bacteriology 190, 1812–1821.

Foster, S.J., (1995). Molecular characterization and functional analysis of the major autolysin of Staphylococcus aureus 8325/4. Journal of Bacteriology 177, 5723–5725.

Foster, T.J., (2017). Antibiotic resistance in Staphylococcus aureus. Current status and future prospects. FEMS Microbiol Rev 41, 430–449.

Foster, T.J., (2009). Colonization and infection of the human host by staphylococci: adhesion, survival and immune evasion. Veterinary Dermatology 20, 456–470.

Foster, T.J., Geoghegan, J.A., Ganesh, V.K., Höök, M., (2014). Adhesion, invasion and evasion: the many functions of the surface proteins of Staphylococcus aureus. Nat Rev Microbiol 12, 49–62.

Fournier, B., Philpott, D.J., (2005). Recognition of Staphylococcus aureus by the Innate Immune System. Clinical Microbiology Reviews 18, 521–540.

Franchi, L., Eigenbrod, T., Muñoz-Planillo, R., Nuñez, G., (2009). The Inflammasome: A Caspase-1 Activation Platform Regulating Immune Responses and Disease Pathogenesis. Nat Immunol 10, 241.

Frank, K.L., Pozo, J.L. del, Patel, R., (2008). From Clinical Microbiology to Infection Pathogenesis: How Daring To Be Different Works for Staphylococcus lugdunensis. Clinical Microbiology Reviews 21, 111–133.

Gan, L., Chen, S., Jensen, G.J., (2008). Molecular organization of Gram-negative peptidoglycan. PNAS 105, 18953–18957.

Gardete, S., Tomasz, A., (2014). Mechanisms of vancomycin resistance in Staphylococcus aureus. J. Clin. Invest. 124, 2836–2840.

Geisinger, E., Isberg, R.R., (2017). Interplay Between Antibiotic Resistance and Virulence During Disease Promoted by Multidrug-Resistant Bacteria. J Infect Dis 215, S9–S17.

Georgopapadakou, N.H., Dix, B.A., Mauriz, Y.R., (1986). Possible physiological functions of penicillin-binding proteins in Staphylococcus aureus. Antimicrobial Agents and Chemotherapy 29, 333–336.

Gibert, L., Didi, J., Marlinghaus, L., Lesouhaitier, O., Legris, S., Szabados, F., Pons, J.-L., Pestel-Caron, M., (2014). The major autolysin of Staphylococcus lugdunensis, AtlL, is involved in cell separation, stress-induced autolysis and contributes to bacterial pathogenesis. FEMS Microbiol Lett 352, 78–86.

Girardin, S.E., Boneca, I.G., Viala, J., Chamaillard, M., Labigne, A., Thomas, G., Philpott, D.J., Sansonetti, P.J., (2003). Nod2 Is a General Sensor of Peptidoglycan through Muramyl Dipeptide (MDP) Detection. J. Biol. Chem. 278, 8869–8872.

Glauner, B., (1988). Separation and quantification of muropeptides with high-performance liquid chromatography. Analytical Biochemistry 172, 451–464.

Glauner, B., Höltje, J.V., Schwarz, U., (1988). The composition of the murein of Escherichia coli. J. Biol. Chem. 263, 10088–10095.

Goffin, C., Ghuysen, J.-M., (2002). Biochemistry and comparative genomics of SxxK superfamily acyltransferases offer a clue to the mycobacterial paradox: presence of penicillin-susceptible target proteins versus lack of efficiency of penicillin as therapeutic agent. Microbiol. Mol. Biol. Rev. 66, 702–738, table of contents.

Goffin, C., Ghuysen, J.-M., (1998). Multimodular Penicillin-Binding Proteins: An Enigmatic Family of Orthologs and Paralogs. Microbiol. Mol. Biol. Rev. 62, 1079–1093.

Golding, C.G., Lamboo, L.L., Beniac, D.R., Booth, T.F., (2016). The scanning electron microscope in microbiology and diagnosis of infectious disease. Sci Rep 6, 1–8.

Gonzalez-Delgado, L.S., Walters-Morgan, H., Salamaga, B., Robertson, A.J., Hounslow, A.M., Jagielska, E., Sabała, I., Williamson, M.P., Lovering, A.L., Mesnage, S., (2020). Two-site recognition of Staphylococcus aureus peptidoglycan by lysostaphin SH3b. Nat Chem Biol 16, 24–30.

Götz, F., Heilmann, C., Stehle, T., (2014). Functional and structural analysis of the major amidase (Atl) in Staphylococcus. International Journal of Medical Microbiology, Pathophysiology of Staphylococci in the Post-Genomic Era 304, 156–163.

Green, E.R., Mecsas, J., (2016). Bacterial Secretion Systems – An overview. Microbiol Spectr 4.

Grice, E.A., Kong, H.H., Conlan, S., Deming, C.B., Davis, J., Young, A.C., Bouffard, G.G., Blakesley, R.W., Murray, P.R., Green, E.D., Turner, M.L., Segre, J.A., (2009). Topographical and Temporal Diversity of the Human Skin Microbiome. Science 324, 1190–1192.

Grilo, I.R., Ludovice, A.M., Tomasz, A., Lencastre, H. de, Sobral, R.G., (2014). The glucosaminidase domain of Atl – the major Staphylococcus aureus autolysin – has DNA-binding activity. MicrobiologyOpen 3, 247–256.

Gründling, A., Schneewind, O., (2007). Synthesis of glycerol phosphate lipoteichoic acid in Staphylococcus aureus. PNAS 104, 8478–8483.

Guinane, C.M., Cotter, P.D., Ross, R.P., Hill, C., (2006). Contribution of Penicillin-Binding Protein Homologs to Antibiotic Resistance, Cell Morphology, and Virulence of Listeria monocytogenes EGDe. Antimicrobial Agents and Chemotherapy 50, 2824–2828.

Hamilton, S.M., Alexander, J.A.N., Choo, E.J., Basuino, L., da Costa, T.M., Severin, A., Chung, M., Aedo, S., Strynadka, N.C.J., Tomasz, A., Chatterjee, S.S., Chambers, H.F., (2017). High-Level Resistance of Staphylococcus aureus to β-Lactam Antibiotics Mediated by Penicillin-Binding Protein 4 (PBP4). Antimicrob. Agents Chemother. 61.

Hardt, P., Engels, I., Rausch, M., Gajdiss, M., Ulm, H., Sass, P., Ohlsen, K., Sahl, H.-G., Bierbaum, G., Schneider, T., Grein, F., (2017). The cell wall precursor lipid II acts as a molecular signal for the Ser/Thr kinase PknB of Staphylococcus aureus. International Journal of Medical Microbiology 307, 1–10.

Hashimoto, M., Tawaratsumida, K., Kariya, H., Kiyohara, A., Suda, Y., Krikae, F., Kirikae, T., Götz, F., (2006). Not Lipoteichoic Acid but Lipoproteins Appear to Be the Dominant Immunobiologically Active Compounds in Staphylococcus aureus. The Journal of Immunology 177, 3162–3169.

Hayhurst, E.J., Kailas, L., Hobbs, J.K., Foster, S.J., (2008). Cell wall peptidoglycan architecture in Bacillus subtilis. PNAS 105, 14603–14608.

Hecker, M., Becher, D., Fuchs, S., Engelmann, S., (2010). A proteomic view of cell physiology and virulence of Staphylococcus aureus. International Journal of Medical Microbiology, Pathophysiology of staphylococci in the post-genomic era 300, 76–87.

Heilmann, C., Hussain, M., Peters, G., Götz, F., (1997). Evidence for autolysin-mediated primary attachment of Staphylococcus epidermidis to a polystyrene surface. Molecular Microbiology 24, 1013–1024.

Henk, W., Todd, W., Enright, F., Mitchell, P., (1995). The morphological effects of two antimicrobial peptides, hecate-1 and melittin, on Escherichia coli. Scanning Microsc 9, 501–507.

Henze, U., Sidow, T., Wecke, J., Labischinski, H., Berger-Bächi, B., (1993). Influence of femB on methicillin resistance and peptidoglycan metabolism in Staphylococcus aureus. Journal of Bacteriology 175, 1612–1620.

Henze, U.U., Berger-Bächi, B., (1995). Staphylococcus aureus penicillin-binding protein 4 and intrinsic beta-lactam resistance. Antimicrobial Agents and Chemotherapy 39, 2415–2422.

Herbomel, P., Thisse, B., Thisse, C., (1999). Ontogeny and behaviour of early macrophages in the zebrafish embryo. Development 126, 3735–3745.

Hermann, C., Spreitzer, I., Schröder, N.W.J., Morath, S., Lehner, M.D., Fischer, W., Schütt, C., Schumann, R.R., Hartung, T., (2002). Cytokine induction by purified lipoteichoic acids from various bacterial species – Role of LBP, sCD14, CD14 and failure to induce IL-12 and subsequent IFN-γ release. European Journal of Immunology 32, 541–551.

Hernández, S.B., Cava, F., Pucciarelli, M.G., Portillo, F.G., Pedro, M.A. de, Casadesús, J., (2015). Bile-induced peptidoglycan remodelling in Salmonella enterica. Environmental Microbiology 17, 1081–1089.

Hesse, L., Bostock, J., Dementin, S., Blanot, D., Mengin-Lecreulx, D., Chopra, I., (2003). Functional and Biochemical Analysis of Chlamydia trachomatis MurC, an Enzyme Displaying UDP-N-Acetylmuramate:Amino Acid Ligase Activity. Journal of Bacteriology 185, 6507–6512.

Higgins, J., Loughman, A., van Kessel, K.P.M., van Strijp, J.A.G., Foster, T.J., (2006). Clumping factor A of Staphylococcus aureus inhibits phagocytosis by human polymorphonuclear leucocytes. FEMS Microbiol. Lett. 258, 290–296.

Hoebe, K., Georgel, P., Rutschmann, S., Du, X., Mudd, S., Crozat, K., Sovath, S., Shamel, L., Hartung, T., Zähringer, U., Beutler, B., (2005). CD36 is a sensor of diacylglycerides. Nature 433, 523–527.

Höltje, J.-V., Kopp, U., Ursinus, A., Wiedemann, B., (1994). The negative regulator of β-lactamase induction AmpD is a N-acetyl-anhydromuramyl-l-alanine amidase. FEMS Microbiol Lett 122, 159–164.

Horn, J., Stelzner, K., Rudel, T., Fraunholz, M., (2018). Inside job: Staphylococcus aureus host-pathogen interactions. Int. J. Med. Microbiol. 308, 607–624.

Horsburgh, M.J., Aish, J.L., White, I.J., Shaw, L., Lithgow, J.K., Foster, S.J., (2002). σB Modulates Virulence Determinant Expression and Stress Resistance: Characterization of a Functional rsbU Strain Derived from Staphylococcus aureus 8325-4. Journal of Bacteriology 184, 5457–5467.

Houston, P., Rowe, S.E., Pozzi, C., Waters, E.M., O'Gara, J.P., (2011). Essential Role for the Major Autolysin in the Fibronectin-Binding Protein-Mediated Staphylococcus aureus Biofilm Phenotype. Infection and Immunity 79, 1153–1165.

Howden, B.P., Davies, J.K., Johnson, P.D.R., Stinear, T.P., Grayson, M.L., (2010). Reduced vancomycin susceptibility in Staphylococcus aureus, including vancomycin-intermediate and heterogeneous

vancomycin-intermediate strains: resistance mechanisms, laboratory detection, and clinical implications. Clin. Microbiol. Rev. 23, 99–139.

Howden, B.P., McEvoy, C.R.E., Allen, D.L., Chua, K., Gao, W., Harrison, P.F., Bell, J., Coombs, G., Bennett-Wood, V., Porter, J.L., Robins-Browne, R., Davies, J.K., Seemann, T., Stinear, T.P., (2011). Evolution of Multidrug Resistance during Staphylococcus aureus Infection Involves Mutation of the Essential Two Component Regulator WalKR. PLOS Pathogens 7, e1002359.

Huang, B., Babcock, H., Zhuang, X., (2010). Breaking the diffraction barrier: super-resolution imaging of cells. Cell 143, 1047–1058.

Irazoki, O., Hernandez, S.B., Cava, F., (2019). Peptidoglycan Muropeptides: Release, Perception, and Functions as Signaling Molecules. Front. Microbiol. 10.

Jacobs, C., Huang, L. j., Bartowsky, E., Normark, S., Park, J. t., (1994). Bacterial cell wall recycling provides cytosolic muropeptides as effectors for beta-lactamase induction. The EMBO Journal 13, 4684–4694.

Jander, G., Rahme, L.G., Ausubel, F.M., (2000). Positive Correlation between Virulence of Pseudomonas aeruginosa Mutants in Mice and Insects. J Bacteriol 182, 3843–3845.

Jault, C., Pichon, L., Chluba, J., (2004). Toll-like receptor gene family and TIR-domain adapters in Danio rerio. Mol. Immunol. 40, 759–771.

Jensen, S.O., Lyon, B.R., (2009). Genetics of antimicrobial resistance in Staphylococcus aureus. Future Microbiol 4, 565–582.

Jevons, M.P., (1961). "Celbenin" - resistant Staphylococci. Br Med J 1, 124–125.

Jim, K.K., Engelen-Lee, J., van der Sar, A.M., Bitter, W., Brouwer, M.C., van der Ende, A., Veening, J.-W., van de Beek, D., Vandenbroucke-Grauls, C.M.J.E., (2016). Infection of zebrafish embryos with live fluorescent Streptococcus pneumoniae as a real-time pneumococcal meningitis model. Journal of Neuroinflammation 13, 188.

Jong, N.W.M. de, Ramyar, K.X., Guerra, F.E., Nijland, R., Fevre, C., Voyich, J.M., McCarthy, A.J., Garcia, B.L., Kessel, K.P.M. van, Strijp, J.A.G. van, Geisbrecht, B.V., Haas, P.-J.A., (2017). Immune evasion by a staphylococcal inhibitor of myeloperoxidase. PNAS 114, 9439–9444.

Jonge, B.L. de, Chang, Y.S., Gage, D., Tomasz, A., (1992a). Peptidoglycan composition in heterogeneous Tn551 mutants of a methicillin-resistant Staphylococcus aureus strain. J. Biol. Chem. 267, 11255–11259.

Jonge, B.L. de, Chang, Y.S., Gage, D., Tomasz, A., (1992b). Peptidoglycan composition of a highly methicillin-resistant Staphylococcus aureus strain. The role of penicillin binding protein 2A. J. Biol. Chem. 267, 11248–11254.

Jonsson, I.-M., Arvidson, S., Foster, S., Tarkowski, A., (2004). Sigma Factor B and RsbU Are Required for Virulence in Staphylococcus aureus-Induced Arthritis and Sepsis. Infection and Immunity 72, 6106–6111.

Kajimura, J., Fujiwara, T., Yamada, S., Suzawa, Y., Nishida, T., Oyamada, Y., Hayashi, I., Yamagishi, J., Komatsuzawa, H., Sugai, M., (2005). Identification and molecular characterization of an N-acetylmuramyl-l-alanine amidase Sle1 involved in cell separation of Staphylococcus aureus. Molecular Microbiology 58, 1087–1101.

Karavolos, M.H., Horsburgh, M.J., Ingham, E., Foster, S.J., (2003). Role and regulation of the superoxide dismutases of Staphylococcus aureus. Microbiology (Reading, Engl.) 149, 2749–2758.

Katayama, Y., Ito, T., Hiramatsu, K., (2000). A new class of genetic element, staphylococcus cassette chromosome mec, encodes methicillin resistance in Staphylococcus aureus. Antimicrob. Agents Chemother. 44, 1549–1555.

Kawai, Y., Marles-Wright, J., Cleverley, R.M., Emmins, R., Ishikawa, S., Kuwano, M., Heinz, N., Bui, N.K., Hoyland, C.N., Ogasawara, N., Lewis, R.J., Vollmer, W., Daniel, R.A., Errington, J., (2011). A widespread family of bacterial cell wall assembly proteins. The EMBO Journal 30, 4931–4941.

Kemp, M.W., Massey, R.C., (2007). The use of insect models to study human pathogens. Drug Discovery Today: Disease Models, Infectious diseases / Respiratory diseases 4, 105–110.

Kengatharan, K.M., De Kimpe, S., Robson, C., Foster, S.J., Thiemermann, C., (1998). Mechanism of Gram-positive Shock: Identification of Peptidoglycan and Lipoteichoic Acid Moieties Essential in the Induction of Nitric Oxide Synthase, Shock, and Multiple Organ Failure. J Exp Med 188, 305–315.

Kennedy, A.D., Wardenburg, J.B., Gardner, D.J., Long, D., Whitney, A.R., Braughton, K.R., Schneewind, O., DeLeo, F.R., (2010). Targeting of alpha-hemolysin by active or passive immunization decreases severity of USA300 skin infections in a mouse model. J Infect Dis 202, 1050–1058.

Kenyon, C., (1988). The nematode Caenorhabditis elegans. Science 240, 1448–1453.

Kim, H.K., Missiakas, D., Schneewind, O., (2014). Mouse models for infectious diseases caused by Staphylococcus aureus. Journal of Immunological Methods, Analysis of Human Infectious Diseases in Murine Models 410, 88–99.

Kim, S.J., Chang, J., Rimal, B., Yang, H., Schaefer, J., (2018). Surface proteins and the formation of biofilms by Staphylococcus aureus. Biochimica et Biophysica Acta (BBA) - Biomembranes 1860, 749–756.

Kim, S.J., Chang, J., Singh, M., (2015). Peptidoglycan architecture of Gram-positive bacteria by solid-state NMR. Biochimica et Biophysica Acta (BBA) - Biomembranes, NMR Spectroscopy for Atomistic Views of Biomembranes and Cell Surfaces 1848, 350–362.

Kim, S.J., Singh, M., Preobrazhenskaya, M., Schaefer, J., (2013). Staphylococcus aureus Peptidoglycan Stem Packing by Rotational-Echo Double Resonance NMR Spectroscopy. Biochemistry 52, 3651–3659.

Kimpe, S.J.D., Kengatharan, M., Thiemermann, C., Vane, J.R., (1995). The cell wall components peptidoglycan and lipoteichoic acid from Staphylococcus aureus act in synergy to cause shock and multiple organ failure. PNAS 92, 10359–10363.

Kimura, Y., Hisano, Y., Kawahara, A., Higashijima, S., (2014). Efficient generation of knock-in transgenic zebrafish carrying reporter/driver genes by CRISPR/Cas9-mediated genome engineering. Sci Rep 4, 6545.

Kiser, K.B., Cantey-Kiser, J.M., Lee, J.C., (1999). Development and Characterization of a Staphylococcus aureus Nasal Colonization Model in Mice. Infect Immun 67, 5001–5006.

Klemsz, M.J., McKercher, S.R., Celada, A., Van Beveren, C., Maki, R.A., (1990). The macrophage and B cell-specific transcription factor PU.1 is related to the ets oncogene. Cell 61, 113–124.

Knop, J., Hanses, F., Leist, T., Archin, N.M., Buchholz, S., Gläsner, J., Gessner, A., Wege, A.K., (2015). Staphylococcus aureus Infection in Humanized Mice: A New Model to Study Pathogenicity Associated With Human Immune Response. J. Infect. Dis. 212, 435–444.

Kobayashi, S.D., Malachowa, N., DeLeo, F.R., (2015). Pathogenesis of Staphylococcus aureus Abscesses. Am J Pathol 185, 1518–1527.

Kohler, T., Weidenmaier, C., Peschel, A., (2009). Wall Teichoic Acid Protects Staphylococcus aureus against Antimicrobial Fatty Acids from Human Skin. Journal of Bacteriology 191, 4482–4484.

Komatsuzawa, H., Ohta, K., Labischinski, H., Sugai, M., Suginaka, H., (1999). Characterization of fmtA, a Gene That Modulates the Expression of Methicillin Resistance in Staphylococcus aureus. Antimicrobial Agents and Chemotherapy 43, 2121–2125.

Komatsuzawa, H., Ohta, K., Sugai, M., Fujiwara, T., Glanzmann, P., Berger-Bachi, B., Suginaka, H., (2000). Tn551-mediated insertional inactivation of the fmtB gene encoding a cell wall-associated

protein abolishes methicillin resistance in Staphylococcus aureus. Journal of Antimicrobial Chemotherapy 45, 421–431.

Komatsuzawa, H., Sugai, M., Nakashima, S., Yamada, S., Matsumoto, A., Oshida, T., Suginaka, H., (1997). Subcellular Localization of the Major Autolysin, ATL and Its Processed Proteins in Staphylococcus aureus. Microbiology and Immunology 41, 469–479.

Korgaonkar, A., Trivedi, U., Rumbaugh, K.P., Whiteley, M., (2013). Community surveillance enhances Pseudomonas aeruginosa virulence during polymicrobial infection. PNAS 110, 1059–1064.

Kouidmi, I., Levesque, R.C., Paradis-Bleau, C., (2014). The biology of Mur ligases as an antibacterial target. Molecular Microbiology 94, 242–253.

Koymans, K.J., Bisschop, A., Vughs, M.M., Van Kessel, K.P.M., De Haas, C.J.C., Van Strijp, J.A.G., (2016). Staphylococcal Superantigen-Like Protein 1 and 5 (SSL1 & SSL5) Limit Neutrophil Chemotaxis and Migration through MMP-Inhibition. International Journal of Molecular Sciences 17, 1072.

Koymans, K.J., Feitsma, L.J., Bisschop, A., Huizinga, E.G., van Strijp, J.A.G., de Haas, C.J.C., McCarthy, A.J., (2018). Molecular basis determining species specificity for TLR2 inhibition by staphylococcal superantigen-like protein 3 (SSL3). Vet. Res. 49, 115.

Kubica, M., Guzik, K., Koziel, J., Zarebski, M., Richter, W., Gajkowska, B., Golda, A., Maciag-Gudowska, A., Brix, K., Shaw, L., Foster, T., Potempa, J., (2008). A potential new pathway for Staphylococcus aureus dissemination: the silent survival of S. aureus phagocytosed by human monocyte-derived macrophages. PLoS ONE 3, e1409.

Kühner, D., Stahl, M., Demircioglu, D.D., Bertsche, U., (2014). From cells to muropeptide structures in 24 h: Peptidoglycan mapping by UPLC-MS. Sci Rep 4, 1–7.

Lawrence, T., (2009). The Nuclear Factor NF-κB Pathway in Inflammation. Cold Spring Harb Perspect Biol 1.

Lazarevic, V., Karamata, D., (1995). The tagGH operon of Bacillus subtilis 168 encodes a two-component ABC transporter involved in the metabolism of two wall teichoic acids. Molecular Microbiology 16, 345–355.

Lelouard, H., Henri, S., De Bovis, B., Mugnier, B., Chollat–Namy, A., Malissen, B., Méresse, S., Gorvel, J., (2010). Pathogenic Bacteria and Dead Cells Are Internalized by a Unique Subset of Peyer's Patch Dendritic Cells That Express Lysozyme. Gastroenterology 138, 173-184.e3.

292

Łeski, T.A., Tomasz, A., (2005). Role of penicillin-binding protein 2 (PBP2) in the antibiotic susceptibility and cell wall cross-linking of Staphylococcus aureus: evidence for the cooperative functioning of PBP2, PBP4, and PBP2A. J. Bacteriol. 187, 1815–1824.

Lioliou, E., Fechter, P., Caldelari, I., Jester, B.C., Dubrac, S., Helfer, A.-C., Boisset, S., Vandenesch, F., Romby, P., Geissmann, T., (2016). Various checkpoints prevent the synthesis of Staphylococcus aureus peptidoglycan hydrolase LytM in the stationary growth phase. RNA Biology 13, 427–440.

Liu, Z.-Q., Deng, G.-M., Foster, S., Tarkowski, A., (2001). Staphylococcal peptidoglycans induce arthritis. Arthritis Research 3, 375–380.

Lo, C.-W., Lai, Y.-K., Liu, Y.-T., Gallo, R.L., Huang, C.-M., (2011). Staphylococcus aureus Hijacks a Skin Commensal to Intensify Its Virulence: Immunization Targeting β-Hemolysin and CAMP Factor. J Invest Dermatol 131, 401–409.

Löffler, B., Hussain, M., Grundmeier, M., Brück, M., Holzinger, D., Varga, G., Roth, J., Kahl, B.C., Proctor, R.A., Peters, G., (2010). Staphylococcus aureus Panton-Valentine Leukocidin Is a Very Potent Cytotoxic Factor for Human Neutrophils. PLOS Pathogens 6, e1000715.

Loskill, P., Pereira, P.M., Jung, P., Bischoff, M., Herrmann, M., Pinho, M.G., Jacobs, K., (2014). Reduction of the Peptidoglycan Crosslinking Causes a Decrease in Stiffness of the Staphylococcus aureus Cell Envelope. Biophysical Journal 107, 1082–1089.

Lovering, A.L., Safadi, S.S., Strynadka, N.C.J., (2012). Structural Perspective of Peptidoglycan Biosynthesis and Assembly. Annual Review of Biochemistry 81, 451–478.

Lowy, F.D., (2003). Antimicrobial resistance: the example of Staphylococcus aureus. J. Clin. Invest. 111, 1265–1273.

Loza-Correa, M., Ayala, J.A., Perelman, I., Hubbard, K., Kalab, M., Yi, Q.-L., Taha, M., de Pedro, M.A., Ramirez-Arcos, S., (2019). The peptidoglycan and biofilm matrix of Staphylococcus epidermidis undergo structural changes when exposed to human platelets. PLoS One 14.

Lund, L.D., Ingmer, H., Frøkiær, H., (2016). D-Alanylation of Teichoic Acids and Loss of Poly-N-Acetyl Glucosamine in Staphylococcus aureus during Exponential Growth Phase Enhance IL-12 Production in Murine Dendritic Cells. PLoS One 11.

Lund, V.A., Wacnik, K., Turner, R.D., Cotterell, B.E., Walther, C.G., Fenn, S.J., Grein, F., Wollman, A.J., Leake, M.C., Olivier, N., Cadby, A., Mesnage, S., Jones, S., Foster, S.J., (2018). Molecular coordination of Staphylococcus aureus cell division. eLife 7, e32057.

Ma, D., Liu, F., (2015). Genome Editing and Its Applications in Model Organisms. Genomics Proteomics Bioinformatics 13, 336–344.

Macheboeuf, P., Contreras-Martel, C., Job, V., Dideberg, O., Dessen, A., (2006). Penicillin binding proteins: key players in bacterial cell cycle and drug resistance processes. FEMS Microbiol. Rev. 30, 673–691.

Madison, B., (2001). Application of stains in clinical microbiology. Biotechnic & Histochemistry 76, 119–125.

Mahapatra, S., Crick, D.C., Brennan, P.J., (2000). Comparison of the UDP-N-Acetylmuramate:l-Alanine Ligase Enzymes from Mycobacterium tuberculosis andMycobacterium leprae. Journal of Bacteriology 182, 6827–6830.

Mainiero, M., Goerke, C., Geiger, T., Gonser, C., Herbert, S., Wolz, C., (2010). Differential Target Gene Activation by the Staphylococcus aureus Two-Component System saeRS. Journal of Bacteriology 192, 613–623.

Mainous, A.G., Hueston, W.J., Everett, C.J., Diaz, V.A., (2006). Nasal Carriage of Staphylococcus aureus and Methicillin-Resistant S aureus in the United States, 2001–2002. Ann Fam Med 4, 132–137.

Malachowa, N., Kobayashi, S.D., Braughton, K.R., DeLeo, F.R., (2013). Mouse Model of Staphylococcus aureus Skin Infection, in: Allen, I.C. (Ed.), Mouse Models of Innate Immunity: Methods and Protocols, Methods in Molecular Biology. Humana Press, Totowa, NJ, pp. 109–116.

Malachowa, N., Kobayashi, S.D., Porter, A.R., Braughton, K.R., Scott, D.P., Gardner, D.J., Missiakas, D.M., Schneewind, O., DeLeo, F.R., (2016). Contribution of Staphylococcus aureus Coagulases and Clumping Factor A to Abscess Formation in a Rabbit Model of Skin and Soft Tissue Infection. PLOS ONE 11, e0158293.

Malanovic, N., Lohner, K., (2016). Gram-positive bacterial cell envelopes: The impact on the activity of antimicrobial peptides. Biochimica et Biophysica Acta (BBA) - Biomembranes, Antimicrobial peptides, cell membrane and microbial surface interaction 1858, 936–946.

Mani, N., Tobin, P., Jayaswal, R.K., (1993). Isolation and characterization of autolysis-defective mutants of Staphylococcus aureus created by Tn917-lacZ mutagenesis. Journal of Bacteriology 175, 1493–1499.

Martin, F.J., Gomez, M.I., Wetzel, D.M., Memmi, G., O'Seaghdha, M., Soong, G., Schindler, C., Prince, A., (2009). Staphylococcus aureus activates type I IFN signaling in mice and humans through the Xr repeated sequences of protein A. J Clin Invest 119, 1931–1939.

Martinon, F., Tschopp, J., (2005). NLRs join TLRs as innate sensors of pathogens. Trends in Immunology 26, 447–454.

Matias, V.R.F., Beveridge, T.J., (2007). Cryo-electron microscopy of cell division in Staphylococcus aureus reveals a mid-zone between nascent cross walls. Molecular Microbiology 64, 195–206.

Matias, V.R.F., Beveridge, T.J., (2006). Native Cell Wall Organization Shown by Cryo-Electron Microscopy Confirms the Existence of a Periplasmic Space in Staphylococcus aureus. Journal of Bacteriology 188, 1011–1021.

Mazmanian, S.K., Liu, G., Jensen, E.R., Lenoy, E., Schneewind, O., (2000). Staphylococcus aureus sortase mutants defective in the display of surface proteins and in the pathogenesis of animal infections. Proceedings of the National Academy of Sciences 97, 5510–5515.

Mazmanian, S.K., Skaar, E.P., Gaspar, A.H., Humayun, M., Gornicki, P., Jelenska, J., Joachmiak, A., Missiakas, D.M., Schneewind, O., (2003). Passage of Heme-Iron Across the Envelope of Staphylococcus aureus. Science 299, 906–909.

McAdow, M., Kim, H.K., Dedent, A.C., Hendrickx, A.P.A., Schneewind, O., Missiakas, D.M., (2011). Preventing Staphylococcus aureus sepsis through the inhibition of its agglutination in blood. PLoS Pathog. 7, e1002307.

McCarthy, H., Waters, E.M., Bose, J.L., Foster, S., Bayles, K.W., O'Neill, E., Fey, P.D., O'Gara, J.P., (2016). The major autolysin is redundant for Staphylococcus aureus USA300 LAC JE2 virulence in a murine device-related infection model. FEMS Microbiol Lett 363.

McVicker, G., Prajsnar, T.K., Williams, A., Wagner, N.L., Boots, M., Renshaw, S.A., Foster, S.J., (2014). Clonal Expansion during Staphylococcus aureus Infection Dynamics Reveals the Effect of Antibiotic Intervention. PLoS Pathog 10.

Medzhitov, R., Preston-Hurlburt, P., Janeway, C.A., (1997). A human homologue of the Drosophila Toll protein signals activation of adaptive immunity. Nature 388, 394–397.

Memmi, G., Filipe, S.R., Pinho, M.G., Fu, Z., Cheung, A., (2008). Staphylococcus aureus PBP4 is essential for beta-lactam resistance in community-acquired methicillin-resistant strains. Antimicrob. Agents Chemother. 52, 3955–3966.

Mercer, K.L.N., Weiss, D.S., (2002). The Escherichia coli cell division protein FtsW is required to recruit its cognate transpeptidase, FtsI (PBP3), to the division site. J. Bacteriol. 184, 904–912.

Merle, N.S., Church, S.E., Fremeaux-Bacchi, V., Roumenina, L.T., (2015). Complement System Part I - Molecular Mechanisms of Activation and Regulation. Front Immunol 6, 262.

Misawa, Y., Kelley, K.A., Wang, X., Wang, L., Park, W.B., Birtel, J., Saslowsky, D., Lee, J.C., (2015). Staphylococcus aureus Colonization of the Mouse Gastrointestinal Tract Is Modulated by Wall Teichoic Acid, Capsule, and Surface Proteins. PLoS Pathog 11.

Miyata, S., Kozuka, S., Yasuda, Y., Chen, Y., Moriyama, R., Tochikubo, K., Makino, S., (1997). Localization of germination-specific spore-lytic enzymes in Clostridium perfringens S40 spores detected by immunoelectron microscopy. FEMS Microbiol Lett 152, 243–247.

Mohammad, M., Na, M., Welin, A., Svensson, M.N.D., Ali, A., Jin, T., Pullerits, R., (2016). RAGE Deficiency Impairs Bacterial Clearance in Murine Staphylococcal Sepsis, but Has No Significant Impact on Staphylococcal Septic Arthritis. PLOS ONE 11, e0167287.

Mohammadi, T., van Dam, V., Sijbrandi, R., Vernet, T., Zapun, A., Bouhss, A., Diepeveen-de Bruin, M., Nguyen-Distèche, M., de Kruijff, B., Breukink, E., (2011). Identification of FtsW as a transporter of lipid-linked cell wall precursors across the membrane. EMBO J. 30, 1425–1432.

Monk, I.R., Shaikh, N., Begg, S.L., Gajdiss, M., Sharkey, L.K.R., Lee, J.Y.H., Pidot, S.J., Seemann, T., Kuiper, M., Winnen, B., Hvorup, R., Collins, B.M., Bierbaum, G., Udagedara, S.R., Morey, J.R., Pulyani, N., Howden, B.P., Maher, M.J., McDevitt, C.A., King, G.F., Stinear, T.P., (2019). Zinc-binding to the cytoplasmic PAS domain regulates the essential WalK histidine kinase of Staphylococcus aureus. Nat Commun 10, 1–13.

Montanaro, L., Speziale, P., Campoccia, D., Ravaioli, S., Cangini, I., Pietrocola, G., Giannini, S., Arciola, C.R., (2011). Scenery of Staphylococcus implant infections in orthopedics. Future Microbiology 6, 1329–1349.

Monteiro, J.M., Fernandes, P.B., Vaz, F., Pereira, A.R., Tavares, A.C., Ferreira, M.T., Pereira, P.M., Veiga, H., Kuru, E., VanNieuwenhze, M.S., Brun, Y.V., Filipe, S.R., Pinho, M.G., (2015). Cell shape dynamics during the staphylococcal cell cycle. Nat Commun 6, 1–12.

Morath, S., Stadelmaier, A., Geyer, A., Schmidt, R.R., Hartung, T., (2002). Synthetic Lipoteichoic Acid from Staphylococcus aureus Is a Potent Stimulus of Cytokine Release. J Exp Med 195, 1635–1640.

Morris, E.K., Caruso, T., Buscot, F., Fischer, M., Hancock, C., Maier, T.S., Meiners, T., Müller, C., Obermaier, E., Prati, D., Socher, S.A., Sonnemann, I., Wäschke, N., Wubet, T., Wurst, S., Rillig, M.C., (2014). Choosing and using diversity indices: insights for ecological applications from the German Biodiversity Exploratories. Ecology and Evolution 4, 3514–3524.

Moynihan, P.J., Sychantha, D., Clarke, A.J., (2014). Chemical biology of peptidoglycan acetylation and deacetylation. Bioorganic Chemistry 54, 44–50.

Mulder, C.P.H., Bazeley-White, E., Dimitrakopoulos, P.G., Hector, A., Scherer-Lorenzen, M., Schmid, B., (2004). Species evenness and productivity in experimental plant communities. Oikos 107, 50–63.

Müller, S., Wolf, A.J., Iliev, I.D., Berg, B.L., Underhill, D.M., Liu, G.Y., (2015). Poorly Cross-Linked Peptidoglycan in MRSA Due to mecA Induction Activates the Inflammasome and Exacerbates Immunopathology. Cell Host Microbe 18, 604–612.

Münch, D., Roemer, T., Lee, S.H., Engeser, M., Sahl, H.G., Schneider, T., (2012). Identification and in vitro Analysis of the GatD/MurT Enzyme-Complex Catalyzing Lipid II Amidation in Staphylococcus aureus. PLOS Pathogens 8, e1002509.

Muñoz-Planillo, R., Franchi, L., Miller, L.S., Núñez, G., (2009). A Critical Role for Hemolysins and Bacterial Lipoproteins in Staphylococcus aureus-Induced Activation of the Nlrp3 Inflammasome. J Immunol 183, 3942–3948.

Nanninga, N., (1991). Cell division and peptidoglycan assembly in Eschenchia coli. Molecular Microbiology 5, 791–795.

Navarre, W.W., Schneewind, O., (1999). Surface Proteins of Gram-Positive Bacteria and Mechanisms of Their Targeting to the Cell Wall Envelope. Microbiol. Mol. Biol. Rev. 63, 174–229.

Needham, A.J., Kibart, M., Crossley, H., Ingham, P.W., Foster, S.J., (2004). Drosophila melanogaster as a model host for Staphylococcus aureus infection. Microbiology, 150, 2347–2355.

Neuhaus, F.C., Baddiley, J., (2003). A Continuum of Anionic Charge: Structures and Functions of d-Alanyl-Teichoic Acids in Gram-Positive Bacteria. Microbiol. Mol. Biol. Rev. 67, 686–723.

Nikaido, H., Vaara, M., (1985). Molecular basis of bacterial outer membrane permeability. Microbiol Rev 49, 1–32.

Ohlsen, K., Donat, S., (2010). The impact of serine/threonine phosphorylation in Staphylococcus aureus. International Journal of Medical Microbiology, Pathophysiology of staphylococci in the post-genomic era 300, 137–141.

Okonog, K., Noji, Y., Nakao, M., Imada, A., (1995). The possible physiological roles of penicillin-binding proteins of methicillin-susceptible and methicillin-resistantStaphylococcus aureus. J Infect Chemother 1, 50–58.

Oku, Y., Kurokawa, K., Matsuo, M., Yamada, S., Lee, B.-L., Sekimizu, K., (2009). Pleiotropic Roles of Polyglycerolphosphate Synthase of Lipoteichoic Acid in Growth of Staphylococcus aureus Cells. Journal of Bacteriology 191, 141–151.

Oshida, T., Sugai, M., Komatsuzawa, H., Hong, Y.M., Suginaka, H., Tomasz, A., (1995). A Staphylococcus aureus autolysin that has an N-acetylmuramoyl-L-alanine amidase domain and an endo-beta-N-acetylglucosaminidase domain: cloning, sequence analysis, and characterization. PNAS 92, 285–289.

Ozinsky, A., Underhill, D.M., Fontenot, J.D., Hajjar, A.M., Smith, K.D., Wilson, C.B., Schroeder, L., Aderem, A., (2000). The repertoire for pattern recognition of pathogens by the innate immune system is defined by cooperation between Toll-like receptors. PNAS 97, 13766–13771.

Park, B., Nizet, V., Liu, G.Y., (2008). Role of Staphylococcus aureus Catalase in Niche Competition against Streptococcus pneumoniae. Journal of Bacteriology 190, 2275–2278.

Pasquina-Lemonche, L., Burns, J., Turner, R.D., Kumar, S., Tank, R., Mullin, N., Wilson, J.S., Chakrabarti, B., Bullough, P.A., Foster, S.J., Hobbs, J.K., (2020). The architecture of the Gram-positive bacterial cell wall. Nature 582, 294–297.

Pasztor, L., Ziebandt, A.-K., Nega, M., Schlag, M., Haase, S., Franz-Wachtel, M., Madlung, J., Nordheim, A., Heinrichs, D.E., Goetz, F., (2010). The staphylococcal major autolysin (ATL) is involved in excretion of cytoplasmic proteins. J. Biol. Chem. jbc.M110.167312.

Patti, G.J., Chen, J., Schaefer, J., Gross, M.L., (2008). Characterization of structural variations in the peptidoglycan of vancomycin-susceptible Enterococcus faecium: understanding glycopeptide-antibiotic binding sites using mass spectrometry. J. Am. Soc. Mass Spectrom. 19, 1467–1475.

Pazos, M., Peters, K., Vollmer, W., (2017). Robust peptidoglycan growth by dynamic and variable multi-protein complexes. Current Opinion in Microbiology, Cell regulation 36, 55–61.

Percy, M.G., Gründling, A., (2014). Lipoteichoic Acid Synthesis and Function in Gram-Positive Bacteria. Annual Review of Microbiology 68, 81–100.

Pereira, S.F.F., Henriques, A.O., Pinho, M.G., de Lencastre, H., Tomasz, A., (2009). Evidence for a dual role of PBP1 in the cell division and cell separation of Staphylococcus aureus. Mol Microbiol 72, 1423–1437.

Pereira, S.F.F., Henriques, A.O., Pinho, M.G., de Lencastre, H., Tomasz, A., (2007). Role of PBP1 in cell division of Staphylococcus aureus. J. Bacteriol. 189, 3525–3531.

Perkins, H.R., (1971). Homoserine and diaminobutyric acid in the mucopeptide-precursor-nucleotides and cell walls of some plant-pathogenic corynebacteria. Biochem J 121, 417–423.

Peterson, P.K., Wilkinson, B.J., Kim, Y., Schmeling, D., Douglas, S.D., Quie, P.G., Verhoef, J., (1978). The key role of peptidoglycan in the opsonization of Staphylococcus aureus. J Clin Invest 61, 597–609.

Pinho, M.G., Errington, J., (2003). Dispersed mode of Staphylococcus aureus cell wall synthesis in the absence of the division machinery. Mol. Microbiol. 50, 871–881.

Pinho, M.G., Filipe, S.R., de Lencastre, H., Tomasz, A., (2001a). Complementation of the essential peptidoglycan transpeptidase function of penicillin-binding protein 2 (PBP2) by the drug resistance protein PBP2A in Staphylococcus aureus. J. Bacteriol. 183, 6525–6531.

298

Pinho, M.G., Filipe, S.R., de Lencastre, H., Tomasz, A., (2001b). Complementation of the Essential Peptidoglycan Transpeptidase Function of Penicillin-Binding Protein 2 (PBP2) by the Drug Resistance Protein PBP2A in Staphylococcus aureus. Journal of Bacteriology 183, 6525–6531.

Pinho, M.G., Kjos, M., Veening, J.-W., (2013). How to get (a)round: mechanisms controlling growth and division of coccoid bacteria. Nat. Rev. Microbiol. 11, 601–614.

Pinho, M.G., Lencastre, H. de, Tomasz, A., (2001c). An acquired and a native penicillin-binding protein cooperate in building the cell wall of drug-resistant staphylococci. PNAS 98, 10886–10891.

Pinho, M.G., Lencastre, H. de, Tomasz, A., (2000). Cloning, Characterization, and Inactivation of the Gene pbpC, Encoding Penicillin-Binding Protein 3 ofStaphylococcus aureus. Journal of Bacteriology 182, 1074–1079.

Pollitt, E.J.G., Szkuta, P.T., Burns, N., Foster, S.J., (2018). Staphylococcus aureus infection dynamics. PLOS Pathogens 14, e1007112.

Pollitt, E.J.G., West, S.A., Crusz, S.A., Burton-Chellew, M.N., Diggle, S.P., (2014). Cooperation, Quorum Sensing, and Evolution of Virulence in Staphylococcus aureus. Infection and Immunity 82, 1045–1051.

Popham, Helin, J., Costello, C.E., Setlow, P., (1996a). Analysis of the peptidoglycan structure of Bacillus subtilis endospores. Journal of Bacteriology 178, 6451–6458.

Popham, Helin, J., Costello, C.E., Setlow, P., (1996b). Muramic lactam in peptidoglycan of Bacillus subtilis spores is required for spore outgrowth but not for spore dehydration or heat resistance. PNAS 93, 15405–15410.

Porayath, C., Suresh, M.K., Biswas, R., Nair, B.G., Mishra, N., Pal, S., (2018). Autolysin mediated adherence of Staphylococcus aureus with Fibronectin, Gelatin and Heparin. International Journal of Biological Macromolecules, Biological Macromolecules for Delivery, Imaging & Therapy (BMDIT-2018) 110, 179–184.

Portillo, F.G., Pucciarelli, M.G., (2012). Remodeling of the Listeria monocytogenes cell wall inside eukaryotic cells. Communicative & Integrative Biology 5, 160–162.

Prajsnar, T.K., Cunliffe, V.T., Foster, S.J., Renshaw, S.A., (2008). A novel vertebrate model of Staphylococcus aureus infection reveals phagocyte-dependent resistance of zebrafish to non-host specialized pathogens. Cellular Microbiology 10, 2312–2325.

Prajsnar, T.K., Hamilton, R., Garcia-Lara, J., McVicker, G., Williams, A., Boots, M., Foster, S.J., Renshaw, S.A., (2012). A privileged intraphagocyte niche is responsible for disseminated infection of Staphylococcus aureus in a zebrafish model. Cellular Microbiology 14, 1600–1619.

Prajsnar, T.K., Renshaw, S.A., Ogryzko, N.V., Foster, S.J., Serror, P., Mesnage, S., (2013). Zebrafish as a Novel Vertebrate Model To Dissect Enterococcal Pathogenesis. Infection and Immunity 81, 4271–4279.

Prajsnar, T.K., Serba, J.J., Dekker, B.M., Gibson, J.F., Masud, S., Fleming, A., Johnston, S.A., Renshaw, S.A., Meijer, A.H., (2020). The autophagic response to Staphylococcus aureus provides an intracellular niche in neutrophils. Autophagy 1–15.

Prince, A., Wang, H., Kitur, K., Parker, D., (2017). Humanized Mice Exhibit Increased Susceptibility to Staphylococcus aureus Pneumonia. J Infect Dis 215, 1386–1395.

Proctor, R., (2015). Recent developments for Staphylococcus aureus vaccines: clinical and basic science challenges. eCM 30, 315–326.

Proctor, R.A., (2012). Challenges for a Universal Staphylococcus aureus Vaccine. Clin Infect Dis 54, 1179–1186.

Qamar, A., Golemi-Kotra, D., (2012). Dual Roles of FmtA in Staphylococcus aureus Cell Wall Biosynthesis and Autolysis. Antimicrobial Agents and Chemotherapy 56, 3797–3805.

Quereda, J.J., Portillo, F.G., Pucciarelli, M.G., (2016). Listeria monocytogenes remodels the cell surface in the blood-stage. Environmental Microbiology Reports 8, 641–648.

Quintela, J.C., Pedro, M.A.D., Zo¨llner, P., Allmaier, G., Portillo, F.G., (1997). Peptidoglycan structure of Salmonella typhimurium growing within cultured mammalian cells. Molecular Microbiology 23, 693–704.

Radkov, A.D., Hsu, Y.-P., Booher, G., VanNieuwenhze, M.S., (2018). Imaging Bacterial Cell Wall Biosynthesis. Annu Rev Biochem 87, 991–1014.

Raetz, C.R.H., Whitfield, C., (2002). Lipopolysaccharide endotoxins. Annu. Rev. Biochem. 71, 635–700.

Ragland, S.A., Criss, A.K., (2017). From bacterial killing to immune modulation: Recent insights into the functions of lysozyme. PLOS Pathogens 13, e1006512.

Rahman, M.M., Hunter, H.N., Prova, S., Verma, V., Qamar, A., Golemi-Kotra, D., (2016). The Staphylococcus aureus Methicillin Resistance Factor FmtA Is a d-Amino Esterase That Acts on Teichoic Acids. mBio 7.

Rajagopal, M., Walker, S., (2017). Envelope Structures of Gram-Positive Bacteria. Curr. Top. Microbiol. Immunol. 404, 1–44.

Rammelkamp, C.H., Maxon, T., (1942). Resistance of Staphylococcus aureus to the Action of Penicillin. Proceedings of the Society for Experimental Biology and Medicine 51, 386–389.

Rauch, S., DeDent, A.C., Kim, H.K., Bubeck Wardenburg, J., Missiakas, D.M., Schneewind, O., (2012). Abscess formation and alpha-hemolysin induced toxicity in a mouse model of Staphylococcus aureus peritoneal infection. Infect. Immun. 80, 3721–3732.

Reddy, P.N., Srirama, K., Dirisala, V.R., (2017). An Update on Clinical Burden, Diagnostic Tools, and Therapeutic Options of Staphylococcus aureus. Infect Dis (Auckl) 10.

Reed, P., Atilano, M.L., Alves, R., Hoiczyk, E., Sher, X., Reichmann, N.T., Pereira, P.M., Roemer, T., Filipe, S.R., Pereira-Leal, J.B., Ligoxygakis, P., Pinho, M.G., (2015). Staphylococcus aureus Survives with a Minimal Peptidoglycan Synthesis Machine but Sacrifices Virulence and Antibiotic Resistance. PLoS Pathog. 11, e1004891.

Reed, P., Veiga, H., Jorge, A.M., Terrak, M., Pinho, M.G., (2011). Monofunctional Transglycosylases Are Not Essential for Staphylococcus aureus Cell Wall Synthesis. Journal of Bacteriology 193, 2549–2556.

Reichmann, N.T., Gründling, A., (2011). Location, synthesis and function of glycolipids and polyglycerolphosphate lipoteichoic acid in Gram-positive bacteria of the phylum Firmicutes. FEMS Microbiol Lett 319, 97–105.

Reichmann, N.T., Tavares, A.C., Saraiva, B.M., Jousselin, A., Reed, P., Pereira, A.R., Monteiro, J.M., Sobral, R.G., VanNieuwenhze, M.S., Fernandes, F., Pinho, M.G., (2019). SEDS–bPBP pairs direct lateral and septal peptidoglycan synthesis in Staphylococcus aureus. Nat Microbiol 4, 1368–1377.

Reizner, W., Hunter, J.G., O'Malley, N.T., Southgate, R.D., Schwarz, E.M., Kates, S.L., (2014). A systematic review of animal models for Staphylococcus aureus osteomyelitis. Eur Cell Mater 27, 196–212.

Reynolds, E.S., (1963). THE USE OF LEAD CITRATE AT HIGH pH AS AN ELECTRON-OPAQUE STAIN IN ELECTRON MICROSCOPY. J Cell Biol 17, 208–212.

Rico-Pérez, G., Pezza, A., Pucciarelli, M.G., Pedro, M.A. de, Soncini, F.C., Portillo, F.G., (2016). A novel peptidoglycan D,L-endopeptidase induced by Salmonella inside eukaryotic cells contributes to virulence. Molecular Microbiology 99, 546–556.

Rieux, V., Carbon, C., Azoulay-Dupuis, E., (2001). Complex Relationship between Acquisition of β-Lactam Resistance and Loss of Virulence in Streptococcus pneumoniae. J Infect Dis 184, 66–72.

Rivera, L., López-Patiño, M.A., Milton, D.L., Nieto, T.P., Farto, R., (2015). Effective qPCR methodology to quantify the expression of virulence genes in Aeromonas salmonicida subsp. salmonicida. J. Appl. Microbiol. 118, 792–802.

Rohrer, S., Berger-Bächi, B., (2003). FemABX Peptidyl Transferases: a Link between Branched-Chain Cell Wall Peptide Formation and β-Lactam Resistance in Gram-Positive Cocci. Antimicrobial Agents and Chemotherapy 47, 837–846.

Rojas, E.R., Billings, G., Odermatt, P.D., Auer, G.K., Zhu, L., Miguel, A., Chang, F., Weibel, D.B., Theriot, J.A., Huang, K.C., (2018). The outer membrane is an essential load-bearing element in Gram-negative bacteria. Nature 559, 617–621.

Romaniuk, J.A.H., Cegelski, L., (2015). Bacterial cell wall composition and the influence of antibiotics by cell-wall and whole-cell NMR. Philos Trans R Soc Lond B Biol Sci 370.

Rooijakkers, S.H.M., van Strijp, J.A.G., (2007). Bacterial complement evasion. Mol. Immunol. 44, 23–32.

Rooijen, N.V., Sanders, A., (1994). Liposome mediated depletion of macrophages: mechanism of action, preparation of liposomes and applications. Journal of Immunological Methods 174, 83–93.

Ruiz, N., Kahne, D., Silhavy, T.J., (2006). Advances in understanding bacterial outer-membrane biogenesis. Nat Rev Microbiol 4, 57–66.

Russo, T.A., MacDonald, U., Beanan, J.M., Olson, R., MacDonald, I.J., Sauberan, S.L., Luke, L.W., Umland, T.C., (2009). Penicillin-binding protein 7/8 contributes to the survival of Acinetobacter baumannii in vitro and in vivo. J Infect Dis 199, 513–521.

Sabath, L.D., (1982). Mechanisms of resistance to beta-lactam antibiotics in strains of Staphylococcus aureus. Ann. Intern. Med. 97, 339–344.

Salamaga, B., Prajsnar, T.K., Jareño-Martinez, A., Willemse, J., Bewley, M.A., Chau, F., Belkacem, T.B., Meijer, A.H., Dockrell, D.H., Renshaw, S.A., Mesnage, S., (2017). Bacterial size matters: Multiple mechanisms controlling septum cleavage and diplococcus formation are critical for the virulence of the opportunistic pathogen Enterococcus faecalis. PLOS Pathogens 13, e1006526.

Salgado-Pabón, W., Schlievert, P.M., (2014). Models matter: the search for an effective Staphylococcus aureus vaccine. Nat Rev Microbiol 12, 585–591.

Saralahti, A., Piippo, H., Parikka, M., Henriques-Normark, B., Rämet, M., Rounioja, S., (2014). Adult zebrafish model for pneumococcal pathogenesis. Developmental & Comparative Immunology 42, 345–353.

Sauvage, E., Kerff, F., Terrak, M., Ayala, J.A., Charlier, P., (2008). The penicillin-binding proteins: structure and role in peptidoglycan biosynthesis. FEMS Microbiol Rev 32, 234–258.

Schade, J., Weidenmaier, C., (2016). Cell wall glycopolymers of Firmicutes and their role as nonprotein adhesins. FEBS Letters 590, 3758–3771.

Scheffers, D.-J., (2005). Dynamic localization of penicillin-binding proteins during spore development in Bacillus subtilis. Microbiology (Reading, Engl.) 151, 999–1012.

Scheffers, D.-J., Tol, M.B., (2015). LipidII: Just Another Brick in the Wall? PLoS Pathog 11.

Schindelin, J., Arganda-Carreras, I., Frise, E., Kaynig, V., Longair, M., Pietzsch, T., Preibisch, S., Rueden, C., Saalfeld, S., Schmid, B., Tinevez, J.-Y., White, D.J., Hartenstein, V., Eliceiri, K., Tomancak, P., Cardona, A., (2012). Fiji: an open-source platform for biological-image analysis. Nat Methods 9, 676–682.

Schindler, C.A., Schuhardt, V.T., (1965). Purification and properties of lysostaphin—A lytic agent for Staphylococcus aureus. Biochimica et Biophysica Acta (BBA) - General Subjects 97, 242–250.

Schindler, C.A., Schuhardt, V.T., (1964). LYSOSTAPHIN: A NEW BACTERIOLYTIC AGENT FOR THE STAPHYLOCOCCUS. Proc Natl Acad Sci U S A 51, 414–421.

Schleifer, K.H., Kandler, O., (1972). Peptidoglycan types of bacterial cell walls and their taxonomic implications. Bacteriol Rev 36, 407–477.

Schneewind, O., Missiakas, D.M., (2012). Protein secretion and surface display in Gram-positive bacteria. Philosophical Transactions of the Royal Society B: Biological Sciences 367, 1123–1139.

Schneider, T., Senn, M.M., Berger-Bächi, B., Tossi, A., Sahl, H.-G., Wiedemann, I., (2004). In vitro assembly of a complete, pentaglycine interpeptide bridge containing cell wall precursor (lipid II-Gly5) of Staphylococcus aureus. Molecular Microbiology 53, 675–685.

Schulz, D., Grumann, D., Trübe, P., Pritchett-Corning, K., Johnson, S., Reppschläger, K., Gumz, J., Sundaramoorthy, N., Michalik, S., Berg, S., van den Brandt, J., Fister, R., Monecke, S., Uy, B., Schmidt, F., Bröker, B.M., Wiles, S., Holtfreter, S., (2017). Laboratory Mice Are Frequently Colonized with Staphylococcus aureus and Mount a Systemic Immune Response—Note of Caution for In vivo Infection Experiments. Front Cell Infect Microbiol 7.

Serruto, D., Rappuoli, R., Scarselli, M., Gros, P., Strijp, J.A.G. van, (2010). Molecular mechanisms of complement evasion: learning from staphylococci and meningococci. Nat Rev Microbiol 8, 393–399.

Severin, A., Tabei, K., Tenover, F., Chung, M., Clarke, N., Tomasz, A., (2004). High Level Oxacillin and Vancomycin Resistance and Altered Cell Wall Composition in Staphylococcus aureus Carrying the Staphylococcal mecA and the Enterococcal vanA Gene Complex. J. Biol. Chem. 279, 3398–3407.

Shimada, T., Park, B.G., Wolf, A.J., Brikos, C., Goodridge, H.S., Becker, C.A., Reyes, C.N., Miao, E.A., Aderem, A., Götz, F., Liu, G.Y., Underhill, D.M., (2010). Staphylococcus aureus Evades Lysozyme-Based Peptidoglycan Digestion that Links Phagocytosis, Inflammasome Activation, and IL-1β Secretion. Cell Host & Microbe 7, 38–49.

Shwartz, A., Goessling, W., Yin, C., (2019). Macrophages in Zebrafish Models of Liver Diseases. Front. Immunol. 10.

Sifri, C.D., Begun, J., Ausubel, F.M., Calderwood, S.B., (2003). Caenorhabditis elegans as a Model Host for Staphylococcus aureus Pathogenesis. Infection and Immunity 71, 2208–2217.

Silhavy, T.J., Kahne, D., Walker, S., (2010). The Bacterial Cell Envelope. Cold Spring Harb Perspect Biol 2, a000414.

Smith, D.J., (2008). Ultimate resolution in the electron microscope? Materials Today 11, 30–38.

Snowden, M.A., Perkins, H.R., (1990). Peptidoglycan cross-linking in Staphylococcus aureus. European Journal of Biochemistry 191, 373–377.

Sobral, R., Tomasz, A., (2019). The Staphylococcal Cell Wall 21.

Soldo, B., Lazarevic, V., Karamata, D., (2002). tagO is involved in the synthesis of all anionic cell-wall polymers in Bacillus subtilis 168aaThe EMBL accession number for the nucleotide sequence reported in this paper is AJ004803. Microbiology, 148, 2079–2087.

Stapleton, M.R., Horsburgh, M.J., Hayhurst, E.J., Wright, L., Jonsson, I.-M., Tarkowski, A., Kokai-Kun, J.F., Mond, J.J., Foster, S.J., (2007). Characterization of IsaA and SceD, Two Putative Lytic Transglycosylases of Staphylococcus aureus. Journal of Bacteriology 189, 7316–7325.

Steele, V.R., Bottomley, A.L., Garcia-Lara, J., Kasturiarachchi, J., Foster, S.J., (2011). Multiple essential roles for EzrA in cell division of Staphylococcus aureus. Molecular Microbiology 80, 542–555.

Strandén, A.M., Ehlert, K., Labischinski, H., Berger-Bächi, B., (1997). Cell wall monoglycine cross-bridges and methicillin hypersusceptibility in a femAB null mutant of methicillin-resistant Staphylococcus aureus. Journal of Bacteriology 179, 9–16.

Stryjewski, M.E., Corey, G.R., (2014). Methicillin-Resistant Staphylococcus aureus: An Evolving Pathogen. Clin Infect Dis 58, S10–S19.

Su, F., Juarez, M.A., Cooke, C.L., Lapointe, L., Shavit, J.A., Yamaoka, J.S., Lyons, S.E., (2007). Differential regulation of primitive myelopoiesis in the zebrafish by Spi-1/Pu.1 and C/ebp1. Zebrafish 4, 187–199.

Swaim, L.E., Connolly, L.E., Volkman, H.E., Humbert, O., Born, D.E., Ramakrishnan, L., (2006). Mycobacterium marinum Infection of Adult Zebrafish Causes Caseating Granulomatous Tuberculosis and Is Moderated by Adaptive Immunity. Infection and Immunity 74, 6108–6117.

Sycuro, L.K., Pincus, Z., Gutierrez, K.D., Biboy, J., Stern, C.A., Vollmer, W., Salama, N.R., (2010). Peptidoglycan Crosslinking Relaxation Promotes Helicobacter pylori's Helical Shape and Stomach Colonization. Cell 141, 822–833.

Szurmant, H., Mohan, M.A., Imus, P.M., Hoch, J.A., (2007). YycH and YycI Interact To Regulate the Essential YycFG Two-Component System in Bacillus subtilis. J Bacteriol 189, 3280–3289.

Taguchi, A., Welsh, M.A., Marmont, L.S., Lee, W., Sjodt, M., Kruse, A.C., Kahne, D., Bernhardt, T.G., Walker, S., (2019). FtsW is a peptidoglycan polymerase that is functional only in complex with its cognate penicillin-binding protein. Nat Microbiol 4, 587–594.

Takahashi, J., Komatsuzawa, H., Yamada, S., Nishida, T., Labischinski, H., Fujiwara, T., Ohara, M., Yamagishi, J., Sugai, M., (2002). Molecular Characterization of an atl Null Mutant of Staphylococcus aureus. Microbiology and Immunology 46, 601–612.

Takeda, K., Kaisho, T., Akira, S., (2003). Toll-like receptors. Annu. Rev. Immunol. 21, 335–376.

Takeuchi, O., Hoshino, K., Akira, S., (2000). Cutting edge: TLR2-deficient and MyD88-deficient mice are highly susceptible to Staphylococcus aureus infection. J. Immunol. 165, 5392–5396.

Taylor, S.C., Nadeau, K., Abbasi, M., Lachance, C., Nguyen, M., Fenrich, J., (2019). The Ultimate qPCR Experiment: Producing Publication Quality, Reproducible Data the First Time. Trends in Biotechnology 37, 761–774.

Thänert, R., Goldmann, O., Beineke, A., Medina, E., (2017). Host-inherent variability influences the transcriptional response of Staphylococcus aureus during in vivo infection. Nat Commun 8.

Thwaites, G.E., Gant, V., (2011). Are bloodstream leukocytes Trojan Horses for the metastasis of Staphylococcus aureus ? Nat Rev Microbiol 9, 215–222.

Torres, V.J., Pishchany, G., Humayun, M., Schneewind, O., Skaar, E.P., (2006). Staphylococcus aureus IsdB is a hemoglobin receptor required for heme iron utilization. J. Bacteriol. 188, 8421–8429.

Touhami, A., Jericho, M.H., Beveridge, T.J., (2004). Atomic force microscopy of cell growth and division in Staphylococcus aureus. J. Bacteriol. 186, 3286–3295.

Trede, N.S., Langenau, D.M., Traver, D., Look, A.T., Zon, L.I., (2004). The Use of Zebrafish to Understand Immunity. Immunity 20, 367–379.

Turner, R.D., Mesnage, S., Hobbs, J.K., Foster, S.J., (2018). Molecular imaging of glycan chains couples cell-wall polysaccharide architecture to bacterial cell morphology. Nat Commun 9, 1–8.

Turner, R.D., Ratcliffe, E.C., Wheeler, R., Golestanian, R., Hobbs, J.K., Foster, S.J., (2010a). Peptidoglycan architecture can specify division planes in Staphylococcus aureus. Nat Commun 1, 1–9.

Turner, R.D., Thomson, N.H., Kirkham, J., Devine, D., (2010b). Improvement of the pore trapping method to immobilize vital coccoid bacteria for high-resolution AFM: a study of Staphylococcus aureus. J Microsc 238, 102–110.

Turner, R.D., Vollmer, W., Foster, S.J., (2014). Different walls for rods and balls: the diversity of peptidoglycan. Molecular Microbiology 91, 862–874.

Typas, A., Banzhaf, M., Gross, C.A., Vollmer, W., (2012). From the regulation of peptidoglycan synthesis to bacterial growth and morphology. Nat Rev Microbiol 10, 123–136.

Ukpanah, M.A., Upla, P.U., (2017). Why is Staphylococcus aureus Such a Successful Pathogen? Microbiology Research Journal International 1–22.

Valentino, M.D., Foulston, L., Sadaka, A., Kos, V.N., Villet, R.A., Maria, J.S., Lazinski, D.W., Camilli, A., Walker, S., Hooper, D.C., Gilmore, M.S., (2014). Genes Contributing to Staphylococcus aureus Fitness in Abscess- and Infection-Related Ecologies. mBio 5.

van der Vaart, M., Spaink, H.P., Meijer, A.H., (2012). Pathogen Recognition and Activation of the Innate Immune Response in Zebrafish. Advances in Hematology 2012, 1–19.

van Kessel, K.P.M., Bestebroer, J., van Strijp, J.A.G., (2014). Neutrophil-Mediated Phagocytosis of Staphylococcus aureus. Front Immunol 5.

Verdrengh, M., Tarkowski, A., (2000). Role of macrophages in Staphylococcus aureus–induced arthritis and sepsis. Arthritis & Rheumatism 43, 2276–2282.

Vermassen, A., Leroy, S., Talon, R., Provot, C., Popowska, M., Desvaux, M., (2019). Cell Wall Hydrolases in Bacteria: Insight on the Diversity of Cell Wall Amidases, Glycosidases and Peptidases Toward Peptidoglycan. Front. Microbiol. 10.

Viljoen, A., Foster, S.J., Fantner, G.E., Hobbs, J.K., Dufrêne, Y.F., (2020). Scratching the Surface: Bacterial Cell Envelopes at the Nanoscale. mBio 11.

Vollmer, W., (2008). Structural variation in the glycan strands of bacterial peptidoglycan. FEMS Microbiol Rev 32, 287–306.

Vollmer, W., Bertsche, U., (2008). Murein (peptidoglycan) structure, architecture and biosynthesis in Escherichia coli. Biochimica et Biophysica Acta (BBA) - Biomembranes, Structural proteomics of the cell envelope of Gram-negative bacteria 1778, 1714–1734.

Vollmer, W., Blanot, D., De Pedro, M.A., (2008a). Peptidoglycan structure and architecture. FEMS Microbiol Rev 32, 149–167.

Vollmer, W., Höltje, J.-V., (2001). Morphogenesis of Escherichia coli. Current Opinion in Microbiology 4, 625–633.

Vollmer, W., Joris, B., Charlier, P., Foster, S., (2008b). Bacterial peptidoglycan (murein) hydrolases. FEMS Microbiol Rev 32, 259–286.

Vollmer, W., Seligman, S.J., (2010). Architecture of peptidoglycan: more data and more models. Trends in Microbiology 18, 59–66.

Vollmer, W., Tomasz, A., (2002). Peptidoglycan N-Acetylglucosamine Deacetylase, a Putative Virulence Factor in Streptococcus pneumoniae. Infection and Immunity 70, 7176–7178.

von Köckritz-Blickwede, M., Rohde, M., Oehmcke, S., Miller, L.S., Cheung, A.L., Herwald, H., Foster, S., Medina, E., (2008). Immunological mechanisms underlying the genetic predisposition to severe Staphylococcus aureus infection in the mouse model. Am. J. Pathol. 173, 1657–1668.

Wada, A., Watanabe, H., (1998). Penicillin-binding protein 1 of Staphylococcus aureus is essential for growth. J. Bacteriol. 180, 2759–2765.

Walter, J., Loach, D.M., Alqumber, M., Rockel, C., Hermann, C., Pfitzenmaier, M., Tannock, G.W., (2007). d-Alanyl ester depletion of teichoic acids in Lactobacillus reuteri 100-23 results in impaired colonization of the mouse gastrointestinal tract. Environmental Microbiology 9, 1750–1760.

Wang, Q.M., Peery, R.B., Johnson, R.B., Alborn, W.E., Yeh, W.-K., Skatrud, P.L., (2001). Identification and Characterization of a Monofunctional Glycosyltransferase from Staphylococcus aureus. Journal of Bacteriology 183, 4779–4785.

Wang, R., Braughton, K.R., Kretschmer, D., Bach, T.-H.L., Queck, S.Y., Li, M., Kennedy, A.D., Dorward, D.W., Klebanoff, S.J., Peschel, A., DeLeo, F.R., Otto, M., (2007). Identification of novel cytolytic peptides as key virulence determinants for community-associated MRSA. Nat. Med. 13, 1510–1514.

Wang, T.-S.A., Manning, S.A., Walker, S., Kahne, D., (2008). Isolated Peptidoglycan Glycosyltransferases from Different Organisms Produce Different Glycan Chain Lengths. J. Am. Chem. Soc. 130, 14068–14069.

Wang, W., Chen, J., Chen, G., Du, X., Cui, P., Wu, J., Zhao, J., Wu, N., Zhang, W., Li, M., Zhang, Y., (2015). Transposon Mutagenesis Identifies Novel Genes Associated with Staphylococcus aureus Persister Formation. Front. Microbiol. 6.

Wanner, S., Schade, J., Keinhörster, D., Weller, N., George, S.E., Kull, L., Bauer, J., Grau, T., Winstel, V., Stoy, H., Kretschmer, D., Kolata, J., Wolz, C., Bröker, B.M., Weidenmaier, C., (2017). Wall teichoic acids mediate increased virulence in Staphylococcus aureus. Nat Microbiol 2, 1–12.

Ward, J.B., Perkins, H.R., (1973). The direction of glycan synthesis in a bacterial peptidoglycan. Biochem J 135, 721–728.

Watson, S.P., Clements, M.O., Foster, S.J., (1998). Characterization of the Starvation-Survival Response of Staphylococcus aureus. Journal of Bacteriology 180, 1750–1758.

Weidenmaier, C., Peschel, A., Xiong, Y.-Q., Kristian, S.A., Dietz, K., Yeaman, M.R., Bayer, A.S., (2005). Lack of Wall Teichoic Acids in Staphylococcus aureus Leads to Reduced Interactions with Endothelial Cells and to Attenuated Virulence in a Rabbit Model of Endocarditis. J Infect Dis 191, 1771–1777.

Wertheim, H.F.L., Walsh, E., Choudhurry, R., Melles, D.C., Boelens, H.A.M., Miajlovic, H., Verbrugh, H.A., Foster, T., Belkum, A. van, (2008). Key Role for Clumping Factor B in Staphylococcus aureus Nasal Colonization of Humans. PLOS Medicine 5, e17.

Wheeler, R., (2012). Peptidoglycan architecture and dynamics in Gram-positive bacteria. University of Sheffield.

Wheeler, R., Mesnage, S., Boneca, I.G., Hobbs, J.K., Foster, S.J., (2011). Super-resolution microscopy reveals cell wall dynamics and peptidoglycan architecture in ovococcal bacteria. Molecular Microbiology 82, 1096–1109.

Wheeler, R., Turner, R.D., Bailey, R.G., Salamaga, B., Mesnage, S., Mohamad, S.A.S., Hayhurst, E.J., Horsburgh, M., Hobbs, J.K., Foster, S.J., (2015). Bacterial Cell Enlargement Requires Control of Cell Wall Stiffness Mediated by Peptidoglycan Hydrolases. mBio 6.

Wyke, A.W., Ward, J.B., Hayes, M.V., Curtis, N.A., (1981a). A role in vivo for penicillin-binding protein-4 of Staphylococcus aureus. Eur. J. Biochem. 119, 389–393.

308

Wyke, A.W., Ward, J.B., Hayes, M.V., Curtis, N.A.C., (1981b). A Role in vivo for Penicillin-Binding Protein-4 of Staphylococcus aureus. European Journal of Biochemistry 119, 389–393.

Xia, G., Corrigan, R.M., Winstel, V., Goerke, C., Gründling, A., Peschel, A., (2011). Wall Teichoic Acid-Dependent Adsorption of Staphylococcal Siphovirus and Myovirus. Journal of Bacteriology 193, 4006–4009.

Yanagihara, Y., Kamisango, K.-I., Yasuda, S., Kobayashi, S., Mifuchi, I., Azuma, I., Yamamura, Y., Johnson, R.C., (1984). Chemical Compositions of Cell Walls and Polysaccharide Fractions of Spirochetes. Microbiology and Immunology 28, 535–544.

Yang, X., Lyu, Z., Miguel, A., McQuillen, R., Huang, K.C., Xiao, J., (2017). GTPase activity–coupled treadmilling of the bacterial tubulin FtsZ organizes septal cell wall synthesis. Science 355, 744–747.

Yokoyama, R., Itoh, S., Kamoshida, G., Takii, T., Fujii, S., Tsuji, T., Onozaki, K., (2012). Staphylococcal Superantigen-Like Protein 3 Binds to the Toll-Like Receptor 2 Extracellular Domain and Inhibits Cytokine Production Induced by Staphylococcus aureus, Cell Wall Component, or Lipopeptides in Murine Macrophages. Infection and Immunity 80, 2816–2825.

Yousif, S.Y., Broome-Smith, J.K., Spratt, B.G., (1985). Lysis of Escherichia coli by beta-lactam antibiotics: deletion analysis of the role of penicillin-binding proteins 1A and 1B. J. Gen. Microbiol. 131, 2839–2845.

Yunck, R., Cho, H., Bernhardt, T.G., (2016). Identification of MltG as a potential terminase for peptidoglycan polymerization in bacteria. Molecular Microbiology 99, 700–718.

Zähringer, U., Lindner, B., Inamura, S., Heine, H., Alexander, C., (2008). TLR2 – promiscuous or specific? A critical re-evaluation of a receptor expressing apparent broad specificity. Immunobiology 213, 205–224.

Zaman, S.B., Hussain, M.A., Nye, R., Mehta, V., Mamun, K.T., Hossain, N., (2017). A Review on Antibiotic Resistance: Alarm Bells are Ringing. Cureus 9.

Zapun, A., Contreras-Martel, C., Vernet, T., (2008a). Penicillin-binding proteins and β-lactam resistance. FEMS Microbiol Rev 32, 361–385.

Zapun, A., Vernet, T., Pinho, M.G., (2008b). The different shapes of cocci. FEMS Microbiol. Rev. 32, 345–360.

Zhang, X., Ma, Y.-F., Wang, L., Jiang, N., Qin, C.-H., Hu, Y.-J., Yu, B., (2017). A rabbit model of implant-related osteomyelitis inoculated with biofilm after open femoral fracture. Exp Ther Med 14, 4995–5001.

Zhou, X., Cegelski, L., (2012). Nutrient-Dependent Structural Changes in S. aureus Peptidoglycan Revealed by Solid-State NMR Spectroscopy. Biochemistry 51, 8143–8153.

Zhou, X., Halladin, D.K., Rojas, E.R., Koslover, E.F., Lee, T.K., Huang, K.C., Theriot, J.A., (2015). Mechanical crack propagation drives millisecond daughter cell separation in Staphylococcus aureus. Science 348, 574–578.

Zuber, B., Chami, M., Houssin, C., Dubochet, J., Griffiths, G., Daffé, M., (2008). Direct Visualization of the Outer Membrane of Mycobacteria and Corynebacteria in Their Native State. Journal of Bacteriology 190, 5672–5680.
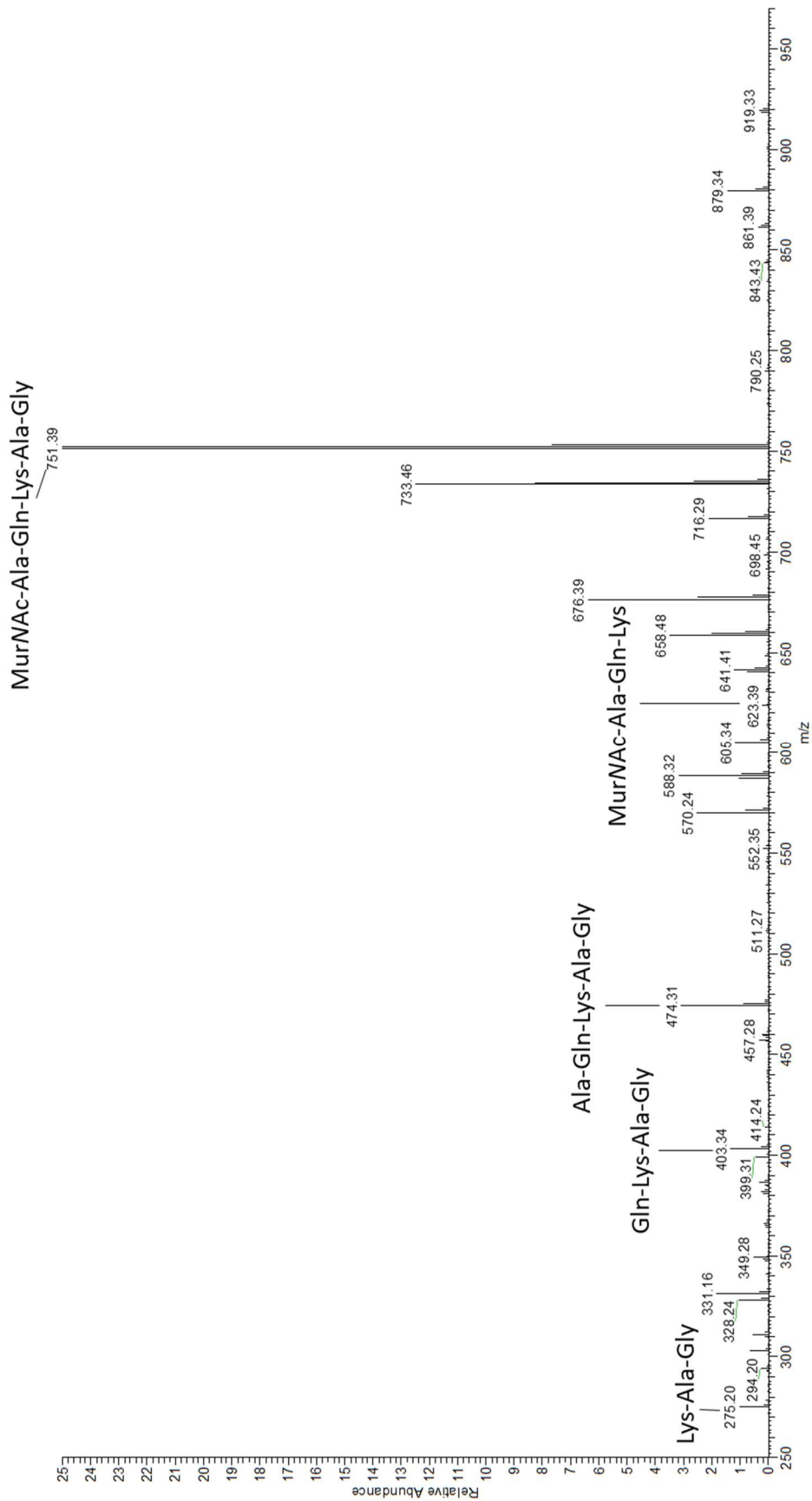
Appendix 1

The chemical structures and labelled MS/MS ion spectra of *S. aureus* muropeptides observed in Chapter 3 and Table 3.1.
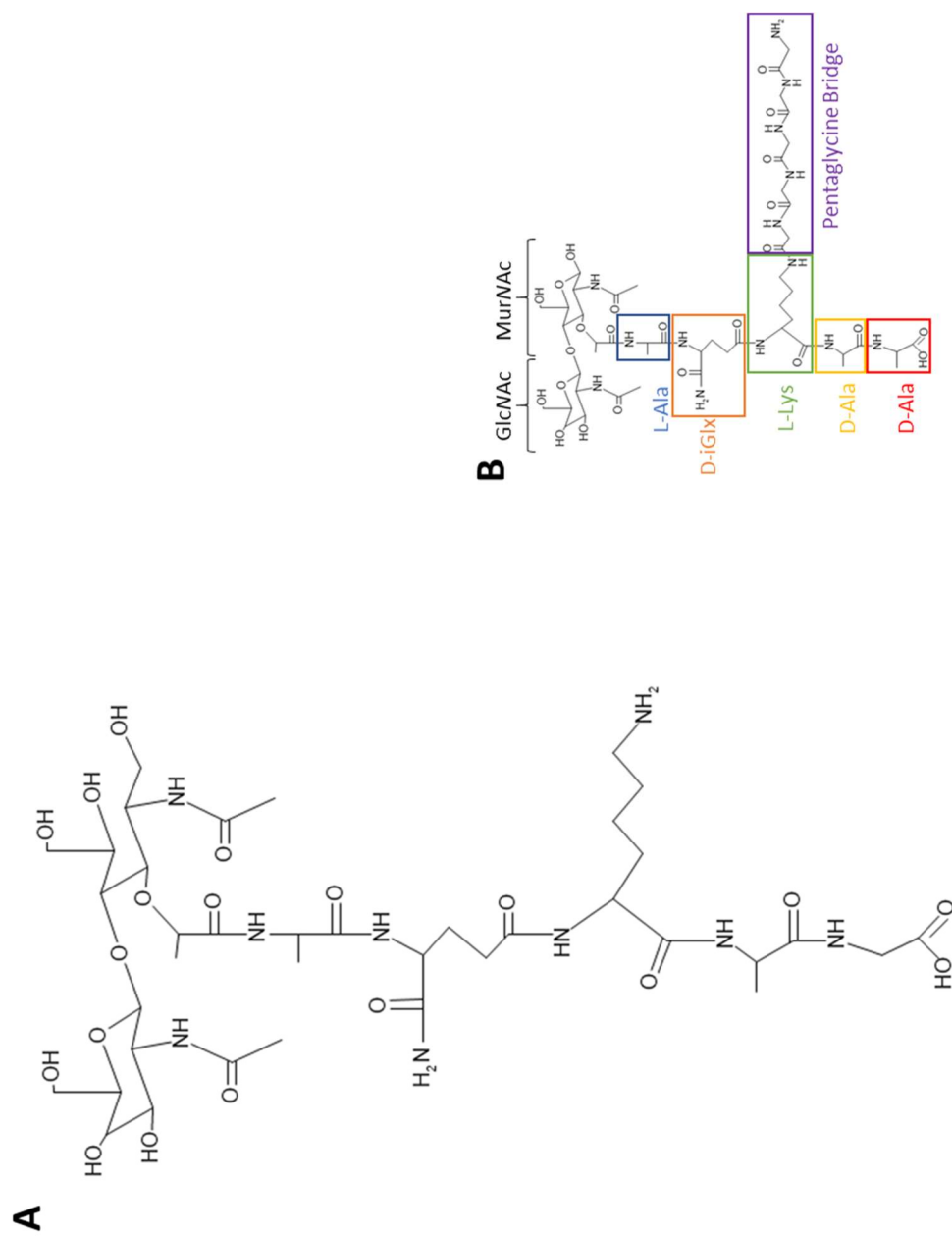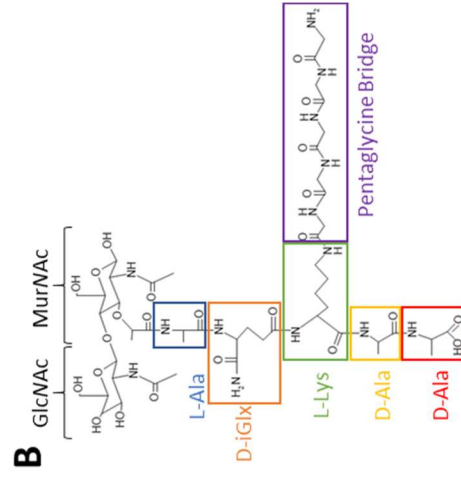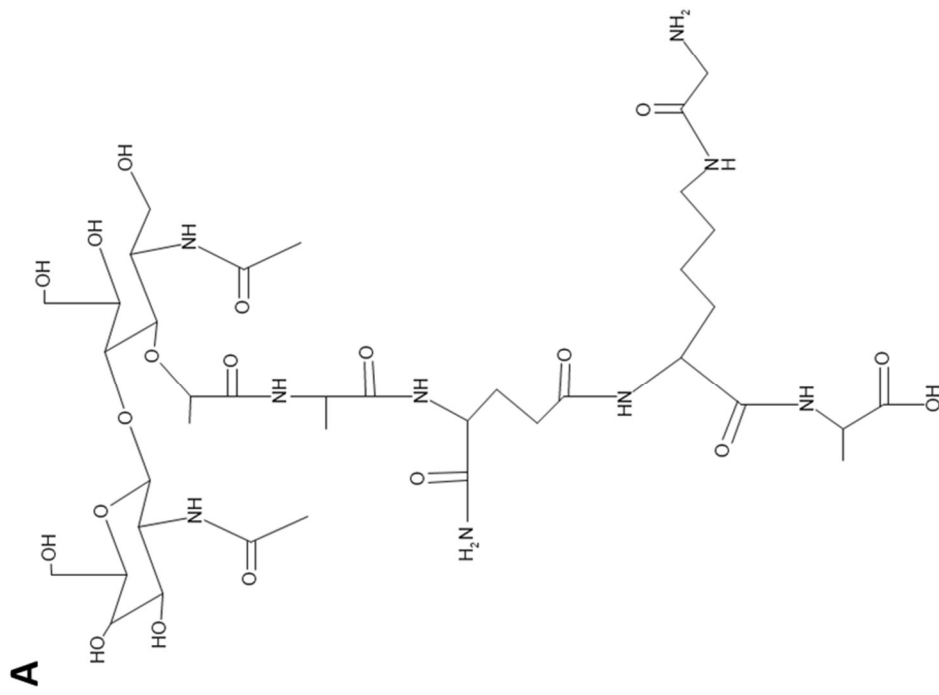
Appendix 1 Figure 1 The chemical structure of muropeptide 1: GM-(Ala-iGln,Lys,Ala,Gly)

(A) Calculated neutral mass 953.40 Da. (B) Reference muropeptide.
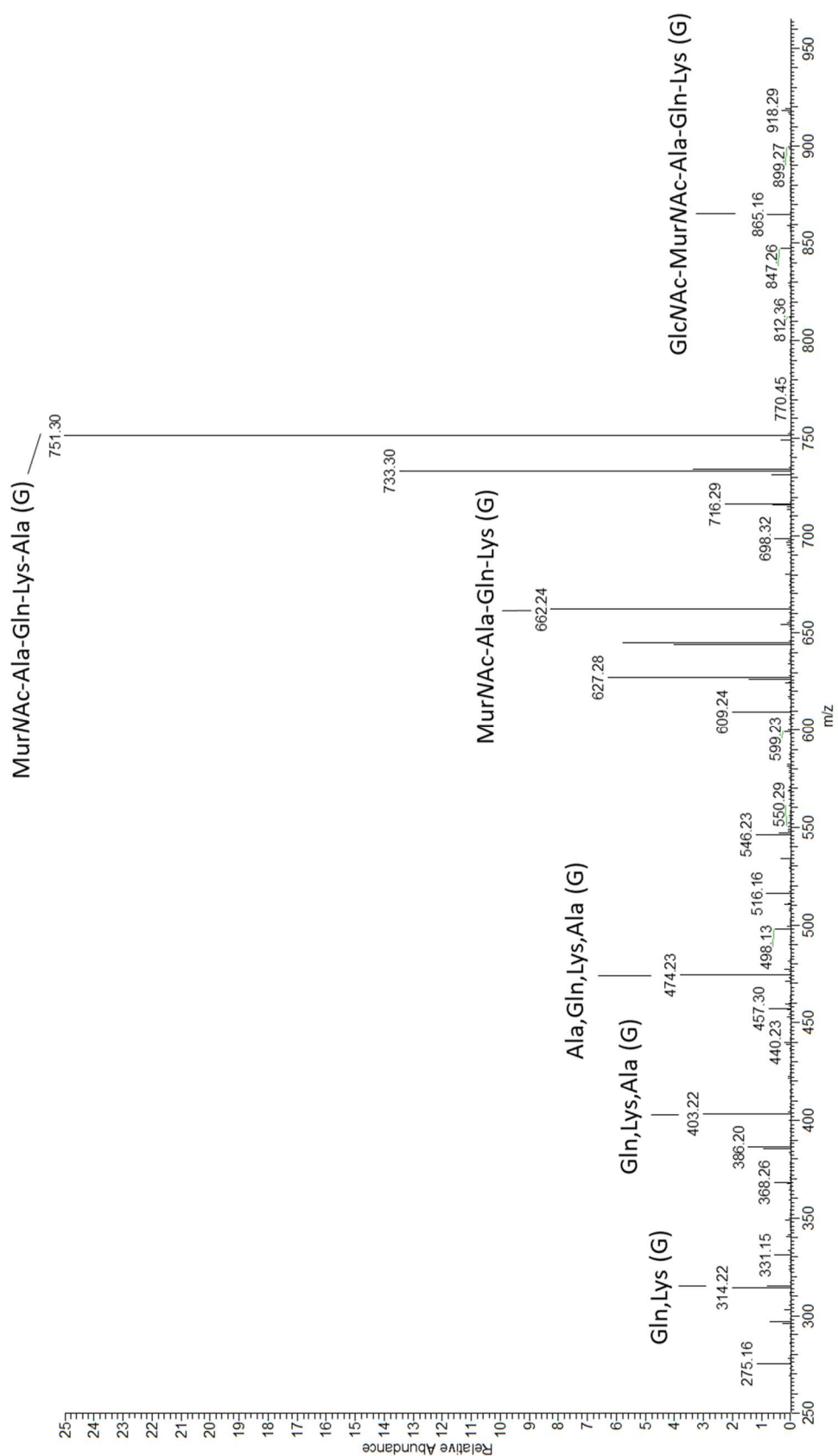
Appendix 1 Figure 2 Representative ion spectrum of muropeptide 1: GM-(Ala-iGln,Lys,Ala,Gly)

Selected ion peaks from MS/MS analysis have been labelled with corresponding structures.
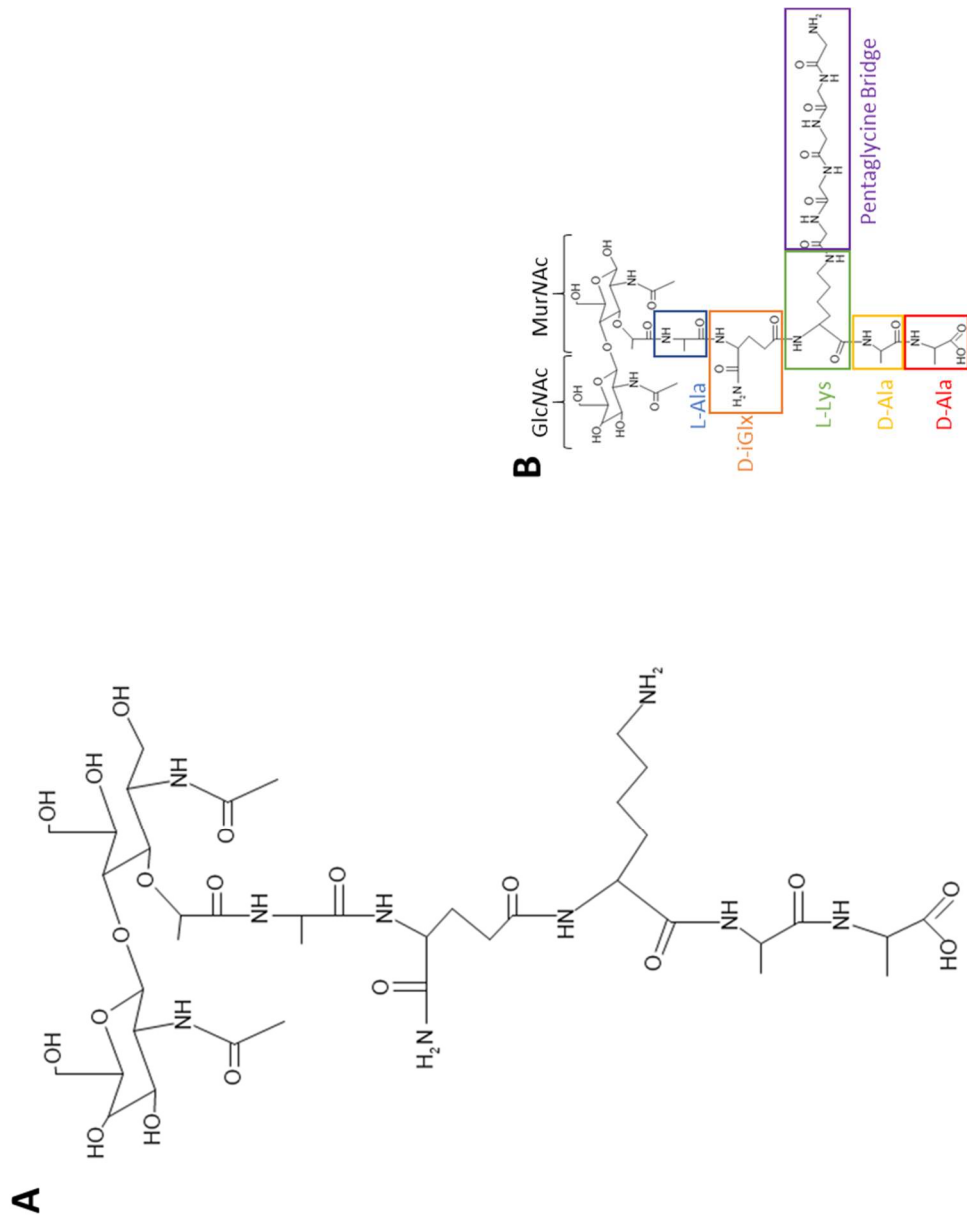
Appendix 1 Figure 3 The chemical structure of muropeptide 2: GM-tetrapeptide (G)

(A) Calculated neutral mass 953.40 Da. (B) Reference muropeptide.

Appendix 1 Figure 4 Representative ion spectrum of muropeptide 2: GM-tetrapeptide (G)

Selected ion peaks from MS/MS analysis have been labelled with corresponding structures.

315

Appendix 1 Figure 5 The chemical structure of muropeptide 3: GM-pentapeptide (Gln)

(A) Calculated neutral mass 967.47 Da. (B) Reference muropeptide.

Appendix 1 Figure 6 Representative ion spectrum of muropeptide 3: GM-pentapeptide (Gln)

Selected ion peaks from MS/MS analysis have been labelled with corresponding structures.

317

Appendix 1 Figure 7 The chemical structure of muropeptide 4: GM-tetrapeptide (Gln) (GG)

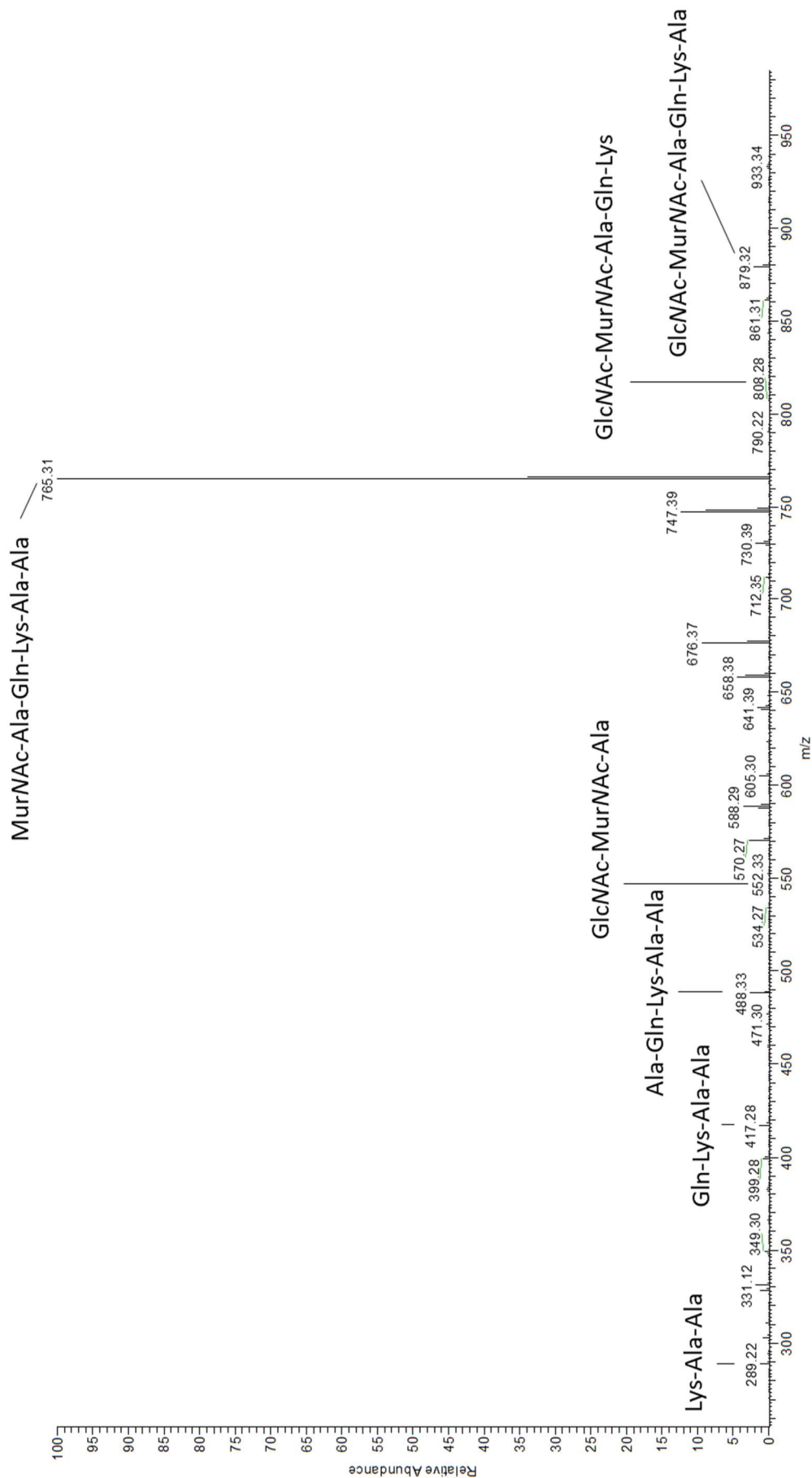(A) Calculated neutral mass 1010.48 Da. (B) Reference muropeptide.

Appendix 1 Figure 8 Representative ion spectrum of muropeptide 4: GM-tetrapeptide (Gln) (GG)

Selected ion peaks from MS/MS analysis have been labelled with corresponding structures.

320

Appendix 1 Figure 9 The chemical structure of muropeptide 5: GM-pentapeptide (Gln) (G)

(A) Calculated neutral mass 1024.49 Da. (B) Reference muropeptide.

Appendix 1 Figure 10 Representative ion spectrum of muropeptide 5: GM-pentapeptide (Gln) (G)

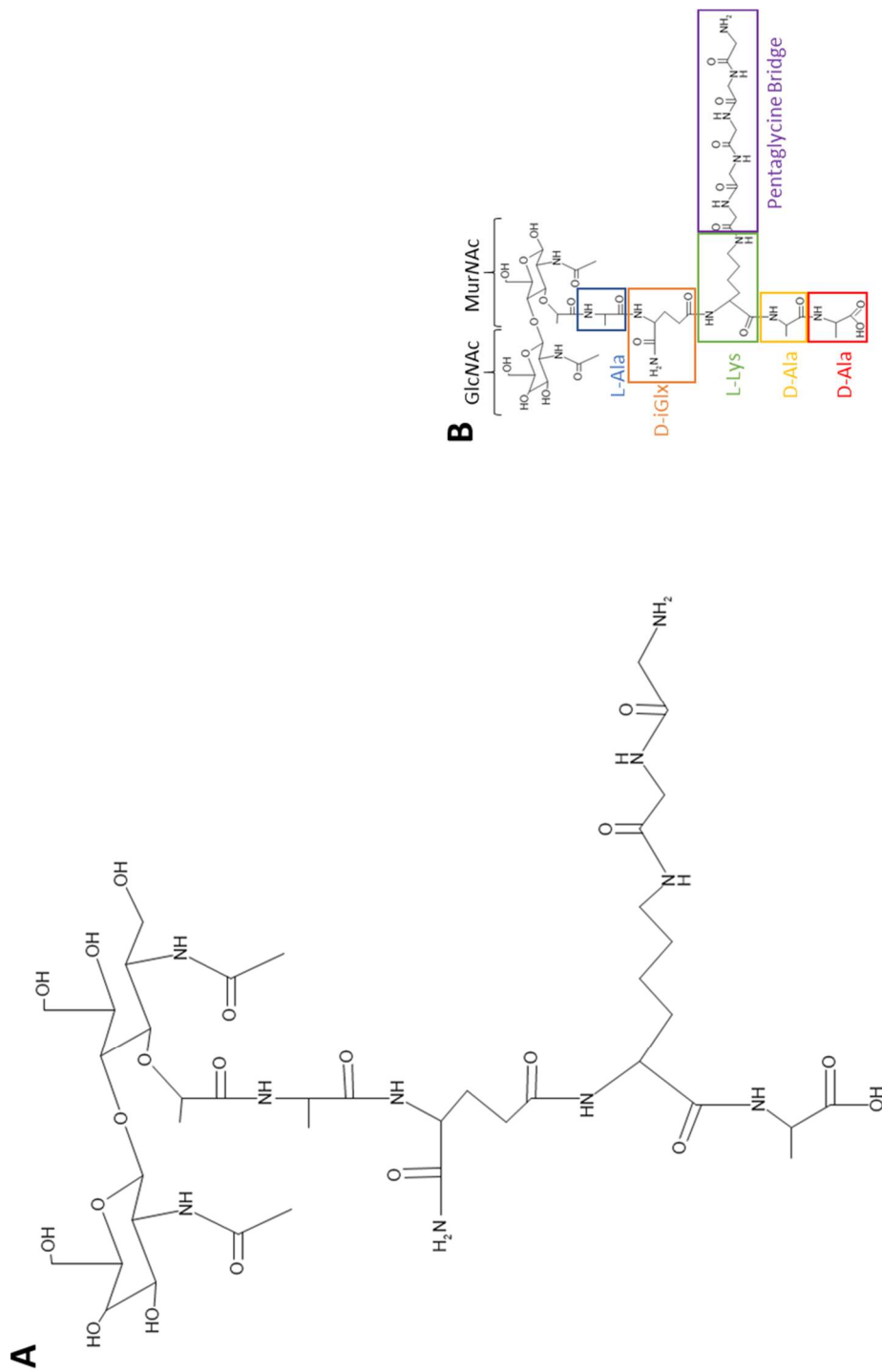Selected ion peaks from MS/MS analysis have been labelled with corresponding structures.

Appendix 1 Figure 11 The chemical structure of muropeptide 6: GM-tetrapeptide (Gln) (GGG)

(A) Calculated neutral mass 1067.50 Da. (B) Reference muropeptide.
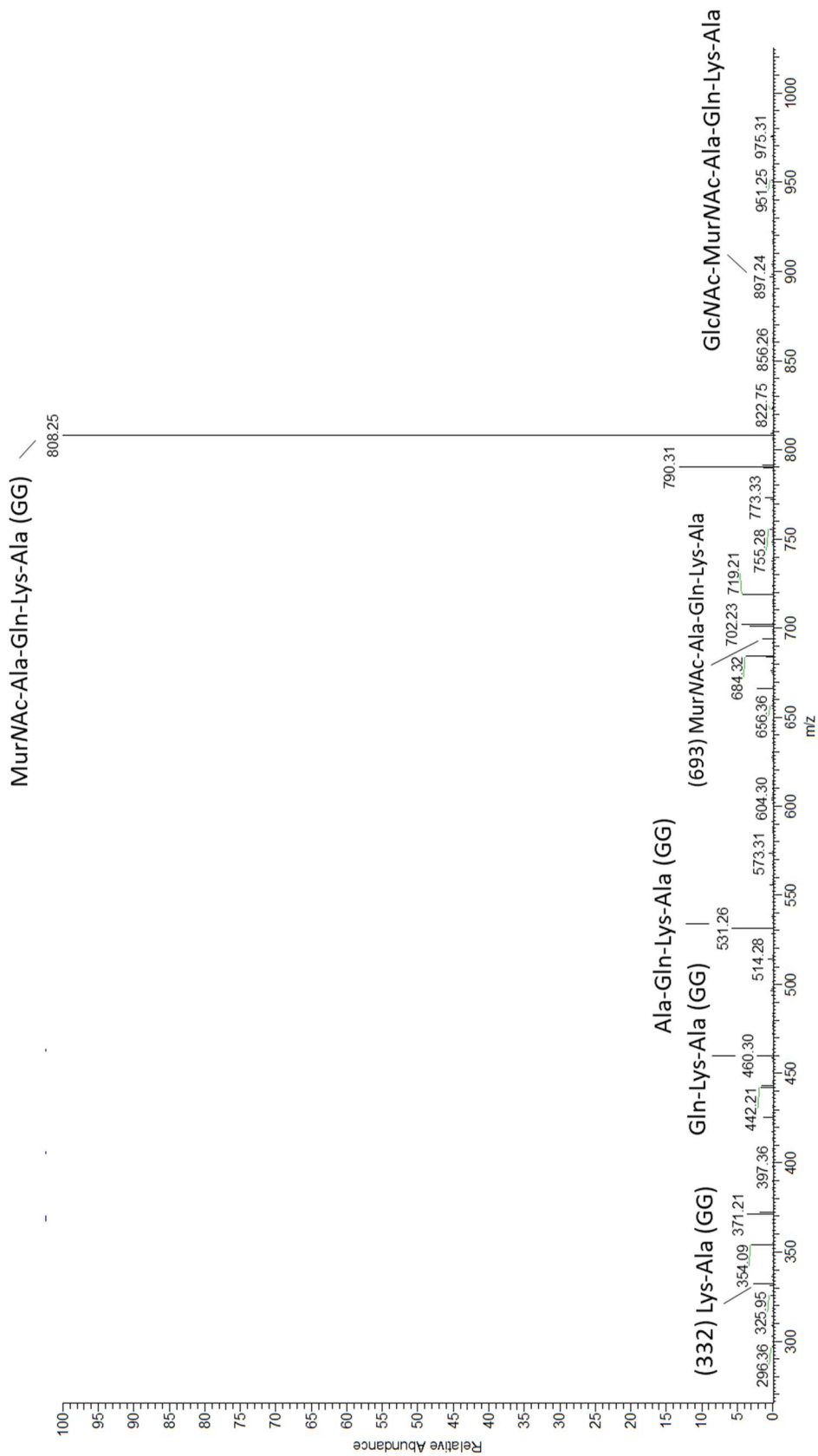
Appendix 1 Figure 12 Representative ion spectrum of muropeptide 6: GM-tetrapeptide (Gln) (GGG)

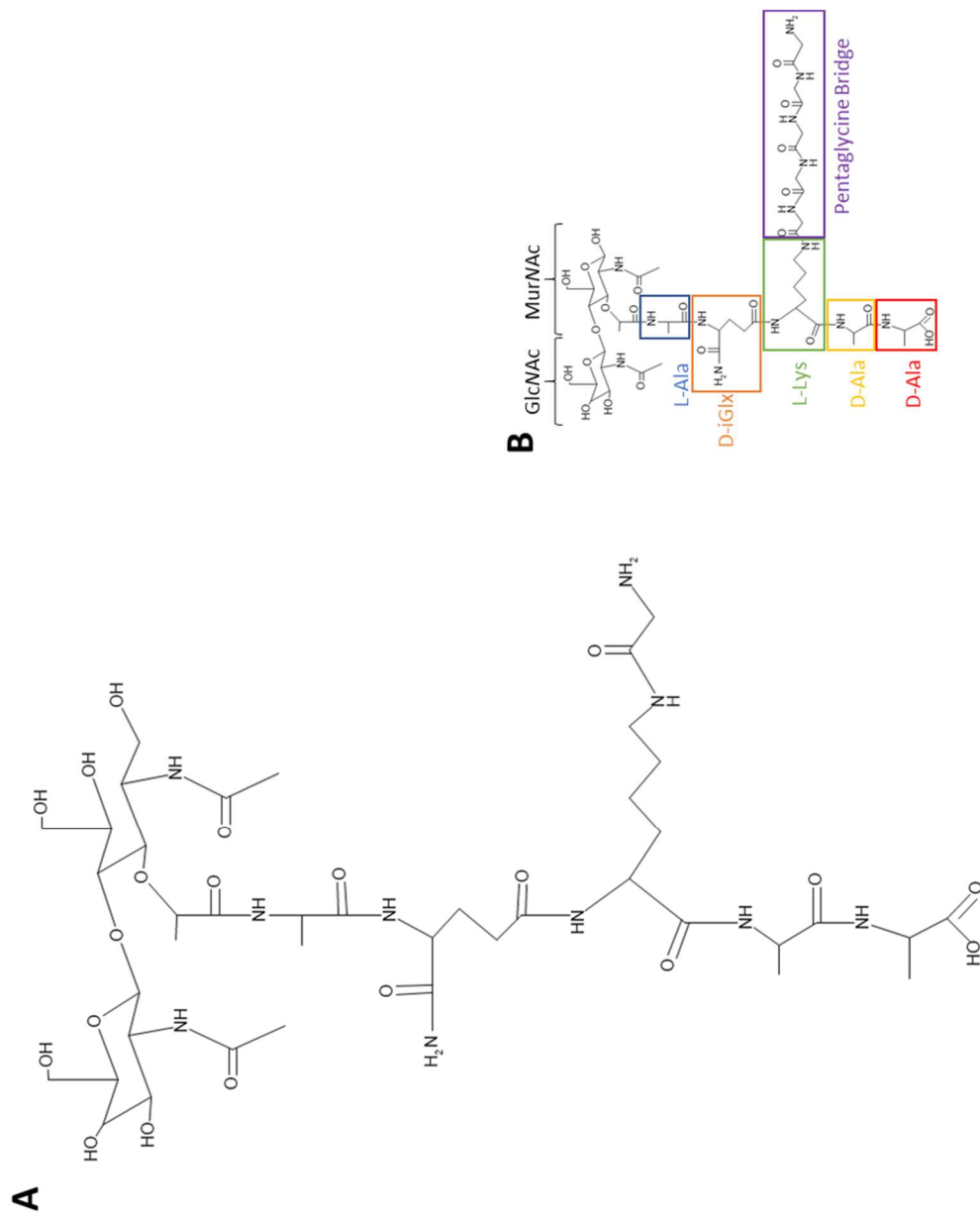Selected ion peaks from MS/MS analysis have been labelled with corresponding structures.

Appendix 1 Figure 13 The chemical structure of muropeptide 7: GM-pentapeptide (Gln) (GG)

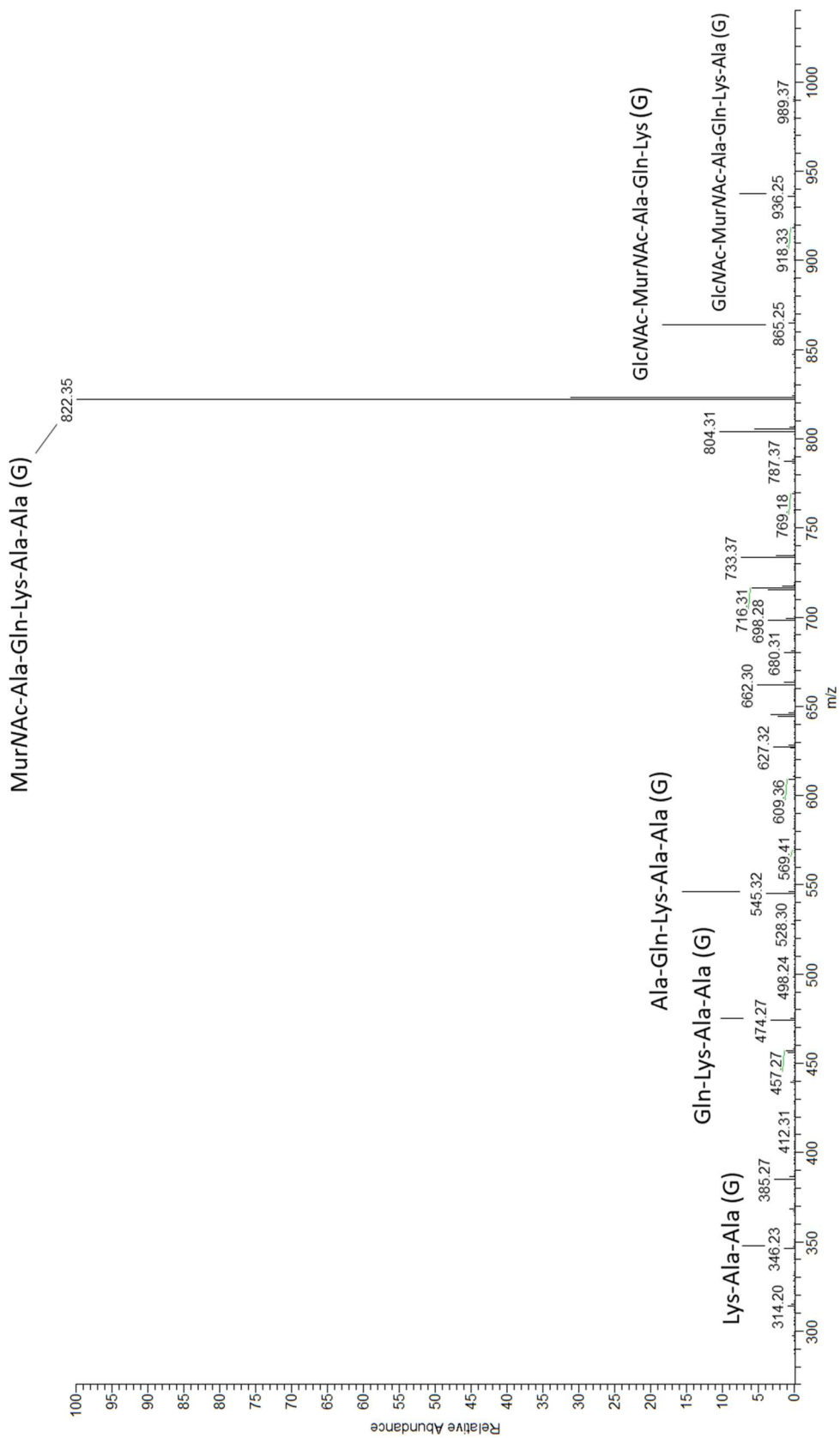(A) Calculated neutral mass 1081.51 Da. (B) Reference muropeptide.

Appendix 1 Figure 14 Representative ion spectrum of muropeptide 7: GM-pentapeptide (Gln) (GG)

Selected ion peaks from MS/MS analysis have been labelled with corresponding structures.

Appendix 1 Figure 15 The chemical structure of muropeptide 8: GM-pentapeptide (Glu) (GG)

(A) Calculated neutral mass 1082.50 Da. (B) Reference muropeptide.

Appendix 1 Figure 16 Representative ion spectrum of muropeptide 8: GM-pentapeptide (Glu) (GG)

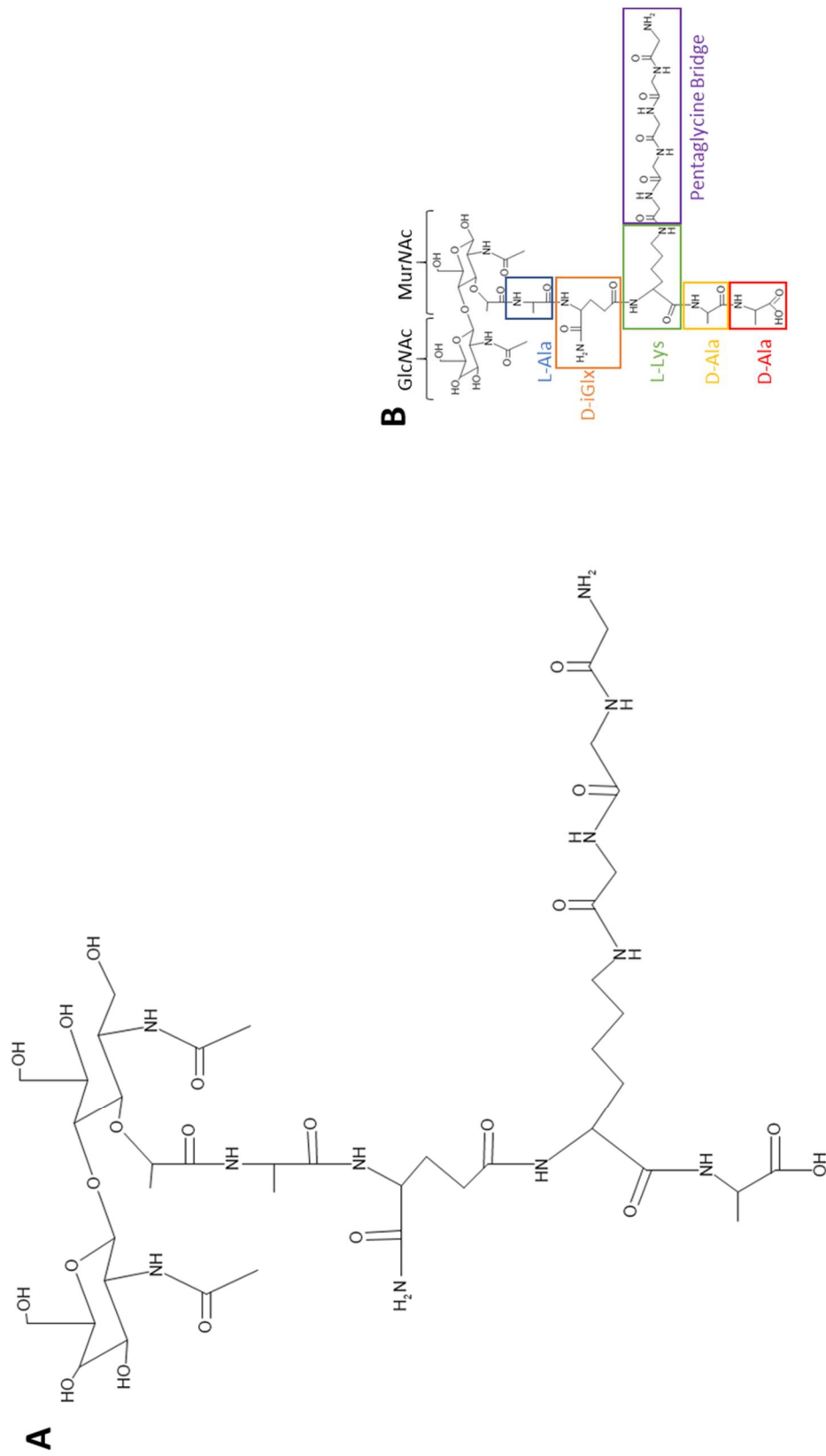Selected ion peaks from MS/MS analysis have been labelled with corresponding structures.

Appendix 1 Figure 17 The chemical structure of muropeptide 9: GM-tetrapeptide (Gln) (GGGG)

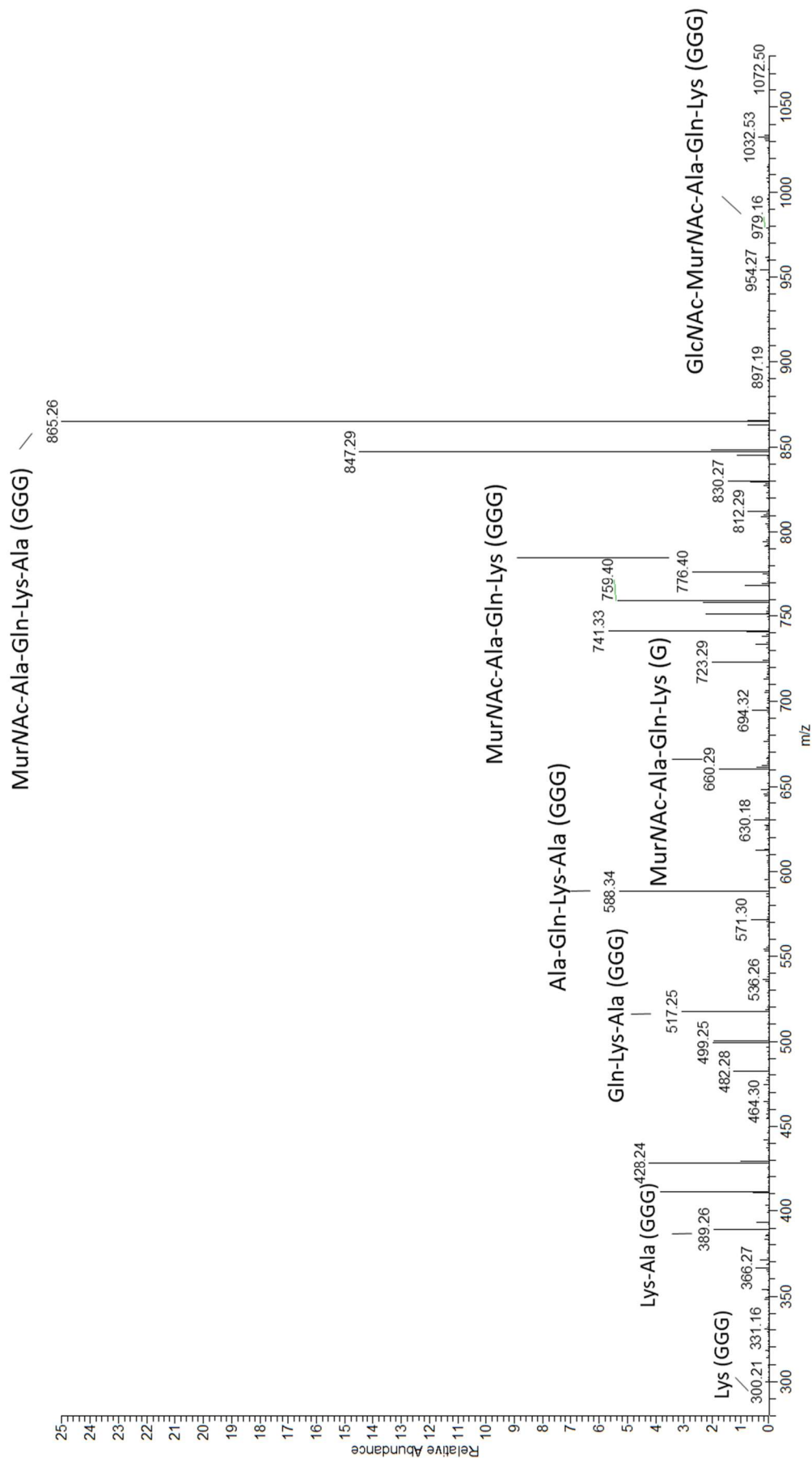(A) Calculated neutral mass 1124.52 Da. (B) Reference muropeptide.

Appendix 1 Figure 18 Representative ion spectrum of muropeptide 9: GM-tetrapeptide (Gln) (GGGG)

Selected ion peaks from MS/MS analysis have been labelled with corresponding structures.

329

Appendix 1 Figure 19 The chemical structure of muropeptide 10: GM-pentapeptide (Gln) (GGG)

(A) Calculated neutral mass 1138.54 Da. (B) Reference muropeptide.

Appendix 1 Figure 20 Representative ion spectrum of muropeptide 10: GM-pentapeptide (Gln) (GGG)

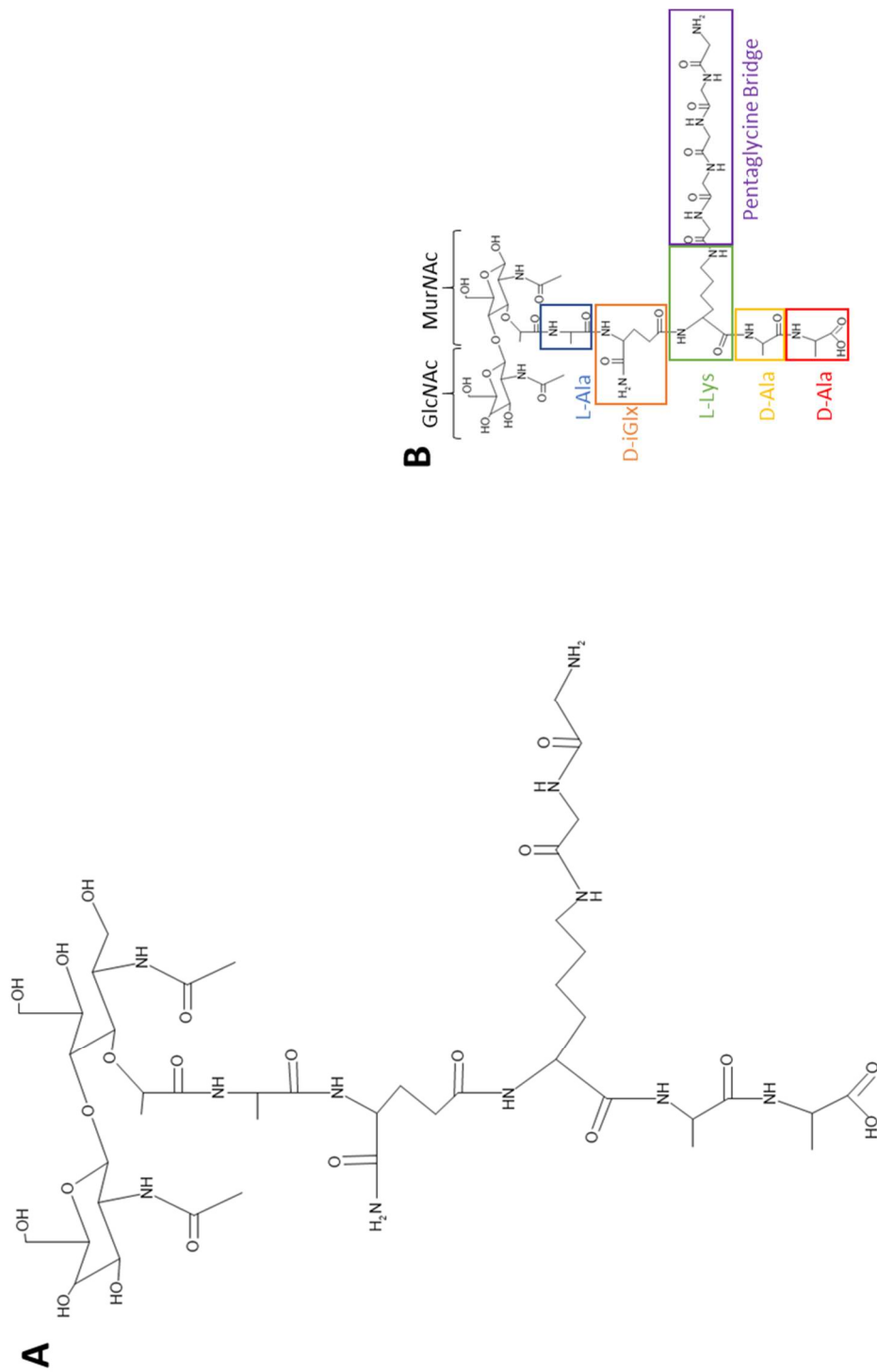Selected ion peaks from MS/MS analysis have been labelled with corresponding structures.

332
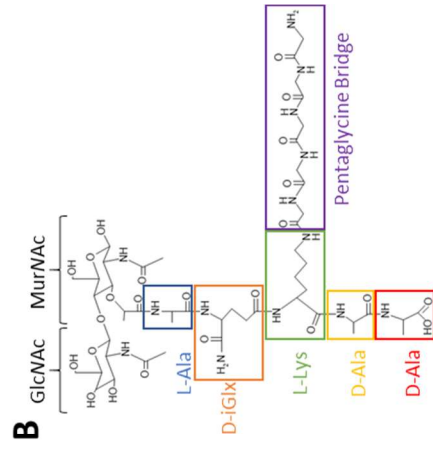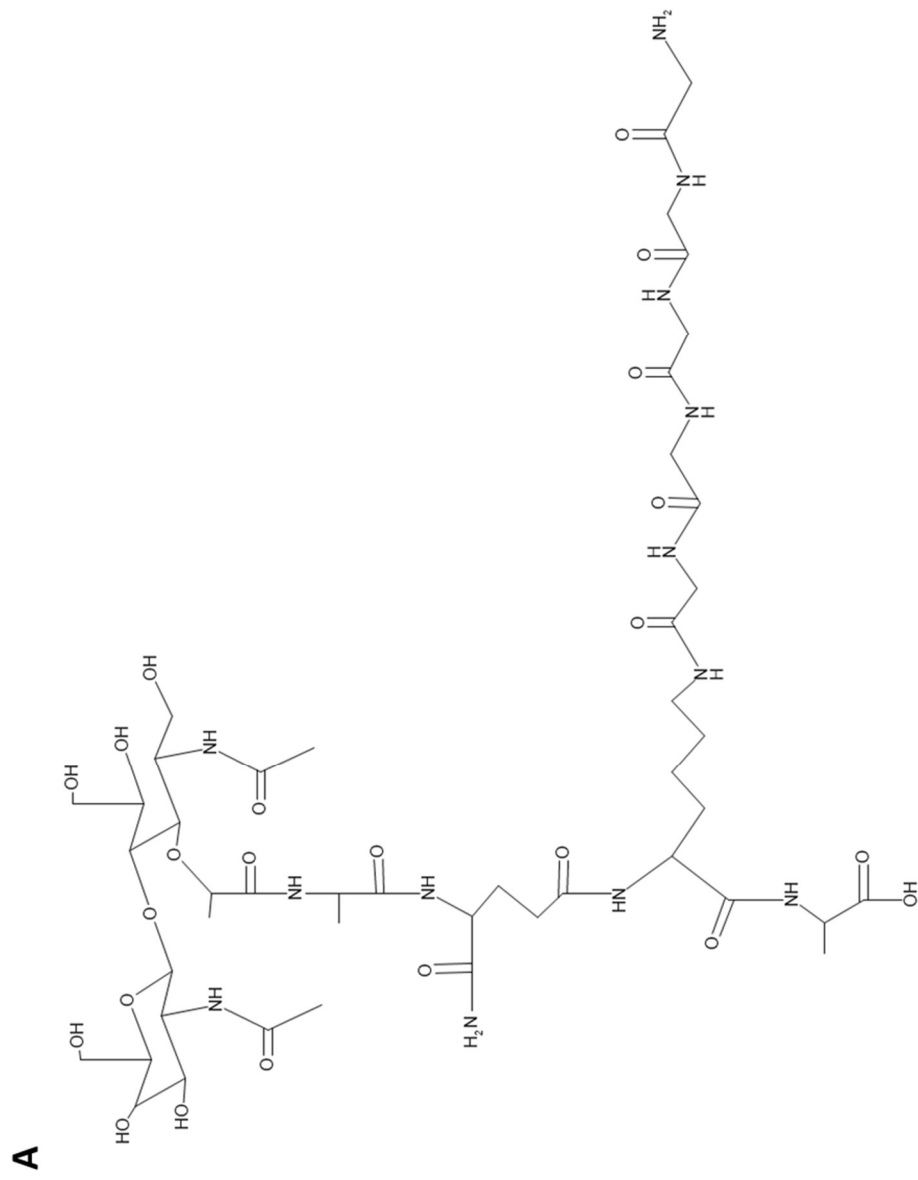
Appendix 1 Figure 21 The chemical structure of muropeptide 11: GM-tetrapeptide (Gln) (GGGGG)

(A) Calculated neutral mass 1181.54 Da. (B) Reference muropeptide.
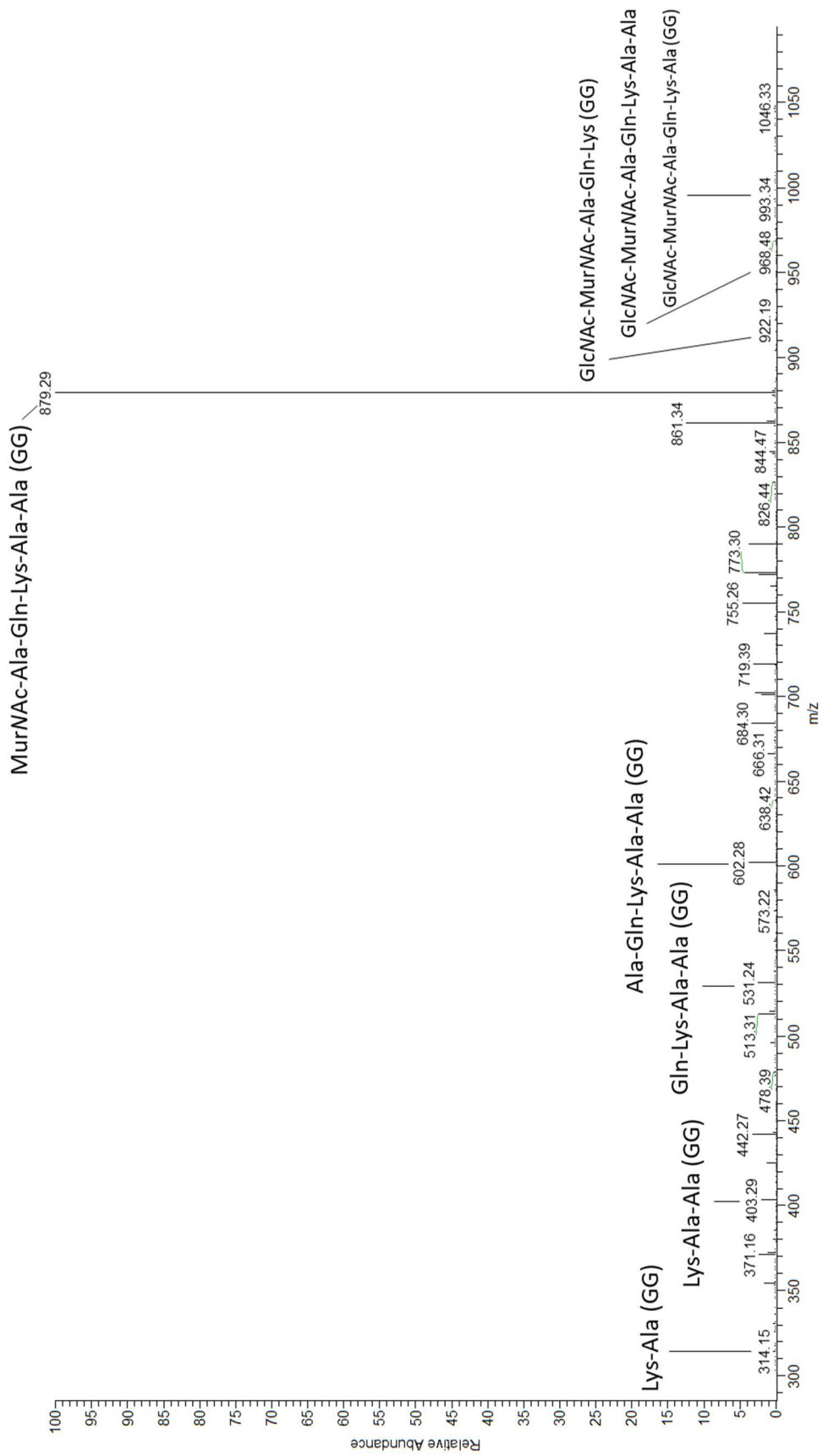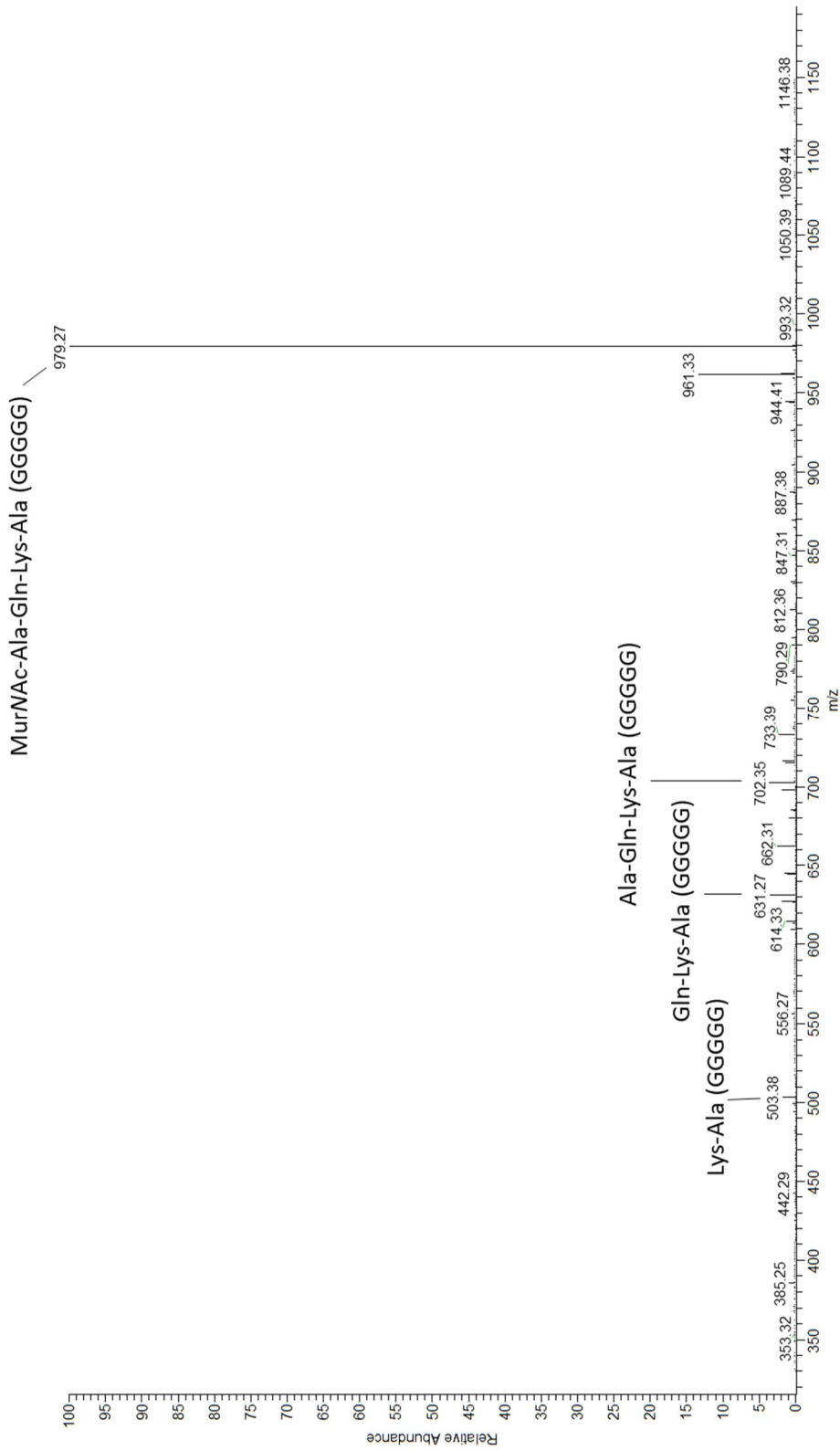
Appendix 1 Figure 22 Representative ion spectrum of muropeptide 11: GM-tetrapeptide (Gln) (GGGGG)

Selected ion peaks from MS/MS analysis have been labelled with corresponding structures.
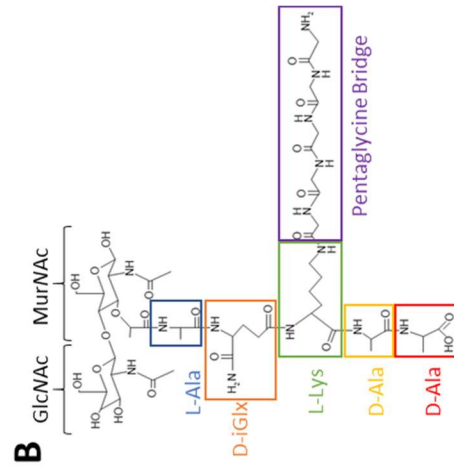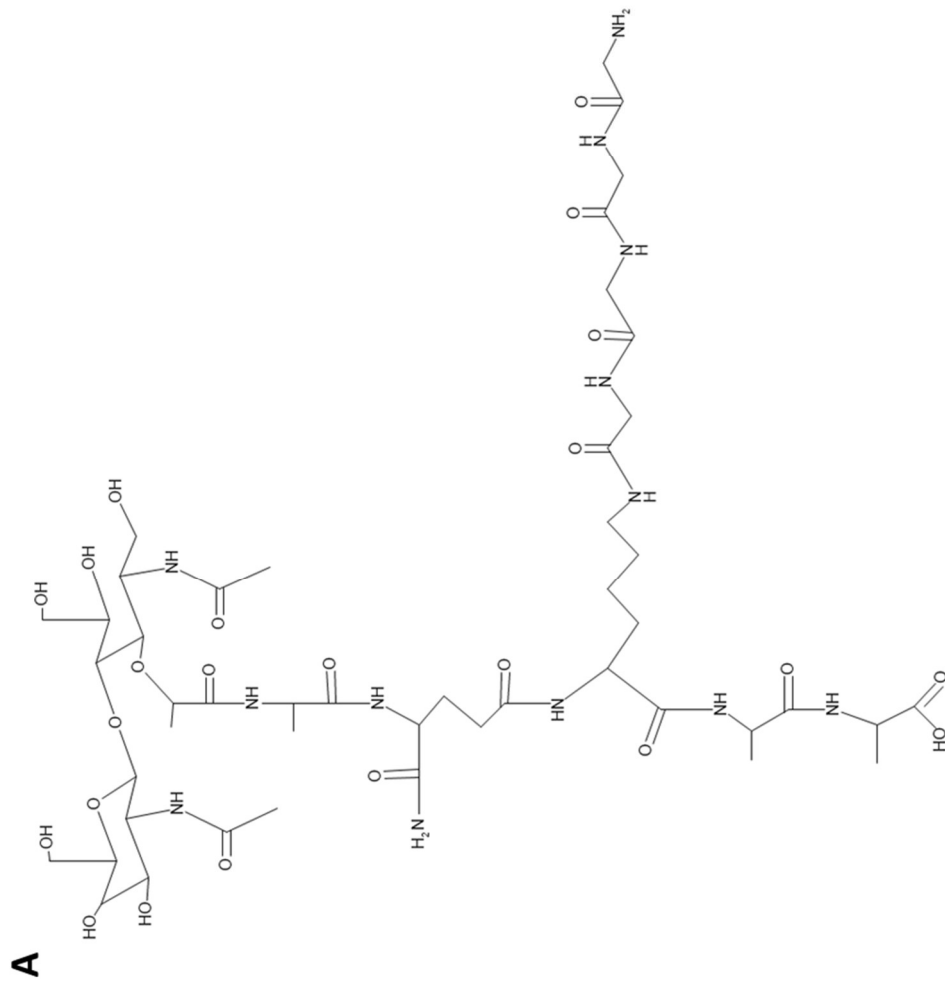
Appendix 1 Figure 23 The chemical structure of muropeptide 12: GM-pentapeptide (Gln) (GGGG)

(A) Calculated neutral mass 1195.56 Da. (B) Reference muropeptide.

334
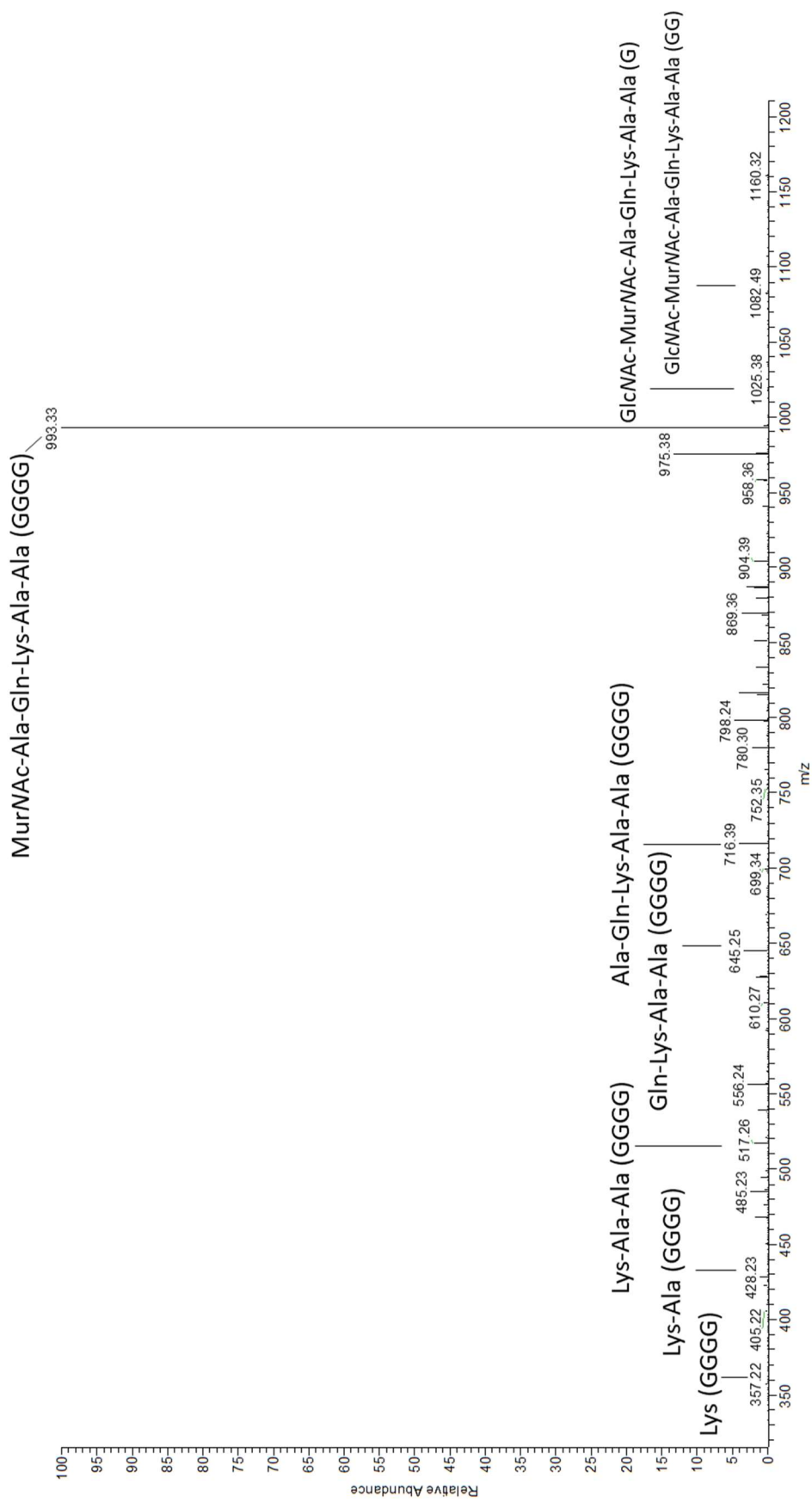
Appendix 1 Figure 24 Representative ion spectrum of muropeptide 12: GM-pentapeptide (Gln) (GGGG)

Selected ion peaks from MS/MS analysis have been labelled with corresponding structures.
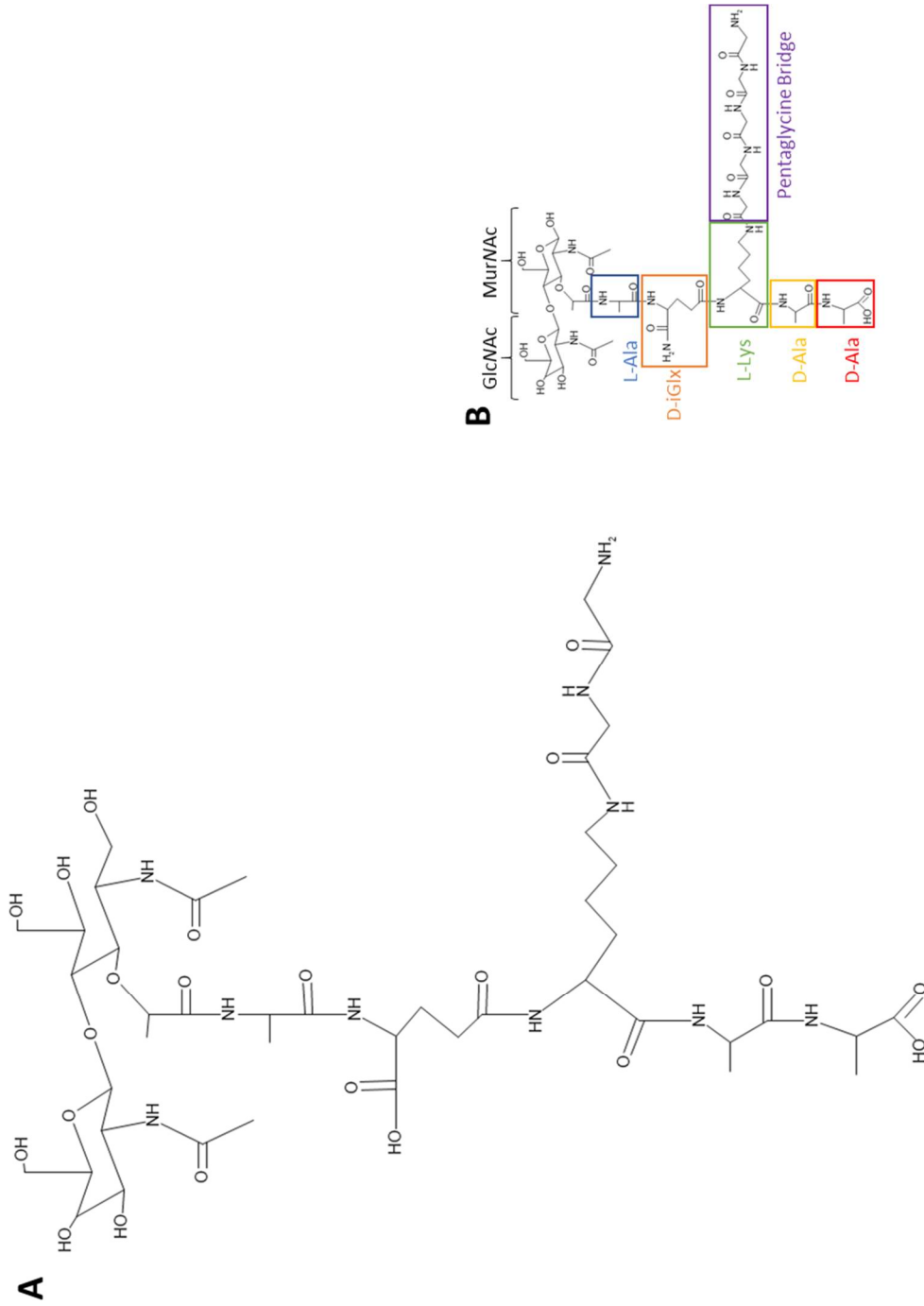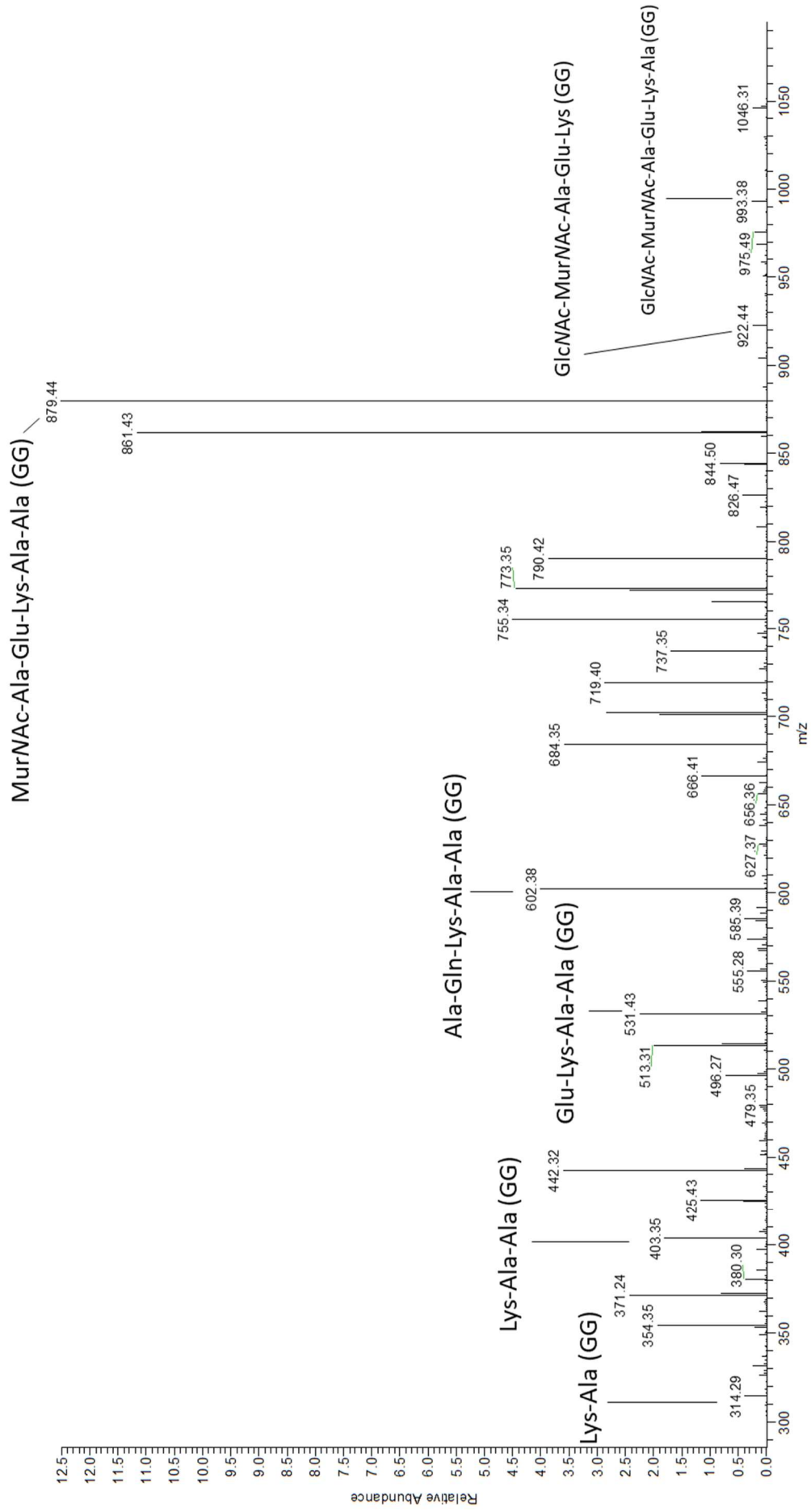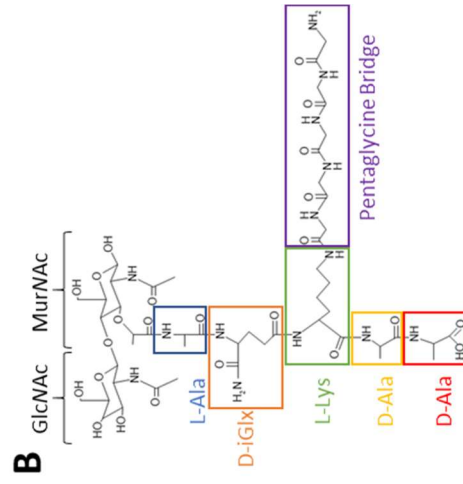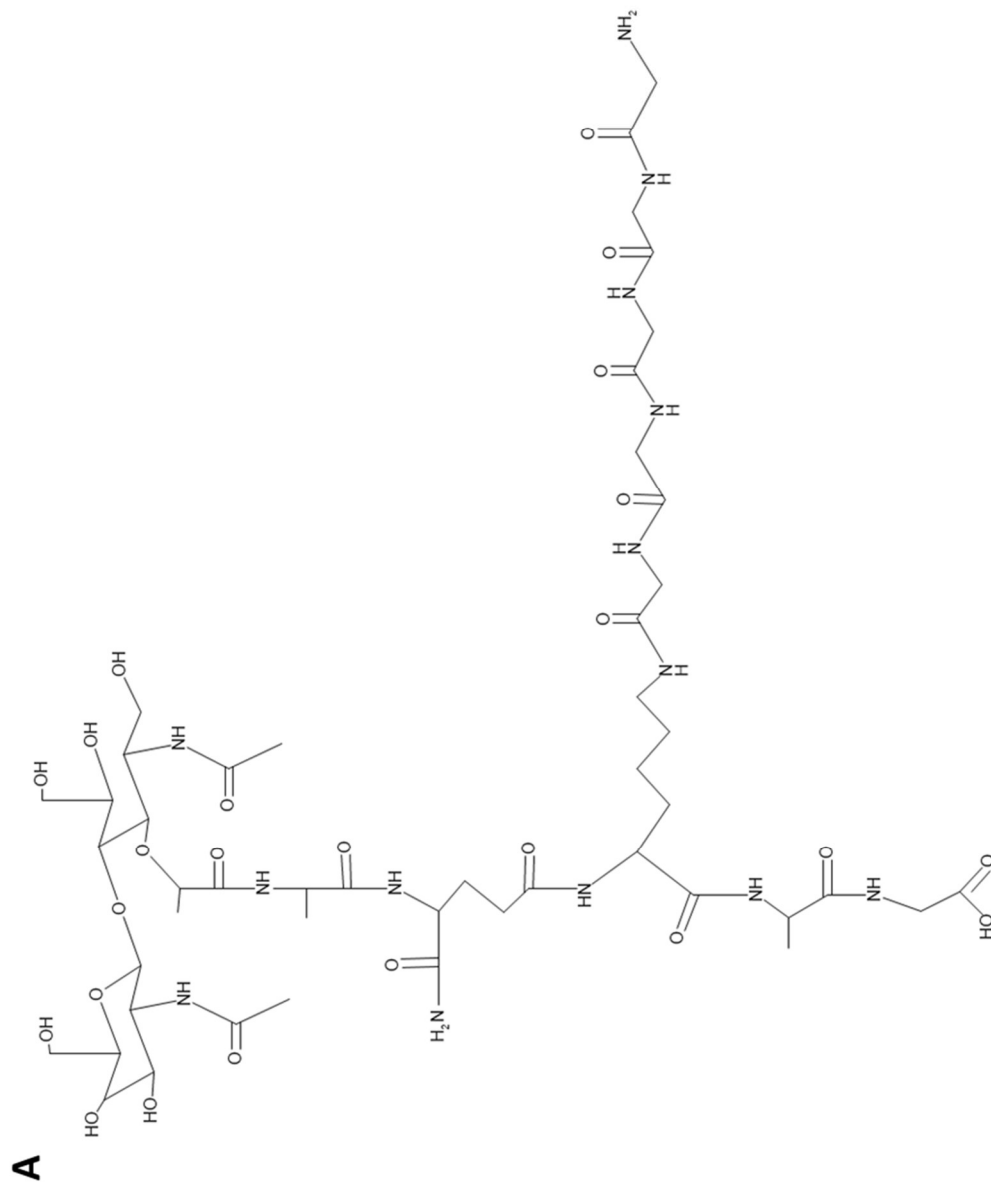
Appendix 1 Figure 25 The chemical structure of muropeptide 13: GM-pentapeptide (Ala,Gln,Lys,Ala,Gln) (GGGGG)

(A) Calculated neutral mass 1238.54 Da. (B) Reference muropeptide.
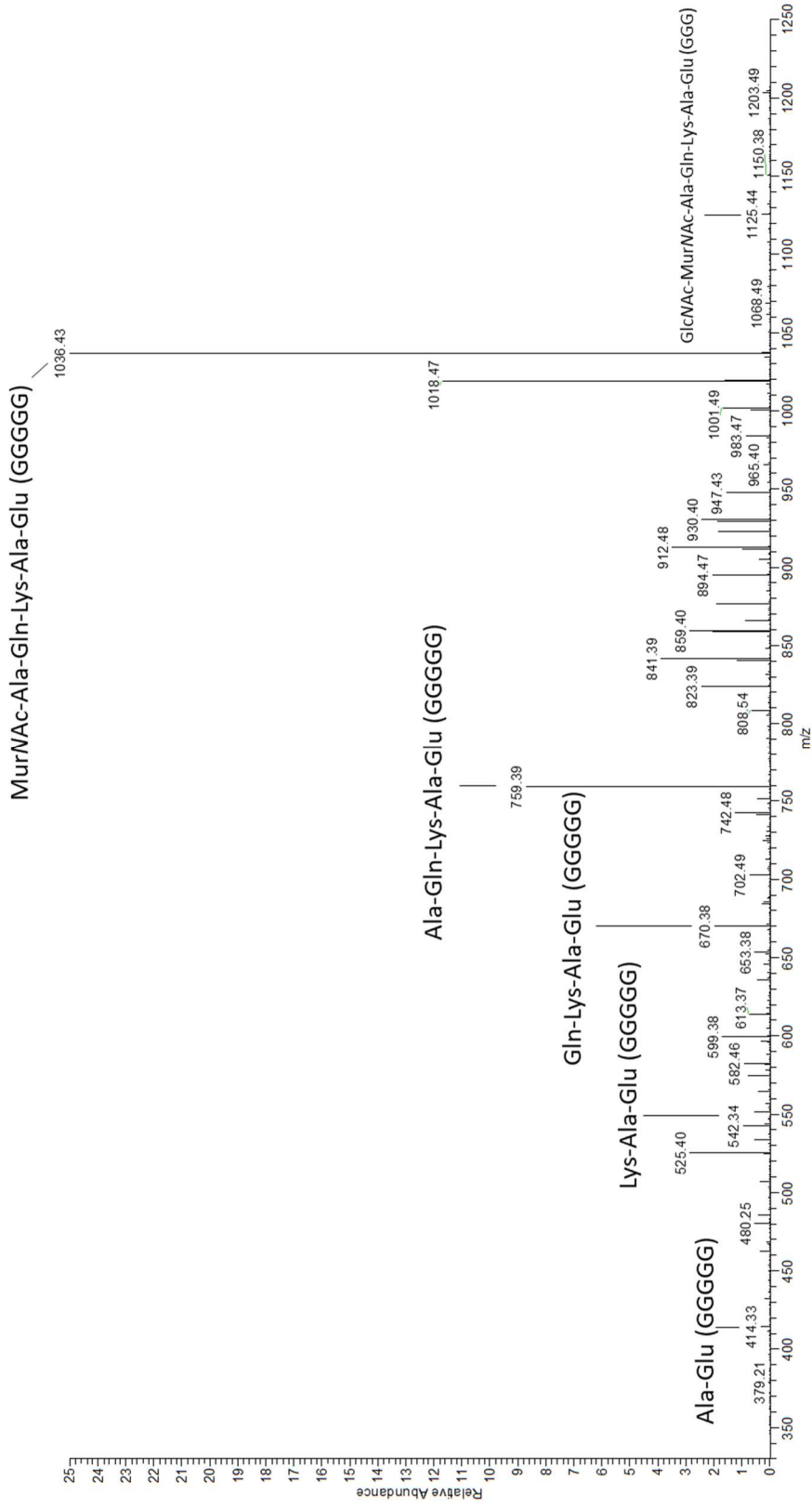
Appendix 1 Figure 26 Representative ion spectrum of muropeptide 13: GM-pentapeptide (Ala,Gln,Lys,Ala,Gln) (GGGGG)

Selected ion peaks from MS/MS analysis have been labelled with corresponding structures.

A

B
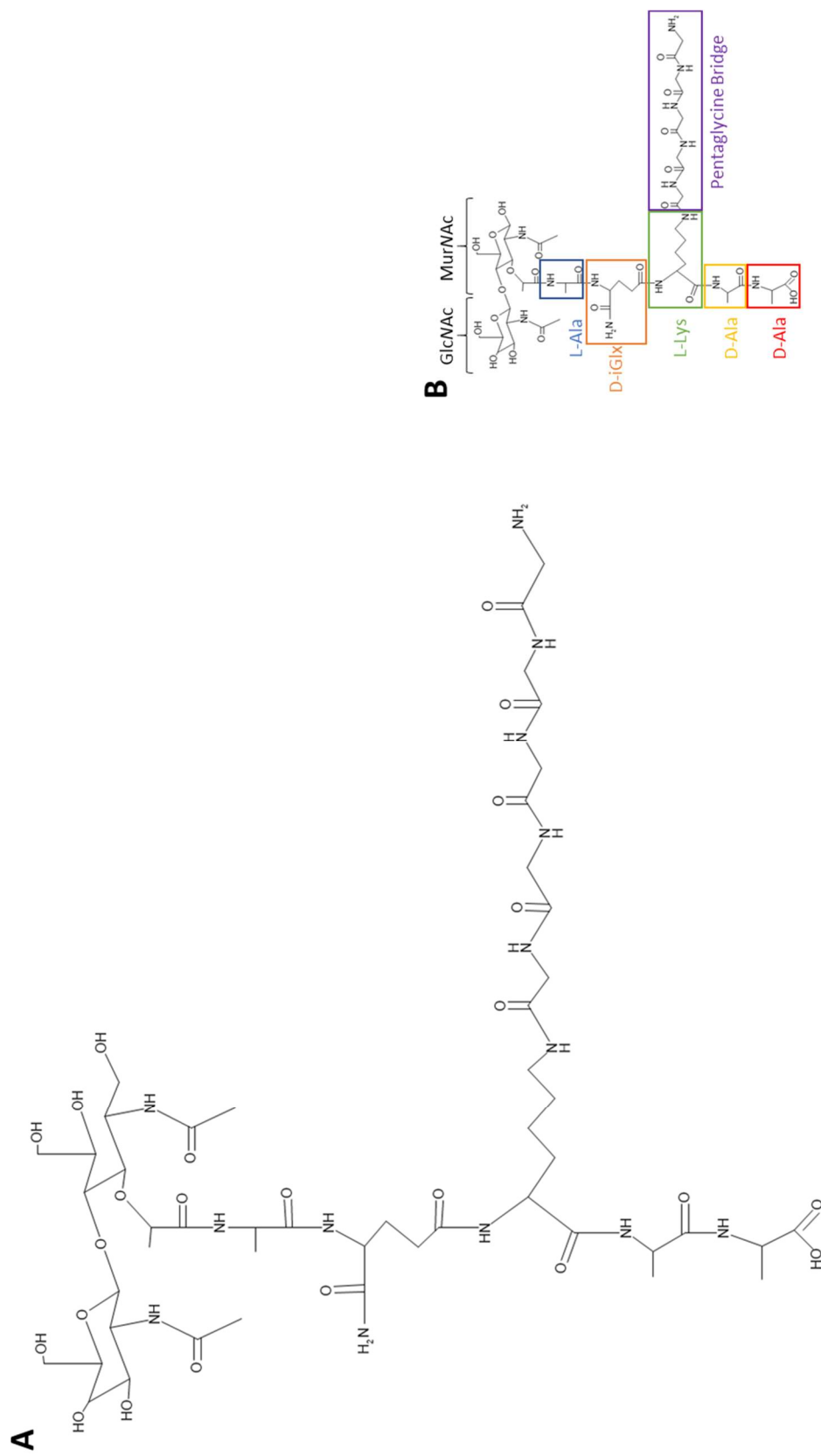
Appendix 1 Figure 27 The chemical structure of muropeptide 14: GM-pentapeptide (Gln) (GGGGG)

(A) Calculated neutral mass 1252.58 Da. (B) Reference muropeptide.
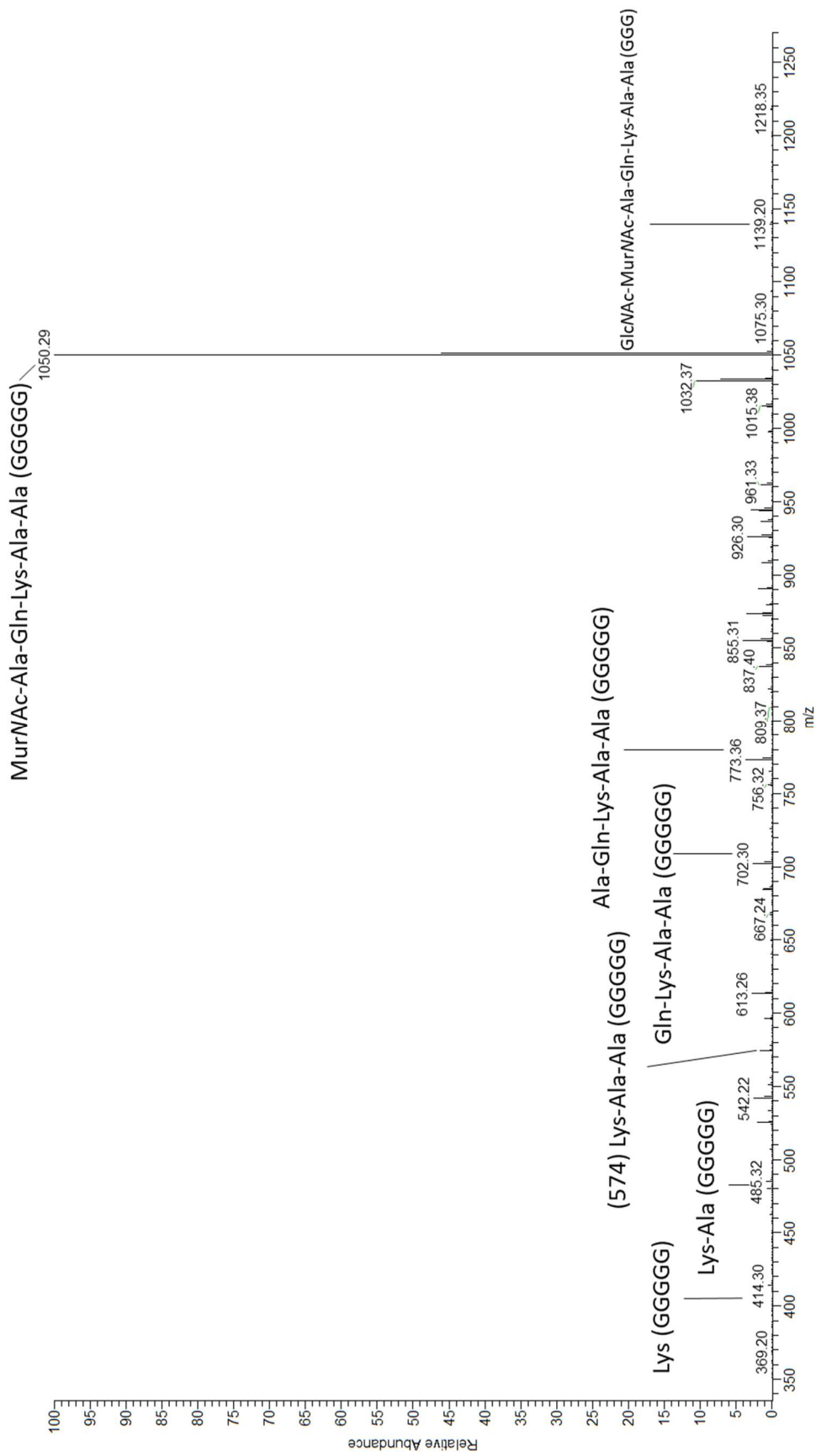
Appendix 1 Figure 28 Representative ion spectrum of muropeptide 14: GM-pentapeptide (Gln) (GGGGG)

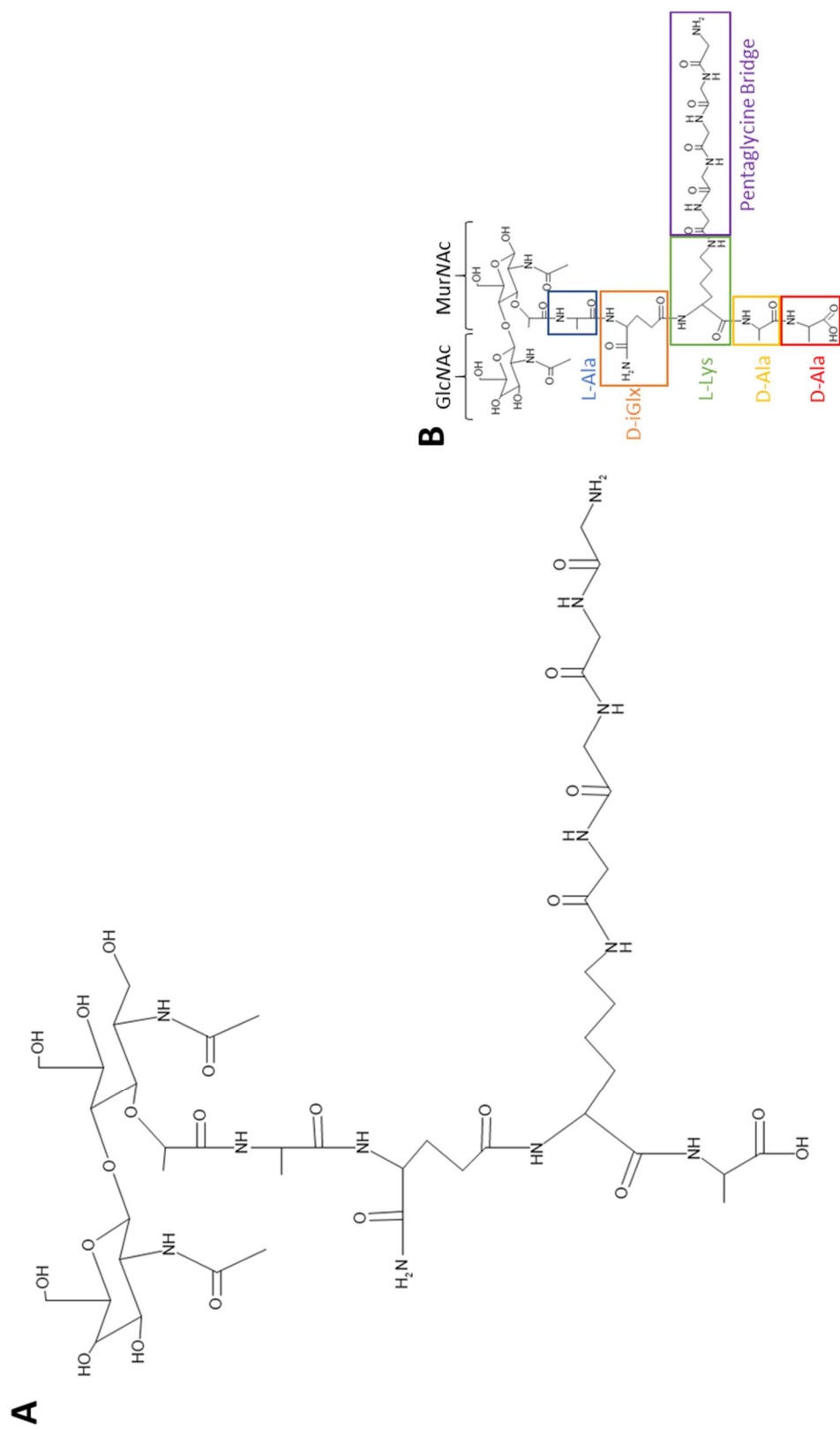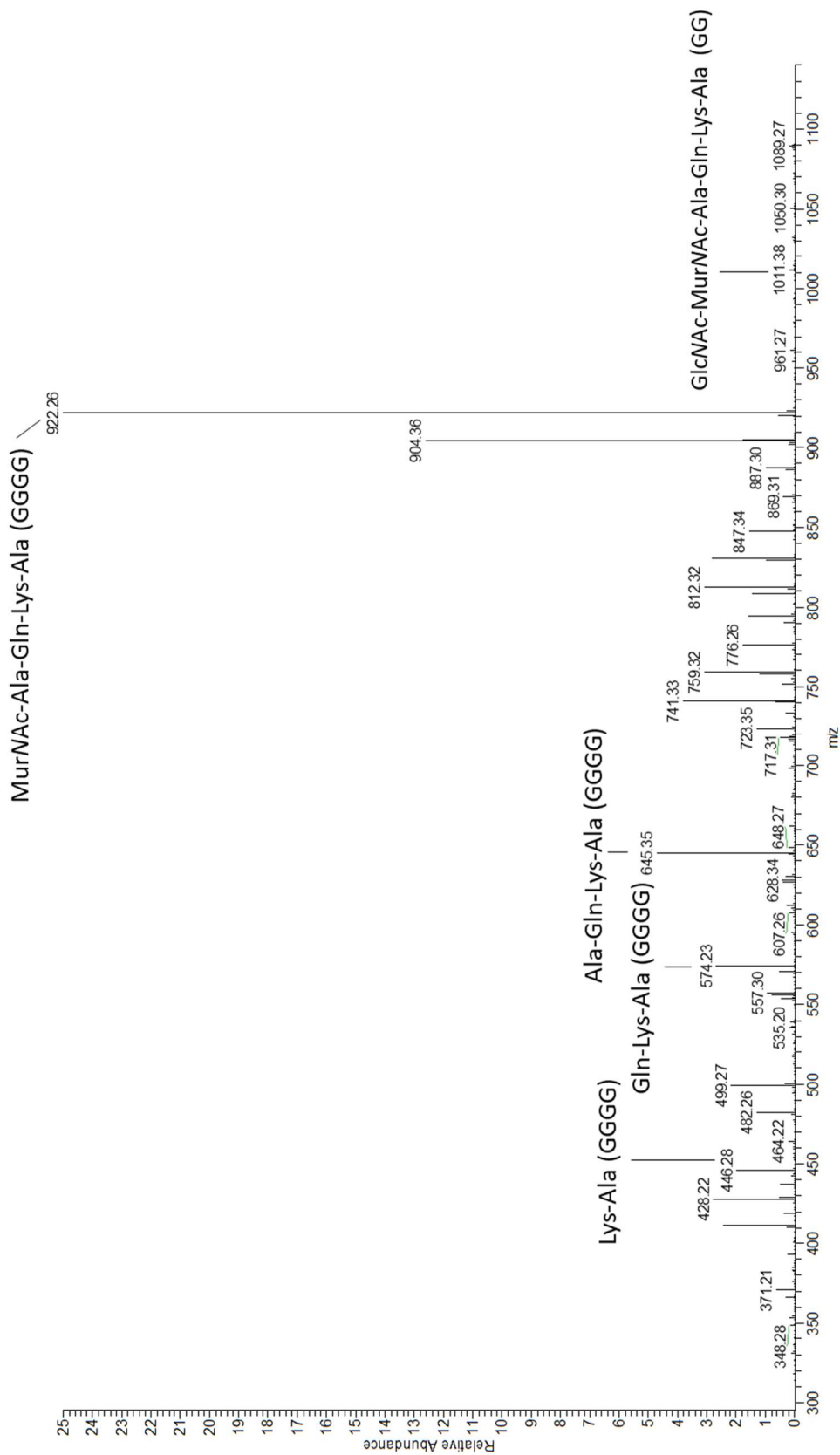Selected ion peaks from MS/MS analysis have been labelled with corresponding structures.
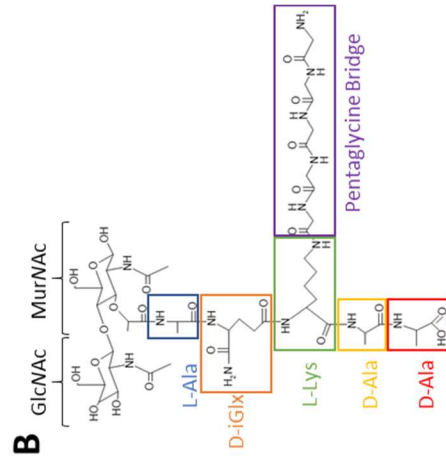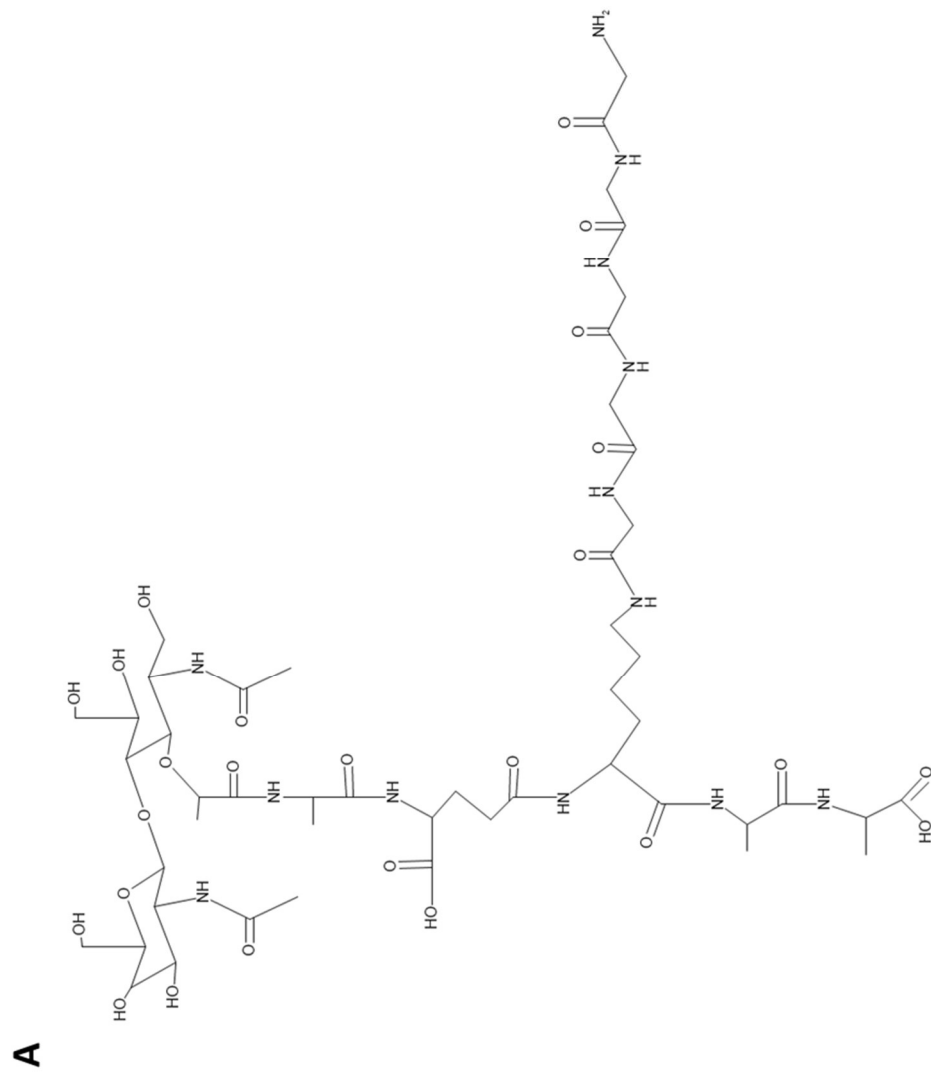
Appendix 1 Figure 29 The chemical structure of muropeptide 15: GM-pentapeptide (Glu) (GGGGG)

(A) Calculated neutral mass 1253.56 Da. (B) Reference muropeptide.
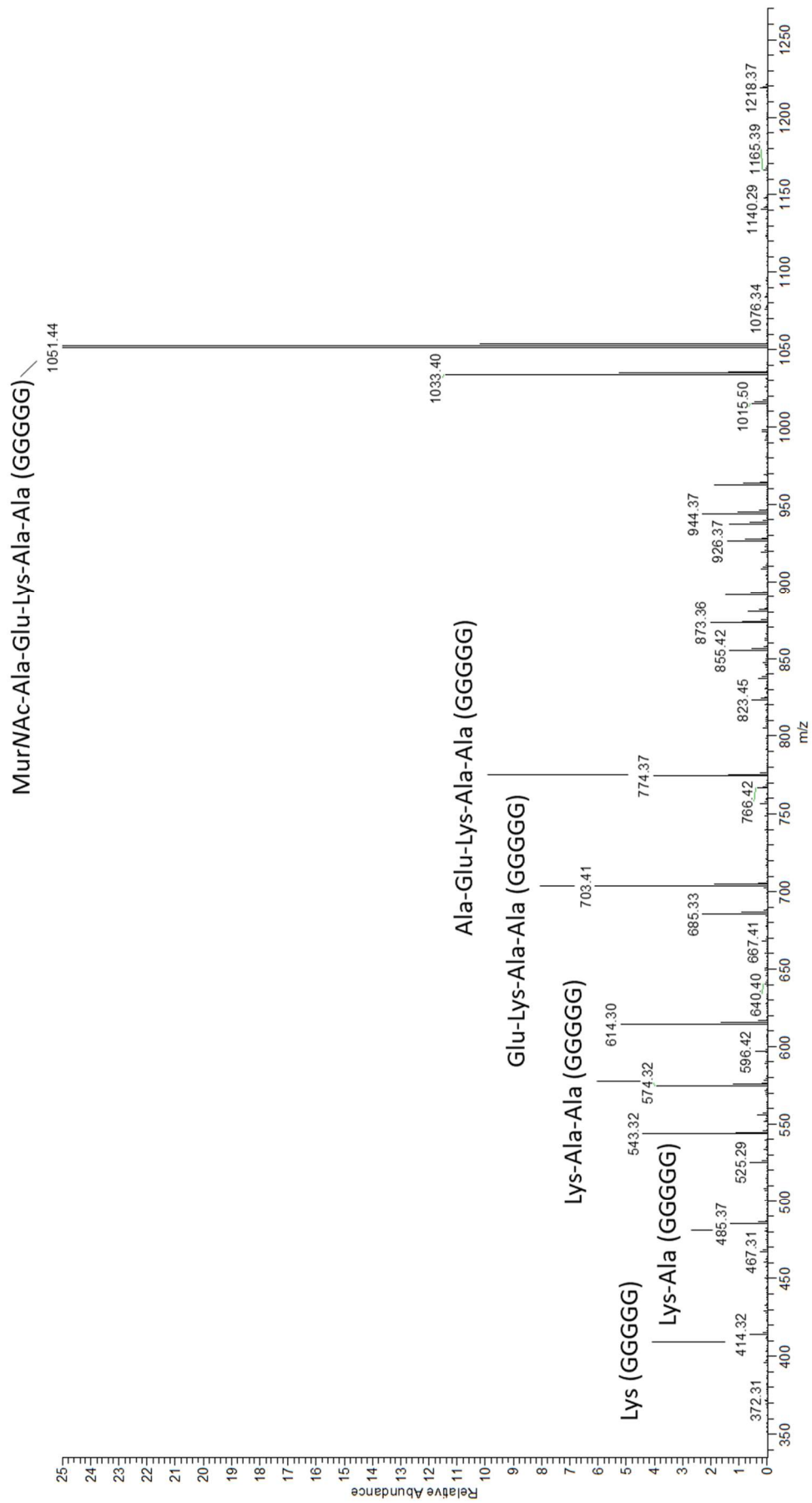
Appendix 1 Figure 30 Representative ion spectrum of muropeptide 15: GM-pentapeptide (Glu) (GGGGG)

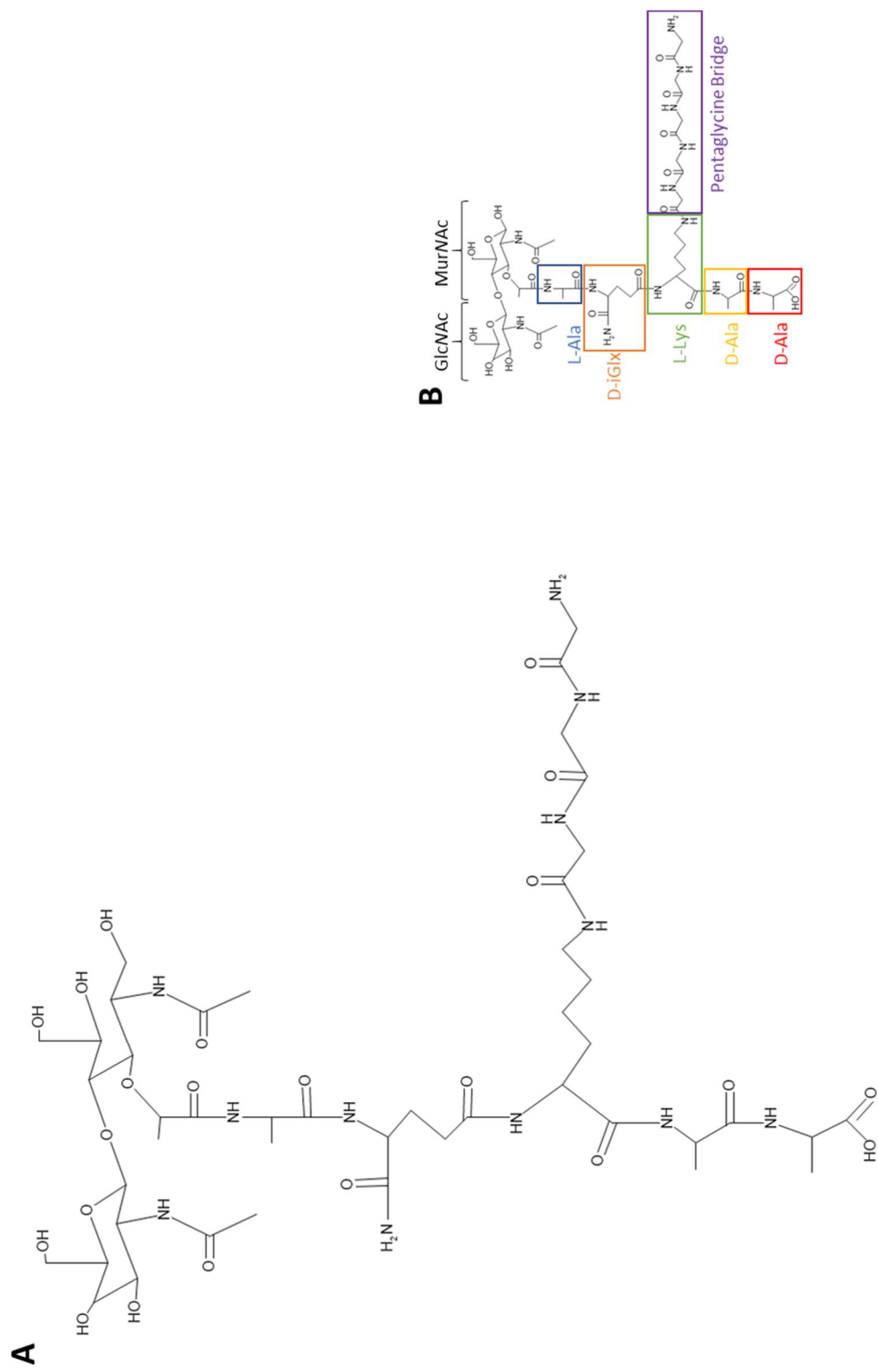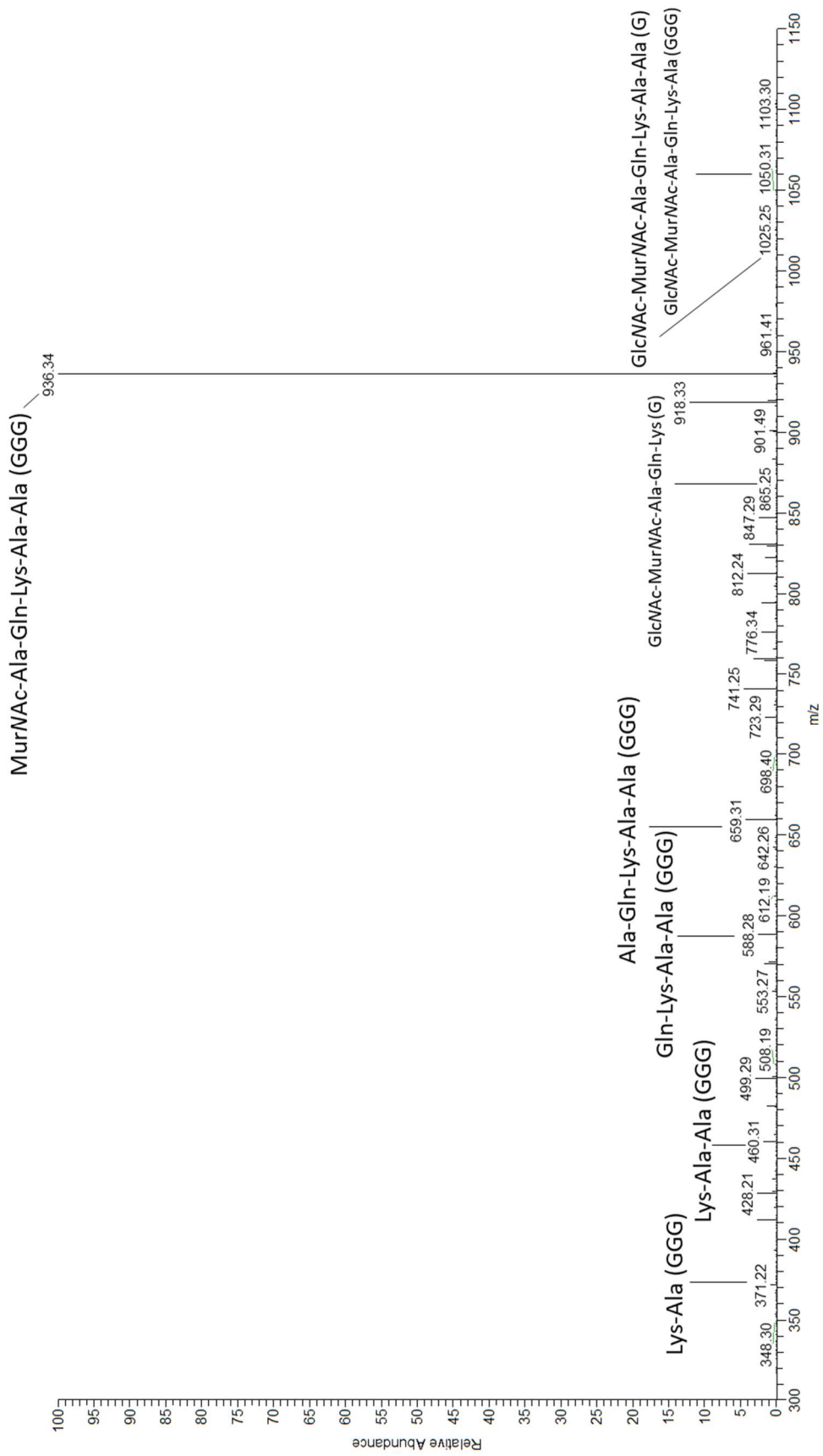Selected ion peaks from MS/MS analysis have been labelled with corresponding structures.
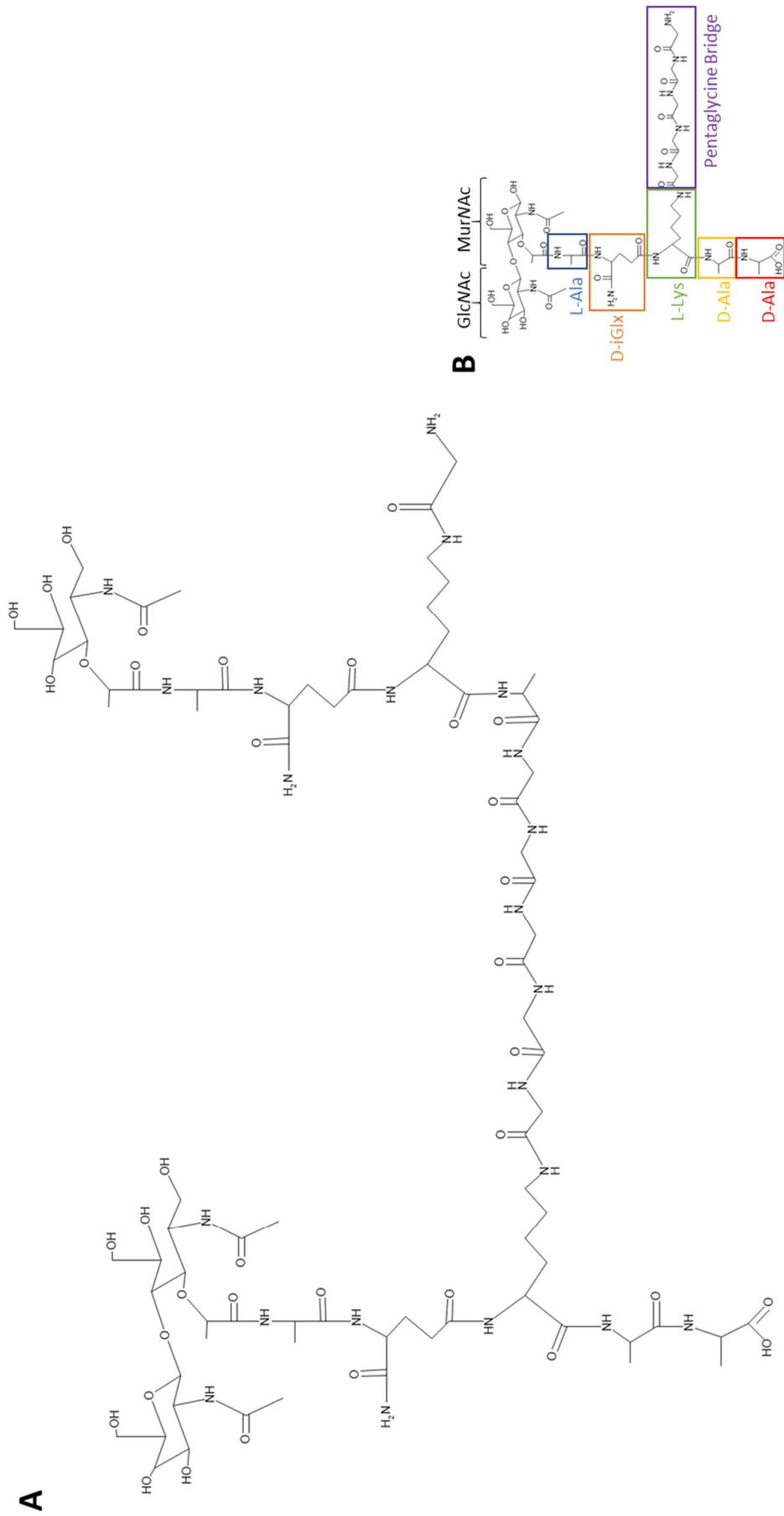
Appendix 1 Figure 31 The chemical structure of muropeptide 16: GM-pentapeptide (GGGGG) – M – tetrapeptide (G)

(A) Calculated neutral mass 1984.94 Da. (B) Reference muropeptide.
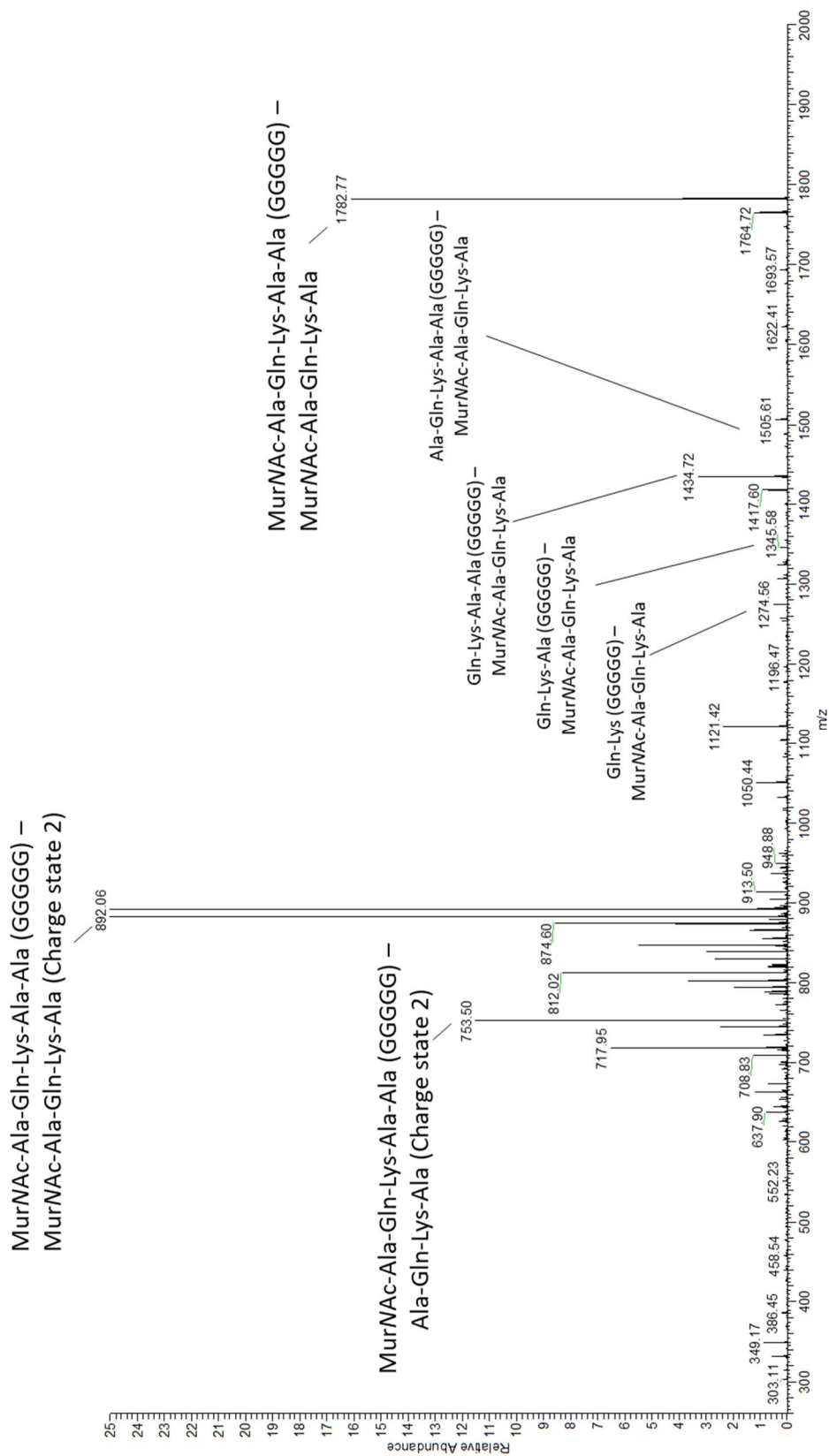
Appendix 1 Figure 32 Representative ion spectrum of muropeptide 16: GM-pentapeptide (GGGGG) – M – tetrapeptide (G)

Selected ion peaks from MS/MS analysis have been labelled with corresponding structures.

344
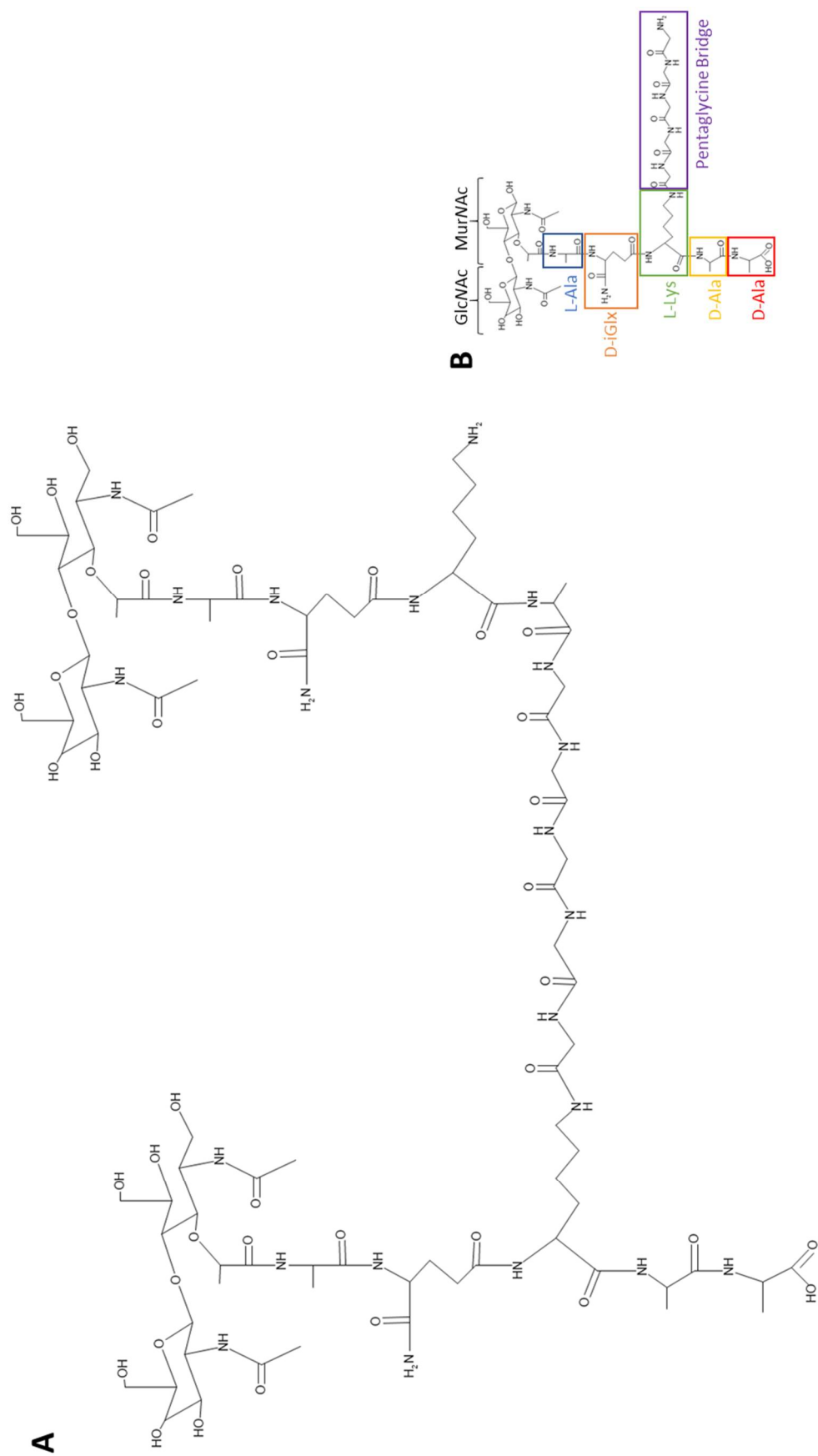
Appendix 1 Figure 33 The chemical structure of muropeptide 17: GM-pentapeptide (GGGGG) – GM – tetrapeptide

(A) Calculated neutral mass 2131.00 Da. (B) Reference muropeptide.
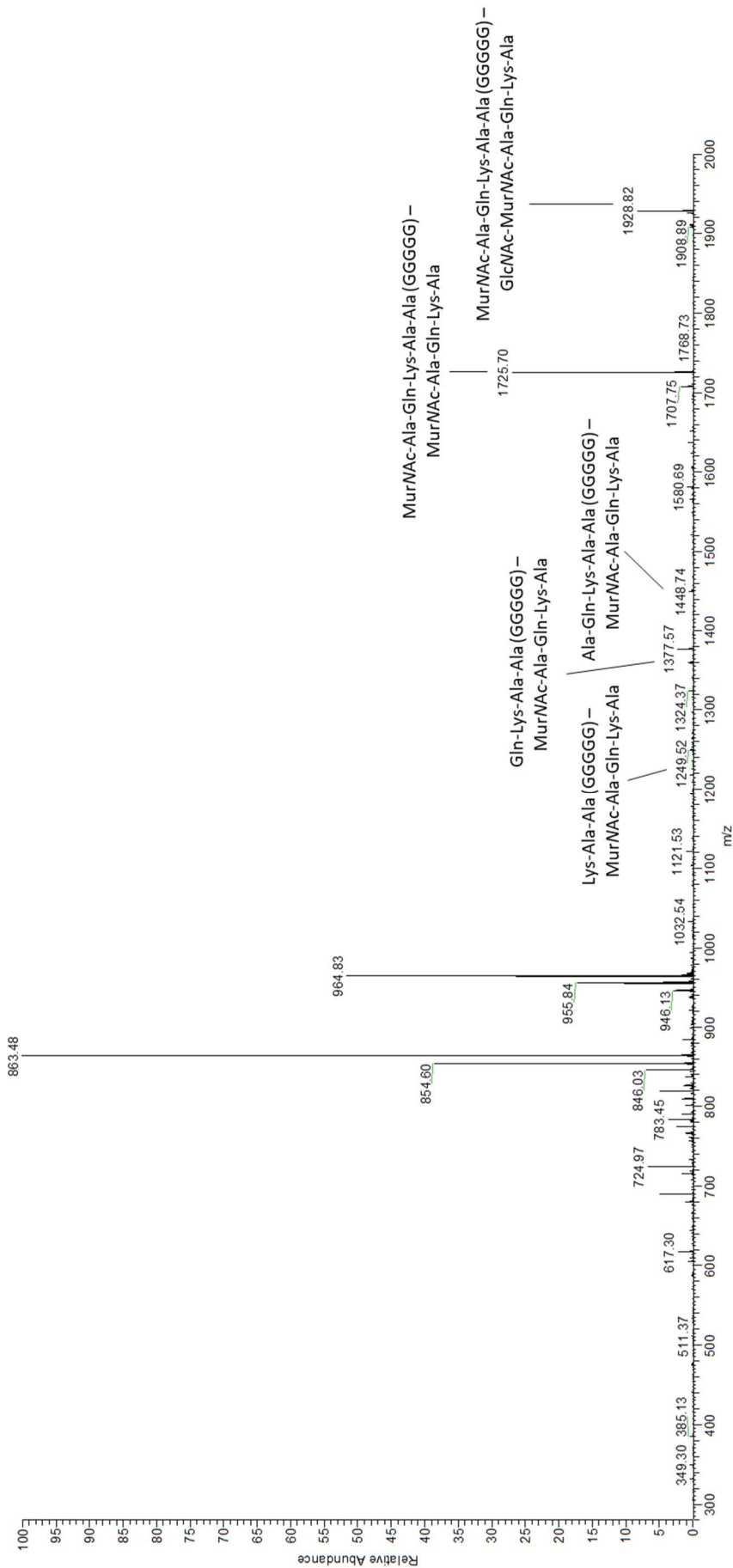
Appendix 1 Figure 34 Representative ion spectrum of muropeptide 17: GM-pentapeptide (GGGGG) – GM – tetrapeptide

Selected ion peaks from MS/MS analysis have been labelled with corresponding structures.

345
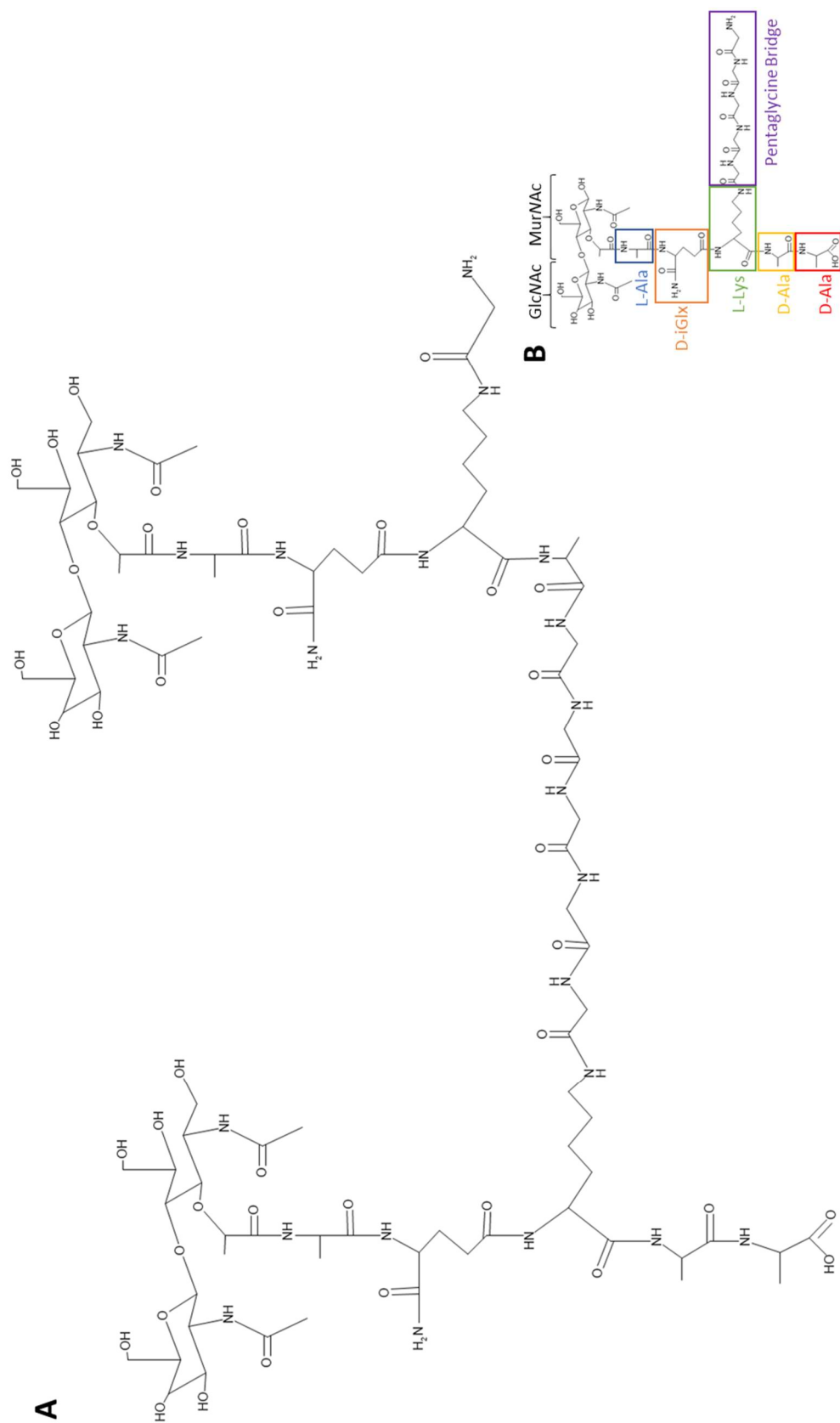
Appendix 1 Figure 35 The chemical structure of muropeptide 18: GM-pentapeptide (GGGGG) – GM – tetrapeptide (G)

(A) Calculated neutral mass 2188.02 Da. (B) Reference muropeptide.
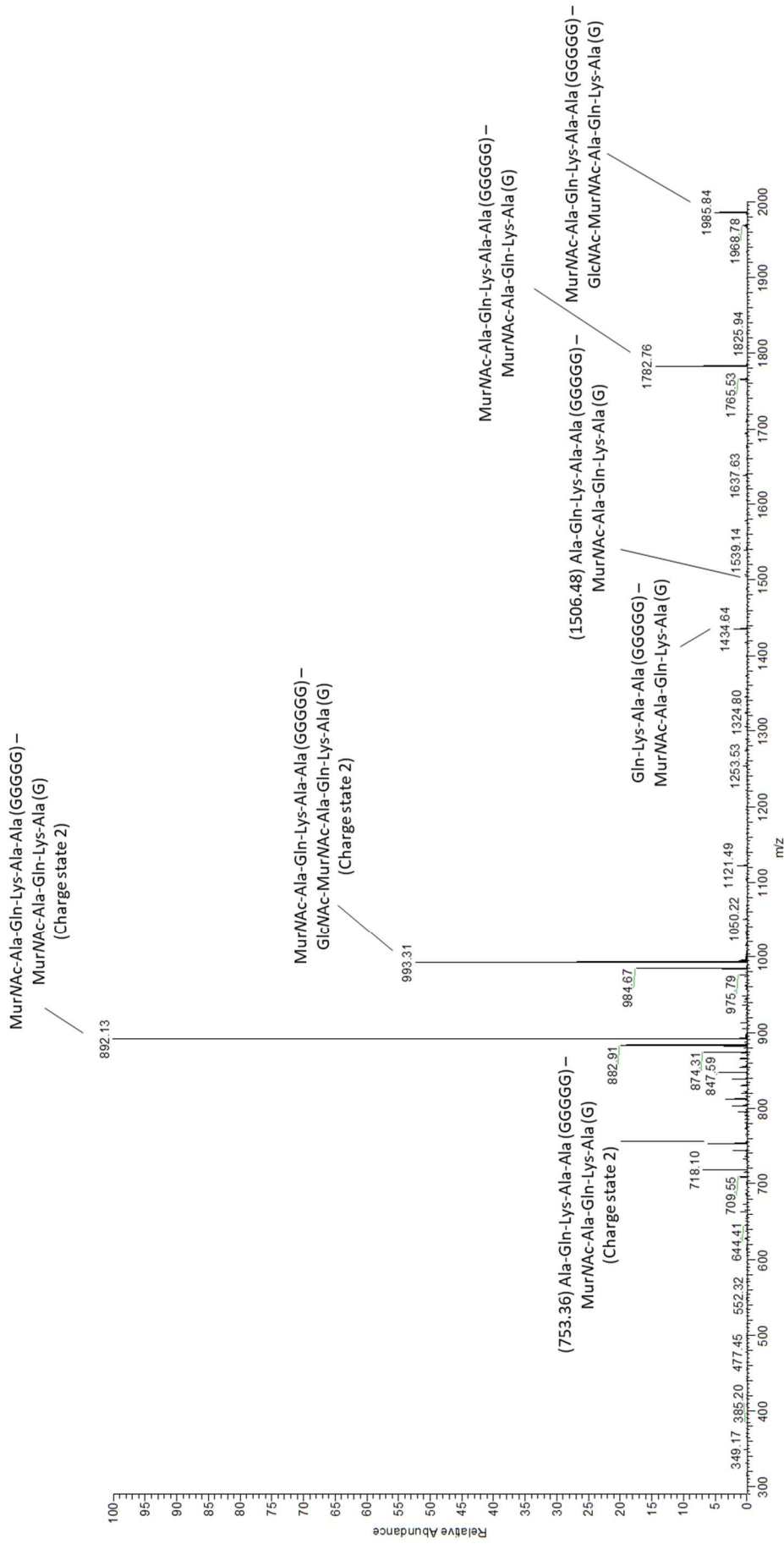
Appendix 1 Figure 36 Representative ion spectrum of muropeptide 18: GM-pentapeptide (GGGGG) – GM – tetrapeptide (G)

Selected ion peaks from MS/MS analysis have been labelled with corresponding structures.
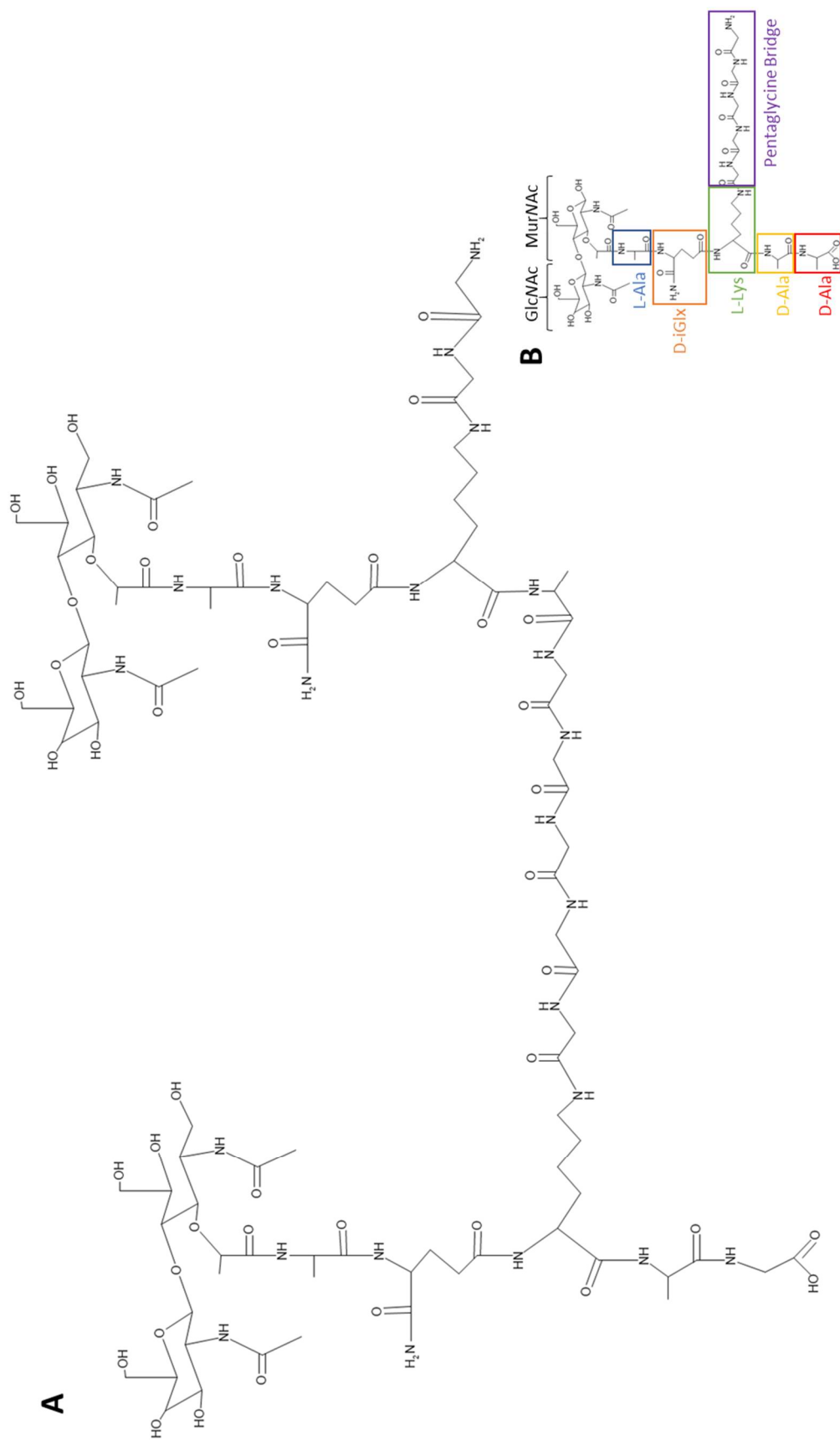
Appendix 1 Figure 37 The chemical structure of muropeptide 19: GM-pentapeptide (Ala-Gln-Lys-Ala-Gly) (GGGGG) – GM – tetrapeptide (G)

(A) Calculated neutral mass 2231.08 Da. (B) Reference muropeptide.
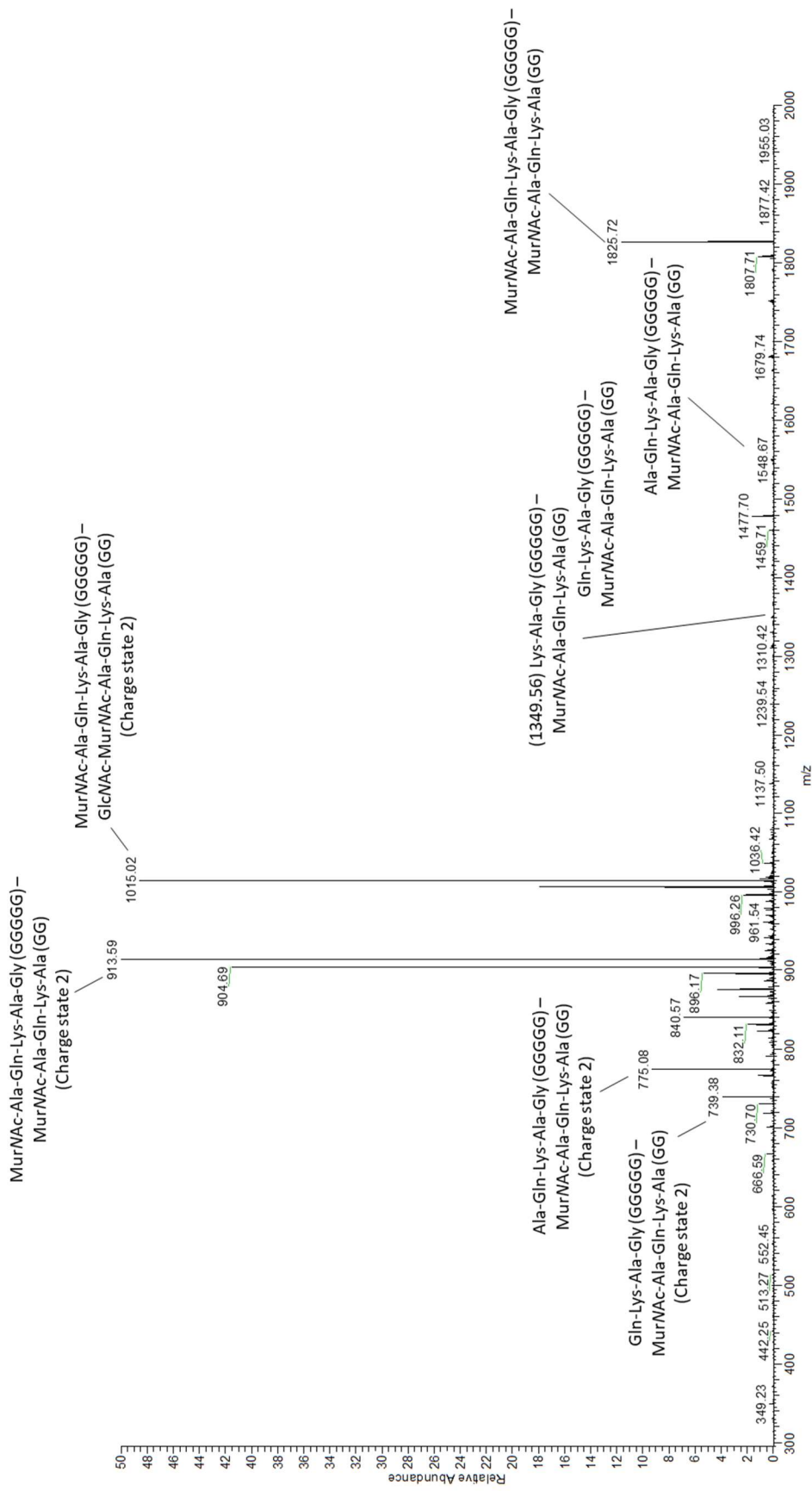
Appendix 1 Figure 38 Representative ion spectrum of muropeptide 19: GM-pentapeptide (GGGGG) – GM – tetrapeptide (G)

Selected ion peaks from MS/MS analysis have been labelled with corresponding structures.

350
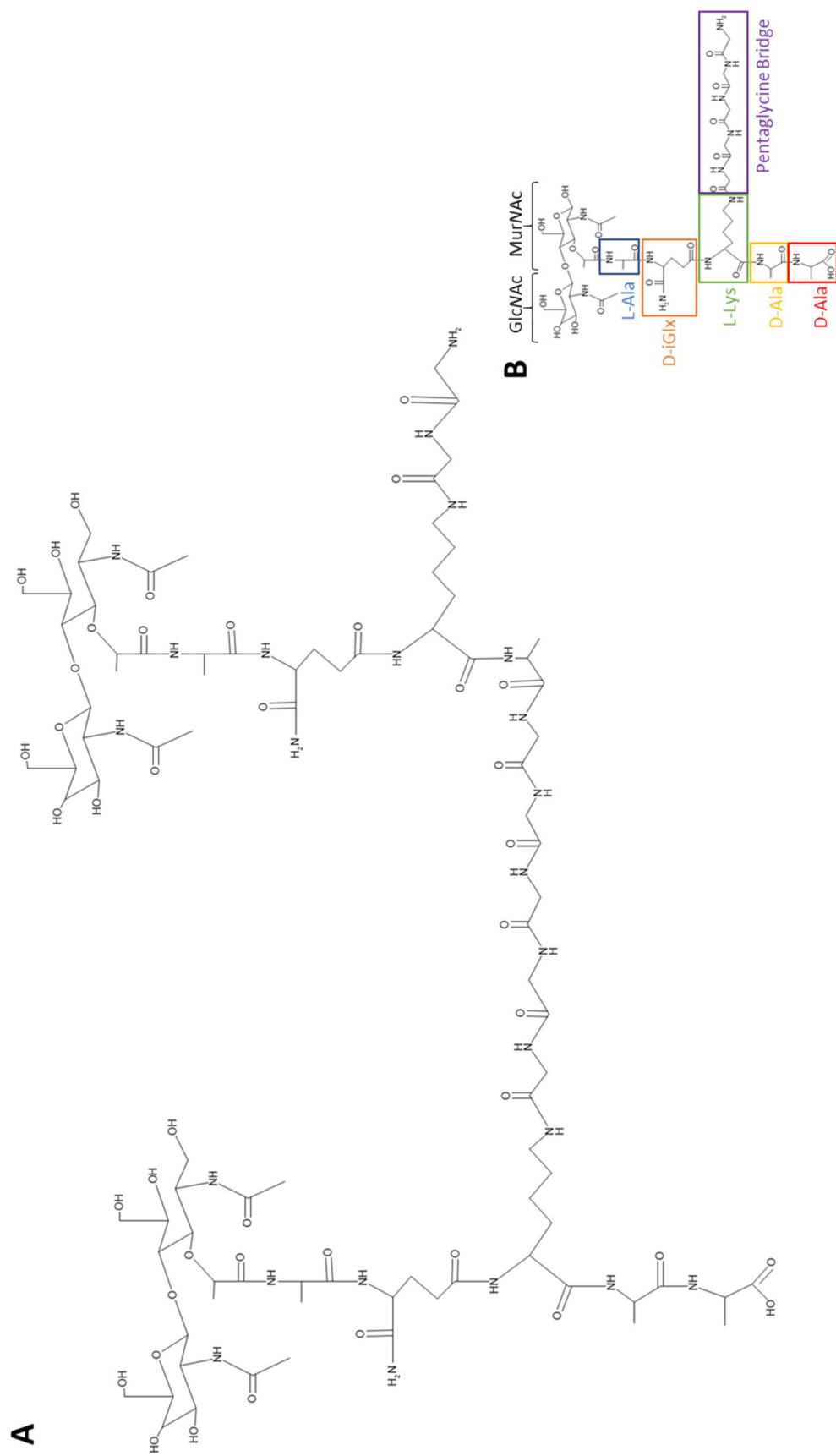
Appendix 1 Figure 39 The chemical structure of muropeptide 20: GM-pentapeptide (GGGGG) – GM – tetrapeptide (GG)

(A) Calculated neutral mass 2245.04 Da. (B) Reference muropeptide.
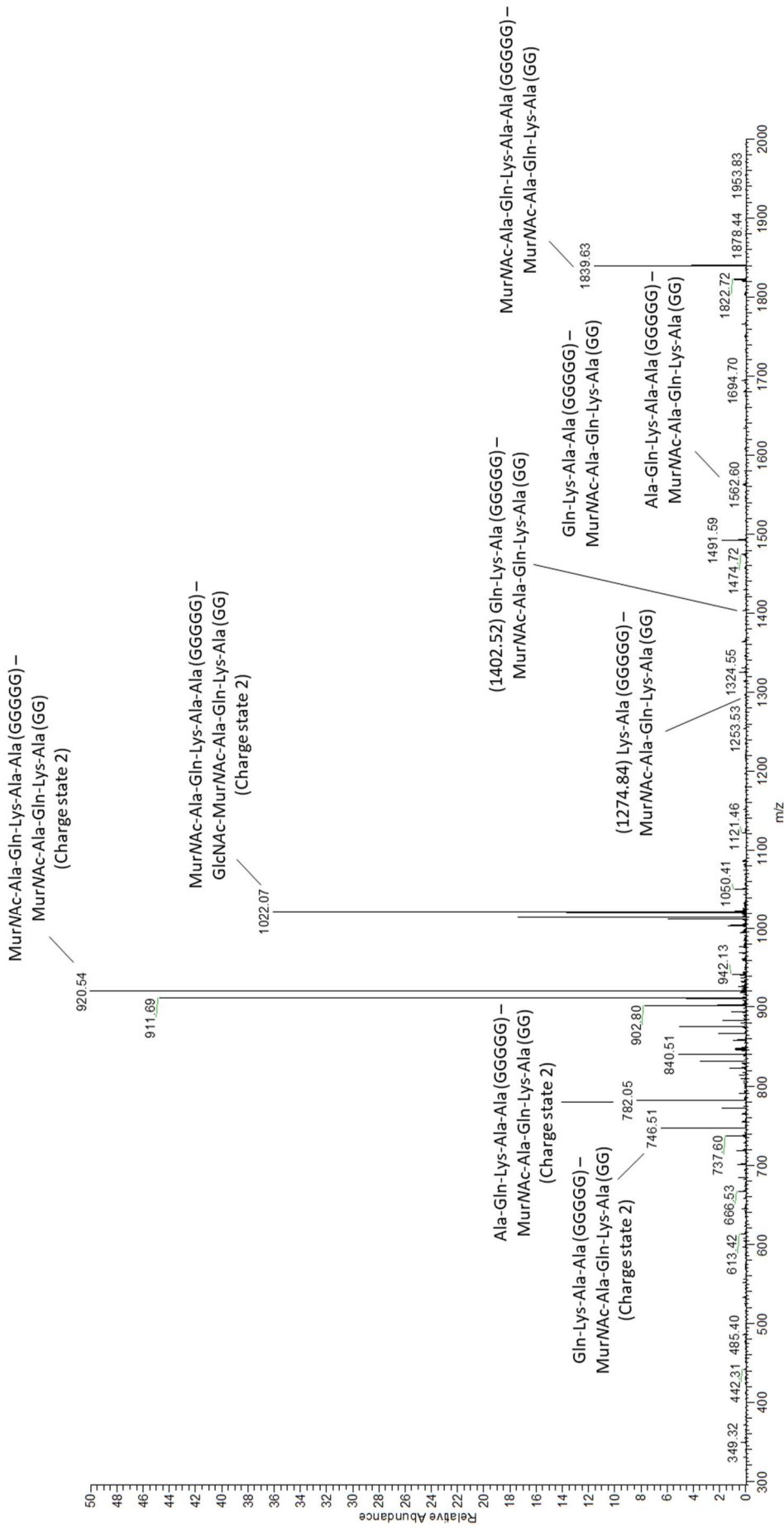
Appendix 1 Figure 40 Representative ion spectrum of muropeptide 20: GM-pentapeptide (GGGGG) – GM – tetrapeptide (GG)

Selected ion peaks from MS/MS analysis have been labelled with corresponding structures.
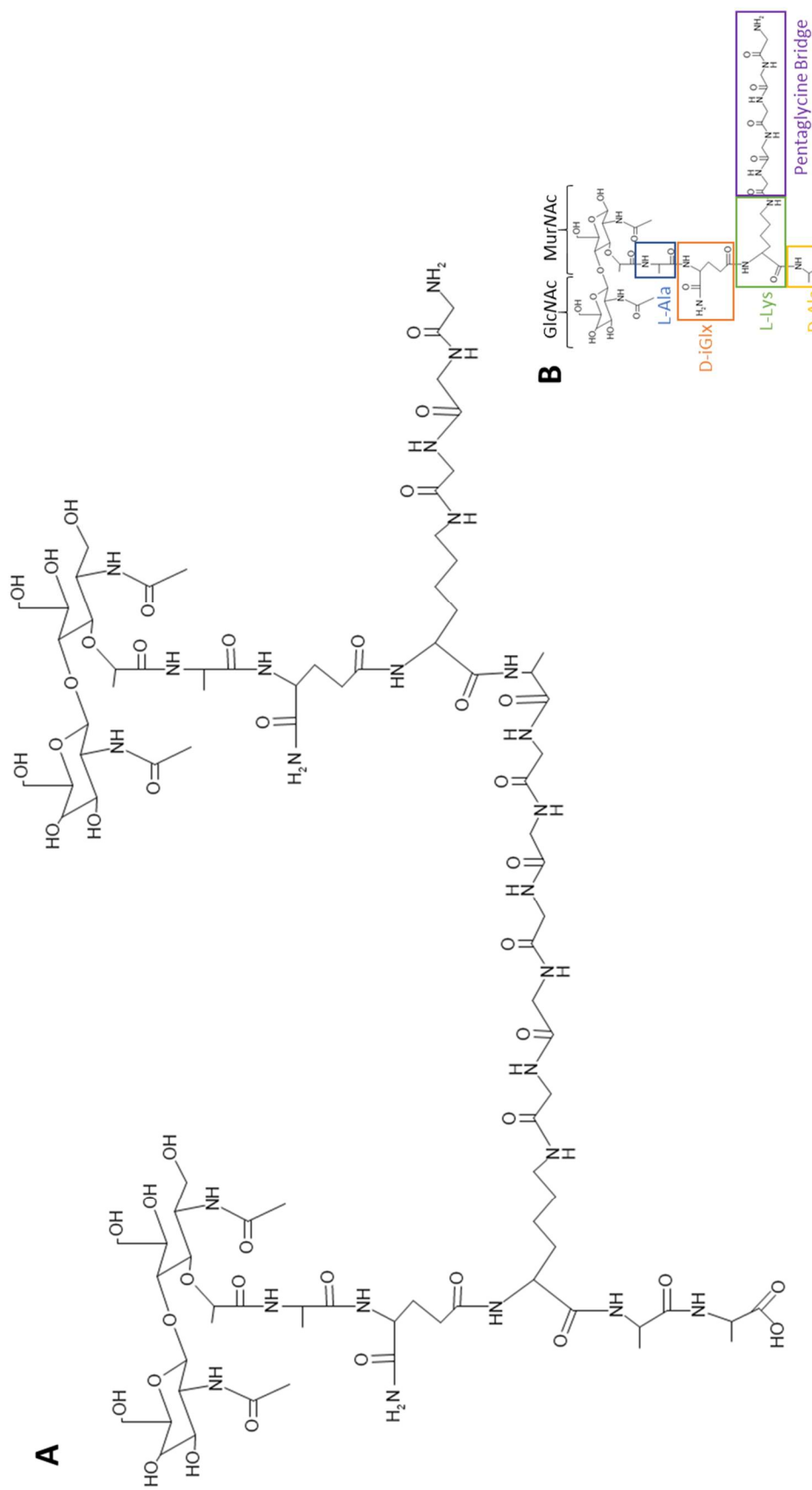
Appendix 1 Figure 41 The chemical structure of muropeptide 21: GM-pentapeptide (GGGGG) – GM – tetrapeptide (GGG)

(A) Calculated neutral mass 2302.07 Da. (B) Reference muropeptide.
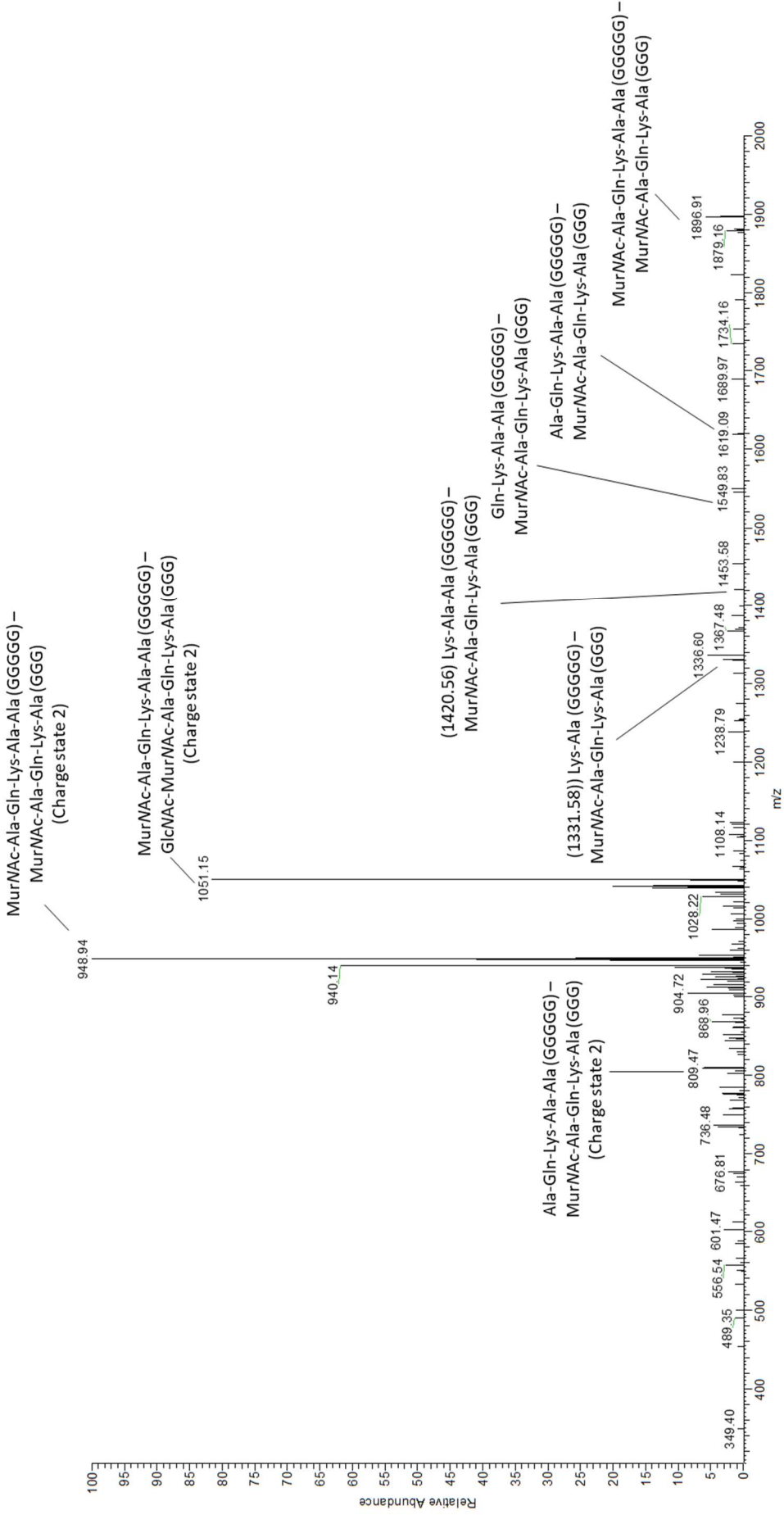
Appendix 1 Figure 42 Representative ion spectrum of muropeptide 21: GM-pentapeptide (GGGGG) – GM – tetrapeptide (GGG)

Selected ion peaks from MS/MS analysis have been labelled with corresponding structures.

353
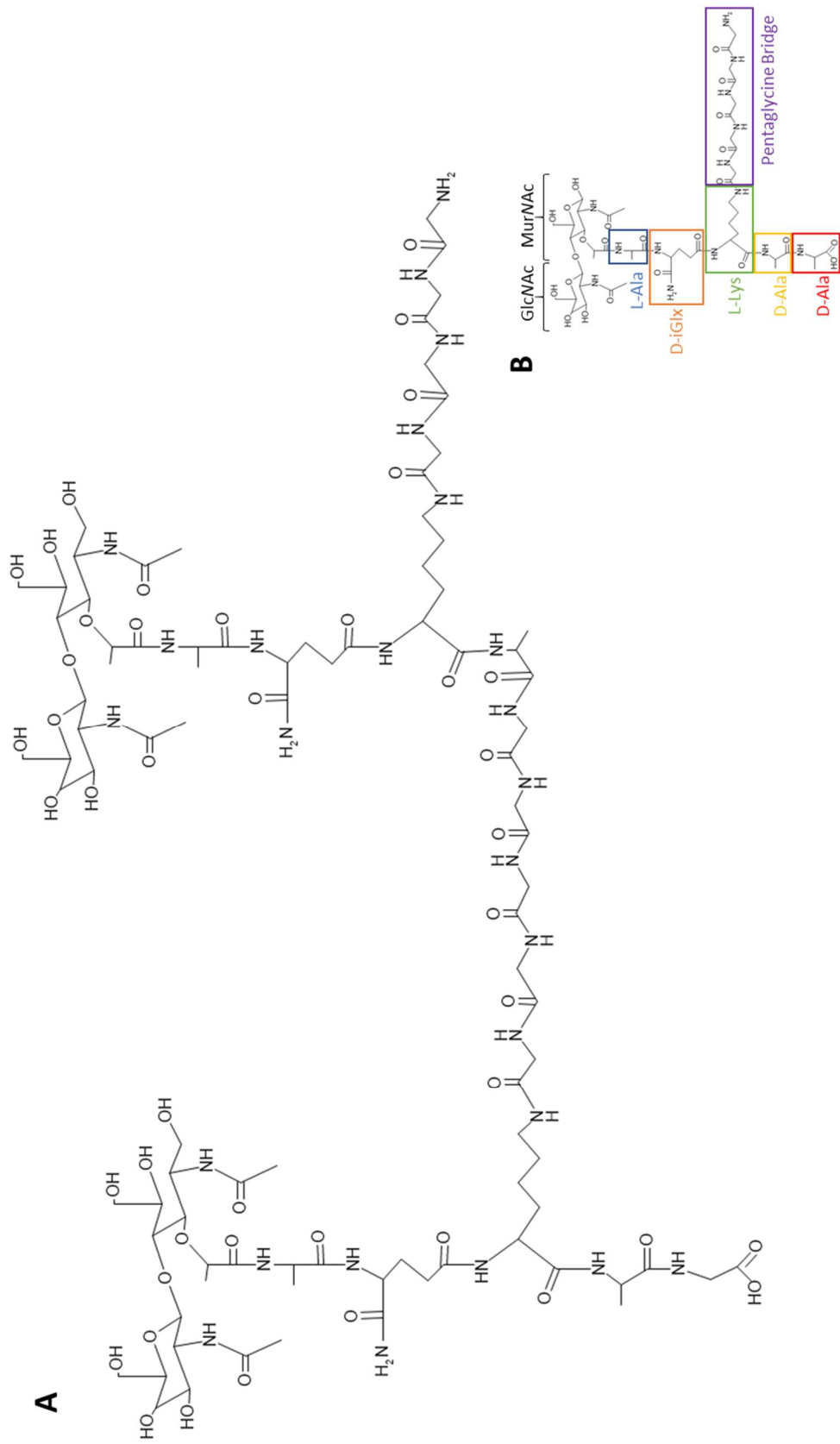
Appendix 1 Figure 43 The chemical structure of muropeptide 22: GM-pentapeptide (Ala-iGln-Lys-Ala-Gly) (GGGGG) – GM – tetrapeptide (GGGG)

(A) Calculated neutral mass 2345.09 Da. (B) Reference muropeptide.
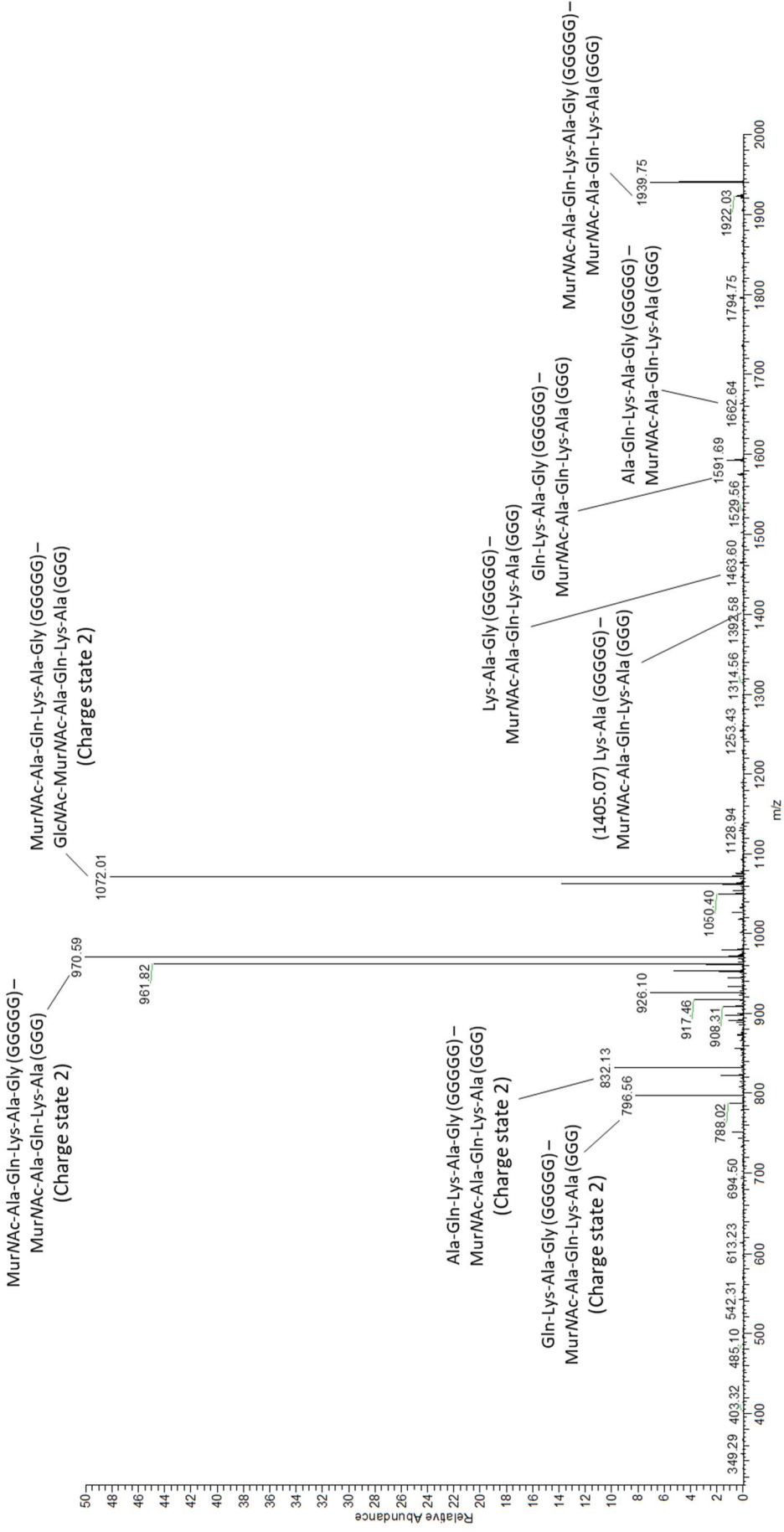
Appendix 1 Figure 44 Representative ion spectrum of muropeptide 22: GM-pentapeptide (Ala-iGln-Lys-Ala-Gly) (GGGGG) – GM – tetrapeptide (GGGG)

Selected ion peaks from MS/MS analysis have been labelled with corresponding structures.
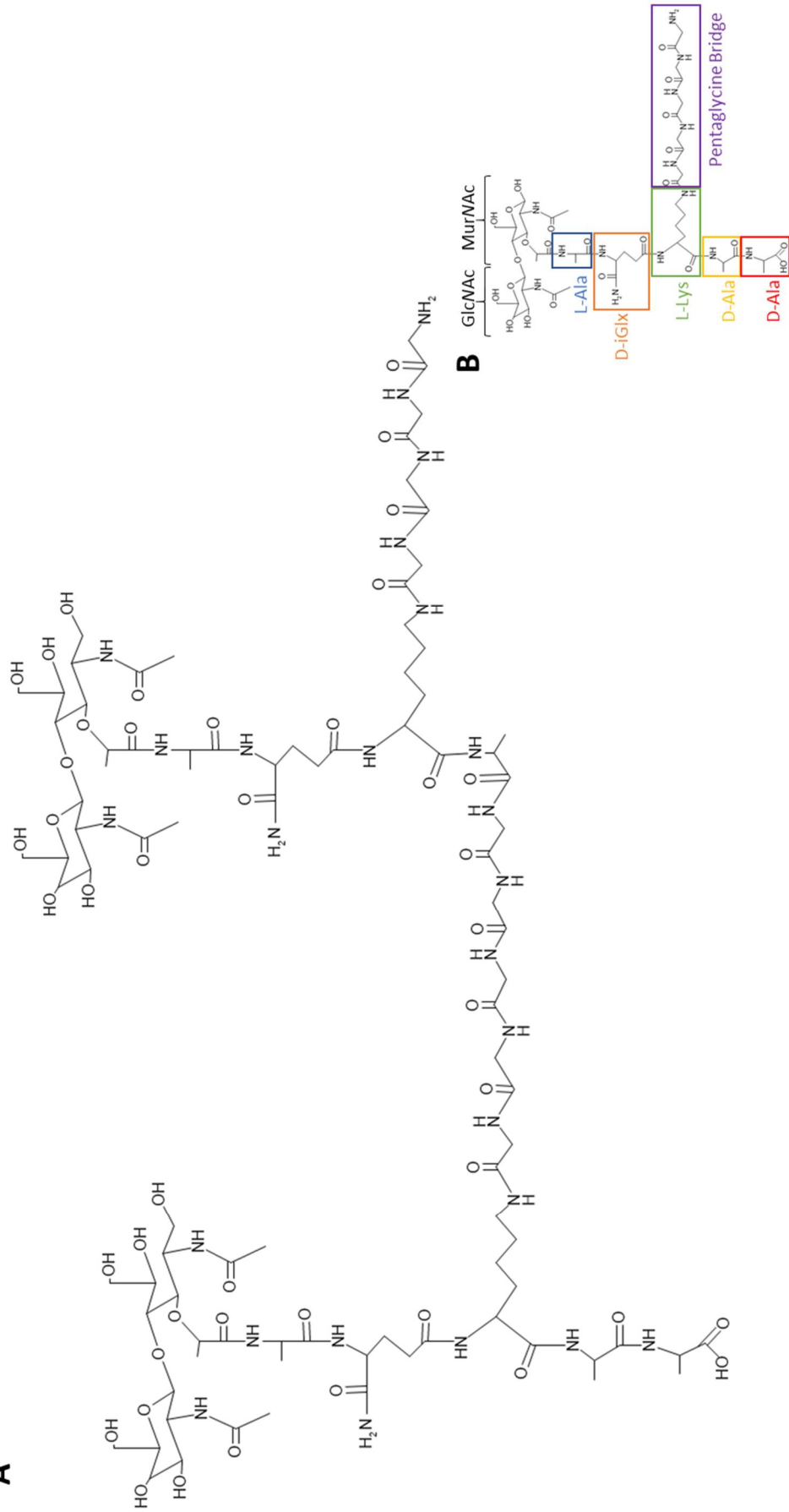
Appendix 1 Figure 45 The chemical structure of muropeptide 23: GM-pentapeptide (GGGGG) – GM – tetrapeptide (GGGG)

(A) Calculated neutral mass 2359.09 Da. (B) Reference muropeptide.

Appendix 1 Figure 46 Representative ion spectrum of muropeptide 23: GM-pentapeptide (GGGGG) – GM – tetrapeptide (GGGG)

Selected ion peaks from MS/MS analysis have been labelled with corresponding structures.
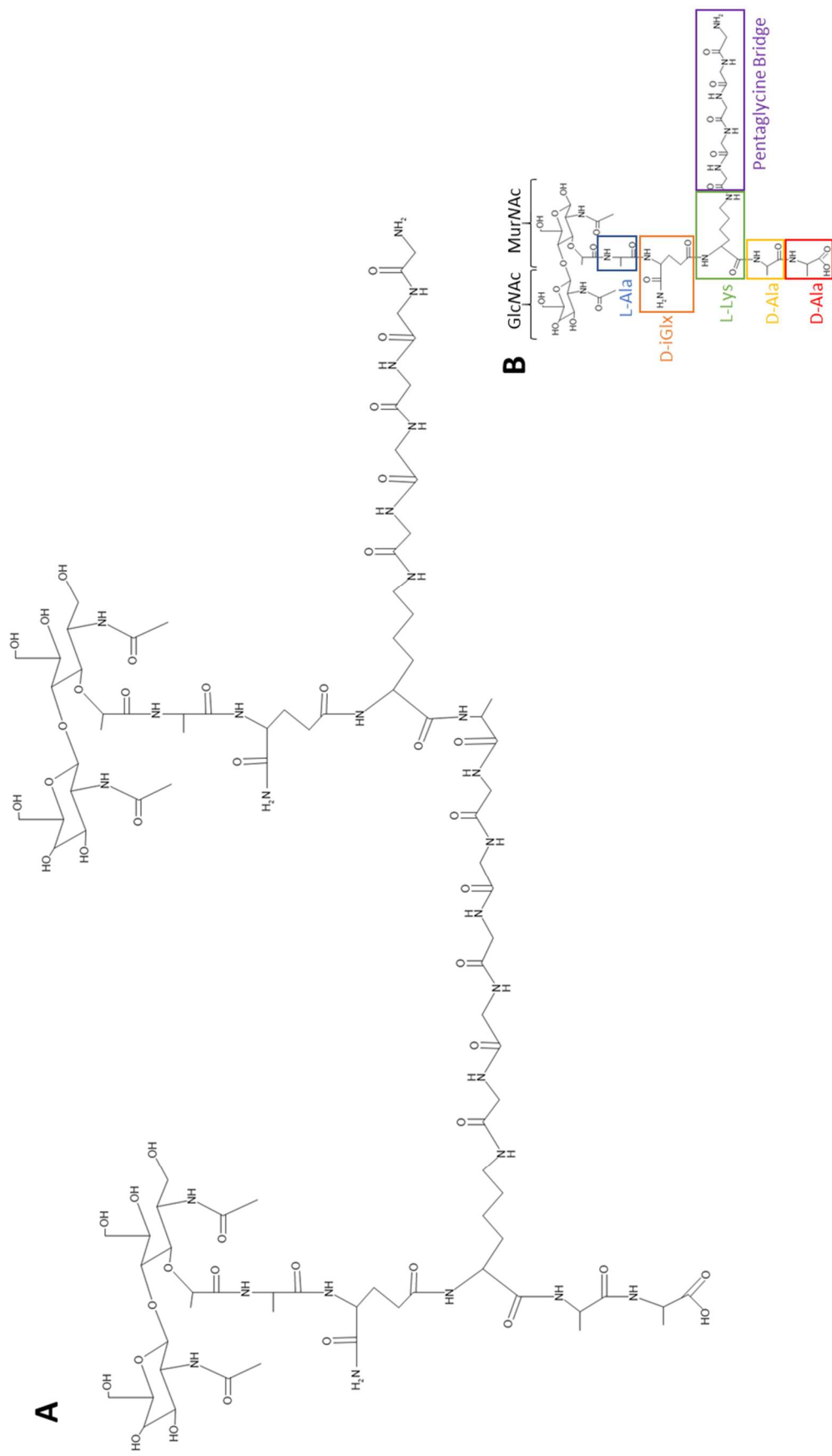
Appendix 1 Figure 47 The chemical structure of muropeptide 24: GM-pentapeptide (GGGGG) – GM – tetrapeptide (GGGGG)

(A) Calculated neutral mass 2417.49 Da. (B) Reference muropeptide.
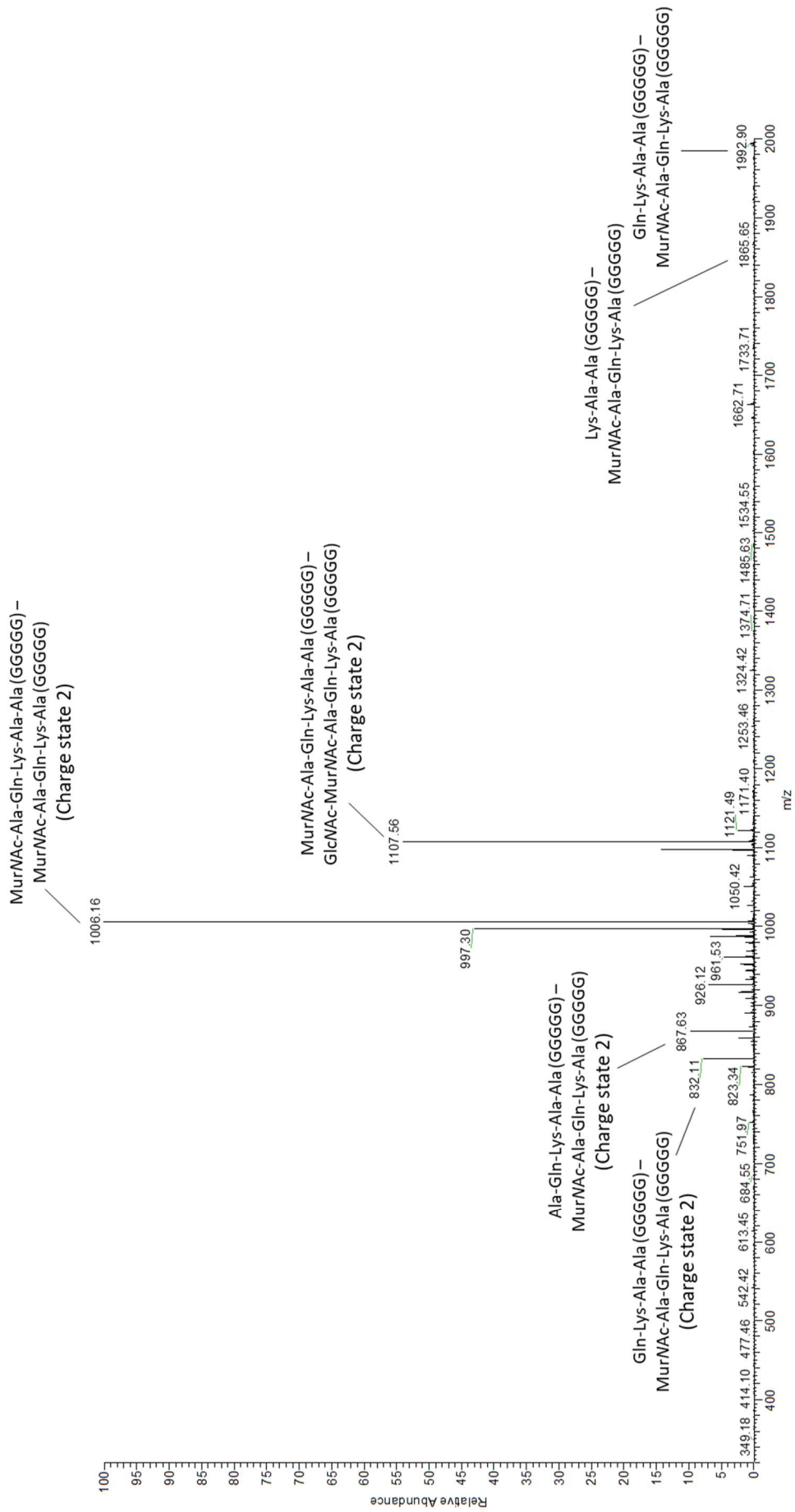
Appendix 1 Figure 48 Representative ion spectrum of muropeptide 24: GM-pentapeptide (GGGGG) – GM – tetrapeptide (GGGGG)

Selected ion peaks from MS/MS analysis have been labelled with corresponding structures.
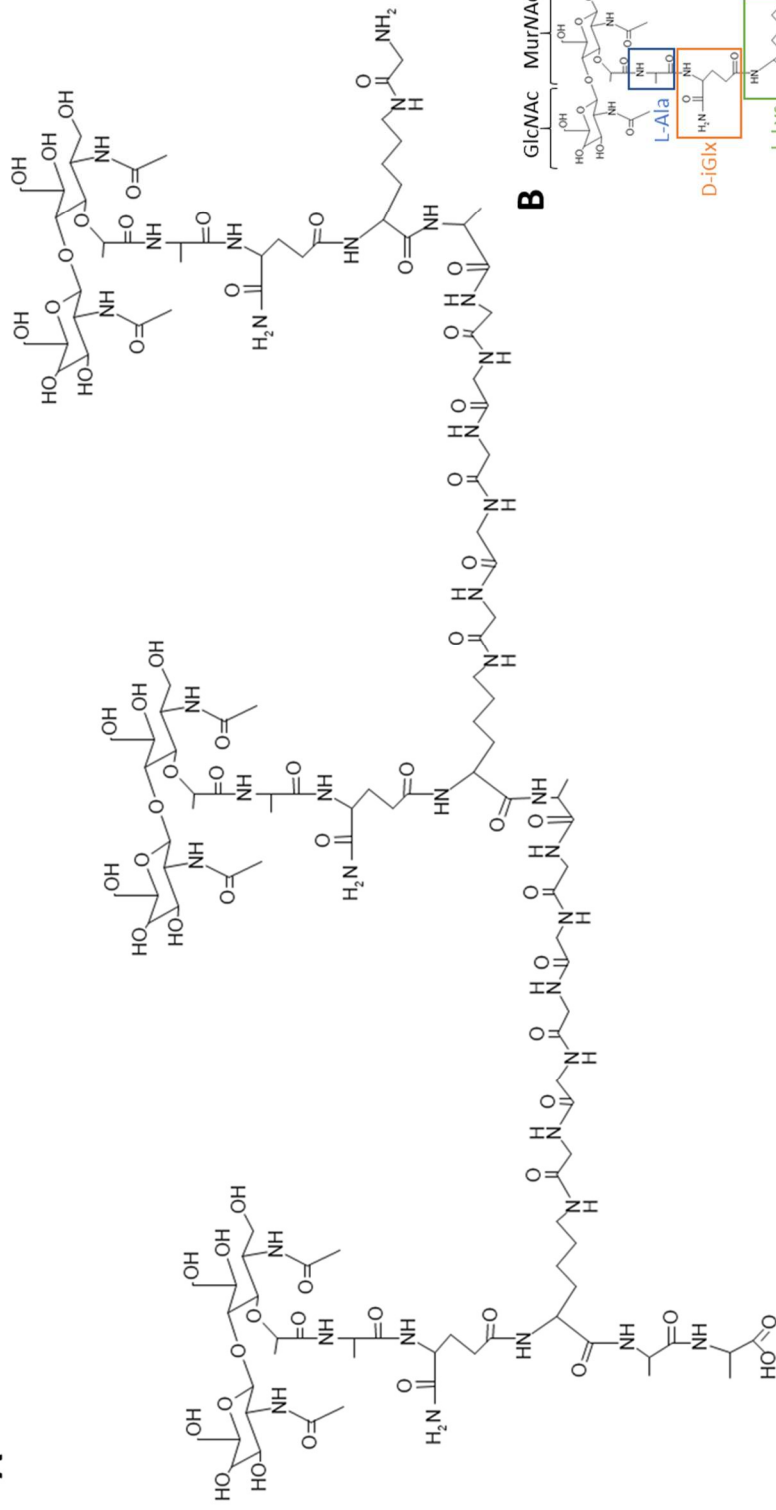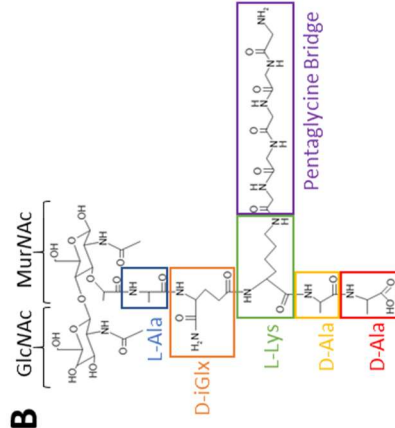
Appendix 1 Figure 49 The chemical structure of muropeptide 25: GM-pentapeptide (GGGGG) – GM – tetrapeptide (GGGGG) – GM – tetrapeptide (G)

(A) Calculated neutral mass 3351.36 Da. (B) Reference muropeptide.
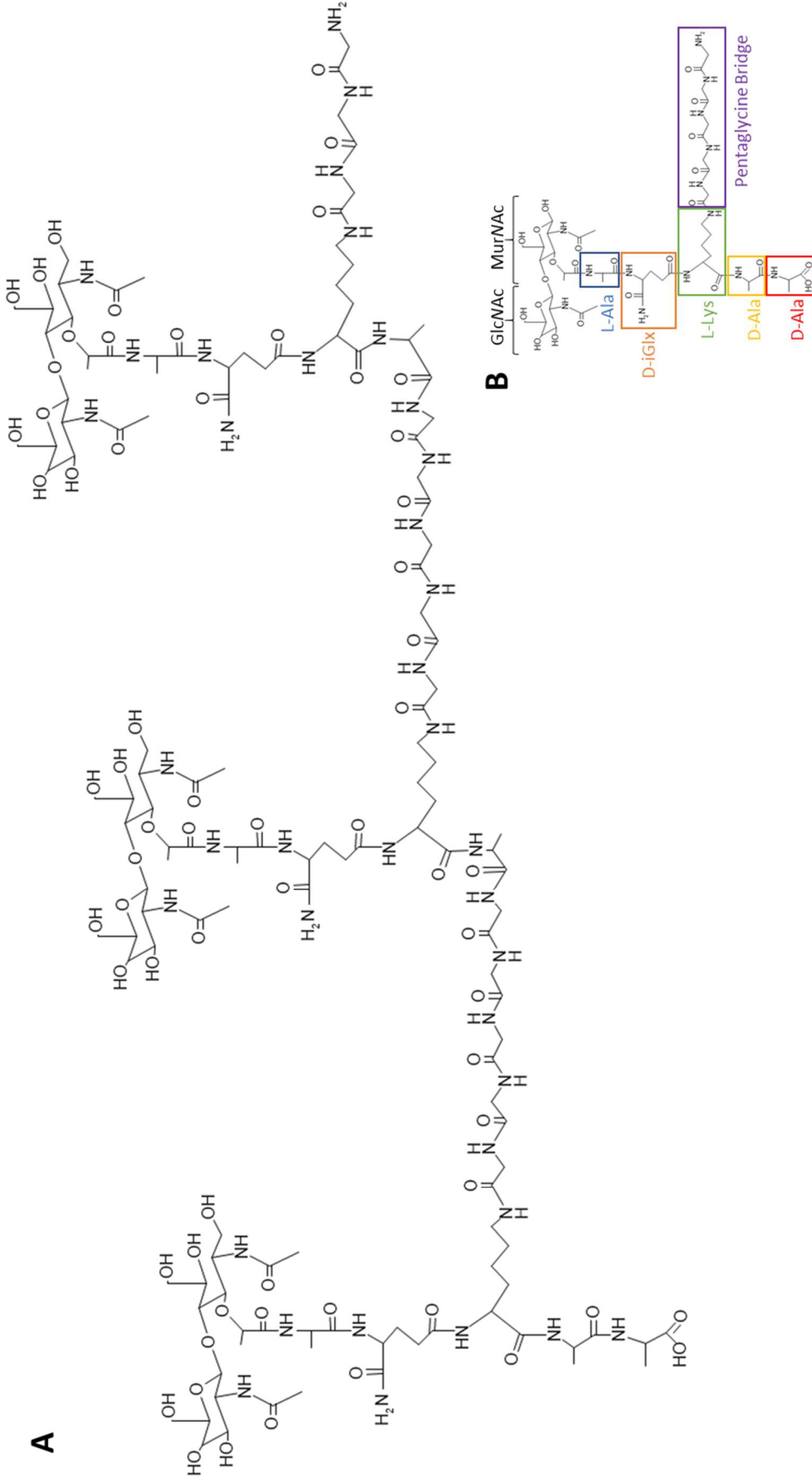
Appendix 1 Figure 50 The chemical structure of muropeptide 26: GM-pentapeptide (GGGGG) – GM – tetrapeptide (GGGGG) – GM – tetrapeptide (GGG)

(A) Calculated neutral mass 3465.53 Da. (B) Reference muropeptide.
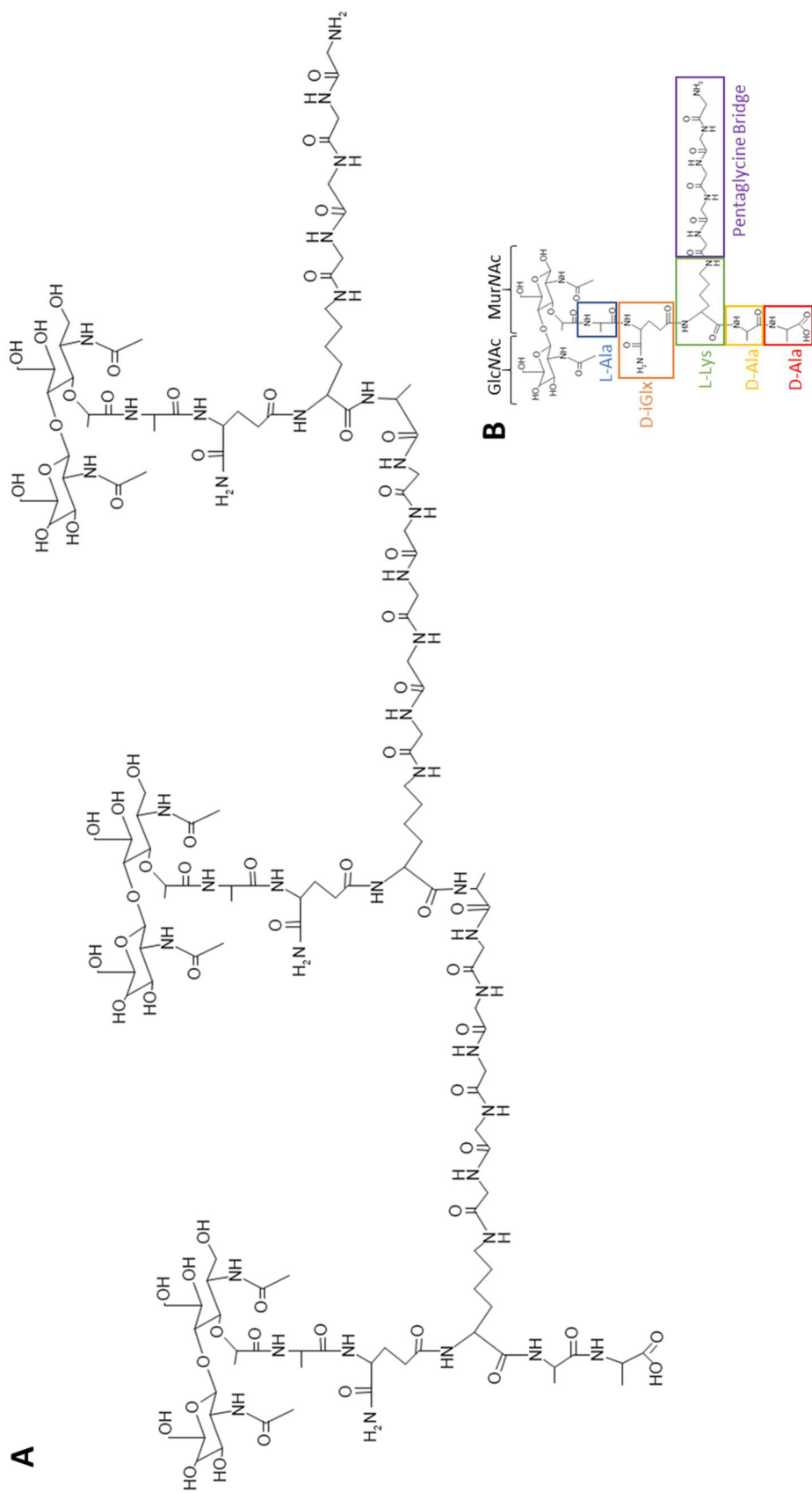
Appendix 1 Figure 51 The chemical structure of muropeptide 27: GM-pentapeptide (GGGGG) – GM – pentapeptide (GGGGG) – GM – tetrapeptide (GGGG) – GM – tetrapeptide (GGGG)

(A) Calculated neutral mass 3522.64 Da. (B) Reference muropeptide.
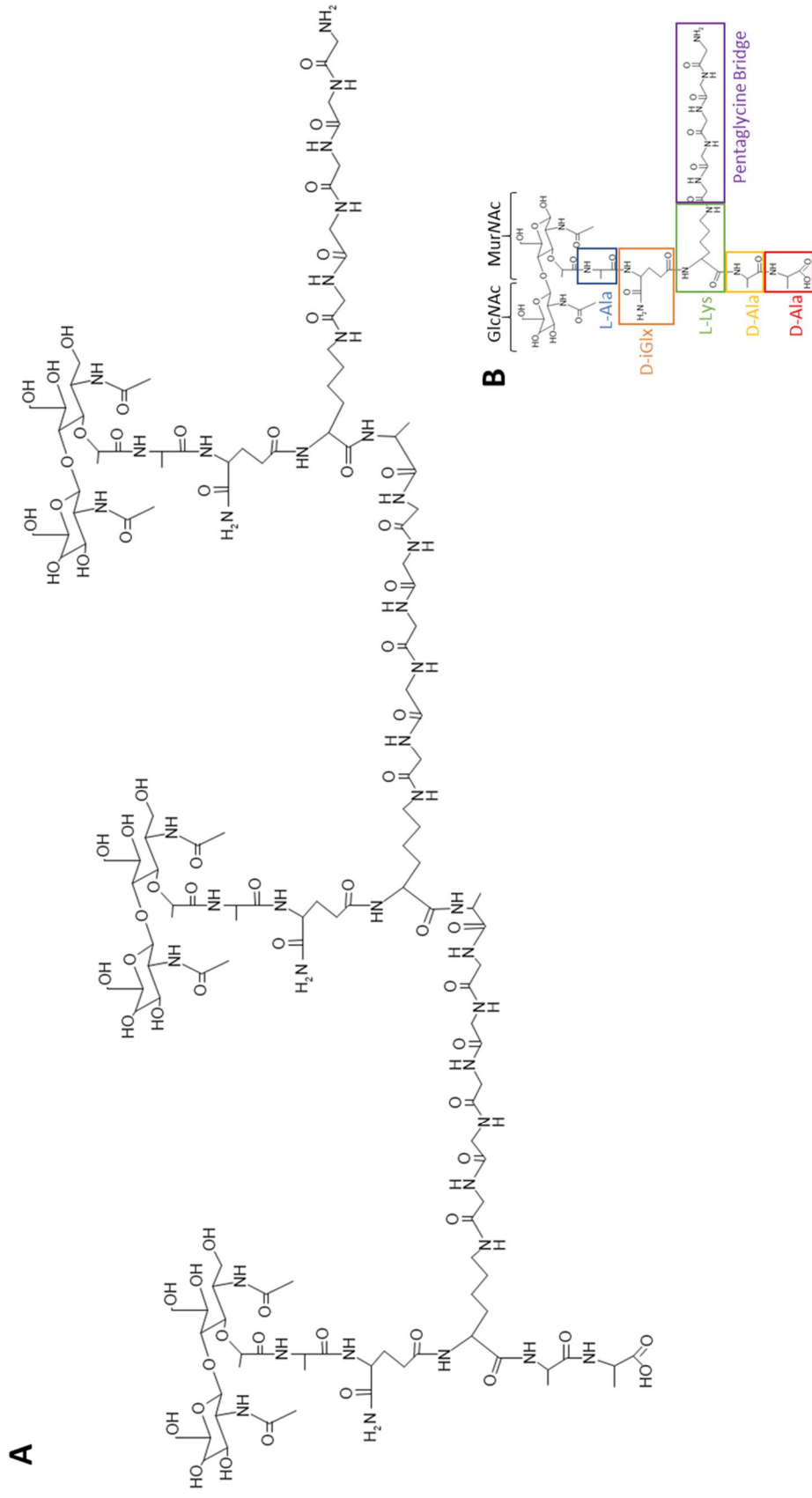
Appendix 1 Figure 52 The chemical structure of muropeptide 28: GM–pentapeptide (GGGGG) – GM – tetrapeptide (GGGGG) – GM – tetrapeptide (GGGGG)

(A) Calculated neutral mass 3579.64 Da. (B) Reference muropeptide.

Appendix 1 Figure 53 The chemical structure of muropeptide 29: GM-tetrapeptide (GGGGG) – GM – tetrapeptide (GGGGG) – GM – tetrapeptide (GGGGG) – GM – tetrapeptide (GGGGG) – GM – tetrapeptide (GGGGG)

(A) Calculated neutral mass 4744.13 Da. (B) Reference muropeptide.
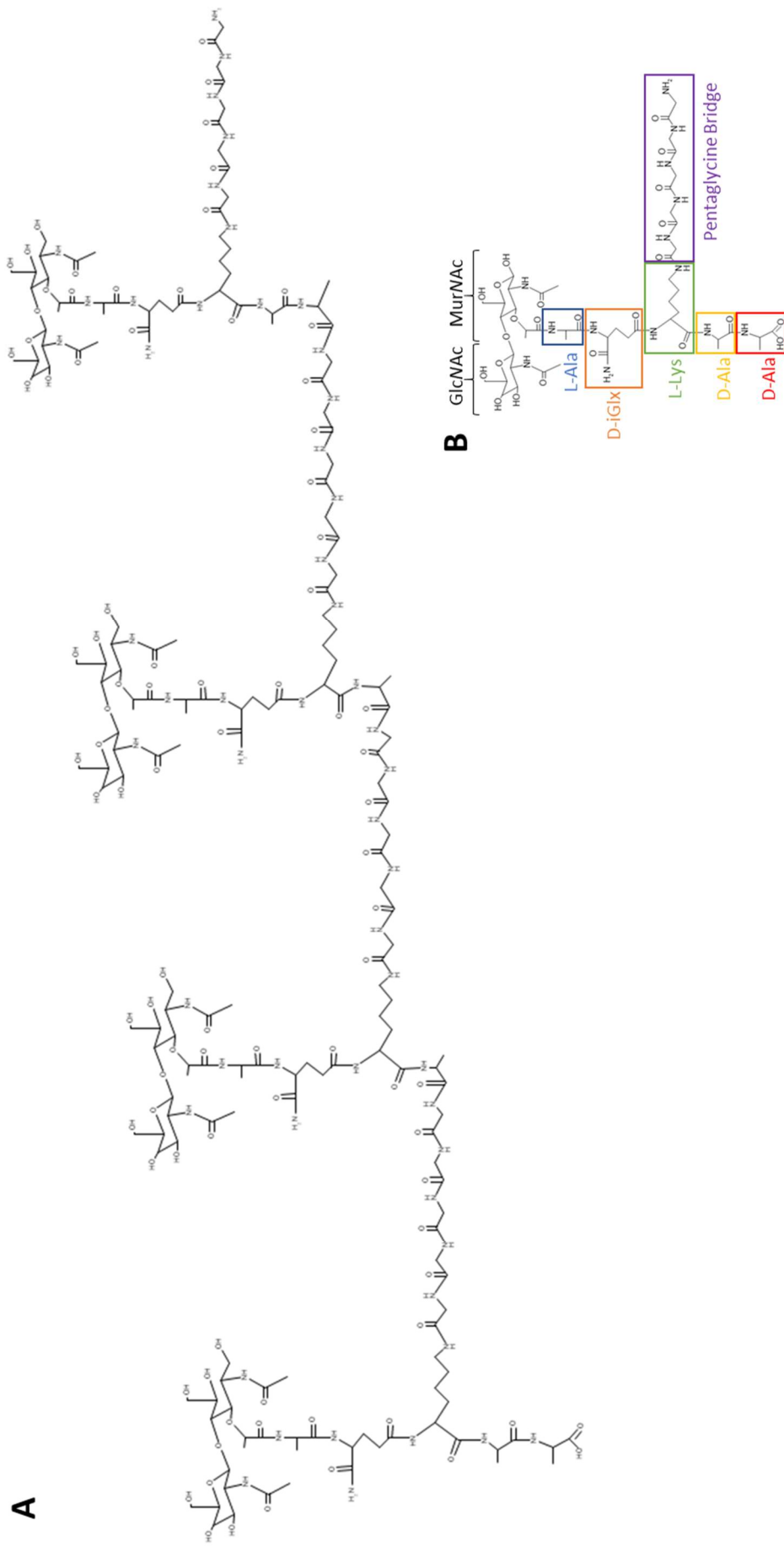
Appendix 1 Figure 54 The chemical structure of muropeptide 30: GM-pentapeptide (GGGGG) – GM – tetrapeptide (GGGGG) – GM – tetrapeptide (GGGGG) – GM – tetrapeptide (GGGGG) – GM – tetrapeptide (GGGGG)

(A) Calculated neutral mass 4814.21 Da. (B) Reference muropeptide.
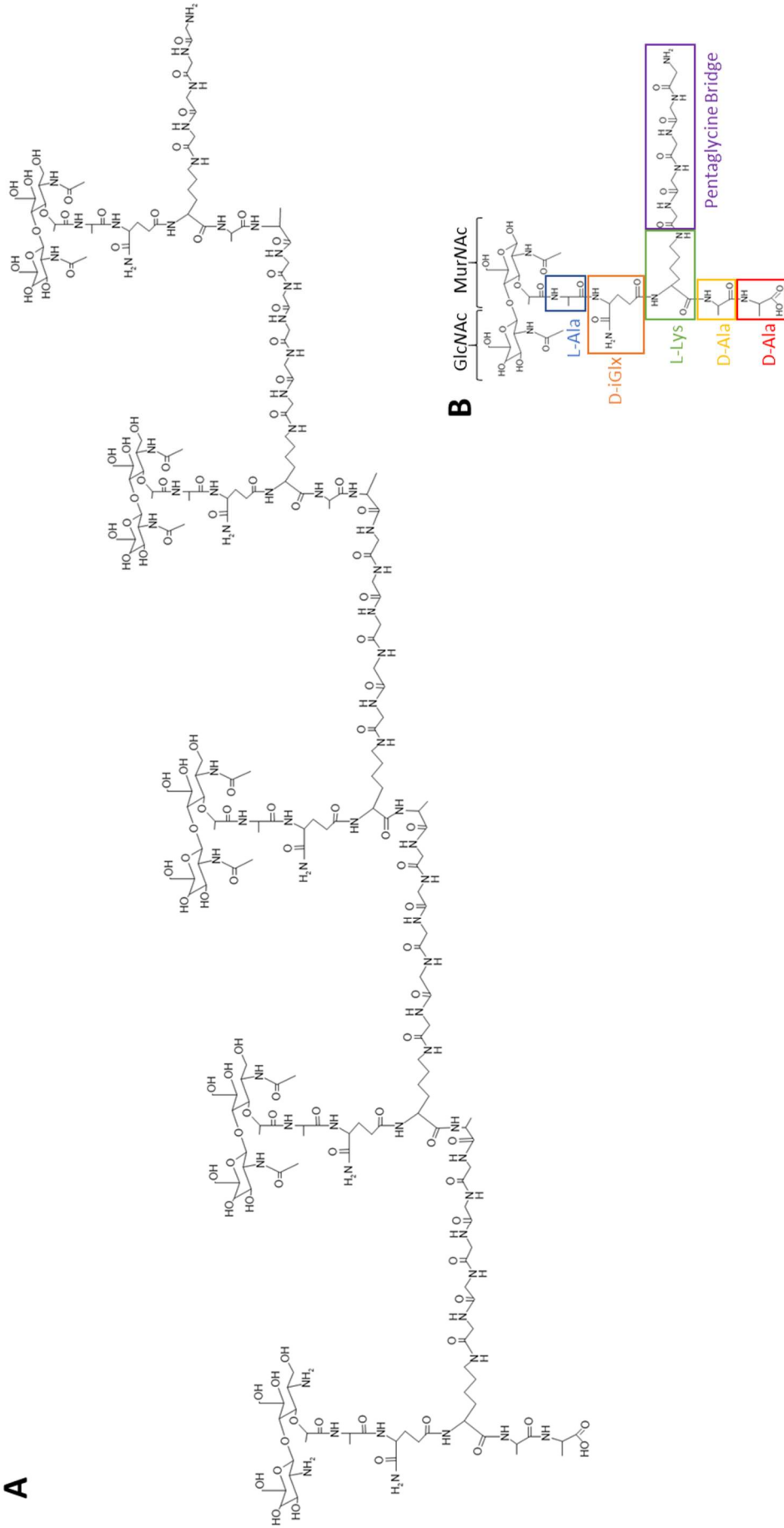
Appendix 1 Figure 55 The chemical structure of muropeptide 31: GM-pentapeptide (GGGGG) – GM – tetrapeptide (GGGGG) – GM – tetrapeptide (GGGGG) – GM – tetrapeptide (GGGGG) – GM – tetrapeptide (GGGGG) – GM – tetrapeptide (GGGGG) (loss of 2 acetyl groups)

(A) Calculated neutral mass 5907.73 Da. (B) Reference muropeptide.
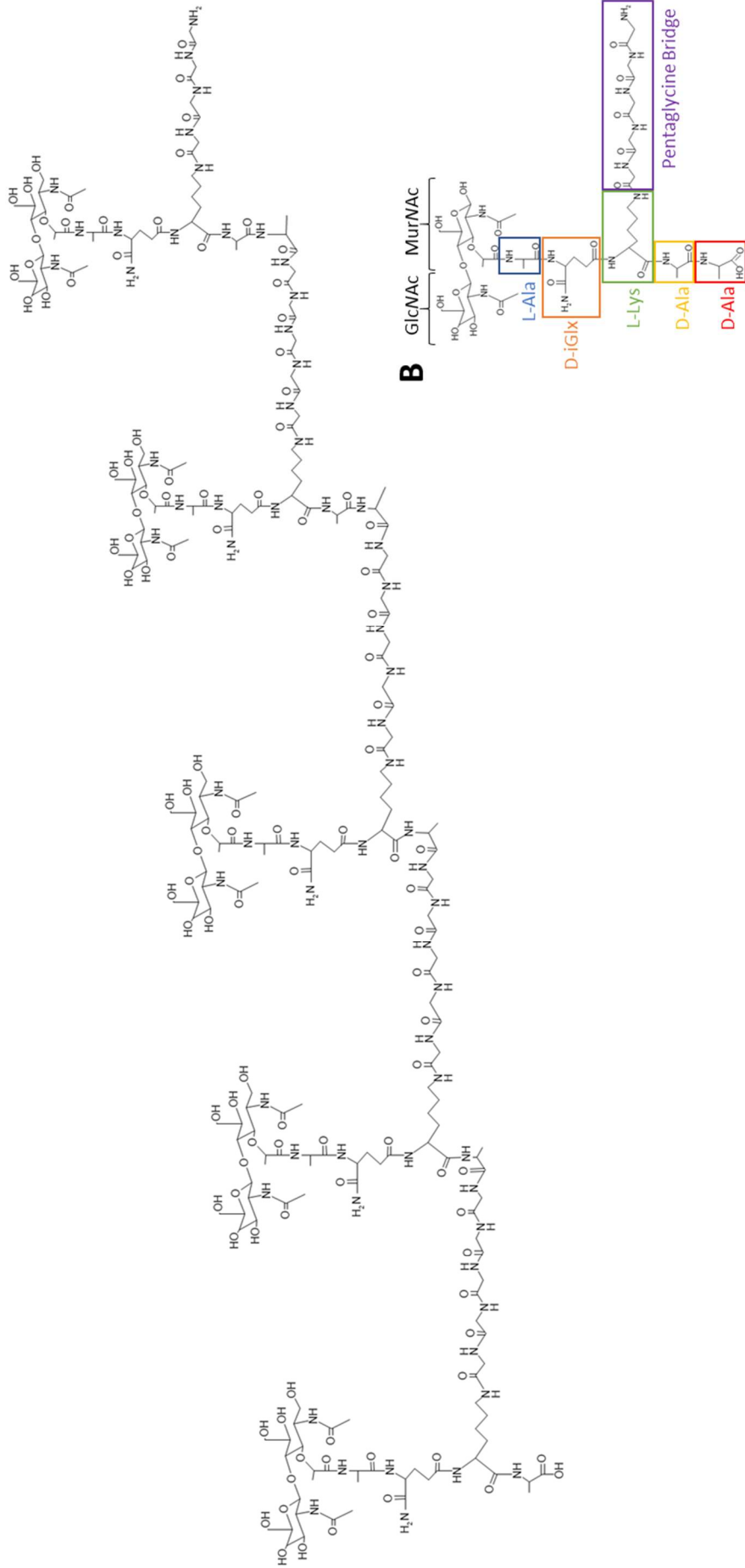
Appendix 1 Figure 56 The chemical structure of muropeptide 32: GM-tetrapeptide (GGGGG) – GM – tetrapeptide (GGGGG) – GM – tetrapeptide (GGGGG) – GM – tetrapeptide (GGGGG) – GM – tetrapeptide (GGGGG) – GM – tetrapeptide (GGGGG) – GM – tetrapeptide (GGGGG)

(A) Calculated neutral mass 5920.68 Da. (B) Reference muropeptide.
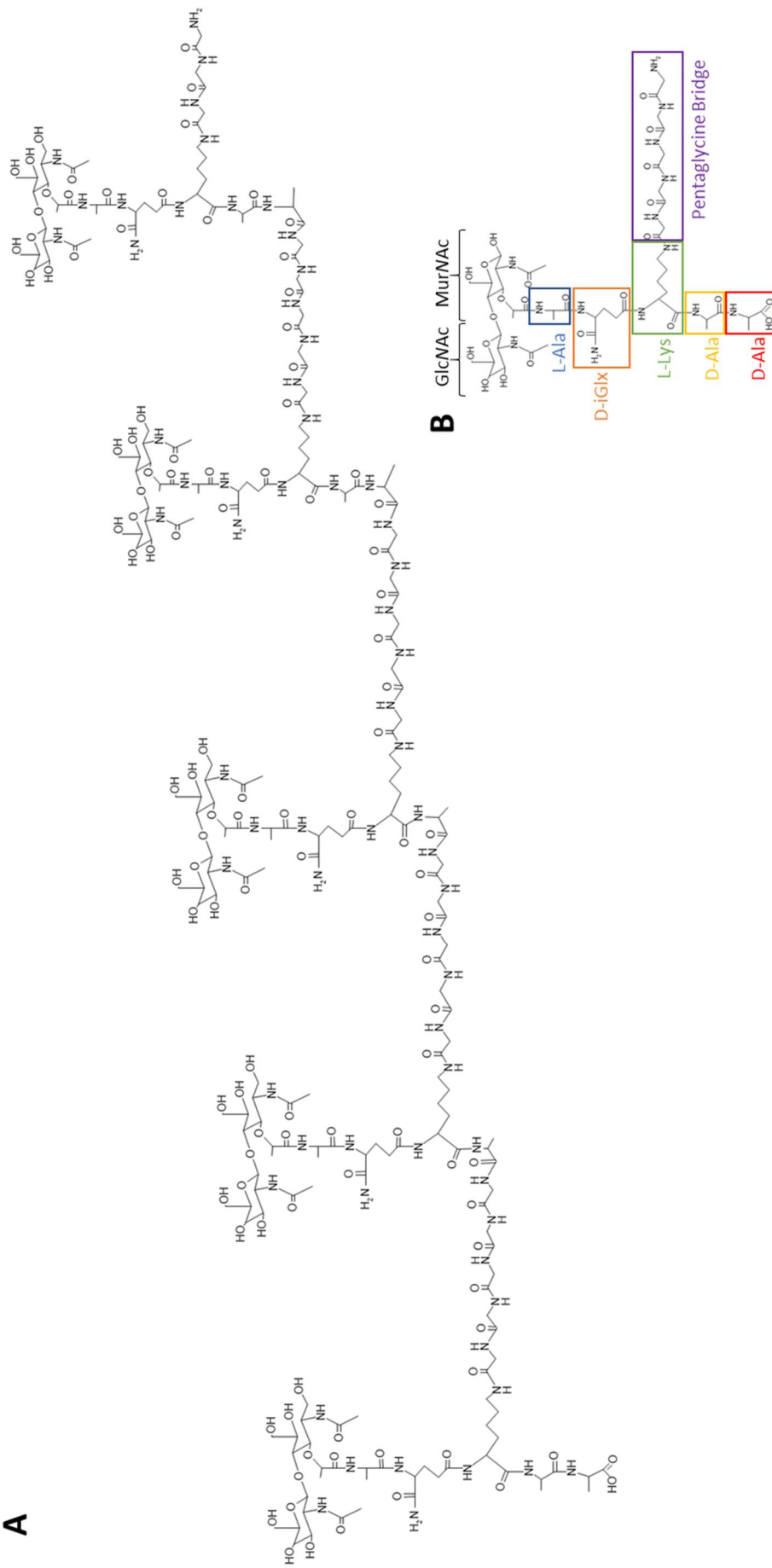
Appendix 1 Figure 57 The chemical structure of muropeptide 33: GM-pentapeptide (GGGGG) – GM – tetrapeptide (GGGGG) – GM – tetrapeptide (GGGGG) – GM – tetrapeptide (GGGGG) – GM – tetrapeptide (GGGGG) – GM – tetrapeptide (GGGG)

(A) Calculated neutral mass 5934.70 Da. (B) Reference muropeptide.

Appendix 1 Figure 58 The chemical structure of muropeptide 34: GM-pentapeptide (GGGGG) – GM – tetrapeptide (GGGGG) – GM – tetrapeptide (GGGGG) – GM – tetrapeptide (GGGGG) – GM – tetrapeptide (GGGGG) – GM – tetrapeptide (GGGGG)

(A) Calculated neutral mass 5991.75 Da. (B) Reference muropeptide.

Appendix 2

Raw data relating to Chapter 3 for the identification of muropeptide species. The identified peaks were integrated (Chapter 2.17) using the UV chromatogram, giving the area of the peak, which is presented as a percentage of the total of identified muropeptides for each repeat.

Table 1

UV retention time (min)	Observed mass (Da)	Charge state (Z)	Calculated neutral mass (Da)	Calculated protonated mass (Da)	Structure	Area of peak (µAU²)	% of measured peaks
29.66	1011.43	1	1010.48	1011.48	GM-Tetrapeptide(Gln) (G)	95354	0.10
30	1068.12	1	1067.50	1068.51	GM-Tetrapeptide(Gln) (GG)	1755175	1.78
31.69	1025.13	1	1024.50	1025.50	GM-Pentapeptide(Gln) (G)	3597231	3.65
32.57	563.05	2	1124.52	1125.53	GM-Tetrapeptide(Gln) (GGGG)	1141429	1.16
32.89	1082.13	1	1081.51	1082.52	GM-Pentapeptide(Gln) (GG)	155034	0.16
33.25	1139.17	1	1138.54	1139.54	GM-Pentapeptide(Gln) (GGG)	11540220	11.70
42.29	1066.16	2	2131.00	2132.01	GM-pentapeptide (GGGGG) - GM-tetrapeptide	1647840	1.67
44.44	1094.68	2	2188.02	2189.03	GM-pentapeptide (GGGGG) - GM-tetrapeptide(G)	1627802	1.65
45.19	1123.21	2	2245.04	2246.05	GM-pentapeptide (GGGGG) - GM-tetrapeptide(GG)	21840966	22.15
46.38	1180.19	2	2359.09	2360.10	GM-pentapeptide (GGGGG) - GM-tetrapeptide(GGGG)	459587	0.47
47.36	1209.20	2	2417.49	2418.50	GM-pentapeptide (GGGGG) - GM-tetrapeptide (GGGGG)	1293504	1.31
56.45	1193.88	3	3579.64	3580.65	GM-tetrapeptide (GGGGG) - GM-tetrapeptide (GGGGG)- GM-tetrapeptide (GGGGG)	19030052	19.30
70.75	1187.01	4	4744.13	4745.14	GM-pentapeptide (GGGGG) - GM-tetrapeptide (GGGGG) - GM-tetrapeptide (GGGGG)- GM-tetrapeptide (GGGGG)	18510532	18.77
87.19	1498.89	4	5991.75	5992.76	GM-pentapeptide (GGGGG) - GM-tetrapeptide (GGGGG)- GM-tetrapeptide (GGGGG)- GM-tetrapeptide (GGGGG)- GM-tetrapeptide (GGGGG)	15920087	16.14

Table 2

UV retention time (min)	Observed mass (Da)	Charge state (Z)	Calculated neutral mass (Da)	Calculated protonated mass (Da)	Structure	Area of peak (µAU²)	% of measured peaks
30.54	954.15	1	953.46	954.46	GM-Tetrapeptide(Gln) (G)	2251672	2.41
31.53	1025.43	1	1024.50	1025.50	GM-Pentapeptide(Gln) (G)	4363105	4.66
32.83	1182.47	1	1181.54	1182.55	GM-Tetrapeptide(Gln) (GGGG)	1789308	1.91
33.71	1253.61	1	1252.58	1253.59	GM-Pentapeptide(Gln) (GGGGG)	14251163	15.24
35.66	1083.12	1	1082.50	1083.51	GM-Pentapeptide(Glu) (GG)	509564	0.54
42.89	1066.17	2	2131.00	2132.01	GM-pentapeptide (GGGGG) - GM-tetrapeptide	1581820	1.69
44.5	993.14	2	1984.94	1985.95	GM-pentapeptide (GGGGG) - M-tetrapeptide(G)	585875	0.63
45.09	1094.68	2	2188.02	2189.03	GM-pentapeptide (GGGGG) - GM-tetrapeptide(G)	1592376	1.70
45.6	1123.21	2	2302.07	2303.07	GM-pentapeptide (GGGGG) - GM-tetrapeptide(GG)	575326	0.62
45.91	1209.28	2	2417.49	2418.50	GM-pentapeptide (GGGGG) - GM-tetrapeptide (GGGGG)	9137041	9.77
57.61	1193.94	3	3579.64	3580.65	GM-tetrapeptide (GGGGG) - GM-tetrapeptide (GGGGG)- GM-tetrapeptide (GGGGG)	24094382	25.76
71.38	1582.29	3	4744.13	4745.14	GM-pentapeptide (GGGGG) - GM-tetrapeptide (GGGGG) - GM-tetrapeptide (GGGGG)- GM-tetrapeptide (GGGGG)	19140300	20.46
86.88	1498.79	4	5991.75	5992.76	GM-pentapeptide (GGGGG) - GM-tetrapeptide (GGGGG)- GM-tetrapeptide (GGGGG)- GM-tetrapeptide (GGGGG)- GM-tetrapeptide (GGGGG)	13665800	14.61

Table 3

UV retention time (min)	Observed mass (Da)	Charge state (Z)	Calculated neutral mass (Da)	Calculated protonated mass (Da)	Structure	Area of peak (µAU²)	% of measured peaks
28.49	968.10	1	967.47	968.48	GM-Pentapeptide(Gln)	777927	0.83
30.06	1011.47	1	1010.48	1011.48	GM-Tetrapeptide(Gln) (GG)	133649	0.14
30.35	1068.1	1	1067.50	1068.51	GM-Tetrapeptide(Gln) (GGG)	2772561	2.98
31.07	563.06	2	1124.52	1125.53	GM-Tetrapeptide(Gln) (GGGG)	2791406	3.00
31.83	1025.13	1	1024.50	1025.50	GM-Pentapeptide(Gln) (G)	5448645	5.85
32.68	1182.12	1	1181.51	1182.55	GM-Tetrapeptide(Gln) (GGGG)	1660747	1.78
35	1082.409	1	1081.51	1082.52	GM-Tetrapeptide(Gln) (GGG)	49127	0.05
33.31	1255.18	1	1252.58	1253.59	GM-Pentapeptide(Gln) (GGGGG)	12676527	13.60
41.69	1066.14	2	2131.00	2132.01	GM-pentapeptide (GGGGG) - GM-tetrapeptide	302122	0.32
43.35	993.18	2	1984.94	1985.95	GM-pentapeptide (GGGGG) - M-tetrapeptide	740070	0.79
44.17	1123.21	2	2302.07	2303.07	GM-pentapeptide (GGGGG) - GM-tetrapeptide(G)	1168609	1.25
44.47	1209.16	2	2417.49	2418.50	GM-pentapeptide (GGGGG) - GM-tetrapeptide(GG)	7150740	7.67
56.04	1194.23	3	3579.64	3580.65	GM-pentapeptide (GGGGG) - GM-tetrapeptide (GGGGG) - GM-tetrapeptide (GGGGG)	27050239	29.03
69.59	1582.31	3	4744.13	4745.14	GM-tetrapeptide (GGGGG) - GM-tetrapeptide (GGGGG) - GM-tetrapeptide (GGGGG)- GM-tetrapeptide (GGGGG)	17408711	18.68
85.02	1484.69	4	5934.70	5935.70	GM-pentapeptide (GGGGG) - GM-tetrapeptide (GGGGG) - GM-tetrapeptide (GGGGG)- GM-tetrapeptide (GGGGG)- GM-tetrapeptide (GGGGG)	13052334	14.01

Appendix 2 Table 1 Identified muropeptides and peak integration for NewHG *kan^R* (SJF 3680) grown to exponential phase in TSB

UV retention time (min)	Observed mass (Da)	Charge state (Z)	Calculated neutral mass (Da)	Calculated protonated mass (Da)	Structure	Area of peak (µAU²)	% of measured peaks
31.08	968.16	1	967.47	968.48	GM-Pentapeptide(Gln)	1611130	7.73
33.77	1025.21	1	1024.50	1025.50	GM-Pentapeptide(Gln)(G)	3723043	17.88
34.46	1125.25	1	1124.52	1125.53	GM-Tetrapeptide(Gln)(GGGG)	875593	4.20
35.05	598.61	2	1195.56	1196.56	GM-Pentapeptide(Gln) (GGGG)	4532727	21.77
35.58	1253.25	1	1252.58	1253.59	GM-Pentapeptide(Gln) (GGGGG)	436435	2.10
41.03	1066.19	2	2131.00	2132.01	GM-pentapeptide (GGGGG) - GM-tetrapeptide	718741	3.45
43	1095.20	2	2188.02	2189.03	GM-pentapeptide (GGGGG) - GM-tetrapeptide(G)	338756	1.63
43.29	1209.24	2	2417.49	2418.50	GM-pentapeptide (GGGGG) - GM-tetrapeptide (GGGGG)	1790624	8.60
49.05	1118.03	3	3351.36	3352.37	GM-pentapeptide (GGGGG) - GM-tetrapeptide (GGGGG)- GM-tetrapeptide (G)	4454112	21.39
57.94	1582.26	3	4744.13	4745.14	GM-tetrapeptide (GGGGG) - GM-tetrapeptide (GGGGG)- GM-tetrapeptide (GGGGG)- GM-tetrapeptide (GGGGG)	2341546	11.25

UV retention time (min)	Observed mass (Da)	Charge state (Z)	Calculated neutral mass (Da)	Calculated protonated mass (Da)	Structure	Area of peak (µAU²)	% of measured peaks
27.09	968.17	1	967.47	968.48	GM-Pentapeptide(Gln)	1395253	7.80
30.52	954.43	1	953.46	954.46	GM-Tetrapeptide(Gln)(G)	181263	1.01
31.5	1011.15	1	1010.48	1011.48	GM-Tetrapeptide(Gln)(GG)	1586741	8.87
32.8	1025.41	1	1024.50	1025.50	GM-Pentapeptide(Gln) (G)	77104	0.43
33.2	1082.17	1	1081.51	1082.52	GM-Pentapeptide(Gln) (GG)	847040	4.74
33.46	1139.16	1	1138.54	1139.54	GM-Pentapeptide(Gln) (GGG)	201401	1.13
34	1196.24	1	1195.56	1196.56	GM-Pentapeptide(Gln) (GGGG)	215422	1.20
34.34	627.11	2	1252.58	1253.59	GM-Pentapeptide(Gln) (GGGGG)	2060673	11.52
43.7	1066.18	2	2131.00	2132.01	GM-pentapeptide (GGGGG) - GM-tetrapeptide	939232	5.25
45.76	1095.17	2	2188.02	2189.03	GM-pentapeptide (GGGGG) - GM-tetrapeptide(G)	607415	3.40
46.38	1152.14	2	2302.07	2303.07	GM-pentapeptide (GGGGG) - GM-tetrapeptide(GGG)	466105	2.61
46.67	1209.20	2	2417.49	2418.50	GM-pentapeptide (GGGGG) - GM-tetrapeptide (GGGGG)	1401812	7.84
58.8	1194.28	3	3579.64	3580.65	GM-pentapeptide (GGGGG) - GM-tetrapeptide (GGGGG)- GM-tetrapeptide (GGGGG)	3894760	21.78
72.69	1582.25	3	4744.13	4745.14	GM-tetrapeptide (GGGGG) - GM-tetrapeptide (GGGGG)- GM-tetrapeptide (GGGGG)- GM-tetrapeptide (GGGGG)	2845760	15.92
88.01	1498.84	4	5991.75	5992.76	GM-pentapeptide (GGGGG) - GM-tetrapeptide (GGGGG)- GM-tetrapeptide (GGGGG)- GM-tetrapeptide (GGGGG)- GM-tetrapeptide (GGGGG)	1160765	6.49

UV retention time (min)	Observed mass (Da)	Charge state (Z)	Calculated neutral mass (Da)	Calculated protonated mass (Da)	Structure	Area of peak (µAU²)	% of measured peaks
27.9	968.13	1	967.47	968.48	GM-Pentapeptide(Gln)	1066417	7.14
32.23	1011.46	1	1010.48	1011.48	GM-Tetrapeptide(Gln)(GG)	1854402	12.42
32.74	1025.46	1	1024.50	1025.50	GM-Pentapeptide(Gln) (G)	90498	0.61
33.14	1125.17	1	1124.52	1125.53	GM-Tetrapeptide(Gln)(GGGG)	678159	4.54
33.48	1082.49	1	1081.51	1082.52	GM-Pentapeptide(Gln) (GG)	104022	0.70
33.73	1139.17	1	1138.54	1139.54	GM-Pentapeptide(Gln) (GGG)	112005	0.75
34.05	1196.21	1	1195.56	1196.56	GM-Pentapeptide(Gln) (GGGG)	1899417	12.72
34.71	1253.47	1	1252.58	1253.59	GM-Pentapeptide(Gln) (GGGGG)	486675	3.26
42.52	1066.60	2	2131.00	2132.01	GM-pentapeptide (GGGGG) - GM-tetrapeptide	860958	5.77
44.48	1095.13	2	2188.02	2189.03	GM-pentapeptide (GGGGG) - GM-tetrapeptide(G)	561346	3.76
45.32	1209.18	2	2417.49	2418.50	GM-pentapeptide (GGGGG) - GM-tetrapeptide (GGGGG)	1488009	9.97
56.96	1194.18	3	3579.64	3580.65	GM-pentapeptide (GGGGG) - GM-tetrapeptide (GGGGG)- GM-tetrapeptide (GGGGG)	4069909	27.26
71.27	1582.19	3	4744.13	4745.14	GM-tetrapeptide (GGGGG) - GM-tetrapeptide (GGGGG)- GM-tetrapeptide (GGGGG)- GM-tetrapeptide (GGGGG)	1658858	11.11

Appendix 2 Table 2 Identified muropeptides and peak integration for NewHG *kan^R* (SJF 3680) grown to stationary phase in TSB

UV retention time (min)	Observed mass (Da)	Charge state (Z)	Calculated neutral mass (Da)	Calculated protonated mass (Da)	Structure	Area of peak (µAU²)	% of measured peaks
26.15	968.15	1	967.47	968.48	GM-Pentapeptide(Gln)	3481010	3.85
31.36	1025.16	1	1024.50	1025.50	GM-Pentapeptide(Gln) (G)	2416119	2.67
32.52	1082.27	1	1081.51	1082.52	GM-Pentapeptide(Gln) (GG)	670679	0.74
32.72	570.10	2	1138.54	1139.54	GM-Pentapeptide(Gln) (GGG)	639604	0.71
32.92	1253.21	1	1252.58	1253.59	GM-Pentapeptide(Gln) (GGGGG)	13864833	15.35
42.68	1066.56	2	2131.00	2132.01	GM-pentapeptide (GGGGG) - GM-tetrapeptide	1448306	1.60
45.03	1095.19	2	2188.02	2189.03	GM-pentapeptide (GGGGG) - GM-tetrapeptide(G)	3570065	3.95
45.42	1209.15	2	2417.49	2418.50	GM-pentapeptide (GGGGG) - GM-tetrapeptide (GGGGG)	18906766	20.93
58.15	1194.18	3	3579.64	3580.65	GM-tetrapeptide (GGGGG) - GM-tetrapeptide (GGGGG)- GM-tetrapeptide (GGGGG)	17797853	19.70
73.82	1187.01	4	4744.13	4745.14	GM-tetrapeptide (GGGGG) - GM-tetrapeptide (GGGGG)- GM-tetrapeptide (GGGGG)- GM-tetrapeptide (GGGGG)	15286835	16.92
90.42	1477.83	4	5907.73	5908.74	GM-pentapeptide (GGGGG) - GM-tetrapeptide (GGGGG)- GM-tetrapeptide (GGGGG)- GM-tetrapeptide (GGGGG) (loss of 2 acetyl Groups)	12247606	13.56

UV retention time (min)	Observed mass (Da)	Charge state (Z)	Calculated neutral mass (Da)	Calculated protonated mass (Da)	Structure	Area of peak (µAU²)	% of measured peaks
26.49	968.07	1	967.47	968.48	GM-Pentapeptide(Gln)	1365101	4.33
30.95	1025.20	1	1024.50	1025.50	GM-Pentapeptide(Gln) (G)	1582109	5.02
32.31	1082.26	1	1081.51	1082.52	GM-Pentapeptide(Gln) (GG)	196934	0.63
32.63	1139.12	1	1138.54	1139.54	GM-Pentapeptide(Gln) (GGG)	335136	1.06
32.83	626.99	2	1252.58	1253.59	GM-Pentapeptide(Gln) (GGGGG)	4642485	14.74
42.79	1066.44	2	2131.00	2132.01	GM-pentapeptide (GGGGG) - GM-tetrapeptide	452248	1.44
44.87	1094.86	2	2188.02	2189.03	GM-pentapeptide (GGGGG) - GM-tetrapeptide(G)	1128157	3.58
45.72	1209.06	2	2417.49	2418.50	GM-pentapeptide (GGGGG) - GM-tetrapeptide (GGGGG)	7149466	22.70
58.05	1194.11	3	3579.64	3580.65	GM-tetrapeptide (GGGGG) - GM-tetrapeptide (GGGGG)- GM-tetrapeptide (GGGGG)	6514392	20.69
69.65	1186.91	4	4744.13	4745.14	GM-tetrapeptide (GGGGG) - GM-tetrapeptide (GGGGG)- GM-tetrapeptide (GGGGG)- GM-tetrapeptide (GGGGG)	5348651	16.98
85.35	1477.69	4	5907.73	5908.74	GM-pentapeptide (GGGGG) - GM-tetrapeptide (GGGGG)- GM-tetrapeptide (GGGGG)- GM-tetrapeptide (GGGGG) (loss of 2 acetyl Groups)	2776380	8.82

UV retention time (min)	Observed mass (Da)	Charge state (Z)	Calculated neutral mass (Da)	Calculated protonated mass (Da)	Structure	Area of peak (µAU²)	% of measured peaks
28.18	968.29	1	967.47	968.48	GM-Pentapeptide(Gln)	2341537	1.96
31.99	1025.10	1	1024.50	1025.50	GM-Pentapeptide(Gln) (G)	7509452	6.28
32.76	1068.10	1	1067.50	1068.51	GM-Tetrapeptide(Gln) (GGG)	2195358	1.84
33	1082.24	1	1081.51	1082.52	GM-Pentapeptide(Gln) (GGG)	945594	0.79
33.34	1253.13	1	1252.58	1253.59	GM-Pentapeptide(Gln) (GGGGG)	21409254	17.90
42.35	1066.42	2	2131.00	2132.01	GM-pentapeptide (GGGGG) - GM-tetrapeptide	2407161	2.01
44.2	1094.58	2	2188.02	2189.03	GM-pentapeptide (GGGGG) - GM-tetrapeptide(G)	3223614	2.70
44.7	1123.56	2	2245.04	2246.05	GM-pentapeptide (GGGGG) - GM-tetrapeptide(GG)	1388442	1.16
44.99	1209.10	2	2417.49	2418.50	GM-pentapeptide (GGGGG) - GM-tetrapeptide (GGGGG)	23791265	19.89
58.2	895.85	4	3579.64	3580.65	GM-pentapeptide (GGGGG) - GM-tetrapeptide (GGGGG)- GM-tetrapeptide (GGGGG)- GM-tetrapeptide (GGGGG)	22708252	18.99
72.18	1187.26	4	4744.13	4745.14	GM-pentapeptide (GGGGG) - GM-tetrapeptide (GGGGG)- GM-tetrapeptide (GGGGG)- GM-tetrapeptide (GGGGG)	18541003	15.33
89.75	1477.77	4	5907.73	5908.74	GM-pentapeptide (GGGGG) - GM-tetrapeptide (GGGGG)- GM-tetrapeptide (GGGGG) (loss of 2 acetyl Groups)	13350299	11.16

Appendix 2 Table 3 Identified muropeptides and peak integration for NewHG *kan^R* (SJF 3680) grown to exponential phase in porcine serum

Table 1

UV retention time (min)	Observed mass (Da)	Charge state (Z)	Calculated neutral mass (Da)	Calculated protonated mass (Da)	Structure	Area of peak (µAU²)	% of measured peaks
25.79	968.41	1	967.47	968.48	GM-Pentapeptide(Gln)	3161621	4.39
30.92	1025.11	1	1024.50	1025.50	GM-Pentapeptide(Gln)(G)	4945203	6.87
32.05	1082.33	1	1081.51	1082.52	GM-Pentapeptide(Gln)(GG)	1034286	1.44
32.25	570.80	2	1138.54	1139.54	GM-Pentapeptide(Gln)(GGG)	1384675	1.92
32.42	1253.16	1	1252.58	1253.59	GM-Pentapeptide(Gln)(GGGG)	1968425	2.73
42.31	1066.37	2	2131.00	2132.01	GM-pentapeptide (GGGGG) - GM-tetrapeptide	1919100	2.67
44.19	1095.14	2	2188.02	2189.03	GM-pentapeptide (GGGGG) - GM-tetrapeptide(G)	2916765	4.05
44.6	1123.65	2	2245.04	2246.05	GM-pentapeptide (GGGGG) - GM-tetrapeptide(GG)	4298405	5.97
44.87	1209.15	2	2417.49	2418.50	GM-pentapeptide (GGGGG) - GM-tetrapeptide (GGGG)	20383929	28.32
56.61	1175.17	3	3579.64	3580.65	GM-pentapeptide (GGGGG) - GM-tetrapeptide (GGGGG)- GM-tetrapeptide (GGGG)	13736471	19.08
71.23	1187.01	4	4744.13	4745.14	GM-pentapeptide (GGGGG) - GM-tetrapeptide (GGGGG)- GM-tetrapeptide (GGGGG)- GM-tetrapeptide (GGGG)	12074323	16.77
86.15	1477.83	4	5907.73	5908.74	GM-pentapeptide (GGGGG) - GM-tetrapeptide (GGGGG)- GM-tetrapeptide (GGGGG)- GM-tetrapeptide (GGGGG) (loss of 2 acetyl Groups)	4160022	5.78

Table 2

UV retention time (min)	Observed mass (Da)	Charge state (Z)	Calculated neutral mass (Da)	Calculated protonated mass (Da)	Structure	Area of peak (µAU²)	% of measured peaks
26.26	484.57	2	967.47	968.48	GM-Pentapeptide(Gln)	1266040	3.76
31.45	513.06	2	1024.50	1025.50	GM-Pentapeptide(Gln)(G)	1954917	5.80
32.72	1082.09	1	1081.51	1082.52	GM-Pentapeptide(Gln)(GG)	202506	0.60
33.03	1139.12	1	1138.54	1139.54	GM-Pentapeptide(Gln)(GGG)	358919	1.06
33.23	627.08	2	1252.58	1253.59	GM-Pentapeptide(Gln)(GGGG)	4783027	14.19
42.1	1066.57	2	2131.00	2132.01	GM-pentapeptide (GGGGG) - GM-tetrapeptide	381055	1.13
44.81	1095.21	2	2188.02	2189.03	GM-pentapeptide (GGGGG) - GM-tetrapeptide(G)	1030170	3.06
45.4	1123.56	2	2245.04	2246.05	GM-pentapeptide (GGGGG) - GM-tetrapeptide(GG)	942467	2.80
45.69	806.75	3	2417.49	2418.50	GM-pentapeptide (GGGGG) - GM-tetrapeptide (GGGG)	7039109	20.88
57.77	1194.08	3	3579.64	3580.65	GM-pentapeptide (GGGGG) - GM-tetrapeptide (GGGGG)- GM-tetrapeptide (GGGG)	6287202	18.65
73.47	1186.97	4	4744.13	4745.14	GM-pentapeptide (GGGGG) - GM-tetrapeptide (GGGGG)- GM-tetrapeptide (GGGGG)- GM-tetrapeptide (GGGG)	5891614	17.48
88.32	1477.81	4	5907.73	5908.74	GM-pentapeptide (GGGGG) - GM-tetrapeptide (GGGGG)- GM-tetrapeptide (GGGGG)- GM-tetrapeptide (GGGGG) (loss of 2 acetyl Groups)	3571437	10.60

Table 3

UV retention time (min)	Observed mass (Da)	Charge state (Z)	Calculated neutral mass (Da)	Calculated protonated mass (Da)	Structure	Area of peak (µAU²)	% of measured peaks
25.48	968.13	1	967.47	968.48	GM-Pentapeptide(Gln)	5365022	2.74
30.16	1025.07	1	1024.50	1025.50	GM-Pentapeptide(Gln)(G)	7730589	3.95
31.01	541.59	2	1081.51	1082.52	GM-Pentapeptide(Gln)(GG)	3554249	1.82
31.6	570.51	2	1138.54	1139.54	GM-Pentapeptide(Gln)(GGG)	1107192	0.57
31.81	1253.61	1	1252.58	1253.59	GM-Pentapeptide(Gln)(GGGG)	29432087	15.05
41.43	1066.1	2	2131.00	2132.01	GM-pentapeptide (GGGGG) - GM-tetrapeptide	7291615	3.73
43.76	1095.14	2	2188.02	2189.03	GM-pentapeptide (GGGGG) - GM-tetrapeptide(G)	3576988	1.83
44.15	1123.54	2	2245.04	2246.05	GM-pentapeptide (GGGGG) - GM-tetrapeptide(GG)	6430393	3.29
44.51	806.83	3	2417.49	2418.50	GM-pentapeptide (GGGGG) - GM-tetrapeptide (GGGG)	29474103	15.07
56.16	895.80	4	3579.64	3580.65	GM-pentapeptide (GGGGG) - GM-tetrapeptide (GGGGG)- GM-tetrapeptide (GGGG)	46589912	23.82
70.73	1187.17	4	4744.13	4745.14	GM-pentapeptide (GGGGG) - GM-tetrapeptide (GGGGG)- GM-tetrapeptide (GGGGG)- GM-tetrapeptide (GGGG)	32150089	16.44
85.66	1182.63	5	5907.73	5908.74	GM-pentapeptide (GGGGG) - GM-tetrapeptide (GGGGG)- GM-tetrapeptide (GGGGG)- GM-tetrapeptide (GGGGG) (loss of 2 acetyl Groups)	22903075	11.71

Appendix 2 Table 4 Identified muropeptides and peak integration for NewHG *kan^R* (SJF 3680) grown to stationary phase in porcine serum

A

UV retention time (min)	Observed mass (Da)	Charge state (Z)	Calculated neutral mass (Da)	Calculated protonated mass (Da)	Structure	Area of peak (µAU²)	% of measured peaks
29.37	968.48	1	967.47	968.48	GM-Pentapeptide(Gln)	7317764	3.33
30.84	1011.43	1	1010.48	1011.48	GM-Tetrapeptide(Gln) (GG)	2594962	1.18
31.45	1068.49	1	1067.50	1068.51	GM-Tetrapeptide(Gln) (GGG)	10243369	4.66
32.6	1025.48	1	1024.50	1025.50	GM-Pentapeptide(Gln) (G)	5613305	2.55
32.84	1139.90	1	1138.54	1139.54	GM-Pentapeptide(Gln) (GG)	2666818	1.21
34.16	1253.47	1	1252.58	1253.59	GM-Pentapeptide(Gln) (GGGG)	36103847	16.41
41.13	1066.54	2	2131.00	2132.01	GM-pentapeptide (GGGGG) - GM-tetrapeptide	2063489	0.94
41.72	1095.07	2	2188.02	2189.03	GM-pentapeptide (GGGGG) - GM-tetrapeptide(G)	10531943	4.79
43.01	1123.60	2	2245.04	2246.05	GM-pentapeptide (GGGGG) - GM-tetrapeptide(GG)	3018373	1.37
43.39	1209.10	2	2417.49	2418.50	GM-pentapeptide (GGGGG) - GM-tetrapeptide (GGGG)	17967977	8.17
51.88	1733.90	2	3465.53	3466.54	GM-pentapeptide (GGGGG) - GM-tetrapeptide (GGG)	1834645	0.83
52.52	1194.30	3	3579.64	3580.65	GM-pentapeptide (GGGGG)- GM-tetrapeptide (GGGGG)	42887724	19.49
67.63	1582.67	3	4744.13	4745.14	GM-tetrapeptide (GGGGG) - GM-tetrapeptide (GGGGG)- GM-tetrapeptide (GGGGG)	39700154	18.05
90.46	1185.14	5	5920.68	5921.69	GM-tetrapeptide (GGGGG) - GM-tetrapeptide (GGGGG) - GM-tetrapeptide (GGGGG)- GM-tetrapeptide (GGGGG)	37461608	17.03

B

UV retention time (min)	Observed mass (Da)	Charge state (Z)	Calculated neutral mass (Da)	Calculated protonated mass (Da)	Structure	Area of peak (µAU²)	% of measured peaks
28.23	968.44	1	967.47	968.48	GM-Pentapeptide(Gln)	5040650	1.37
29.27	1011.41	1	1010.48	1011.48	GM-Tetrapeptide(Gln) (GG)	3657171	1.00
29.84	1068.47	1	1067.50	1068.51	GM-Tetrapeptide(Gln) (GGG)	9939334	2.71
30.08	1125.28	1	1124.52	1125.53	GM-Tetrapeptide(Gln) (GGGG)	670956	0.18
31.31	1082.40	1	1081.51	1082.52	GM-Pentapeptide(Gln) (G)	5260955	1.43
32.39	1253.48	1	1252.58	1253.59	GM-Pentapeptide(Glu) (GGGG)	66372872	18.08
34.77	1254.42	1	1253.56	1254.57	GM-Pentapeptide(Glu) (GGGG)	37012219	10.08
40.81	1066.45	2	2131.00	2132.01	GM-pentapeptide (GGGGG) - GM-tetrapeptide	7367432	2.01
41.4	1095.15	2	2188.02	2189.03	GM-pentapeptide (GGGGG) - GM-tetrapeptide(G)	8637034	2.35
42.53	1123.51	2	2245.04	2246.05	GM-pentapeptide (GGGGG) - GM-tetrapeptide(GG)	16466879	4.49
43.03	1209.69	2	2417.49	2418.50	GM-pentapeptide (GGGGG) - GM-tetrapeptide (GGGG)	21554696	5.87
52.65	1194.23	3	3579.64	3580.65	GM-pentapeptide (GGGGG) - GM-tetrapeptide (GGGGG)- GM-tetrapeptide (GGGGG)	71823461	19.57
67.35	1582.27	3	4744.13	4745.14	GM-tetrapeptide (GGGGG) - GM-tetrapeptide (GGGGG)- GM-tetrapeptide (GGGGG)	72955406	19.88
89.4	1199.41	5	5991.75	5992.76	GM-tetrapeptide (GGGGG) - GM-tetrapeptide (GGGGG)- GM-tetrapeptide (GGGGG)- GM-tetrapeptide (GGGGG)	40270617	10.97

C

UV retention time (min)	Observed mass (Da)	Charge state (Z)	Calculated neutral mass (Da)	Calculated protonated mass (Da)	Structure	Area of peak (µAU²)	% of measured peaks
24.56	954.37	1	953.4	954.4	GM-Pentapeptide(Ala-iGln-Lys-Ala-Gly)	2092735	1.15
25.02	968.44	1	967.47	968.48	GM-Pentapeptide(Gln)	18782232	10.29
27.08	1011.47	1	1010.48	1011.48	GM-Pentapeptide(Gln) (G)	1576707	0.86
27.65	1068.46	1	1067.50	1068.51	GM-Tetrapeptide(Gln) (GGG)	11291197	6.19
28.2	1125.5	1	1124.52	1125.53	GM-Tetrapeptide(Gln) (GGGG)	44805215	24.54
30.97	1182.47	1	1181.54	1182.55	GM-Tetrapeptide(Gln) (GGGGG)	6904000	3.78
31.94	1239.53	1	1238.54	1239.54	GM-Pentapeptide(Ala-iGln-Lys-Ala-Gly)Gly5	11133883	6.10
42.02	1116.54	2	2231.08	2232.09	GM-pentapeptide(Ala-iGln-Lys-Ala-Gly) (GGGGG) - GM-tetrapeptide(GG)	52771051	28.91
43.63	1095.02	2	2188.02	2189.03	GM-pentapeptide (GGGGG) - GM-tetrapeptide(G)	6479309	3.55
44.18	1173.54	2	2345.087	2346.095	GM-pentapeptide (Ala-iGln-Lys-Ala-Gly) (GGGGG) - GM-tetrapeptide(GGG)	10335219	5.66
54.08	1194.24	3	3579.64	3580.65	GM-pentapeptide (GGGGG) - GM-tetrapeptide (GGGGG)- GM-tetrapeptide (GGGGG)	8895587	4.87
69.55	1582.39	3	4744.13	4745.14	GM-tetrapeptide (GGGGG) - GM-tetrapeptide (GGGGG)- GM-tetrapeptide (GGGGG)	7479586	4.10

D

UV retention time (min)	Observed mass (Da)	Charge state (Z)	Calculated neutral mass (Da)	Calculated protonated mass (Da)	Structure	Area of peak (µAU²)	% of measured peaks
26.49	968.43	1	967.47	968.48	GM-Pentapeptide(Gln)	1259304	0.81
30.47	1025.43	1	1024.50	1025.50	GM-Pentapeptide(Gln) (G)	4787222	3.06
30.66	1068.43	1	1067.50	1068.51	GM-Tetrapeptide(Gln) (GGG)	5827398	3.73
31.23	1182.53	1	1181.54	1182.55	GM-Tetrapeptide(Gln) (GGGGG)	4458671	2.85
31.92	1253.57	1	1252.58	1253.59	GM-Pentapeptide(Gln) (GGGG)	33632804	21.51
41.64	1066.51	2	2131.00	2132.01	GM-pentapeptide (GGGGG) - GM-tetrapeptide	7717803	4.94
43.55	1095.01	2	2188.02	2189.03	GM-pentapeptide (GGGGG) - GM-tetrapeptide(G)	4419211	2.83
44.34	1209.10	2	2417.49	2418.50	GM-pentapeptide (GGGGG) - GM-tetrapeptide (GGGG)	28632633	18.31
52.65	1194.02	3	3579.64	3580.65	GM-pentapeptide (GGGGG) - GM-tetrapeptide (GGGGG)- GM-tetrapeptide (GGGGG)	34721748	22.21
68.38	1582.62	3	4744.13	4745.14	GM-tetrapeptide (GGGGG) - GM-tetrapeptide (GGGGG) - GM-tetrapeptide (GGGGG)- GM-tetrapeptide (GGGGG)	30892685	19.76

Appendix 2 Table 5 Identified muropeptides and peak integration for NewHG _kan^R_ (SJF 3680) grown in CDM

(A) NewHG _kan^R_ (SJF 3680) grown in CDM to exponential phase, (B) NewHG _kan^R_ (SJF 3680) grown in CDM to stationary phase, (C) NewHG _kan^R_ (SJF 3680) grown in CDM containing 125 mM glycine, (D) NewHG _kan^R_ (SJF 3680) grown in CDM lacking glucose.

UV retention time (min)	Observed mass (Da)	Charge state (Z)	Calculated neutral mass (Da)	Calculated protonated mass (Da)	Structure	Area of peak (μAU²)	% of measured peaks
30.59	954.15	1	953.46	954.46	GM-Tetrapeptide(Gln) (G)	127005	2.68
31.45	513.02	1	1024.50	1025.50	GM-Pentapeptide(Gln) (G)	421883	8.90
32.37	563.44	2	1124.52	1125.53	GM-Tetrapeptide(Gln) (GGGG)	155394	3.28
32.69	1082.03	1	1081.51	1082.52	GM-Pentapeptide(Gln) (GG)	88455	1.87
33.04	570.07	1	1138.54	1139.54	GM-Pentapeptide(Gln) (GGG)	67071	1.42
33.34	627.08	2	1252.58	1253.59	GM-Pentapeptide(Gln) (GGGG)	896838	18.93
42.63	1066.30	2	2131.00	2132.01	GM-pentapeptide (GGGGG) - GM-tetrapeptide	151557	3.20
44.78	1094.98	2	2188.02	2189.03	GM-pentapeptide (GGGGG) - GM-tetrapeptide(G)	200563	4.23
45.4	1123.45	2	2245.04	2246.05	GM-pentapeptide (GGGGG) - GM-tetrapeptide(GG)	321133	6.78
45.75	1209.48	2	2417.49	2418.50	GM-pentapeptide (GGGGG) - GM-tetrapeptide (GGGGG)	1066850	22.51
58.6	1194.30	3	3579.64	3580.65	GM-pentapeptide (GGGGG) - GM-tetrapeptide (GGGGG)- GM-tetrapeptide (GGGGG)	780868	16.48
73.04	1186.83	4	4814.21	4815.22	GM-tetrapeptide (GGGGG) - GM-tetrapeptide (GGGGG) - GM-tetrapeptide (GGGGG)- GM-tetrapeptide (GGGGG)	460963	9.73

UV retention time (min)	Observed mass (Da)	Charge state (Z)	Calculated neutral mass (Da)	Calculated protonated mass (Da)	Structure	Area of peak (μAU²)	% of measured peaks
29.43	954.32	1	953.46	954.46	GM-Tetrapeptide(Gln) (G)	350575	6.40
30.84	1025.35	1	1024.50	1025.50	GM-Pentapeptide(Gln) (G)	557820	10.19
31.76	1182.43	1	1181.54	1182.55	GM-Tetrapeptide(Gln) (GGGGG)	905240	16.53
32.52	1196.48	1	1195.56	1196.56	GM-Pentapeptide(Gln) (GGGG)	390446	7.13
33.15	1253.39	1	1252.58	1253.59	GM-Pentapeptide(Gln) (GGGGG)	970851	17.73
45.14	1209.53	2	2417.49	2418.50	GM-pentapeptide (GGGGG) - GM-tetrapeptide (GGGGG)	1314932	24.01
56.36	1194.4	3	3579.64	3580.65	GM-pentapeptide (GGGGG) - GM-tetrapeptide (GGGGG)- GM-tetrapeptide (GGGGG)	985898	18.00

Appendix 2 Table 6 Identified muropeptides and peak integration for NewHG *kan^R* (SJF 3680) recovered from infected murine kidneys 72 hpi.